

INVESTIGATIONS OF HIGH VALENT METAL REACTIVITY USING THE LIGAND  
DONOR PARAMETER

By

Brennan Shay Billow

A DISSERTATION

Submitted to  
Michigan State University  
in partial fulfillment of the requirements  
for the degree of

Chemistry – Doctor of Philosophy

2018



# ABSTRACT

## INVESTIGATIONS OF HIGH VALENT METAL REACTIVITY USING THE LIGAND DONOR PARAMETER

By

Brennan Shay Billow

Understanding the chemistry of high valent metals stands to open the door to a new realm of chemical transformations. Unfortunately, a relative lack of research into chemical processes using high valent metals has led to a dearth of information in comparison to processes involving low valent metals. Recently, our group has set about developing new tools for the development of high valent metal-based catalysts. Specifically, development of the ligand donor parameter (LDP) stands to uncover a wealth of information involving high valent metal-ligand interactions. In the following chapters the application of LDP in chromium-, titanium-, and uranium-based systems will be discussed. These studies have led to better perception of metal-ligand bonds, improved understanding of titanium-based catalysis, and discovery of exciting new uranium complexes.



To My Family and Friends



## ACKNOWLEDGMENTS

I hope that all who have assisted me in my pursuit of academic achievement already know they have my unending gratitude. Still, I would be remiss if I did not address those who have been most influential to my growth as a scientist and as a person.

I owe the most to my parents and family, without their support and encouragement I could not have done this. Despite their less-than-subtle reminders that I always had the option to “swing a hammer” for the rest of my life, they always pushed me to achieve more.

I was also able to find a home away from home in the chemistry department, complete with an academic family. Professor Aaron Odom, Dr. Tanner “McDanner” McDaniel, and Kelly Aldrich make up what I consider to be my immediate academic family. The discussions, advice, and encouragement they provided is what kept chemistry exciting. Of course, there were others in the group as well. Without the other past and current group members, the extended academic family, none of the progress I have made would have been possible. Especially, Dr. Ross Bemowski and Dr. Amrendra Singh, both of whom helped jump start both my graduate studies, as well as, my 4<sup>th</sup> floor aviation experiments.

The list of those I consider to be extended academic family goes on. I owe thanks to my committee, Professor Mitch Smith, Professor Tom Hamann, and Professor Ben Levine for their insight and criticism. I wish there were more opportunities to meet with everyone, our few meetings were both productive and enjoyable. Furthermore, the (formerly) open door policy in the 4<sup>th</sup> and 5<sup>th</sup> floor of the chemistry building led to a truly collaborative and friendly environment. I hope no one allows recent “safety and security advancements” to spoil that atmosphere.



I was also fortunate enough to spend time in the lab of Dr. James (Jim) Boncella. Everyone at LANL welcomed me as both a co-worker and friend, so much so that I decided to go back.

To Dr. Richard Staples and Dr. Dan Holmes I am also especially grateful. The hundreds of hours I spent in the X-ray lab and NMR facilities might have been thousands if not for your expertise and guidance. Besides that, your counsel and willingness to listen won't be forgotten. Further, the support staff in the chemistry building are far too often under appreciated. Without the folks like Glenn, Scott, and Bob, our lab would have ceased to function a long time ago.

I also owe thanks to Oscar, while not in the Odom group, I consider you as much of a family member as anyone. All of my future employers have you to thank for my (at times distracting) skiing addiction. But, as other group members can confirm, it helped keep me sane during even the most stressful times.

Of course, I also need to thank those who most influenced my interest in chemistry in the first place. Ms. Winczewski, Dr. Dan Adsmond, and Dr. Colleen Partigianoni, without the passion each of you displayed for chemistry, my interests in the field might have never been realized.



## TABLE OF CONTENTS

LIST OF TABLES .....	viii
LIST OF FIGURES .....	x
LIST OF SCHEMES.....	xxi
KEY TO SYMBOLS AND ABBREVIATIONS .....	xxii
Chapter 1. Introduction.....	1
1.1 Background and Motivation.....	1
1.2 Tolman's Cone Angle and Electronic Parameter .....	1
1.3 Advancements in Modeling Ancillary Ligands .....	3
1.4 Considerations for High Valent Metals.....	6
1.5 Titanium Catalysis.....	7
1.6 Ligand Donor Parameter .....	9
1.7 Quantitatively Modeling Reactions.....	14
1.8 Conclusions .....	14
REFERENCES .....	16
Chapter 2. Investigations of Chromium(VI) Nitrido Cyclopentadienyl Bonding System .....	19
2.1 Introduction .....	19
2.2 Synthesis and Characterization .....	20
2.3 Bonding Analysis .....	24
2.4 Conclusions .....	28
2.5 Experimental .....	28
REFERENCES .....	44
Chapter 3. Analysis of Phosphines as Ligand on High Valent Transition Metals .....	47
3.1 Introduction .....	47
3.2 Synthesis.....	47
3.3 Initial LDP Analysis.....	48
3.4 Anion and Solvent Dependence .....	50
3.5 Entropy Analysis .....	54
3.6 Phosphine Analysis .....	58
3.7 Phosphine Bonding Analysis .....	61
3.8 Conclusions .....	65
3.9 Experimental .....	65
REFERENCES .....	145
Chapter 4. Developing a Model for the Optimization and Development of Titanium Catalyzed Hydroamination .....	148
4.1 Introduction .....	148
4.2 Ligand Analysis Considerations.....	149
4.3 Synthesis and Characterization of the Chromium Complexes.....	152



4.4	Modeling the Hydroamination Kinetics .....	154
4.5	Testing Ligand Variety.....	161
4.6	Investigating Anomalies.....	165
4.7	Other Applications of the Model.....	168
4.8	Conclusions .....	173
4.9	Experimental .....	175
	REFERENCES.....	238
Chapter 5. Preliminary Investigations of Uranium-Ligand Interactions .....		242
5.1	Introduction .....	242
5.2	Reaction Design .....	244
5.3	Catalyst Design and Synthesis .....	246
5.4	Catalysis .....	252
5.5	Future Work .....	254
5.6	Conclusions .....	257
5.7	Experimental .....	258
	REFERENCES.....	277
Chapter 6. Synthesis and Characterization of Uranium-Terphenyl Complexes.....		280
6.1	Investigating Imido Synthesis .....	280
6.2	Steric Bulk as a Method to Slow Ligand Redistribution.....	281
6.3	Comparisons Between Amide and Imides of Bulky Ligands .....	283
6.4	Bis(Amide) Species as a Way to Access Low Valent Uranium .....	290
6.5	Generation of a Neutral Uranium(II) .....	294
6.6	Oxidation of the Uranium(II) .....	297
6.7	Spectroscopic Analysis .....	299
6.8	Conclusions .....	301
6.9	Experimental .....	301
	REFERENCES.....	351
Chapter 7. Reduction of Dinitrogen to Hydrazine.....		354
7.1	Introduction .....	354
7.2	Ammonia as an Energy Storage Solution .....	356
7.3	Alternative Methods for Nitrogen Fixation.....	357
7.4	Reproduction of Shilov's Results.....	359
7.5	Monitoring Hydrazine Formation .....	360
7.6	Moving to More Complex Systems .....	362
7.7	Catalyst Synthesis .....	363
7.8	Looking Forward.....	364
7.9	Conclusions .....	365
7.10	Experimental .....	365
	REFERENCES.....	370



## LIST OF TABLES

Table 3-1. Initial LDP measurements for PR <sub>3</sub> ligands. All compounds used SbF <sub>6</sub> as the counter ion. All values are based on at least one good LDP measurement performed, but results here were not necessarily performed in triplicate due to decomposition of the complexes. As such, the values are reported only to the tenths. ....	49
Table 3-2. LDP measurements of [NCr(N <sup>i</sup> Pr <sub>2</sub> ) <sub>2</sub> (PPhMe <sub>2</sub> )] <sup>+</sup> X <sup>-</sup> . ....	52
Table 3-3. Summary of Eyring analyses of the various phosphine complexes. The entropy analysis error was determined from a linear least squares fit of the experimentally data as reported by Lente. <sup>17</sup> <sup>a</sup> Values in CD <sub>3</sub> CN use SbF <sub>6</sub> as an anion. These ΔH <sup>‡</sup> values include the, admittedly crude, assumption of a constant entropy of -9 e.u. <sup>b</sup> These values were run at 3 constant temperatures, as such the precision is high and the error for the measurement is low, this does not necessarily mean the ΔH <sup>‡</sup> values are more accurate than the other values here, especially in light of the entropy assumption. <sup>c</sup> Values in CDCl <sub>3</sub> use BAr <sup>F</sup> <sub>24</sub> as the anion. ΔH <sup>‡</sup> values are from the Eyring analysis. ....	56
Table 3-4. Parameters used to model the trialkyl phosphines against ΔH <sup>‡</sup> . ΔH <sup>‡</sup> values taken from Table 3-3. ....	59
Table 3-5. Experimental ΔH <sup>‡</sup> values (including ΔG <sup>‡</sup> ) for [NCr(N <sup>i</sup> Pr <sub>2</sub> ) <sub>2</sub> PE <sub>3</sub> ]SbF <sub>6</sub> salts in CD <sub>3</sub> CN. <sup>a</sup> ΔH <sup>‡</sup> value in CD <sub>3</sub> CN was measured via <i>in situ</i> generated species stabilized with excess phosphine. <sup>b</sup> Measured ΔH <sup>‡</sup> was taken in multiple trials, taking a single measurement on three different samples due to compound instability. As a result, three different temperatures were calibrated, one for each separate run. The reported ΔG <sup>‡</sup> is approximate, as it is an average from 3 (close) temperatures. ....	75
Table 4-1. Summary of the titanium catalysts use for hydroamination, the chromium complexes used to parameterize the ligands, and the rates of catalysis. ....	156
Table 4-2. Summary of the validation set of bis-aryloxide ligands. ....	162
Table 4-3. Table showing the fitting parameters and rate constant for catalyst 3. ....	165
Table 4-4. Table summarizing the rate constant and fitting parameters for catalyst 6. ....	167
Table 4-5. Spin saturation transfer data. <sup>a</sup> Determined from the rate constant for isopropyl group exchange using the Eyring Equation with the assumption that the transmission coefficient is unity. <sup>b</sup> Assuming ΔS <sup>‡</sup> = -9 cal•mol <sup>-1</sup> •K <sup>-1</sup> . <sup>c</sup> Pyrr = pyrrolide, Ind = indolide, tol = <i>p</i> -tolyl. <sup>d</sup> Determined by line shape analysis. <sup>e</sup> The 6-Br-SNap ligand was only used as a surrogate for 2-naphthylthiolate (SNap) to obtain the % V <sub>bur</sub> value. Consequently, its LDP was not employed in this study; however, we include the LDP for completeness. ....	175



Table 6-1. Selected bond lengths and angles. <sup>a</sup>The centroid refers to the Cp\* centroid-U-Arene centroid angle in **2-6**, and the Arene centroid-U-Arene centroid angle in **7**..... 329

Table 6-2. Selected bond lengths and angles. <sup>a</sup>The white rows are the values from the diethyl ether crystallized structure, the grey rows are from the hexane crystallized structure. .... 330



## LIST OF FIGURES

Figure 1-1. Representation of Tolman Cone Angle <sup>1</sup> .....	3
Figure 1-2. Comparison of different NHC ligand profiles and resulting cone angle. ....	4
Figure 1-3. Top: Graphical representation of % $V_{bur}$ . Black shaded area represents buried volume. Bottom: Steric map output from SambVca 2.0 program. <sup>9</sup> The x and y axis are distance from center in Å. The map cuts off at 3.5 Å due to our defined radius. The colored contour represents the distance in angstroms in the z direction (perpendicular to the plane of the page). ....	5
Figure 1-4. Hydroamination catalytic cycle. <sup>19</sup> .....	8
Figure 1-5. Representative chromium structure for LDP determination. <sup>24</sup> .....	9
Figure 1-6. LDP values of previously reported ligands. <sup>24</sup> .....	13
Figure 2-1. Representation of the three typical binding modes of cyclopentadienyl. ....	19
Figure 2-2. Crystals structures of <b>1</b> , <b>3</b> , <b>4</b> , and <b>5</b> . Ellipsoids displayed at the 50% probability level. All hydrogens, solvents in the lattice, and counterion from <b>5</b> , removed for clarity. ....	22
Figure 2-3. Mayer bond order analysis of <b>1-5</b> . ....	25
Figure 2-4. Cr-C bond lengths and averages for compounds <b>1-5</b> . ....	25
Figure 2-5. Mayer bond order analysis of the literature reported “standards.” <sup>15, 20-21</sup> .....	26
Figure 2-6. M-C bond lengths and averages for the literature reported “standards.” .....	27
Figure 2-7. $\text{NCr}(\text{N}^i\text{Pr}_2)_2(\text{Cp})$ ( <b>1</b> ) $^1\text{H}$ NMR .....	33
Figure 2-8. $\text{NCr}(\text{N}^i\text{Pr}_2)_2(\text{Cp})$ ( <b>1</b> ) $^{13}\text{C}$ NMR .....	34
Figure 2-9. $\text{NCr}(\text{N}^i\text{Pr}_2)_2(\text{Ind})$ ( <b>2</b> ) $^1\text{H}$ NMR .....	35
Figure 2-10. $\text{NCr}(\text{N}^i\text{Pr}_2)_2(\text{Ind})$ ( <b>2</b> ) $^{13}\text{C}$ NMR .....	36
Figure 2-11. $\text{NCr}(\text{N}^i\text{Pr}_2)(\text{O}_2\text{CPh})(\text{Cp})$ ( <b>3</b> ) $^1\text{H}$ NMR (13 °C) .....	37
Figure 2-12. $\text{NCr}(\text{N}^i\text{Pr}_2)(\text{O}_2\text{CPh})(\text{Cp})$ ( <b>3</b> ) $^{13}\text{C}$ NMR (13 °C) .....	38
Figure 2-13. $\text{NCr}(\text{N}^i\text{Pr}_2)(\text{Cp})\text{Cl}$ ( <b>4</b> ) $^1\text{H}$ NMR .....	39
Figure 2-14. $\text{NCr}(\text{N}^i\text{Pr}_2)(\text{Cp})\text{Cl}$ ( <b>4</b> ) $^{13}\text{C}$ NMR .....	40



Figure 2-15. $[\text{NCr}(\text{N}^i\text{Pr}_2)(\text{Cp})(\text{NCMe})][\text{SbF}_6]$ ( <b>5</b> ) $^1\text{H}$ NMR (In Situ Reaction) .....	41
Figure 2-16. $[\text{NCr}(\text{N}^i\text{Pr}_2)(\text{Cp})(\text{NCMe})][\text{SbF}_6]$ ( <b>5</b> ) $^{13}\text{C}$ NMR (In Situ Reaction) .....	42
Figure 2-17. $[\text{NCr}(\text{N}^i\text{Pr}_2)(\text{Cp})(\text{NCMe})][\text{SbF}_6]$ ( <b>5</b> ) $^{19}\text{F}$ NMR (In Situ Reaction) .....	43
Figure 3-1. Various anions explored in this study. ....	50
Figure 3-2. $^{14}\text{N}$ NMR analysis of $[\text{NCr}(\text{N}^i\text{Pr}_2)_2(\text{PMePh}_2)]^+\text{X}^-$ in $\text{CDCl}_3$ where $\text{X} = \text{SbF}_6$ (right) and $\text{PF}_6$ (left). The peak at 309 ppm (labelled with a *) represents dissolved $\text{N}_2$ , which was referenced as an internal standard. ....	51
Figure 3-3. Plot of $\Delta\text{H}^\ddagger$ vs model predicted $\Delta\text{H}^\ddagger$ using $\Delta\text{H}^\ddagger$ values determine from $\text{CD}_3\text{CN}$ with an assumption of constant $\Delta\text{S}^\ddagger$ . ....	59
Figure 3-4. Lewis structures depicting the typical resonance forms of a low valent metal-phosphine interaction. The contribution of $\delta$ is dependent on the identity of the E groups. ....	61
Figure 3-5. Resonance forms discovered in NRT analysis of $[\text{NCr}(\text{NH}_2)_2(\text{P}(\text{OMe})_3)]^+$ . ....	63
Figure 3-6. NRT analysis of $[\text{NCr}(\text{NH}_2)_2(\text{PPhMe}_2)]^+$ .....	64
Figure 3-7. Eyring Plot for $\text{NCr}(\text{N}^i\text{Pr}_2)_2\text{I}$ in $\text{CD}_3\text{CN}$ . The value obtained was -1 e.u. ( $\pm 0.5$ ). ....	76
Figure 3-8. Eyring Plot analysis of $\text{NCr}(\text{N}^i\text{Pr}_2)_2\text{I}$ in $\text{CDCl}_3$ . The value obtained for $\Delta\text{S}^\ddagger$ was -0.6(0.3). ....	77
Figure 3-9. Eyring Plot analysis of $\text{NCr}(\text{N}^i\text{Pr}_2)_2\text{OPh}$ in $\text{CDCl}_3$ . The value obtained for $\Delta\text{S}^\ddagger$ was -3.1(0.5). ....	78
Figure 3-10. Eyring Plot analysis of $\text{NCr}(\text{N}^i\text{Pr}_2)_3$ in $\text{CDCl}_3$ . The value obtained for $\Delta\text{S}^\ddagger$ was -5.7(0.7). ....	79
Figure 3-11. Eyring Plot analysis of $\text{NCr}(\text{N}^i\text{Pr}_2)_2\text{Pyr}^{3\text{C}_6\text{H}_3(\text{CF}_3)_2}$ in $\text{CDCl}_3$ . The value obtained for $\Delta\text{S}^\ddagger$ was -3.7(0.4) .....	80
Figure 3-12. $^1\text{H}$ NMR Spectrum for $[\text{NCr}(\text{N}^i\text{Pr}_2)_2(\text{PMe}_3)]\text{SbF}_6$ ( <b>3a</b> ) in $\text{CD}_3\text{CN}$ .....	81
Figure 3-13. $^{13}\text{C}$ NMR Spectrum for $[\text{NCr}(\text{N}^i\text{Pr}_2)_2(\text{PMe}_3)]\text{SbF}_6$ ( <b>3a</b> ) in $\text{CD}_3\text{CN}$ .....	82
Figure 3-14. $^{31}\text{P}$ NMR Spectrum for $[\text{NCr}(\text{N}^i\text{Pr}_2)_2(\text{PMe}_3)]\text{SbF}_6$ ( <b>3a</b> ) in $\text{CD}_3\text{CN}$ .....	83
Figure 3-15. $^{19}\text{F}$ NMR Spectrum for $[\text{NCr}(\text{N}^i\text{Pr}_2)_2(\text{PMe}_3)]\text{SbF}_6$ ( <b>3a</b> ) in $\text{CD}_3\text{CN}$ .....	84
Figure 3-16. $^1\text{H}$ NMR Spectrum for $[\text{NCr}(\text{N}^i\text{Pr}_2)_2(\text{P}^n\text{Bu}_3)]\text{SbF}_6$ ( <b>3b</b> ) in $\text{CDCl}_3$ .....	85
Figure 3-17. $^{13}\text{C}$ NMR Spectrum for $[\text{NCr}(\text{N}^i\text{Pr}_2)_2(\text{P}^n\text{Bu}_3)]\text{SbF}_6$ ( <b>3b</b> ) in $\text{CDCl}_3$ .....	86
Figure 3-18. $^{31}\text{P}$ NMR Spectrum for $[\text{NCr}(\text{N}^i\text{Pr}_2)_2(\text{P}^n\text{Bu}_3)]\text{SbF}_6$ ( <b>3b</b> ) in $\text{CDCl}_3$ .....	87



Figure 3-19. $^{19}\text{F}$ NMR Spectrum for $[\text{NCr}(\text{N}^i\text{Pr}_2)_2(\text{P}^n\text{Bu}_3)]\text{SbF}_6$ ( <b>3b</b> ) in $\text{CDCl}_3$ .....	88
Figure 3-20. $^1\text{H}$ NMR Spectrum for $[\text{NCr}(\text{N}^i\text{Pr}_2)_2(\text{P}^i\text{Bu}_3)]\text{SbF}_6$ ( <b>3c</b> ) in $\text{CDCl}_3$ .....	89
Figure 3-21. $^{13}\text{C}$ NMR Spectrum for $[\text{NCr}(\text{N}^i\text{Pr}_2)_2(\text{P}^i\text{Bu}_3)]\text{SbF}_6$ ( <b>3c</b> ) in $\text{CDCl}_3$ .....	90
Figure 3-22. $^{31}\text{P}$ NMR Spectrum for $[\text{NCr}(\text{N}^i\text{Pr}_2)_2(\text{P}^i\text{Bu}_3)]\text{SbF}_6$ ( <b>3c</b> ) in $\text{CDCl}_3$ .....	91
Figure 3-23. $^{19}\text{F}$ NMR Spectrum for $[\text{NCr}(\text{N}^i\text{Pr}_2)_2(\text{P}^i\text{Bu}_3)]\text{SbF}_6$ ( <b>3c</b> ) in $\text{CDCl}_3$ .....	92
Figure 3-24. $^1\text{H}$ NMR Spectrum for $[\text{NCr}(\text{N}^i\text{Pr}_2)_2(\text{P}^i\text{Pr}_3)]\text{SbF}_6$ ( <b>3d</b> ) in $\text{CDCl}_3$ .....	93
Figure 3-25. $^{13}\text{C}$ NMR Spectrum for $[\text{NCr}(\text{N}^i\text{Pr}_2)_2(\text{P}^i\text{Pr}_3)]\text{SbF}_6$ ( <b>3d</b> ) in $\text{CDCl}_3$ .....	94
Figure 3-26. $^{31}\text{P}$ NMR Spectrum for $[\text{NCr}(\text{N}^i\text{Pr}_2)_2(\text{P}^i\text{Pr}_3)]\text{SbF}_6$ ( <b>3d</b> ) in $\text{CDCl}_3$ .....	95
Figure 3-27. $^{19}\text{F}$ NMR Spectrum for $[\text{NCr}(\text{N}^i\text{Pr}_2)_2(\text{P}^i\text{Pr}_3)]\text{SbF}_6$ ( <b>3d</b> ) in $\text{CDCl}_3$ .....	96
Figure 3-28. $^1\text{H}$ NMR Spectrum for $[\text{NCr}(\text{N}^i\text{Pr}_2)_2(\text{PCy}_3)]\text{SbF}_6$ ( <b>3e</b> ) in $\text{CDCl}_3$ .....	97
Figure 3-29. $^{13}\text{C}$ NMR Spectrum for $[\text{NCr}(\text{N}^i\text{Pr}_2)_2(\text{PCy}_3)]\text{SbF}_6$ ( <b>3e</b> ) in $\text{CDCl}_3$ .....	98
Figure 3-30. $^{31}\text{P}$ NMR Spectrum for $[\text{NCr}(\text{N}^i\text{Pr}_2)_2(\text{PCy}_3)]\text{SbF}_6$ ( <b>3e</b> ) in $\text{CDCl}_3$ .....	99
Figure 3-31. $^{19}\text{F}$ NMR Spectrum for $[\text{NCr}(\text{N}^i\text{Pr}_2)_2(\text{PCy}_3)]\text{SbF}_6$ ( <b>3e</b> ) in $\text{CDCl}_3$ .....	100
Figure 3-32. $^{14}\text{N}$ NMR Spectrum for $[\text{NCr}(\text{N}^i\text{Pr}_2)_2(\text{PCy}_3)]\text{SbF}_6$ ( <b>3e</b> ) in $\text{CDCl}_3$ .....	101
Figure 3-33. $^1\text{H}$ NMR Spectrum for $[\text{NCr}(\text{N}^i\text{Pr}_2)_2(\text{PPhMe}_2)]\text{SbF}_6$ ( <b>3e</b> ) in $\text{CDCl}_3$ .....	102
Figure 3-34. $^{13}\text{C}$ NMR Spectrum for $[\text{NCr}(\text{N}^i\text{Pr}_2)_2(\text{PPhMe}_2)]\text{SbF}_6$ ( <b>3e</b> ) in $\text{CDCl}_3$ .....	103
Figure 3-35. $^{31}\text{P}$ NMR Spectrum for $[\text{NCr}(\text{N}^i\text{Pr}_2)_2(\text{PPhMe}_2)]\text{SbF}_6$ ( <b>3e</b> ) in $\text{CDCl}_3$ .....	104
Figure 3-36. $^{19}\text{F}$ NMR Spectrum for $[\text{NCr}(\text{N}^i\text{Pr}_2)_2(\text{PPhMe}_2)]\text{SbF}_6$ ( <b>3e</b> ) in $\text{CDCl}_3$ .....	105
Figure 3-37. $^1\text{H}$ NMR Spectrum for $[\text{NCr}(\text{N}^i\text{Pr}_2)_2(\text{PPh}_2\text{Me})]\text{SbF}_6$ ( <b>3g</b> ) in $\text{CDCl}_3$ .....	106
Figure 3-38. $^{13}\text{C}$ NMR Spectrum for $[\text{NCr}(\text{N}^i\text{Pr}_2)_2(\text{PPh}_2\text{Me})]\text{SbF}_6$ ( <b>3g</b> ) in $\text{CDCl}_3$ .....	107
Figure 3-39. $^{31}\text{P}$ NMR Spectrum for $[\text{NCr}(\text{N}^i\text{Pr}_2)_2(\text{PPh}_2\text{Me})]\text{SbF}_6$ ( <b>3g</b> ) in $\text{CDCl}_3$ .....	108
Figure 3-40. $^{19}\text{F}$ NMR Spectrum for $[\text{NCr}(\text{N}^i\text{Pr}_2)_2(\text{PPh}_2\text{Me})]\text{SbF}_6$ ( <b>3g</b> ) in $\text{CDCl}_3$ .....	109
Figure 3-41. $^1\text{H}$ NMR Spectrum for $[\text{NCr}(\text{N}^i\text{Pr}_2)_2(\text{PPhEt}_2)]\text{SbF}_6$ ( <b>3h</b> ) in $\text{CDCl}_3$ .....	110
Figure 3-42. $^{13}\text{C}$ NMR Spectrum for $[\text{NCr}(\text{N}^i\text{Pr}_2)_2(\text{PPhEt}_2)]\text{SbF}_6$ ( <b>3h</b> ) in $\text{CDCl}_3$ .....	111
Figure 3-43. $^{31}\text{P}$ NMR Spectrum for $[\text{NCr}(\text{N}^i\text{Pr}_2)_2(\text{PPhEt}_2)]\text{SbF}_6$ ( <b>3h</b> ) in $\text{CDCl}_3$ .....	112



Figure 3-44. $^{19}\text{F}$ NMR Spectrum for $[\text{NCr}(\text{N}^i\text{Pr}_2)_2(\text{PPhEt}_2)]\text{SbF}_6$ ( <b>3h</b> ) in $\text{CDCl}_3$ .....	113
Figure 3-45. $^1\text{H}$ NMR Spectrum for $[\text{NCr}(\text{N}^i\text{Pr}_2)_2(\text{PPh}_2\text{Et})]\text{SbF}_6$ ( <b>3i</b> ) in $\text{CDCl}_3$ .....	114
Figure 3-46. $^{13}\text{C}$ NMR Spectrum for $[\text{NCr}(\text{N}^i\text{Pr}_2)_2(\text{PPh}_2\text{Et})]\text{SbF}_6$ ( <b>3i</b> ) in $\text{CDCl}_3$ .....	115
Figure 3-47. $^{31}\text{P}$ NMR Spectrum for $[\text{NCr}(\text{N}^i\text{Pr}_2)_2(\text{PPh}_2\text{Et})]\text{SbF}_6$ ( <b>3i</b> ) in $\text{CDCl}_3$ .....	116
Figure 3-48. $^{19}\text{F}$ NMR Spectrum for $[\text{NCr}(\text{N}^i\text{Pr}_2)_2(\text{PPh}_2\text{Et})]\text{SbF}_6$ ( <b>3i</b> ) in $\text{CDCl}_3$ .....	117
Figure 3-49. $^1\text{H}$ NMR Spectrum for $[\text{NCr}(\text{N}^i\text{Pr}_2)_2(\text{PPh}_2^n\text{Bu})]\text{PF}_6$ ( <b>3j</b> ) in $\text{CDCl}_3$ .....	118
Figure 3-50. $^{13}\text{C}$ NMR Spectrum for $[\text{NCr}(\text{N}^i\text{Pr}_2)_2(\text{PPh}_2^n\text{Bu})]\text{PF}_6$ ( <b>3j</b> ) in $\text{CDCl}_3$ .....	119
Figure 3-51. $^{31}\text{P}$ NMR Spectrum for $[\text{NCr}(\text{N}^i\text{Pr}_2)_2(\text{PPh}_2^n\text{Bu})]\text{PF}_6$ ( <b>3j</b> ) in $\text{CDCl}_3$ .....	120
Figure 3-52. $^{19}\text{F}$ NMR Spectrum for $[\text{NCr}(\text{N}^i\text{Pr}_2)_2(\text{PPh}_2^n\text{Bu})]\text{PF}_6$ ( <b>3j</b> ) in $\text{CDCl}_3$ .....	121
Figure 3-53. $^{14}\text{N}$ NMR Spectrum for $[\text{NCr}(\text{N}^i\text{Pr}_2)_2(\text{PPh}_2^n\text{Bu})]\text{PF}_6$ ( <b>3j</b> ) in $\text{CDCl}_3$ .....	122
Figure 3-54. $^1\text{H}$ NMR Spectrum for $[\text{NCr}(\text{N}^i\text{Pr}_2)_2(\text{PPh}_2\text{Cy})]\text{SbF}_6$ ( <b>3k</b> ) in $\text{CDCl}_3$ .....	123
Figure 3-55. $^{13}\text{C}$ NMR Spectrum for $[\text{NCr}(\text{N}^i\text{Pr}_2)_2(\text{PPh}_2\text{Cy})]\text{SbF}_6$ ( <b>3k</b> ) in $\text{CDCl}_3$ .....	124
Figure 3-56. $^{31}\text{P}$ NMR Spectrum for $[\text{NCr}(\text{N}^i\text{Pr}_2)_2(\text{PPh}_2\text{Cy})]\text{SbF}_6$ ( <b>3k</b> ) in $\text{CDCl}_3$ .....	125
Figure 3-57. $^{19}\text{F}$ NMR Spectrum for $[\text{NCr}(\text{N}^i\text{Pr}_2)_2(\text{PPh}_2\text{Cy})]\text{SbF}_6$ ( <b>3k</b> ) in $\text{CDCl}_3$ .....	126
Figure 3-58. $^1\text{H}$ NMR Spectrum for $[\text{NCr}(\text{N}^i\text{Pr}_2)_2(\text{PPhCy}_2)]\text{SbF}_6$ ( <b>3l</b> ) in $\text{CDCl}_3$ .....	127
Figure 3-59. $^{13}\text{C}$ NMR Spectrum for $[\text{NCr}(\text{N}^i\text{Pr}_2)_2(\text{PPhCy}_2)]\text{SbF}_6$ ( <b>3l</b> ) in $\text{CDCl}_3$ .....	128
Figure 3-60. $^{31}\text{P}$ NMR Spectrum for $[\text{NCr}(\text{N}^i\text{Pr}_2)_2(\text{PPhCy}_2)]\text{SbF}_6$ ( <b>3l</b> ) in $\text{CDCl}_3$ .....	129
Figure 3-61. $^{19}\text{F}$ NMR Spectrum for $[\text{NCr}(\text{N}^i\text{Pr}_2)_2(\text{PPhCy}_2)]\text{SbF}_6$ ( <b>3l</b> ) in $\text{CDCl}_3$ .....	130
Figure 3-62. $^{14}\text{N}$ NMR Spectrum for $[\text{NCr}(\text{N}^i\text{Pr}_2)_2(\text{PPhCy}_2)]\text{SbF}_6$ ( <b>3l</b> ) in $\text{CDCl}_3$ .....	131
Figure 3-63. $^1\text{H}$ NMR Spectrum for $[\text{NCr}(\text{N}^i\text{Pr}_2)_2(\text{P}(\text{OEt})_3)]\text{SbF}_6$ ( <b>3m</b> ) in $\text{CDCl}_3$ .....	132
Figure 3-64. $^{13}\text{C}$ NMR Spectrum for $[\text{NCr}(\text{N}^i\text{Pr}_2)_2(\text{P}(\text{OEt})_3)]\text{SbF}_6$ ( <b>3m</b> ) in $\text{CDCl}_3$ .....	133
Figure 3-65. $^{31}\text{P}$ NMR Spectrum for $[\text{NCr}(\text{N}^i\text{Pr}_2)_2(\text{P}(\text{OEt})_3)]\text{SbF}_6$ ( <b>3m</b> ) in $\text{CDCl}_3$ .....	134
Figure 3-66. $^{19}\text{F}$ NMR Spectrum for $[\text{NCr}(\text{N}^i\text{Pr}_2)_2(\text{P}(\text{OEt})_3)]\text{SbF}_6$ ( <b>3m</b> ) in $\text{CDCl}_3$ .....	135
Figure 3-67. $^1\text{H}$ NMR Spectrum for $[\text{NCr}(\text{N}^i\text{Pr}_2)_2(\text{P}(\text{O}^i\text{Pr})_3)]\text{SbF}_6$ ( <b>3n</b> ) in $\text{CDCl}_3$ .....	136
Figure 3-68. $^{13}\text{C}$ NMR Spectrum for $[\text{NCr}(\text{N}^i\text{Pr}_2)_2(\text{P}(\text{O}^i\text{Pr})_3)]\text{SbF}_6$ ( <b>3n</b> ) in $\text{CDCl}_3$ .....	137



Figure 3-69. $^{31}\text{P}$ NMR Spectrum for $[\text{NCr}(\text{N}^i\text{Pr}_2)_2(\text{P}(\text{O}^i\text{Pr}_3)_3)]\text{SbF}_6$ ( <b>3n</b> ) in $\text{CDCl}_3$ .....	138
Figure 3-70. $^{19}\text{F}$ NMR Spectrum for $[\text{NCr}(\text{N}^i\text{Pr}_2)_2(\text{P}(\text{O}^i\text{Pr}_3)_3)]\text{SbF}_6$ ( <b>3n</b> ) in $\text{CDCl}_3$ .....	139
Figure 3-71. $^{14}\text{N}$ NMR Spectrum for $[\text{NCr}(\text{N}^i\text{Pr}_2)_2(\text{P}(\text{O}^i\text{Pr}_3)_3)]\text{SbF}_6$ ( <b>3n</b> ) in $\text{CDCl}_3$ .....	140
Figure 3-72. $^1\text{H}$ NMR Spectrum for $[\text{NCr}(\text{N}^i\text{Pr}_2)_2(\text{NCCH}_3)]\text{SbF}_6$ ( <b>2</b> ) in $\text{CDCl}_3$ .....	141
Figure 3-73. $^{13}\text{C}$ NMR Spectrum for $[\text{NCr}(\text{N}^i\text{Pr}_2)_2(\text{NCCH}_3)]\text{SbF}_6$ ( <b>2</b> ) in $\text{CDCl}_3$ .....	142
Figure 3-74. $^{19}\text{F}$ NMR Spectrum for $[\text{NCr}(\text{N}^i\text{Pr}_2)_2(\text{NCCH}_3)]\text{SbF}_6$ ( <b>2</b> ) in $\text{CDCl}_3$ .....	143
Figure 3-75. $^{14}\text{N}$ NMR Spectrum for $[\text{NCr}(\text{N}^i\text{Pr}_2)_2(\text{NCCH}_3)]\text{SbF}_6$ ( <b>2</b> ) in $\text{CDCl}_3$ .....	144
Figure 4-1. Plot displaying the calculate vs. experimental rate constant. The y-axis was calculated by using the experimental LDP and % $V_{\text{bur}}$ values in the model described above. The error bars are displayed at the 95% confidence level. ....	160
Figure 4-2. Plot displaying the calculate vs. experimental rate constant for the full set of ligands tested. The y-axis was calculated by using the experimental LDP and % $V_{\text{bur}}$ values in the model described above. The error bars are displayed at the 95% confidence level. The grey square are the aryloxide points and were not included in the regression. ....	163
Figure 4-3. Expanded model displaying the poor fit for catalyst <b>3</b> . ....	166
Figure 4-4. Representations of the proposed possible catalyst structures the hydroamination reaction using $\text{Ti}(\text{NMe}_2)_4$ as a catalyst.....	169
Figure 4-5. Series of ligands with the computationally modelled LDP fit against the experimental LDP. The orange point is the predicted imido value fit to the best fit line of the model. ....	170
Figure 4-6. Fit of the computed and experimental LDP values including a steric term to account for the truncated chromium molecule in the calculations. The orange point is the imido theoretical value fit to the best fit line. ....	172
Figure 4-7. Plot of the predicted imido value to our model. The orange diamond is $-\text{Ti}(\text{NPh})$ , the green diamond is $-\text{Ti}(\text{NHPh})_2$ , and the purple diamond is $-\text{Ti}(\text{NMe}_2)_2$ . ....	173
Figure 4-8. DOSY spectrum of $\text{Ti}(\text{dithioBINAP})(\text{NMe}_2)_2$ ( <b>6</b> ) at 25 °C. ....	177
Figure 4-9. Molecular weight calibration of $\text{Ti}(\text{dithioBINAP})(\text{NMe}_2)_2$ ( <b>6</b> ) at 25 °C. ....	178
Figure 4-10. Molecular weight calibration of $\text{Ti}(\text{dithioBINAP})(\text{NMe}_2)_2$ ( <b>6</b> ) at 50 °C. ....	180
Figure 4-11. Molecular weight calibration of $\text{Ti}(\text{dithioBINAP})(\text{NMe}_2)_2$ ( <b>6</b> ) with addition of aniline (4 equiv.) at 50 °C. ....	181
Figure 4-12. Representative Plots for Kinetics Plot of [1-phenylpropyne] vs time with $\text{Ti}(\text{NMe}_2)_2(\text{bis-phenoxide}^{2t\text{Bu-4Me}})$ ( <b>5</b> ) .....	194



Figure 4-13. $^1\text{H}$ NMR Spectrum of $\text{NCr}(\text{N}^i\text{Pr}_2)_2(\text{Ind}^{3\text{Me}})$ in $\text{CDCl}_3$ .....	195
Figure 4-14. $^{13}\text{C}$ NMR Spectrum of $\text{NCr}(\text{N}^i\text{Pr}_2)_2(\text{Ind}^{3\text{Me}})$ in $\text{CDCl}_3$ .....	196
Figure 4-15. $^{14}\text{N}$ NMR Spectrum of $\text{NCr}(\text{N}^i\text{Pr}_2)_2(\text{Ind}^{3\text{Me}})$ in $\text{CDCl}_3$ .....	197
Figure 4-16. $^1\text{H}$ NMR Spectrum of $\text{NCr}(\text{N}^i\text{Pr}_2)_2(\text{Ind}^{3\text{Me}5\text{F}})$ in $\text{CDCl}_3$ .....	198
Figure 4-17. $^{13}\text{C}$ NMR Spectrum of $\text{NCr}(\text{N}^i\text{Pr}_2)_2(\text{Ind}^{3\text{Me}5\text{F}})$ in $\text{CDCl}_3$ .....	199
Figure 4-18. $^{19}\text{F}$ NMR Spectrum of $\text{NCr}(\text{N}^i\text{Pr}_2)_2(\text{Ind}^{3\text{Me}5\text{F}})$ in $\text{CDCl}_3$ .....	200
Figure 4-19. $^{14}\text{N}$ NMR Spectrum of $\text{NCr}(\text{N}^i\text{Pr}_2)_2(\text{Ind}^{3\text{Me}5\text{F}})$ in $\text{CDCl}_3$ .....	201
Figure 4-20. $^1\text{H}$ NMR Spectrum of $\text{NCr}(\text{N}^i\text{Pr}_2)_2(\text{Pyr}^{\text{Me}})$ in $\text{CDCl}_3$ .....	202
Figure 4-21. $^{13}\text{C}$ NMR Spectrum of $\text{NCr}(\text{N}^i\text{Pr}_2)_2(\text{Pyr}^{\text{Me}})$ in $\text{CDCl}_3$ .....	203
Figure 4-22. $^{14}\text{N}$ NMR Spectrum of $\text{NCr}(\text{N}^i\text{Pr}_2)_2(\text{Pyr}^{\text{Me}})$ in $\text{CDCl}_3$ .....	204
Figure 4-23. $^1\text{H}$ NMR Spectrum of $\text{NCr}(\text{N}^i\text{Pr}_2)_2(\text{Pyr}^{2-[\text{C}_6\text{H}_3(\text{CF}_3)_2]})$ in $\text{CDCl}_3$ .....	205
Figure 4-24. $^{13}\text{C}$ NMR Spectrum of $\text{NCr}(\text{N}^i\text{Pr}_2)_2(\text{Pyr}^{2-[\text{C}_6\text{H}_3(\text{CF}_3)_2]})$ in $\text{CDCl}_3$ .....	206
Figure 4-25. $^{19}\text{F}$ NMR Spectrum of $\text{NCr}(\text{N}^i\text{Pr}_2)_2(\text{Pyr}^{2-[\text{C}_6\text{H}_3(\text{CF}_3)_2]})$ in $\text{CDCl}_3$ .....	207
Figure 4-26. $^{14}\text{N}$ NMR Spectrum of $\text{NCr}(\text{N}^i\text{Pr}_2)_2(\text{Pyr}^{2-[\text{C}_6\text{H}_3(\text{CF}_3)_2]})$ in $\text{CDCl}_3$ .....	208
Figure 4-27. $^1\text{H}$ NMR Spectrum of $\text{NCr}(\text{N}^i\text{Pr}_2)_2(\text{Pyr}^{\text{Ph}})$ in $\text{CDCl}_3$ .....	209
Figure 4-28. $^{13}\text{C}$ NMR Spectrum of $\text{NCr}(\text{N}^i\text{Pr}_2)_2(\text{Pyr}^{\text{Ph}})$ in $\text{CDCl}_3$ .....	210
Figure 4-29. $^{14}\text{N}$ NMR Spectrum of $\text{NCr}(\text{N}^i\text{Pr}_2)_2(\text{Pyr}^{\text{Ph}})$ in $\text{CDCl}_3$ .....	211
Figure 4-30. $^1\text{H}$ NMR Spectrum of $\text{NCr}(\text{N}^i\text{Pr}_2)_2(\text{Pyr}^{\text{Tol}})$ in $\text{CDCl}_3$ .....	212
Figure 4-31. $^{13}\text{C}$ NMR Spectrum of $\text{NCr}(\text{N}^i\text{Pr}_2)_2(\text{Pyr}^{\text{Tol}})$ in $\text{CDCl}_3$ .....	213
Figure 4-32. $^{14}\text{N}$ NMR Spectrum of $\text{NCr}(\text{N}^i\text{Pr}_2)_2(\text{Pyr}^{\text{Tol}})$ in $\text{CDCl}_3$ .....	214
Figure 4-33. $^1\text{H}$ NMR Spectrum of $\text{NCr}(\text{N}^i\text{Pr}_2)_2(\text{OPh}^{2,4\text{-diMe}})$ in $\text{CDCl}_3$ .....	215
Figure 4-34. $^{13}\text{C}$ NMR Spectrum of $\text{NCr}(\text{N}^i\text{Pr}_2)_2(\text{OPh}^{2,4\text{-diMe}})$ in $\text{CDCl}_3$ .....	216
Figure 4-35. $^{14}\text{N}$ NMR Spectrum of $\text{NCr}(\text{N}^i\text{Pr}_2)_2(\text{OPh}^{2,4\text{-diMe}})$ in $\text{CDCl}_3$ .....	217
Figure 4-36. $^1\text{H}$ NMR Spectrum of $\text{NCr}(\text{N}^i\text{Pr}_2)_2(\text{OPh}^{2\text{-tBu-4-Me}})$ in $\text{CDCl}_3$ .....	218
Figure 4-37. $^{13}\text{C}$ NMR Spectrum of $\text{NCr}(\text{N}^i\text{Pr}_2)_2(\text{OPh}^{2\text{-tBu-4-Me}})$ in $\text{CDCl}_3$ .....	219



Figure 4-38. $^{14}\text{N}$ NMR Spectrum of $\text{NCr}(\text{N}^i\text{Pr}_2)_2(\text{OPh}^{2\text{-tBu-4-Me}})$ in $\text{CDCl}_3$ .	220
Figure 4-39. $^1\text{H}$ NMR Spectrum of $\text{NCr}(\text{N}^i\text{Pr}_2)_2(\text{OPh}^{2,4,5\text{-triMe}})$ in $\text{CDCl}_3$ .	221
Figure 4-40. $^1\text{H}$ NMR Spectrum of $\text{NCr}(\text{N}^i\text{Pr}_2)_2(\text{OPh}^{2,4,5\text{-triMe}})$ in $\text{CDCl}_3$ at $-29^\circ\text{C}$ .	222
Figure 4-41. $^1\text{H}$ NMR Spectrum of $\text{NCr}(\text{N}^i\text{Pr}_2)_2(\text{OPh}^{2,4,5\text{-triMe}})$ in $\text{CDCl}_3$ at $-29^\circ\text{C}$ .	223
Figure 4-42. $^{14}\text{N}$ NMR Spectrum of $\text{NCr}(\text{N}^i\text{Pr}_2)_2(\text{OPh}^{2,4,5\text{-triMe}})$ in $\text{CDCl}_3$ .	224
Figure 4-43. $^1\text{H}$ NMR Spectrum of $\text{NCr}(\text{N}^i\text{Pr}_2)_2(\text{OPh}^{2\text{-tBu-4,5-diMe}})$ in $\text{CDCl}_3$ .	225
Figure 4-44. $^{13}\text{C}$ NMR Spectrum of $\text{NCr}(\text{N}^i\text{Pr}_2)_2(\text{OPh}^{2\text{-tBu-4,5-diMe}})$ in $\text{CDCl}_3$ .	226
Figure 4-45. $^{14}\text{N}$ NMR Spectrum of $\text{NCr}(\text{N}^i\text{Pr}_2)_2(\text{OPh}^{2\text{-tBu-4,5-diMe}})$ in $\text{CDCl}_3$ .	227
Figure 4-46. $^1\text{H}$ NMR Spectrum of $\text{NCr}(\text{N}^i\text{Pr}_2)_2(\text{OPh}^{2\text{-Me-4-OMe}})$ in $\text{CDCl}_3$ .	228
Figure 4-47. $^1\text{H}$ NMR Spectrum of $\text{NCr}(\text{N}^i\text{Pr}_2)_2(\text{OPh}^{2\text{-Me-4-OMe}})$ in $\text{CDCl}_3$ at $-26^\circ\text{C}$ .	229
Figure 4-48. $^{13}\text{C}$ NMR Spectrum of $\text{NCr}(\text{N}^i\text{Pr}_2)_2(\text{OPh}^{2\text{-Me-4-OMe}})$ in $\text{CDCl}_3$ .	230
Figure 4-49. $^{14}\text{N}$ NMR Spectrum of $\text{NCr}(\text{N}^i\text{Pr}_2)_2(\text{OPh}^{2\text{-Me-4-OMe}})$ in $\text{CDCl}_3$ .	231
Figure 4-50. $^1\text{H}$ NMR Spectrum of $\text{NCr}(\text{N}^i\text{Pr}_2)_2(\text{OPh}^{2\text{-tBu-4-OMe}})$ in $\text{CDCl}_3$ .	232
Figure 4-51. $^{13}\text{C}$ NMR Spectrum of $\text{NCr}(\text{N}^i\text{Pr}_2)_2(\text{OPh}^{2\text{-tBu-4-OMe}})$ in $\text{CDCl}_3$ .	233
Figure 4-52. $^{14}\text{N}$ NMR Spectrum of $\text{NCr}(\text{N}^i\text{Pr}_2)_2(\text{OPh}^{2\text{-tBu-4-OMe}})$ in $\text{CDCl}_3$ .	234
Figure 4-53. $^1\text{H}$ NMR Spectrum of $\text{NCr}(\text{N}^i\text{Pr}_2)_2(\text{S Nap})$ in $\text{CDCl}_3$ .	235
Figure 4-54. $^{13}\text{C}$ NMR Spectrum of $\text{NCr}(\text{N}^i\text{Pr}_2)_2(\text{S Nap})$ in $\text{CDCl}_3$ .	236
Figure 4-55. $^{14}\text{N}$ NMR Spectrum of $\text{NCr}(\text{N}^i\text{Pr}_2)_2(\text{S Nap})$ in $\text{CDCl}_3$ .	237
Figure 5-1. Plot of the LDP versus the $E_{1/2}$ values of a U(V)/U(VI) redox couple for a series of ligands.	244
Figure 5-2. Comparison of the olefinic region of the $^1\text{H}$ NMR spectrum before (top) and after (bottom) catalysis showing complete cyclization.	249
Figure 5-3. Structures of <i>top</i> : $\text{Cp}^*\text{UI}_2(\text{PyPyr}^{\text{Me}3})(\text{thf})$ ( <b>3a</b> ), $\text{Cp}^*\text{UI}_2(\text{PyPyr}^{\text{Me}2})(\text{thf})$ ( <b>5</b> ), <i>bottom</i> : $\text{Cp}^*\text{UCl}_2(\text{PyPyr}^{\text{Me}2\text{Tol}})(\text{thf})$ ( <b>4a</b> ), and $\text{Cp}^*\text{UI}_2(\text{PyPyr}^{\text{Me}2\text{Tol}})(\text{thf})$ ( <b>4b</b> ), Hydrogens and co-crystallized solvents removed for clarity.	251
Figure 5-4. Comparison of the solid-state structures of $(\kappa^2(\text{N-C})\text{-CH}_2\text{SiMe}_2\text{NTMS})\text{U}(\text{Cp}^*)(\text{PyPyr}^{\text{Me}3})$ ( <b>6</b> ) (left) and $(\kappa^2(\text{N-C})\text{-CH}_2\text{SiMe}_2\text{NTMS})\text{U}(\text{Cp}^*)(\text{PyPyr}^{\text{Me}2})$ ( <b>7</b> ) (right).	254



Figure 5-5. Crystals structures of $\text{U}(\text{PyPyr}^{\text{Me}3})_4$ and $\text{U}(\text{PyPyr}^{\text{Me}2\text{Cl}})_4$ byproducts. The structure of $\text{U}(\text{PyPyr}^{\text{Me}3})_4$ crystallizes with four-fold symmetry, the grown structure is shown. Hydrogens and co-crystallized solvents removed for purity.....	255
Figure 5-6. Crystal structure of $\text{UI}_2(\text{PyPyr}^{\text{tBu}2})_2$ ( <b>6</b> ). Hydrogens and co-crystallized diethyl ether molecules removed for clarity. ....	256
Figure 5-7. Crude $^1\text{H}$ NMR of $[\text{N}(\text{TMS})\text{Cy}]_2\text{U}(\text{PyPyr}^{\text{Me}2})_2$ , <b>1</b> . ....	264
Figure 5-8. Crude $^1\text{H}$ NMR of $[\text{N}(\text{TMS})\text{Cy}]\text{U}(\text{PyPyr}^{\text{Me}2})_3$ , <b>2</b> .....	265
Figure 5-9. Crude $^1\text{H}$ NMR of $\text{U}(\text{PyPyr}^{\text{Me}2})_4$ . There are still signals present for <b>2</b> , but the majority of the $\text{N}(\text{TMS})\text{Cy}$ amides have been displaced. ....	266
Figure 5-10. $^1\text{H}$ NMR of $\text{Cp}^*\text{UCl}_2(\text{PyPyr}^{\text{Me}3})(\text{thf})$ ( <b>3a</b> ). ....	267
Figure 5-11. Best $^1\text{H}$ NMR of $\text{Cp}^*\text{UI}_2(\text{PyPyr}^{\text{Me}3})(\text{thf})$ , ( <b>3b</b> ). The spectrum contains impurities from unknown species that are not removed by recrystallization.....	268
Figure 5-12. $^1\text{H}$ NMR of $\text{Cp}^*\text{UCl}_2(\text{PyPyr}^{\text{Me}2\text{Tol}})(\text{thf})$ , ( <b>4a</b> ).....	269
Figure 5-13. $^1\text{H}$ NMR of $\text{Cp}^*\text{UI}_2(\text{PyPyr}^{\text{Me}2\text{Tol}})(\text{thf})$ ( <b>4b</b> ).....	270
Figure 5-14. $^1\text{H}$ NMR of $\text{Cp}^*\text{UI}_2(\text{PyPyr}^{\text{Me}2})(\text{thf})$ ( <b>5</b> ).....	271
Figure 5-15. $^1\text{H}$ NMR of $(\kappa^2(\text{N-C})\text{-CH}_2\text{SiMe}_2\text{NTMS})\text{U}(\text{Cp}^*)(\text{PyPyr}^{\text{Me}3})$ ( <b>6</b> ).....	272
Figure 5-16. Crude $^1\text{H}$ NMR of $(\kappa^2(\text{N-C})\text{-CH}_2\text{SiMe}_2\text{NTMS})\text{U}(\text{Cp}^*)(\text{PyPyr}^{\text{Me}2})$ ( <b>7</b> ). ....	273
Figure 5-17. Arrayed Spectra from the catalysis of <b>6</b> (10 mol%, 65 °C, $\text{C}_6\text{D}_6$ ) with DPAP. Each spectrum was taken in 10-minute intervals. The reaction appears to be complete after ~150 minutes (spectrum 15).....	274
Figure 5-18. Arrayed Spectra from the catalysis of <b>6</b> (5 mol%, 65 °C, $\text{C}_6\text{D}_6$ ) with DPAP. Each spectrum was taken in 10-minute intervals. The reaction appears to be complete after ~330 minutes (spectrum 33).....	275
Figure 5-19. Arrayed Spectra from the catalysis of <b>7</b> (5 mol%, 65 °C, $\text{C}_6\text{D}_6$ ) with DPAP. Each spectrum was taken in 10-minute intervals. The reaction appears to be complete after ~190 minutes (spectrum 19).....	276
Figure 6-1. Single crystal structure of $(\text{Cp}^*)\text{UI}(\text{NAr}^{\text{iPr}6})$ ( <b>2</b> ). Solvent molecules and hydrogens removed for clarity.....	281
Figure 6-2. Single crystal structure of $(\text{Cp}^*)\text{UI}(\text{NHAr}^{\text{iPr}6})$ ( <b>3</b> ). Hydrogens (except NH) and solvent removed for clarity. ....	284
Figure 6-3. Single crystal structure of $(\text{Cp}^*)\text{UI}(\text{NHAr}^{\text{Me}6})$ ( <b>5</b> ). Hydrogens (except NH) removed for clarity.....	285



Figure 6-4. Single crystal structure of (Cp*)UI(NAr <sup>Me6</sup> )(thf) <sub>2</sub> , <b>4</b> . Hydrogens (except NH) removed for clarity.....	287
Figure 6-5. Single crystal structure of (Cp*)U(NHAr <sup>Me6</sup> ) <sub>2</sub> , <b>6</b> . Hydrogens (except NH) removed for clarity.....	289
Figure 6-6. <i>Top</i> : Single crystal structure of <b>7</b> . Hydrogens (except NH's) removed for clarity. <i>Bottom</i> : Synthesis of UI(NHAr <sup>Me6</sup> ) <sub>2</sub> <b>7</b> . ....	290
Figure 6-7. <i>Top</i> : Crystal structure of UI(NHAr <sup>iPr6</sup> ) <sub>2</sub> <b>8</b> . Hydrogens (excepts N-H's) and solvent molecule removed for clarity. <i>Bottom</i> : Synthesis of (I)U(NHAr <sup>iPr6</sup> ) <sub>2</sub> ( <b>8</b> ).....	292
Figure 6-8. Contrasting solid state structures of <b>8</b> when crystallized from diethyl ether (green) and n-hexane (light blue). ....	293
Figure 6-9. Crystal structure of U(NHAr <sup>iPr6</sup> ) <sub>2</sub> ( <b>9</b> ). Hydrogens, except N-H's, and solvent molecule removed for clarity. The structure is grown to show the full molecule, but <b>9</b> crystallizes as half of the molecule with a 2-fold rotational axis.....	295
Figure 6-10. <i>Top</i> : Crystal structure of [U(NHAr <sup>iPr6</sup> ) <sub>2</sub> ][BAr <sup>F</sup> <sub>24</sub> ] ( <b>10</b> ) Hydrogens, except N-H's, anion, disorder, and solvent molecule removed for clarity. <i>Bottom</i> : Space filling structures of <b>8</b> (left) and <b>10</b> (right).....	297
Figure 6-11. EPR spectra of (a) (I)U(NHAr <sup>iPr6</sup> ) <sub>2</sub> ( <b>8</b> ) and (b) [U(NHAr <sup>iPr6</sup> ) <sub>2</sub> ][BAr <sup>F</sup> <sub>24</sub> ] ( <b>10</b> ). Measurement parameters for both spectra were: microwave frequency, 9.40 GHz, microwave power, 0.79 mW; field modulation amplitude, 1 mT; and sample temperature, 6 K. ....	298
Figure 6-12. Temperature dependence of the magnetic susceptibility for UI(NHAr <sup>iPr6</sup> ) <sub>2</sub> ( <b>8</b> ) (black squares), U(NHAr <sup>iPr6</sup> ) <sub>2</sub> ( <b>9</b> ) (red circles), and [U(NHAr <sup>iPr6</sup> ) <sub>2</sub> ][BAr <sup>F</sup> <sub>24</sub> ] ( <b>10</b> ) (blue diamonds) collected at 5000 Oe.....	301
Figure 6-13. <sup>1</sup> H NMR spectrum of (Cp*)UI(NAr <sup>iPr6</sup> ) in C <sub>6</sub> D <sub>6</sub> .....	309
Figure 6-14. <sup>1</sup> H NMR spectrum of (Cp*)UI(NHAr <sup>iPr6</sup> ) in C <sub>6</sub> D <sub>6</sub> .....	310
Figure 6-15. <sup>1</sup> H NMR spectrum of (Cp*)UI(NAr <sup>Me6</sup> ) in C <sub>6</sub> D <sub>6</sub> .....	311
Figure 6-16. Crude <sup>1</sup> H NMR spectrum of (Cp*)UI(NHAr <sup>Me6</sup> ) in C <sub>6</sub> D <sub>6</sub> .....	312
Figure 6-17. Crude <sup>1</sup> H NMR of (Cp*)U(NHAr <sup>Me6</sup> ) <sub>2</sub> in C <sub>6</sub> D <sub>6</sub> . Inset shows the broad peaks attributed to fluxionality. ....	313
Figure 6-18. <sup>1</sup> H NMR spectrum of UI(NHAr <sup>Me6</sup> ) <sub>2</sub> in C <sub>6</sub> D <sub>6</sub> .....	314
Figure 6-19. <sup>1</sup> H NMR Spectrum of UI(NHAr <sup>iPr6</sup> ) <sub>2</sub> ( <b>8</b> ) at -30 °C in toluene-d <sub>8</sub> .....	315
Figure 6-20. <sup>1</sup> H NMR Spectrum of UI(NHAr <sup>iPr6</sup> ) <sub>2</sub> ( <b>8</b> ) at ambient temperature in toluene-d <sub>8</sub> ....	316
Figure 6-21. <sup>1</sup> H NMR Spectrum of U(NHAr <sup>iPr6</sup> ) <sub>2</sub> ( <b>9</b> ) at 25 °C in toluene-d <sub>8</sub> .....	317



Figure 6-22. $^1\text{H}$ NMR Spectrum of $[\text{U}(\text{NHA}^{\text{iPr}_6})_2]^+ [\text{BAr}^{\text{F}_{24}}]^-$ ( <b>10</b> ) at 25 °C in THF- $\text{d}_8$ .....	318
Figure 6-23. UV-vis/NIR spectrum of <b>2</b> in 1 mm cuvette .....	319
Figure 6-24. UV-vis/NIR spectrum of <b>3</b> in 1 mm cuvette .....	320
Figure 6-25. UV-vis/NIR spectrum of <b>6</b> in 1 mm cuvette. ....	320
Figure 6-26. UV-vis/NIR spectrum of <b>8</b> at low concentration ( $\sim 0.5$ mM). ....	321
Figure 6-27. NIR spectrum of <b>8</b> at high concentration ( $\sim 10$ mM). ....	321
Figure 6-28. UV-vis/NIR spectrum of <b>9</b> at low concentration ( $\sim 0.5$ mM). ....	322
Figure 6-29. UV-vis/NIR spectrum of <b>10</b> at low concentration ( $\sim 0.5$ mM). ....	322
Figure 6-30. EPR spectra of (I) $\text{U}(\text{NHA}^{\text{iPr}_6})_2$ ( <b>8</b> ), $\text{U}(\text{NHA}^{\text{iPr}_6})_2$ ( <b>9</b> ), and $\text{U}(\text{NHA}^{\text{iPr}_6})_2^+$ ( <b>10</b> ). Measurement parameters for both spectra were: microwave frequency = 9.40 GHz, microwave power = 0.79 mW, field modulation amplitude = 1 mT, and sample temperature = 6 K. ....	324
Figure 6-31. Parallel and perpendicular EPR spectra for <b>8</b> . Instrument conditions for these scans were: (a) perpendicular mode: microwave frequency = 9.643 GHz, and (b) parallel mode: microwave frequency = 9.441 GHz. Conditions common to the two spectra are: microwave power = 1.0 mW, field modulation amplitude = 1.6 mT, field modulation frequency = 10 kHz, and sample temperature = 5 K. ....	325
Figure 6-32. Temperature dependence of magnetic susceptibility ( $\mu_{\text{eff}}$ ) for <b>8</b> collected at 5000 Oe. .....	327
Figure 6-33. Temperature dependence of magnetic susceptibility ( $\mu_{\text{eff}}$ ) for <b>9</b> collected at 5000 Oe. .....	327
Figure 6-34. Temperature dependence of magnetic susceptibility ( $\mu_{\text{eff}}$ ) for <b>10</b> collected at 5000 Oe. ....	328
Figure 6-35. Temperature dependence of solution state magnetic susceptibility ( $\mu_{\text{eff}}$ ) for <b>9</b> . ....	328
Figure 6-36. Full structure of ( <b>2</b> ) including solvent. ....	331
Figure 6-37. Full structure of ( <b>3</b> ) including solvent and molecular disorder. ....	333
Figure 6-38. Full structure of ( <b>4</b> ) .....	335
Figure 6-39. Full structure of ( <b>5</b> ) .....	337
Figure 6-40. Full structure of ( <b>6</b> ) .....	339
Figure 6-41. Full structure of ( <b>7</b> ) .....	341



Figure 6-42. Full structure of <b>(8)</b> solvent and molecular disorder .....	343
Figure 6-43. Full structure of <b>(8)</b> including solvent and molecular disorder.....	345
Figure 6-44. Full structure of <b>(9)</b> including solvent.....	347
Figure 6-45. Full structure of <b>(10)</b> including anion, solvent, and molecular disorder .....	349
Figure 7-1. Concentration of CO <sub>2</sub> in the atmosphere measured from 1958 to 2018 at the Manua Loa Observatory. Figure taken from reference 3.....	354
Figure 7-2. Heterometallic cluster reported by Shilov to be the active species in his dinitrogen reduction system. <sup>36</sup> .....	358
Figure 7-3. Molybdenum cluster isolated from attempts at catalyst synthesis. Hydrogens are removed from the tetrabutyl ammonium for clarity. ....	364
Figure 7-4. GC/MS trace of an aliquot of the reaction solution from a reaction that produced hydrazine according to the indicator solution. <sup>48</sup> The indicated peak at 13.424 represents the peak for stilbene. ....	368
Figure 7-5 GC/MS trace of an equal aliquot from the same solution shown in Figure 7-4 spiked with 0.25 µg hydrazine (added as hydrate). <sup>48</sup> The indicated peak at 13.424 represents the peak for stilbene. ....	369



## LIST OF SCHEMES

Scheme 1-1. General synthesis of chromium starting materials for LDP analysis. <sup>a</sup> Synthesized using literature procedure. <sup>26</sup> .....	12
Scheme 2-1. Synthesis of $\text{NCr}(\text{N}^i\text{Pr}_2)_2(\text{Cp})$ , <b>1</b> , and $\text{NCr}(\text{N}^i\text{Pr}_2)(\text{Cp})(\text{O}_2\text{CPh})$ , <b>3</b> , from $\text{NCr}(\text{N}^i\text{Pr}_2)\text{I}$ . .....	21
Scheme 2-2. Synthesis of $\text{NCr}(\text{N}^i\text{Pr}_2)(\text{Cp})(\text{Cl})$ , <b>4</b> . .....	23
Scheme 2-3. In situ synthesis of $\text{NCr}(\text{N}^i\text{Pr}_2)_2\text{Cp}(\text{NCMe})$ , <b>5</b> . .....	24
Scheme 3-1. General procedure for the synthesis of $\text{PR}_3$ complexes from $\text{NCr}(\text{N}^i\text{Pr}_2)_2\text{I}$ . $\text{X} = \text{SbF}_6$ , $\text{PF}_6$ , $\text{BAr}^{\text{F}}_{24}$ , $\text{BAr}^{\text{F}}_{20}$ , $\text{BPh}_4$ , $\text{Al}(\text{O}^t\text{Bu}^{\text{F}}_9)_4$ .....	48
Scheme 4-1. General procedures for synthesis of the chromium complexes. ....	154
Scheme 4-2. Reaction scheme for the hydroamination kinetics experiments. ....	155
Scheme 4-3. Comparison of the molecular weight of the monomer and dimerized catalyst. ....	179
Scheme 5-1. Example of an intramolecular hydroamination.....	246
Scheme 5-2. Proposed synthesis of the uranium precatalysts.....	247
Scheme 5-3. Attempted synthesis of $\text{U}(\text{PyPyr})_2\text{Cl}_2$ from $\text{UCl}_4$ . ....	248
Scheme 5-4. Synthesis of mixed amide PyPyr compounds.....	248
Scheme 5-5. Synthesis of $\text{Cp}^*\text{UX}_2(\text{PyPyr})(\text{thf})$ from $\text{UX}_4$ starting materials. ....	252
Scheme 5-6. Synthesis of $(\kappa^2(\text{N-C})\text{-CH}_2\text{SiMe}_2\text{NTMS})\text{U}(\text{Cp}^*)(\text{PyPyr}^{\text{Me}3})$ ( <b>6</b> ) from $\text{UCl}_4$ . ....	253
Scheme 6-1. Reaction of $(\text{Cp}^*)\text{U}(\text{I})_2(\text{thf})_3$ with $\text{DiPPN}_3$ . ....	280
Scheme 6-2. Top. Discovery of $(\text{Cp}^*)\text{UI}(\text{NAr}^{i\text{Pr}})$ ( <b>2</b> ) from $(\text{Cp}^*)\text{U}(\text{I})_2(\text{thf})_3$ and $\text{N}_3\text{Ar}^{i\text{Pr}6}$ disproportionation. Middle. Rational synthesis of <b>2</b> . Bottom. Synthesis of $(\text{Cp}^*)\text{UI}(\text{NAr}^{i\text{Pr}6})$ ( <b>3</b> ) from $(\text{Cp}^*)\text{U}(\text{I})_2(\text{thf})_3$ and $\text{NaNAr}^{i\text{Pr}6}$ .....	282
Scheme 6-3. Synthesis of $(\text{Cp}^*)\text{UI}(\text{NAr}^{\text{Me}6})$ ( <b>4</b> ) and $(\text{Cp}^*)\text{UI}(\text{NAr}^{\text{Me}6})$ ( <b>5</b> ). ....	286
Scheme 6-4. Synthesis of $(\text{Cp}^*)\text{U}(\text{NAr}^{\text{Me}6})_2$ ( <b>6</b> ). ....	288
Scheme 6-5. Synthesis of $\text{U}(\text{NAr}^{i\text{Pr}6})_2$ ( <b>9</b> ) from <b>8</b> . ....	294
Scheme 6-6. Synthesis of $[\text{U}(\text{NAr}^{i\text{Pr}6})_2][\text{BAr}^{\text{F}}_{24}]$ ( <b>10</b> ) from <b>9</b> . ....	297



## KEY TO SYMBOLS AND ABBREVIATIONS

LDP	Ligand Donor Parameter
IR	Infrared Radiation
$\theta$	Tolman Cone Angle
Å	Angstrom
$\nu$	Tolman Electronic Parameter
% V <sub>bur</sub>	Percent Buried Volume
NHC	N-Heterocyclic Carbene
HVM	High Valent Metal
Cp	Cyclopentadiene
NBO	Natural Bond Orbital
NMR	Nuclear Magnetic Resonance
THF	Tetrahydrofuran
HPCC	High Power Computing Cluster
MBO	Mayer Bond Order
G09	Gaussian 09
DOSY	Diffusion Ordered Spectroscopy
ROESY	Rotating-frame Overhauser Spectroscopy
e.u.	Entropy unit
$\chi_d$	Corrected phosphine electronic parameter
$\Delta H^\ddagger$	Enthalpy of Activation
$\Delta S^\ddagger$	Entropy of Activation



$\Delta G^\ddagger$	Free Energy of Activation
DFT	Density Functional Theory
NRT	Natural Resonance Theory
AN	Acceptor Number
Std. Dev.	Standard Deviation
Pyrr.	Pyrrole
Et	Ethyl
Ph	Phenyl
Nap	Naphthyl
h	hour(s)
H <sub>2</sub> dpm	5,5-dimethyldipyrrolylmethane
dim	Diindolylmethane
SST	Spin Saturation Transfer
DOE	Department of Energy
SCGSR	Science Graduate Student Research
LANL	Los Alamos National Laboratory
PyPyr	2-2'-pyridylpyrrole
TMS	trimethylsilyl
RT	Room Temperature
Cp*	Pentamethylcyclopentadiene
UV	Ultraviolet Radiation
Vis	Visible Radiation
DPAP	2,2-diphenyl-1-amino-4-pentene



DiPP	Diisopropylphenyl
Ar <sup>iPr6</sup>	2,6-bis(2,4,6-triisopropylphenyl)-phenyl
Ar <sup>Me6</sup>	2,6-bis(2,4,6-trimethylphenyl)-phenyl
SQUID	Superconducting Quantum Interference Device
Ppm	Parts Per Million
PDMAB	<i>p</i> -dimethylaminobenzaldehyde
PC	L- $\alpha$ -dipalmitoylphosphatidylcholine
Equiv.	Equivalents
Cy	Cyclohexyl
GC	Gas Chromatography
GC/MS	Gas Chromatography/Mass Spectrometry



# Chapter 1. Introduction

## 1.1 Background and Motivation

Transition metal catalyzed reactions find use in all scales of modern chemistry. Whether it is an academician using a metathesis reaction for the final step in a natural product synthesis, or multibillion-dollar polymerizations, the catalysts employed need to work well. One of the most common endeavors to improve those catalysts is to modify the ancillary ligands (a ligand that does not directly participate in bond making and bond breaking in the catalytic cycle). Ligand manipulations allow a researcher to tune subtle electronic and steric factors that can control everything from catalytic rates and product selectivity, to substrate scope and catalyst stability. For those who have been in the field for many years, and have years of knowledge and experience, making productive changes to a ligand is often based on intuition. Unfortunately, in many cases, that wealth of knowledge from experience is not always available. Young graduate students charged with designing new catalysts, new industry researchers trying to make processes more energy efficient and cheaper, or new catalyst design where little literature background is available, are all examples of this knowledge gap. That considered, it is a wonder there are not more tools available for researchers to use in catalyst development.

## 1.2 Tolman's Cone Angle and Electronic Parameter

When Chadwick Tolman published his methods of quantitatively characterizing various phosphine ligands, it was a huge advance in catalyst development.<sup>1</sup> Parameterizing phosphine ligands based on quantitative values for size and donor ability made it possible to develop educated ligand design ideas with minimal prior knowledge. Tolman's electronic parameter is based on  $\text{Ni}(\text{CO})_3\text{L}$  complexes, where L represents various phosphine-type ligands.<sup>2</sup> Using IR spectroscopy, Tolman measured the  $A_1$  stretching frequencies of the CO ligands to gain insight into how much



electron density the Ni is gaining from the L donation. When a ligand, L, donates more electron density to the Ni, the Ni can donate density into a  $\pi$  antibonding orbital of the CO ligands. This back donation causes a measurable change in the IR stretch of the CO ligands. So, as a  $\text{PR}_3$  donates more electron density to the metal, the  $\nu$  value decreases. The change in this frequency, when referenced to  $(\text{CO})_3\text{NiP}(\text{tBu})_3$  is known as Tolman's electronic parameter, or  $\nu$ .

Tolman's cone angle ( $\theta$ ) is a simple and effective method for comparing the sterics of various phosphines.<sup>1,3</sup> Tolman made models of each phosphine and arranged the models in a steric conformation that was as small as possible. The cone was then generated by making a cylindrical cone with its apex 2.28 Å from the P atom and the sides of the cone just touching the edges of the outermost atoms of the substituents. The measurement,  $\theta$ , is the apex angle of the cone. A diagram is shown in Figure 1-1 below.

Folding the ligand into the smallest possible conformation allowed the comparisons between phosphines to be systematic rather than random due to orientation of the model. The 2.28 Å distance effectively adjusted the measurements to a P-Ni bond length. Both assumptions are quite crude, but considering the simplicity of the measurement, the Tolman cone angle has proven to be quite useful. The parameter  $\theta$  set a standard for turning qualitative descriptions of ligand size into a quantitative measure.



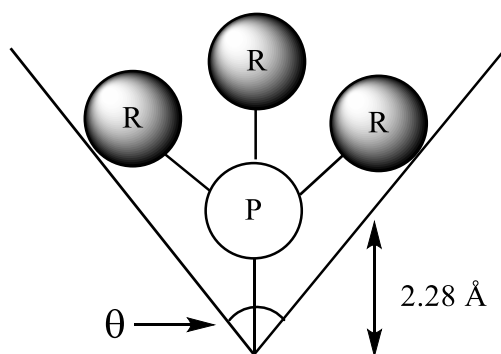


Figure 1-1. Representation of Tolman Cone Angle<sup>1</sup>

### 1.3 Advancements in Modeling Ancillary Ligands

Since Tolman's report of cone angle there have been developments made to improve the system. The most useful advances have been modelling sterics based on experimental structural data, rather than models, and measuring sterics of ligands with less regular shapes.<sup>4-8</sup> One method that has proven to be useful to our research is percent buried volume ( $\%V_{\text{bur}}$ ).<sup>4,9</sup> This program allows a user to define a radius from the metal center (3.5 Å is the program default) and project a sphere around the metal center at that radius. The program calculates the percentage of the sphere occupied by a given ligand. In this way, percent buried volume differs from the Tolman cone angle in that only atoms *within* the sphere contribute sterically, rather than a steric projection of the entire ligand. As a result, Cavallo's program enables users to define steric parameters for ligands that are less symmetric than phosphines. Take, for example, N-heterocyclic carbene (NHC) ligands. This class of ligands is becoming more prevalent. For instance, Grubb's second generation catalyst reported by Hoveyda uses an NHC ligand.<sup>10</sup> These ligands are far from cylindrical. If we were to try to define a cone angle for NHC ligands, which profile should be used? Figure 1-2 shows how choosing a different profile drastically changes the output.



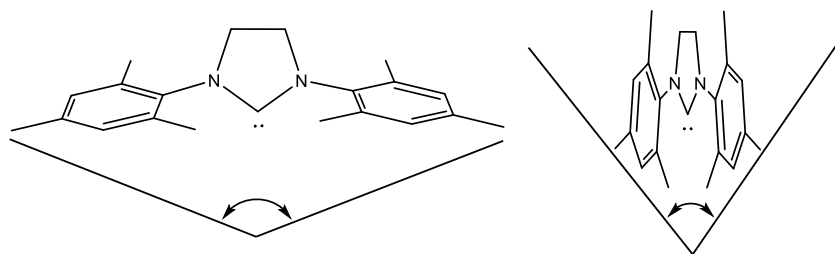


Figure 1-2. Comparison of different NHC ligand profiles and resulting cone angle.

Because of the enormous difference in profiles, it is likely that neither extreme is accurate by a cone angle approximation. Even Tolman's system to evaluate asymmetric phosphines, which is simply averaging the  $\theta$  values for each R-group, cannot be applied to NHC ligands. A program like % $V_{\text{bur}}$  is much more useful in situations like this. Figure 1-3 shows how the buried volume program differs. The ligand in the figure is a 2-aryl substituted pyrrole, because % $V_{\text{bur}}$  simply measures sterics of the ligand close to the metal, the shape of the ligand is irrelevant. As mentioned, the program also uses structural data such as a crystal structure or theoretically optimized structures to calculate the steric parameter. The recent update to the program has also made it possible to get a multidimensional steric map to see where the most sterically crowded areas of the ligand are (Figure 1-3, bottom).<sup>9</sup>



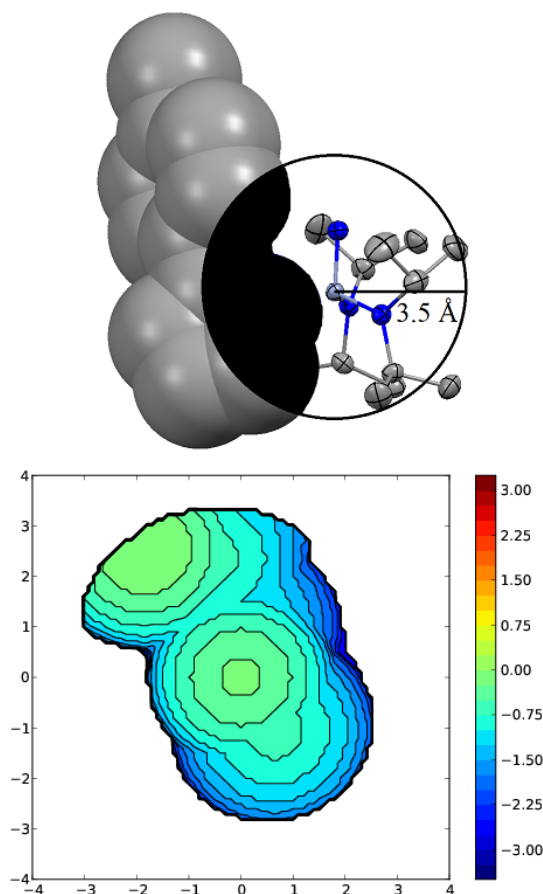


Figure 1-3. Top: Graphical representation of % $V_{\text{bur}}$ . Black shaded area represents buried volume. Bottom: Steric map output from SambVca 2.0 program.<sup>9</sup> The x and y axis are distance from center in Å. The map cuts off at 3.5 Å due to our defined radius. The colored contour represents the distance in angstroms in the z direction (perpendicular to the plane of the page).

Like the steric parameter, there are limitations to the Tolman electronic parameter ( $\nu$ ). Since Tolman's original report, developments have been made to improve accuracy, risks associated with the measurement (the starting material  $\text{Ni}(\text{CO})_4$  is very toxic), and its application to modeling reactions.<sup>11-13</sup> Despite the innovations, if a chemist wants to develop a reaction based on a metal in a high oxidation state, Ti(IV) for example, phosphines are rarely going to be the ligand of choice.

Other methods of ligand parameterization, including Lever's analysis of electrochemical potentials of Ru complexes and Gusev's computational expansion of the Tolman parameter, support a wider variety of ligands.<sup>12,14</sup> In Lever's study, ligands were analyzed by their effect on



the redox potential of Ru(III)/Ru(II). In Gusev's study, the detailed theoretical analysis includes a wide variety of L-type ligands. In either case though, the numbers are still not necessarily applicable to metals in higher oxidation states. This is primarily due to the differences in bonding between a ligand and a metal in a high or low oxidation state. More specifically, the high electronegativity of HVMs, and the availability of acceptor orbitals, means bonding between ligands and HVMs is very dependent on ligand to metal  $\pi$ -interactions. In contrast,  $\pi$ -interactions in low valent metal systems are usually metal to ligand based. Because of this, the preferred ligand choice in each system is quite different. Low valent metals often bond more strongly to good  $\pi$ -accepting ligands while high valent metals typically prefer  $\pi$ -donating ligands.

#### **1.4 Considerations for High Valent Metals**

The difference in metal-ligand interaction leads to a vastly different set of ancillary ligands in HVM-based catalysts. Ancillary ligands vary from alkoxides (e.g. Kulinkovich cyclopropanation and Sharpless epoxidation catalysts) to pyrroles (e.g. Odom group's hydroamination catalysts), to cyclopentadienyl (Cp) rings and amides (e.g. Dow's ethylene polymerization catalysts).<sup>15-19</sup> The wide variety of ligands employed in HVM catalysis poses the most significant hurdle in comparing one ligand set to another. Traditionally, the only way to compare ligands against each other was to use metrics such as  $pK_a$ , or Hammett parameters.<sup>20-21</sup> Such metrics deployed in discussions about ligands on HVM's still fail to make a complete description. Simple values based on interactions of the ligand with a proton do not accurately represent the interaction of the same ligand with a HVM. Much like the differences between low and high valent metals, interactions between a ligand and proton cannot accurately account for the  $\pi$ -effects of the ligand.



## 1.5 Titanium Catalysis

The lack of tools to develop high valent metal catalyzed reactions is unfortunate. There are many advantages to using high valent metals in catalysis. One such advantage is the abundance of early transition metals.<sup>19</sup> While metals such as Pd, Pt, Ru, and Ir catalyze a number of incredibly useful reactions, the cost associated with using these elements can be a deterrent. That alone, though, does not warrant investigation of alternatives. The real driving force for using early transition metals is the difference in reactivity they display.

Our group has developed a number of interesting transformations based on a series of titanium catalysts, but this dissertation will focus on only hydroamination.<sup>19, 22</sup> A general mechanism for hydroamination is shown in Figure 1-4. This mechanism is adapted from a report by Bergman where many intermediates in the reaction were isolable through stoichiometric reactions.<sup>23</sup>



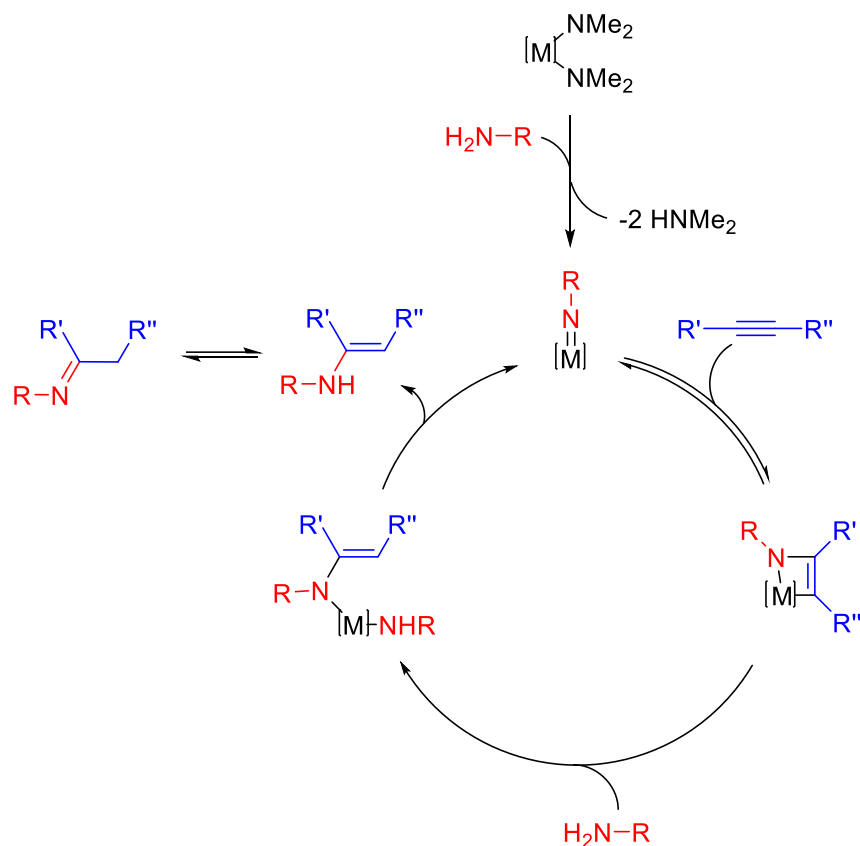


Figure 1-4. Hydroamination catalytic cycle.<sup>19</sup>

The mechanism for hydroamination that Bergman elucidated (shown above), proposed a rate-limiting step where  $\alpha$ -elimination of amine results in regeneration of a metal imide.<sup>23</sup> This step is dependent on proton transfer from one coordinated amide to another. Making the metal center more Lewis acidic may increase this rate by increasing the acidity of the protons on the dative amine, thereby increasing the rate of protonation. The first step to make a catalyst more Lewis acidic, is to adjust the ancillary ligands. Here again, though, what changes can be made to make the metal center more Lewis acidic?



## 1.6 Ligand Donor Parameter

In 2011 the Odom group answered this question with a report measuring various ligand donation abilities for HVM systems.<sup>24</sup> The system that was developed employed a Cr(VI) metal center as the reporter. Because the output is derived from a  $d^0$  metal, the results are better suited for application in HVM catalysis. The ligand donation parameter, LDP, is a measurement system that could be regarded as the high valent analogue to the Tolman electronic parameter. In place of the traditional carbonyl  $A_1$  stretching frequency as a reporter, the LDP system uses a Cr-N bond rotation to measure donation from the ligand under investigation. A model complex is shown in Figure 1-5 below.

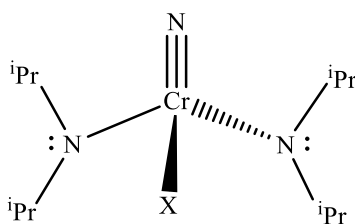


Figure 1-5. Representative chromium structure for LDP determination.<sup>24</sup>

The LDP system has been described in detail in the original publication, but we will briefly discuss it here.<sup>24</sup> The LDP system functions through a competition for electron density. The highly electronegative Cr(VI) center has available  $\pi$ -acceptor orbitals. Depending on the X ligand under study, availability of the acceptor orbitals is variable. When X is a poor donor, the acceptor orbitals are more vacant, allowing the  $N^iPr_2$  groups to donate their nitrogen lone pair from the nitrogen to the chromium. This donation creates double bond character in the Cr-N bond, hindering rotation about it. Thus, when X is a poor donor the barrier to rotation about the Cr-N bond is high and, if X is a strong donor, the Cr-N bond has mostly single bond in character, and the barrier to rotation is low.



The barrier to rotation is measured using a simple series of NMR experiments to determine a rate of rotation about the Cr-N bond.<sup>24-25</sup> It is important to note that this is only possible because the hindered rotation of the Cr-N bond creates unique chemical shifts for the *syn*- and *anti*-isopropyl groups, and the rate of rotation about the Cr-N bonds lie within the window of the NMR time scale. Using the Eyring equation, we can convert the rate of rotation into a free energy of activation, and, using an assumption about the entropy, we can convert the free energy value to a temperature independent enthalpy of activation,  $\Delta H^\ddagger$ . In short, an X ligand that donates substantial electron density to a metal center will result in a low  $\Delta H^\ddagger$  and an X ligand that is a poor electron density donor will have a high  $\Delta H^\ddagger$ , or LDP. It is worth noting that in this system, the competition for electron density is based on both  $\sigma$  and  $\pi$  effects, so the LDP is a sum of all electron density donation.

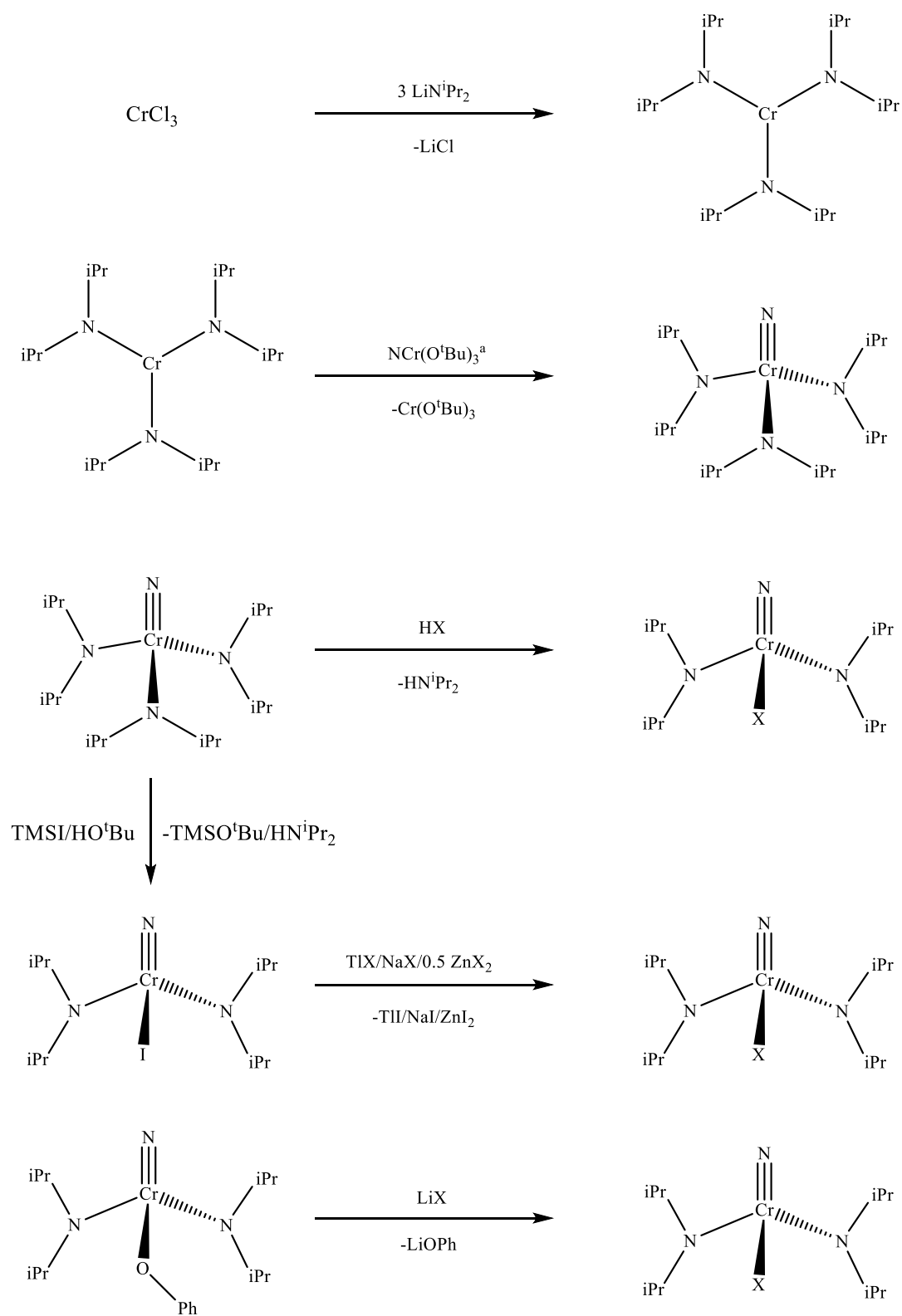
It is worth stating that we measure and report LDP values to two decimal places, for example the LDP of pyrrole is 13.64 kcal/mol. This is not meant to imply that we can accurately measure a  $\Delta H^\ddagger$  to the hundredth of a kcal. Rather, this is indicative of the precision with which we can perform these measurements. Different researchers on different instruments can reproduce LDP values with standard deviations of only calories. Thus, the difference between ligands is considered quite accurate.

Much like the Tolman system, the Odom group aimed to provide a complete characterization of the ligands studied. This means providing a steric analysis of the ligands as well. Fortunately, almost all of the chromium complexes synthesized are crystalline, so detailed steric analysis was also performed.<sup>24</sup>



In general, the synthesis of the chromium complexes used in the LDP analysis is quite straightforward. Scheme 1-1 highlights the most common synthetic strategies to access molecules to study.





Scheme 1-1. General synthesis of chromium starting materials for LDP analysis. <sup>a</sup>Synthesized using literature procedure.<sup>26</sup>



Over the years since the original LDP publication, a vast array of ligands has been investigated using the LDP method. The values that were determined at the time of the original publication are displayed in Figure 1-6.

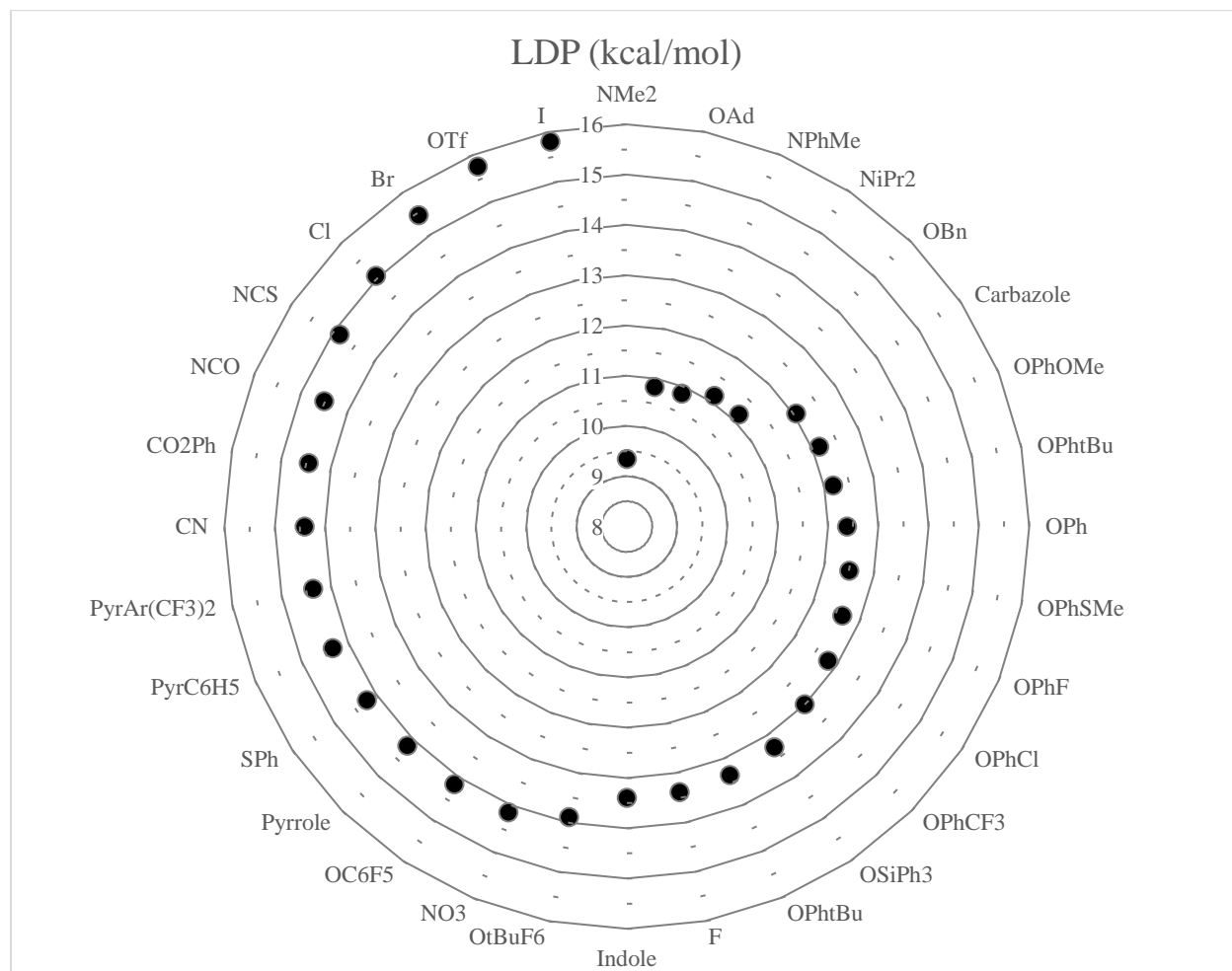


Figure 1-6. LDP values of previously reported ligands.<sup>24</sup>

As can be seen in Figure 1-6, the halides increase in donor ability as they decrease in size, with fluoride being the strongest donor. This effect correlates directly with the orbital overlap from NBO calculations.<sup>27</sup> Additionally, it was shown that the series of *para*-substituted phenols fit well against their respective Hammett parameters.<sup>24</sup> In short, the values derived from the chromium system were benchmarked against a variety of other metrics including orbital overlap, angular



overlap model, Hammett parameters,  $^{13}\text{C}$  NMR data, spectrochemical data, and  $\text{p}K_{\text{a}}$ 's.<sup>24, 27</sup> All of these correlations proved that LDP was, in fact, an accurate representation of a ligand's donation ability to a high valent transition metal, but they undersell the utility of the LDP system.

### 1.7 Quantitatively Modeling Reactions

The goal for the ligand donor parameterization is to analyze reactions such as HVM catalyzed transformations, and use the knowledge gained to improve the reactions. As Tolman highlighted, it is simple to model a property of a compound,  $Z$  (IR stretching frequencies, reaction rates, etc.) as a function of sterics or a function of electronics. It is also quite easy to measure the same property as a function of both parameters though. Equation 1 below highlights the simplest case where a property,  $Z$ , shows dependence on both sterics and electronics.

$$Z = a(\nu) + b(\theta) + c \quad (1)$$

In this equation,  $a$ ,  $b$ , and  $c$  are all fitting parameters that scale with the relative magnitude of the effects of the electronics and sterics. For example, if  $a$  is a large value relative to  $b$ , it implies that the electronics have a large effect on property  $Z$ . Furthermore, the sign of the fitting parameters gives information about how each parameter affects  $Z$ . If, for instance,  $Z$  represents a reaction rate constant and  $b$  is a negative number, it implies that as the sterics increase, the rate of reaction is slowed.

### 1.8 Conclusions

Reaction models of this type can be useful at any point in the phases of catalyst development. Models like Equation 1 can provide a wealth of information about a reaction, as they detail what property of the ligand should be given highest priority, and how it should be adjusted. This allows a researcher to screen a few reactions, analyze and model the results, and then make educated decisions about what changes to make and new catalysts to design. There is no need for prior



knowledge, only the need to make educated interpretations of data, eliminating dependence on years of experience to successfully develop catalysts. The models, though, are not just useful to initial stages of development. As will be discussed in detail in the coming chapters, these equations can also be deployed in more complex situations and used to discover much more information about a reaction.



## REFERENCES



## REFERENCES

1. Tolman, C. A., *Chem. Rev.* **1977**, 77 (3), 313-348.
2. Tolman, C. A., *J. Am. Chem. Soc.* **1970**, 92 (10), 2953-2956.
3. Tolman, C. A., *J. Am. Chem. Soc.* **1970**, 92 (10), 2956-2965.
4. Poater, A.; Cosenza, B.; Correa, A.; Giudice, S.; Ragone, F.; Scarano, V.; Cavallo, L., *Eur. J. Inorg. Chem.* **2009**, 2009 (13), 1759-1766.
5. Taverner, B. C., *J. Comput. Chem.* **1996**, 17 (14), 1612-1623.
6. Guzei, I. A.; Wendt, M., *Dalton Trans.* **2006**, (33), 3991-3999.
7. White, D. P.; Anthony, J. C.; Oyefeso, A. O., *J. Org. Chem.* **1999**, 64 (21), 7707-7716.
8. Harper, K. C.; Bess, E. N.; Sigman, M. S., *Nat. Chem.* **2012**, 4 (5), 366-374.
9. Falivene, L.; Credendino, R.; Poater, A.; Petta, A.; Serra, L.; Oliva, R.; Scarano, V.; Cavallo, L., *Organometallics* **2016**, 35 (13), 2286-2293.
10. Kingsbury, J. S.; Harrity, J. P. A.; Bonitatebus, P. J.; Hoveyda, A. H., *J. Am. Chem. Soc.* **1999**, 121 (4), 791-799.
11. Liu, H. Y.; Eriks, K.; Prock, A.; Giering, W. P., *Organometallics* **1990**, 9 (6), 1758-1766.
12. Gusev, D. G., *Organometallics* **2009**, 28 (3), 763-770.
13. Nelson, D. J.; Nolan, S. P., *Chem. Soc. Rev.* **2013**, 42 (16), 6723-6753.
14. Lever, A. B. P., *Inorg Chem* **1990**, 29 (6), 1271-1285.
15. Kulinkovich, O. G.; Sviridov, S. V.; Vasilevski, D. A., *Synthesis-Stuttgart* **1991**, 1991 (3), 234-234.
16. Kulinkovich, O. G., *Chem. Rev.* **2003**, 103 (7), 2597-2632.
17. Finn, M. G.; Sharpless, K. B., *J. Am. Chem. Soc.* **1991**, 113 (1), 113-126.
18. Klosin, J.; Fontaine, P. P.; Figueroa, R., *Acc. Chem. Res.* **2015**, 48 (7), 2004-2016.
19. Odom, A. L.; McDaniel, T. J., *Acc. Chem. Res.* **2015**, 48 (11), 2822-2833.
20. Hammett, L. P., *J. Am. Chem. Soc.* **1937**, 59 (1), 96-103.
21. Hansch, C.; Leo, A.; Taft, R. W., *Chem. Rev.* **1991**, 91 (2), 165-195.



22. Odom, A. L., *Dalton Trans.* **2005**, (2), 225-233.
23. Walsh, P. J.; Baranger, A. M.; Bergman, R. G., *J. Am. Chem. Soc.* **1992**, *114* (5), 1708-1719.
24. DiFranco, S. A.; Maciulis, N. A.; Staples, R. J.; Batrice, R. J.; Odom, A. L., *Inorg. Chem.* **2012**, *51* (2), 1187-1200.
25. Jarek, R. L.; Flesher, R. J.; Shin, S. K., *J. Chem. Educ.* **1997**, *74* (8), 978-982.
26. Chiu, H. T.; Chen, Y. P.; Chuang, S. H.; Jen, J. S.; Lee, G. H.; Peng, S. M., *Chem. Commun.* **1996**, (2), 139-140.
27. Bemowski, R. D.; Singh, A. K.; Bajorek, B. J.; DePorre, Y.; Odom, A. L., *Dalton Trans.* **2014**, *43* (32), 12299-12305.



## Chapter 2. Investigations of Chromium(VI) Nitrido Cyclopentadienyl Bonding System

### 2.1 Introduction

One aspect of organometallic chemistry where the utility of the LDP framework can be exploited is in analysis of the cyclopentadienyl ligand. Cyclopentadienyl, or Cp, has been a staple ligand in organometallic and inorganic chemistry for many years and arguably started the field of organometallic chemistry altogether.<sup>1-5</sup> The Cp ligand can bind to a metal center in a variety of ways, including the  $\eta^5$ ,  $\eta^3$ , and  $\eta^1$  binding modes as shown in Figure 2-1. In many cases it is obvious what confirmation the Cp ring takes, but, sometimes, Cp binding is rather ambiguous. Using a few compounds synthesized previously in the group, in addition to new syntheses, we set out to shed some light on binding modes of the cyclopentadienyl ring.<sup>6</sup>

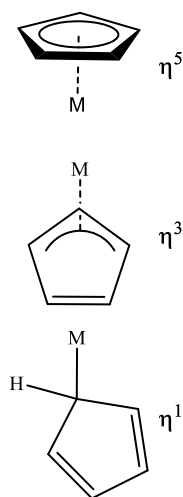


Figure 2-1. Representation of the three typical binding modes of cyclopentadienyl.

The compounds under investigation are a rare class of complexes bearing a nitride and a Cp ligand. It is surprising how few NMCp complexes were known at the time of this study. In fact, prior to this work, only four complexes bearing both a nitride and Cp ligand had been structurally



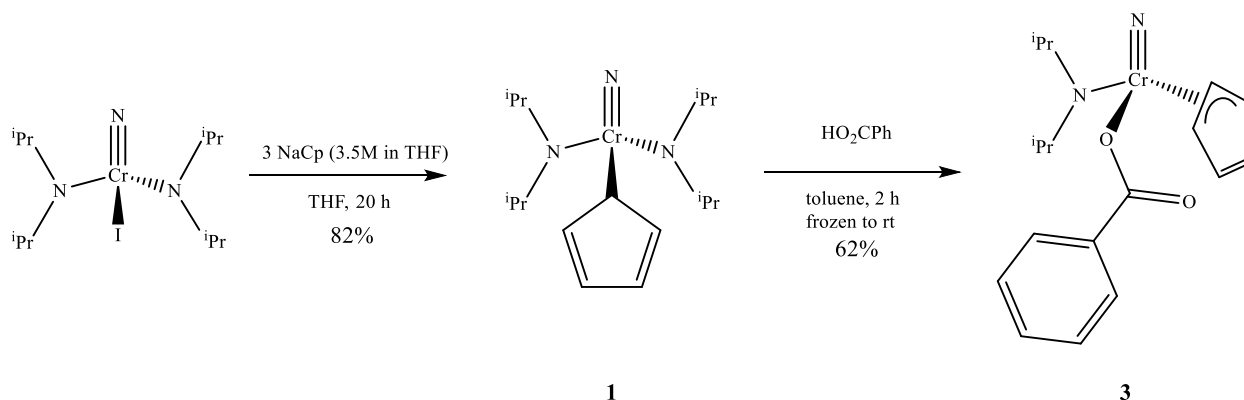
characterized.<sup>7-10</sup> This might seem like a specific molecule moiety to compare, but when we considered the prevalence of group (IV) metallocene complexes in polymerizations, it is surprising that more hasn't been done with the isolobal  $\text{NCr}(\text{N}^i\text{Pr}_2)_2$  framework.<sup>11-14</sup>

## 2.2 Synthesis and Characterization

Previously, a few compounds using the  $\text{NCr}(\text{N}^i\text{Pr}_2)_2$  fragment and Cp-type ligands were made.<sup>6</sup> Namely the  $\text{NCr}(\text{N}^i\text{Pr}_2)_2\text{Cp}$  (**1**) and  $\text{NCr}(\text{N}^i\text{Pr}_2)_2\text{Indenyl}$  (**2**) molecules. Compound **1** was produced through reaction of  $\text{NCr}(\text{N}^i\text{Pr}_2)_2\text{I}$  with a solution of NaCp in THF (scheme 2-2). Compound **2** was produced similarly using metathesis of Li-Indenyl. Interestingly, the preferred binding mode for the Cp ring in **1** and **2** is quite clearly  $\eta^1$ . In this mode, the Cp ring formally donates two electrons, acting only as a  $\sigma$ -donor. It was unclear whether the Cp adopted the confirmation due to electronic or steric effects. We were surprised to see, though, that in the  $^1\text{H}$  NMR, the Cp ring in **1** appears as a sharp singlet, even at low temperature. This is consistent to what is seen in the “ring whizzing”  $\text{Fe}(\text{CO})_2(\eta^5\text{-Cp})(\eta^1\text{-Cp})$  system reported by Wilkinson.<sup>15</sup> Compound **2** also shows interesting characteristics in the  $^1\text{H}$  NMR. The resonance for protons located on the 1 and 3 position of the ring are equivalent due to rapid exchange. We were unable to reach slow exchange on our instrumentation, but the coalescence point of the signal occurs at  $-50\text{ }^\circ\text{C}$ .

To test whether we could induce a haptotropic shift of the Cp ring in **1**, we began attempting to change the ligand framework around the chromium center. Reaction of **1** with benzoic acid results in protonation of an amide and formation of  $\text{NCr}(\text{N}^i\text{Pr}_2)(\text{Cp})(\text{O}_2\text{CPh})$ , **3** (Scheme 2-1).





Scheme 2-1. Synthesis of  $\text{NCr}(\text{N}^i\text{Pr}_2)_2(\text{Cp})$ , **1**, and  $\text{NCr}(\text{N}^i\text{Pr}_2)(\text{Cp})(\text{O}_2\text{CPh})$ , **3**, from  $\text{NCr}(\text{N}^i\text{Pr}_2)\text{I}$ .

With substitution of a diisopropylamido ligand by the benzoate, the competition for  $\pi$  donation is reduced.<sup>16</sup> As a result, the Cp ligand goes to what appears to be an  $\eta^3$  conformation. Importantly, the reduced electron density is not the only factor changing. The steric bulk is significantly reduced in the substitution process as well. Regardless of the cause, there is a significant difference in the Cp ring binding mode between **1** and **3**, which is obvious even with visual comparison of the solid-state structures, see Figure 2-2 below.



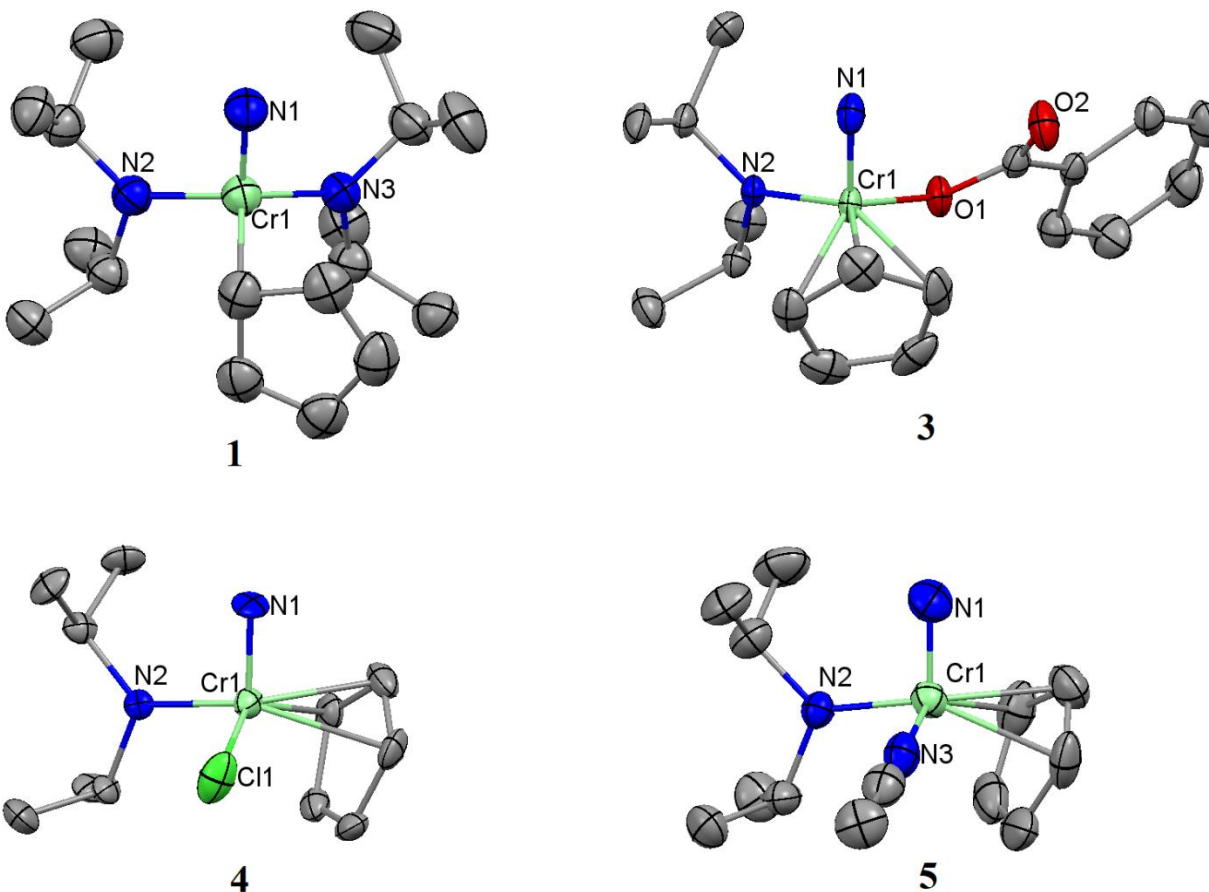
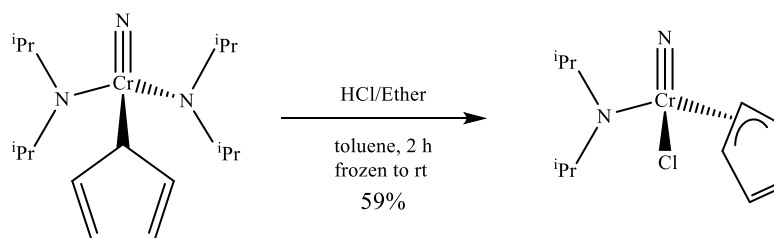


Figure 2-2. Crystals structures of **1**, **3**, **4**, and **5**. Ellipsoids displayed at the 50% probability level. All hydrogens, solvents in the lattice, and counterion from **5**, removed for clarity.

Further reduction of both electron density and steric hinderance can be achieved by protonation of **1** with ethereal hydrochloric acid yielding a substitution of a diisopropylamido with a chloride to make  $\text{NCr}(\text{N}^i\text{Pr}_2)(\text{Cp})(\text{Cl})$  (**4**) (Scheme 2-2). Since chromium is even more electron deficient, and less sterically hindered, with a chloride than the benzoate, we postulated the Cp ring would slip closer to chromium.<sup>16</sup> In the solid state structures, the Cp rings of **3** and **4** are essentially equal in orientation with respect to the Cr metal center.





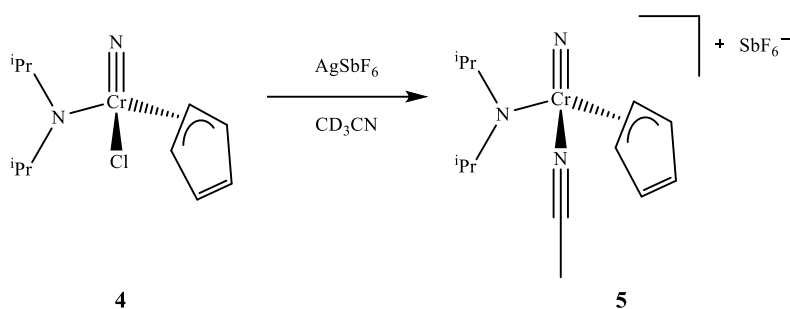
Scheme 2-2. Synthesis of  $\text{NCr}(\text{N}^i\text{Pr}_2)(\text{Cp})(\text{Cl})$ , **4**.

We began to wonder if we could force the Cp to bind even tighter to the Cr. We thought it should be possible to achieve an  $\eta^5$  confirmation since the resulting structures are isoelectronic with classical group(IV) metallocene- type molecules, which are ubiquitous in polymerization catalysis.<sup>11-14</sup>

Treatment of the **4** with silver hexafluoroantimonate, or a similar noncoordinating anion, in acetonitrile yields the  $\text{NCr}(\text{N}^i\text{Pr}_2)\text{Cp}(\text{NCMe})$  (**5**), Scheme 2-3. Compound **5** was only produced *in situ* due to its low thermal stability. We tried a variety of other methods to generate **5** including other noncoordinating anions, super acids (such as  $\text{HSbF}_6$ ), and other metathesis reactions. In most cases **5** was generated (indicated by NMR spectroscopy), but not in isolable quantities. Despite the instability and small reaction scale we were still able to produce X-ray quality single crystals as shown in Figure 2-2.

We were somewhat surprised to find that complex **5** coordinated an equivalent of acetonitrile. It is likely that the Cp engaging in an  $\eta^5$ -interaction does not provide the electron density necessary to stabilize a three coordinate Cr(VI) cation. Still, due to the poorer donation ability of the coordinated acetonitrile, relative to Cl, the Cp ring is once again brought slightly closer to chromium to stabilize the loss of electron density.<sup>17</sup>





Scheme 2-3. In situ synthesis of  $\text{NCr}(\text{N}^i\text{Pr}_2)\text{Cp}(\text{NCMe})$ , **5**.

Thus far, the discussion about the coordination mode has been qualitative based on solid state structure inspection. We wondered if the visual analysis could be a result of packing forces in the solid state. As such, we turned to theory to calculate bond orders of the Cr-C bonds to compare **1**-**5**.

### 2.3 Bonding Analysis

For complexes **1** and **2**, where both diisopropylamido ligands are present to compete for electron density and space, Mayer bond order shows a strong bond ( $>0.7$ ) to only one carbon, while the other four remain essentially nonbonding, classic  $\eta^1$ -Cp binding.<sup>18-19</sup> When electron density is removed from the metal center, as shown in **3** and **4**, three carbons are involved in bonding and the remaining two have only relatively weak interaction with chromium. This appears to be an  $\eta^3$ -interaction. Even when we have removed as much electron density from chromium as possible and made as much space around the metal center as we could, in compound **5**, the Cp ring barely slid closer to an  $\eta^5$  confirmation. Consequently, cationic compound **5** also has the highest average bond order for all five carbons at 0.32 but remains in what appears to be an  $\eta^3$  confirmation. The Mayer bond order analysis is shown in Figure 2-3.



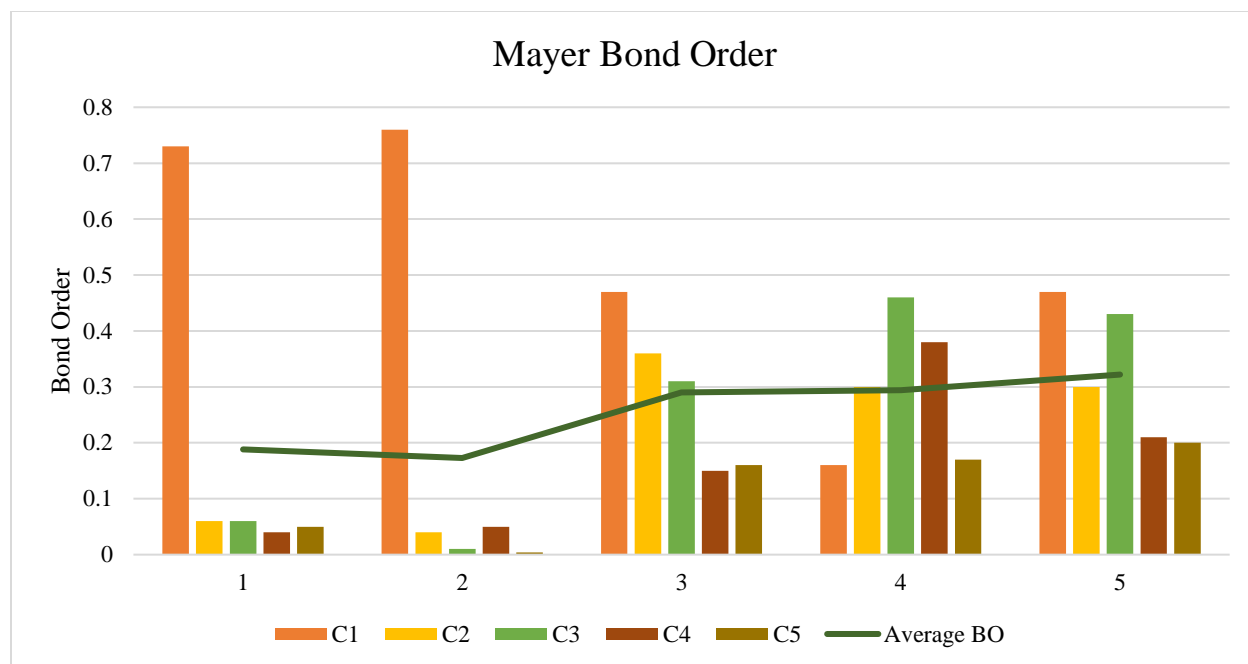


Figure 2-3. Mayer bond order analysis of **1-5**.

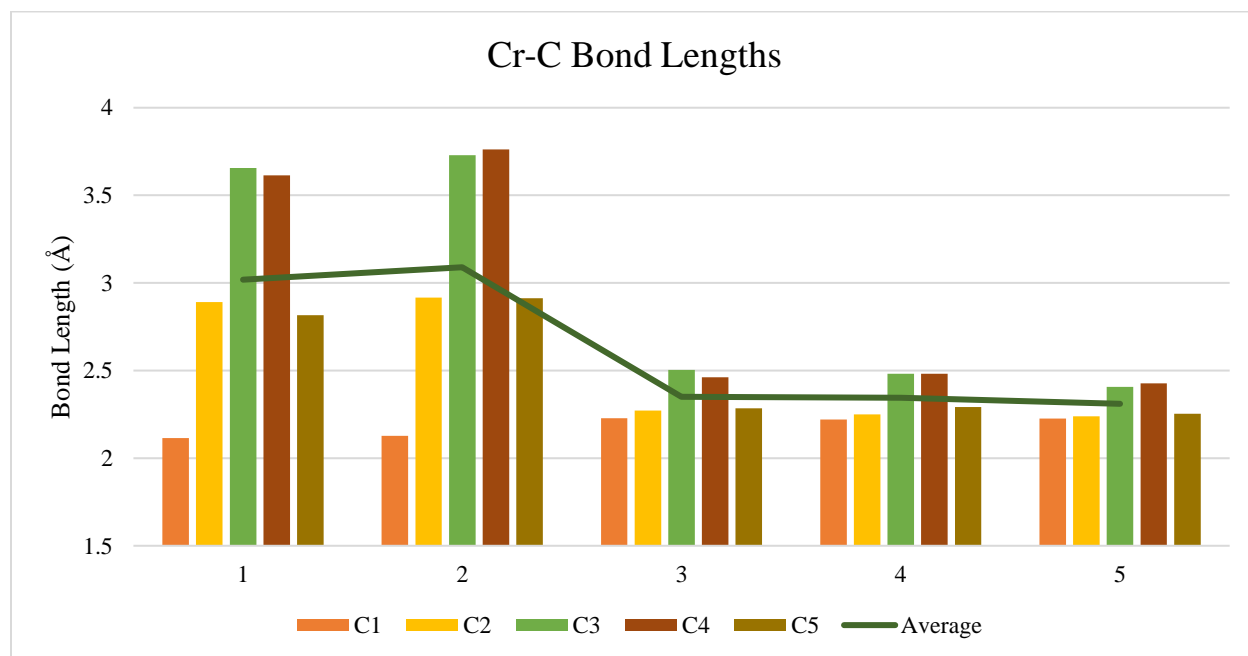


Figure 2-4. Cr-C bond lengths and averages for compounds **1-5**.

Cp is an example of a ligand that can adapt and stabilize changing electronic conditions on a metal. It was quite apparent that as the Lewis acidity and available space, of the Cr center was



increased, the donation of the Cp ring compensated accordingly. It is interesting that in the reaction to form **5**, the complex coordinated an acetonitrile rather than allowing the Cp ring to form a full  $\eta^5$ -interaction. Maybe the Cp ring in **5** is in fact as close to an  $\eta^5$  interaction as the molecule can achieve. To try and get a better understanding, we decided to benchmark our series of coordination modes of **1-5** to some known compounds that could be considered “standards” for the hapticity of Cp.

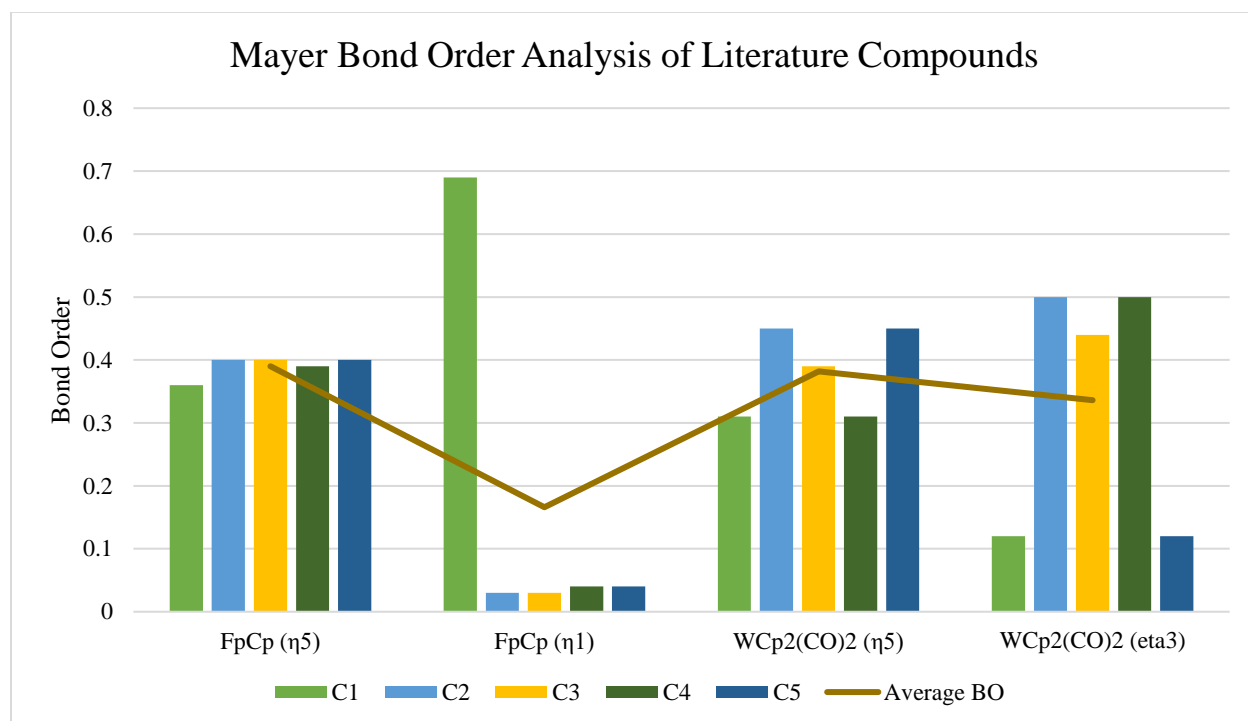


Figure 2-5. Mayer bond order analysis of the literature reported “standards.”<sup>15, 20-21</sup>



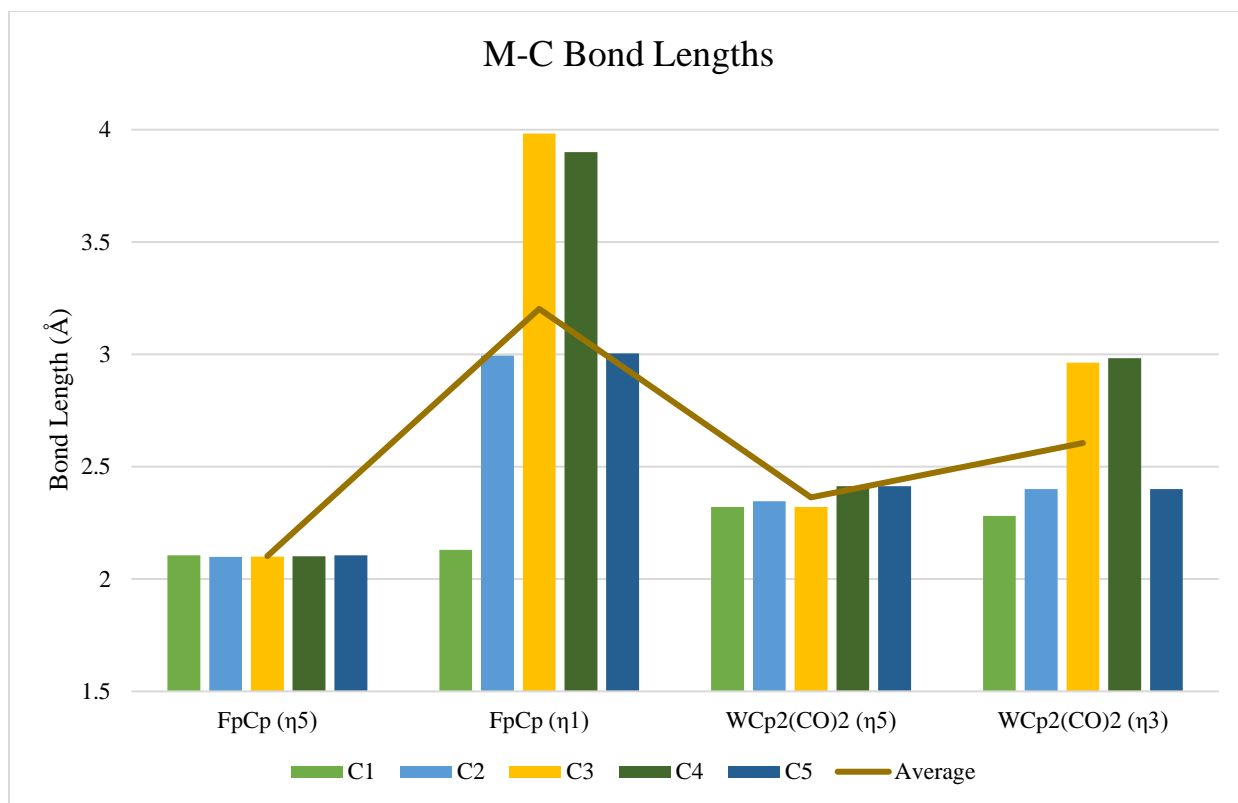


Figure 2-6. M-C bond lengths and averages for the literature reported “standards.”

We selected two complexes from the literature that represent what could be considered as standards for the  $\eta^5$ ,  $\eta^3$ , and  $\eta^1$  coordination modes. The Fe complex  $\text{Fe}(\eta^5\text{-Cp})(\eta^1\text{-Cp})(\text{CO})_2$ , [Fe], has ideal examples of the  $\eta^1$  and  $\eta^5$  coordination modes.<sup>15, 20</sup> The tungsten complex  $\text{W}(\eta^5\text{-Cp})(\eta^3\text{-Cp})(\text{CO})_2$ , [W], on the other hand, has ideal examples of both the  $\eta^5$  and  $\eta^3$  coordination modes.<sup>21</sup> A MBO analysis of those model complexes is shown in Figure 2-5. It is immediately obvious when comparing **1** and **2** to [Fe] that, in the chromium complexes bearing both diisopropylamide ligands, the Cp and indenyl rings are in a  $\eta^1$  confirmation. Both the Mayer bond order and crystallographic bond lengths agree well on that point. The remaining complexes **3**, **4** and **5**, however, are clearly somewhere between the  $\eta^1$  and  $\eta^5$  conformations of the [Fe] complex.

Comparing to the [W] complex, the Cp rings in **3** and **4** appear quite close to an  $\eta^3$  confirmation, which agrees well with the crystallographic bond lengths. Complex **5** on the other hand does not



make the distinction so clear. The distribution of bond lengths, especially, looks more like the  $\eta^5$  coordinated Cp ring in the [W] molecule, while the Mayer bond order calculations more closely resemble the  $\eta^3$  mode. When compared to the [Fe]  $\eta^5$  ring, it seems unreasonable to classify it as a true  $\eta^5$  ring. The Cp ring in complex **5** is likely best described as a strong  $\eta^3$  interaction.

## 2.4 Conclusions

As with most concepts in chemistry, these various coordination modes are simply “bookkeeping” methods of tallying things like electron counts and formal charges. They should not be considered as the only allowed modes, and, in fact, should be considered a continuum as highlighted with complex **5** here, which seems intermediate to  $\eta^5$  and  $\eta^3$ . Regardless, this study highlights the flexibility of the Cp ligand to stabilize a variety of states at a metal center. It can compensate for both steric and electronic perturbations at the metal center, which is a likely reason for its deployment in so many organometallic systems.<sup>3-5, 11-13</sup>

## 2.5 Experimental

**Experimental taken from recent publication: This can be located at:**

*Organometallics*, **2015**, 34(18), 4567

*General Considerations.* All reactions and manipulations were carried out in an MBraun glovebox under a nitrogen atmosphere and/or using standard Schlenk techniques. Ethereal solvents, pentane, and toluene were purchased from Aldrich Chemical Co. and purified by passing through alumina columns to remove water after sparging with dinitrogen to remove oxygen. Silver hexfluoroantimonate was purchased from Aldrich Chemical Co. and used as received. *Tert*-butanol was purchased from Jade Chemical Co. and dried over 3 Å molecular sieves to remove water after being sparged with dry nitrogen to remove oxygen. Trimethylsilyl iodide was purchased from



Oakwood Chemical and distilled under dry nitrogen. FpCp was prepared using the literature procedure.<sup>9</sup>

All NMR solvents were purchased from Cambridge Isotopes Laboratories, Inc. Deuterated chloroform and acetonitrile were dried over 3 Å sieves and freeze–pump–thaw degassed. The NMR solvents were stored in the glove box in glass containers with a stopcock. Spectra were taken on Varian instruments located in the Max T. Rogers Instrumentation Facility at Michigan State University. These include a UNITYplus 500 spectrometer equipped with a 5 mm pulsed-field-gradient (PFG) switchable broadband probe and operating at 499.955 MHz (<sup>1</sup>H) and 125.77 (<sup>13</sup>C). <sup>1</sup>H NMR chemical shifts are reported relative to residual CHCl<sub>3</sub> in CDCl<sub>3</sub> as 7.26 ppm. <sup>13</sup>C NMR chemical shifts are reported relative to <sup>13</sup>C in CDCl<sub>3</sub> as 77.0 ppm. Single crystal X-ray diffraction data was collected in the Center for Crystallographic Research at MSU.

*Synthesis of NCr(N<sup>i</sup>Pr)<sub>2</sub>(Cp) (1):* Under an inert atmosphere, a scintillation vial was loaded with NCr(N<sup>i</sup>Pr)<sub>2</sub>(I) (0.500 g, 0.1271 mmol, 1 equiv.), 5 mL THF, and a stirbar. To this a 3.5 M THF solution of sodium cyclopentadienide (1.089 mL, 3.813 mmol, 3 equiv.) was added, and the solution was rapidly stirred for 20 h. The volatiles were removed in vacuo, and the residue was extracted with pentane (3 × 25 mL) and filtered through Celite. The volatiles were removed in vacuo yielding **1** as a brown powder. Diffraction quality crystals were obtained from a concentrated pentane solution of NCr(N<sup>i</sup>Pr)<sub>2</sub>(Cp) held at –30 °C (0.280 g, 1.051 mmol, 82% yield). <sup>1</sup>H NMR (CDCl<sub>3</sub>, –60 °C, 500 MHz): 6.16 (s, 5H, Cp), 4.88 (sept, *J*<sub>HH</sub> = 6.4, 2H, CH(CH<sub>3</sub>)<sub>2</sub>), 3.59 (sept, *J*<sub>HH</sub> = 6.3, 2H, CH(CH<sub>3</sub>)<sub>2</sub>), 1.72 (d, *J*<sub>HH</sub> = 6.3, 6H, CH(CH<sub>3</sub>)<sub>2</sub>), 1.42 (d, *J*<sub>HH</sub> = 6.4, 6H, CH(CH<sub>3</sub>)<sub>2</sub>), 1.04 (d, *J*<sub>HH</sub> = 6.2, 6H, CH(CH<sub>3</sub>)<sub>2</sub>). <sup>13</sup>C NMR (CDCl<sub>3</sub>, 25 °C, 125 MHz): 115.0, 58.3, 55.2, 30.4, 30.3, 23.3, 18.0. Anal. Calcd. for C<sub>17</sub>H<sub>33</sub>CrN<sub>3</sub>: C, 61.60; H, 10.03; N, 12.68. Found: C, 61.59; H, 9.97; N, 12.65. Mp: 90–92 °C (sub).



*Synthesis of  $\text{NCr}(\text{N}^i\text{Pr}_2)_2(\text{Ind})$  (**2**):* To a partially frozen solution of  $\text{NCr}(\text{N}^i\text{Pr}_2)_2(\text{I})$  (100 mg, 0.254 mmol, 1 equiv.) in ether (3 mL), a suspension of lithiated indene (34.2 mg, 0.280 mmol, 1.1 equiv.) in ether (2 mL) was added. This dark mixture was allowed to warm to room temperature and stirred for 18 h. The volatiles were then removed in vacuo, and the residue extracted with pentane, filtered through Celite, and evaporated to a dark orange/brown solid. The solids were dissolved in a minimal amount of pentane and chilled to  $-30\text{ }^\circ\text{C}$  overnight providing **2** as dark orange crystals (26 mg, 27% yield).  $^1\text{H}$  NMR ( $\text{CDCl}_3$ ,  $25\text{ }^\circ\text{C}$ , 500 MHz): 7.59 (dd,  $J_{\text{HH}} = 5.6, 3.2$ , 2 H, Ar), 7.02–7.07 (m, 3 H, Ar and  $\beta$ -Ind), 5.65 (br, 2 H, Ar), 4.82 (sept,  $J_{\text{HH}} = 6.3$ , 2 H,  $\text{CH}(\text{CH}_3)_2$ ), 3.48 (sept,  $J_{\text{HH}} = 6.3$ , 2 H,  $\text{CH}(\text{CH}_3)_2$ ), 1.46 (d, 12 H,  $\text{CH}(\text{CH}_3)_2$ ), 1.04 (d,  $J_{\text{HH}} = 6.4$ , 6 H,  $\text{CH}(\text{CH}_3)_2$ ), 0.90 (d,  $J_{\text{HH}} = 6.2$ , 6 H,  $\text{CH}(\text{CH}_3)_2$ ).  $^{13}\text{C}$  NMR ( $\text{CDCl}_3$ ,  $25\text{ }^\circ\text{C}$ , 125 MHz): (6 of the signals for the indenyl ligand are not observed due to broadening from fluxionality on the  $^{13}\text{C}$  NMR time scale) 136.7, 123.1, 122.4, 57.2, 54.8, 30.7, 29.3, 23.4, 19.9, 14.2. Anal. Calcd. for  $\text{C}_{21}\text{H}_{35}\text{CrN}_3$ : C, 66.11; H, 9.25; N, 11.01. Found: C, 65.68; H, 9.60; N, 10.95. Mp: 131–133  $^\circ\text{C}$  (dec.)

*Synthesis of  $\text{NCr}(\text{N}^i\text{Pr}_2)(\text{O}_2\text{CPh})(\text{Cp})$  (**3**):* Under an inert atmosphere a scintillation vial was loaded with **1** (0.178 g, 0.537 mmol, 1 equiv.), a stir bar, and toluene (4 mL). The vial was moved to a liquid nitrogen cooled cold well for 10 min. The reaction was stirred vigorously and benzoic acid (0.066 mg, 0.537 mmol, 1 equiv.) in toluene (6 mL) was added dropwise over 5 min. The solution turned dark red and was allowed to stir at room temperature for 2 h. The volatiles were removed in vacuo, and the residue was dissolved in 2 mL of toluene. The solution was filtered over Celite, layered with an equal volume of pentane, and held at  $-35\text{ }^\circ\text{C}$  yielding crystals of **3** (0.117 g, 0.333 mmol, 62%).  $^1\text{H}$  NMR (500 MHz,  $\text{CDCl}_3$ ,  $13\text{ }^\circ\text{C}$ ): 7.95 (dd,  $J_{\text{HH}} = 8.25\text{ Hz}$ ,  $J_{\text{HH}} = 1.5\text{ Hz}$ , 2 H, Ph), 7.41 (tt,  $J_{\text{HH}} = 7.0\text{ Hz}$ ,  $J_{\text{HH}} = 2.5\text{ Hz}$ , 1 H, Ph), 7.34 (t,  $J_{\text{HH}} = 7.5\text{ Hz}$ , 2 H, Ph),



6.14 (s, 5 H, C<sub>5</sub>H<sub>5</sub>), 5.56 (sept,  $J_{\text{HH}} = 6.0$  Hz, 1 H, NCH(CH<sub>3</sub>)<sub>2</sub>), 4.31 (sept,  $J_{\text{HH}} = 6.0$  Hz, 1 H, NCH(CH<sub>3</sub>)<sub>2</sub>), 2.11 (d,  $J_{\text{HH}} = 6.0$  Hz, 3 H, NCH(CH<sub>3</sub>)<sub>2</sub>), 1.75 (d,  $J_{\text{HH}} = 6.0$  Hz, 3 H, NCH(CH<sub>3</sub>)<sub>2</sub>), 1.29 (d,  $J_{\text{HH}} = 6.0$  Hz, 3 H, NCH(CH<sub>3</sub>)<sub>2</sub>), 1.11 (d,  $J_{\text{HH}} = 6.0$  Hz, 3 H, NCH(CH<sub>3</sub>)<sub>2</sub>). <sup>13</sup>C NMR (125 MHz, CDCl<sub>3</sub>, 13 °C): 170.74, 135.26, 130.77, 129.66, 127.83, 108.22, 73.71, 63.71, 31.06, 29.83, 20.64, 20.15. FT-IR (KBr): 1639.2 cm<sup>-1</sup> (ν<sub>s</sub> CO<sub>2</sub>), 1415.5 cm<sup>-1</sup> (ν<sub>a</sub> CO<sub>2</sub>). Satisfactory elemental analysis was not obtained after several attempts.

*Synthesis of NCr(N<sup>i</sup>Pr<sub>2</sub>)(Cp)Cl (4):* Under an inert atmosphere, a Schlenk flask was loaded with **1** (50 mg, 0.151 mmol, 1 equiv.) and ether (5 mL). To the solution of **1**, 2.0 M HCl (0.226 mL, 0.453 mmol, 3 equiv.) in ether was added rapidly. The dark mixture turns reddish, and some precipitate forms during addition. This mixture was stirred at room temperature for 30 min. The volatiles were then removed in vacuo, and the residue was washed with pentane (2 × 5 mL). The solid was then extracted with ether, filtered through Celite, and concentrated to ~2 mL. This dark solution was cooled to -30 °C overnight providing **4** as dark red crystals (24 mg, 59%). <sup>1</sup>H NMR (CDCl<sub>3</sub>, 25 °C, 500 MHz): 6.09 (s, 5 H, Cp), 5.23 (sept,  $J_{\text{HH}} = 6.5$ , 1 H, CH(CH<sub>3</sub>)<sub>2</sub>), 4.36 (sept,  $J_{\text{HH}} = 6.3$ , 1 H, CH(CH<sub>3</sub>)<sub>2</sub>), 2.17 (d,  $J_{\text{HH}} = 6.3$ , 3 H, CH(CH<sub>3</sub>)<sub>2</sub>), 1.80 (d,  $J_{\text{HH}} = 6.4$ , 3 H, CH(CH<sub>3</sub>)<sub>2</sub>), 1.26 (d,  $J_{\text{HH}} = 6.5$ , 3 H, CH(CH<sub>3</sub>)<sub>2</sub>), 1.20 (d,  $J_{\text{HH}} = 6.5$ , 6 H, CH(CH<sub>3</sub>)<sub>2</sub>). <sup>13</sup>C NMR (CDCl<sub>3</sub>, 25 °C, 125 MHz): 108.9, 74.7, 64.4, 30.8, 29.3, 20.2, 17.8. Anal. Calcd. for C<sub>11</sub>H<sub>19</sub>ClCrN<sub>2</sub>: C, 49.53; H, 7.18; N, 10.50. Found: C, 49.50; H, 7.56; N, 10.45. Mp: 121-123 °C (dec.)

*Synthesis of [NCr(N<sup>i</sup>Pr<sub>2</sub>)(Cp)(NCMe)][SbF<sub>6</sub>] (5):* Under an inert atmosphere, a scintillation vial was loaded with **4** (25 mg, 0.124 mmol, 1 equiv.) and CD<sub>3</sub>CN (1 mL). To this, a solution of AgSbF<sub>6</sub> (85 mg, 0.248 mmol, 2 equiv.) in CD<sub>3</sub>CN (1 mL) was added. The reaction was allowed to proceed and was monitored by <sup>1</sup>H NMR. After 4 d it was observed that all starting material peaks had disappeared. The volatiles were removed in vacuo, and the residue was washed with ether (5



mL). The solids were extracted with chloroform (1 mL), filtered through Celite, layered with ether, and chilled to  $-30\text{ }^{\circ}\text{C}$  for recrystallization. Despite being of quality for single crystal diffraction, the crystals obtained by this technique were unstable, and the bulk material was consistently impure. As a result, only the in situ  $^1\text{H}$  NMR and single crystal X-ray diffraction were successful for the characterization of this compound.  $^1\text{H}$  NMR ( $\text{CD}_3\text{CN}$ ,  $25\text{ }^{\circ}\text{C}$ , 500 MHz): 6.24 (s, 5 H, Cp), 5.33 (sept,  $J_{\text{HH}} = 6.3$ , 1 H,  $\text{CH}(\text{CH}_3)_2$ ), 4.67 (sept,  $J_{\text{HH}} = 6.2$ , 1 H,  $\text{CH}(\text{CH}_3)_2$ ), 2.15 (d,  $J_{\text{HH}} = 6.2$ , 3 H,  $\text{CH}(\text{CH}_3)_2$ ), 1.78 (d,  $J_{\text{HH}} = 6.2$ , 3 H,  $\text{CH}(\text{CH}_3)_2$ ), 1.28 (d,  $J_{\text{HH}} = 6.8$ , 3 H,  $\text{CH}(\text{CH}_3)_2$ ), 1.22 (d,  $J_{\text{HH}} = 6.4$ , 3 H,  $\text{CH}(\text{CH}_3)_2$ ).  $^{13}\text{C}$  NMR ( $\text{CD}_3\text{CN}$ ,  $25\text{ }^{\circ}\text{C}$ , 125 MHz): 129.19, 110.30, 78.55, 67.60, 49.45, 31.81, 30.41, 20.99, 19.06.  $^{19}\text{F}$  NMR ( $\text{CD}_3\text{CN}$ ,  $25\text{ }^{\circ}\text{C}$ , 470 MHz):  $-113.65$  to  $-134.23$  (m).

*General Procedure for FT-IR Carboxylate Denticity Determination.* All FT-IR analysis was done on a Mattson Galaxy Series FTIR 3000 spectrometer. Samples were prepared by pressing  $\sim 10$  mg of each compound into anhydrous KBr. The symmetric and asymmetric carbonyl stretches were identified by comparison to its isotopologue,  $^{13}\text{C}$  labeled at the carbonyl carbon. Difference between the stretches in the sample were compared to the difference in the symmetric ( $\nu_s = 1415.5\text{ cm}^{-1}$ ) and asymmetric ( $\nu_a = 1594.8\text{ cm}^{-1}$ ) stretches in a sample of sodium benzoate in KBr, which had a value for  $\Delta(\text{NaO}_2\text{CPh})$  of  $179.3\text{ cm}^{-1}$ .

*Computational Details:* All calculations were done at the High-Performance Computing Center (HPCC) at Michigan State University. The optimization of structures was done using G09 with DFT and the B3PW91 functional. Due to the size of the structures, only double zeta basis sets were used in most cases with 6-31G\*\* used for all the chromium and iron complexes. In the case of the molybdenum and tungsten, the SDD basis was used. The Mayer Bond Order calculations were done on a departmental cluster using BORDER. In the case of the chromium complexes, the basis set dependence of the Mayer Bond Orders was examined. For example, for compound **1** the



calculation was carried out with 3-21G, 6-31G, 6-31G\*\*, and SDD. Bond orders using these different basis sets were generally comparable and either 6-31G\*\* or SDD were employed for all the complexes. For example, the Cr–N(nitrido) bond orders in **1** with the different basis sets were 2.71, 2.72, 2.68, and 2.89, respectively. The highest bond order between Cr–C(Cp) in **1** was 0.60, 0.71, 0.73, 0.71, respectively.

## NMR Spectra

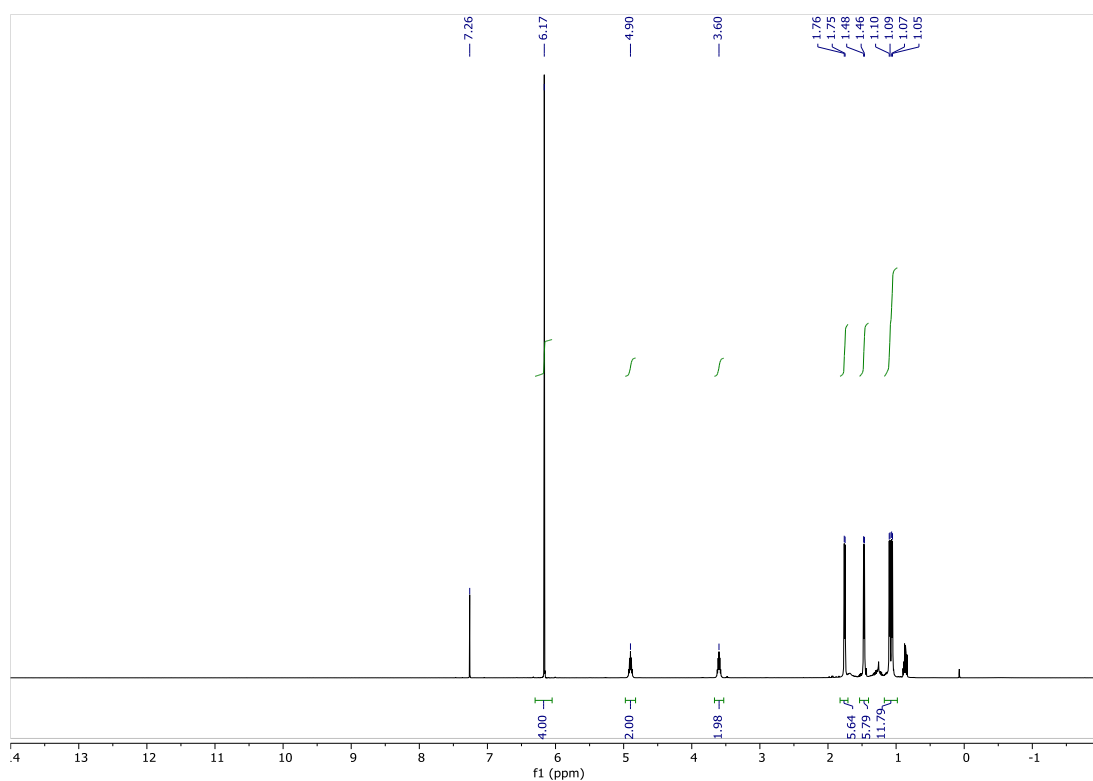


Figure 2-7. NCr(N<sup>i</sup>Pr)<sub>2</sub>(Cp) (**1**) <sup>1</sup>H NMR



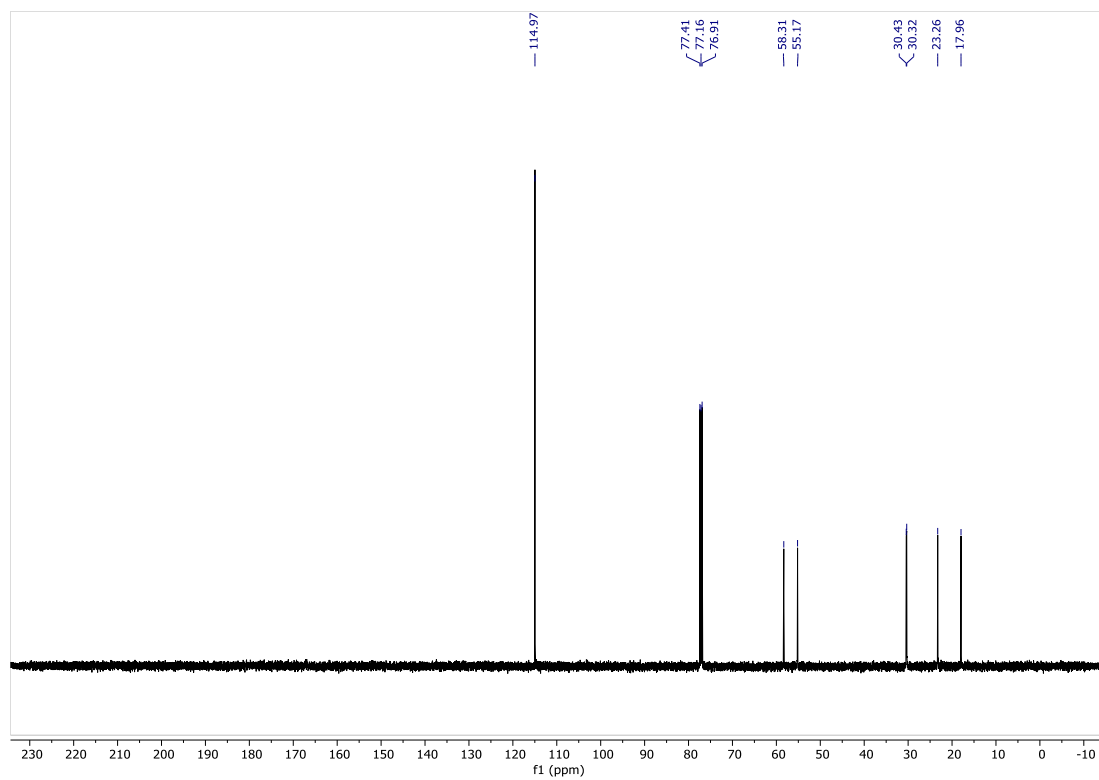


Figure 2-8. NCr(NiPr<sub>2</sub>)<sub>2</sub>(Cp) (**1**) <sup>13</sup>C NMR



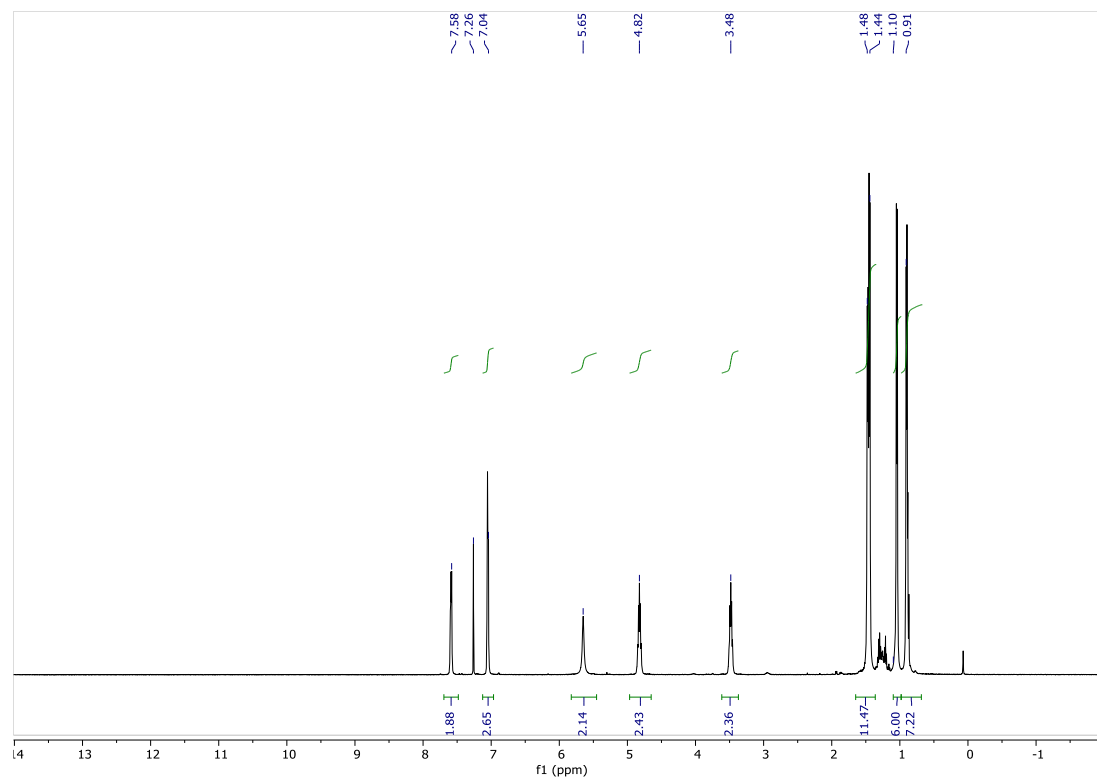


Figure 2-9. NCr(NiPr<sub>2</sub>)<sub>2</sub>(Ind) (2) <sup>1</sup>H NMR



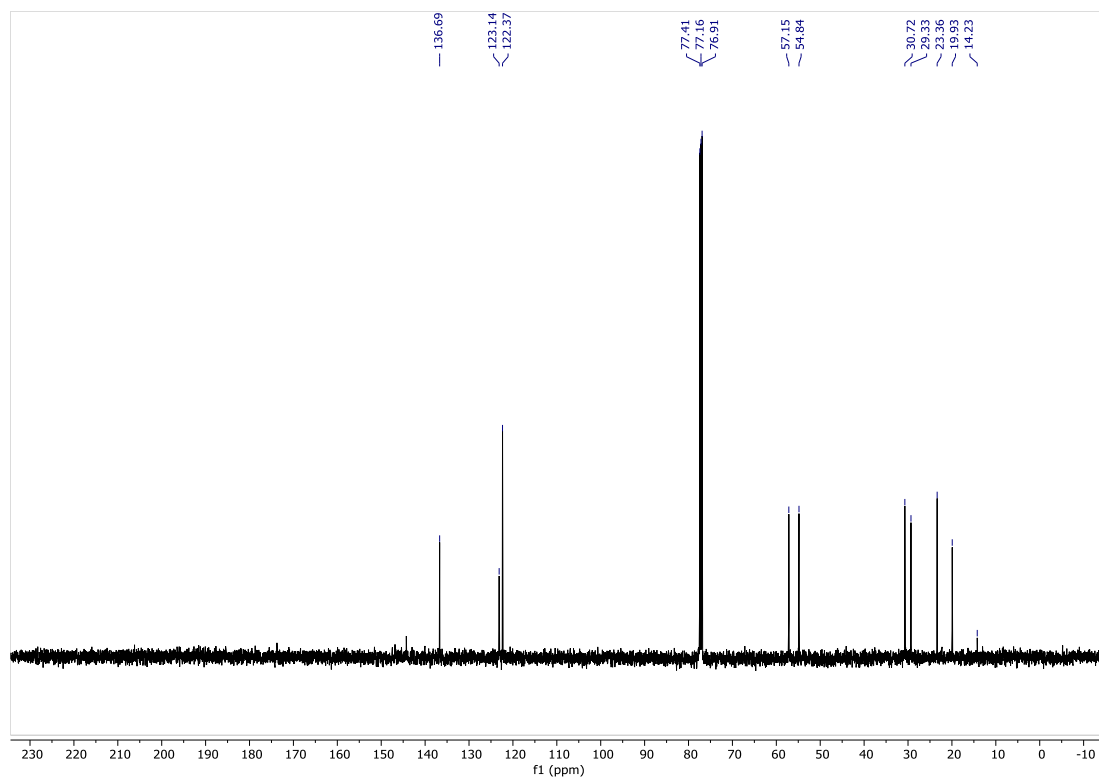


Figure 2-10.  $\text{NCr}(\text{NiPr}_2)_2(\text{Ind})$  (**2**)  $^{13}\text{C}$  NMR



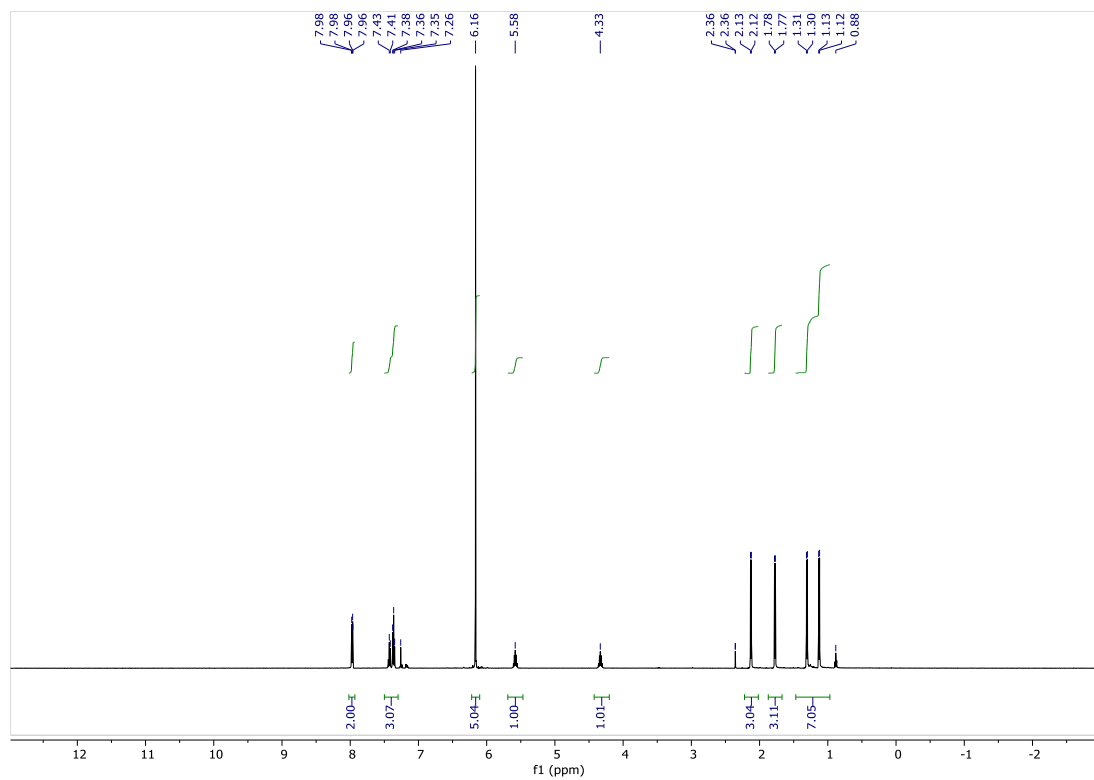


Figure 2-11.  $\text{NCr}(\text{N}^i\text{Pr}_2)(\text{O}_2\text{CPh})(\text{Cp})$  (3) <sup>1</sup>H NMR (13 °C)



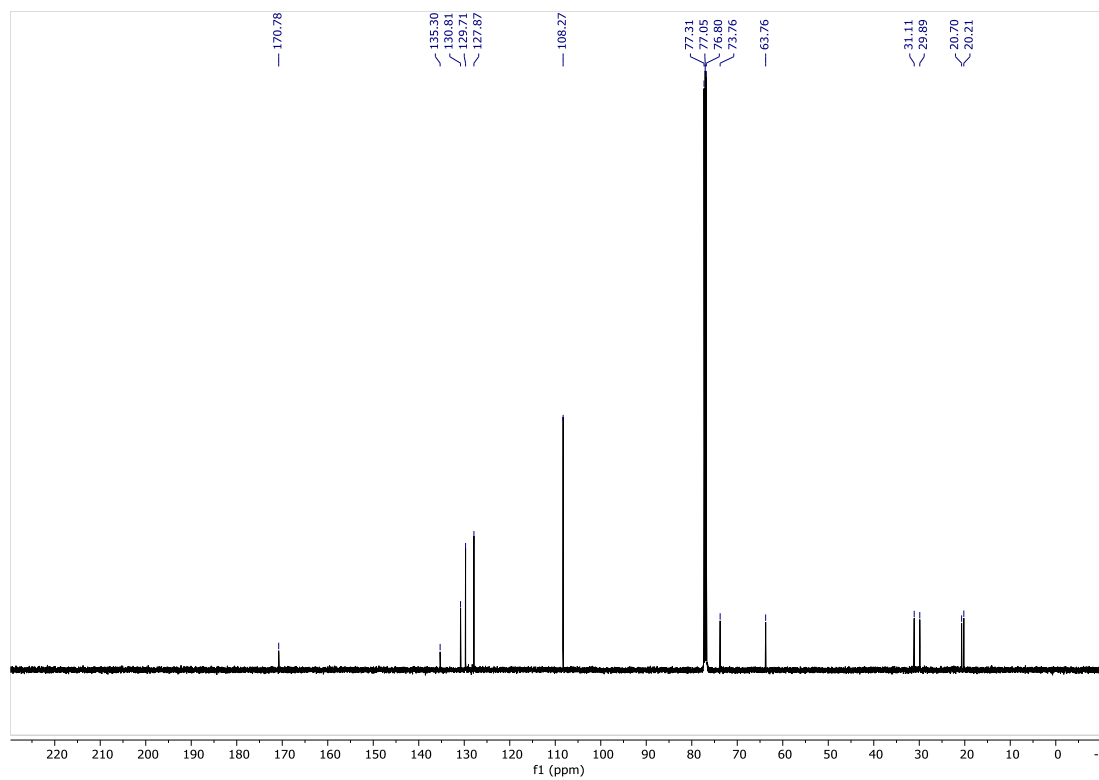


Figure 2-12. NCr(NiPr<sub>2</sub>)(O<sub>2</sub>CPh)(Cp) (**3**) <sup>13</sup>C NMR (13 °C)



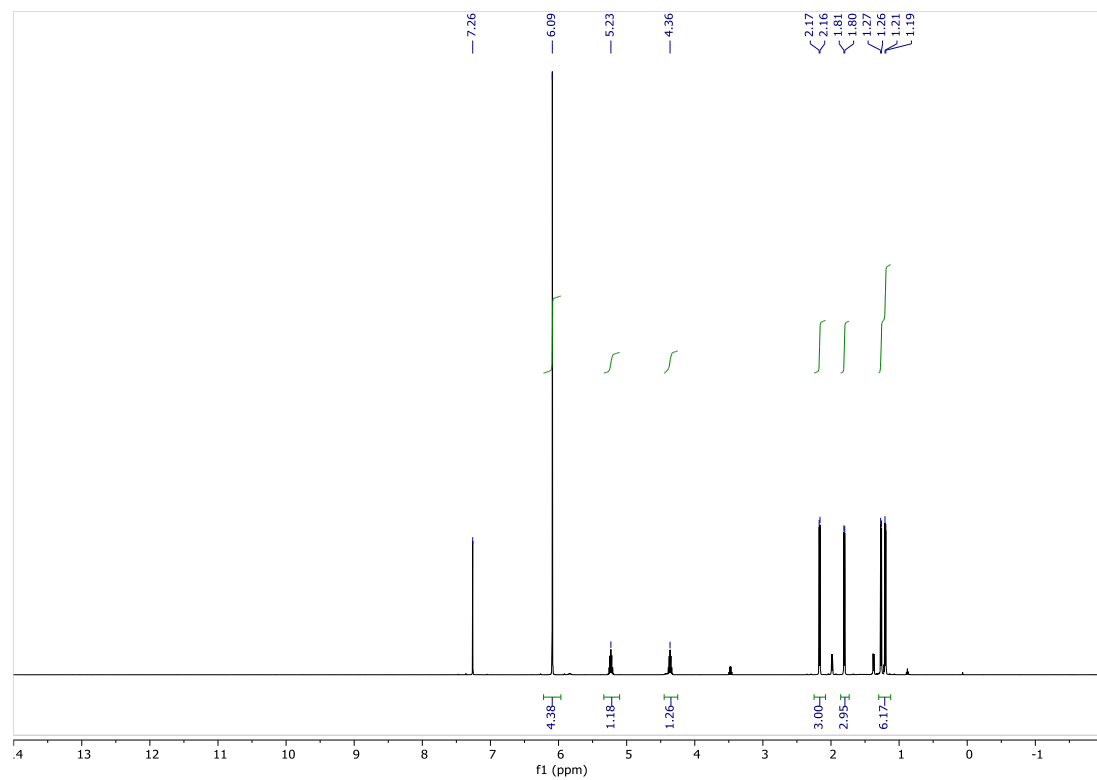


Figure 2-13. NCr(NiPr<sub>2</sub>)(Cp)Cl (**4**) <sup>1</sup>H NMR



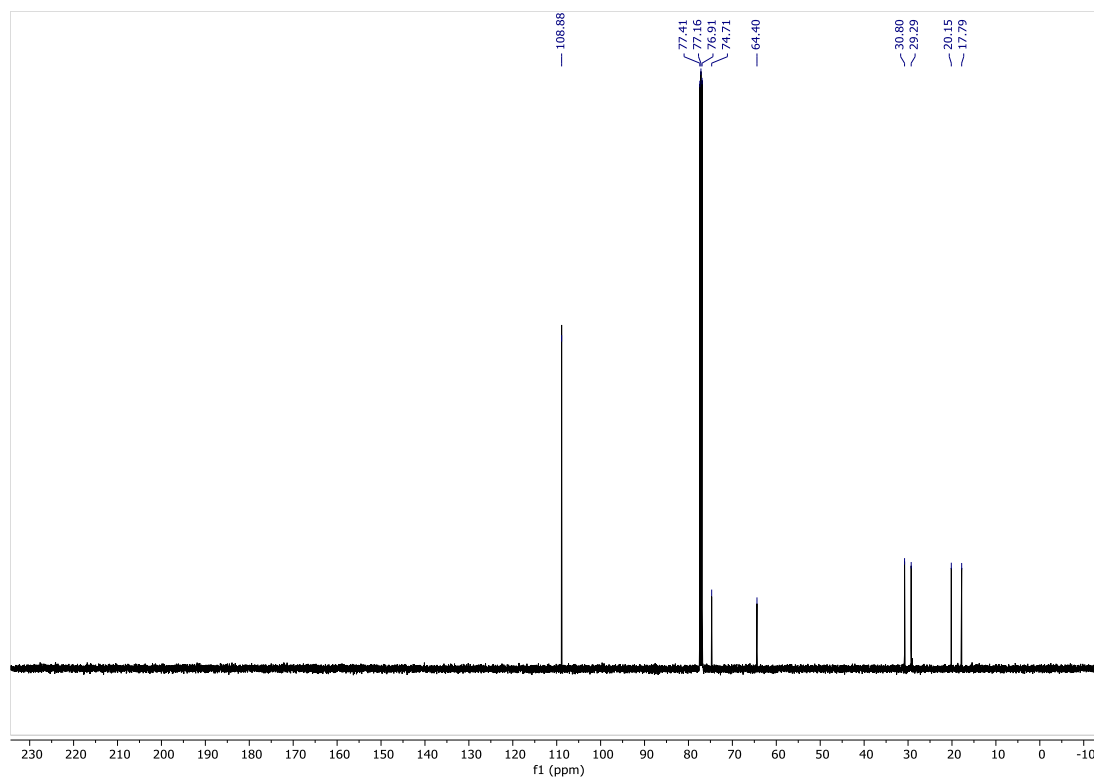


Figure 2-14.  $\text{NCr}(\text{N}^i\text{Pr}_2)(\text{Cp})\text{Cl}$  (4)  $^{13}\text{C}$  NMR



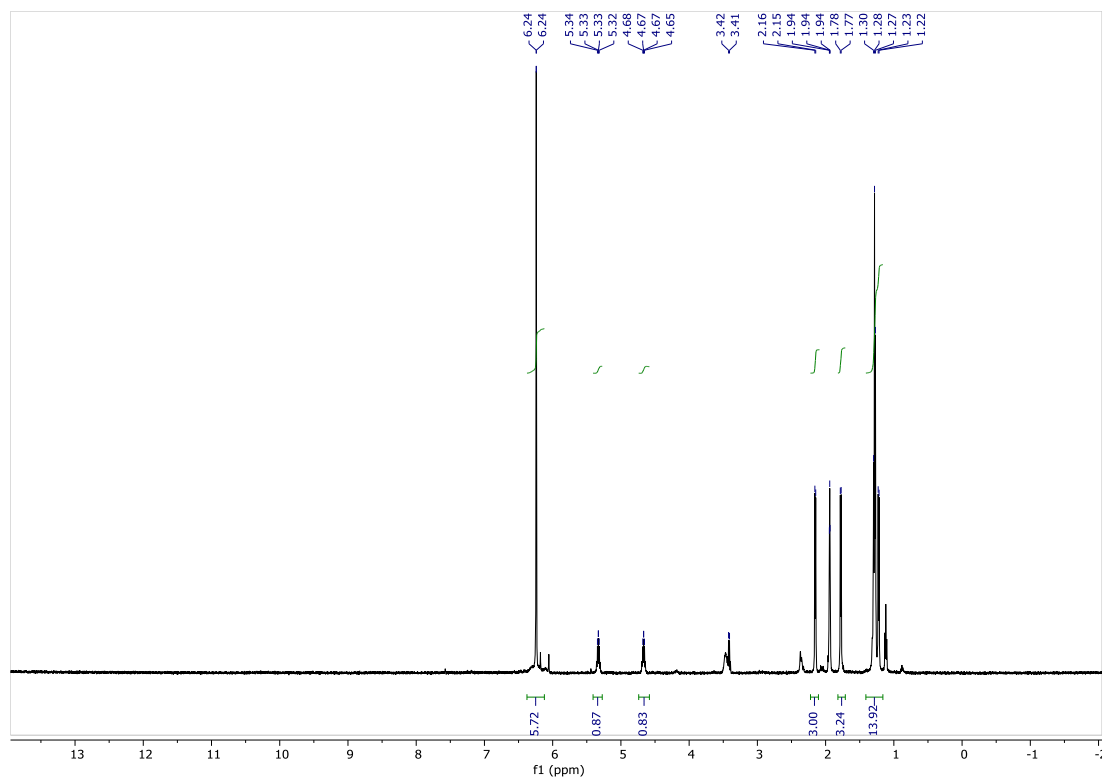


Figure 2-15.  $[\text{NCr}(\text{N}^i\text{Pr}_2)(\text{Cp})(\text{NCMe})][\text{SbF}_6]$  (5)  $^1\text{H}$  NMR (In Situ Reaction)



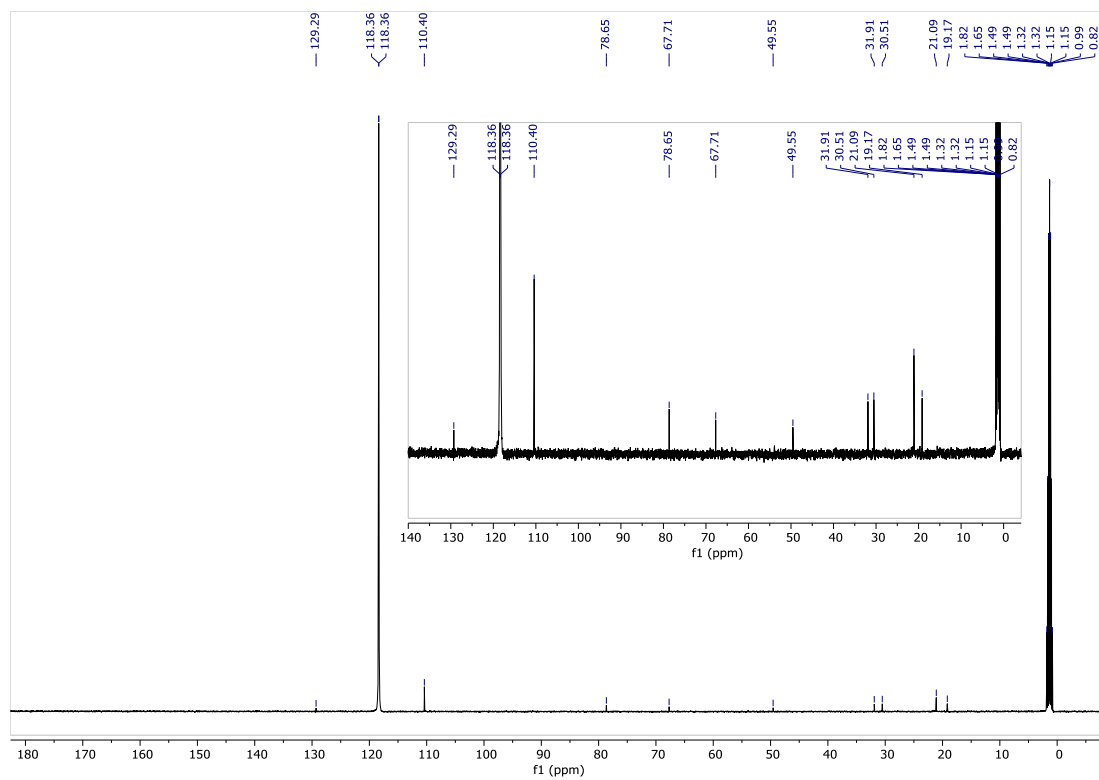


Figure 2-16.  $[\text{NCr}(\text{N}^i\text{Pr}_2)(\text{Cp})(\text{NCMe})][\text{SbF}_6]$  (**5**) <sup>13</sup>C NMR (In Situ Reaction)



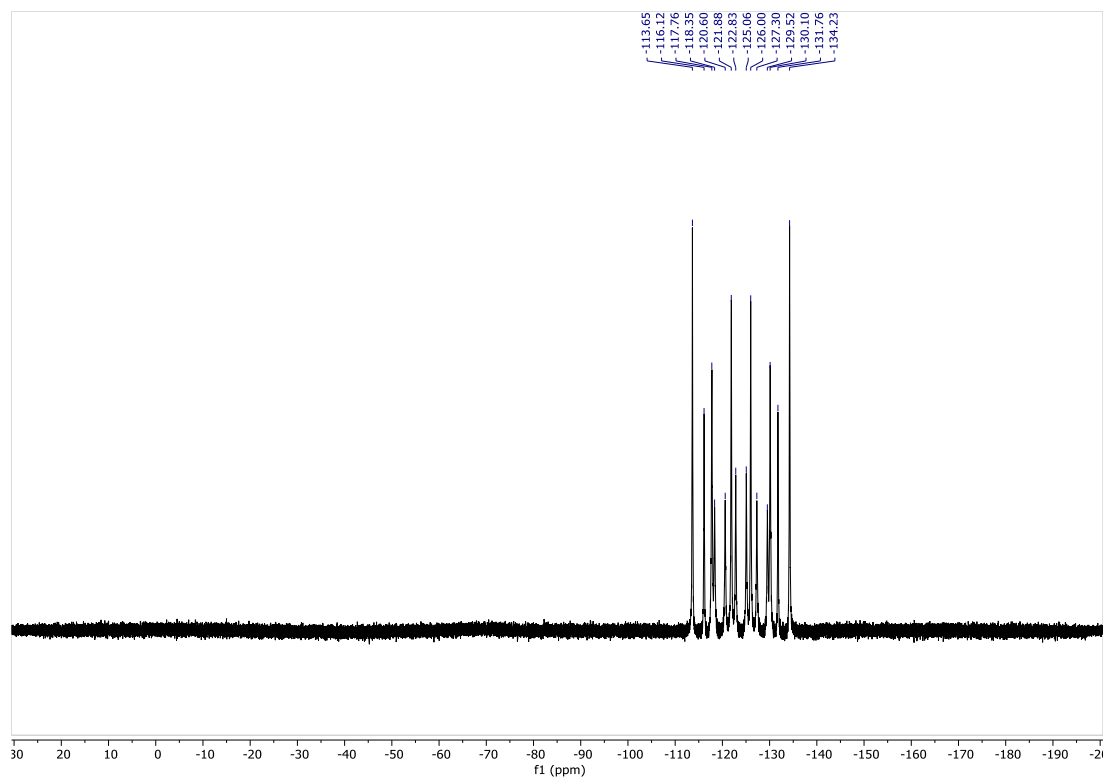


Figure 2-17.  $[\text{NCr}(\text{N}^i\text{Pr}_2)(\text{Cp})(\text{NCMe})][\text{SbF}_6]$  (**5**)  $^{19}\text{F}$  NMR (In Situ Reaction)



## REFERENCES



## REFERENCES

1. Kealy, T. J.; Pauson, P. L., *Nature* **1951**, *168* (4285), 1039-1040.
2. Wilkinson, G.; Rosenblum, M.; Whiting, M. C.; Woodward, R. B., *J. Am. Chem. Soc.* **1952**, *74* (8), 2125-2126.
3. Field, L. D.; Lindall, C. M.; Masters, A. F.; Clentsmith, G. K. B., *Coord. Chem. Rev.* **2011**, *255* (15-16), 1733-1790.
4. Cotton, F. A., *J. Organomet. Chem.* **2001**, *637-639* (0), 18-26.
5. MacDonald, M. R.; Fieser, M. E.; Bates, J. E.; Ziller, J. W.; Furche, F.; Evans, W. J., *J. Am. Chem. Soc.* **2013**, *135* (36), 13310-13313.
6. DiFranco, S. A. Single-Site Molybdenum(Iv) Mediated Bond Cleavage Reactions and Ligand Parameterization Using a Cr(Vi) Nitrido Platform. Michigan State University, 2013.
7. Shin, J. H.; Bridgewater, B. M.; Churchill, D. G.; Baik, M.-H.; Friesner, R. A.; Parkin, G., *J. Am. Chem. Soc.* **2001**, *123* (41), 10111-10112.
8. Koch, J. L.; Shapley, P. A., *Organometallics* **1997**, *16* (19), 4071-4076.
9. Johnson, C. E.; Kysor, E. A.; Findlater, M.; Jasinski, J. P.; Metell, A. S.; Queen, J. W.; Abernethy, C. D., *Dalton Trans.* **2010**, *39* (14), 3482-3488.
10. Miyazaki, T.; Tanaka, H.; Tanabe, Y.; Yuki, M.; Nakajima, K.; Yoshizawa, K.; Nishibayashi, Y., *Angew. Chem. Int. Ed.* **2014**, *53* (43), 11488-11492.
11. Bochmann, M., *J. Chem. Soc. Dalton. Trans.* **1996**, (3), 255-270.
12. Alt, H. G.; Koppl, A., *Chem. Rev.* **2000**, *100* (4), 1205-1221.
13. Resconi, L.; Cavallo, L.; Fait, A.; Piemontesi, F., *Chem. Rev.* **2000**, *100* (4), 1253-1346.
14. Hoffmann, R., *Angew. Chem. Int. Ed.* **1982**, *21* (10), 711-724.
15. Piper, T. S.; Wilkinson, G., *J. Inorg. Nucl. Chem.* **1956**, *3* (2), 104-124.
16. DiFranco, S. A.; Maciulis, N. A.; Staples, R. J.; Batrice, R. J.; Odom, A. L., *Inorg. Chem.* **2012**, *51* (2), 1187-1200.
17. Aldrich, K. E.; Billow, B. S.; Holmes, D.; Bemowski, R. D.; Odom, A. L., *Organometallics* **2017**, *36* (7), 1227-1237.
18. Mayer, I., *J. Comput. Chem.* **2007**, *28* (1), 204-221.



19. Mayer, I., *Border 1.0*, 2005.
20. Billow, B. S.; Bemowski, R. D.; DiFranco, S. A.; Staples, R. J.; Odom, A. L., *Organometallics* **2015**, *34* (18), 4567-4573.
21. Huttner, G.; Brintzinger, H. H.; Bell, L. G.; Friedrich, P.; Bejenke, V.; Neugebauer, D., *J. Organomet. Chem.* **1978**, *145* (3), 329-333.



## Chapter 3. Analysis of Phosphines as Ligand on High Valent Transition Metals

### 3.1 Introduction

Phosphines are one of the most frequently employed ligands in catalysis. As we discussed in chapter 1, much effort has gone into the development and understanding of phosphine-metal interactions.<sup>1-4</sup> The sheer number of different phosphine ligands makes these research efforts necessary, as the choice of phosphine can dramatically affect the outcome of a catalytic reaction. Take for example Grubbs first generation catalyst.<sup>5</sup> The choice of phosphine between two seemingly similar ligands,  $\text{PPh}_3$  and  $\text{PCy}_3$ , is the difference between an inactive species and a commercially available olefin metathesis catalyst. The choice of phosphine becomes even more complex when choosing between the extremely wide variety of ligands designed for cross coupling reactions.<sup>6-7</sup>

A highlight of the research discussed in chapter 2 was the realization of Cr(VI) cations. Former group members had some results synthesizing cationic complexes, but very little had been accomplished with them.<sup>8</sup> In an effort to learn more about the donor ability of neutral donor ligands, such as phosphines, to HVMs we began investigating them using the LDP method. Since phosphines are one of the most prevalent ligands in catalysis, and our system is essentially the high valent analogue to the Tolman electronic parameter, we set out to help improve the understanding of phosphine-metal bonding.

### 3.2 Synthesis

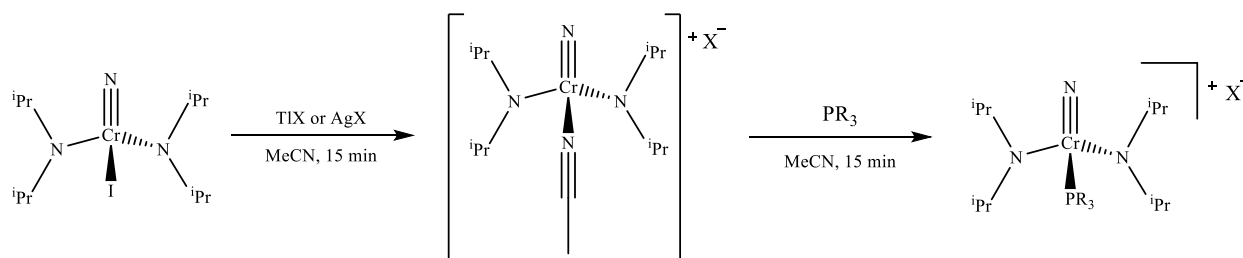
*This project was undertaken in close collaboration with Kelly Aldrich. Much of the work performed in this chapter was a shared effort, but the ion pairing analysis and computational*



studies were primarily Kelly's work. As such, efforts were made in the respective sections to explicitly give credit to Kelly, but all of the contents of this chapter were a collaborative effort to some degree.

Naturally, analysis of L-type ligands (neutral, two-electron donor ligands) in the LDP system requires formation of a cationic chromium complex. It is preferable to use a noncoordinating ion for charge balance to avoid competing exchange reactions with the L-type ligands. There are a number of noncoordinating ions to choose from and synthesis of cationic chromium complexes works reasonably well with most of them. One notable exception is triflate. The triflate anion is actually quite coordinating in this system and can easily outcompete L-type ligands.

The synthesis of the chromium phosphine complexes is quite simple. Addition of AgX or TlX, where X = SbF<sub>6</sub>, PF<sub>6</sub>, BAr<sup>F</sup><sub>24</sub>, BAr<sup>F</sup><sub>20</sub>, BPh<sub>4</sub>, Al(O<sup>t</sup>Bu<sup>F</sup><sub>9</sub>)<sub>4</sub>, to an acetonitrile solution of NCr(N<sup>i</sup>Pr)<sub>2</sub>I results in immediate precipitation of either AgI or TlI, generating [NCr(N<sup>i</sup>Pr)<sub>2</sub>(MeCN)]<sup>+</sup>X<sup>-</sup>. Addition of a slight excess of PR<sub>3</sub> to the resulting solution generates the desired [NCr(N<sup>i</sup>Pr)<sub>2</sub>PR<sub>3</sub>]<sup>+</sup>X<sup>-</sup> complex. The reaction sequence is shown in Scheme 2-1.



Scheme 3-1. General procedure for the synthesis of PR<sub>3</sub> complexes from NCr(N<sup>i</sup>Pr)<sub>2</sub>I. X = SbF<sub>6</sub>, PF<sub>6</sub>, BAr<sup>F</sup><sub>24</sub>, BAr<sup>F</sup><sub>20</sub>, BPh<sub>4</sub>, Al(O<sup>t</sup>Bu<sup>F</sup><sub>9</sub>)<sub>4</sub>

### 3.3 Initial LDP Analysis

We realized that changing the LDP framework from a neutral species to an ionic one was likely to cause some complications, but we began by analyzing the complexes using our standard method.



On synthesizing the first few complexes, we realized immediately there were some surprises in the LDP assessments of the phosphines. The first issue we encountered was the high barriers to rotation of the Cr-N bond. Because the phosphine complexes have extremely high barriers compared to the previously studied ligands, values >17 kcal/mol, the measurements required elevated temperatures. This was an immediate problem as triplicate LDP results usually require ~1.5 to 2 h at temperature, and several of the compounds were not stable on that timescale. For all of the measurements in Table 3-1 below, the complexes had at least one good LDP measurement performed, but triplicate results could not be easily obtained. Still though, the small series of phosphine complexes we analyzed did not follow the expected trends.

<b>Phosphine Group</b>	<b>LDP (kcal/mol)</b>
<b>PMe<sub>3</sub></b>	17.2
<b>PPhMe<sub>2</sub></b>	17.0
<b>PMePh<sub>2</sub></b>	16.2
<b>PCy<sub>3</sub></b>	17.2
<b>PBu<sub>3</sub></b>	17.3

Table 3-1. Initial LDP measurements for PR<sub>3</sub> ligands. All compounds used SbF<sub>6</sub> as the counter ion. All values are based on at least one good LDP measurement performed, but results here were not necessarily performed in triplicate due to decomposition of the complexes. As such, the values are reported only to the tenths.

It is important to realize there are a number of things that could potentially affect the numbers, but the values for the cursory analysis highlighted some surprising results. The LDP of the PR<sub>3</sub> ligands follows the opposite trend one would expect based on Tolman's  $\nu$  values.<sup>9</sup> The trialkyl phosphines are reported to be the best electron density donors, and the more aryl substituents that are added, the worse donors they become. We see the opposite trend in our data. Before drawing conclusions, we decided to make sure our measurements were actually an accurate measure of the PR<sub>3</sub> donor ability.



### 3.4 Anion and Solvent Dependence

The first thing we investigated was the ionic species dependence on the counterion. To test this, we synthesized a series of  $[\text{N}(\text{Cr}(\text{N}^i\text{Pr}_2)_2(\text{PPhMe}_2))^+ \text{X}^-]$  complexes with a series of counterions,  $\text{X} = \text{SbF}_6, \text{PF}_6, \text{BAr}^{\text{F}}_{24}, \text{BAr}^{\text{F}}_{20}, \text{BPh}_4, \text{Al}(\text{O}^i\text{Bu}^{\text{F}}_9)_4$ . The anions are displayed below in Figure 3-1.

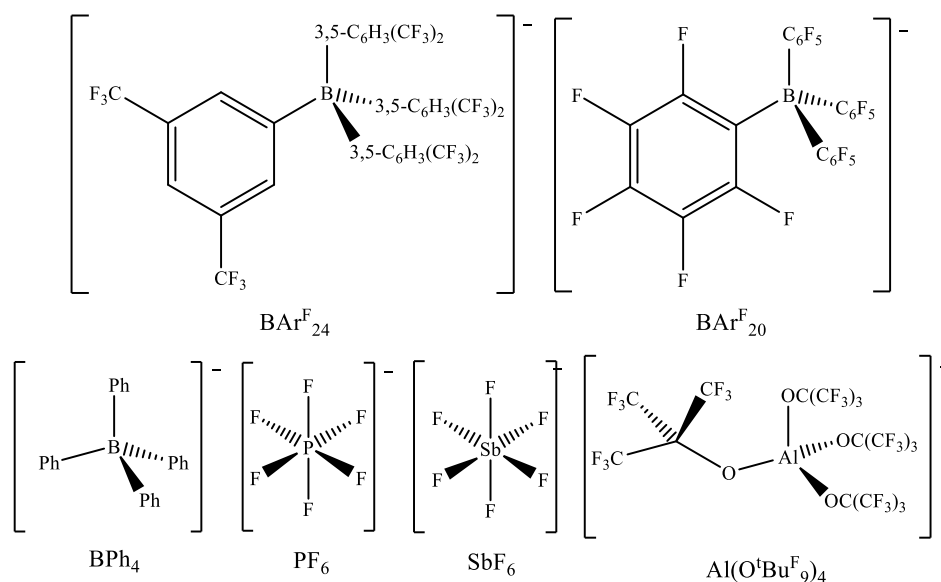


Figure 3-1. Various anions explored in this study.

Even before performing an LDP analysis on the series of  $[\text{Cr}]\text{PR}_3^+ \text{X}^-$  salts, we realized the anions were not equal. Surprisingly, the various ions did not give equivalent NMR spectra. Specifically, in the <sup>14</sup>N NMR spectrum, the signal for the nitride was missing in the complexes synthesized using the SbF<sub>6</sub> anion. When we synthesized the PF<sub>6</sub> version of the same phosphine complexes, the signal for the nitride was apparent (Figure 3-2). We hypothesized that the anions were in such close proximity to the chromium fragment in solution, that the quadrupolar Sb nucleus was broadening the nitride resonance into the baseline. In other words, we thought the SbF<sub>6</sub> anion



was ion paired with the Cr cation. This ion pairing, if it was the cause, should be solvent dependent.<sup>10</sup>

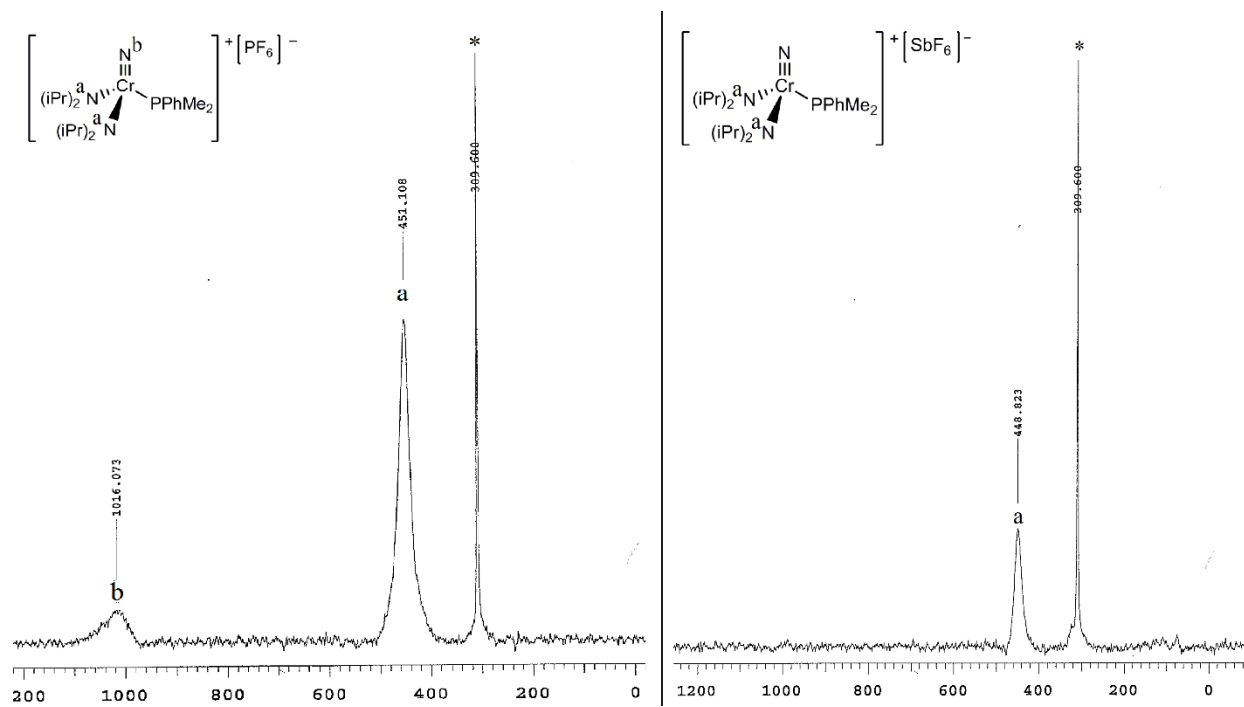


Figure 3-2.  $^{14}\text{N}$  NMR analysis of  $[\text{N}(\text{iPr})_2\text{Cr}(\text{PMePh}_2)]^+\text{X}^-$  in  $\text{CDCl}_3$  where  $\text{X} = \text{SbF}_6$  (right) and  $\text{PF}_6$  (left). The peak at 309 ppm (labelled with a \*) represents dissolved  $\text{N}_2$ , which was referenced as an internal standard.

To test this theory, we ran LDP analyses of the anion series in two different solvents,  $\text{CDCl}_3$  which is our standard solvent for the measurement, and  $\text{CD}_3\text{CN}$  which is a more polar solvent. The two solvents tested were chosen to highlight any differences in ion pairing between the cation and anion. The results are shown in Table 3-2.



The results of the series were interesting. The LDP values with different anions in  $\text{CDCl}_3$  were all quite different. This led us to believe that ion pairing in solution does indeed affect the Cr-N bond rotation, and it does so in a non-systematic way. For example, the  $\text{SbF}_6$  anion in  $\text{CDCl}_3$  has an LDP nearly 0.5 kcal/mol greater than that of the  $\text{BAr}_4$  anions. This lends some support to what we saw in the  $^{14}\text{N}$  NMR spectrum. If the  $\text{SbF}_6$  anion is close enough to the cation to hinder bond rotation, it could be close enough to broaden the nitride resonance in the  $^{14}\text{N}$  NMR spectrum. Surprising was the contrasting results between the two solvents. The same measurements in  $\text{CD}_3\text{CN}$  led to much more consistent results. We postulated that this was due to the increased solvation of the ions by the more polar solvent. If the ions were separated in solution by the acetonitrile molecule, the anion would not be in a proximity where the Cr-N bond rotation is hindered.

Anion	LDP (kcal/mol) in $\text{CDCl}_3$	LDP (kcal/mol) in $\text{CD}_3\text{CN}$
<b><math>\text{SbF}_6</math></b>	16.99	16.53
<b><math>\text{PF}_6</math></b>	16.96	16.53
<b><math>\text{BAr}^{\text{F}}_{24}</math></b>	16.60	16.58
<b><math>\text{BAr}^{\text{F}}_{20}</math></b>	16.64	16.62
<b><math>\text{BPh}_4</math></b>	16.57	16.47
<b><math>\text{Al}(\text{O}^t\text{Bu}^{\text{F}}_9)_4</math></b>	16.66	16.62

Table 3-2. LDP measurements of  $[\text{NCr}(\text{N}^i\text{Pr}_2)_2(\text{PPhMe}_2)]^+\text{X}^-$ .

We wondered how much the charge distribution in the noncoordinating anion affected the ion pairing. The  $\text{BAr}_4$  anions have the negative charge highly delocalized, but there are known anions with even more charge distribution.<sup>11-12</sup> At the time of the study, some of the weakest coordinating anion were carboranes and perfluoroaluminates.<sup>13</sup> The extremely charge delocalized carborane anion, though, was explosive. Fortunately, the  $\text{Al}(\text{O}^t\text{Bu}^{\text{F}}_9)_4$  anion has nearly the same charge distribution and, as such, is considered equally noncoordinating thanks to the 36 F atoms around



the periphery. These anions are easily prepared and are extremely stable.<sup>12</sup> Moreover, they provide interesting contrast to the BAr<sub>4</sub> anions since they are based on an alkyl fluorocarbon periphery rather than an aryl one.

Despite all of this, the aluminate anion hindered Cr-N bond rotation slightly more than the BAr<sub>4</sub> anions. Presumably, the flexible alkyl substituents can interact with the <sup>i</sup>Pr groups of the amides easier than the rigid aryl substituents. We attempted synthesis of the hydrocarbon analogue of the aluminate, Al(O<sup>t</sup>Bu)<sub>4</sub>, to test that theory, but we could only produce the lithium and potassium salts, which were unsuccessful in the synthesis of [NCr(N<sup>i</sup>Pr<sub>2</sub>)<sub>2</sub>(PR<sub>3</sub>)]<sup>+</sup>(Al(O<sup>t</sup>Bu)<sub>4</sub>)<sup>-</sup>.

The results of testing the series of anions suggested that, regardless of how delocalized the charge was in the anion, LDP alone was probably not going to be an adequate indication of ion interaction. In light of this, Kelly tested the ion pairing dependence on solvent and anion identity using a series of detailed analyses including diffusion ordered spectroscopy (DOSY) NMR, LDP, and DFT.<sup>14-15</sup> The DOSY study showed equal diffusion coefficients of the cation and anion in solution. This suggests the ions are diffusing together in solution, or in other words, they are tightly ion paired. DFT analysis even suggested ions like SbF<sub>6</sub><sup>-</sup> paired to the chromium complex in a specific way, directly above the nitride, confirming our suspicions from the <sup>14</sup>N NMR. When the ions are in this position, the electronegative fluorides can hydrogen bond to the protons on the <sup>i</sup>Pr groups of the amides. This means the SbF<sub>6</sub><sup>-</sup> anion might be able to hinder bond rotation both sterically and through noncovalent bonding interactions.

In CD<sub>3</sub>CN, the DOSY experiment showed different diffusion rates for each cation and anion. As we suspected, the higher polarity of acetonitrile meant the ions could be completely solvated, separating the cation from the anion. This is consistent with the lower LDP values in the more polar solvent.



Kelly also studied the ion pairing using ROESY NMR.<sup>14</sup> The ROESY experiment shows through space correlations in the  $^1\text{H}$  NMR. The larger  $\text{BAr}^{\text{F}}_{24}$  ion was ion paired in  $\text{CDCl}_3$ , but the pairing was non-specific, meaning the aromatic  $^1\text{H}$  signal from the anion correlated weakly with all of the proton signals in the chromium complex. The lower effect of the LDP value in  $\text{CDCl}_3$  for the  $\text{BAr}_4$  ions may be due to the ion spending some time by the amides, some by the phosphine ligand, and some solvated. In  $\text{CD}_3\text{CN}$ , though, there were no correlation signals. While this is a negative result, it is what we would expect if the acetonitrile completely solvates the ions.

In brief, Kelly's analysis of the ion pairing in various solvents seemed pretty conclusive. The easiest modification we could make to the LDP method was switching to  $\text{CD}_3\text{CN}$  as a solvent. This allows us our choice of anions, and for synthetic ease, we chose the  $\text{SbF}_6$  anion.

### 3.5 Entropy Analysis

Because LDP analysis of the cationic complexes required using a different solvent, we realized that one of the assumptions we had made in all LDP measurements in the past may not translate to the  $\text{PR}_3$  complexes. In the previous LDP studies, the assumption was that the entropy of activation,  $\Delta S^\ddagger$ , was equal to -9 e.u. This number was established for the original LDP publication by investigating a number of chromium complexes with Eyring plot analysis in  $\text{CDCl}_3$ . All of the values determined were small, negative values. The number that was established over the largest temperature range was that using the  $\text{N}(\text{C}(\text{iPr})_2)_2\text{I}$  complex.<sup>16</sup> Since this value had the most reliable data backing the value, the  $\Delta S^\ddagger$  for the iodide complex has been used for all ligands. Throughout the studies we have done since the original publication, we have not had cause to question that value. Even in situations where it would have become obvious that the assumed value was incorrect, specifically doing LDP measurements at different temperatures for the same ligand, the assumption seemed to hold.



We first became suspicious of the entropy assumption when we investigated some of the phosphine complexes at varied temperatures. The LDP values determined in  $\text{CD}_3\text{CN}$  at varying temperatures were not self-consistent. Considering we changed our analysis from chloroform to acetonitrile and the complexes from neutral to ionic, it seemed prudent to reinvestigate our original assumption. We performed numerous analyses of the  $\text{PR}_3$  complexes and the results are outlined in Table 3-3.



Ligand	$\Delta H^\ddagger$ (CD <sub>3</sub> CN) <sup>a,b</sup>	$\Delta S^\ddagger$ (CD <sub>3</sub> CN) <sup>a</sup>	$\Delta H^\ddagger$ (CDCl <sub>3</sub> ) <sup>c</sup>	$\Delta S^\ddagger$ (CDCl <sub>3</sub> ) <sup>c</sup>
PMe <sub>3</sub>	16.64±.2		18.71±.3	-3.4±1
P <sup>n</sup> Bu <sub>3</sub>	16.77±.2		18.91±.3	-2.8±1
P <sup>i</sup> Bu <sub>3</sub>	17.13±.2		17.76±.4	-5.7±1
P <sup>i</sup> Pr <sub>3</sub>	17.17±.2		19.47±.5	-3.0±2
PCy <sub>3</sub>	17.27±.2		19.46±.2 <sup>b</sup>	-
PPhMe <sub>2</sub>	16.53±.2	-4.7±1	18.79±.4	-2.1±1
PPh <sub>2</sub> Me	16.16±.2		16.9±.4	-8.2±1
PPhEt <sub>2</sub>	16.65±.2		16.96±.4	-6.7±1
PPh <sub>2</sub> Et	16.15±.2		17.98±.3	-4.0±1
PPh <sub>2</sub> <sup>n</sup> Bu	16.31±.2	-25±4	18.17±.1	-3.4±1
PPh <sub>2</sub> Cy	16.43±.2		18.11±1	-5.5±3
PPhCy <sub>2</sub>	16.37±.2		-	-
P(OEt) <sub>3</sub>	15.73±.2	-38±3	16.99±.4	-6.1±1
P(O <sup>i</sup> Pr) <sub>3</sub>	15.91±.2		17.12±.4	-6.0±1
P(NC <sub>4</sub> H <sub>8</sub> ) <sub>3</sub>	16.21±.2		19.52±.5	-1.0±2
PPh <sub>3</sub>	-	-	18.00±.7	-4.1±2
I	-	-1.3±1	18.05±.1	-0.6±1
OPh	-	-	13.50±.1	-3.1±1
Pyrr <sup>3</sup> -C <sub>6</sub> H <sub>3</sub> (CF <sub>3</sub> ) <sub>2</sub>	-	-	15.50±.1	-3.7±1
N <sup>i</sup> Pr <sub>2</sub>	-	-	11.48±.2	-5.7±1

Table 3-3. Summary of Eyring analyses of the various phosphine complexes. The entropy analysis error was determined from a linear least squares fit of the experimentally data as reported by Lente.<sup>17</sup> <sup>a</sup>Values in CD<sub>3</sub>CN use SbF<sub>6</sub> as an anion. These  $\Delta H^\ddagger$  values include the, admittedly crude, assumption of a constant entropy of -9 e.u. <sup>b</sup>These values were run at 3 constant temperatures, as such the precision is high and the error for the measurement is low, this does not necessarily mean the  $\Delta H^\ddagger$  values are more accurate than the other values here, especially in light of the entropy assumption. <sup>c</sup>Values in CDCl<sub>3</sub> use BAR<sup>F</sup><sub>24</sub> as the anion.  $\Delta H^\ddagger$  values are from the Eyring analysis.



We decided it would also be sensible to reevaluate the anionic ligands to confirm the assumption of a constant  $\Delta S^\ddagger$  value, especially since our techniques for the LDP measurement had improved since the original publication.<sup>18</sup> For this analysis we determined  $\Delta S^\ddagger$  for the  $\text{NCr}(\text{N}^i\text{Pr}_2)_2\text{I}$ ,  $\text{NCr}(\text{N}^i\text{Pr}_2)_2\text{OPh}$ ,  $\text{NCr}(\text{N}^i\text{Pr}_2)_2\text{Pyr}^{3-\text{C}_6\text{H}_3(\text{CF}_3)_2}$  and  $\text{NCr}(\text{N}^i\text{Pr}_2)_3$  which represent a wide range of donor ability and buried volumes. The results for those four experiments are shown at the bottom of Table 3-3. The results line up well with those previously reported. This result was unsurprising given the successful deployment of the LDP system in modelling. We averaged the data from the four points to come to a  $\Delta S^\ddagger$  value of -3.5 e.u. Given the circumstances, the value of the entropy is inconsequential as long as we can assume the value is constant for all of the ligands measured. The accuracy of the  $\Delta H^\ddagger$  value is not the critical factor in the LDP assessment of ligands. As mentioned in chapter 1, the important aspect of the LDP measurement is precision and the relative difference from one ligand to another. Since the value seems reasonably constant for the anionic ligands, our assumption of a constant  $\Delta S^\ddagger$  does not seem unreasonable.

It is important to note too, the entropy values for the  $\text{PR}_3$  complexes in chloroform match quite well to the anionic ligand values. Again, this supports our assumption about constant  $\Delta S^\ddagger$  values in  $\text{CDCl}_3$ . Unfortunately, the Cr-N bond rotation is hindered in chloroform by intermolecular interactions from ion pairing, precluding the use of  $\text{CDCl}_3$  for the phosphine LDP measurements. The entropy values in acetonitrile, though, seem to vary widely.

We wondered if we could shed some light on the cause of the fluctuating entropy. To test whether entropy was dependent on solvent, we analyzed the  $\Delta S^\ddagger$  of  $\text{NCr}(\text{N}^i\text{Pr}_2)_2\text{I}$  in  $\text{CD}_3\text{CN}$ . The value, determined over a temperature range of 41 K, matched almost exactly the value we determined from  $\text{CDCl}_3$  at -1.3 (0.5) e.u. Since the value of a neutral complex in  $\text{CD}_3\text{CN}$  matches



the values of both ionic and neutral species in  $\text{CDCl}_3$ , we suspect the substantial changes in  $\Delta S^\ddagger$  comes from varying solvation spheres surrounding the cationic chromium molecule.

### 3.6 Phosphine Analysis

Unfortunately, the investigation into the entropy of our LDP system only highlighted the cause of the mismatching  $\text{PR}_3$  values at different temperatures, it did not solve the problem. As a result, direct, quantitative comparison of neutral donors is still not achievable using the LDP method. We were still able to make qualitative comparisons between the phosphines, though, but we will discuss the donor ability in terms of  $\Delta H^\ddagger$  to emphasize these values do not fall on the previously discussed LDP scale.

We could not analyze the entropy value of the alkyl phosphines due to extremely limited temperature windows where the complexes were stable. Since the complexes were similar and the LDP measurements were performed at similar temperatures, we thought the entropy differences between them might be negligible. We compared the set of trialkyl phosphine complexes to see if an analysis was possible. We fit the  $\Delta H^\ddagger$  data from  $\text{CD}_3\text{CN}$  to the Tolman type equation below.<sup>1</sup>

$$\Delta H^\ddagger = a(\chi_d) + b(\theta) + c \quad (1)$$

In Equation 1,  $\chi_d$  is the adapted Tolman electronic parameter by Prock and Giering.<sup>19</sup> The values scale like Tolman's  $\nu$  value, but were corrected for  $\pi$ -effects and are meant to be a true  $\sigma$ -donor value.<sup>3</sup> We decided this would be the simplest model for the trialkylphosphines since there should be minimal influence from  $\pi$ -effects. Modelling the data in Table 3-4 using Equation 1 with a least squares fit gives Equation 2 below.

$$\Delta H^\ddagger = 0.135(\chi_d) + 0.030(\theta) + 11.98 \quad (2)$$



Ligand	$\Delta H^\ddagger$ (CD <sub>3</sub> CN)	$\Delta H^\ddagger$ (CDCl <sub>3</sub> )	TCA (°)	$\chi_d$
PMe <sub>3</sub>	16.64	18.71	118	8.55
P <sup>n</sup> Bu <sub>3</sub>	16.77	18.91	136	5.25
P <sup>i</sup> Bu <sub>3</sub>	17.13	17.76	143	5.70
P <sup>i</sup> Pr <sub>3</sub>	17.17	19.47	160	3.45
PCy <sub>3</sub>	17.27	19.46	170	1.40

Table 3-4. Parameters used to model the trialkyl phosphines against  $\Delta H^\ddagger$ .  $\Delta H^\ddagger$  values taken from Table 3-3.

One test of the fit can be seen in Figure 3-3. The plot is the model predicted  $\Delta H^\ddagger$  plotted against the experimentally measured  $\Delta H^\ddagger$  values. Plots of this type give an indication of how well the data is modelled based on the regression. A good linear fit means there is good correlation between the  $\Delta H^\ddagger$  and the  $\theta$  and  $\chi_d$  values. Fortunately, this model gives quite a good fit for the alkyl phosphines. The best fit line for the plot shows that there is an almost exact 1:1 ratio from the model predicted and actual  $\Delta H^\ddagger$  values with a decent fit.

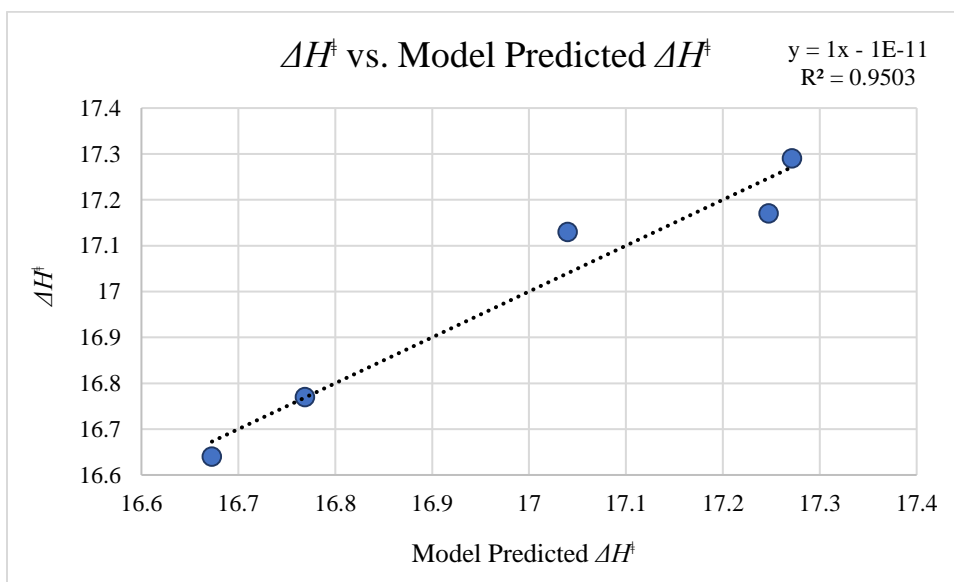


Figure 3-3. Plot of  $\Delta H^\ddagger$  vs model predicted  $\Delta H^\ddagger$  using  $\Delta H^\ddagger$  values determine from CD<sub>3</sub>CN with an assumption of constant  $\Delta S^\ddagger$ .



While this is not quantitative, the model can tell us a bit about the  $\Delta H^\ddagger$  measurement of the  $\text{PR}_3$  complexes. In the model there is a dependence on both sterics and electronics. Equation 2 highlights some phenomena that agree, logically, with what we expect to see. First, the  $a$  term is 0.135. The magnitude is somewhat meaningless, but the sign is important. The positive correlation between  $\Delta H^\ddagger$  and  $\chi_d$  means as the sigma donor ability increases (smaller  $\chi_d$ ), the  $\Delta H^\ddagger$  also reflects a better donor ability (smaller  $\Delta H^\ddagger$ ). Conversely, as  $\theta$  increases, the  $b$  term indicates that steric hinderance increases the barrier to Cr-N bond rotation, shown in the positive correlation between  $\theta$  and  $\Delta H^\ddagger$ .

When we extended the model in Equation 2 to the whole series of  $\text{PR}_3$  ligands, there was no correlation. This is unsurprising since we specifically chose the  $\chi_d$  value to remove  $\pi$  effects for the trialkylphosphines and the other  $\text{PR}_3$  ligands have groups that are likely heavily influenced by  $\pi$  effects, as well as different values of  $\Delta S^\ddagger$ .

We were surprised to see that the series of the alkyl/aryl phosphines still followed the trend that adding aryl substituents increased donor ability (lower  $\Delta H^\ddagger$ ) regardless of the conditions (Table 3-3). Even more shocking, though, was the trend of the  $\text{P(OR)}_3$  ligands. Much like the alkyl vs. aryl phosphines, the phosphites are expected to be far worse  $\sigma$ -donors due to the electron withdrawing substituents. Every number we have measured with these ligands suggests they are, in fact, *better* donors to Cr(VI). It seems unlikely that the difference in  $\Delta H^\ddagger$  between the values for the phosphites and phosphines are within the error of even these crude measurements. For example, in  $\text{CDCl}_3$  where only steric interactions of the anion affect the measurement, the  $\text{P(OEt)}_3$  complex has a  $\Delta H^\ddagger$  of 16.99 kcal/mol compared to a  $\Delta H^\ddagger$  of 18.71 kcal/mol for  $\text{PMe}_3$ .



We can say with some degree of certainty that the sterics of the  $\text{PR}_3$  ligands are not the cause of this difference in donation. While it is true that the Tolman cone angle ( $\theta$ ) of  $\text{PMe}_3$  is larger than that of  $\text{P(OEt)}_3$ ,  $118^\circ$  and  $109^\circ$ , respectively, the  $\text{P(O}^i\text{Pr)}_3$  ligand has a  $\theta = 130^\circ$  but it still has a lower  $\Delta H^\ddagger$  than  $\text{PMe}_3$ . Since we could only get qualitative data from experiment, we sought an explanation through theory.

### 3.7 Phosphine Bonding Analysis

To gain better understanding of the difference in  $\Delta H^\ddagger$ , Kelly analyzed the phosphine complexes using natural bond orbital theory (NBO) with DFT optimized structures. The findings were quite surprising. Decades of information about phosphines involved in late metal catalysts have led to a wealth of information about phosphine bonding to metal centers.<sup>20-22</sup> The resonance forms shown in Figure 3-4 highlight the accepted bonding modes of a phosphine and a late transition metal.

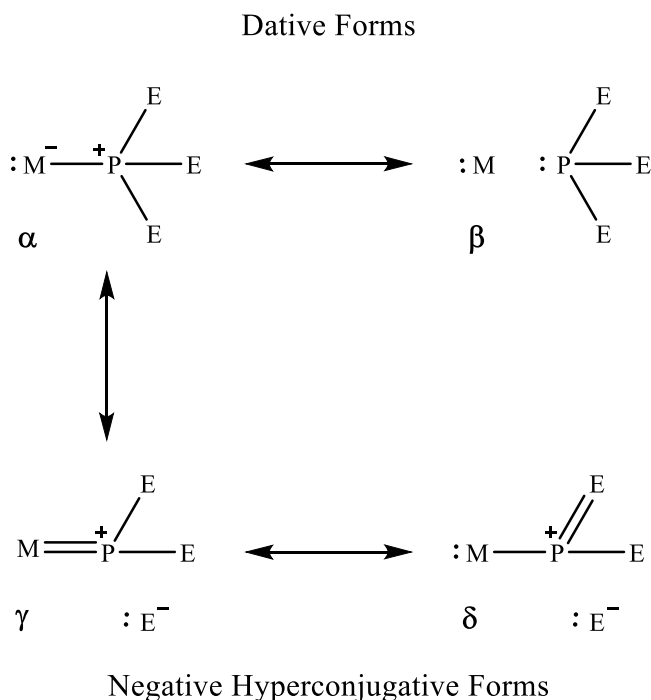


Figure 3-4. Lewis structures depicting the typical resonance forms of a low valent metal-phosphine interaction. The contribution of  $\delta$  is dependent on the identity of the E groups.



As described in the introduction, Cr(VI) is far from a low valent metal. Still, the interactions between chromium and an alkyl phosphine ligand are not substantially different than those expected for a metal like Ni or Pd. The resonance forms that contributed to the Cr-P bond were simple Lewis pair resonance forms. The contributions to the resonance form, calculated by NRT, were 69% bound ( $\alpha$ ) and 30% unbound ( $\beta$ ) (the resonance forms are defined in the figures). The high contribution of  $\beta$  may account for the high  $\Delta H^\ddagger$  we see in the alkyl phosphines, as well as their instability at elevated temperature.

When the same analysis was performed on the phosphite ligand, there were additional resonance forms found to contribute. Figure 3-5 below details the findings, but in short, the phosphite ligand was found to interact through hyperconjugative resonance forms that resemble the opposite of the bonding picture we see with late transition metal form  $\gamma$ . Since the oxygens on the phosphite have an available lone pair, they can donate into a P-O  $\sigma^*$  orbital, resonance form  $\delta$ . Form  $\delta$  is unsurprising as these resonance forms are well established as a resonance phenomenon within the phosphite ligand itself and have little dependence on M.<sup>23-24</sup> What was shocking was the phosphite was also found to have a resonance form where a lone pair from oxygen donates into a Cr-P  $\sigma^*$  orbital, resulting in what could be considered a net reduction of Cr. We postulate the contributions from  $\delta$  and  $\epsilon$  decrease the contribution of the nonbonding resonance for  $\beta$ , resulting in an overall higher bond order with chromium.



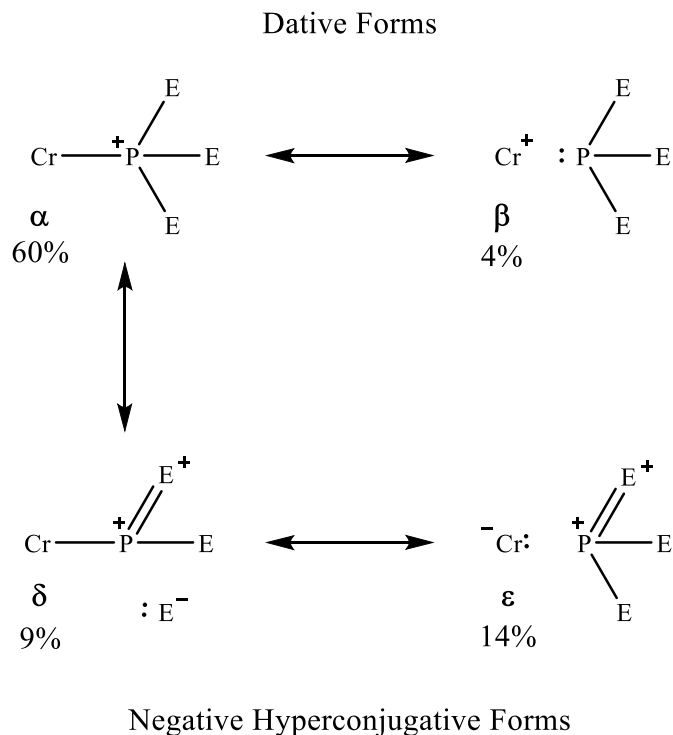


Figure 3-5. Resonance forms discovered in NRT analysis of  $[\text{NCr}(\text{NH}_2)_2(\text{P}(\text{OMe})_3)]^+$ .

Still, though, this resonance form is very unexpected. Why would the resonance form  $\epsilon$  account for 14% of the bonding interaction between Cr and P? The answer could lie in the electronegativity of the formally  $d^0$  Cr(VI) atom. Because of the high formal charge, the Cr could potentially compete for electron density with the O atoms. It is difficult to assign an electronegativity to the chromium atom in our system, especially since the coordination environment should vary the electronegativity, but the Sanderson electronegativity of Cr(VI) is 3.37, between Cl (3.48) and Br (3.21).<sup>25</sup>

To get a better measure on the Lewis acidity of the chromium system, we turned to a method developed by Gutmann.<sup>26-27</sup> The acceptor number (AN) system is based on the  $^{31}\text{P}$  NMR shift of a coordinated  $\text{OPEt}_3$  ligand. A spectrum is acquired on a sample of free phosphine oxide in dichloroethane, then remeasured with the test species present. The shift of the free phosphine oxide versus the coordinated one is then compared to a scale of previously measured standards. The scale



is based on a range of 0-100 where 0 is hexane and 100 is  $\text{SbCl}_5$ . Our chromium system has an of 100, equal to that of  $\text{SbCl}_5$ . For comparison, other common Lewis acids like  $\text{B}(\text{C}_6\text{F}_5)_3$  and  $\text{BBr}_3$  have ANs of 78 and 90.3, respectively.<sup>28</sup> As we suspected, the high oxidation state and poor donor ability of the phosphine ligands means that the chromium atom in our system is extremely Lewis acidic. This comes as no surprise since  $d^0$  metals,  $\text{TiCl}_4$  for example, have been used as Lewis acids in organic synthesis.<sup>29</sup> These findings lend some support to resonance form  $\epsilon$  as a reasonable resonance form in the chromium system.

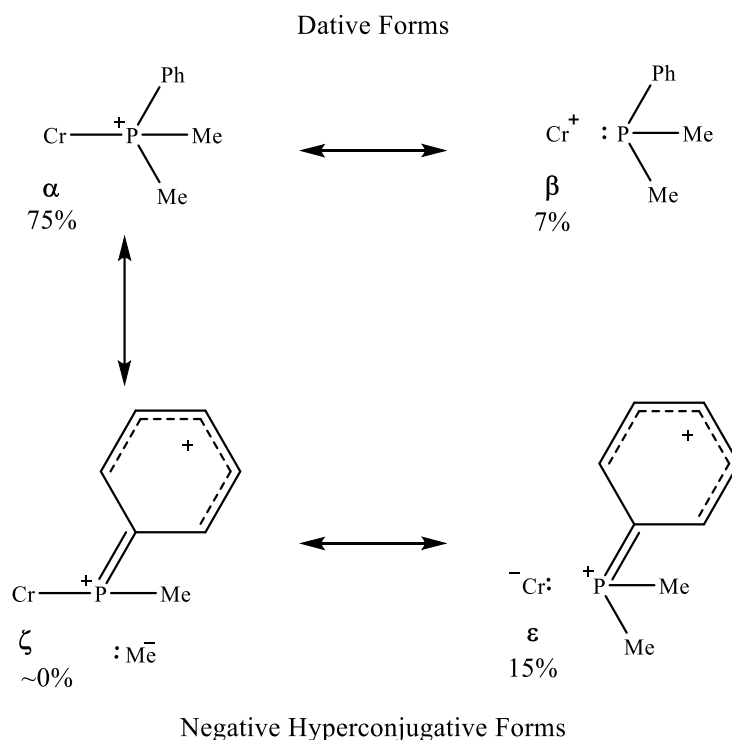


Figure 3-6. NRT analysis of  $[\text{NCr}(\text{NH}_2)_2(\text{PPhMe}_2)]^+$

Further NRT analysis of the arylphosphines and trisamidophosphines yielded related results to the phosphite. In the analysis of  $\text{PPhMe}_2$  as a ligand, NRT highlighted the same  $\epsilon$  resonance form, where the phenyl group delocalized a positive charge in the ring (Figure 3-6). This resonance form could explain why we see a decrease of  $\Delta H^\ddagger$  when more phenyl groups are added to the phosphine.



### 3.8 Conclusions

Regrettably, we were unable to perform a full, quantitative bonding analysis of the phosphine ligands. The hurdle that the inconsistent  $\Delta S^\ddagger$  value in acetonitrile and the inconsistent interactions of the anion in chloroform imposed, provided no workaround. Despite this, our qualitative investigations led to some exciting results. The estimated values we observed from the  $\Delta H^\ddagger$  led us to investigate the Cr(VI)-P bonding computationally. In doing so we discovered contrasting bonding pictures between high and low valent metals. The resonance form  $\epsilon$  provides an explanation for the surprisingly strong electron donation from aryl phosphines and phosphites.

Our phosphine study was quite different than the M-PE<sub>3</sub> phosphine studies that Tolman and others have studied.<sup>1</sup> As such, the observed differences in M-P bonding are not shocking. We propose that many systems that could broadly be classified as mid-valent, may incorporate both sorts of metal-phosphine bonding pictures to varying degrees. As such, we hope these bonding descriptors find use in a wide variety of phosphine selection considerations.

### 3.9 Experimental

**This experimental was taken from our recent publications. These can be located at:**

*Organometallics*, **2017**, 36(7), 1227-1237

And

*Polyhedron*, **2018**, accepted

All syntheses were carried out under an N<sub>2</sub> atmosphere, using standard Schlenk techniques or in an MBraun glovebox. All reagents were stored in a glovebox after purification. Diethyl ether, acetonitrile, and dichloromethane were purified by passing them over a neutral alumina column under N<sub>2</sub> and stored over 3 Å molecular sieves. Chloroform was distilled from P<sub>2</sub>O<sub>5</sub> under N<sub>2</sub> and



stored over molecular sieves. Deuterated chloroform from Cambridge Isotope Laboratories was distilled from P<sub>2</sub>O<sub>5</sub> under N<sub>2</sub> and stored over molecular sieves. Deuterated acetonitrile from Cambridge Isotope Laboratories was distilled under N<sub>2</sub> from calcium hydride and stored over 3 Å molecular sieves. The complex NCr(N<sup>i</sup>Pr)<sub>2</sub>I was prepared according to the literature procedure.<sup>18</sup>

Trimethyl-, dimethylphenyl-, and diphenylmethylphosphine were purchased from Aldrich Chemical Co. and used as received. Triethylphosphite and triisopropylphosphite were purchased from Aldrich Chemical Co. and distilled from Na<sub>2</sub>SO<sub>4</sub> under reduced pressure. Triisobutylphosphine, diphenylcyclohexylphosphine, and phenyldicyclohexylphosphine were purchased from Strem Chemical Co. and used as received. Triisopropylphosphine purchased from Strem Chemical Co. was distilled from a 10 wt% solution in hexanes and stored over 3 Å molecular sieves. Tri(*n*-butyl)phosphine purchased from Strem Chemical Co. was distilled under purified N<sub>2</sub> and stored over 3 Å molecular sieves. Triphenyl-, phenyldiethyl-, diphenylethyl-, and tricyclohexylphosphine were purchased from Alfa Aesar and used as received. Silver hexafluoroantimonate and thallium hexafluorophosphate were purchased from Sigma-Aldrich Chemical Co. and used as received. Thallium(I) BAr<sup>F</sup><sub>24</sub><sup>−</sup>, where BAr<sup>F</sup><sub>24</sub><sup>−</sup> = B[3,5-(CF<sub>3</sub>)<sub>2</sub>C<sub>6</sub>H<sub>3</sub>]<sub>4</sub><sup>−</sup>, was prepared using the literature procedure.<sup>30</sup> The KBar<sup>F</sup><sub>20</sub> was supplied as a gift from Boulder Chemical Co. and was used as received. AgAl(O<sup>i</sup>BuF<sub>9</sub>)<sub>4</sub> was prepared following the literature procedure.<sup>12</sup>

Diphenyl(*n*-butyl)phosphine was synthesized by adding 1.7 M <sup>n</sup>BuLi solution (1 equiv) to PPh<sub>2</sub>Cl (1 equiv) in cold (−78 °C) diethyl ether.<sup>31</sup> In the literature preps for these phosphines, they were purified by distillation. However, the syntheses were carried out on much smaller scales than was conducted in the literature. Thus as an alternative method of purification, the diphenyl(*n*-



butyl)phosphine, were run over a short plug of alumina for purification, which provided colorless oils pure by multi-nuclear NMR spectroscopy.

Adequate CHN was not obtained on the complexes under study despite many attempts. The cationic Cr(VI) complexes have been characterized by NMR ( $^1\text{H}$ ,  $^{13}\text{C}$ ,  $^{31}\text{P}$ ,  $^{14}\text{N}$ , and  $^{19}\text{F}$ ), X-ray diffraction, and melting point. All experiments carried out with the chromium complexes in this study were conducted with X-ray quality single crystals in an attempt to ensure purity.

### Synthetic Details

The preparation of the phosphines with various cations followed essentially the same procedure as that below. The exception is the synthesis of  $\text{BAr}^{\text{F}}_{24}$  salts, which were synthesized using Tl in DCM using the same general procedure as that below

*General Procedure for the Synthesis of  $[\text{NCr}(\text{N}^i\text{Pr}_2)_2\text{PE}_3]^+ \text{SbF}_6^-$ :* A 20 mL scintillation vial was charged with 1 equiv of  $\text{NCr}(\text{N}^i\text{Pr}_2)_2\text{I}$ ,<sup>18</sup> acetonitrile (3 mL), and a Teflon-coated stir bar. This mixture was stirred at room temperature giving a dark red-orange solution. Separately, a solution of  $\text{AgSbF}_6$  (1 equiv) was prepared in acetonitrile (1-2 mL). The  $\text{AgSbF}_6$  solution was then added dropwise to the stirred solution of  $\text{NCr}(\text{N}^i\text{Pr}_2)_2\text{I}$ . Upon addition, copious amounts of off-white precipitate formed, and the solution became dark brown. The resultant mixture was stirred for 20 min after complete addition of the Ag solution. The mixture was then filtered over Celite to remove the precipitate. The dark brown solution was once again stirred at room temperature and a solution of  $\text{PR}_3$  (1-2 equiv) in acetonitrile (1-2 mL) was added. (1 equiv of the phosphine was used if it was a solid or high-boiling liquid phosphine that is difficult to remove by recrystallization. 2 equiv of phosphine were used if  $\text{PR}_3$  is a low-boiling liquid easily removed *in vacuo*.) Upon addition of  $\text{PR}_3$ , the solution quickly became yellow-orange. The reaction solution was stirred for 1 h at room



temperature. The volatiles were then removed in vacuo to give a dark residue. This residue was rinsed with small aliquots of cold Et<sub>2</sub>O (3 x 1 mL) to remove any unreacted material. The residue was once more dried in vacuo. The residue was dissolved in a minimal amount of CH<sub>2</sub>Cl<sub>2</sub> or CHCl<sub>3</sub> and layered with Et<sub>2</sub>O or pentane. The layered solution was then stored overnight at –35 °C to yield yellow-orange X-ray quality crystals.

*Synthesis of [NCr(N<sup>i</sup>Pr)<sub>2</sub>PMe<sub>3</sub>]<sup>+</sup> SbF<sub>6</sub><sup>–</sup>:* Following the general procedure, the reaction was carried out with NCr(N<sup>i</sup>Pr)<sub>2</sub>I (89 mg, 0.226 mmol), AgSbF<sub>6</sub> (78 mg, 0.226 mmol), and PMe<sub>3</sub> (35 mg, 0.46 mmol). Yield (68.2 mg, 52.4%). Note: Synthesis for the other anions of this complex were achieved using the same generic procedure. M.p.: 111–113 °C. <sup>1</sup>H NMR (500 MHz, CDCl<sub>3</sub>) δ 5.42 – 5.29 (sept, 2H), 4.08 – 3.93 (sept, 2H), 1.86 (t, J = 4.6 Hz, 6H), 1.69 (d, J = 10.9 Hz, 9H), 1.61 (d, J = 6.3 Hz, 6H), 1.39 (d, J = 6.3 Hz, 6H), 1.27 (d, J = 9.0 Hz, 6H). <sup>13</sup>C NMR (126 MHz, CD<sub>3</sub>CN) δ 59.77 (s), 59.16 (s), 32.06 (s), 30.44 (s), 23.20 (d), 16.79 (s), 16.14 (s), 15.89 (s). <sup>19</sup>F (470 MHz, CDCl<sub>3</sub>) δ -123.1 (d). <sup>31</sup>P NMR (202 MHz, CDCl<sub>3</sub>) δ 6.86 (s).

*Synthesis of [NCr(N<sup>i</sup>Pr)<sub>2</sub>P<sup>n</sup>Bu<sub>3</sub>]<sup>+</sup> SbF<sub>6</sub><sup>–</sup>:* Following the general procedure, the reaction was carried out with NCr(N<sup>i</sup>Pr)<sub>2</sub>I (100 mg, 0.254 mmol), AgSbF<sub>6</sub> (87 mg, 0.254 mmol), and P<sup>n</sup>Bu<sub>3</sub> (51.4 mg, 0.51 mmol). Yield (83.1 mg, 46.4%). M.p.: 50 °C (dec.). <sup>1</sup>H NMR (500 MHz, CDCl<sub>3</sub>): 7.70 (s, 1H), 7.52 (s, 1H), 7.47 (ddd, J = 19.8, 9.9, 5.1 Hz, 1H), 4.95 (sept, J = 12.8, 6.4 Hz, 1H), 3.88 (sept, J = 12.5, 6.3 Hz, 1H), 1.87 (d, J = 10.3 Hz, 1H), 1.65 (d, J = 6.3 Hz, 1H), 1.56 (d, J = 6.3 Hz, 1H), 1.15 (d, J = 6.4 Hz, 1H), 1.10 (d, J = 6.4 Hz, 1H). <sup>13</sup>C NMR (126 MHz, CDCl<sub>3</sub>): 59.85 (d), 58.92, 32.48, 30.30, 25.79 (d), 24.92 (d), 24.56 (d), 23.87, 23.79, 13.85. <sup>31</sup>P NMR (202 MHz, CDCl<sub>3</sub>): 30.0. <sup>19</sup>F NMR (470 MHz, CDCl<sub>3</sub>): –106.55 to –137.63 (m).

*Synthesis of [NCr(N<sup>i</sup>Pr)<sub>2</sub>P<sup>i</sup>Bu<sub>3</sub>]<sup>+</sup> SbF<sub>6</sub><sup>–</sup>:* Following the general procedure, the reaction was carried out with NCr(N<sup>i</sup>Pr)<sub>2</sub>I (50 mg, 0.127 mmol), AgSbF<sub>6</sub> (44 mg, 0.127 mmol), and P<sup>i</sup>Bu<sub>3</sub> (36



mg, 0.254 mmol). Yield (58.6 mg, 64.7%). M.p.: 150 °C (dec.).  $^1\text{H}$  NMR (500 MHz,  $\text{CDCl}_3$ ): 5.36 (sept,  $J = 12.4, 6.2$  Hz, 2H), 4.00 (sept,  $J = 12.4, 6.2$  Hz, 2H), 2.16 (dt,  $J = 18.8, 6.3$  Hz, 3H), 1.97 (dd,  $J = 8.5, 6.3$  Hz, 6H), 1.84 (d,  $J = 6.3$  Hz, 6H), 1.57 (d,  $J = 6.2$  Hz, 6H), 1.37 (d,  $J = 6.2$  Hz, 6H), 1.32 (d,  $J = 6.2$  Hz, 6H), 1.10 (d,  $J = 6.6$  Hz, 18H).  $^{13}\text{C}$  NMR (126 MHz,  $\text{CDCl}_3$ ): 59.50 (d), 59.09, 32.56 (d), 29.40, 25.02, 24.87, 23.94 (d), 23.74, 19.46.  $^{31}\text{P}$  NMR (202 MHz,  $\text{CDCl}_3$ ): 32.8.

*Synthesis of  $[\text{NCr}(\text{N}^i\text{Pr}_2)_2\text{P}^i\text{Pr}_3]^+ \text{SbF}_6^-$ :* Following the general procedure, the reaction was carried out with  $\text{NCr}(\text{N}^i\text{Pr}_2)_2\text{I}$  (52 mg, 0.132 mmol),  $\text{AgSbF}_6$  (45 mg, 0.132 mmol), and  $\text{P}^i\text{Pr}_3$  (33.5 mg, 0.210 mmol). Yield (33.5 mg, 40%). M.p.: 155 °C (dec.).  $^1\text{H}$  NMR (500 MHz,  $\text{CDCl}_3$ ): 5.41 (sept,  $J = 12.5, 6.2$  Hz, 2H), 4.02 (sept,  $J = 12.6, 6.3$  Hz, 2H), 2.46-2.34 (m, 3H), 1.84 (d,  $J = 6.4$  Hz, 6H), 1.58 (d,  $J = 6.3$  Hz, 6H), 1.43 (d,  $J = 7.2$  Hz, 9H), 1.40 (d,  $J = 6.9$  Hz, 15H), 1.34 (d,  $J = 6.2$  Hz, 6H).  $^{13}\text{C}$  NMR (126 MHz,  $\text{CDCl}_3$ ): 59.71, 59.24, 32.74, 29.58, 25.12 (d), 24.14, 23.94, 19.65.  $^{31}\text{P}$  NMR (202 MHz,  $\text{CDCl}_3$ ):  $\delta$  67.0.  $^{19}\text{F}$  NMR (470 MHz,  $\text{CDCl}_3$ ): -105.15 to -139.23 (m,  $J = 1809.1, 1654.8, 1457.8, 1258.2$  Hz).

*Synthesis of  $[\text{NCr}(\text{N}^i\text{Pr}_2)_2\text{PCy}_3]^+ \text{SbF}_6^-$ :* Following the general procedure, the reaction was carried out with  $\text{NCr}(\text{N}^i\text{Pr}_2)_2\text{I}$  (55 mg, 0.140 mmol),  $\text{AgSbF}_6$  (48 mg, 0.140 mmol) and  $\text{PCy}_3$  (40.5 mg, 0.140 mmol). Yield (66 mg, 60%). M.p.: 117 °C (dec.).  $^1\text{H}$  NMR (500 MHz,  $\text{CDCl}_3$ ): 5.35 (sept,  $J = 12.4, 6.2$  Hz, 2H), 4.02 (sept,  $J = 12.6, 6.3$  Hz, 2H), 2.06 (dt,  $J = 21.0, 10.5$  Hz, 6H), 1.99-1.86 (m, 16H), 1.83 (d,  $J = 6.3$  Hz, 8H), 1.78 (s, 4H), 1.58 (d,  $J = 6.3$  Hz, 10H), 1.56-1.41 (m, 6H), 1.39 (d,  $J = 6.2$  Hz, 8H), 1.36 (d,  $J = 6.2$  Hz, 8H), 1.35-1.11 (m, 16H).  $^{13}\text{C}$  NMR (126 MHz,  $\text{CDCl}_3$ ): 59.84, 59.22, 34.84 (d), 32.70, 29.75, 29.65, 27.60 (d), 25.84, 24.30, 23.75.  $^{31}\text{P}$  NMR (202 MHz,  $\text{CDCl}_3$ ): 56.9.  $^{19}\text{F}$  NMR (470 MHz,  $\text{CDCl}_3$ ): -123.19 (d,  $J = 3323.8$  Hz).

*Synthesis of  $[\text{NCr}(\text{N}^i\text{Pr}_2)_2\text{PPhMe}_2]^+ \text{SbF}_6^-$ :* Following the general procedure, the reaction was carried out with  $\text{NCr}(\text{N}^i\text{Pr}_2)_2\text{I}$  (50 mg, 0.127 mmol),  $\text{AgSbF}_6$  (44 mg, 0.127 mmol), and  $\text{PPhMe}_2$



(35 mg, 0.253 mmol). Yield (56.4 mg, 68.4%). Note: Synthesis for the other anions of this complex were achieved using the same generic procedure. M.p.: 152-154°C (dec.).  $^1\text{H}$  NMR (500 MHz,  $\text{CDCl}_3$ )  $\delta$  7.62 (dd,  $J$  = 8.7, 3.1 Hz, 2H), 7.53 (s, 3H), 5.33 (sept,  $J$  = 23.2 Hz, 2H), 3.91 (dt,  $J$  = 12.0, 5.9 Hz, 2H), 1.99 (d,  $J$  = 10.3 Hz, 6H), 1.57 (dd,  $J$  = 11.1, 6.2 Hz, 12H), 1.31 – 1.17 (m, 13H).  $^{13}\text{C}$  NMR (126 MHz,  $\text{CDCl}_3$ )  $\delta$  132.07 (s), 130.38 (d), 129.93 (d), 59.81 (d), 58.73 (s), 32.05 (s), 29.68 (s), 23.40 (s), 22.63 (s), 14.56 (s), 14.32 (s).  $^{19}\text{F}$  NMR (470 MHz,  $\text{CDCl}_3$ )  $\delta$  -122.13 (d,  $J$  = 5077.9 Hz).  $^{31}\text{P}$  NMR (202 MHz,  $\text{CDCl}_3$ )  $\delta$  11.89 (s).  $^{14}\text{N}$  NMR (36 MHz  $\text{CDCl}_3$ , 25 °C)  $\delta$  448.8 (s).

*Synthesis of  $[\text{NCr}(\text{N}^i\text{Pr}_2)_2\text{PPh}_2\text{Me}]^+ \text{SbF}_6^-$ :* Following the general procedure, the reaction was carried out with  $\text{NCr}(\text{N}^i\text{Pr}_2)_2\text{I}$  (50 mg, 0.127 mmol),  $\text{AgSbF}_6$  (43 mg, 0.127 mmol), and  $\text{PPh}_2\text{Me}$  (50 mg, 0.250 mmol). Yield (50.1 mg, 54.9%). M.p.: 138 °C.  $^1\text{H}$  NMR (500 MHz,  $\text{CDCl}_3$ ): 7.94-7.27 (m, 10H), 5.40 (sept,  $J$  = 11.6, 5.7 Hz, 2H), 3.89 (sept,  $J$  = 12.0, 5.9 Hz, 2H), 2.34 (d,  $J$  = 9.2 Hz, 3H), 1.89 (s, 1H), 1.55 (dd,  $J$  = 15.3, 6.2 Hz, 12H), 1.40 (s, 3H), 1.27 (d,  $J$  = 6.0 Hz, 7H), 1.07 (d,  $J$  = 6.0 Hz, 6H).  $^{13}\text{C}$  NMR (126 MHz,  $\text{CDCl}_3$ ): 132.42 (d), 132.09, 131.79 (d), 130.70, 129.92 (d), 129.21, 128.31, 127.93, 59.97 (d), 58.89, 31.99, 29.11, 23.05, 22.25, 12.67 (d).  $^{31}\text{P}$  NMR (202 MHz,  $\text{CDCl}_3$ ): 20.7.  $^{19}\text{F}$  NMR (470 MHz,  $\text{CDCl}_3$ ): -107.41 to -139.91 (m). The X-ray diffraction study was carried out on the  $\text{BAr}^{\text{F}}_{24}^-$  salt, which gave single crystals and was made analogously to the  $\text{SbF}_6^-$  salt.

*Synthesis of  $[\text{NCr}(\text{N}^i\text{Pr}_2)_2\text{PPhEt}_2]^+ \text{SbF}_6^-$ :* Following the general procedure, the reaction was carried out with  $\text{NCr}(\text{N}^i\text{Pr}_2)_2\text{I}$  (50 mg, 0.127 mmol),  $\text{AgSbF}_6$  (43 mg, 0.127 mmol), and  $\text{PPhEt}_2$  (34 mg, 0.246 mmol). Yield (28.1 mg 33.1%). M.p.: 115 °C (dec.).  $^1\text{H}$  NMR (500 MHz,  $\text{CDCl}_3$ ): 7.64-7.50 (m, 5H), 5.21 (sept,  $J$  = 12.5, 6.3 Hz, 2H), 3.90 (sept,  $J$  = 12.5, 6.3 Hz, 2H), 2.48-2.33 (m,  $J$  = 15.0, 10.7, 7.5 Hz, 2H), 2.33-2.21 (m, 2H), 1.65 (d,  $J$  = 6.3 Hz, 6H), 1.57 (d,  $J$  = 6.3 Hz,



6H), 1.31-1.18 (m, 14H), 1.14 (d,  $J = 6.2$  Hz, 6H).  $^{13}\text{C}$  NMR (126 MHz,  $\text{CDCl}_3$ ): 132.09, 130.87 (d), 130.25 (d), 59.65, 58.51, 31.88, 23.53, 22.34, 17.60 (d), 7.16.  $^{31}\text{P}$  NMR (202 MHz,  $\text{CDCl}_3$ ): 34.9.  $^{19}\text{F}$  NMR (470 MHz,  $\text{CDCl}_3$ ):  $-123.30$  (d,  $J = 5888.3$  Hz).

*Synthesis of  $[\text{NCr}(\text{N}^i\text{Pr}_2)_2\text{PPh}_2\text{Et}]^+ \text{SbF}_6^-$ :* Following the general procedure, the reaction was carried out with  $\text{NCr}(\text{N}^i\text{Pr}_2)_2\text{I}$  (100 mg, 0.254 mmol),  $\text{AgSbF}_6$  (87 mg, 0.254 mmol), and  $\text{PPh}_2\text{Et}$  (63 mg, 0.298 mmol). Yield (94 mg, 51.6%). M.p.:  $150\text{ }^\circ\text{C}$  (dec).  $^1\text{H}$  NMR (500 MHz,  $\text{CDCl}_3$ ): 7.60 (dt,  $J = 11.6, 6.1$  Hz, 6H), 7.45-7.28 (m, 4H), 5.20 (sept,  $J = 6.3$  Hz, 2H), 3.93 (sept,  $J = 6.4$  Hz, 2H), 2.62 (p,  $J = 7.3$  Hz, 2H), 1.70 (d,  $J = 6.2$  Hz, 6H), 1.56 (d,  $J = 6.2$  Hz, 6H), 1.24 (d,  $J = 6.3$  Hz, 6H), 1.11 (dt,  $J = 18.0, 7.4$  Hz, 3H), 1.01 (d,  $J = 6.3$  Hz, 6H).  $^{13}\text{C}$  NMR (126 MHz,  $\text{CDCl}_3$ ): 132.98 (d), 132.85 (d), 130.20 (d), 125.36 (d), 60.06, 59.07, 32.31, 29.49, 23.39, 22.60 (d), 22.34, 7.98 (d).  $^{31}\text{P}$  NMR (202 MHz,  $\text{CDCl}_3$ ): 35.3.  $^{19}\text{F}$  NMR (470 MHz,  $\text{CDCl}_3$ ):  $-122.12$  (d,  $J = 5841.6$  Hz).

*Synthesis of  $[\text{NCr}(\text{N}^i\text{Pr}_2)_2\text{PPh}_2^i\text{Bu}]^+ \text{PF}_6^-$ :* A 20 mL scintillation vial was charged with  $\text{NCr}(\text{N}^i\text{Pr}_2)_2\text{I}$  (100 mg, 0.254 mmol),  $\text{CH}_2\text{Cl}_2$  (5 mL),  $\text{PPh}_2^i\text{Bu}$  (61 mg, 0.252 mmol), and a Teflon-coated stir bar. This solution was stirred at room temperature to give a dark red-orange solution. Separately, a suspension of  $\text{TIPF}_6$  was prepared in 2 mL of  $\text{CH}_2\text{Cl}_2$ . The  $\text{TIPF}_6$  suspension was then added dropwise to the stirred solution of  $\text{NCr}(\text{N}^i\text{Pr}_2)_2\text{I}$  and  $\text{PPh}_2^i\text{Bu}$ . A yellow precipitate began to form on addition. After addition, the solution was stirred 3 h at room temperature. Then, the reaction mixture was filtered through Celite to remove the precipitate, and the bright orange filtrate was collected. The volatiles were removed from the filtrate in vacuo, leaving a dark residue. The residue was washed with cold  $\text{Et}_2\text{O}$  (3 x 1 mL), and the solution was again dried in vacuo. The residue was dissolved in a minimal amount of  $\text{CH}_2\text{Cl}_2$  and layered with pentane. The layered solution was stored at  $-35\text{ }^\circ\text{C}$  overnight to get X-ray quality orange crystals. Yield (104 mg, 63%).



M.p.: 74-77 °C (dec).  $^1\text{H}$  NMR (500 MHz,  $\text{CDCl}_3$ ): 7.78-7.47 (m, 10H), 5.22 (sept,  $J = 6.3$  Hz, 2H), 3.93 (sept,  $J = 6.4$  Hz, 2H), 2.53 (q,  $J = 7.8$  Hz, 2H), 1.69 (d,  $J = 6.3$  Hz, 6H), 1.56 (d,  $J = 6.2$  Hz, 6H), 1.38 (dq,  $J = 23.9, 8.0, 7.6$  Hz, 4H), 1.25 (d,  $J = 6.3$  Hz, 6H), 0.99 (d,  $J = 6.3$  Hz, 6H), 0.84 (t,  $J = 7.1$  Hz, 3H).  $^{13}\text{C}$  NMR (126 MHz,  $\text{CDCl}_3$ ): 132.89 (d), 132.80 (d), 130.23 (d), 125.81 (d), 60.11, 59.04, 32.29, 29.44, 29.05 (d), 25.67 (d), 23.99 (d), 23.33, 22.32, 13.60.  $^{31}\text{P}$  NMR (202 MHz,  $\text{CDCl}_3$ ): 32.7.  $^{19}\text{F}$  NMR (470 MHz,  $\text{CDCl}_3$ ): -73.41 (d,  $J = 712.4$  Hz).

*Synthesis of  $[\text{NCr}(\text{N}^i\text{Pr}_2)_2\text{PPh}_2\text{Cy}]^+ \text{SbF}_6^-$* : Following the general procedure, the reaction was carried out with  $\text{NCr}(\text{N}^i\text{Pr}_2)_2\text{I}$  (75 mg, 0.191 mmol),  $\text{AgSbF}_6$  (68 mg, 0.195 mmol), and  $\text{PPh}_2\text{Cy}$  (63 mg, 0.230 mmol). Yield (62.5 mg, 63.8%). M.p.: 168 °C (dec).  $^1\text{H}$  NMR (500 MHz,  $\text{CDCl}_3$ ): 7.63 (m,  $J = 15.0, 7.8$  Hz, 10H), 4.94 (sept,  $J = 6.2$  Hz, 2H), 3.92 (sept,  $J = 6.3$  Hz, 2H), 2.50–2.33 (m, 1H), 2.31–2.14 (m, 2H), 1.93–1.77 (m, 2H), 1.72 (d,  $J = 6.3$  Hz, 6H), 1.57 (d,  $J = 6.2$  Hz, 6H), 1.45–1.33 (m, 6H), 1.20 (d,  $J = 6.3$  Hz, 6H), 1.02 (d,  $J = 6.2$  Hz, 6H), 0.93–0.72 (m, 2H).  $^{13}\text{C}$  NMR (126 MHz,  $\text{CDCl}_3$ ): 133.77 (d,  $J = 10.2$  Hz), 132.89, 129.85 (d,  $J = 10.2$  Hz), 123.03 (d,  $J = 42.8$  Hz), 59.92 (d,  $J = 1.8$  Hz), 58.90, 36.94 (d,  $J = 22.4$  Hz), 32.14 (d,  $J = 1.8$  Hz), 29.05, 26.63 (d,  $J = 12.5$  Hz), 25.46, 23.34, 22.39.  $^{31}\text{P}$  NMR (202 MHz,  $\text{CDCl}_3$ ): 45.2.  $^{19}\text{F}$  NMR (470 MHz,  $\text{CDCl}_3$ ): -106.76 to -136.05 (m). The X-ray diffraction study was done with the  $\text{BPh}_4^-$  salt, which gave single crystals and was made analogously to the  $\text{SbF}_6^-$  salt.

*Synthesis of  $[\text{NCr}(\text{N}^i\text{Pr}_2)_2\text{PPhCy}_2]^+ \text{SbF}_6^-$* : Following the general procedure, the reaction was carried out with  $\text{NCr}(\text{N}^i\text{Pr}_2)_2\text{I}$  (52 mg, 0.132 mmol),  $\text{AgSbF}_6$  (45 mg, 0.132 mmol), and  $\text{PPhCy}_2$  (48.3 mg, 0.176 mmol). Yield (58.2 mg, 56.1%). M.p.: 115 °C (dec).  $^1\text{H}$  NMR (500 MHz,  $\text{CDCl}_3$ ): 7.79-7.37 (m, 5H), 5.38 (sept,  $J = 12.2, 6.1$  Hz, 2H), 3.99 (sept,  $J = 12.2, 6.0$  Hz, 2H), 2.34 (d,  $J = 8.7$  Hz, 2H), 1.91 (d,  $J = 21.6$  Hz, 8H), 1.77 (d,  $J = 6.2$  Hz, 8H), 1.60 (d,  $J = 6.2$  Hz, 6H), 1.44-1.05 (m, 24H).  $^{13}\text{C}$  NMR (126 MHz,  $\text{CDCl}_3$ ): 132.89 (d), 132.49, 130.01 (d), 122.36 (d), 59.96, 59.02,



34.31 (d), 32.28, 29.37, 28.32, 28.04, 27.17-26.56 (m), 25.52, 23.50, 23.19.  $^{31}\text{P}$  NMR (202 MHz,  $\text{CDCl}_3$ ): 49.8.  $^{19}\text{F}$  NMR (470 MHz,  $\text{CDCl}_3$ ): -108.70 to -142.59 (m).

*Synthesis of  $[\text{NCr}(\text{N}^i\text{Pr}_2)_2\text{P}(\text{OEt})_3]^+ \text{SbF}_6^-$ :* Following the general procedure, the reaction was carried out with  $\text{NCr}(\text{N}^i\text{Pr}_2)_2\text{I}$  (100 mg, 0.254 mmol),  $\text{AgSbF}_6$  (87 mg, 0.254 mmol), and  $\text{P}(\text{OEt})_3$  (43 mg, 0.26 mmol). Yield (48.2 mg, 28.3%). M.p.: 149-150 °C.  $^1\text{H}$  NMR (500 MHz,  $\text{CDCl}_3$ ): 5.36 (sept,  $J = 12.6, 6.3$  Hz, 2H), 4.24 (p,  $J = 7.1$  Hz, 6H), 4.03 (sept,  $J = 12.5, 6.1$  Hz, 2H), 1.87 (d,  $J = 6.3$  Hz, 6H), 1.60 (d,  $J = 6.3$  Hz, 6H), 1.45-1.35 (m, 18H), 1.28 (d,  $J = 6.3$  Hz, 9H).  $^{13}\text{C}$  NMR (126 MHz,  $\text{CDCl}_3$ ): 65.06 (d), 60.32 (d), 59.19, 32.14, 30.46, 23.17, 22.81, 16.29 (d).  $^{31}\text{P}$  NMR (202 MHz,  $\text{CDCl}_3$ ): 122.6.  $^{19}\text{F}$  NMR (470 MHz,  $\text{CDCl}_3$ ): -122.86 (d,  $J = 5081.0$  Hz).

*Synthesis of  $[\text{NCr}(\text{N}^i\text{Pr}_2)_2\text{P}(\text{O}^i\text{Pr})_3]^+ \text{SbF}_6^-$ :* Following the general procedure, the reaction was carried out with  $\text{NCr}(\text{N}^i\text{Pr}_2)_2\text{I}$  (50 mg, 0.127 mmol),  $\text{AgSbF}_6$  (43 mg, 0.127 mmol), and  $\text{P}(\text{O}^i\text{Pr})_3$  (38 mg, 0.182 mmol). Yield (44.3 mg, 51%). M.p.: 138-140 °C.  $^1\text{H}$  NMR (500 MHz,  $\text{CDCl}_3$ ): 5.35 (dt,  $J = 12.6, 6.3$  Hz, 2H), 4.89-4.70 (m, 3H), 4.05 (dt,  $J = 12.5, 6.2$  Hz, 2H), 1.92 (d,  $J = 6.3$  Hz, 6H), 1.56 (d,  $J = 6.3$  Hz, 6H), 1.41 (d,  $J = 6.2$  Hz, 18H), 1.38 (d,  $J = 6.3$  Hz, 6H), 1.30 (d,  $J = 6.3$  Hz, 6H).  $^{13}\text{C}$  NMR (126 MHz,  $\text{CDCl}_3$ ): 75.15 (d), 59.98 (d), 59.26, 32.48, 29.97, 24.11 (d), 23.00 (d).  $^{31}\text{P}$  NMR (202 MHz,  $\text{CDCl}_3$ ): 119.1.

*Synthesis of  $[\text{NCr}(\text{N}^i\text{Pr}_2)_2\text{NCCH}_3]^+ \text{SbF}_6^-$ :* A 20 mL scintillation vial was charged with  $\text{NCr}(\text{N}^i\text{Pr}_2)_2\text{I}$  (50 mg, 0.127 mmol), a Teflon-coated stir bar,  $\text{CH}_2\text{Cl}_2$  (4 mL), and acetonitrile (60  $\mu\text{L}$ ). The solution was stirred at room temperature to give a dark red-orange solution. Separately,  $\text{AgSbF}_6$  (43 mg, 0.125 mmol) was suspended in  $\text{CH}_2\text{Cl}_2$  (2 mL). The  $\text{AgSbF}_6$  suspension was then added dropwise to the chromium solution, resulting in rapid formation of an off-white precipitate. Upon complete addition, the solution was stirred 3 h at room temperature. Then, the reaction mixture was filtered over Celite to remove the precipitate, and the red filtrate was collected. The



volatiles were removed from the filtrate in vacuo, leaving a dark brown residue. The residue was washed with cold Et<sub>2</sub>O (3 x 1 mL), and once again, the volatiles were removed in vacuo. The residue was dissolved in a minimal amount of CH<sub>2</sub>Cl<sub>2</sub> and layered with Et<sub>2</sub>O. This solution was stored overnight at -35 °C to give X-ray quality red-orange crystals (30.9 mg, 43.5%). M.p.: 126-129 °C (dec.). <sup>1</sup>H NMR (500 MHz, CDCl<sub>3</sub>): 5.57 (sept, J = 7.5, 6.7 Hz, 2H), 4.07 (sept, J = 6.2 Hz, 2H), 2.58 (s, 3H), 2.02 (d, J = 6.2 Hz, 6H), 1.52 (d, J = 6.2 Hz, 6H), 1.39 (d, J = 6.2 Hz, 6H), 1.20 (d, J = 6.3 Hz, 6H). <sup>13</sup>C NMR (126 MHz, CDCl<sub>3</sub>): 60.34 (d), 59.87, 31.15, 30.91, 22.40, 22.25. <sup>19</sup>F NMR (470 MHz, CDCl<sub>3</sub>): -123.79 (d, J = 6244.7 Hz).

#### Instrumentation and Facilities

All NMR spectra, including LDP and routine characterization data, were recorded utilizing the Max T. Rogers NMR Facility at Michigan State University. These include a UNITYplus 500 spectrometer equipped with a 5 mm switchable broadband probe operating at 36.12 MHz (<sup>14</sup>N); a Varian Inova 500 spectrometer equipped with a 5 mm Pulse Field Gradient (PFG) switchable broadband probe operating at 499.84 MHz (<sup>1</sup>H) and 470.28 MHz (<sup>19</sup>F); a Varian Inova 600 spectrometer equipped with a 5 mm PFG switchable broadband probe operating at 599.89 MHz (<sup>1</sup>H) and 564.30 MHz (<sup>19</sup>F); and an Agilent DDR2 500 MHz NMR spectrometer equipped with a 5 mm PFG OneProbe operating at 499.84 MHz (<sup>1</sup>H), 125.73 MHz (<sup>13</sup>C), and 202.35 (<sup>31</sup>P). <sup>1</sup>H NMR chemical shifts are reported relative to residual CHCl<sub>3</sub> in CDCl<sub>3</sub> as 7.26 ppm. <sup>13</sup>C NMR chemical shifts are reported relative to natural abundance <sup>13</sup>CDCl<sub>3</sub> in *d*-chloroform as 77.0 ppm. Single crystal X-ray diffraction data was collected in the Center for Crystallographic Research at MSU.



Phosphine	Rate Constant	$\Delta G^\ddagger$ (kcal/mol)	$\Delta H^\ddagger$ (kcal/mol)	Std. Dev.	Temperature (°C)
<b>PMe<sub>3</sub></b>	0.58	19.59	16.64	0.03	54.31
<b>P<sup>n</sup>Bu<sub>3</sub></b>	0.36	19.69	16.77	0.005	51.13
<b>P<sup>i</sup>Pr<sub>3</sub></b>	0.46	20.14	17.13	0.02	62.90
<b>P<sup>i</sup>Bu<sub>3</sub></b>	0.52	20.19	17.17	0.02	60.72
<b>PCy<sub>3</sub></b>	0.43	20.32	17.29	0.03	62.96
<b>PPhMe<sub>2</sub></b>	0.57	19.46	16.53	0.01	52.04
<b>PPh<sub>2</sub>Me</b>	0.33	18.96	16.16	0.01	34.71
<b>PPhEt<sub>2</sub></b>	0.45	19.58	16.65	0.02	51.46
<b>PPh<sub>2</sub>Et</b>	1.16	19.09	16.15	0.02	53.62
<b>PPh<sub>2</sub><sup>n</sup>Bu</b>	0.4	19.16	16.31	0.008	43.71
<b>PPh<sub>2</sub>Cy</b>	1.01	19.41	16.43	0.02	57.36
<b>PPhCy<sub>2</sub></b>	0.54	19.26	16.37	0.02	48.25
<b>P(OEt)<sub>3</sub></b>	0.48	18.5	15.73	0.02	34.88
<b>P(O<sup>i</sup>Pr)<sub>3</sub></b>	1.15	18.81	15.91	0.04	48.82

Table 3-5. Experimental  $\Delta H^\ddagger$  values (including  $\Delta G^\ddagger$ ) for [NCr(N<sup>i</sup>Pr<sub>2</sub>)<sub>2</sub>PE<sub>3</sub>]SbF<sub>6</sub> salts in CD<sub>3</sub>CN. <sup>a</sup>  $\Delta H^\ddagger$  value in CD<sub>3</sub>CN was measured via *in situ* generated species stabilized with excess phosphine. <sup>b</sup> Measured  $\Delta H^\ddagger$  was taken in multiple trials, taking a single measurement on three different samples due to compound instability. As a result, three different temperatures were calibrated, one for each separate run. The reported  $\Delta G^\ddagger$  is approximate, as it is an average from 3 (close) temperatures.



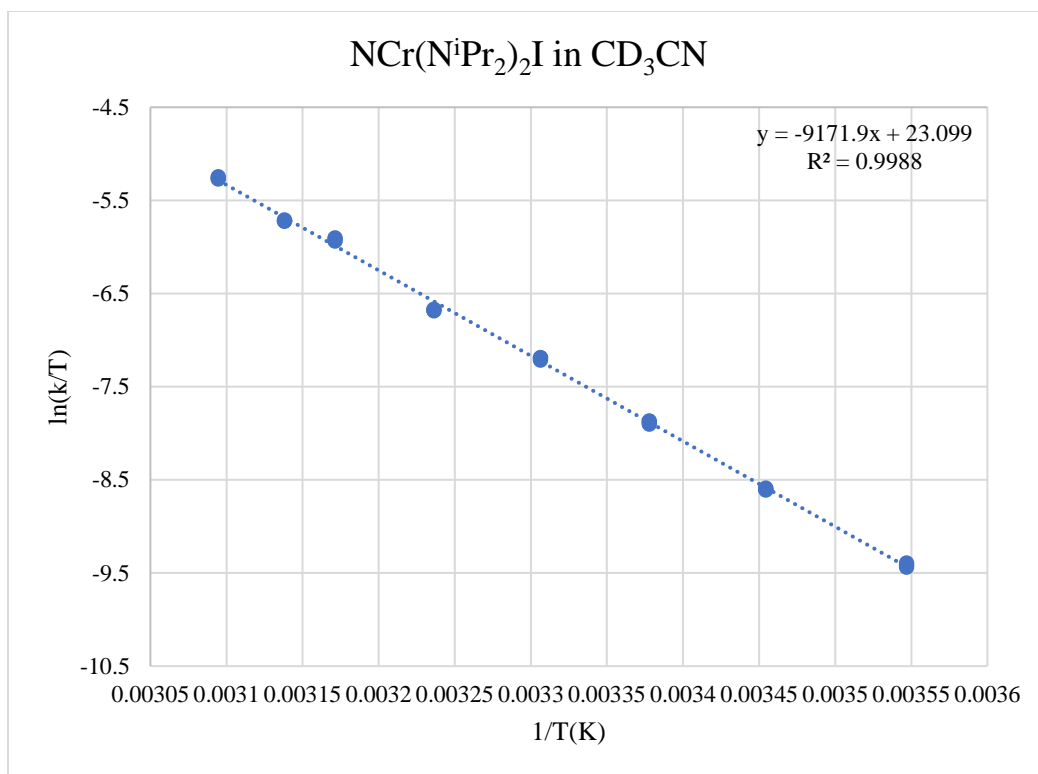


Figure 3-7. Eyring Plot for  $\text{NCr}(\text{N}^i\text{Pr}_2)_2\text{I}$  in  $\text{CD}_3\text{CN}$ . The value obtained was -1 e.u. ( $\pm 0.5$ ).



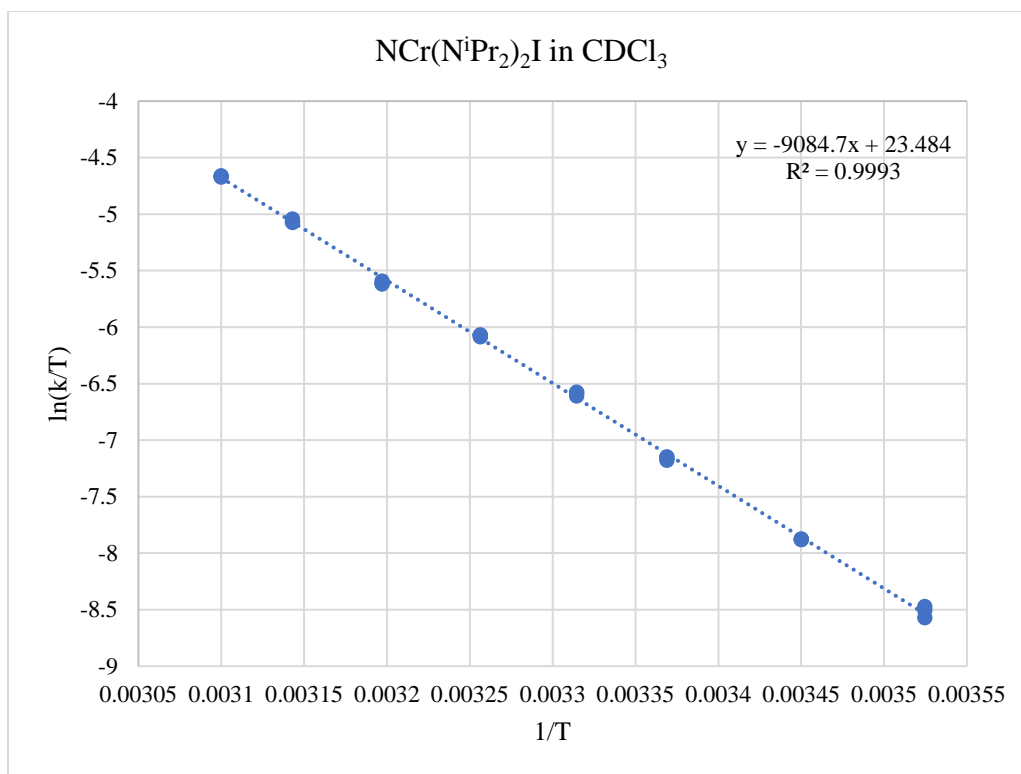


Figure 3-8. Eyring Plot analysis of  $\text{NCr}(\text{N}^i\text{Pr}_2)_2\text{I}$  in  $\text{CDCl}_3$ . The value obtained for  $\Delta S^\ddagger$  was  $-0.6(0.3)$ .



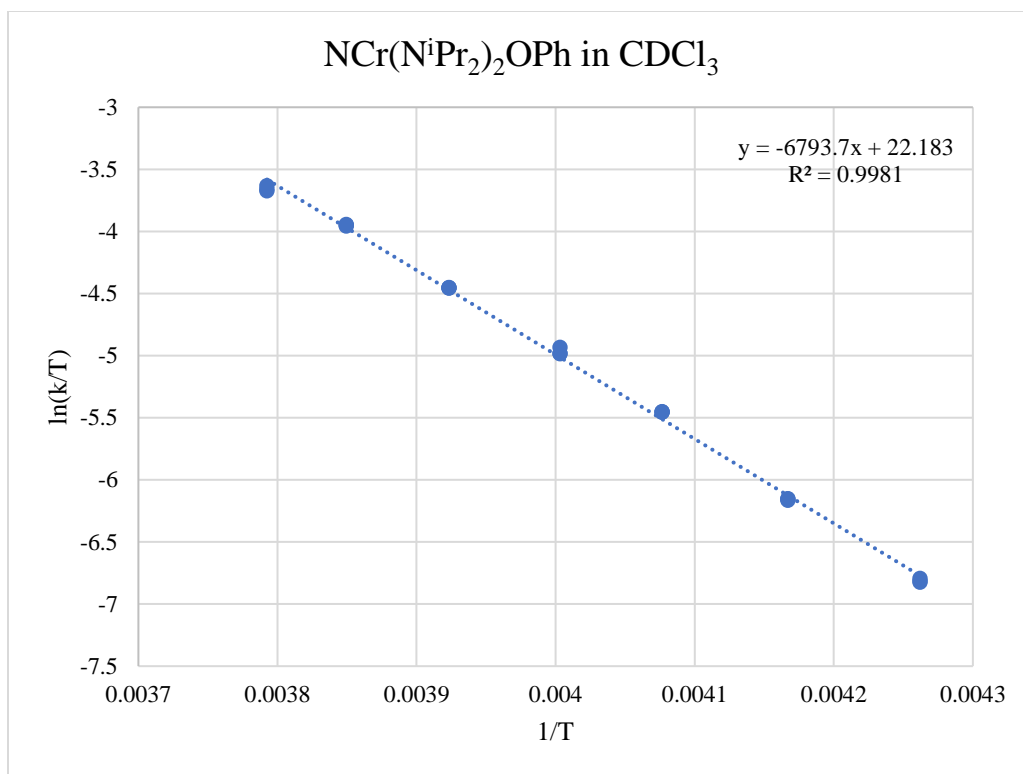


Figure 3-9. Eyring Plot analysis of  $\text{NCr}(\text{N}^i\text{Pr}_2)_2\text{OPh}$  in  $\text{CDCl}_3$ . The value obtained for  $\Delta S^\ddagger$  was  $-3.1(0.5)$ .



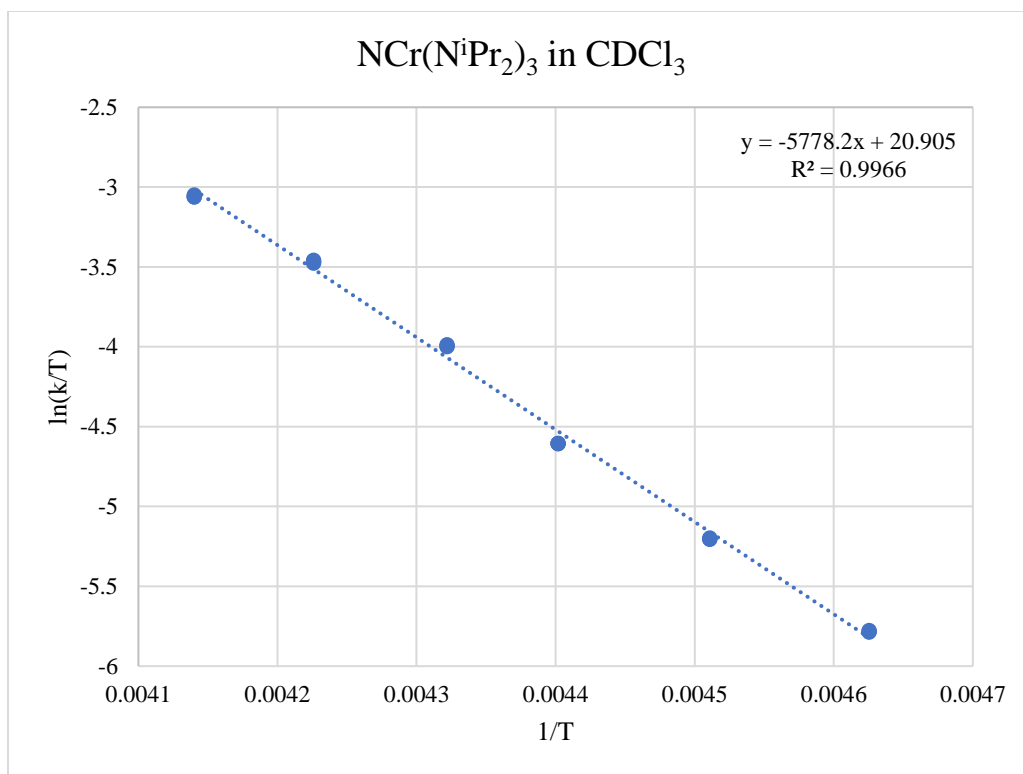


Figure 3-10. Eyring Plot analysis of  $\text{N}(\text{C}(\text{H}_3)_2)_3\text{Cr}(\text{N}(\text{C}(\text{H}_3)_2)_2)_3$  in  $\text{CDCl}_3$ . The value obtained for  $\Delta S^\ddagger$  was  $-5.7(0.7)$



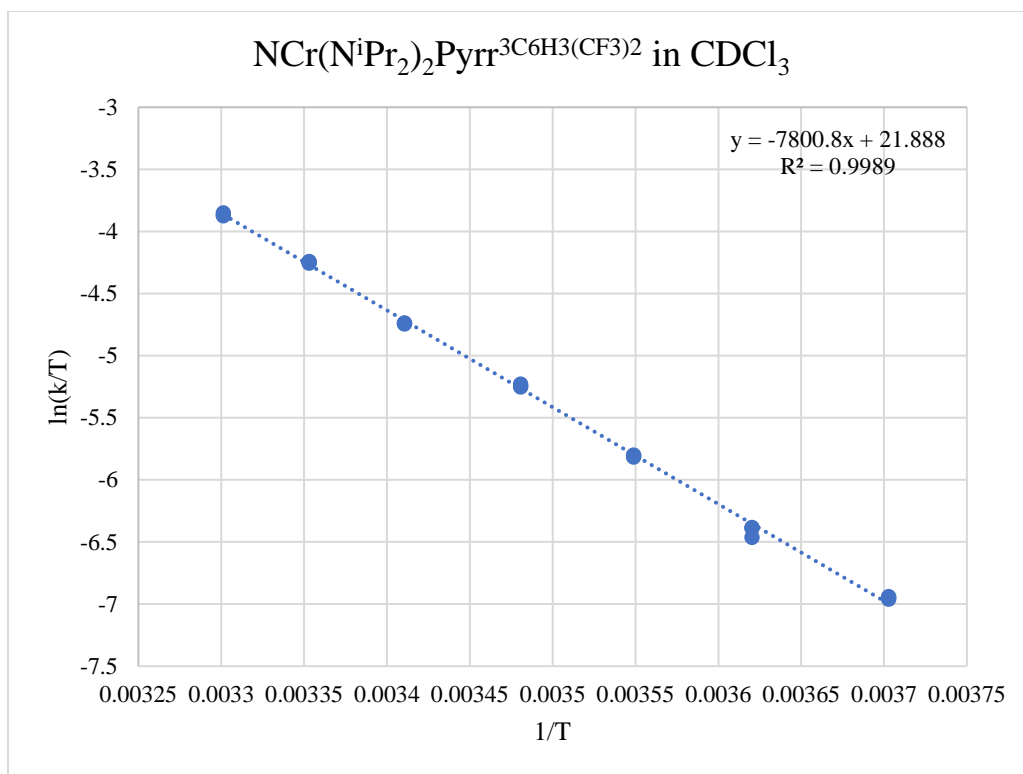


Figure 3-11. Eyring Plot analysis of  $\text{NCr}(\text{N}^i\text{Pr}_2)_2\text{Pyr}^{3\text{C}_6\text{H}_3(\text{CF}_3)_2}$  in  $\text{CDCl}_3$ . The value obtained for  $\Delta S^\ddagger$  was  $-3.7(0.4)$



## NMR Spectra

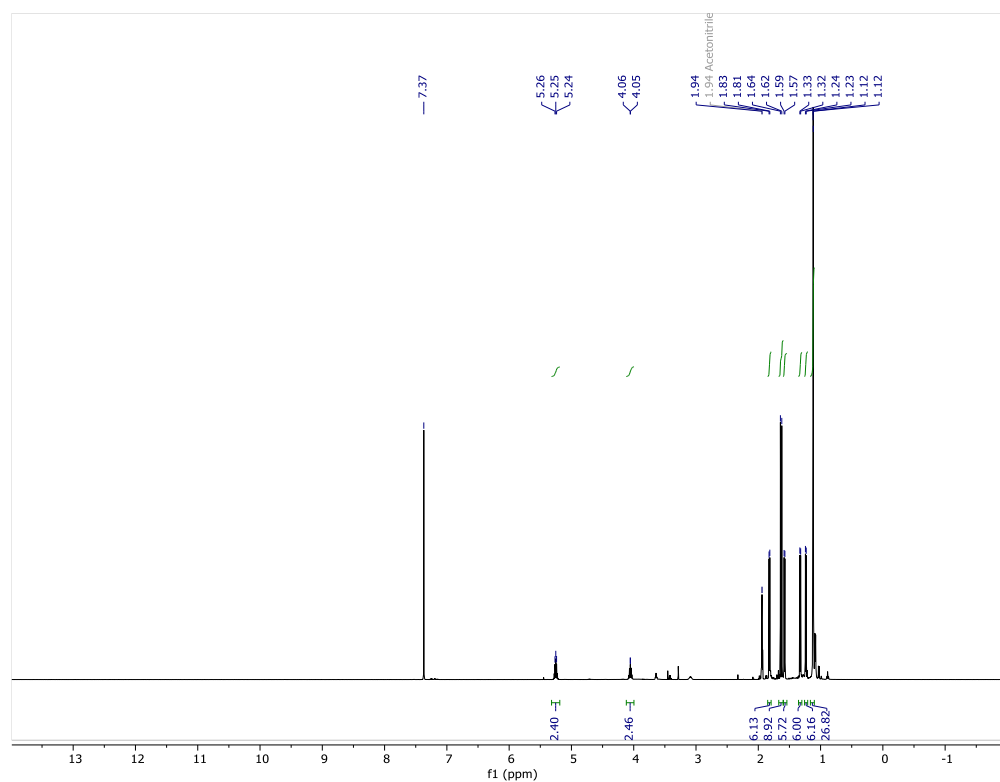


Figure 3-12.  $^1\text{H}$  NMR Spectrum for  $[\text{NCr}(\text{N}^i\text{Pr}_2)_2(\text{PMe}_3)]\text{SbF}_6$  (**3a**) in  $\text{CD}_3\text{CN}$



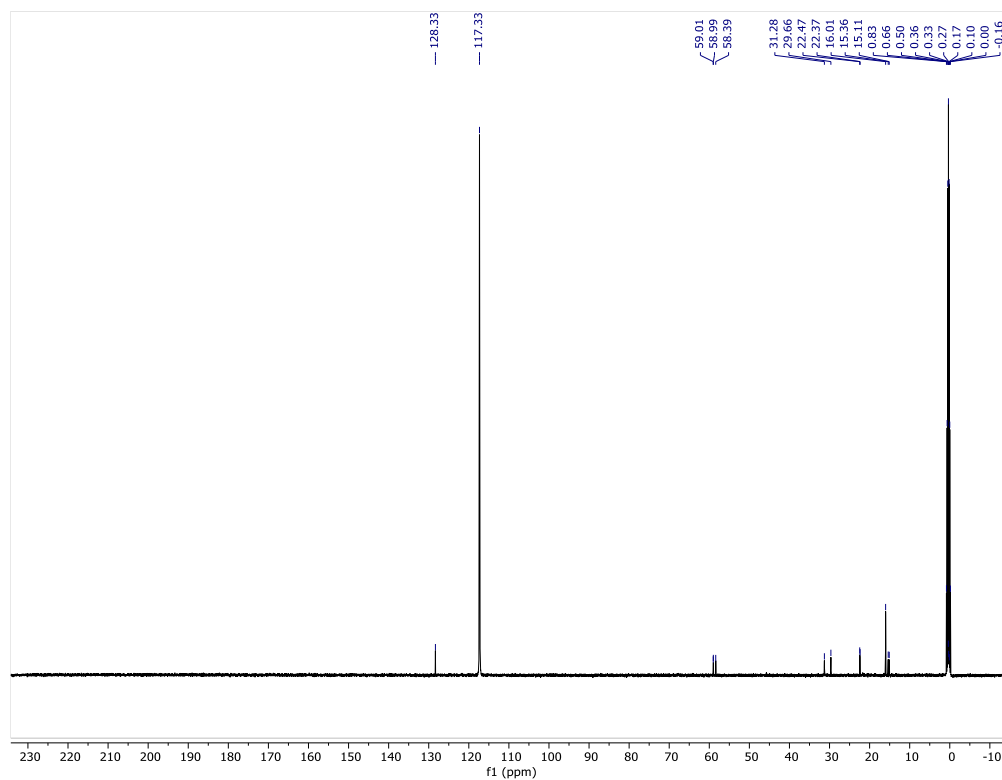


Figure 3-13.  $^{13}\text{C}$  NMR Spectrum for  $[\text{NCr}(\text{N}^i\text{Pr}_2)_2(\text{PMe}_3)]\text{SbF}_6$  (**3a**) in  $\text{CD}_3\text{CN}$



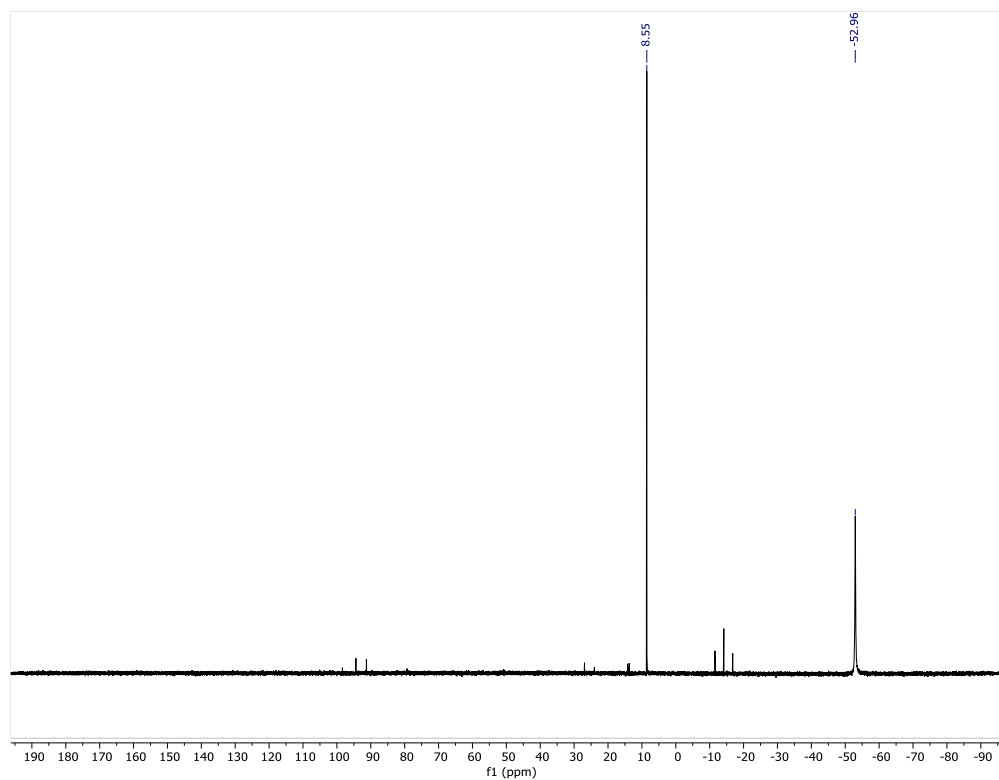


Figure 3-14.  $^{31}\text{P}$  NMR Spectrum for  $[\text{NCr}(\text{N}^i\text{Pr}_2)_2(\text{PMe}_3)]\text{SbF}_6$  (**3a**) in  $\text{CD}_3\text{CN}$



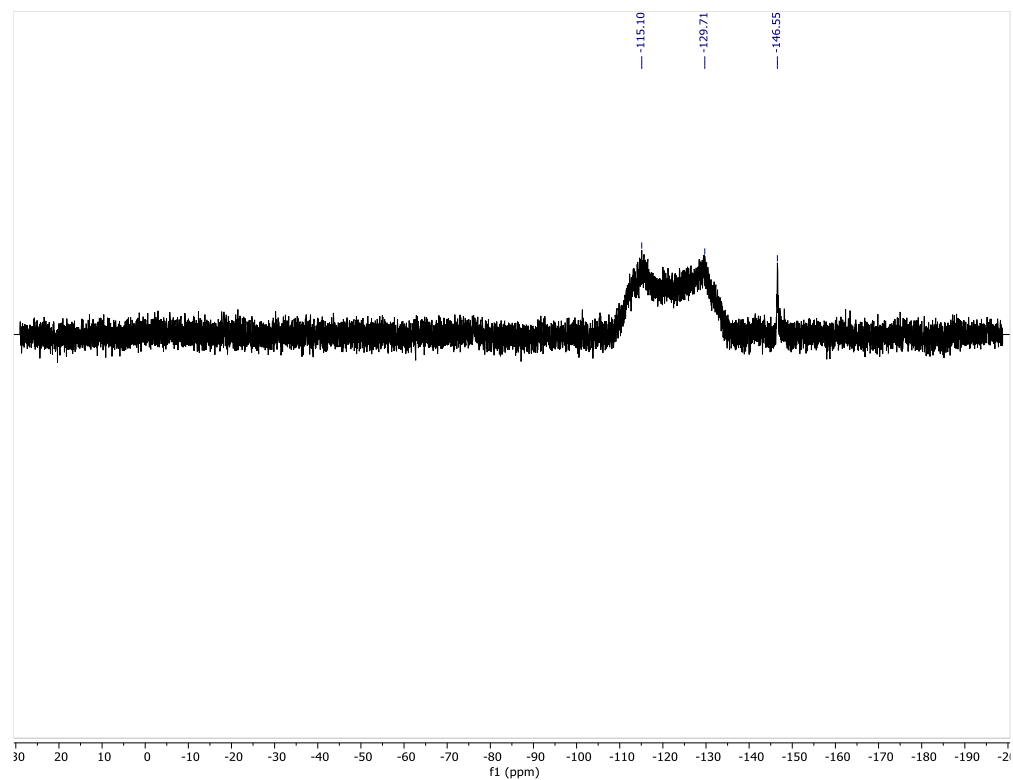


Figure 3-15.  $^{19}\text{F}$  NMR Spectrum for  $[\text{NCr}(\text{N}^i\text{Pr}_2)_2(\text{PMe}_3)]\text{SbF}_6$  (**3a**) in  $\text{CD}_3\text{CN}$



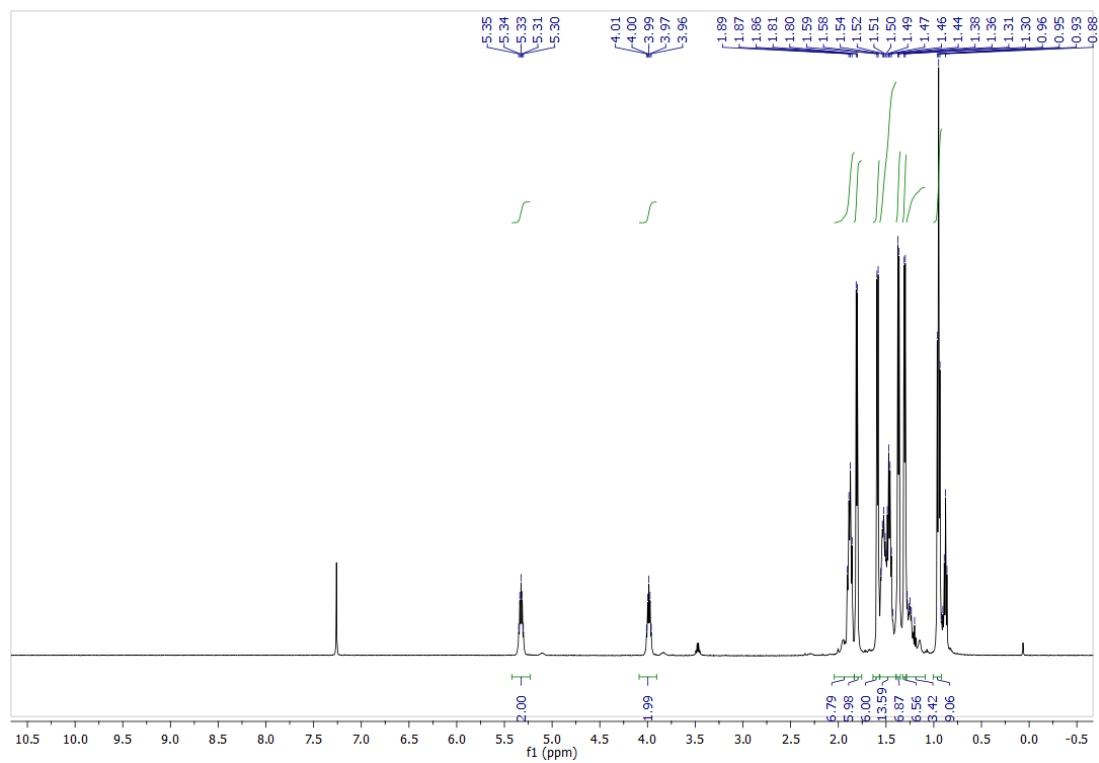


Figure 3-16.  $^1\text{H}$  NMR Spectrum for  $[\text{NCr}(\text{N}^i\text{Pr}_2)_2(\text{P}^n\text{Bu}_3)]\text{SbF}_6$  (**3b**) in  $\text{CDCl}_3$



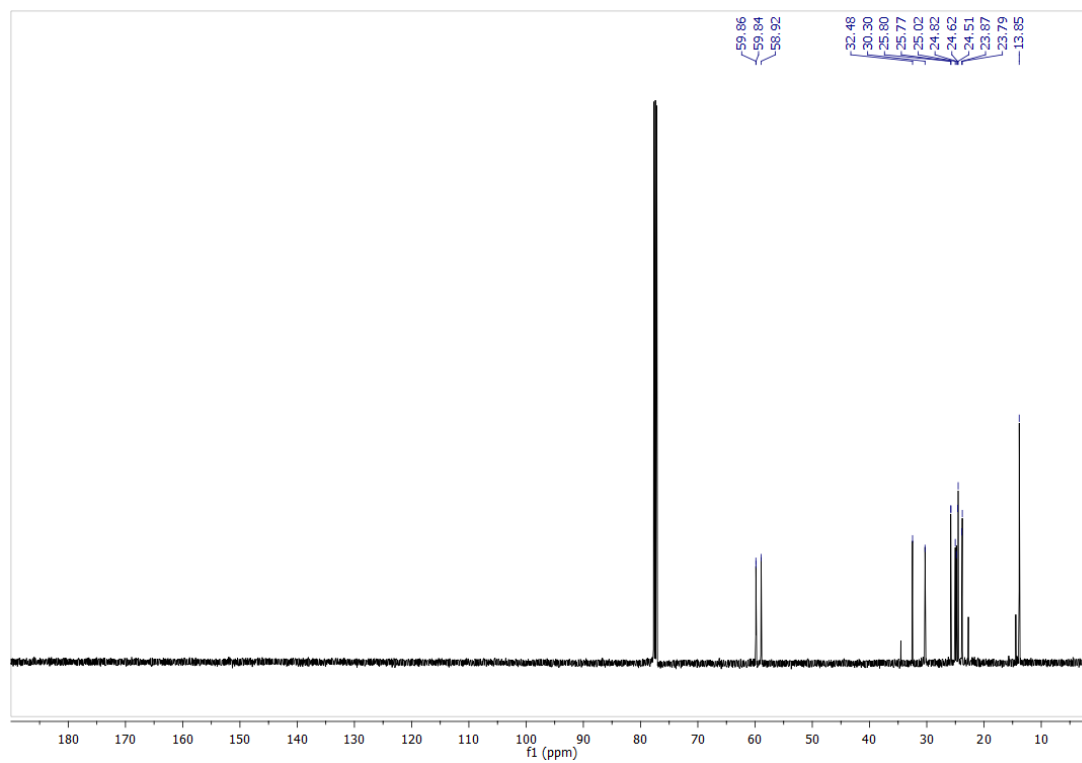


Figure 3-17.  $^{13}\text{C}$  NMR Spectrum for  $[\text{NCr}(\text{N}^i\text{Pr}_2)_2(\text{P}^n\text{Bu}_3)]\text{SbF}_6$  (**3b**) in  $\text{CDCl}_3$



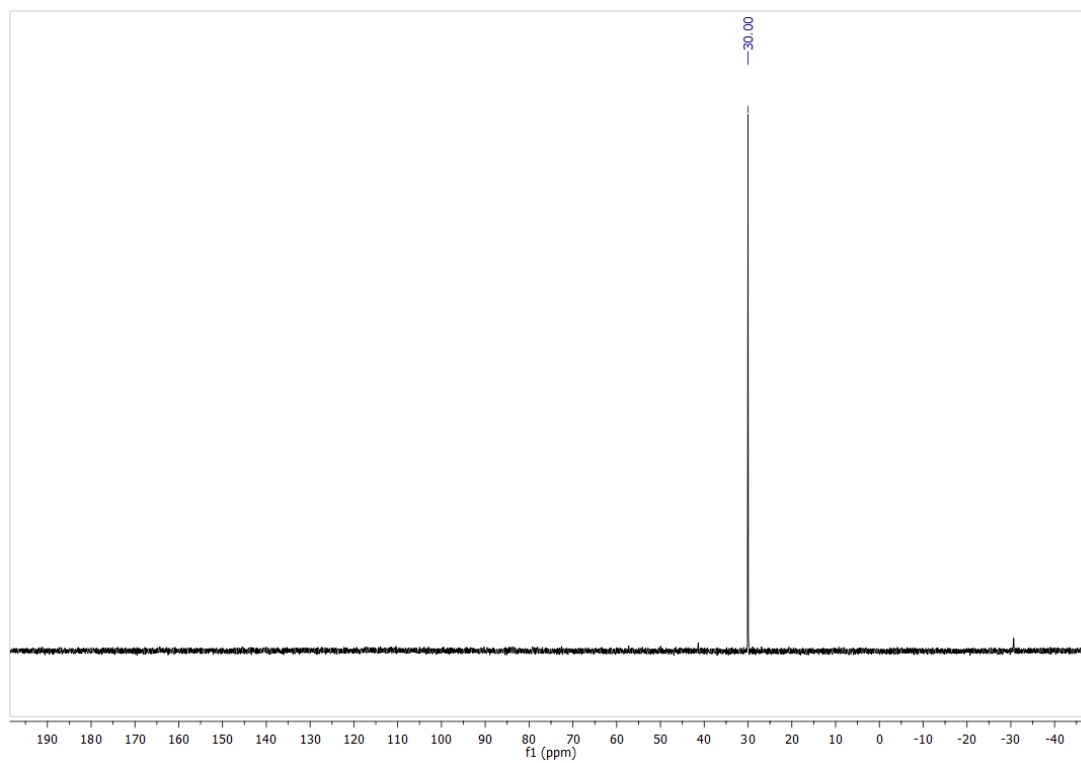


Figure 3-18.  $^{31}\text{P}$  NMR Spectrum for  $[\text{NCr}(\text{N}^i\text{Pr}_2)_2(\text{P}^n\text{Bu}_3)]\text{SbF}_6$  (**3b**) in  $\text{CDCl}_3$



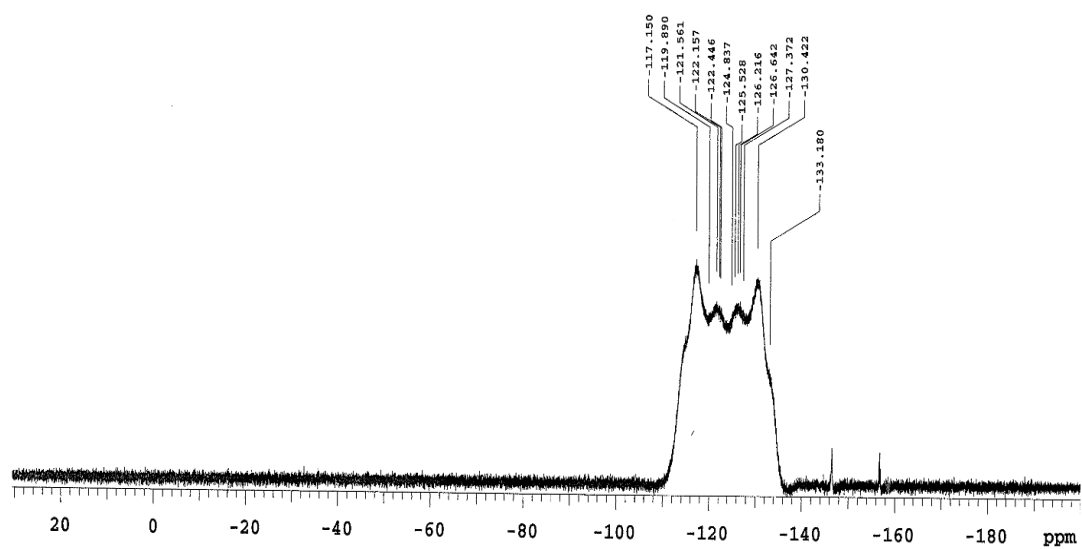


Figure 3-19.  $^{19}\text{F}$  NMR Spectrum for  $[\text{NCr}(\text{N}^i\text{Pr}_2)_2(\text{P}^n\text{Bu}_3)]\text{SbF}_6$  (**3b**) in  $\text{CDCl}_3$



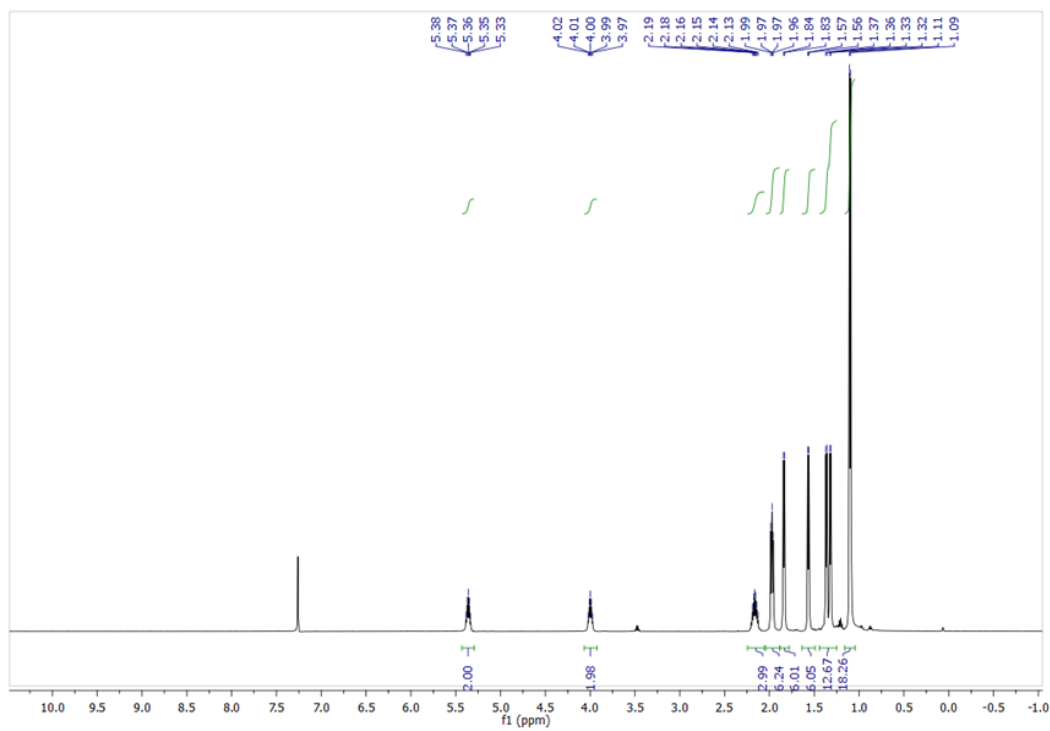


Figure 3-20.  $^1\text{H}$  NMR Spectrum for  $[\text{NCr}(\text{N}^i\text{Pr}_2)_2(\text{P}^i\text{Bu}_3)]\text{SbF}_6$  (**3c**) in  $\text{CDCl}_3$



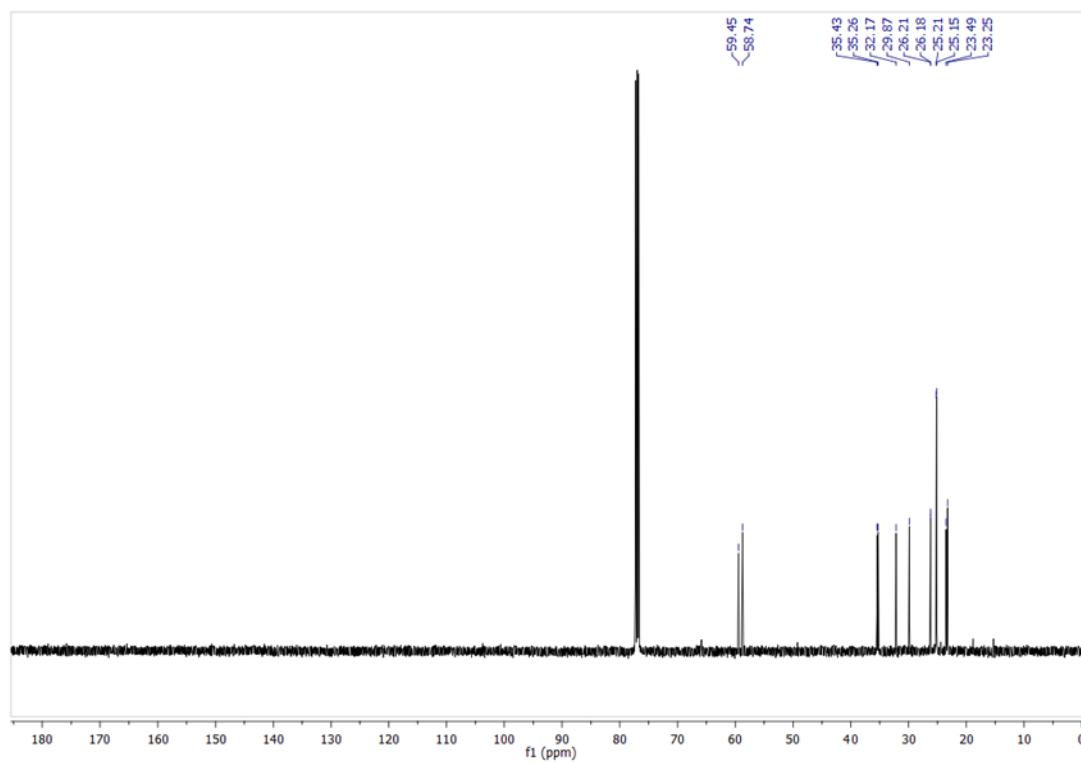


Figure 3-21.  $^{13}\text{C}$  NMR Spectrum for  $[\text{N}(\text{Cr}(\text{N}^i\text{Pr}_2)_2)(\text{P}^i\text{Bu}_3)]\text{SbF}_6$  (**3c**) in  $\text{CDCl}_3$



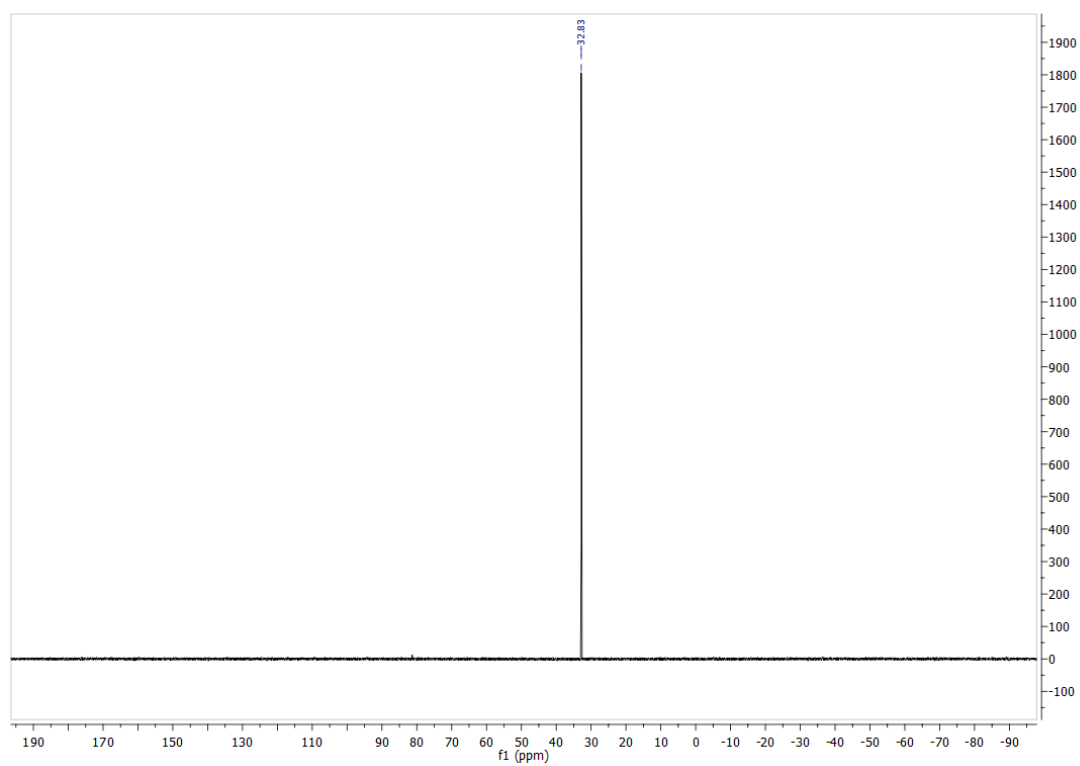


Figure 3-22.  $^{31}\text{P}$  NMR Spectrum for  $[\text{NCr}(\text{N}^i\text{Pr}_2)_2(\text{P}^i\text{Bu}_3)]\text{SbF}_6$  (**3c**) in  $\text{CDCl}_3$



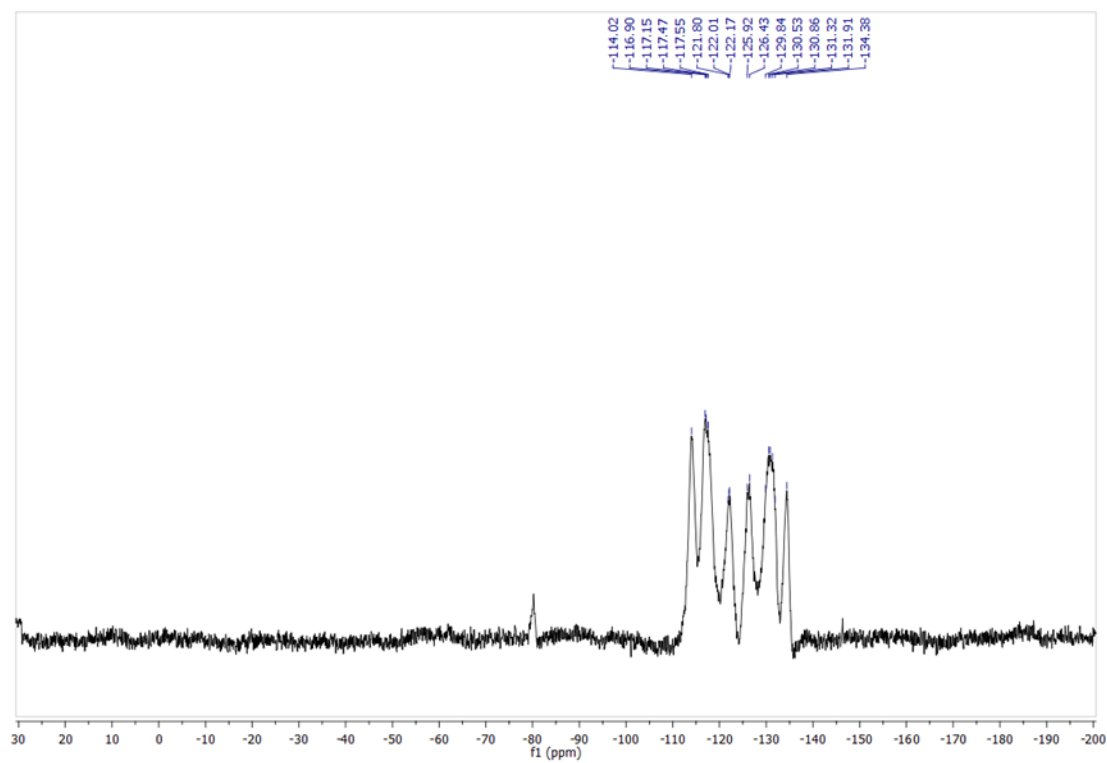


Figure 3-23.  $^{19}\text{F}$  NMR Spectrum for  $[\text{NCr}(\text{N}^i\text{Pr}_2)_2(\text{P}^i\text{Bu}_3)]\text{SbF}_6$  (**3c**) in  $\text{CDCl}_3$



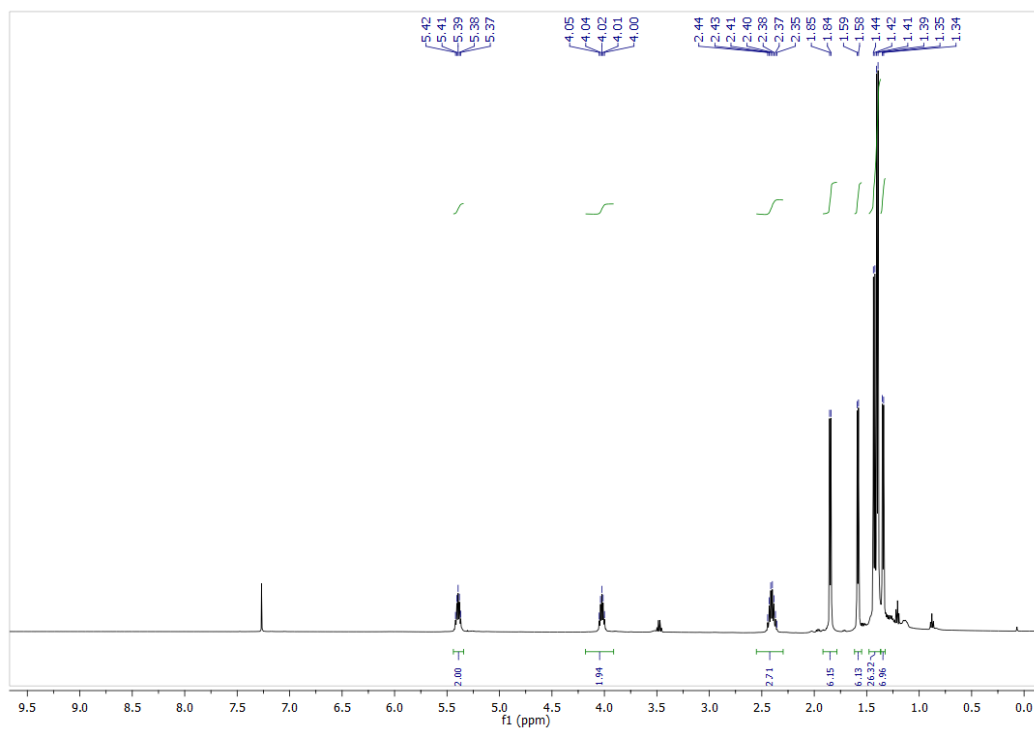


Figure 3-24.  $^1\text{H}$  NMR Spectrum for  $[\text{NCr}(\text{N}^i\text{Pr}_2)_2(\text{P}^i\text{Pr}_3)]\text{SbF}_6$  (**3d**) in  $\text{CDCl}_3$



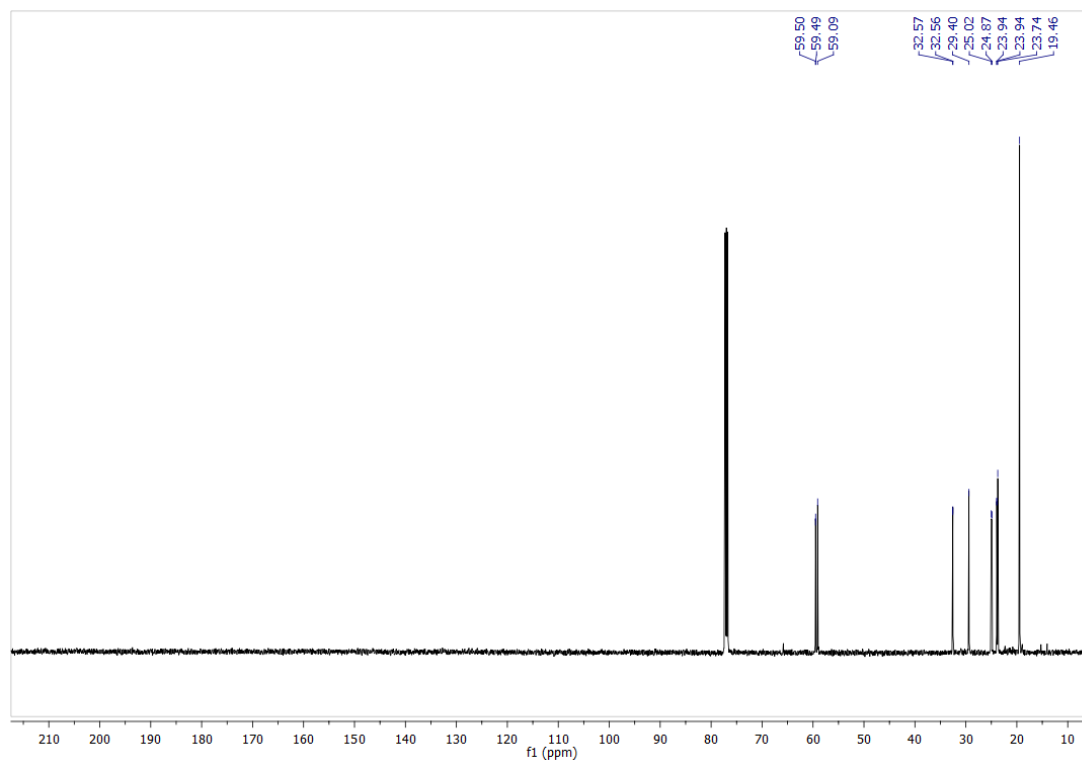


Figure 3-25.  $^{13}\text{C}$  NMR Spectrum for  $[\text{NCr}(\text{N}^i\text{Pr}_2)_2(\text{P}^i\text{Pr}_3)]\text{SbF}_6$  (**3d**) in  $\text{CDCl}_3$



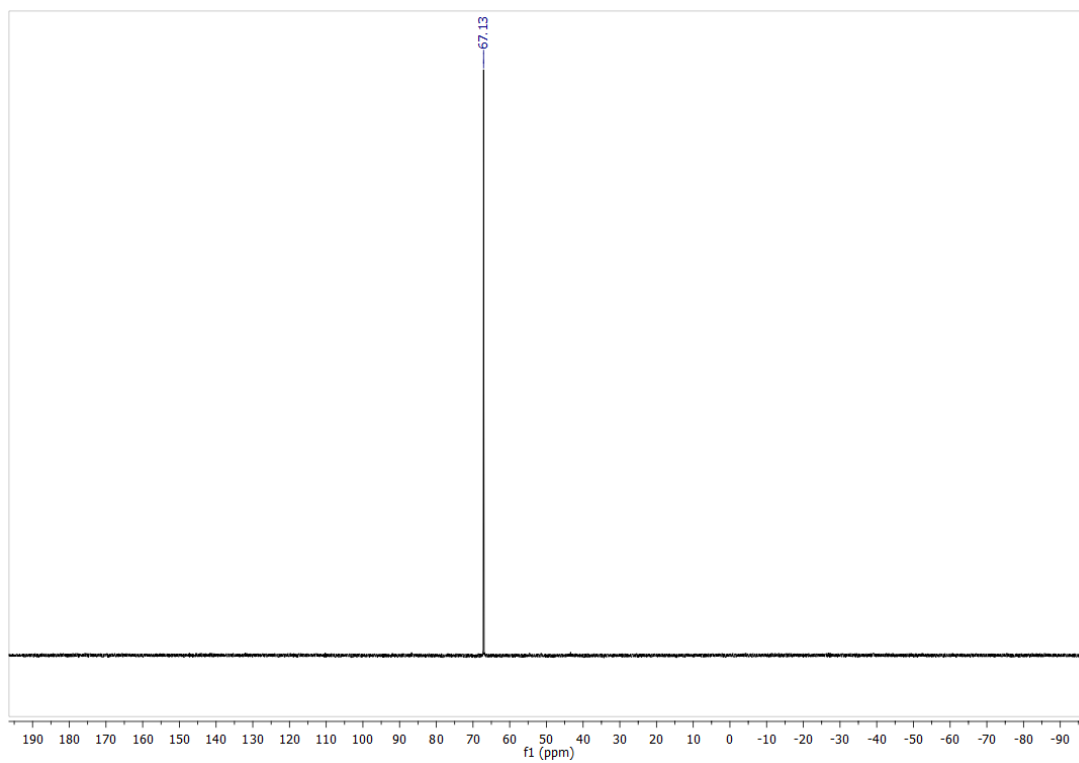


Figure 3-26.  $^{31}\text{P}$  NMR Spectrum for  $[\text{NCr}(\text{N}^i\text{Pr}_2)_2(\text{P}^i\text{Pr}_3)]\text{SbF}_6$  (**3d**) in  $\text{CDCl}_3$



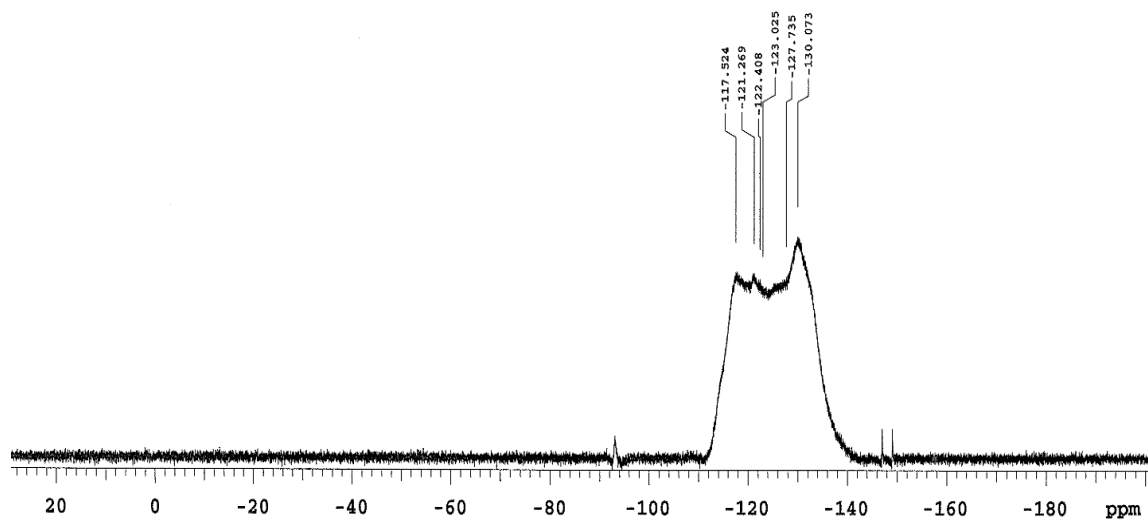


Figure 3-27.  $^{19}\text{F}$  NMR Spectrum for  $[\text{NCr}(\text{N}^i\text{Pr}_2)(\text{P}^i\text{Pr}_3)]\text{SbF}_6$  (**3d**) in  $\text{CDCl}_3$



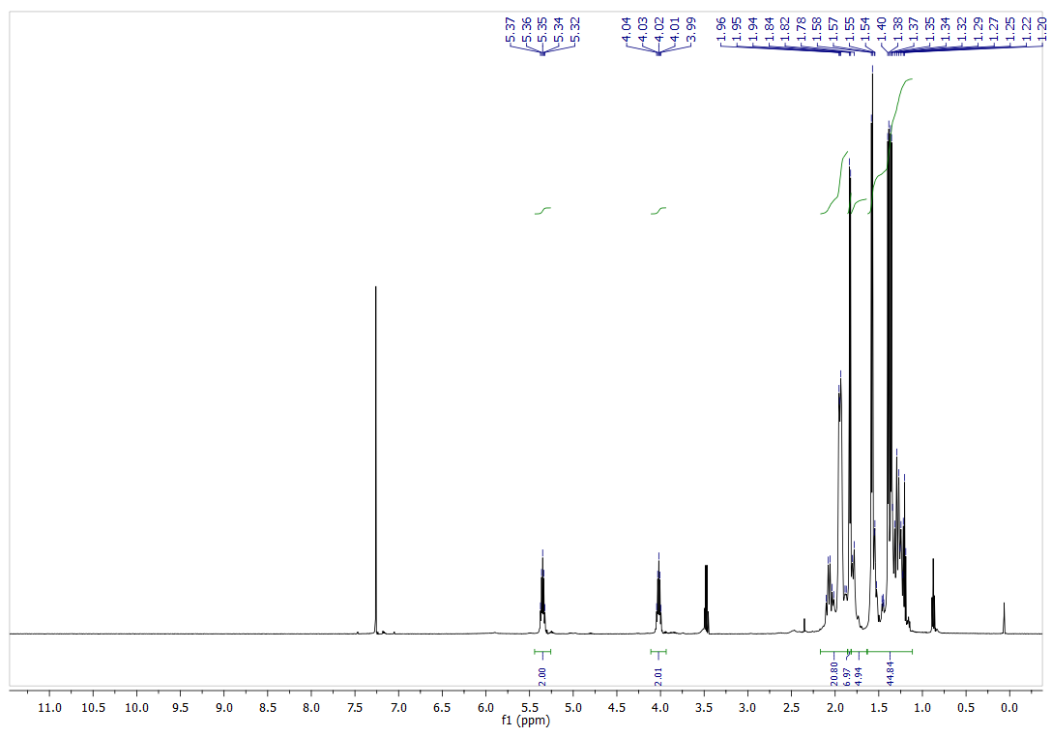


Figure 3-28.  $^1\text{H}$  NMR Spectrum for  $[\text{NCr}(\text{N}^i\text{Pr}_2)_2(\text{PCy}_3)]\text{SbF}_6$  (**3e**) in  $\text{CDCl}_3$



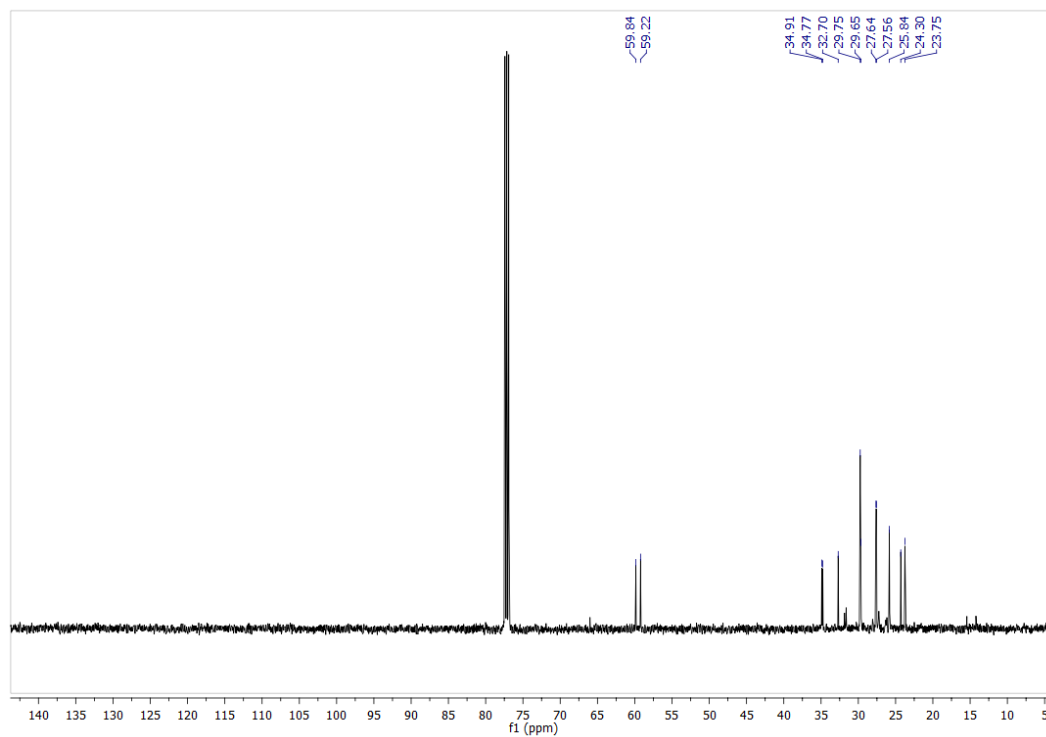


Figure 3-29.  $^{13}\text{C}$  NMR Spectrum for  $[\text{NCr}(\text{N}^i\text{Pr}_2)_2(\text{PCy}_3)]\text{SbF}_6$  (**3e**) in  $\text{CDCl}_3$



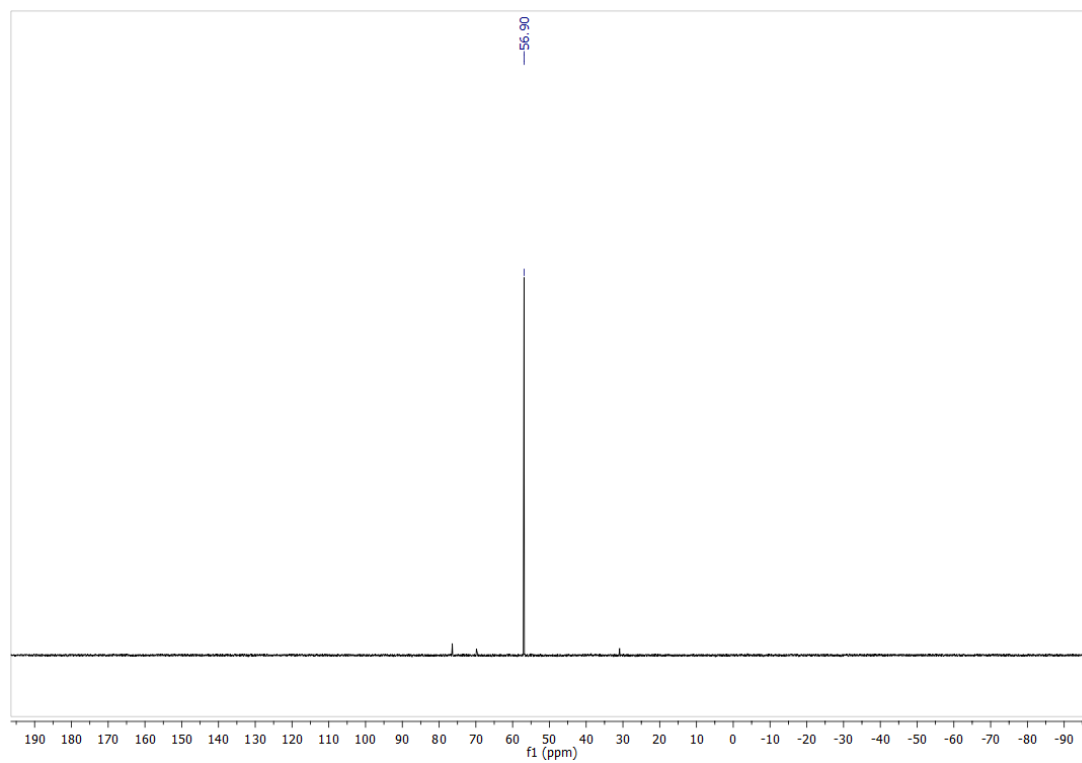


Figure 3-30.  $^{31}\text{P}$  NMR Spectrum for  $[\text{NCr}(\text{N}^i\text{Pr}_2)_2(\text{PCy}_3)]\text{SbF}_6$  (**3e**) in  $\text{CDCl}_3$



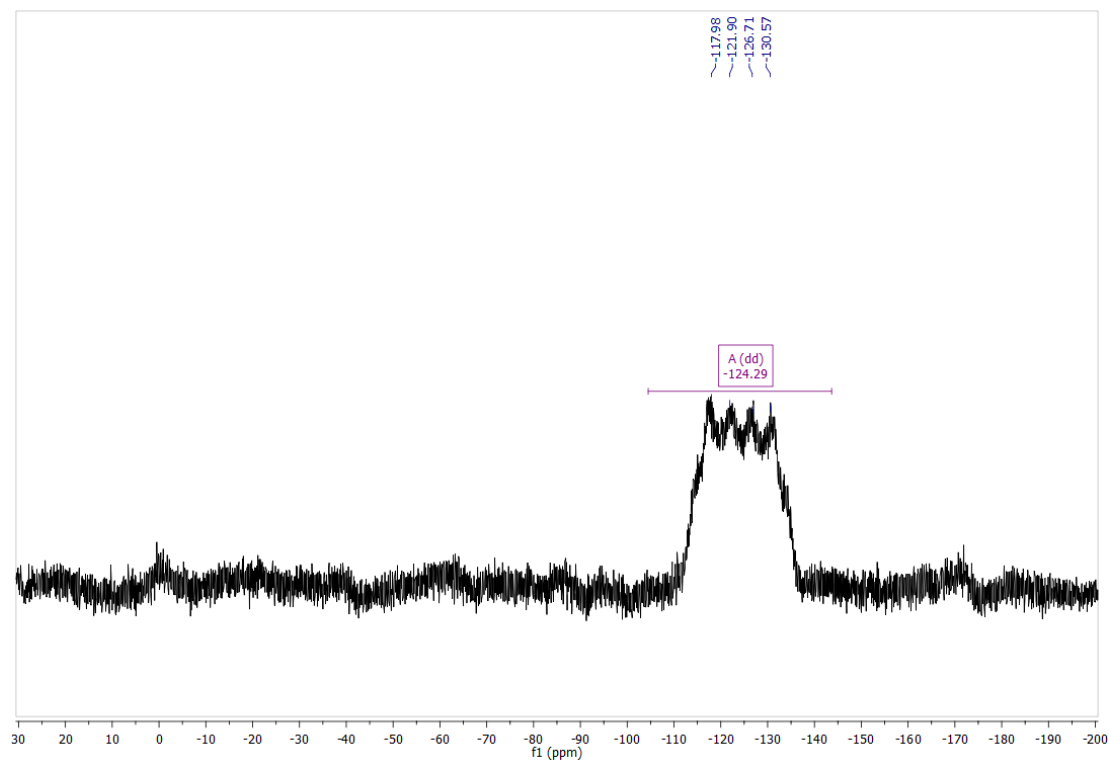


Figure 3-31.  $^{19}\text{F}$  NMR Spectrum for  $[\text{NCr}(\text{N}^i\text{Pr}_2)_2(\text{PCy}_3)]\text{SbF}_6$  (**3e**) in  $\text{CDCl}_3$



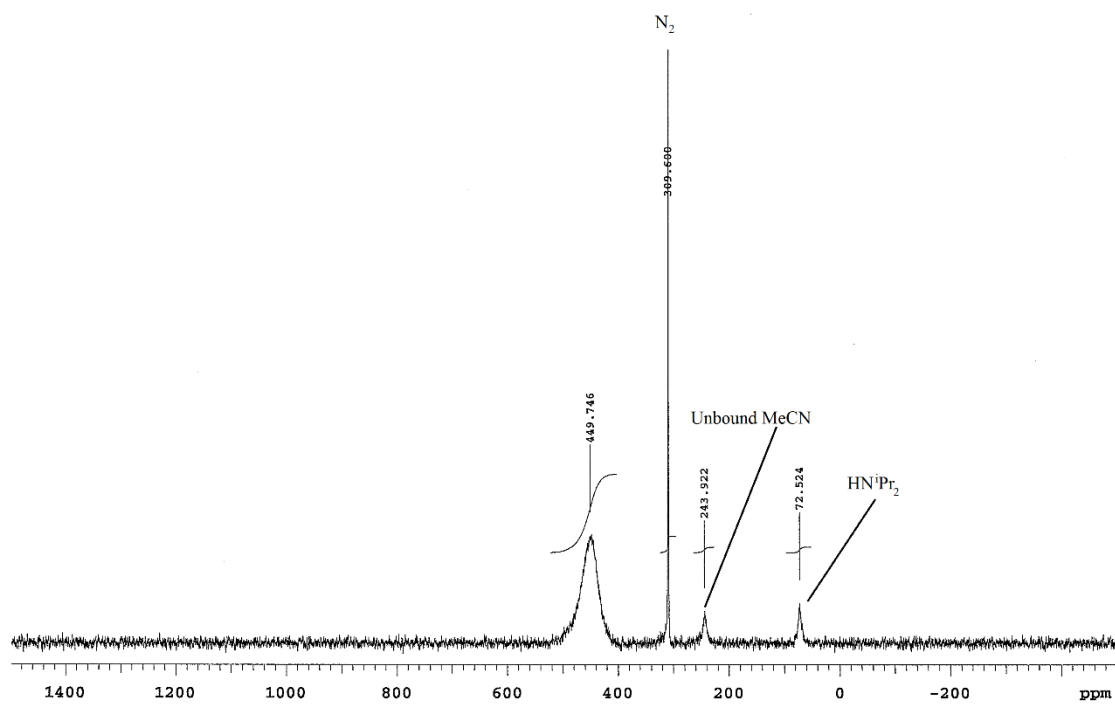


Figure 3-32.  $^{14}\text{N}$  NMR Spectrum for  $[\text{NCr}(\text{N}^i\text{Pr}_2)_2(\text{PCy}_3)]\text{SbF}_6$  (**3e**) in  $\text{CDCl}_3$



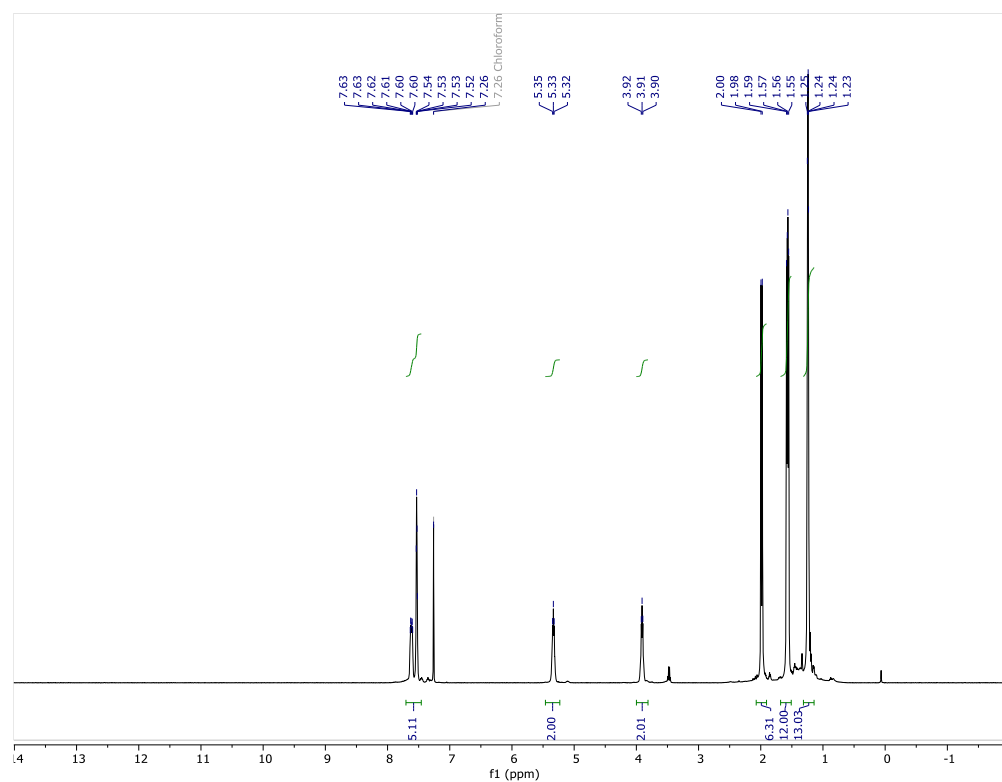


Figure 3-33. <sup>1</sup>H NMR Spectrum for [NCr(N<sup>i</sup>Pr<sub>2</sub>)<sub>2</sub>(PPhMe<sub>2</sub>)]SbF<sub>6</sub> (**3e**) in CDCl<sub>3</sub>



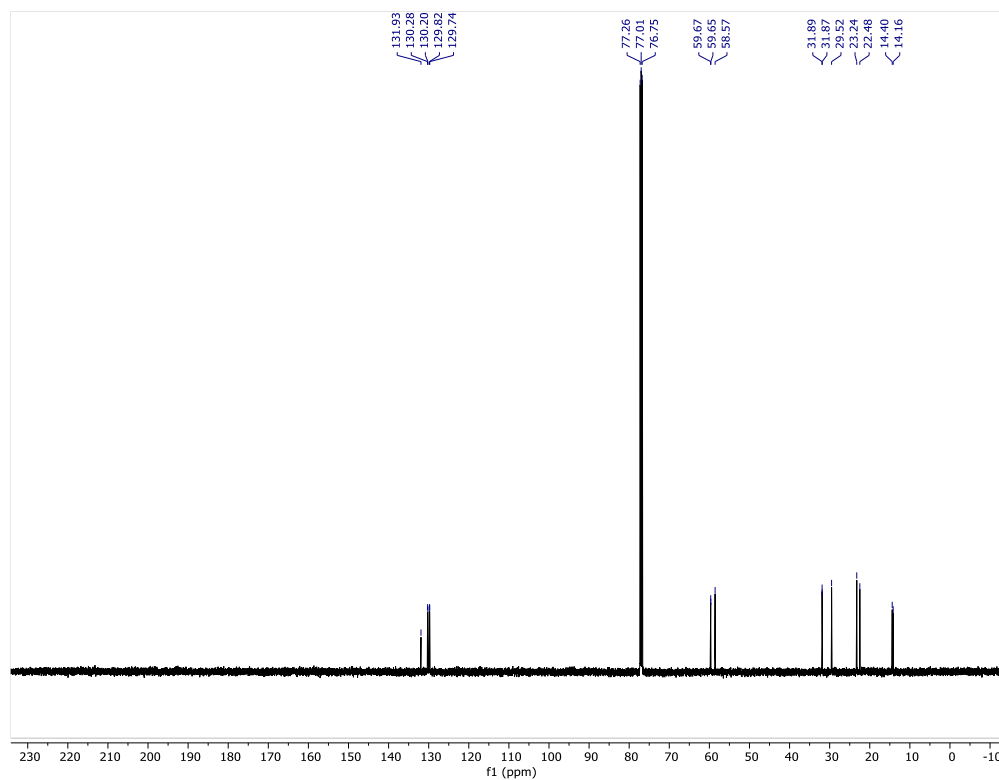


Figure 3-34.  $^{13}\text{C}$  NMR Spectrum for  $[\text{NCr}(\text{N}^i\text{Pr}_2)_2(\text{PPhMe}_2)]\text{SbF}_6$  (**3e**) in  $\text{CDCl}_3$



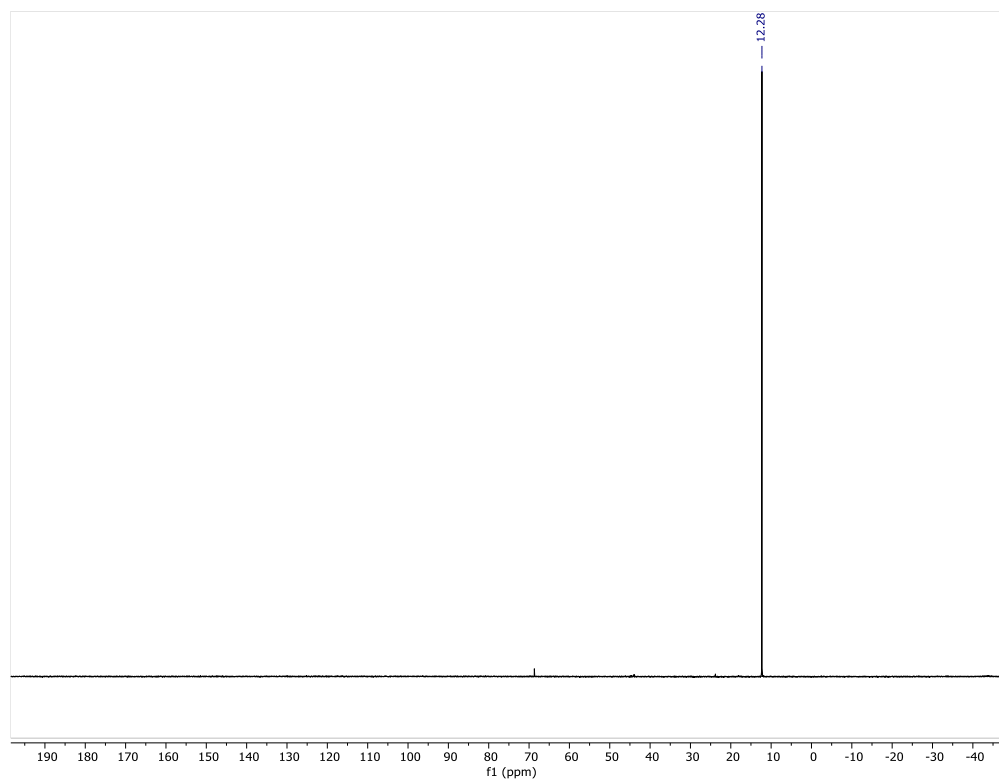


Figure 3-35.  $^{31}\text{P}$  NMR Spectrum for  $[\text{NCr}(\text{N}^i\text{Pr}_2)_2(\text{PPhMe}_2)]\text{SbF}_6$  (**3e**) in  $\text{CDCl}_3$



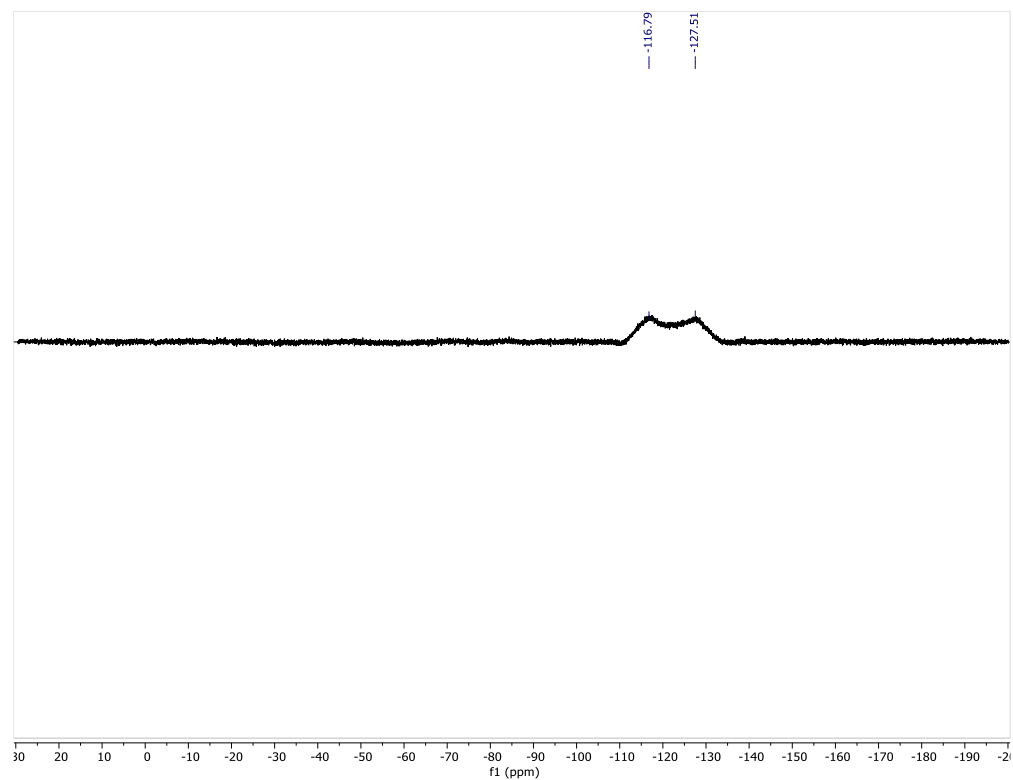


Figure 3-36.  $^{19}\text{F}$  NMR Spectrum for  $[\text{NCr}(\text{N}^i\text{Pr}_2)_2(\text{PPhMe}_2)]\text{SbF}_6$  (**3e**) in  $\text{CDCl}_3$



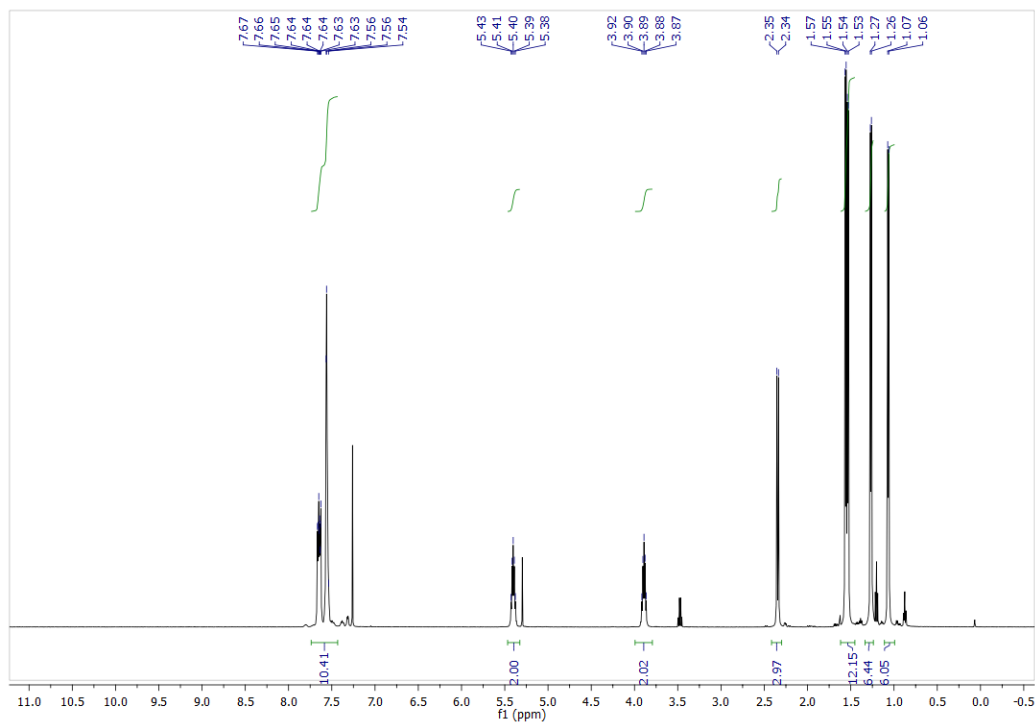


Figure 3-37. <sup>1</sup>H NMR Spectrum for [NCr(N<sup>i</sup>Pr<sub>2</sub>)<sub>2</sub>(PPh<sub>2</sub>Me)]SbF<sub>6</sub> (**3g**) in CDCl<sub>3</sub>



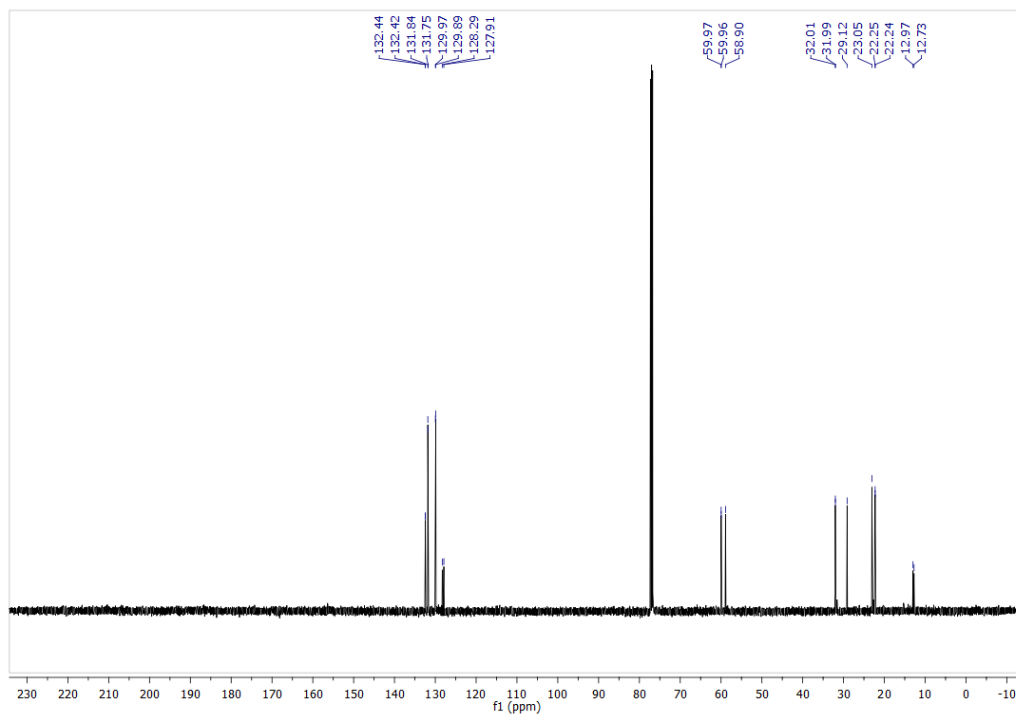


Figure 3-38.  $^{13}\text{C}$  NMR Spectrum for  $[\text{NCr}(\text{N}^i\text{Pr}_2)_2(\text{PPh}_2\text{Me})]\text{SbF}_6$  (**3g**) in  $\text{CDCl}_3$



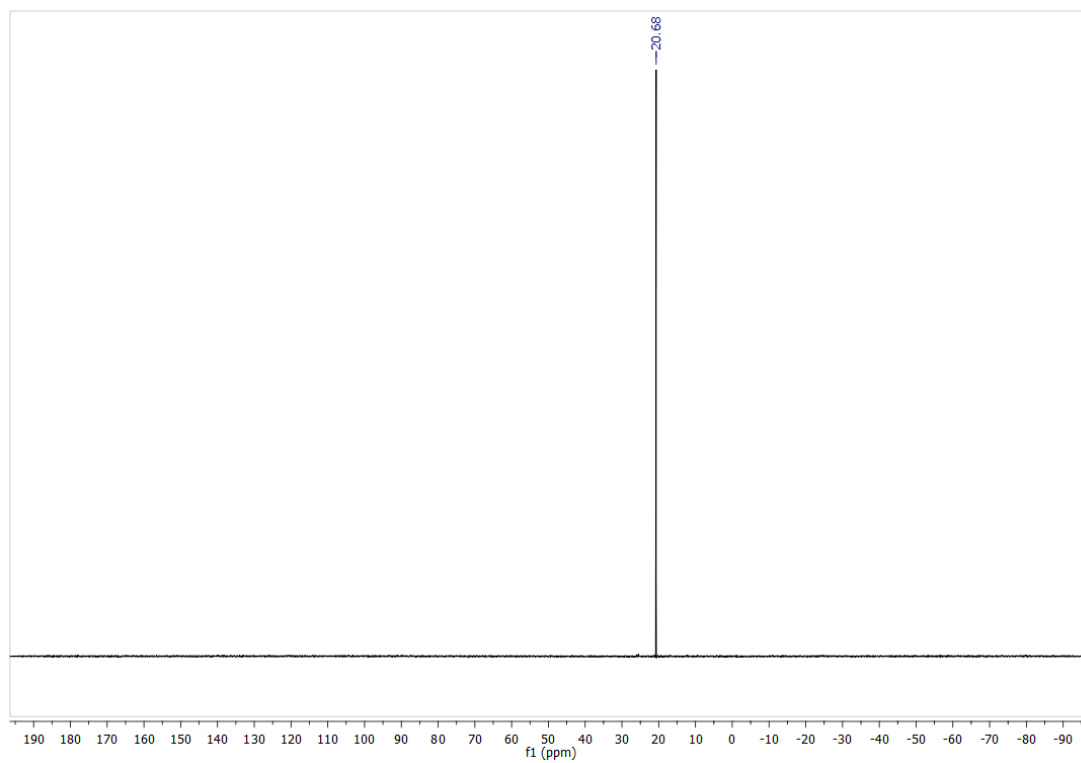


Figure 3-39.  $^{31}\text{P}$  NMR Spectrum for  $[\text{NCr}(\text{N}^i\text{Pr}_2)_2(\text{PPh}_2\text{Me})]\text{SbF}_6$  (**3g**) in  $\text{CDCl}_3$



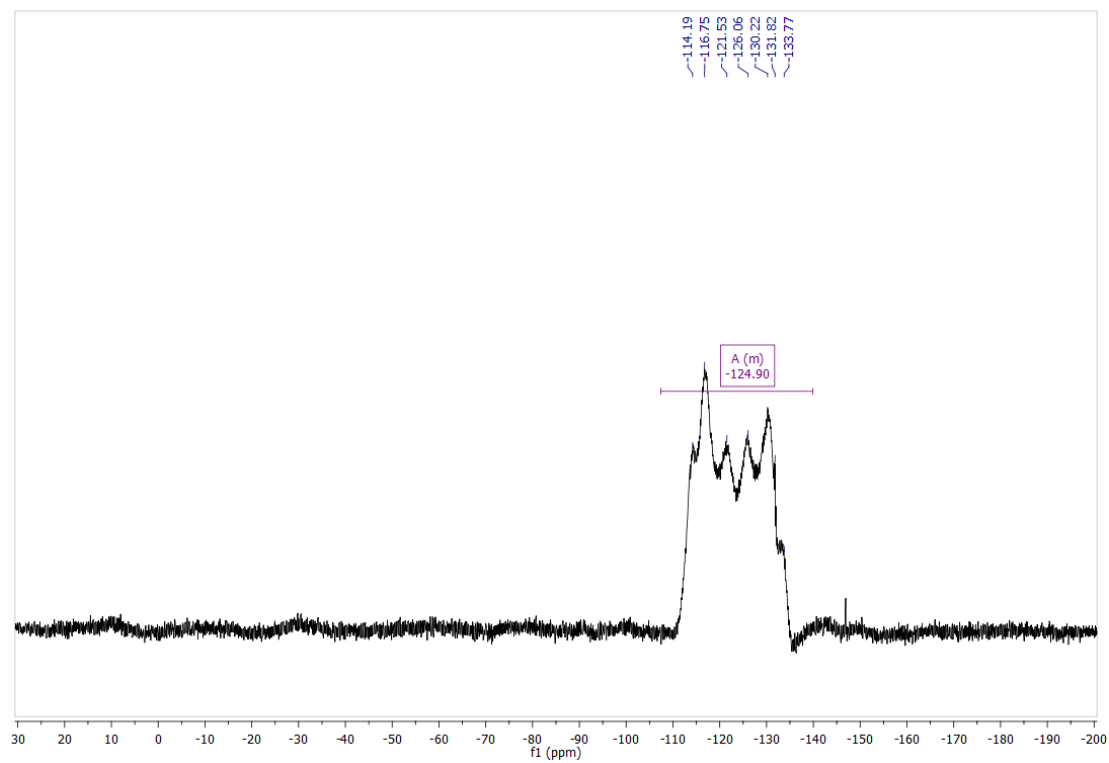


Figure 3-40.  $^{19}\text{F}$  NMR Spectrum for  $[\text{NCr}(\text{N}^i\text{Pr}_2)_2(\text{PPh}_2\text{Me})]\text{SbF}_6$  (**3g**) in  $\text{CDCl}_3$



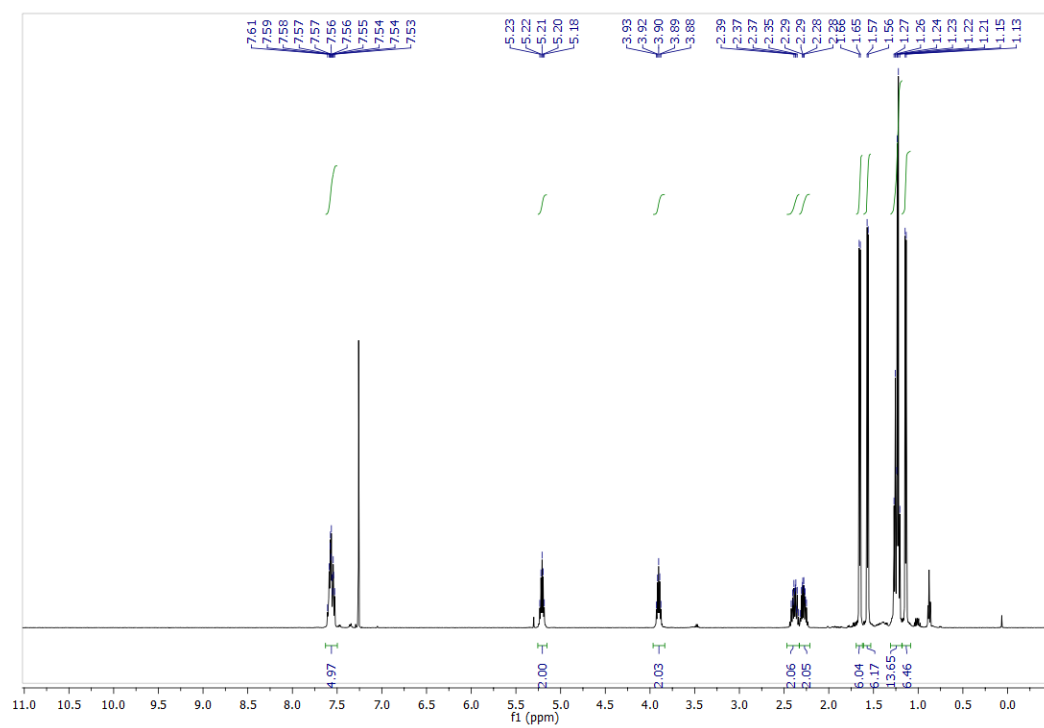


Figure 3-41.  $^1\text{H}$  NMR Spectrum for  $[\text{NCr}(\text{N}^i\text{Pr}_2)_2(\text{PPhEt}_2)]\text{SbF}_6$  (**3h**) in  $\text{CDCl}_3$



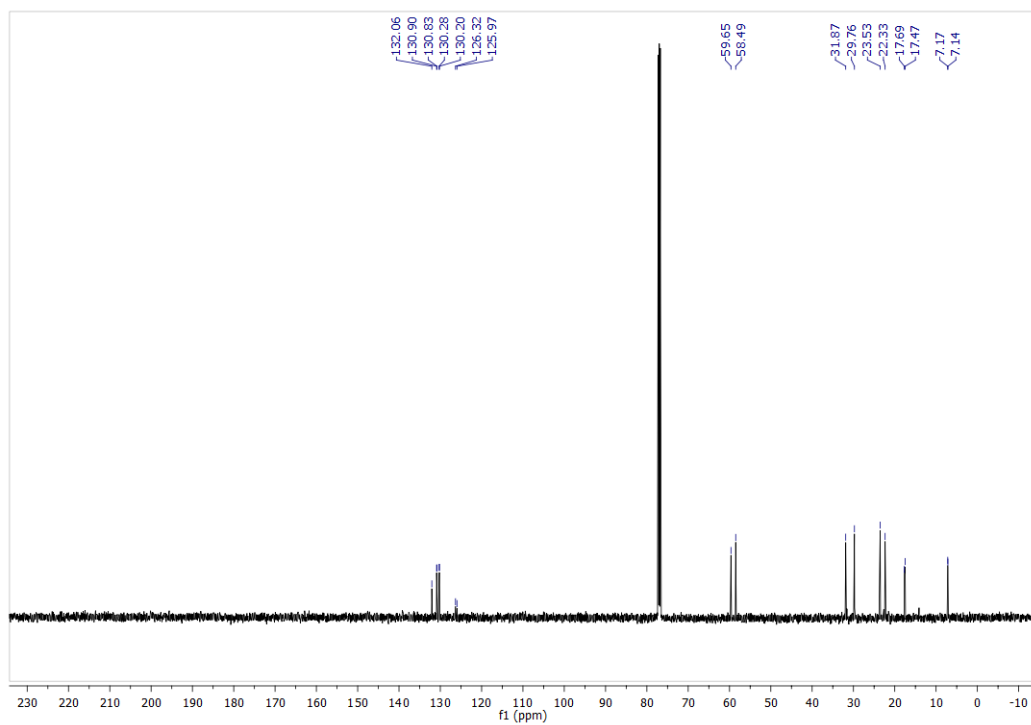


Figure 3-42.  $^{13}\text{C}$  NMR Spectrum for  $[\text{NCr}(\text{N}^i\text{Pr}_2)_2(\text{PPhEt}_2)]\text{SbF}_6$  (**3h**) in  $\text{CDCl}_3$



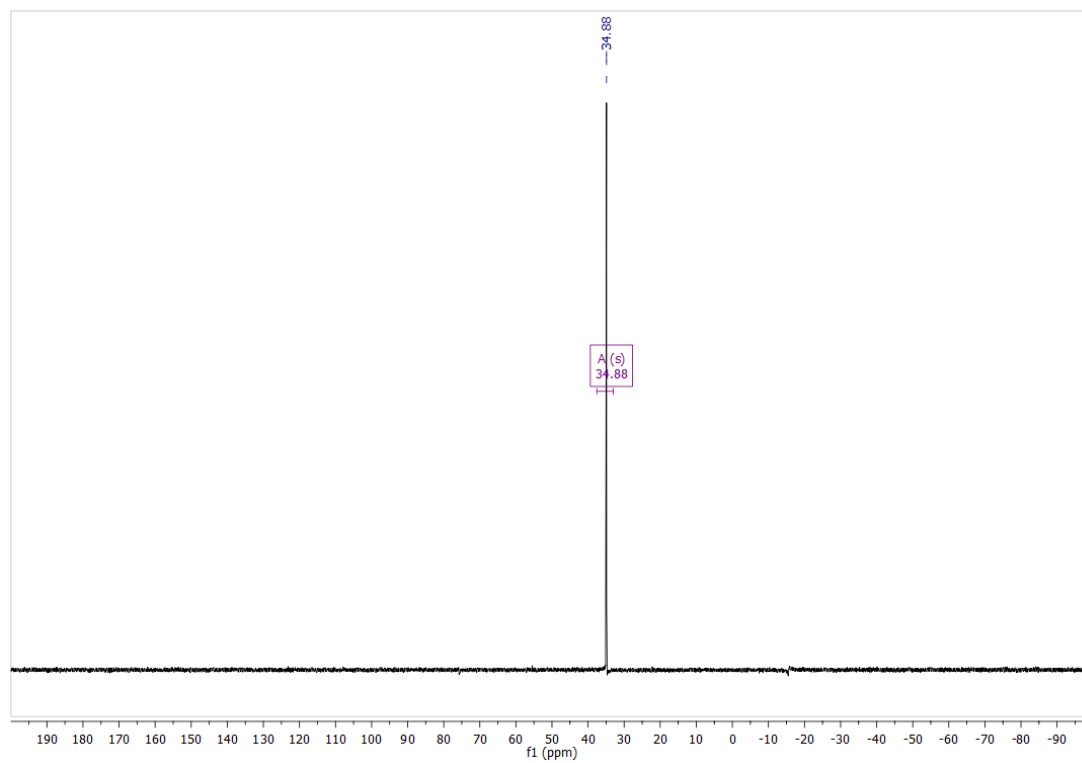


Figure 3-43.  $^{31}\text{P}$  NMR Spectrum for  $[\text{NCr}(\text{N}^i\text{Pr}_2)_2(\text{PPhEt}_2)]\text{SbF}_6$  (**3h**) in  $\text{CDCl}_3$



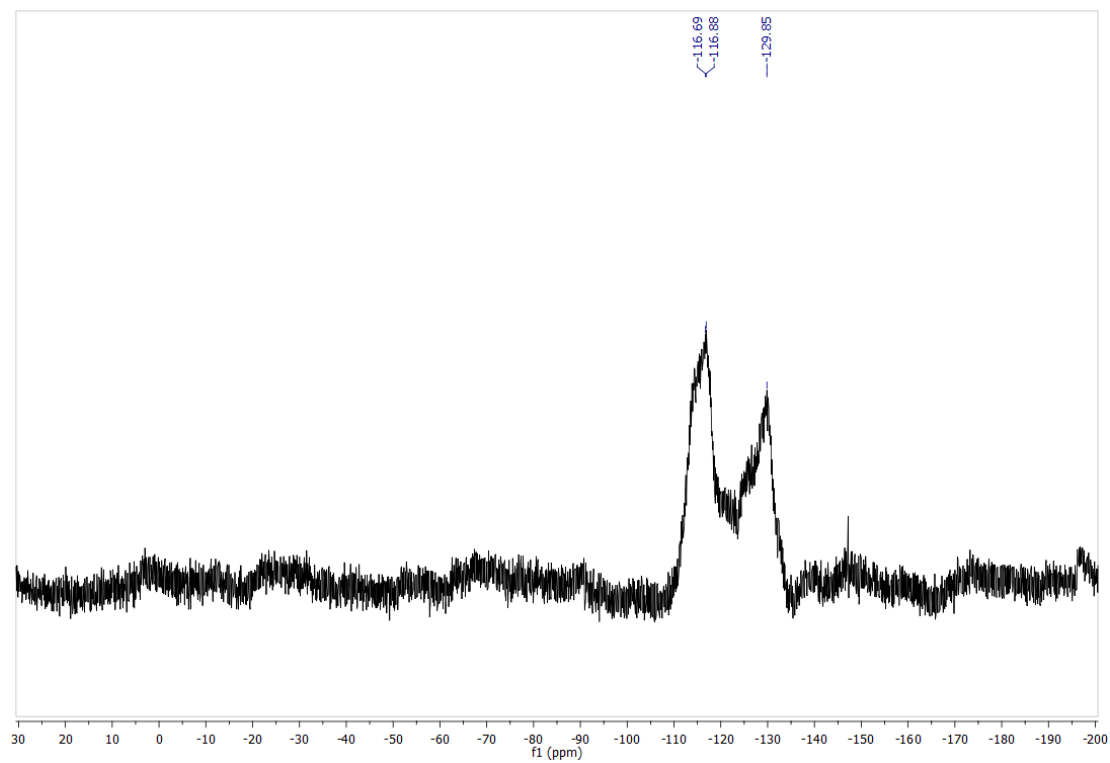


Figure 3-44.  $^{19}\text{F}$  NMR Spectrum for  $[\text{NCr}(\text{N}^i\text{Pr}_2)_2(\text{PPhEt}_2)]\text{SbF}_6$  (**3h**) in  $\text{CDCl}_3$



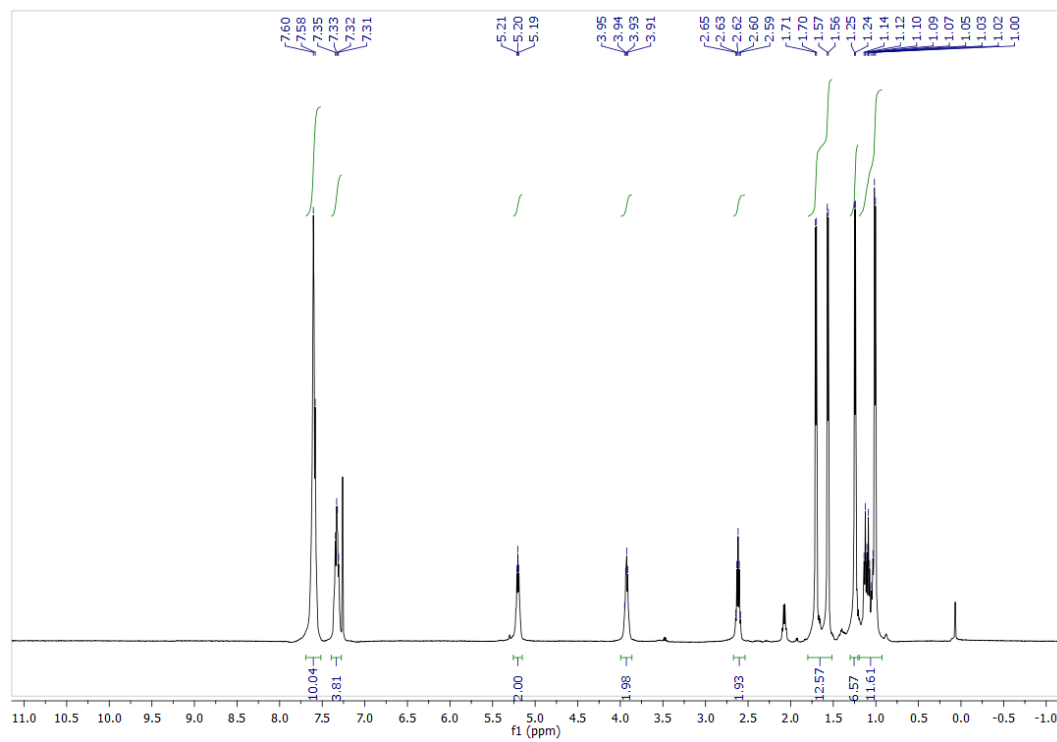


Figure 3-45.  $^1\text{H}$  NMR Spectrum for  $[\text{NCr}(\text{N}^i\text{Pr}_2)_2(\text{PPh}_2\text{Et})]\text{SbF}_6$  (**3i**) in  $\text{CDCl}_3$



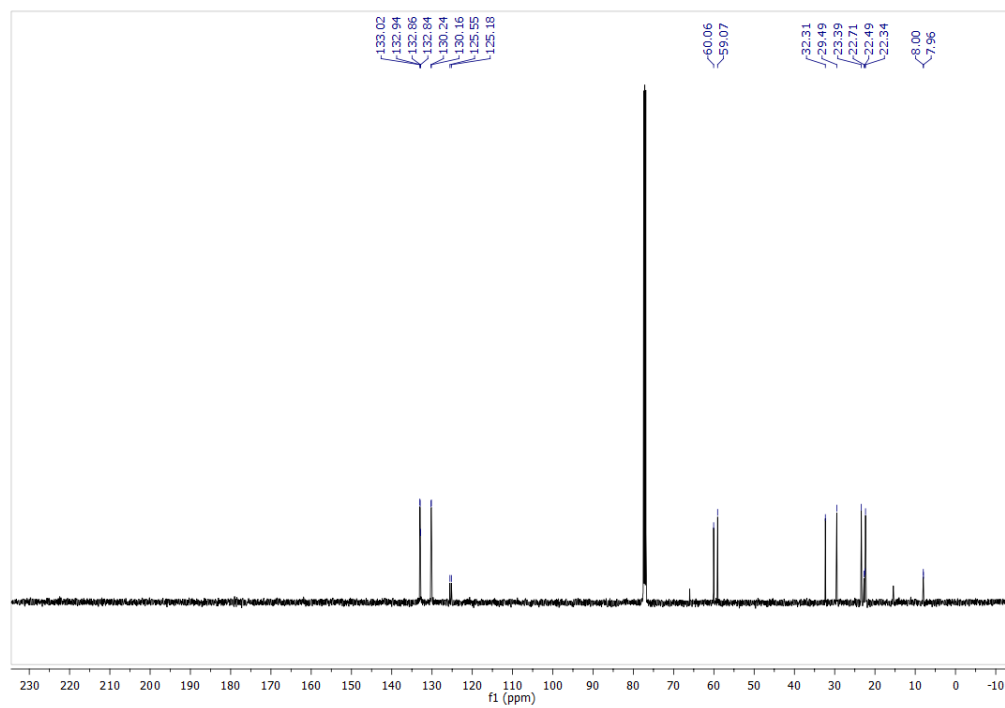


Figure 3-46.  $^{13}\text{C}$  NMR Spectrum for  $[\text{NCr}(\text{N}^i\text{Pr}_2)_2(\text{PPh}_2\text{Et})]\text{SbF}_6$  (**3i**) in  $\text{CDCl}_3$



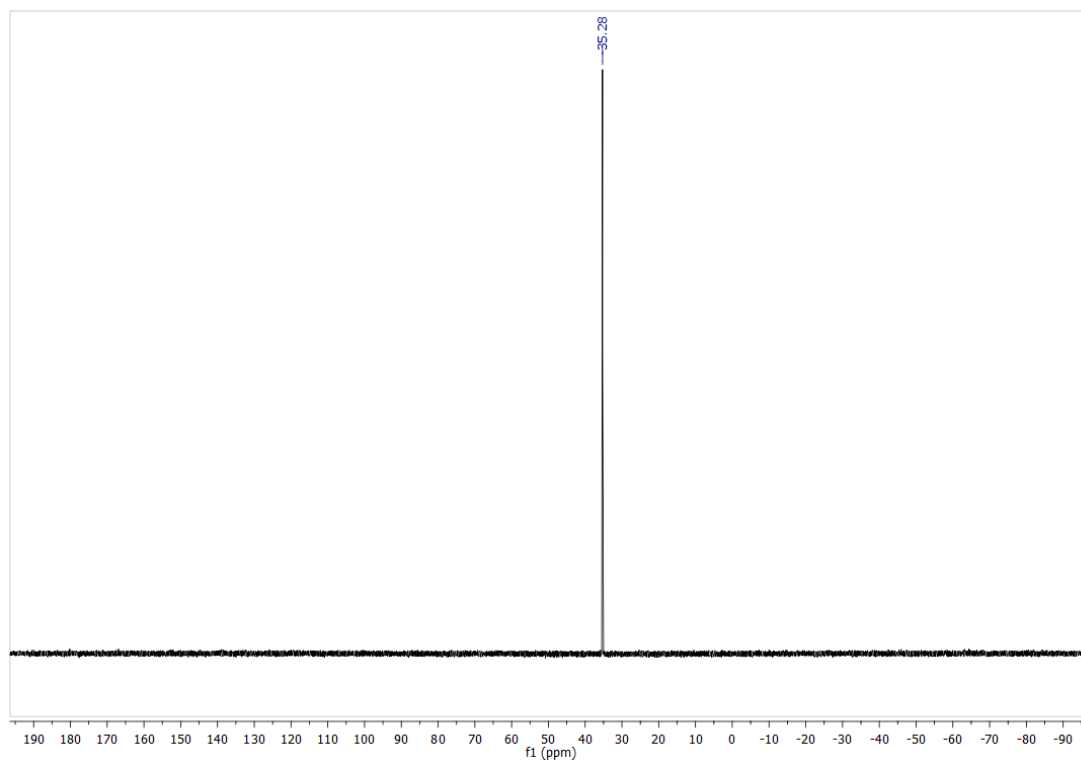


Figure 3-47.  $^{31}\text{P}$  NMR Spectrum for  $[\text{NCr}(\text{N}^i\text{Pr}_2)_2(\text{PPh}_2\text{Et})]\text{SbF}_6$  (**3i**) in  $\text{CDCl}_3$



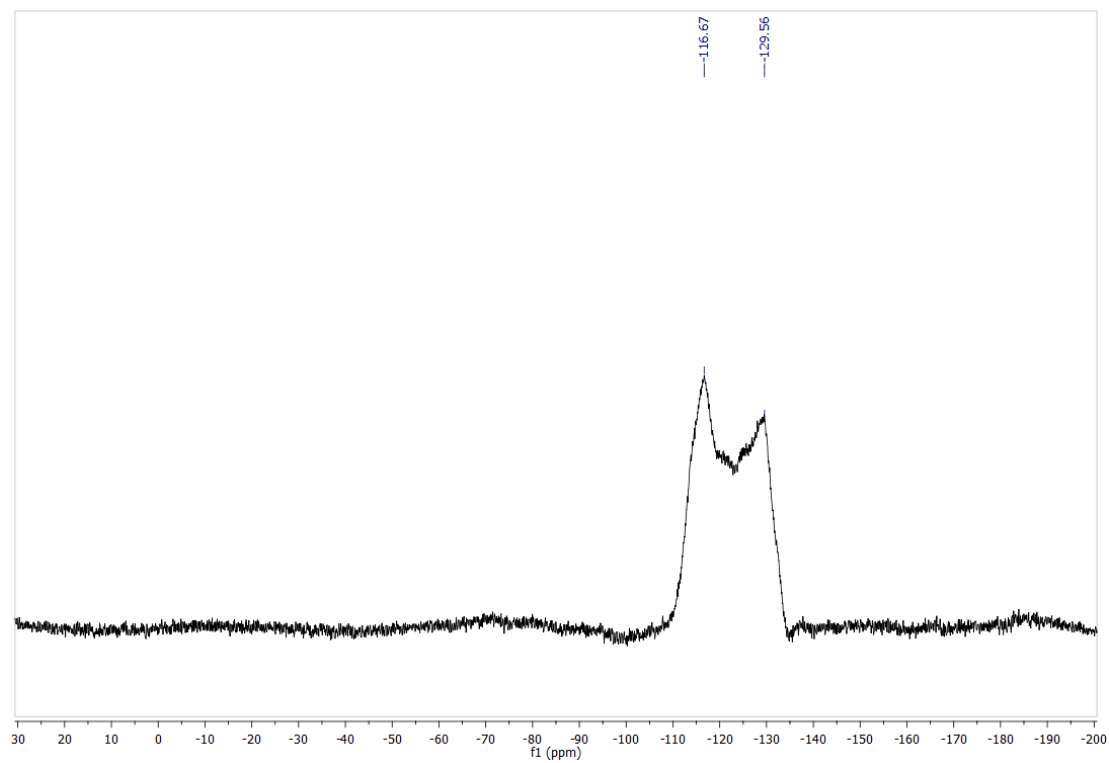


Figure 3-48.  $^{19}\text{F}$  NMR Spectrum for  $[\text{NCr}(\text{N}^i\text{Pr}_2)_2(\text{PPh}_2\text{Et})]\text{SbF}_6$  (**3i**) in  $\text{CDCl}_3$



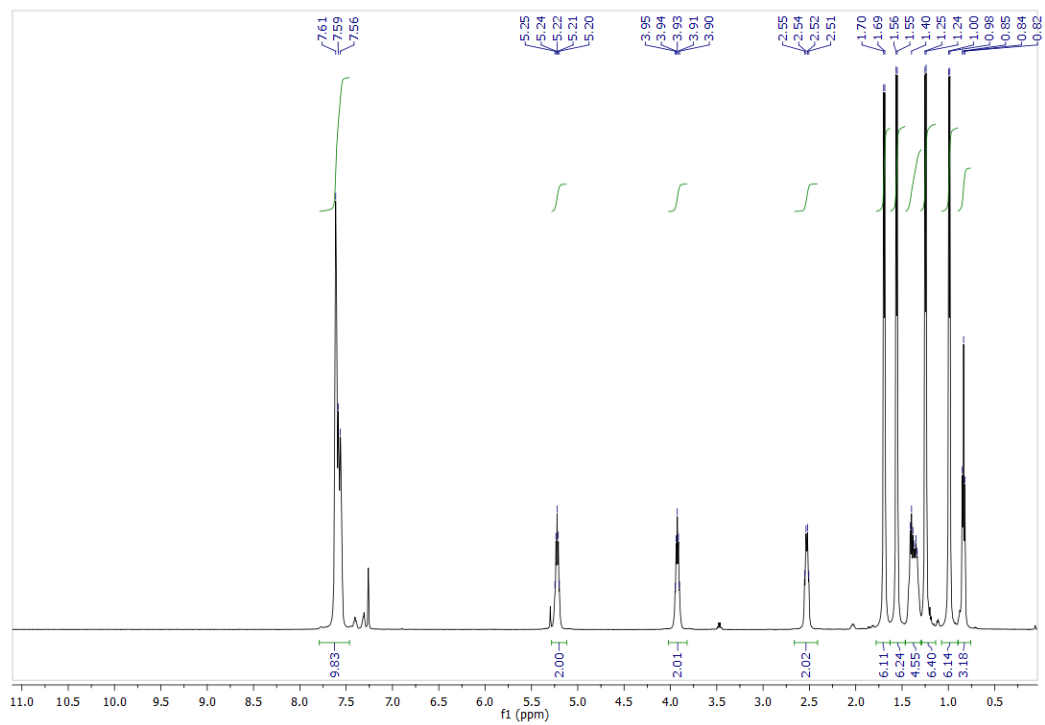


Figure 3-49.  $^1\text{H}$  NMR Spectrum for  $[\text{NCr}(\text{N}^i\text{Pr}_2)_2(\text{PPh}_2^n\text{Bu})]\text{PF}_6$  (**3j**) in  $\text{CDCl}_3$



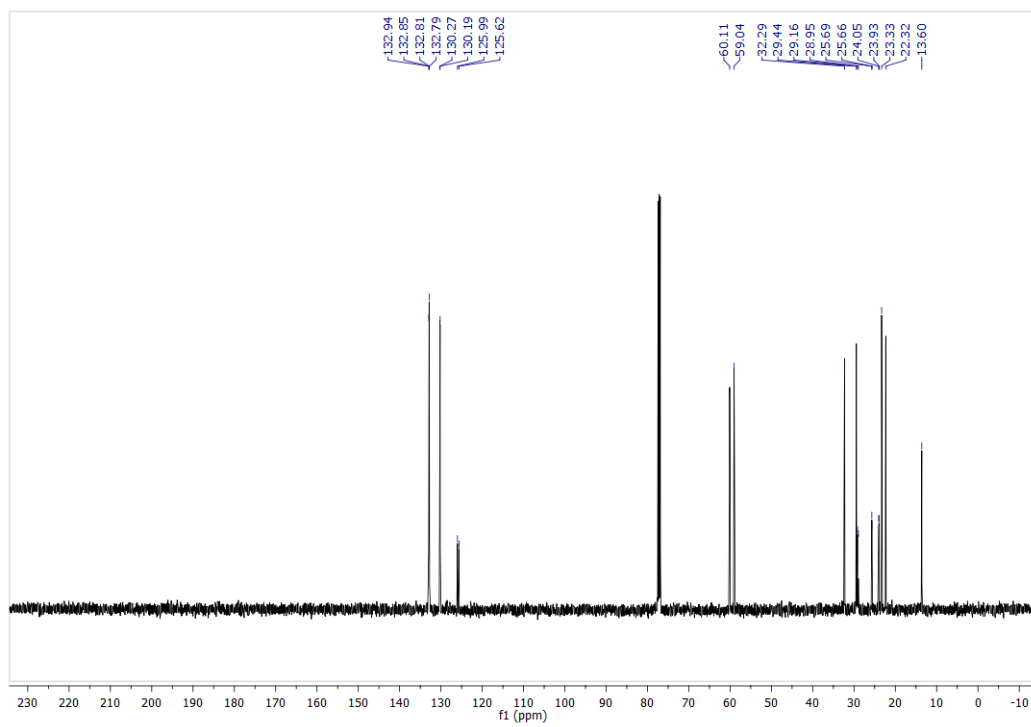


Figure 3-50.  $^{13}\text{C}$  NMR Spectrum for  $[\text{NCr}(\text{N}^i\text{Pr}_2)_2(\text{PPh}_2^n\text{Bu})]\text{PF}_6$  (**3j**) in  $\text{CDCl}_3$



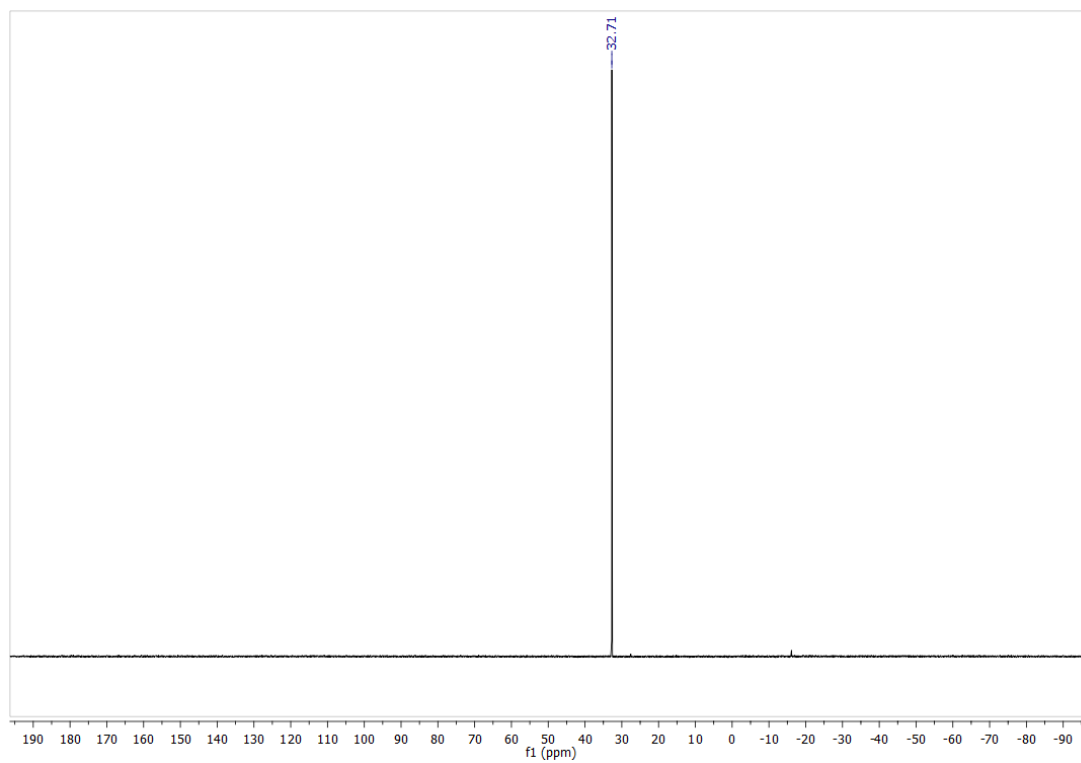


Figure 3-51.  $^{31}\text{P}$  NMR Spectrum for  $[\text{NCr}(\text{N}^i\text{Pr}_2)_2(\text{PPh}_2^n\text{Bu})]\text{PF}_6$  (**3j**) in  $\text{CDCl}_3$



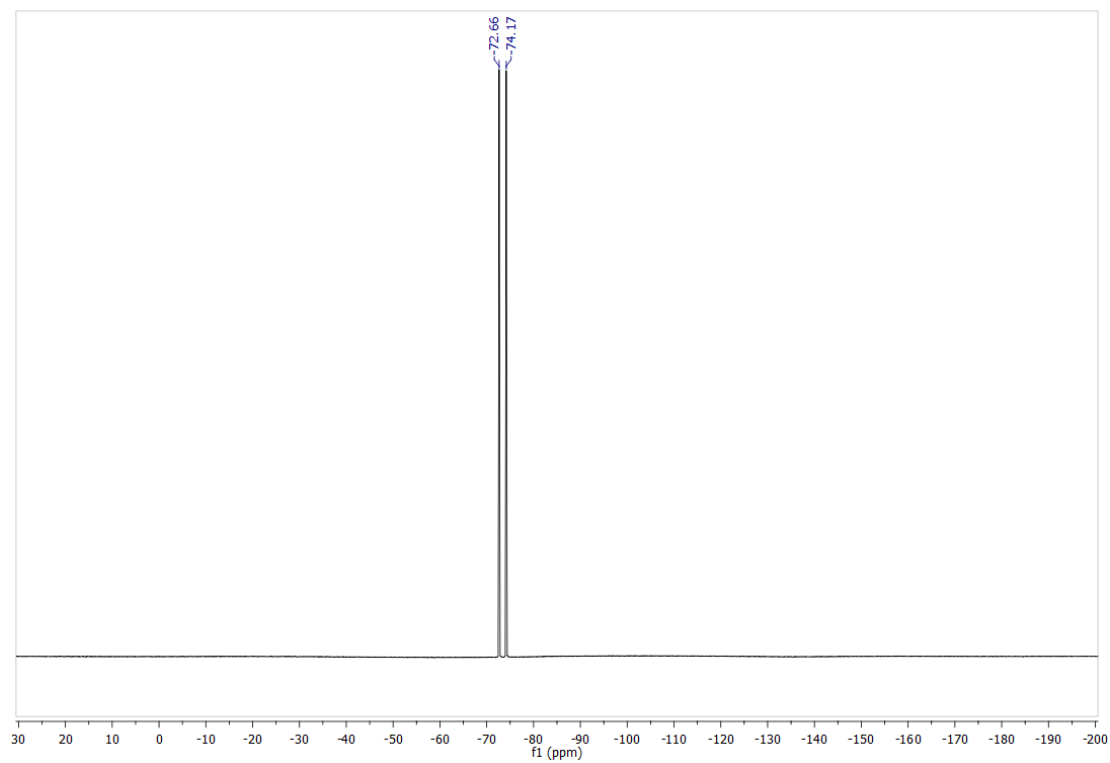


Figure 3-52.  $^{19}\text{F}$  NMR Spectrum for  $[\text{NCr}(\text{N}^i\text{Pr}_2)_2(\text{PPh}_2^n\text{Bu})]\text{PF}_6$  (**3j**) in  $\text{CDCl}_3$



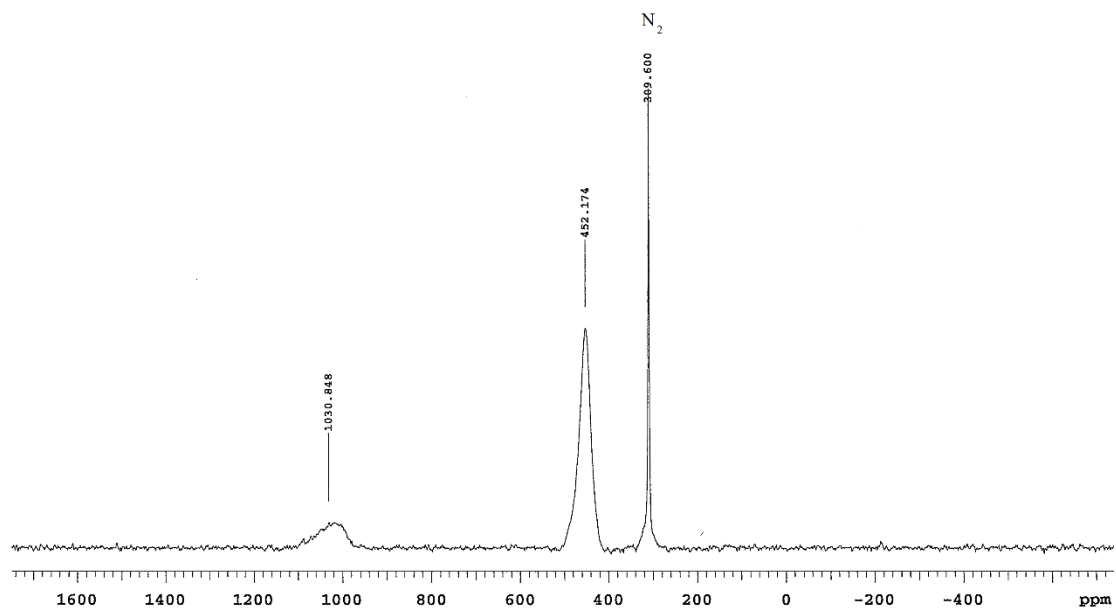


Figure 3-53.  $^{14}\text{N}$  NMR Spectrum for  $[\text{NCr}(\text{N}^i\text{Pr}_2)_2(\text{PPh}_2^n\text{Bu})]\text{PF}_6$  (**3j**) in  $\text{CDCl}_3$



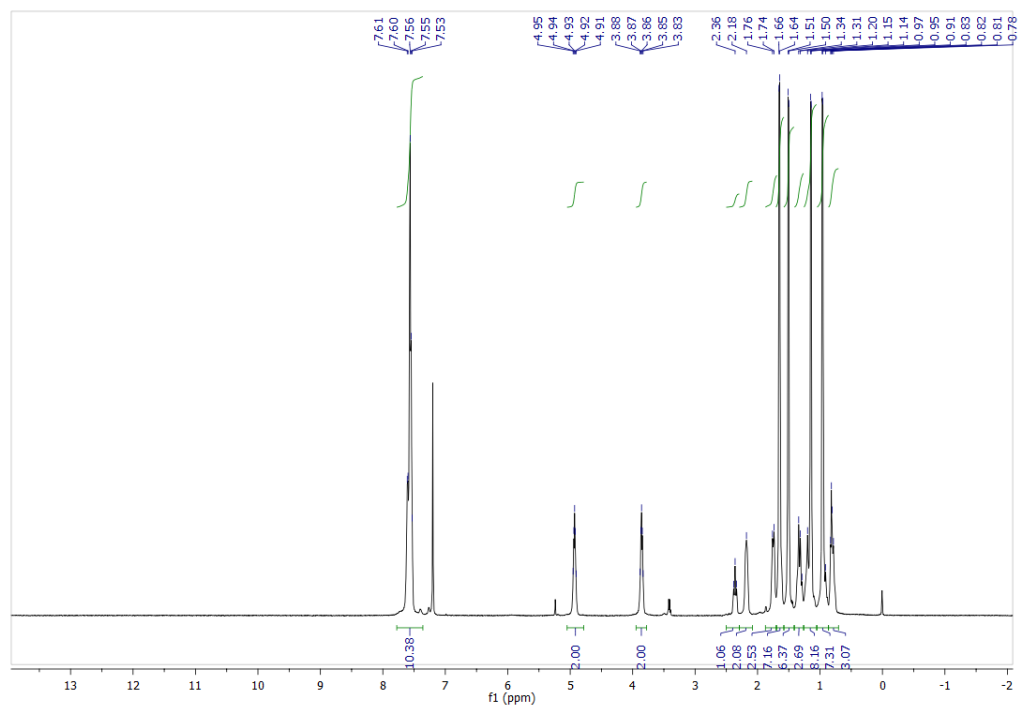


Figure 3-54.  $^1\text{H}$  NMR Spectrum for  $[\text{NCr}(\text{N}^i\text{Pr}_2)_2(\text{PPh}_2\text{Cy})]\text{SbF}_6$  (**3k**) in  $\text{CDCl}_3$



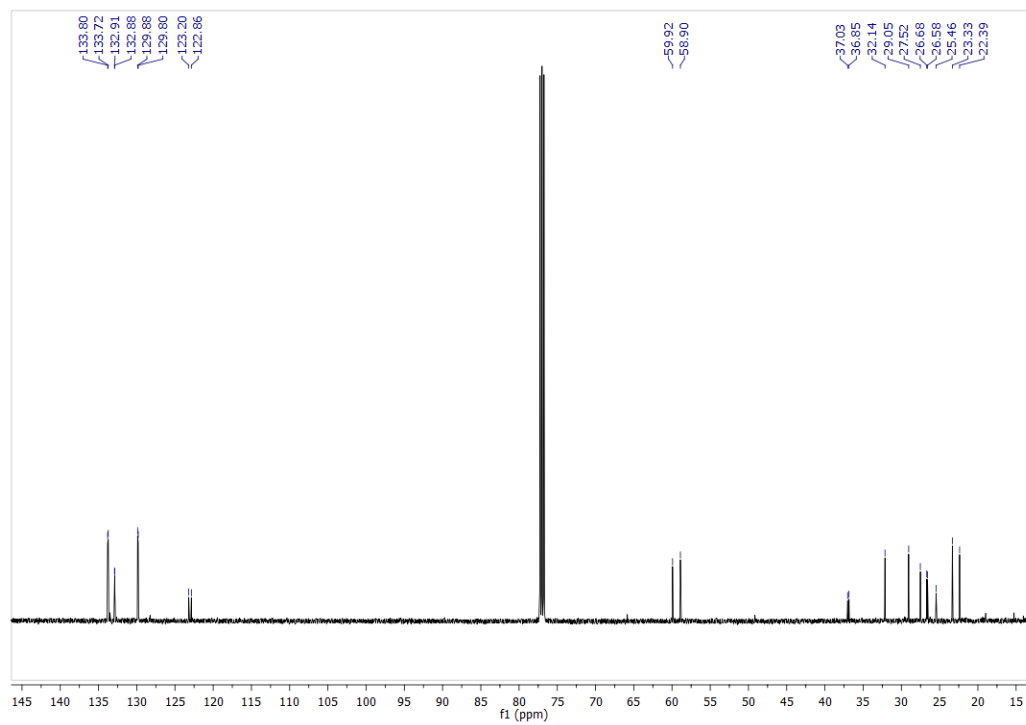


Figure 3-55. <sup>13</sup>C NMR Spectrum for [NCr(N<sup>i</sup>Pr)<sub>2</sub>(PPh<sub>2</sub>Cy)]SbF<sub>6</sub> (**3k**) in CDCl<sub>3</sub>



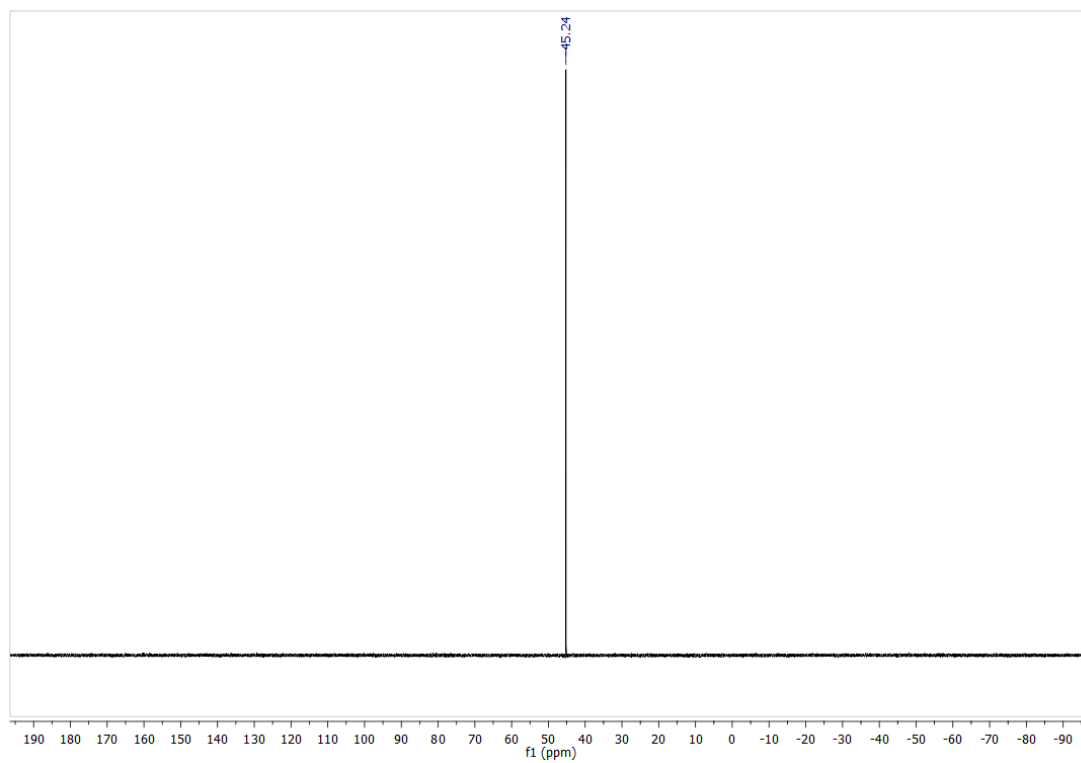


Figure 3-56.  $^{31}\text{P}$  NMR Spectrum for  $[\text{NCr}(\text{N}^i\text{Pr}_2)_2(\text{PPh}_2\text{Cy})]\text{SbF}_6$  (**3k**) in  $\text{CDCl}_3$



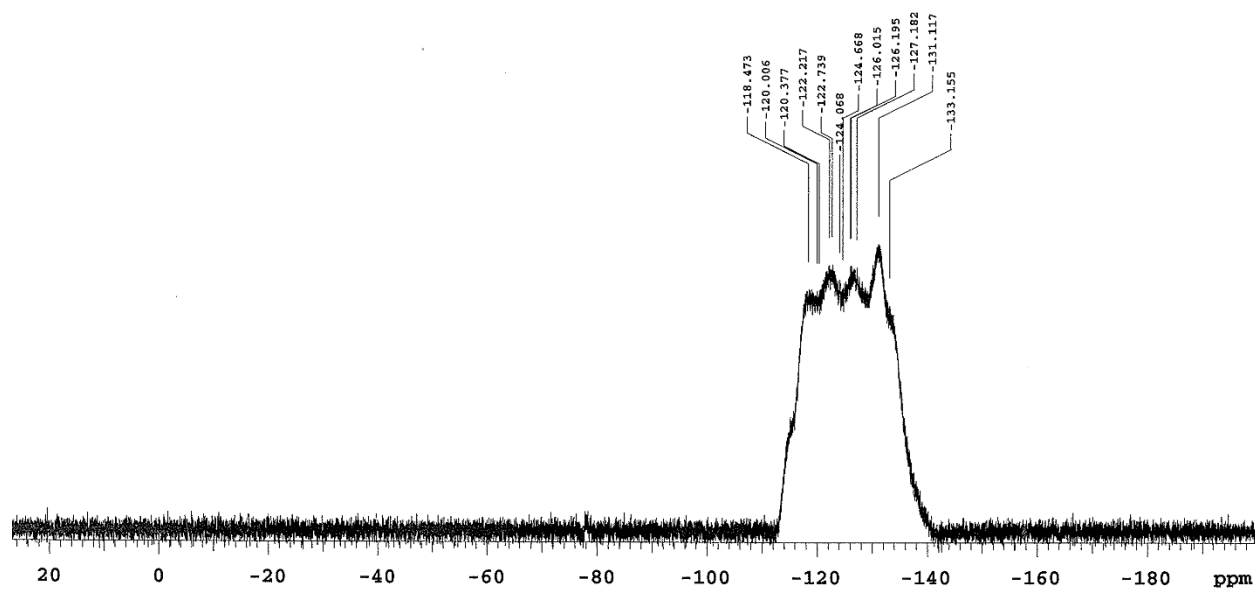


Figure 3-57.  $^{19}\text{F}$  NMR Spectrum for  $[\text{NCr}(\text{N}^i\text{Pr}_2)_2(\text{PPh}_2\text{Cy})]\text{SbF}_6$  (**3k**) in  $\text{CDCl}_3$



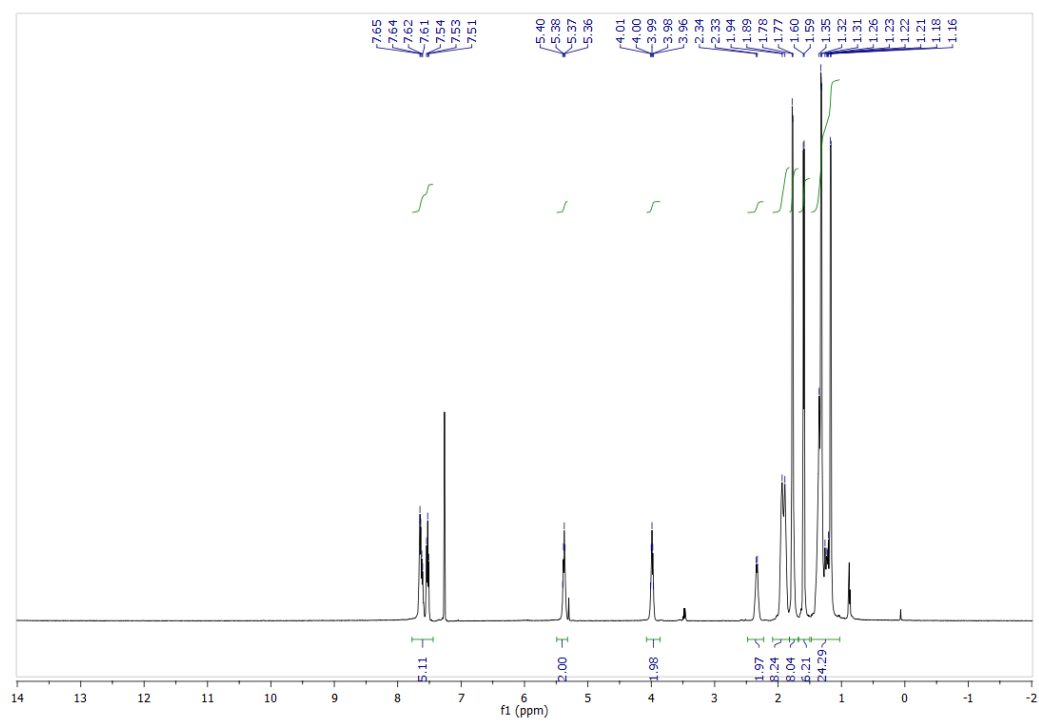


Figure 3-58.  $^1\text{H}$  NMR Spectrum for  $[\text{NCr}(\text{N}^i\text{Pr}_2)_2(\text{PPhCy}_2)]\text{SbF}_6$  (**3I**) in  $\text{CDCl}_3$



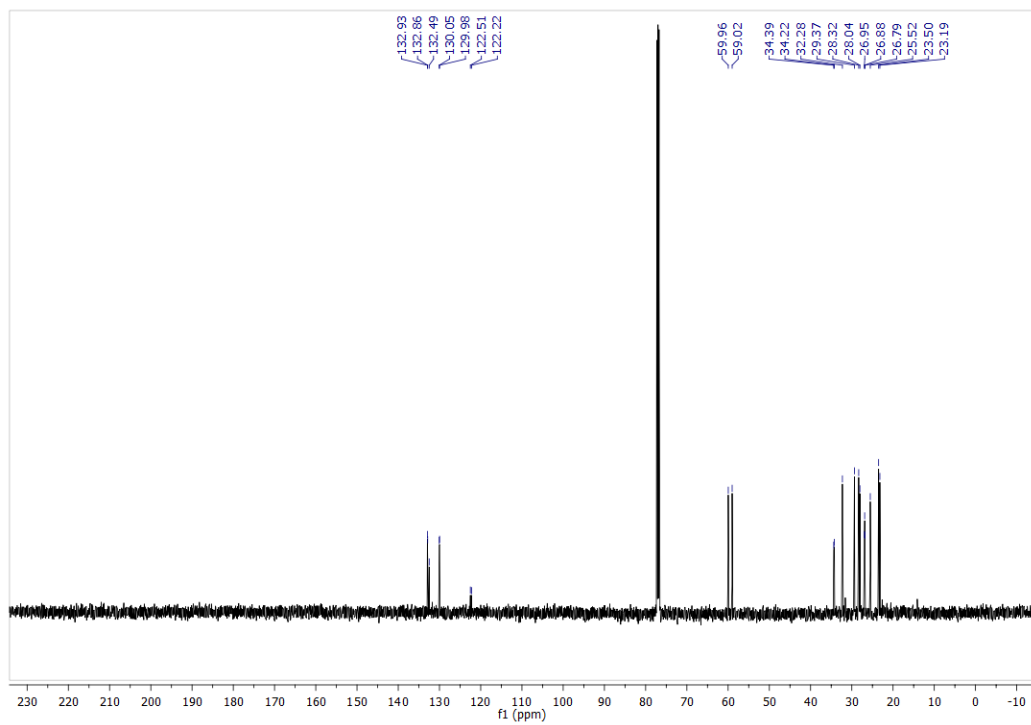


Figure 3-59.  $^{13}\text{C}$  NMR Spectrum for  $[\text{NCr}(\text{N}^i\text{Pr}_2)_2(\text{PPhCy}_2)]\text{SbF}_6$  (**31**) in  $\text{CDCl}_3$



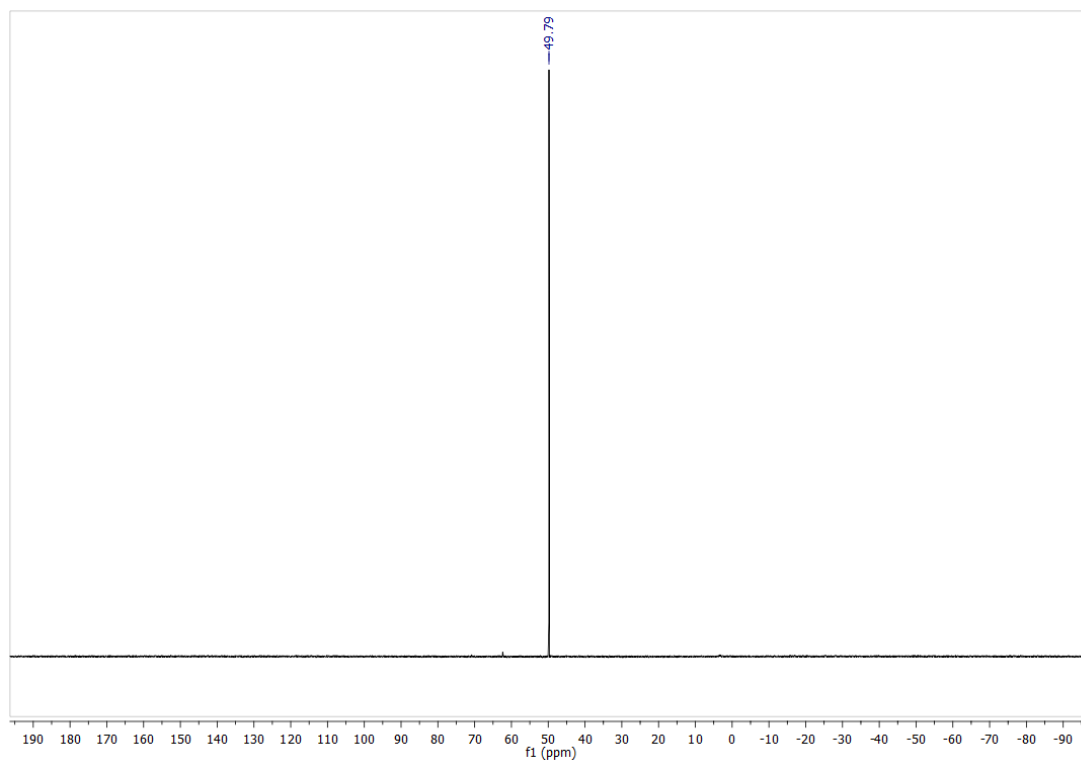


Figure 3-60.  $^{31}\text{P}$  NMR Spectrum for  $[\text{NCr}(\text{N}^i\text{Pr}_2)_2(\text{PPhCy}_2)]\text{SbF}_6$  (**31**) in  $\text{CDCl}_3$



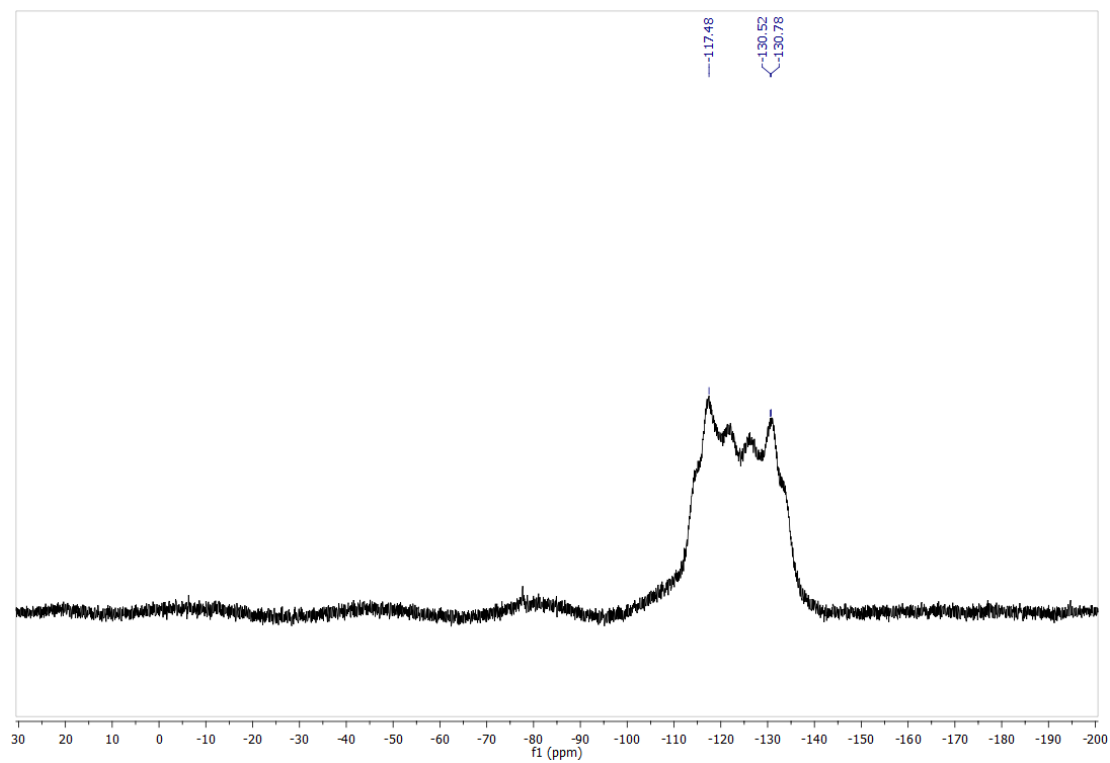


Figure 3-61.  $^{19}\text{F}$  NMR Spectrum for  $[\text{NCr}(\text{N}^i\text{Pr}_2)_2(\text{PPhCy}_2)]\text{SbF}_6$  (**31**) in  $\text{CDCl}_3$



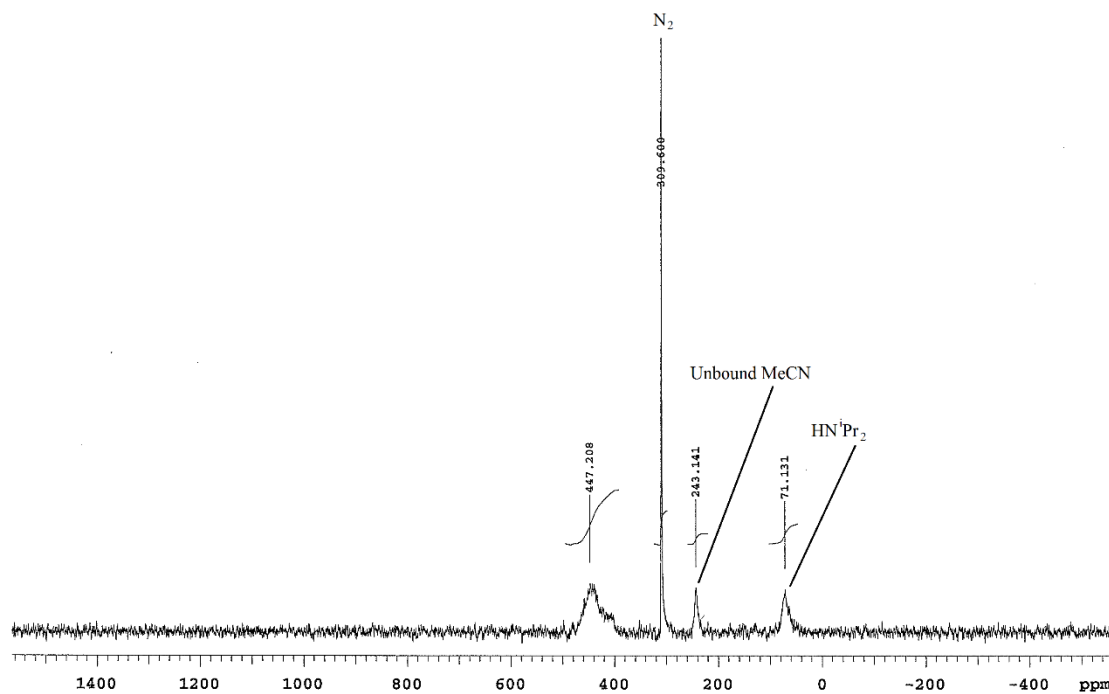


Figure 3-62.  $^{14}\text{N}$  NMR Spectrum for  $[\text{NCr}(\text{N}^i\text{Pr}_2)_2(\text{PPhCy}_2)]\text{SbF}_6$  (**31**) in  $\text{CDCl}_3$



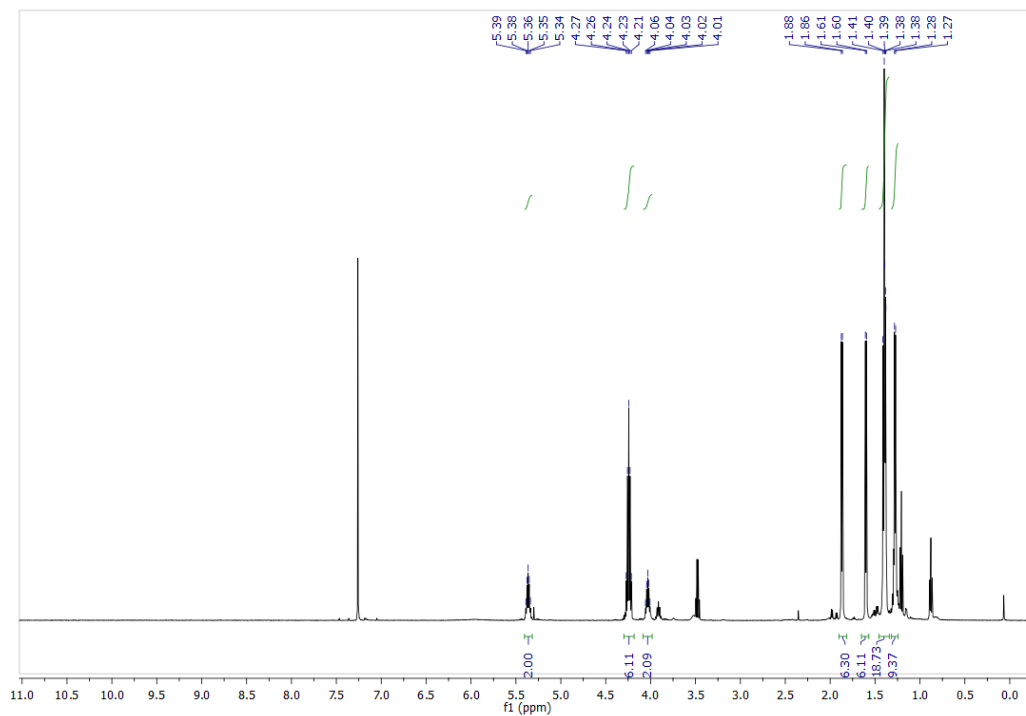


Figure 3-63.  $^1\text{H}$  NMR Spectrum for  $[\text{NCr}(\text{N}^i\text{Pr}_2)_2(\text{P}(\text{OEt})_3)]\text{SbF}_6$  (**3m**) in  $\text{CDCl}_3$



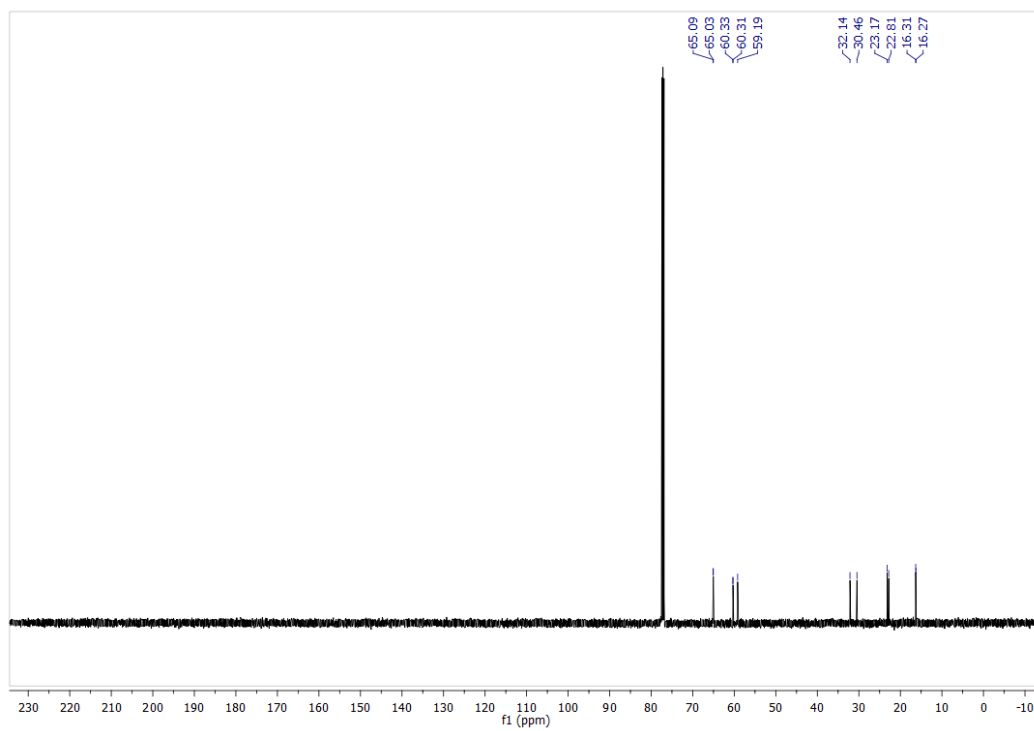


Figure 3-64. <sup>13</sup>C NMR Spectrum for [NCr(N<sup>i</sup>Pr<sub>2</sub>)<sub>2</sub>(P(OEt)<sub>3</sub>)]SbF<sub>6</sub> (**3m**) in CDCl<sub>3</sub>



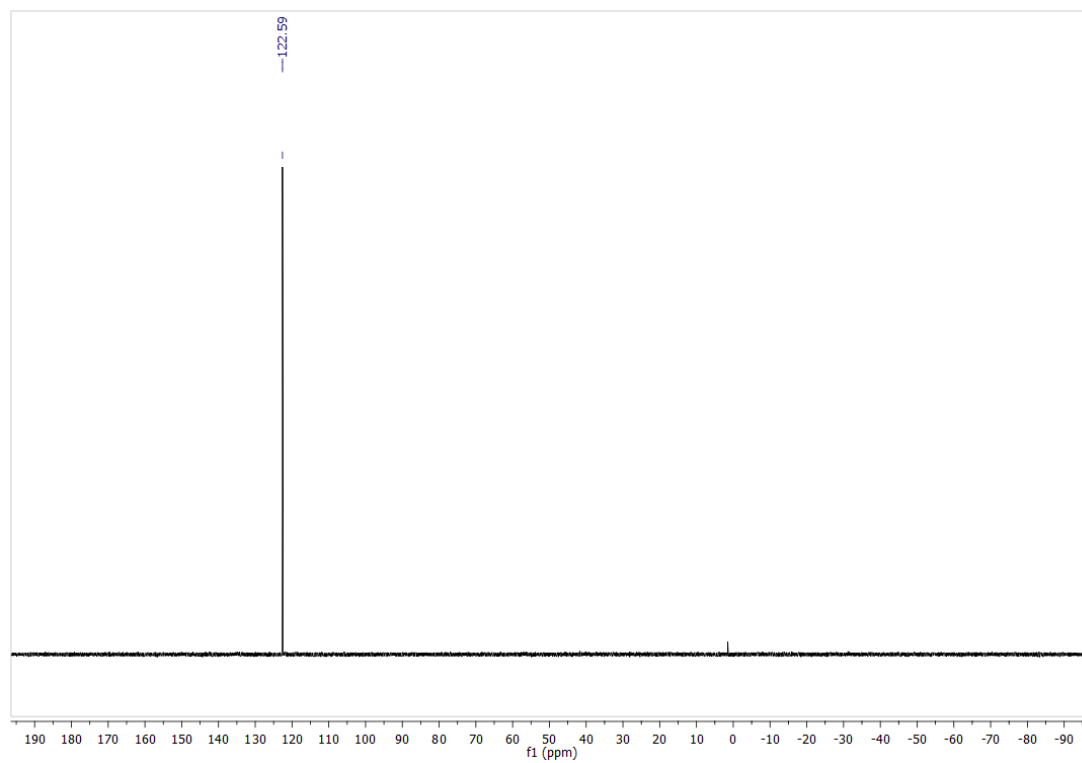


Figure 3-65.  $^{31}\text{P}$  NMR Spectrum for  $[\text{NCr}(\text{N}^i\text{Pr}_2)_2(\text{P}(\text{OEt})_3)]\text{SbF}_6$  (**3m**) in  $\text{CDCl}_3$



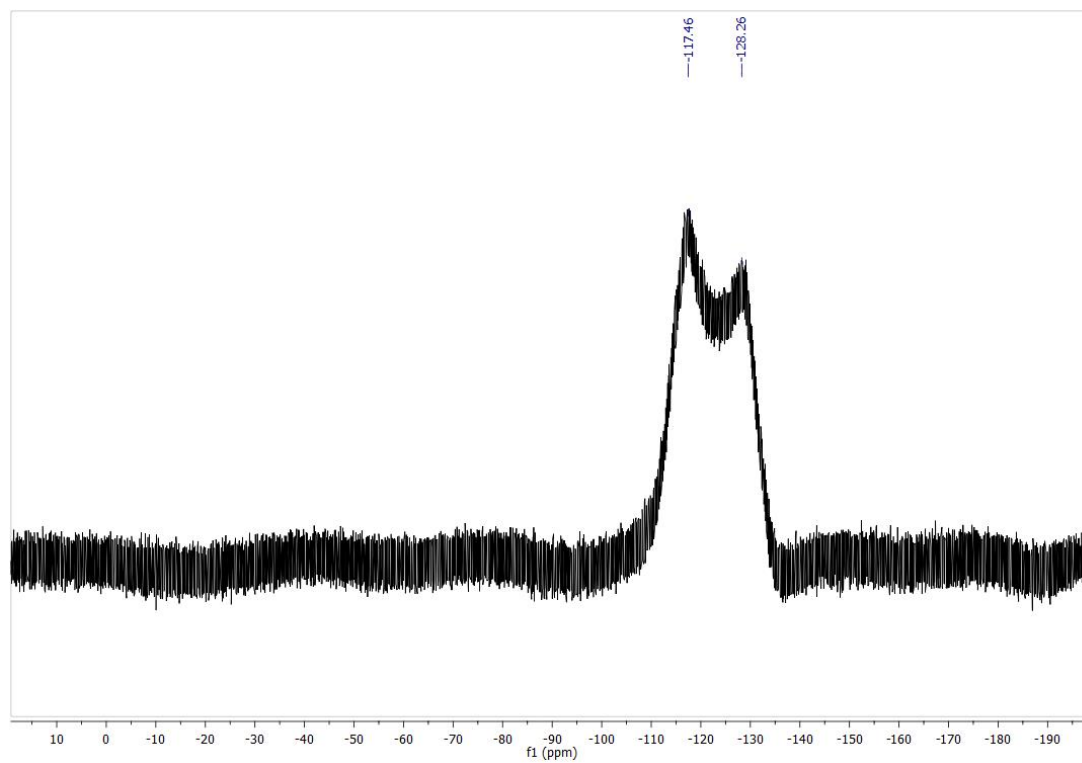


Figure 3-66.  $^{19}\text{F}$  NMR Spectrum for  $[\text{NCr}(\text{N}^i\text{Pr}_2)_2(\text{P}(\text{OEt})_3)]\text{SbF}_6$  (**3m**) in  $\text{CDCl}_3$



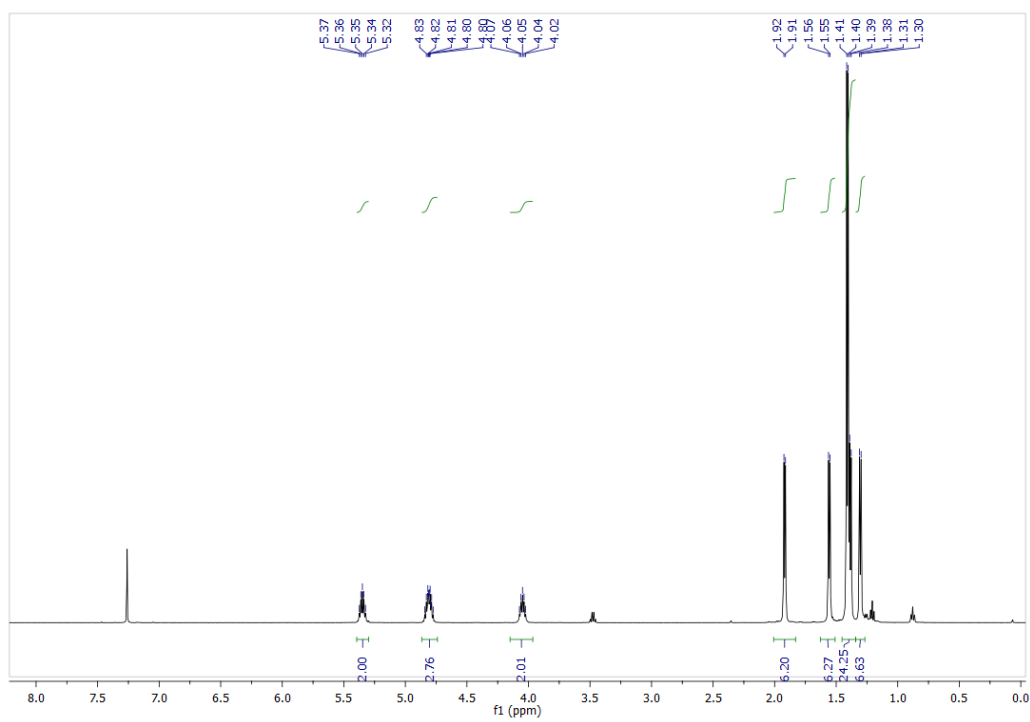


Figure 3-67.  $^1\text{H}$  NMR Spectrum for  $[\text{NCr}(\text{N}^i\text{Pr}_2)_2(\text{P}(\text{O}^i\text{Pr})_3)]\text{SbF}_6$  (**3n**) in  $\text{CDCl}_3$



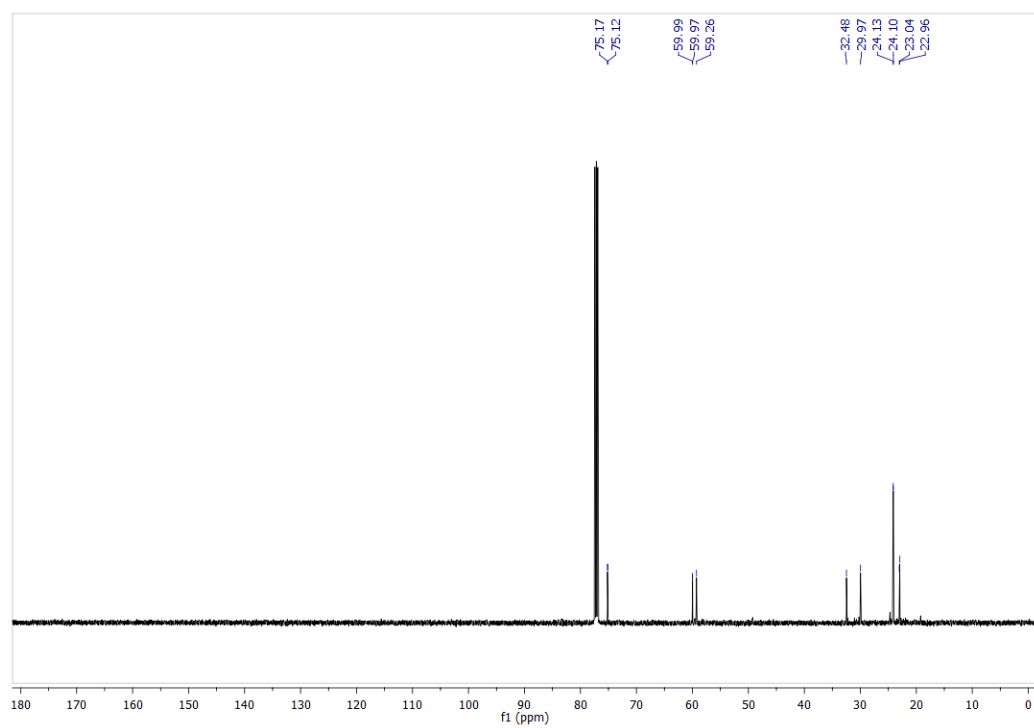


Figure 3-68.  $^{13}\text{C}$  NMR Spectrum for  $[\text{NCr}(\text{N}^i\text{Pr}_2)_2(\text{P}(\text{O}^i\text{Pr})_3)]\text{SbF}_6$  (**3n**) in  $\text{CDCl}_3$



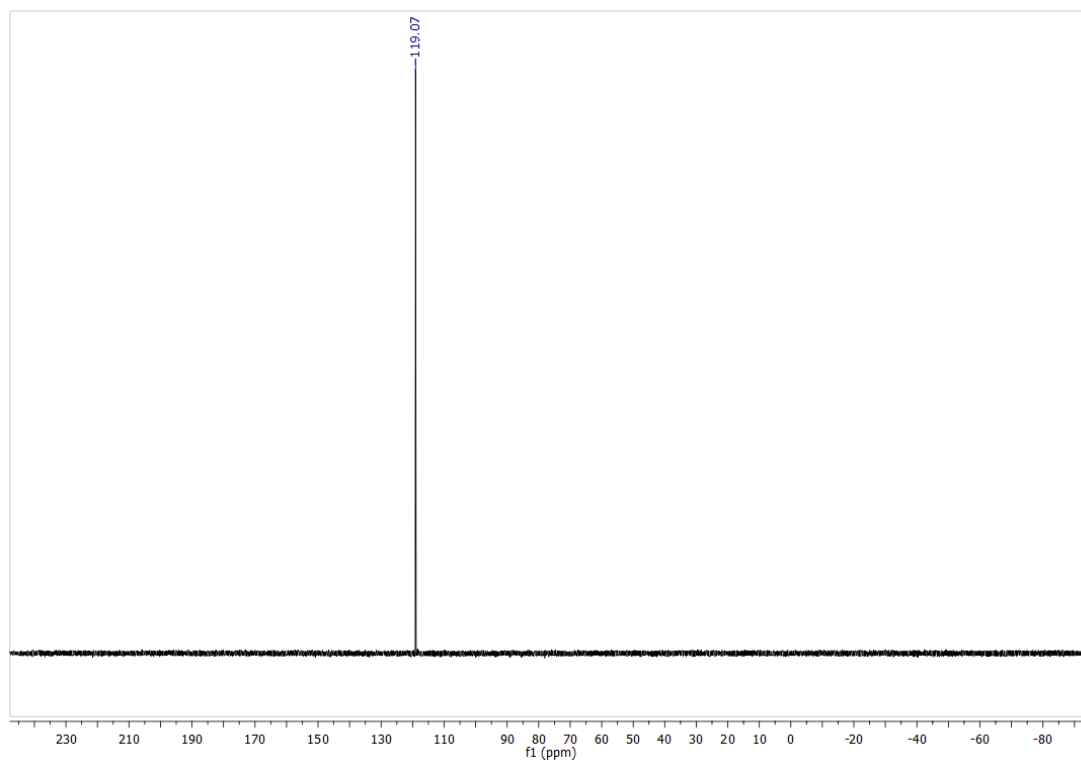


Figure 3-69.  $^{31}\text{P}$  NMR Spectrum for  $[\text{NCr}(\text{N}^i\text{Pr}_2)_2(\text{P}(\text{O}^i\text{Pr})_3)]\text{SbF}_6$  (**3n**) in  $\text{CDCl}_3$



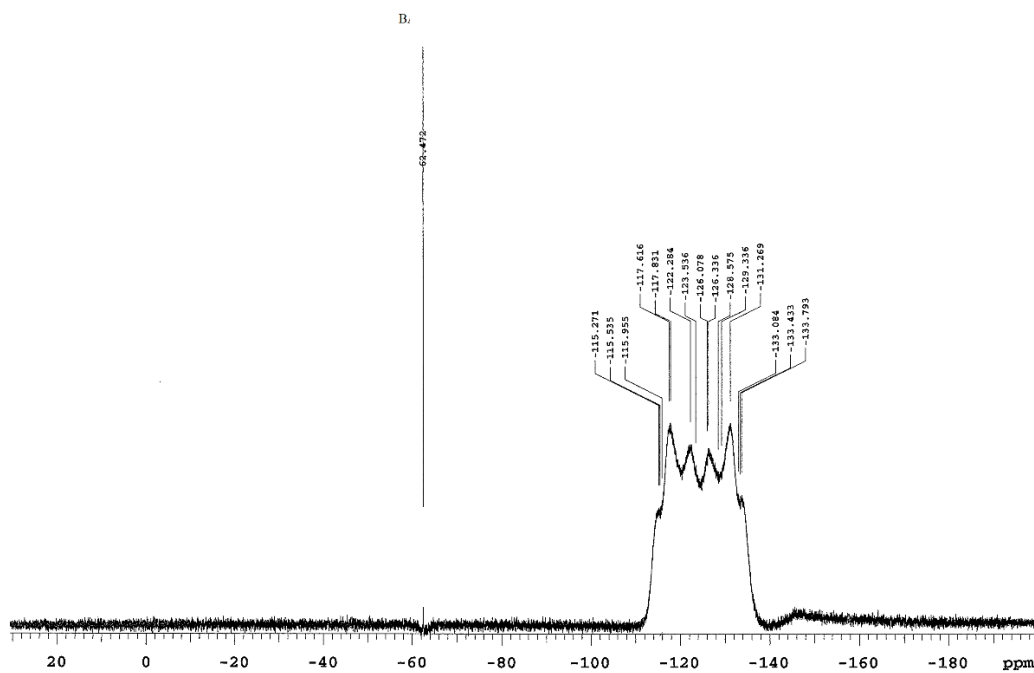


Figure 3-70.  $^{19}\text{F}$  NMR Spectrum for  $[\text{NCr}(\text{N}^i\text{Pr}_2)_2(\text{P}(\text{O}^i\text{Pr})_3)]\text{SbF}_6$  (**3n**) in  $\text{CDCl}_3$



{N

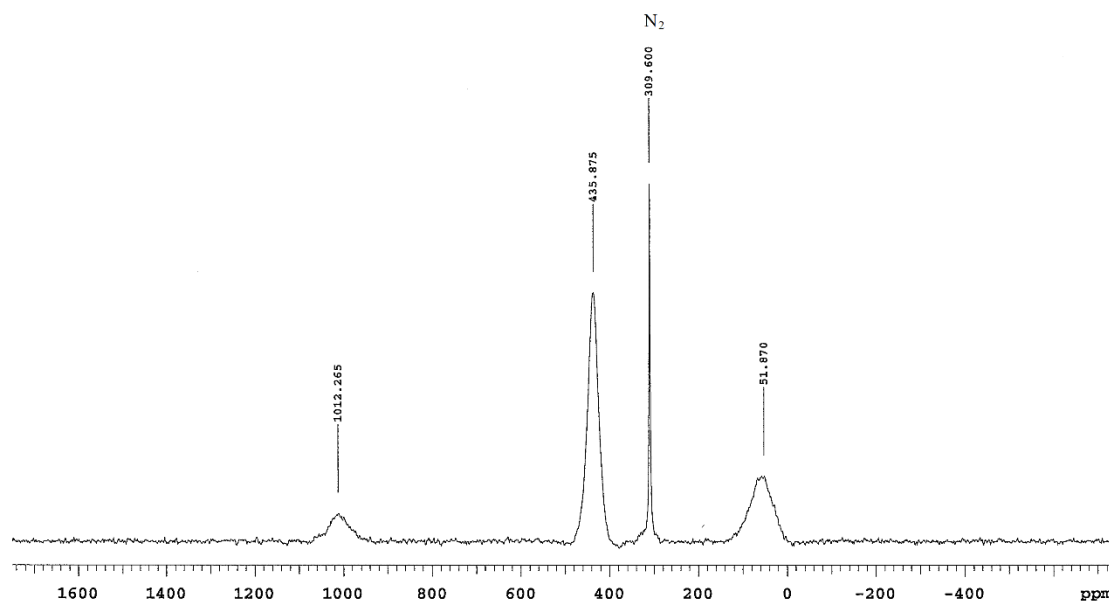


Figure 3-71.  $^{14}\text{N}$  NMR Spectrum for  $[\text{NCr}(\text{N}^i\text{Pr}_2)_2(\text{P}(\text{O}^i\text{Pr})_3)]\text{SbF}_6$  (**3n**) in  $\text{CDCl}_3$



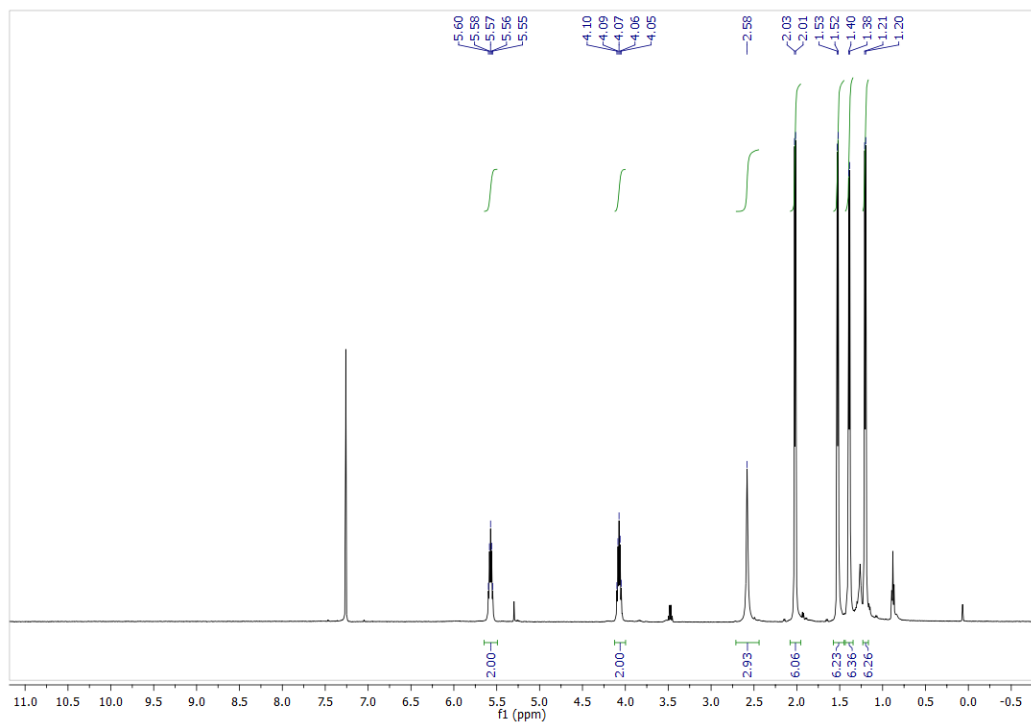


Figure 3-72.  $^1\text{H}$  NMR Spectrum for  $[\text{NCr}(\text{N}^i\text{Pr}_2)_2(\text{NCCH}_3)]\text{SbF}_6$  (**2**) in  $\text{CDCl}_3$



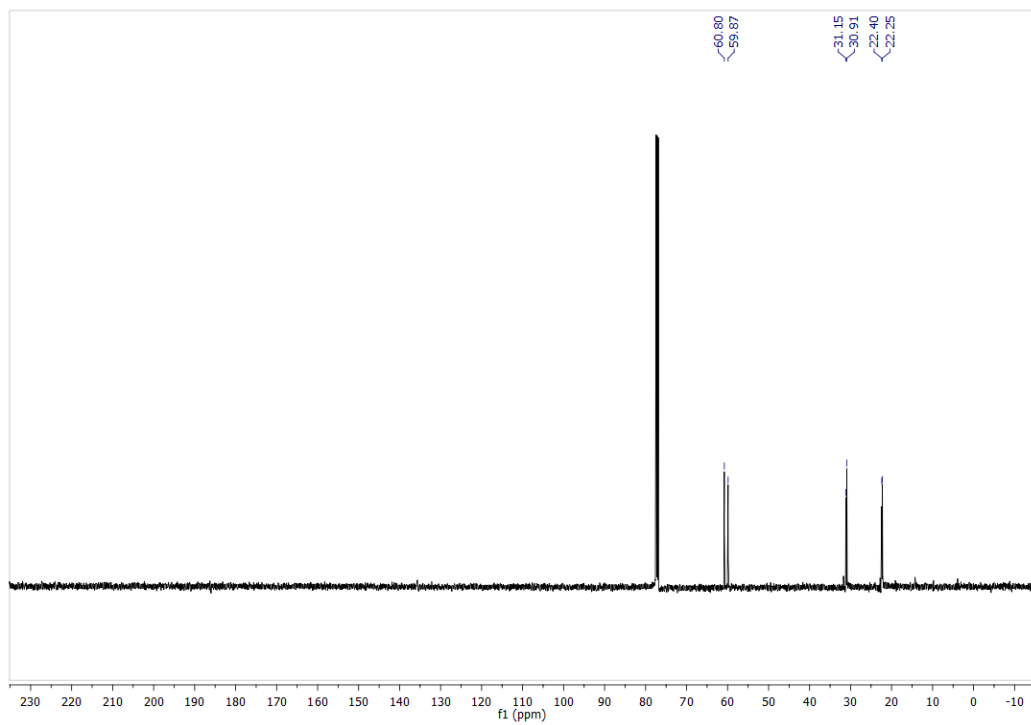


Figure 3-73.  $^{13}\text{C}$  NMR Spectrum for  $[\text{NCr}(\text{NiPr}_2)_2(\text{NCCH}_3)]\text{SbF}_6$  (**2**) in  $\text{CDCl}_3$



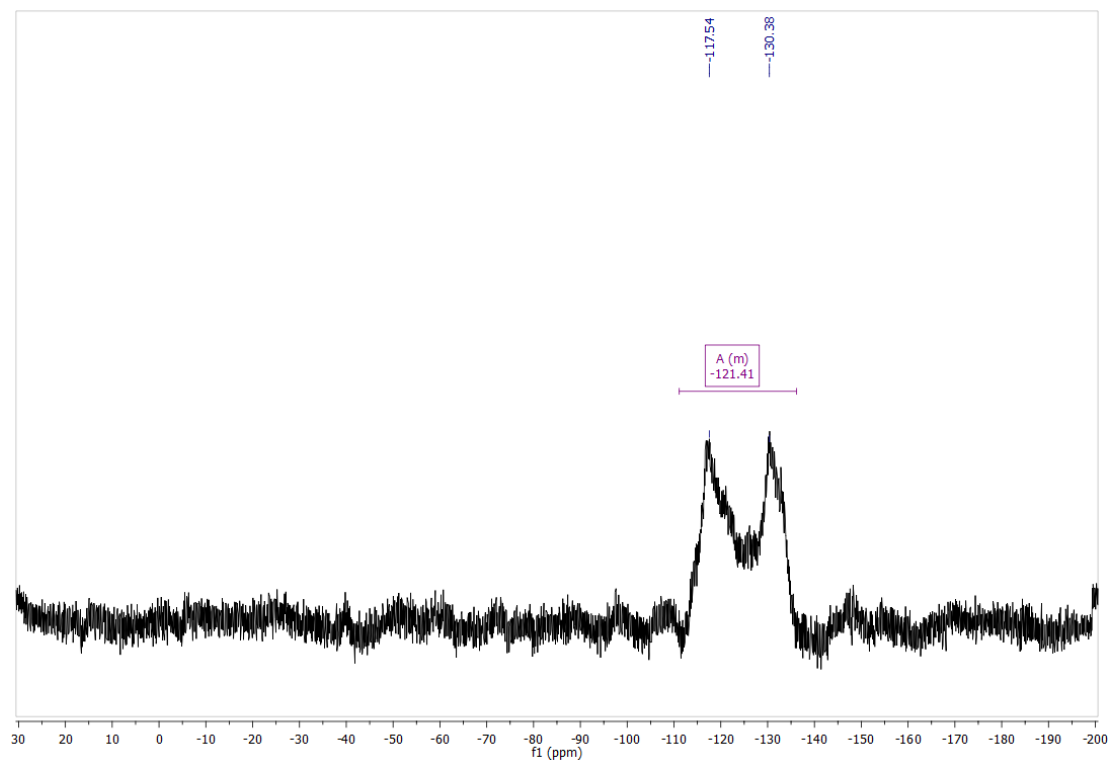


Figure 3-74.  $^{19}\text{F}$  NMR Spectrum for  $[\text{NCr}(\text{N}^i\text{Pr}_2)_2(\text{NCCH}_3)]\text{SbF}_6$  (**2**) in  $\text{CDCl}_3$



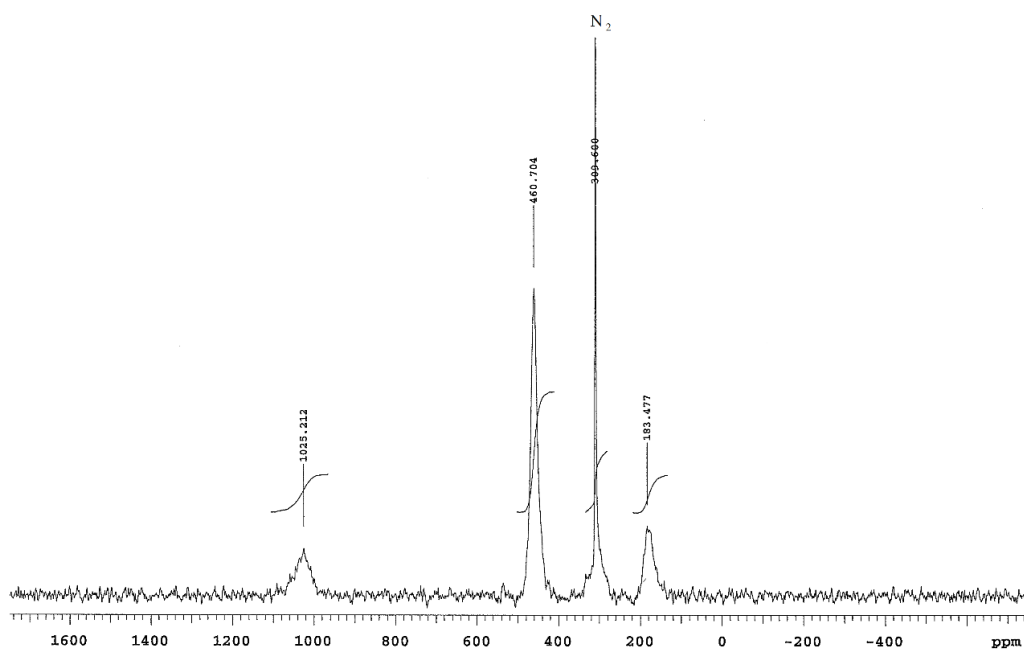


Figure 3-75.  $^{14}\text{N}$  NMR Spectrum for  $[\text{NCr}(\text{N}^i\text{Pr}_2)_2(\text{NCCH}_3)]\text{SbF}_6$  (**2**) in  $\text{CDCl}_3$



## REFERENCES



## REFERENCES

1. Tolman, C. A., *Chem. Rev.* **1977**, 77 (3), 313-348.
2. Fernandez, A. L.; Reyes, C.; Prock, A.; Giering, W. P., *J. Chem. Soc., Perkin Trans. 2* **2000**, (5), 1033-1041.
3. Liu, H. Y.; Eriks, K.; Prock, A.; Giering, W. P., *Organometallics* **1990**, 9 (6), 1758-1766.
4. Wolczanski, P. T., *Organometallics* **2017**, 36 (3), 622-631.
5. Dias, E. L.; Nguyen, S. T.; Grubbs, R. H., *J. Am. Chem. Soc.* **1997**, 119 (17), 3887-3897.
6. Surry, D. S.; Buchwald, S. L., *Angew. Chem. Int. Ed.* **2008**, 47 (34), 6338-6361.
7. Martin, R.; Buchwald, S. L., *Acc. Chem. Res.* **2008**, 41 (11), 1461-1473.
8. DiFranco, S. A. Single-Site Molybdenum(IV) Mediated Bond Cleavage Reactions and Ligand Parameterization Using a Cr(VI) Nitrido Platform. Michigan State University, 2013.
9. Tolman, C. A., *J. Am. Chem. Soc.* **1970**, 92 (10), 2953-2956.
10. Rocchigiani, L.; Macchioni, A., *Dalton Trans.* **2016**, 45 (7), 2785-2790.
11. Krossing, I.; Reisinger, A., *Coord. Chem. Rev.* **2006**, 250 (21-22), 2721-2744.
12. Krossing, I., *Chem. Eur. J.* **2001**, 7 (2), 490-502.
13. Reed, C. A., *Acc. Chem. Res.* **1998**, 31 (3), 133-139.
14. Aldrich, K. E.; Billow, B. S.; Holmes, D.; Bemowski, R. D.; Odom, A. L., *Organometallics* **2017**, 36 (7), 1227-1237.
15. Macchioni, A.; Ciancaleoni, G.; Zuccaccia, C.; Zuccaccia, D., *Chem. Soc. Rev.* **2008**, 37 (3), 479-489.
16. DiFranco, S. A.; Maciulis, N. A.; Staples, R. J.; Batrice, R. J.; Odom, A. L., *Inorg. Chem.* **2012**, 51 (2), 1187-1200.
17. Lente, G.; Fabian, I.; Poe, A. J., *New J. Chem.* **2005**, 29 (6), 759-760.
18. Billow, B. S.; Bemowski, R. D.; DiFranco, S. A.; Staples, R. J.; Odom, A. L., *Organometallics* **2015**, 34 (18), 4567-4573.
19. Fernandez, A.; Reyes, C.; YingLee, T.; Prock, A.; Giering, W. P.; Haar, C. M.; Nolan, S. P., *J. Chem. Soc., Perkin Trans. 2* **2000**, (7), 1349-1357.



20. Mitoraj, M. P.; Michalak, A., *Inorg. Chem.* **2010**, 49 (2), 578-582.
21. Leyssens, T.; Peeters, D.; Orpen, A. G.; Harvey, J. N., *Organometallics* **2007**, 26 (10), 2637-2645.
22. Parkin, G., *J. Chem. Ed.* **2006**, 83 (5), 791.
23. Green, M. L. H.; Parkin, G., *Dalton Trans.* **2016**, 45 (47), 18784-18795.
24. Gillespie, R. J.; Silvi, B., *Coord. Chem. Rev.* **2002**, 233-234, 53-62.
25. Sanderson, R. T., *J. Chem. Ed.* **1988**, 65 (2), 112-118.
26. Mayer, U.; Gutmann, V.; Gerger, W., *Chemical Monthly* **1975**, 106 (6), 1235-1257.
27. Mayer, U.; Gutmann, V. In *Phenomenological Approach to Cation-Solvent Interactions*, Berlin, Heidelberg, Springer Berlin Heidelberg: Berlin, Heidelberg, 1972; pp 113-140.
28. Beckett, M. A.; Strickland, G. C.; Holland, J. R.; Sukumar Varma, K., *Polymer* **1996**, 37 (20), 4629-4631.
29. Crimmins, M. T.; King, B. W.; Tabet, E. A.; Chaudhary, K., *J. Org. Chem.* **2001**, 66 (3), 894-902.
30. Park, J. G.; Jeon, I.-R.; Harris, T. D., *Inorg. Chem.* **2015**, 54 (1), 359-369.
31. Kermagoret, A.; Braunstein, P., *Dalton Trans.* **2008**, (6), 822-831.



## **Chapter 4.      Developing a Model for the Optimization and Development of Titanium Catalyzed Hydroamination**

### **4.1 Introduction**

We have discussed in the previous chapters how LDP can be used to not only parameterize ligands, but also interrogate ligand-metal bonding interactions. We wanted to prove, though, that LDP could also be used to design and optimize high valent metal catalysts. Being the first endeavor in modeling catalysis with the LDP system, we decided it would be wise to start with a catalyst that we knew behaves well and has some simple ancillary ligand variability. With the combined knowledge from our group, the Bergman group, and others, we decided titanium-catalyzed hydroamination made a good platform from which to start.<sup>1-6</sup>

As mentioned in chapter 1, more electronically deficient ligands put on the Ti center should yield faster catalysis due to an increased acidity of the coordinated amide.<sup>7-9</sup> Surprisingly, in a study published in 2006, it was observed that adding electron withdrawing substituents to the 2-position of pyrrole slowed the rate of hydroamination.<sup>9</sup> In a 2011 study, Swartz again added similar electronic withdrawing arenes to the ligand, but this time to the 3-position of the pyrroles.<sup>7</sup> With the withdrawing groups in the 3-position, the rate of catalysis was increased. These observations were attributed to the steric profile of the ligands. When the pyrrole is substituted in the 2-position, the large profile of the electron deficient arenes slows the rate of catalysis. The 3-position on the other hand, meant the large substituents were pointing away from the metal center and did not increase the steric profile of the ligand. The series of studies reported by Swartz highlights the difficulty in designing new and improved catalysts. There is a delicate balance between adding electron withdrawing groups and keeping the steric profile of the ligand small enough. Simply



guessing at how to change the ligand structure can be productive, but it is often a long, intensive process. We hoped we could model the titanium hydroamination catalysis in a way that allowed quantitative understanding of the steric and electronic effects of the ligands.

## 4.2 Ligand Analysis Considerations

The first hurdle in modeling the catalysis was the ligand choice. Since Dr. Doug Swartz, a former Odom group member, had results with both monodentate and bidentate pyrrole ligands, and there seemed to be an easily observable rate difference between pyrrole substitutions, we chose pyrrole-based ligands. But we were hesitant to use monodentate ligands. It has been established that titanium systems undergo ligand redistribution reactions and, from experience in our group, monodentate ligands make this process more facile.<sup>10-13</sup>

Using the  $(X_2)Ti(NMe_2)_2$  ligands as a platform, we could easily manipulate the catalyst by exchanging the bidentate  $X_2$  ancillary ligand.<sup>8-9, 14</sup> The pyrrole platform is an excellent system to manipulate the sterics and electronics of the catalysts. Substitution of the 2-, 3-, and 4-positions of the pyrrole with both sterically and electronically varied groups provides a wide variety of potential catalytic activities. We hoped these types of substitutions would allow enough ligand variation to produce a sound model for the reaction without the need to include any monodentate ligands.

Importantly, the analogous monodentate pyrrole fragments are also isolable and easy to measure with the LDP system.<sup>15</sup> Due to the nature of the LDP system, we are only able to parameterize monodentate ligands. We postulated this problem could be solved by simply measuring one half of the ligand fragment (ignoring the linker) to establish values for steric and electronic parameters.



This brings us to the other critical factor of the ligand analysis, sterics. The system Tolman developed for sterics was incredibly simple.<sup>16-17</sup> By forming a cone around the ligand, he simplified the complicated steric system of a phosphine ligand into a single value. This single value has found much use in the literature and is still commonly used today. Unfortunately, though, the simplicity of  $\theta$  is a limitation on its implementation to other systems. The three-fold symmetry of simple  $\text{PR}_3$  ligands means that a cone around the ligands can be a reasonable approximation of the steric profile. Moving to ligands with less regular profiles means that the conical approximation becomes a less accurate description. Moreover, as substituents are added to the ligands which make them more unsymmetrical, the approximation fails even faster.

As such, we needed to find a way to quantitatively compare the steric profiles of the ligands we planned to study. In the original LDP publication, two steric descriptors were used to compare the ligands reported.<sup>15</sup> The first program treats the metal center as a point light source.<sup>18-19</sup> The program then uses the ligands as solid objects which, when shined with light from the metal center, create shadows. The output for the steric parameter is the percentage of a sphere around the metal center the ligand “shades”. The issue with this, later named, solid angle program is that the ligands essentially become two dimensional. This has two primary issues. The first, substituents such as a phenyl group are treated as a function of the orientation of the group. For example, if a phenyl group is in an orientation where the vector connecting its centroid and the metal center is perpendicular to the aromatic plane, the phenyl group appears large. If the same vector lies in the plane of the phenyl ring, then the group appears small. The second problem is, like the orientation of the ligand, the distance to the metal has a dramatic effect on the measured steric parameter. Small ligands close to the metal are measured as being large while large radii atoms far from the metal center are measured as being quite small. In some cases this can be a true measure of sterics,



for example O<sup>t</sup>Bu is larger than S<sup>t</sup>Bu, but the program seems to treat this scenarios inconsistently. This leads to strange results such as the ordering of the halides of F > Br > I > Cl on Cr(VI).<sup>15</sup>

A better option for comparing the steric profile of ligands is the percent buried volume program, %V<sub>bur</sub>, developed by Cavallo.<sup>20-21</sup> In this program the first coordination sphere around the metal is set to an arbitrary value, generally a radius of 3.5 Å. The program then creates a shell around the metal center at this radius. The volume of the shell occupied by the ligand under investigation is the %V<sub>bur</sub>. The calculation of the %V<sub>bur</sub> of a ligand is based on a crystal structure, and as such, the values are much less approximate than, for example,  $\theta$  which is based on molecular models. It is important to note, though, that since hydrogen positions are calculated in the crystal structures, they are often removed in the %V<sub>bur</sub> calculations, but for our system, they were included. The advantages of the buried volume program were discussed in more detail in chapter 1, but, in brief, it allows a single parameter that accounts for size of ligand, irregularity in shape, and proximity of the ligand to the metal.

For each ligand studied, the chromium complex was used to determine the steric parameters. We decided this was the most reasonable estimation of the ligands sterics. This is in part because we wanted to ignore contributions of the linker in the bidentate ligands to test metallocycle ring size effects, which will be discussed later. But, more importantly, determining the steric parameters from Ti would have meant accepting some inherent, known inaccuracy.

Reactive species are, by definition, unstable. So, the structure of the catalyst employed in the rate limiting step is rarely an isolable species and it is likely to be different from the precatalyst structure. By fully parameterizing the ligands from our Cr system, we have a systematic platform to compare all aspects of various ligands against one another. In the titanium systems, some catalysts have ligands that vary in hapticity depending on the substitution. For example, the crystal



structure of  $(\text{NMe}_2)_2\text{Ti}(\text{dpm})$  has one pyrrole ring bound  $\eta^1$  through only the nitrogen and the other is bound  $\eta^5$  through the aromatic system; other dipyrrole ligands systems have both sides bound  $\eta^1$  through the pyrrole.<sup>14</sup> Since we predicted the ligand was fluxional, it is possible that modeling the sterics from titanium would be inaccurate. Besides that, some of the precatalysts have varying coordination number due to dative coordination of  $\text{HNMe}_2$  ligands. Measuring the %  $V_{\text{bur}}$  from the titanium complexes would have meant we were comparing both changes in ligand and changes in the coordination environment of the metal center.

If, on the other hand, we measure the sterics from the chromium crystal structures, the coordination environment is much more constant. Additionally, because of the sterics at the metal, the ligands are all forced into an  $\eta^1$  configuration. We think this is a more accurate representation for the active species of the Ti complexes, but that will be discussed in detail later. One might be concerned that the steric bulk of the diisopropyl groups would affect the orientation of the ligand on Cr. While this is a possibility, in some sense it relates our system back to the Tolman's  $\theta$  parameter. Tolman configured the phosphines into their smallest possible configuration before measuring  $\theta$ .<sup>16</sup> This achieves a more constant orientation, rather than leaving the R groups arranged at random, providing a more systematic comparison between ligands.

#### 4.3 Synthesis and Characterization of the Chromium Complexes

*This project was undertaken as close collaboration with Tanner McDaniel. The ligands presented in this study that were not commercially available were synthesized by him.<sup>22-23</sup> Tanner also synthesized the titanium catalysts and did kinetic analysis of each catalyst. My part in this investigation was the synthesis of the chromium complexes, evaluation of the LDP parameters, and modeling the experimental data.*



The synthesis and characterization of the chromium species in this study were quite straightforward. Most procedures are either analogous to those from the original LDP publication or subtle derivations thereof.<sup>15, 24</sup>

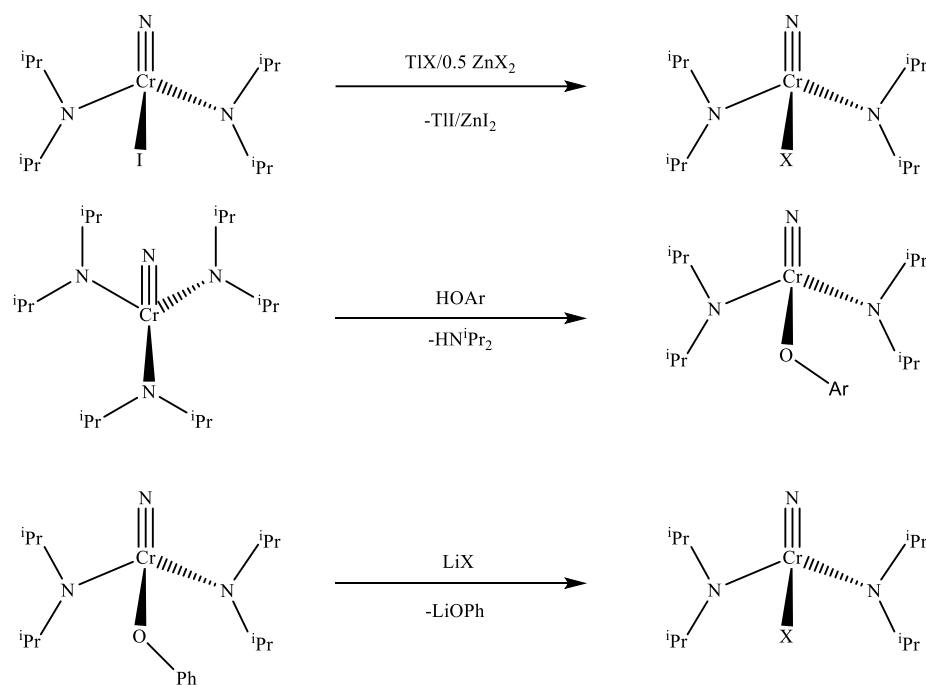
The general procedures for the synthesis of the chromium complexes is shown in Scheme 4-1. For the electron deficient pyrrole ligands, the pyrroles were reacted with TIOEt in ether to produce the TI-Pyrrole. The TI-pyrrole can then be added to a solution of  $\text{N}(\text{iPr})_2\text{CrI}$  in ether, precipitating TII, and generating the desired chromium pyrrole species. For the methyl-substituted pyrroles and indoles it was necessary to use transmetalation *via*  $\text{ZnX}_2$  and  $\text{N}(\text{iPr})_2\text{CrI}$  or  $\text{LiX}$  and  $\text{N}(\text{iPr})_2\text{CrOPh}$ . Synthesis of the aryloxide chromium complexes was achieved using an acid base reaction of the phenol and  $\text{N}(\text{iPr})_2\text{Cr}_3$ .<sup>24</sup>

All of the complexes except  $\text{N}(\text{iPr})_2\text{Cr}(\text{SNap})$  were crystalline and produced X-ray quality single crystals. Crystallographic analysis of all compounds provided the structures used in the percent buried volume analysis. The settings for the buried volume program, SambVca 2, were left to the default settings.<sup>25</sup> The sphere was given a radius of 3.5 Å, hydrogens were not included in the calculation, and the %  $V_{\text{bur}}$  calculation used the Bondi radii of the atoms scaled by 1.17 with a 0.10 mesh size.

The ligand donor parameters were established using our standard method.<sup>15, 26</sup> The bidentate aryloxide ligands used for the catalysis featured a very large <sup>t</sup>Bu group in the 2-position. The monodentate version of these ligands were bound to chromium easily enough, but the LDP values were not in line with what we expected. The values determined were >13 kcal/mol. When compared to unsubstituted phenol, 11.98 kcal/mol, these values did not seem logical. We synthesized the 2-Me substituted versions of each phenol as electronic surrogates and determined the LDP values to be lower than phenol. This is expected as adding alkyl or alkoxy groups to the



aromatic ring should increase the ligand's overall donation ability to the metal center.<sup>15, 27</sup> We suspect that, like the discussion of bulky anions and phosphine ligands in chapter 3, the steric bulk of the 2-<sup>t</sup>Bu phenols sterically crowds the <sup>i</sup>Pr groups of the amides and hinders rotation, artificially inflating the LDP value.<sup>28</sup> As such, we decided to use the LDP values of the methyl-substituted aryloxides for our modeling, but the %  $V_{\text{bur}}$  was calculated using the <sup>t</sup>Bu substituted ligand.

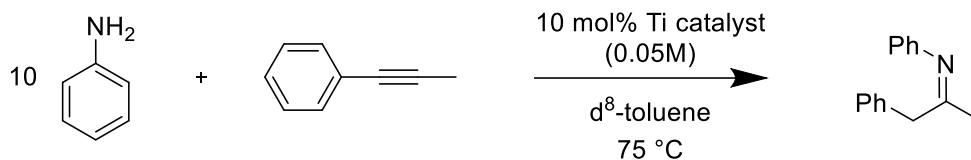


Scheme 4-1. General procedures for synthesis of the chromium complexes.

#### 4.4 Modeling the Hydroamination Kinetics

With the methods to quantitatively compare sterics and electronics of our chosen ligands we set out to begin modeling kinetics. As mentioned above, we aimed to study intermolecular hydroamination. The catalyses were run with a 10-fold excess of aniline to produce pseudo first order kinetics. The overall reaction is shown in Scheme 4-2 below. By monitoring consumption of 1-phenylpropyne, we were able to model reaction progress while ignoring things like regioisomer mixtures.





Scheme 4-2. Reaction scheme for the hydroamination kinetics experiments.

We started the process with a training set of ligands for the catalysis. The training set allows for development of a model based on a series of ligands, which can then be confirmed for accuracy later using another set of different ligands. The advantage of the training set is that we are able to confirm the accuracy of the model rather than influencing the regression by including all data points. For the training set we began with pyrrole- and indole-based bidentate ligands, including the dpm ligand. The initial complexes are shown in Table 4-1 below.



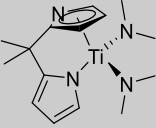
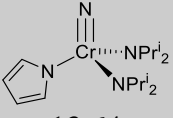
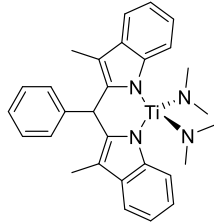
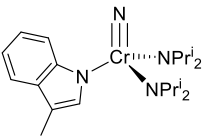
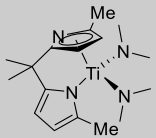
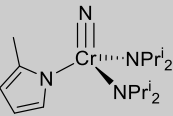
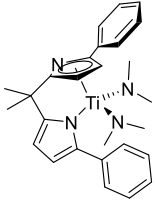
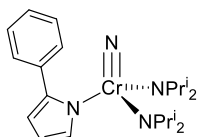
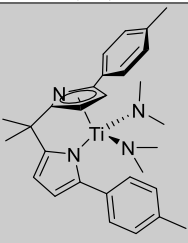
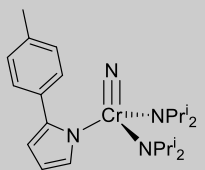
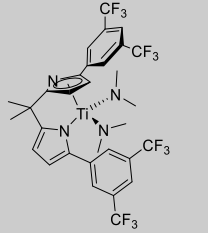
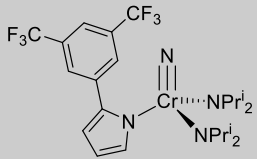
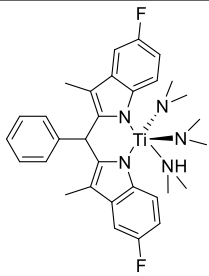
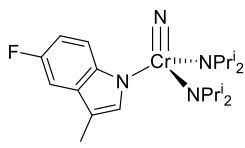
Ti Catalyst	Cr Complex for LDP (kcal/mol)	%V <sub>bur</sub> from Cr	k <sub>obs</sub> x 10 <sup>4</sup> (s <sup>-1</sup> )
 <b>Ti(NMe<sub>2</sub>)<sub>2</sub>(dpm) (1a)</b>	 13.64	20.4	4.16
 <b>Ti(NMe<sub>2</sub>)<sub>2</sub>(dim<sup>3</sup>Me) (2a)</b>	 12.49	22.6	0.662
 <b>Ti(NMe<sub>2</sub>)<sub>2</sub>(dpm<sup>2</sup>Me) (1b)</b>	 13.46	23.7	1.35
 <b>Ti(NMe<sub>2</sub>)<sub>2</sub>(dpm<sup>2</sup>phenyl) (1c)</b>	 14.03	27.1	0.522
 <b>Ti(NMe<sub>2</sub>)<sub>2</sub>(dpm<sup>2</sup>tolyl) (1d)</b>	 13.91	26.7	0.552

Table 4-1. Summary of the titanium catalysts use for hydroamination, the chromium complexes used to parameterize the ligands, and the rates of catalysis.



Table 4-1 (cont'd)

Ti Catalyst	Cr Complex for LDP (kcal/mol)	%V <sub>bur</sub> from Cr	k <sub>obs</sub> x 10 <sup>4</sup> (s <sup>-1</sup> )
 <b>Ti(NMe<sub>2</sub>)<sub>2</sub>(dpm)<sup>2-</sup></b> <b>[C<sub>6</sub>H<sub>3</sub>(CF<sub>3</sub>)<sub>2</sub>] (1e)</b>	 14.32	27.9	0.581
 <b>Ti(NMe<sub>2</sub>)<sub>2</sub>(dim<sup>3Me5F</sup>) (2b)</b>	 12.66	22.6	1.08

It is worth restating that both the sterics and electronics were measured using the monodentate ligand ignoring the linker. As such the bidentate ligands that were synthesized using different carbonyl groups (*via* condensation with acetone or benzaldehyde) are all treated identically.<sup>23</sup> The complexes were modeled using the simplest equation that accounts for both sterics and electronics.

$$k = a(LDP) + b(\%V_{bur}) + c \quad (1)$$

In Equation 1 above,  $k$  is the pseudo first order rate constant of the catalysis,  $a$  and  $b$  are fitting constants that scale the contributions of LDP and %V<sub>bur</sub>, respectively, and  $c$  is simply an intercept in the linear fit. Two different forms of the data can be modeled, and both will be discussed. The first way is to use natural variables, or the actual measured %V<sub>bur</sub> and LDP. These natural variables are the easiest way to generate a model that can predict ideal sterics and electronics of future



catalysts. The other method is to use scaled variables. While the modeling is complicated by scaling the variables, the resulting equation is more informative. The scaling was done using Equation 2 below, where  $x_i$  = scaled variable,  $u_i$  = natural variable,  $u_i^0$  = midpoint of the range of the natural variables, and  $\Delta u_i$  = the difference between the midpoint and the high value (half the full range).

$$x_i = \frac{u_i - u_i^0}{\Delta u_i} \quad (2)$$

The equations for the calculation of  $u_i^0$  and  $\Delta u_i$  are shown below.

$$\Delta u_i = u_i^{high} - u_i^0 \quad (3)$$

$$u_i^0 = \frac{u_i^{high} - u_i^{low}}{2} \quad (4)$$

Using either the scaled or natural variables, a least squares fit to the data was done by solving Equation 5. In Equation 5,  $y$  = single column matrix of the rate constants,  $b$  = single column matrix of the coefficients  $X$  = the model matrix which consists of the scaled or unscaled variables,  $X^t$  = transform of the model matrix. The equation below provides the least square values without being prone to local minima like iterative methods can be and required nothing more than an Excel spreadsheet to calculate the set of coefficients.

$$(X^t \cdot X)^{-1} \cdot X^t \cdot y = b \quad (5)$$



The equation with the natural variables in the matrices is shown in Equation 6. In order to get the  $c$ -coefficient in the fit, a row of ones was added after the LDP and %V<sub>bur</sub> data.

$$\left[ \begin{pmatrix} 12.49 & 13.64 & 12.66 & 13.91 & 14.03 & 13.46 & 14.32 \\ 22.6 & 20.4 & 22.6 & 26.7 & 27.1 & 23.7 & 27.9 \\ 1 & 1 & 1 & 1 & 1 & 1 & 1 \end{pmatrix} \begin{pmatrix} 12.49 & 22.6 & 1 \\ 13.64 & 20.4 & 1 \\ 12.66 & 22.6 & 1 \\ 13.91 & 26.7 & 1 \\ 14.03 & 27.1 & 1 \\ 13.46 & 23.7 & 1 \\ 14.32 & 27.9 & 1 \end{pmatrix}^{-1} \right] \cdot \begin{pmatrix} 12.49 & 13.64 & 12.66 & 13.91 & 14.03 & 13.46 & 14.32 \\ 22.6 & 20.4 & 22.6 & 26.7 & 27.1 & 23.7 & 27.9 \\ 1 & 1 & 1 & 1 & 1 & 1 & 1 \end{pmatrix} \cdot \begin{pmatrix} 0.66 \\ 4.16 \\ 1.08 \\ 0.55 \\ 0.52 \\ 1.35 \\ 0.58 \end{pmatrix} = \begin{pmatrix} a \\ b \\ c \end{pmatrix} \quad (6)$$

Solution of the Equation 6 gives:  $a = 1.75$ ,  $b = -0.635$ , and  $c = -6.88$ . The scaled variable coefficients were found, using the same method, to be:  $a_s = 1.61$ ,  $b_s = -2.25$ , and  $c_s = 1.34$ . While the natural variables give some insight into how each variable affects the model, they are mostly meaningless due to the relative magnitude of the electronic and steric measurements. Scaling the variables affords more information from  $a_s$ ,  $b_s$ , and  $c_s$ . Both equations are displayed below where Equation 7 is made from the natural variables and Equation 8 is made using the scaled variables.

$$k_{obs} = 1.75(LDP) - 0.635(\%V_{bur}) + 6.88 \quad (7)$$

$$k_{obs} = 1.61(LDP) - 2.25(\%V_{bur}) + 1.34 \quad (8)$$

By scaling the changes made to electronics and sterics to an equivalent range, we can see that the steric term,  $b_s$  is larger in magnitude than the electronic term,  $a_s$ . In other words, the sterics play a slightly more significant role in the rate determining step of the hydroamination. Moreover,  $b_s$  is negative, implying that as the steric term increases (ligands become larger) the rate of catalysis is slowed. The electronic term on the other hand is positive. This means that as we increase the



LDP of the ancillary ligand (the ligand is less electron donating) the rate of catalysis increases. In short, small electron deficient ligands yield faster catalysis. A graph of the model is shown Figure 4-1 below. The graph shows the model predicted rate constant vs. the experimental rate constant. A good linear fit implies good correlation between our combination of sterics and electronics and the observed rate.

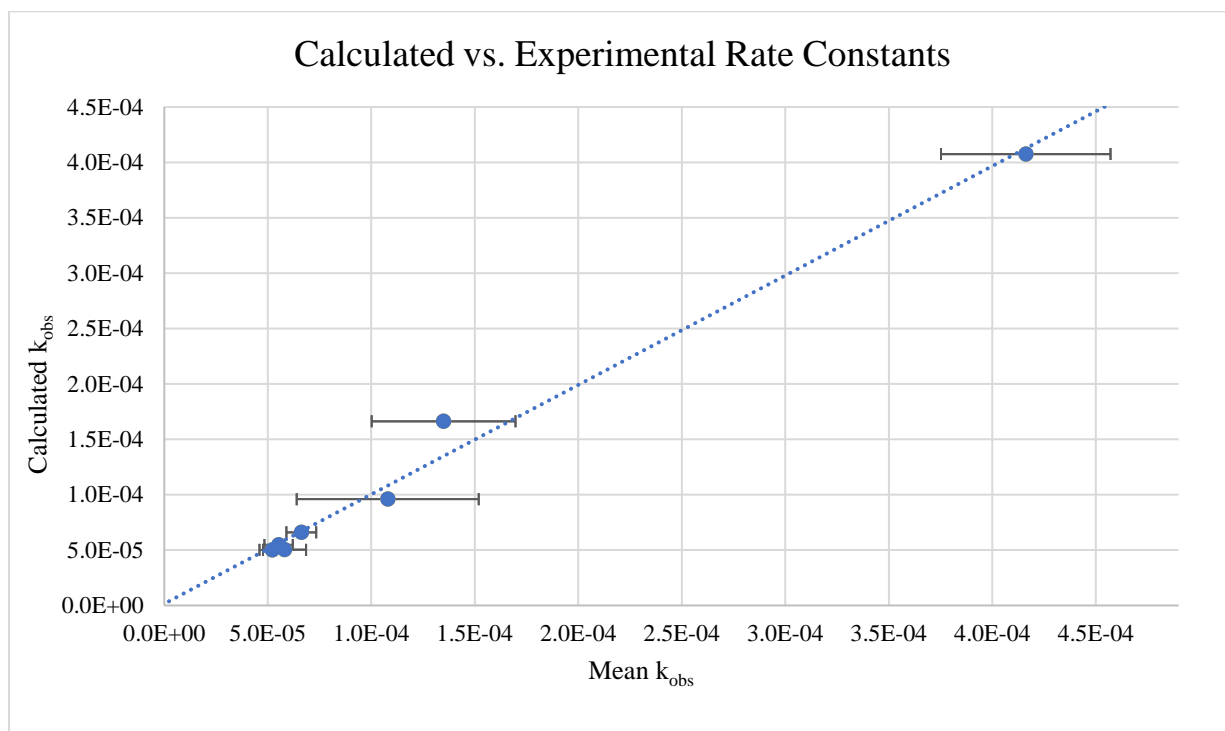


Figure 4-1. Plot displaying the calculate vs. experimental rate constant. The y-axis was calculated by using the experimental LDP and % $V_{bur}$  values in the model described above. The error bars are displayed at the 95% confidence level.

It is incredibly easy to use this model qualitatively, as we already mentioned, the model tells us that smaller electron deficient ligands are better. We can use this model more quantitatively, though. We can take any ligand from the series of ligands we have examined and use the LDP and % $V_{bur}$  to calculate a theoretical rate constant. For example, we know the LDP and % $V_{bur}$  of 2,4-diMe-pyrrole is 12.81 kcal/mol and 22.8%, respectively. Inputting those values into Equation 7



gives a predicted rate of  $1.094 \times 10^{-5} \text{ s}^{-1}$ . In other words, without doing any chemistry, we know that the 2,4-diMe-pyrrole version of dpm should be slower than the unsubstituted dpm.

With the training set developed, we began testing other varieties of ligand sets, specifically we moved to aryloxy based bidentate ligands. We believed that the switch to a different ligand motif was a good test of whether our model would be expandable to other ligand types. Since, if the model was only functional in the range of pyrrole derivatives, it would not be especially useful for catalyst design.

#### **4.5 Testing Ligand Variety**

We set about making a variety of aryloxy derivatives. Unfortunately, the aryloxy-based titanium catalysts are unstable and quite dependent on having steric bulk. As such we were limited in the ligand design. The three catalysts shown in the Table below were synthesized, and the rate determined for the hydroamination reaction. This set of ligands could be considered a validation set for the model.



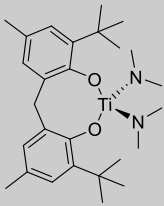
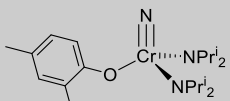
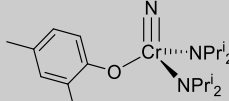
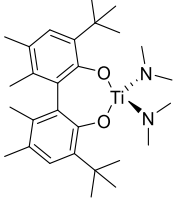
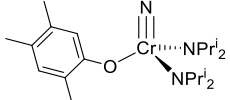
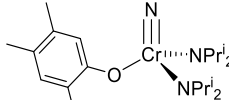
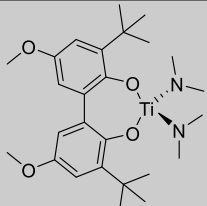
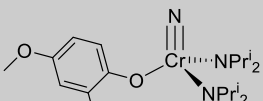
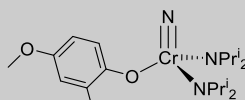
Ti Catalyst	Cr Complex for LDP (kcal/mol)	%V <sub>bur</sub> from Cr	k <sub>obs</sub> x 10 <sup>4</sup> (s <sup>-1</sup> )
 <b>Ti(NMe<sub>2</sub>)<sub>2</sub>(bis-phenoxide<sup>2-tBu-4-Me</sup>) (5)</b>	 11.98	 21.6	0.432
 <b>Ti(NMe<sub>2</sub>)<sub>2</sub>(biphenol<sup>2-tBu-4,5-diMe</sup>) (4a)</b>	 11.87	 21.5	0.244
 <b>Ti(NMe<sub>2</sub>)<sub>2</sub>(biphenol<sup>2-tBu-4-OMe</sup>) (4b)</b>	 11.82	 21.5	0.0546

Table 4-2. Summary of the validation set of bis-aryloxide ligands.

The aryloxide catalysts tested three primary aspects of the model. First, the switch to an oxygen-based ligand using the model derived from pyrrole derivatives. This tests whether there is a dependence on what type of donor is used for the ligand. Second, the ligands form a variety of metallacycle ring sizes. This tests whether metallacycle ring size is an important factor in the catalysis. Third, the aryloxide ligands are all locked into a single conformation, i.e. no haptotropic shifts are possible. This tests our theory about the pyrrole ring in (NMe<sub>2</sub>)<sub>2</sub>Ti(dpm) undergoing a haptotropic shift during the reaction.



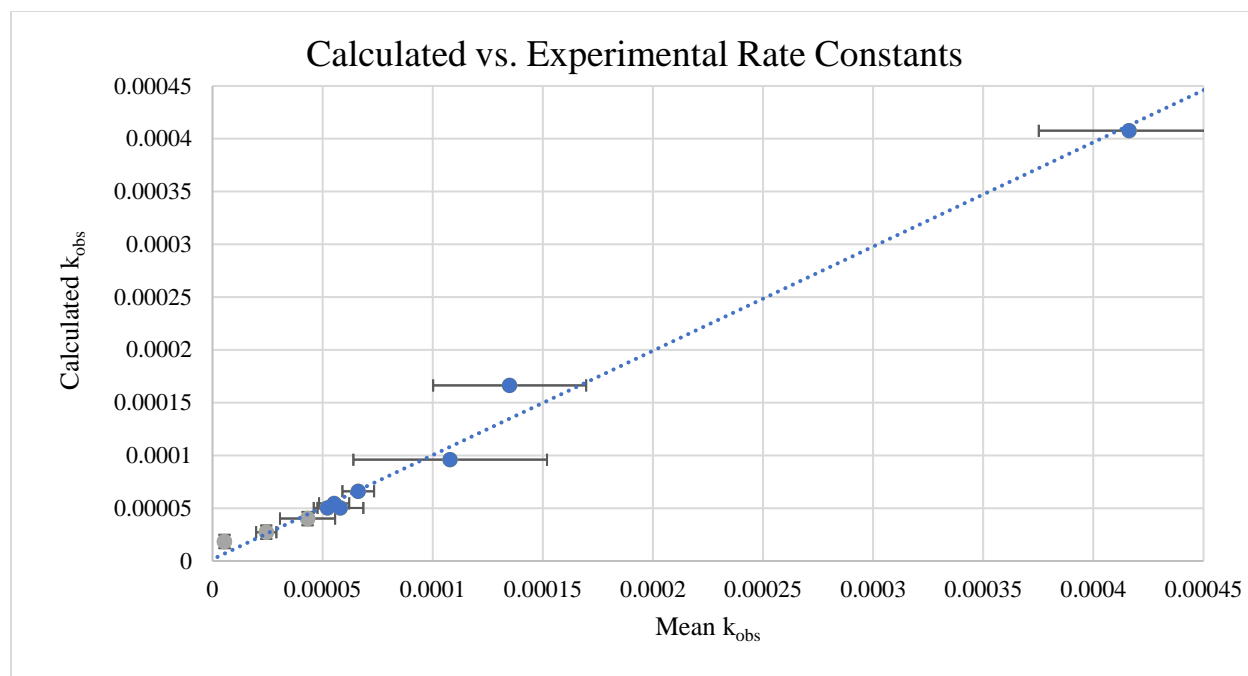


Figure 4-2. Plot displaying the calculated vs. experimental rate constant for the full set of ligands tested. The y-axis was calculated by using the experimental LDP and %Vbur values in the model described above. The error bars are displayed at the 95% confidence level. The grey squares are the aryloxy points and were not included in the regression.

As shown in Figure 4-2, the rate constant of the three aryloxy catalysts (grey points) is small due to both the steric bulk required to prevent side reactions and the strong donor ability of the oxygen-based ligands compared to the pyrroles. Nevertheless, they seem to fit the model very well and, in fact, we were able to draw some conclusions as a result.

With regards to the first point mentioned previously, we have shown in Figure 4-2 that all three aryloxy ligands tested fit the training set model quite well. This supports that the reactivity of the  $(\text{NMe}_2)_2\text{Ti}(\text{X}_2)$  type catalysts for hydroamination are sensitive to the Lewis acidity of the metal center and the sterics of the  $\text{X}_2$  regardless of what the  $\text{X}_2$  is. There seems to be no dependence on the identity of the donor atom. Next, we wondered if changing the metallacycle ring size would have an effect that was unaccounted for in the model. In other words, we wondered if measuring the sterics from the Cr complex was a poor representation of the steric profile of the ligands in



varying ring sizes. In the full set of ligands tested, we interrogated 6-, 7-, and 8-membered rings and, regardless of the ring size, the ligands fit the model.

The final of the three points that the aryloxide derivatives address is the hapticity change. As we have seen (NMe<sub>2</sub>)<sub>2</sub>Ti(dpm) has one pyrrole in an  $\eta^5$  configuration, bound through the aromatic ring.<sup>14</sup> If the ring stayed in that conformation, the %V<sub>bur</sub> would be very different from the  $\eta^1$  conformation and the LDP would likely be very different as well. The aryloxides, and the indoles as well, specifically address this point since the only available coordination mode of the aryloxide ligands is  $\eta^1$ . Since all of our catalysts fit one model, it strongly suggests that the complexes which feature an  $\eta^5$  ring in the crystal structure must undergo a haptotropic shift during the catalysis to  $\eta^1$ . If they did not, the LDP system would not accurately represent the electronic and steric parameters and the catalysts would not fit to the model.



## 4.6 Investigating Anomalies

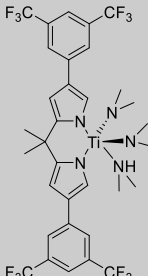
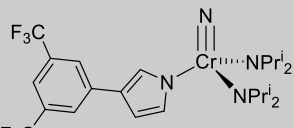
Ti Catalyst	Cr Complex for LDP (kcal/mol)	%V <sub>bur</sub> from Cr	k <sub>obs</sub> x 10 <sup>4</sup> (s <sup>-1</sup> )
 <b>Ti(NMe<sub>2</sub>)<sub>2</sub>(dpms<sup>3</sup>-[C<sub>6</sub>H<sub>3</sub>(CF<sub>3</sub>)<sub>2</sub>])</b> <b>(3)</b>	 14.06	20.3	7.32

Table 4-3. Table showing the fitting parameters and rate constant for catalyst 3.

One of the catalysts tested previously by Swartz was the 3,3'-aryl substituted dpms ligand.<sup>7</sup> By adding electron withdrawing groups to the backside of the ligand, the ligand becomes more electron deficient, but the steric profile is not increased. In Doug's study, this led to much faster turnover for hydroamination.<sup>7</sup> When we studied the catalyst, we noticed that it didn't fit the model very well. In fact, even using 95% confidence level error bars, the catalyst was well off the line (orange point in Figure 4-3).



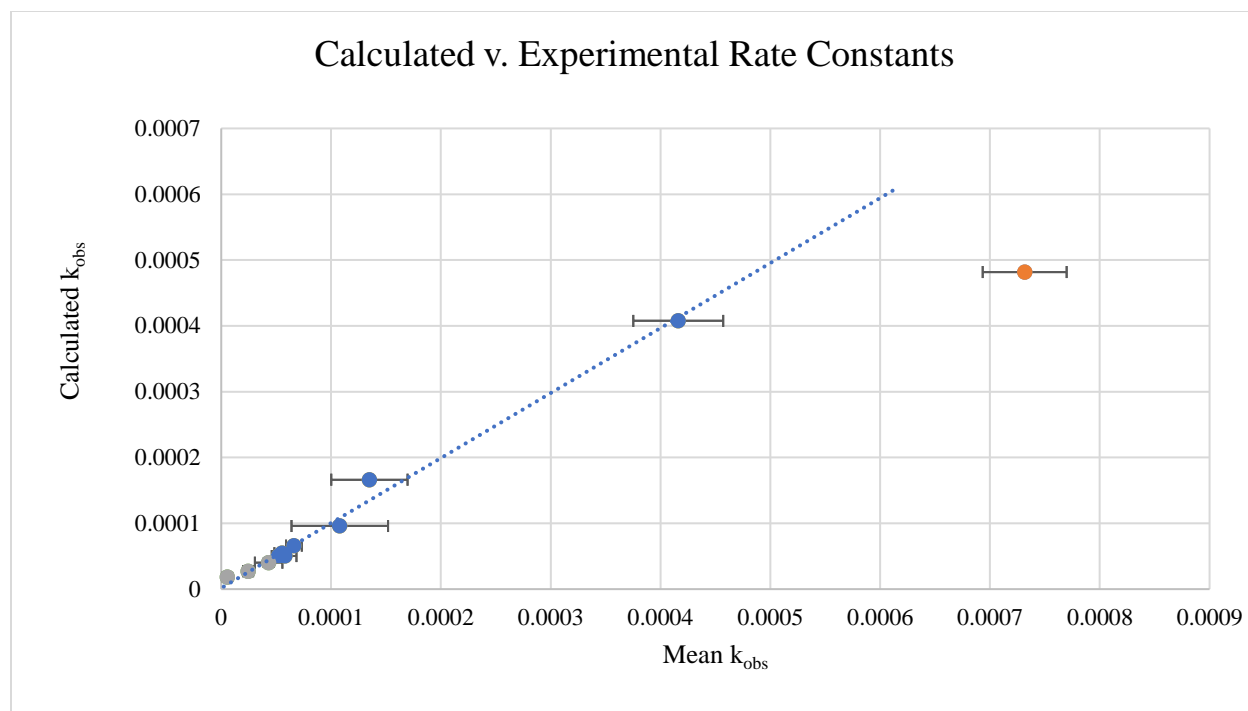


Figure 4-3. Expanded model displaying the poor fit for catalyst **3**.

When we saw how poorly **3** fit, we wondered if the model was better described by a curved fit rather than a linear one. No matter how we tried to fit the data though, the correlation was always poor. We decided to investigate in more detail, what was happening with catalyst **3**. After running a kinetics trial, we checked the solution by GC/MS. The solution had many assorted products. At most, we expect signals from the product isomers, free ligand, and possibly starting materials. But what we found did not match the mass of any of those. The product peak (MW = 209) was the majority of the mixture, but there were additional, much heavier peaks (MW = 325). The heavy peaks match the mass of the product of coupling aniline with two equivalents of 1-phenyl propyne. While the byproduct could never be isolated, and  $^1\text{H}$  NMR was unhelpful due to the massive excess of aniline, this product lines up well with our modeling problem. Since our rates are measured by alkyne consumption, if the catalyst is incorporating extra equivalents of alkyne into the hydroamination product, we would expect to see an artificially faster rate due to alkyne being our



handle for measuring the kinetics. What the model has accomplished is alerting us to a change in the chemistry happening in the reaction. Often, small amounts of by-products in reactions might go overlooked, but by using the model, we knew something was wrong, investigated the reaction, and discovered some potentially exciting chemistry.

From just this short series of tests we were able to learn an immense amount of information about an already well-studied catalytic system. We wanted to go further, though, and use the model to design a catalyst that would display a faster turnover for hydroamination. We also wanted to stick to a relatively simple ligand framework, even the 3-substituted pyrrole in complex 3 was several steps to make and can be a chore to isolate.<sup>7, 23</sup> That said, we consulted our table of LDP values and scanned the less electron-donating ligands. One type of ligand that stood out immediately was thiols. The congeners of the aryloxide-based ligands are poorer donors due to orbital overlap.<sup>29</sup> They also have the advantage of having a longer bond length due to the larger ionic radius, which makes the effective steric profile significantly smaller.

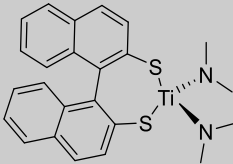
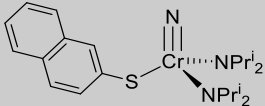
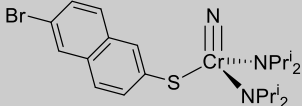
Ti Catalyst	Cr Complex for LDP (kcal/mol)	%V <sub>bur</sub> from Cr	k <sub>obs</sub> x 10 <sup>4</sup> (s <sup>-1</sup> )
 <b>Ti(NMe<sub>2</sub>)<sub>2</sub>(dithioBINAP)</b> <b>(6)</b>	 13.99	 22.3 <sup>a</sup>	0.0794

Table 4-4. Table summarizing the rate constant and fitting parameters for catalyst **6**.

Catalyst **6** was synthesized and tested for hydroamination. Surprisingly, this catalyst also did not fit the model, in fact, it was far slower than predicted. The predicted rate of hydroamination was  $3.48 \times 10^{-4}$  and the experimental rate was far slower at  $0.0794 \times 10^{-4} \text{ s}^{-1}$ .



When we investigated the catalyst more, we discovered the problem. By routine spectroscopy, the catalyst appeared clean, but, when Dr. McDaniel analyzed the solution behavior using diffusion ordered spectroscopy (DOSY) NMR, we discovered the catalyst is a dimer in solution. Crystallization of the complex confirmed this finding. Even heating the complex with an excess of aniline in solution did not make a difference, the compound still behaved as a dimer. The long S-Ti bonds and available lone pair of the sulfur atom mean bridging two metal centers is very favorable, so using thiols that are not extremely sterically protected is unlikely to be successful.

This example highlights another benefit of using a model such as the one we developed. Had LDP and the model not existed, we might have assumed that all thiols were poor catalysts for the reaction due to a strong donor ability. We would have never had cause to investigate the molecular structure of the catalyst to learn *why* it was such a poor catalyst. Instead, we know that with proper ligand development of, say, an unsymmetrical ligand bearing one thiol and one other donor, the catalyst may potentially be improved.

We tried several other ligand ideas as well. Monodentate ligands, halogenated pyrroles, and indoles, and smaller aryloxides all failed for one reason or another. As the ligands become more electron deficient and smaller, stability of the precatalyst suffers as well, making isolation of a new, improved catalyst quite challenging.

#### **4.7 Other Applications of the Model**

Since designing a new catalyst that was an improvement over  $(\text{NMe}_2)_2\text{Ti}(\text{dpm})$  was unsuccessful, we wondered if we might be able to use to the model for another purpose. It is known that  $\text{Ti}(\text{NMe}_2)_4$  is a precatalyst for hydroamination.<sup>30</sup> What is unknown, is the identity of the active species. When  $\text{Ti}(\text{NMe}_2)_4$  is added to a solution of alkyne and amine, what reactions happen to



form an active catalyst? Are all the dimethylamines replaced by anilides? Is imido formation the first step? What ancillary ligands are on the metal center?

To answer this question, we needed to compile a set of possibilities. Our three most likely conjectures at the structure of the catalyst in the slow step were:  $\text{-Ti(NMe}_2)_2$ ,  $\text{-Ti(NPh)}$ , or  $\text{-Ti(NHPh)}_2$  (Figure 4-4). Both LDP and  $\%V_{\text{bur}}$  had previously been investigated for  $\text{NMe}_2$  and  $\text{NHPh}$  using the LDP system, so those were easy to compare. By inputting the values into our model, we had predicted rates for each of the two possibilities. The imido was a little bit more difficult.

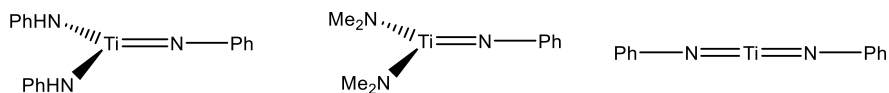


Figure 4-4. Representations of the proposed possible catalyst structures the hydroamination reaction using  $\text{Ti(NMe}_2)_4$  as a catalyst.

We had previously synthesized the  $[\text{NCr(N}^i\text{Pr}_2)_2(\text{NPh})]^- \text{K}^+$  complex. Unfortunately, the donor ability of the imido ligand made rotation so rapid, the rate of rotation could not be monitored using solution state NMR. We turned to theory to get a prediction of the LDP value.

For the calculations, all chromium molecules were truncated to  $\text{NCr(NH}_2)_2\text{X}$  for ease of optimization. The optimizations of structures were done using DFT and were performed using the M06L functional with the TZVP basis set. Optimizations of transition states were done using the Berny algorithm monitoring vibrational frequencies to confirm minima. There was a single negative vibration in the transition state corresponding to  $\text{Cr-N}$  rotation.

The ligand donation parameter calculations were attempted by optimizing the ground state geometry and the transition state in which one amido ligand is rotated  $\sim 90^\circ$ , which caused amido pyramidalization. The electronic energy difference between the ground state and transition state



was calculated and plotted against the experimental LDP values. We selected a variety of ligands including halogens, heterocycles, and phenoxide to include differences in size, a wide variety of electronics, and structures that are simple enough to optimize by computation. These points were used to generate a line relating the computational barrier and the experimental values. The computational barrier for the imido ligand was then fit to this line, and the LDP for the ligand approximated. The fits for the lines generated were compared across multiple levels of theory, revealing that the computational values generated using the B3PW91/cc-pvtz and M06L/TZVP were the best fits. See Figure 4-5 for the B3PW91/cc-pvtz plot (the imido is the orange point).

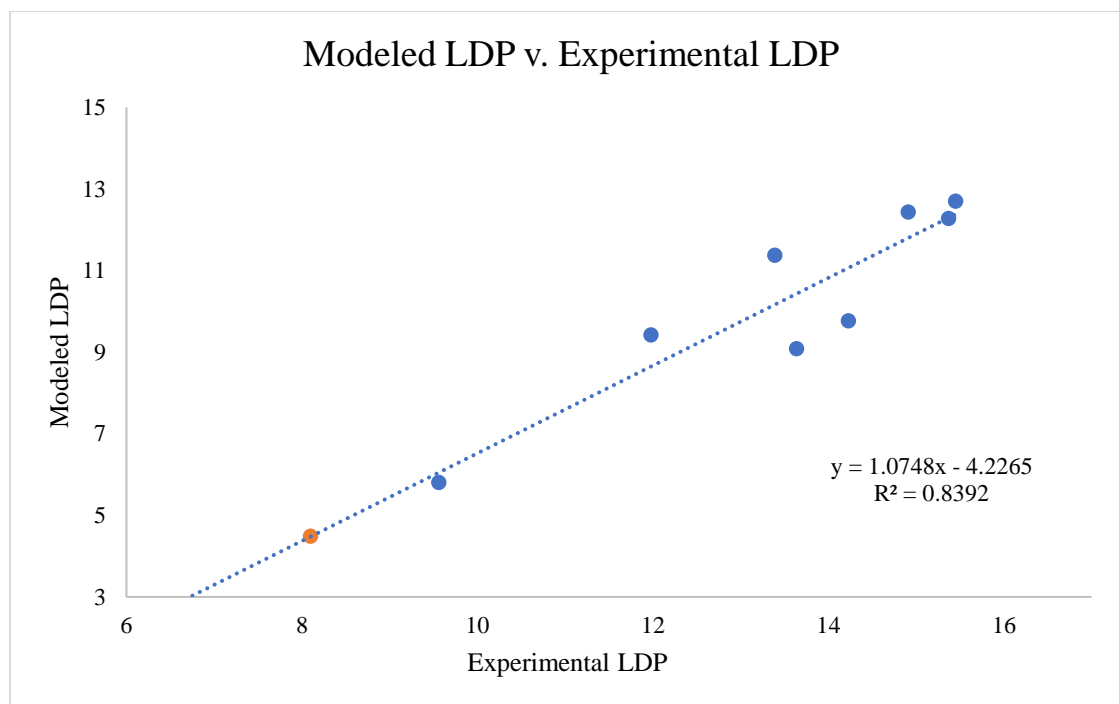


Figure 4-5. Series of ligands with the computationally modelled LDP fit against the experimental LDP. The orange point is the predicted imido value fit to the best fit line of the model.

The fits generated just comparing the calculated barrier to experimental LDP are passable, but the correlation of the model could be improved. If theory accurately calculated the LDP, the slope of the line would be exactly one, and the intercept would be zero. So, as an additional measure, fits were generated using the  $\text{NCr}(\text{NH}_2)_2\text{X}$  model that included the  $\%V_{\text{bur}}$  of the ligand to account



for the switch to a much smaller ancillary ligand. We have established that in some cases, large X ligands can affect the pure electronic measure of the LDP system. As such, since we truncated the Cr molecule for the calculations, we thought including a steric term might help our calculated approximations better match the experimental values. By fitting the computed barrier with a linear regression using the LDP and  $\%V_{\text{bur}}$ , a fit was generated that more accurately related the computationally generated energy barriers to the experimentally derived LDP values. The fit including sterics using M06L/TZVP is displayed below in Figure 4-6. Compared to the fit using the computed barrier and the experimental LDPs, the values from this fit correlate more accurately; the slope of the line is nearly one, and the intercept nearly zero.

Again, the orange point in the figure represents the imido fit to the model. The values for both methods were similar, 8.1 kcal/mol for the first fit and 7.9 kcal/mol for the model including sterics, and the value that included sterics was used due to the higher quality of the fit.



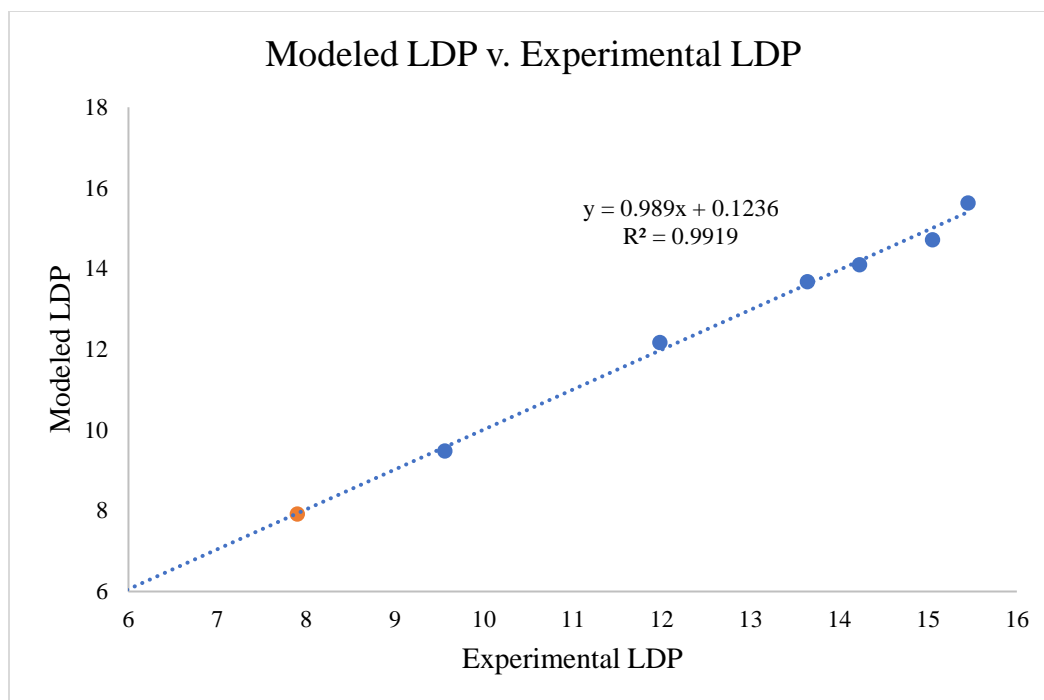


Figure 4-6. Fit of the computed and experimental LDP values including a steric term to account for the truncated chromium molecule in the calculations. The orange point is the imido theoretical value fit to the best fit line.

When we compared the model calculated rate constant values for  $\text{-Ti(NMe}_2)_2$ ,  $\text{-Ti(NPh)}$ , or  $\text{-Ti(NHPh)}_2$  as catalysts, the results were surprising. Neither  $\text{-Ti(NMe}_2)_2$  nor  $\text{-Ti(NHPh)}_2$  were even close to matching the value we determined by kinetics. Both ligands are much stronger donors than all the ligands we used in the training set and validation set, so the predicted rates were slow. The imido, on the other hand, is also a strong donor, but the steric profile of this one dianionic ligand is small when compared to two monoanionic ligands, meaning that the predicted rate is actually quite fast. Figure 4-7 below is a graphical representation of the results.



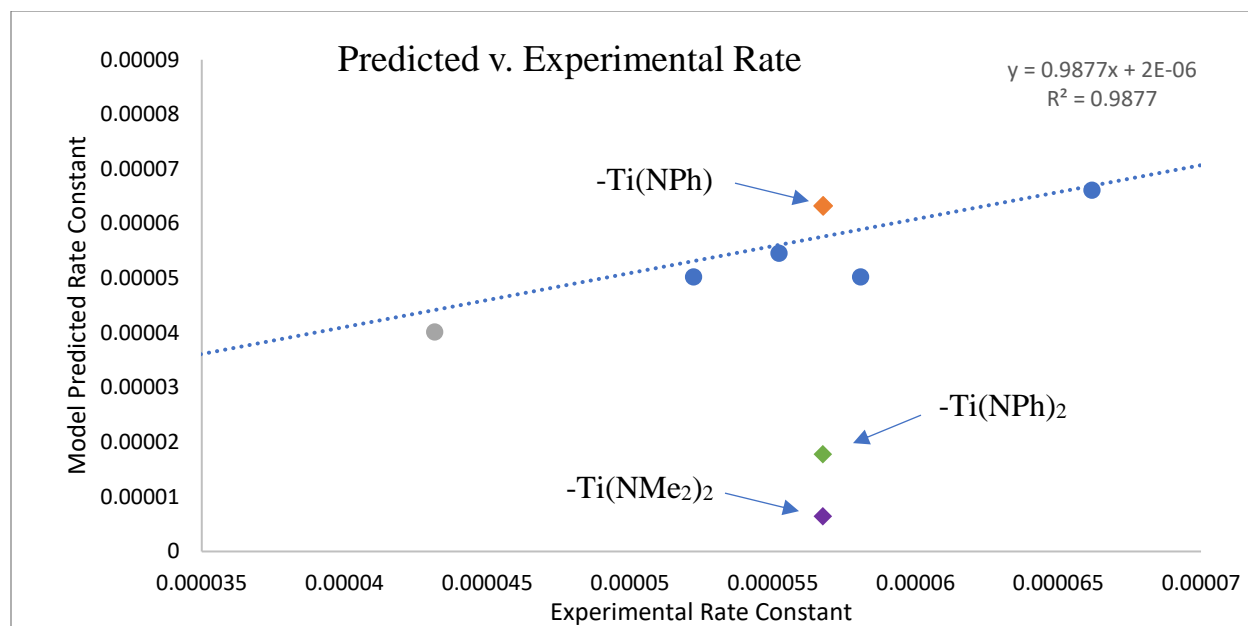


Figure 4-7. Plot of the predicted imido value to our model. The orange diamond is -Ti(NPh), the green diamond is -Ti(NHPh)<sub>2</sub>, and the purple diamond is -Ti(NMe<sub>2</sub>)<sub>2</sub>.

Clearly the imido is the best prediction for the active species in the Ti(NMe<sub>2</sub>)<sub>4</sub>-catalyzed hydroamination. While we are aware this does not definitively prove the mechanism by which the catalysis happens, this is compelling evidence in support of the active species that we would not have without the model.

## 4.8 Conclusions

It is unfortunate we were not able to use the full potential of the model to design an improved hydroamination catalyst immediately. Instead, we have learned that pyrrole is a special ligand. It can stabilize a Lewis acidic metal center through hapticity changes to provide a stable, easy to handle precatalyst that converts to a highly active catalyst. In hindsight, we were never likely to improve much on dpm as a ligand. The ease of synthesis and low cost associated with the ligand make it the ideal partner to a cheap, earth abundant catalyst. Even if a faster catalyst is found, matching the rate of catalysis *and* the simplicity of (NMe<sub>2</sub>)<sub>2</sub>Ti(dpm) will be no small feat.



Even still, the LDP driven model of titanium-catalyzed hydroamination proved to be an incredibly useful tool. The results of our study provided a means to screen potential catalysts while saving the time and energy associated with synthesizing, testing, and modifying a series of molecules. It uncovered a simple method of spotting side reactions that could have easily gone unnoticed. We were able to glean mechanistic information about the haptotropic shift using pyrrolyl-based catalysts. We were even able to shed light on a reaction that was published more than 15 years ago and identify the active species. This study illustrates how LDP can provide an immense amount of information about high valent catalyzed reaction. And as demonstrated, whether the catalyst is brand new or has been used for 15 years, models of this kind can be informative. Hopefully, other high valent metal chemists can employ our methods and use the knowledge gained to transform the way we approach catalyst optimizations.



## 4.9 Experimental

This experimental was taken from our recent publication. This be accessed at:

*Nat. Chem.*, **2017**, 9(9), 837

### Ligand Donation Parameter Considerations

<b>X Ligand<sup>c</sup></b>	<b>Experimental Rate (s<sup>-1</sup>)</b>	<b><math>\Delta G^{\ddagger a}</math> (kcal/mol)</b>	<b>LDP<sup>b</sup> (kcal/mol)</b>	<b>Standard Deviation in LDP (kcal/mol)</b>	<b>Temp (°C)</b>
<b>Pyrr</b>	0.89	16.11	13.64	0.01	1.7
<b>Pyrr<sup>3-</sup></b>	0.42	16.54	14.06	0.04	1.9
<b>Ind<sup>3Me</sup></b>	2.93	14.87	12.49	0.002	-8.4
<b>Ind<sup>3Me5F</sup></b>	2.09	15.05	12.66	0.01	-8.4
<b>Pyrr<sup>Me</sup></b>	1.47	15.95	13.46	0.01	3.5
<b>Pyrr<sup>2-</sup></b>	1.63	16.98	14.32	0.0003	21.8
<b>Pyrr<sup>Ph</sup></b>	0.67	16.54	14.03	0.003	6.2
<b>Pyrr<sup>tol</sup></b>	0.55	16.38	13.91	0.01	1.9
<b>OPh<sup>2,4-diMe</sup></b>	1.05	14.17	11.98	0.01	-29.0
<b>OPh<sup>2-tBu-4-Me</sup></b>	0.86	15.52	13.14	0.01	-8.3
<b>OPh<sup>2,4,5-triMe</sup></b>	2.35	14.11	11.87	0.003	-23.3
<b>OPh<sup>2-tBu-4,5-</sup></b>	1.89	13.89	11.70	0.004	-28.9
<b>OPh<sup>2-Me-4-</sup></b>	3.07	15.55	13.06	0.003	3.7
<b>OPh<sup>2-tBu-</sup></b>	1.95	14.05	11.82	0.01	-26
<b>SNap</b>	1.87	16.60	13.99	.002	17.0
<b>6-Br-SNap<sup>e</sup></b>	1.56	16.77	14.15	0.007	18.0

Table 4-5. Spin saturation transfer data. <sup>a</sup> Determined from the rate constant for isopropyl group exchange using the Eyring Equation with the assumption that the transmission coefficient is unity. <sup>b</sup> Assuming  $\Delta S^{\ddagger} = -9 \text{ cal}\cdot\text{mol}^{-1}\cdot\text{K}^{-1}$ . <sup>c</sup> Pyrr = pyrrolide, Ind = indolide, tol = *p*-tolyl. <sup>d</sup> Determined by line shape analysis. <sup>e</sup> The 6-Br-SNap ligand was only used as a surrogate for 2-naphthylthiolate (SNap) to obtain the %V<sub>bur</sub> value. Consequently, its LDP was not employed in this study; however, we include the LDP for completeness.

### General LDP Procedure

The rate constant for the exchange of the two methyne hydrogens of the isopropyl groups was measured using <sup>1</sup>H NMR spin saturation transfer (SST). The temperature chosen for each experiment was based on that required to reach the slow exchange limit of the complex under



investigation, in these cases between  $-30\text{ }^{\circ}\text{C}$  and  $25\text{ }^{\circ}\text{C}$ .  $T_1$  values were measured using the inversion recovery method. Samples were made between 0.02–0.03 M in  $\text{CDCl}_3$ .  $\Delta S^{\ddagger}$  for this rotation was shown to be  $-9\text{ cal}\cdot\text{mol}^{-1}\cdot\text{K}^{-1}$  for  $\text{NCr}(\text{N}^i\text{Pr}_2)_2\text{I}$  and assumed to be the same for the other compounds.<sup>15</sup>

### General Percent Buried Volume Considerations

In calculating percent buried volume, the ligand structure was taken from the chromium complex crystal structure. The  $\text{NCr}(\text{N}^i\text{Pr}_2)_2$  fragment was deleted, leaving just the X ligand for analysis. This fragment, in conjunction with the bond length from the chromium crystal structure (Cr-X bond length) were used in the SambVca 2.0 program to calculate the  $\%V_{\text{bur}}$ .<sup>25</sup> This method was used for several reasons. First, the chromium molecules are easily crystallizable and provided an experimental basis for the measurement (as opposed to modeling computationally). Second, the chromium molecule is already the model for the electronic term, it was logical to use the same molecule to determine the steric factor. Finally, using just the ligand fragment eliminates as much bias for bonding angles, twisting, and torsions from sterics and crystal packing as possible. In other words, it is a better measure of the ligands sterics towards a more general set of high valent metals. The sphere radius was left at the default 3.5 Å. Other radii were tested, but the default gave the best correlation. Mesh spacing was left at the default value of 0.10, the atomic radii were used as the default Bondi radii scale by 1.17, and for all ligands the H atoms were included in the calculations.

### DOSY Analysis

The DOSY NMR experiments were recorded with a Varian Inova 600 spectrometer equipped with a 5 mm PFG switchable broadband probe operating at 599.89 MHz ( $^1\text{H}$ ). The Varian



Dbppste\_cc (DOSY bipolar pulse pair simulated spin echo convection corrected) pulse sequence was utilized for all experiments. Following literature methods,<sup>31-33</sup> the molecular weight of Ti(dithioBINAP)(NMe<sub>2</sub>)<sub>2</sub> (**6**) was analyzed using DOSY techniques. The internal molecular weight standards chosen for this experiment included ferrocene (FeCp<sub>2</sub>), tetrakis(trimethylsilyl)silane (Si(TMS)<sub>4</sub>), and toluene. The experiment that was performed at room temperature was carried out in a threaded J. Young tube that was sealed with a Teflon stopper. The experiments that were performed at 50 °C were carried out utilizing a capillary tube (2 mm) to reduce and convection errors in the experiments and improve accuracy. An example of the DOSY spectrum obtained by this method is shown below in Figure 4-8.

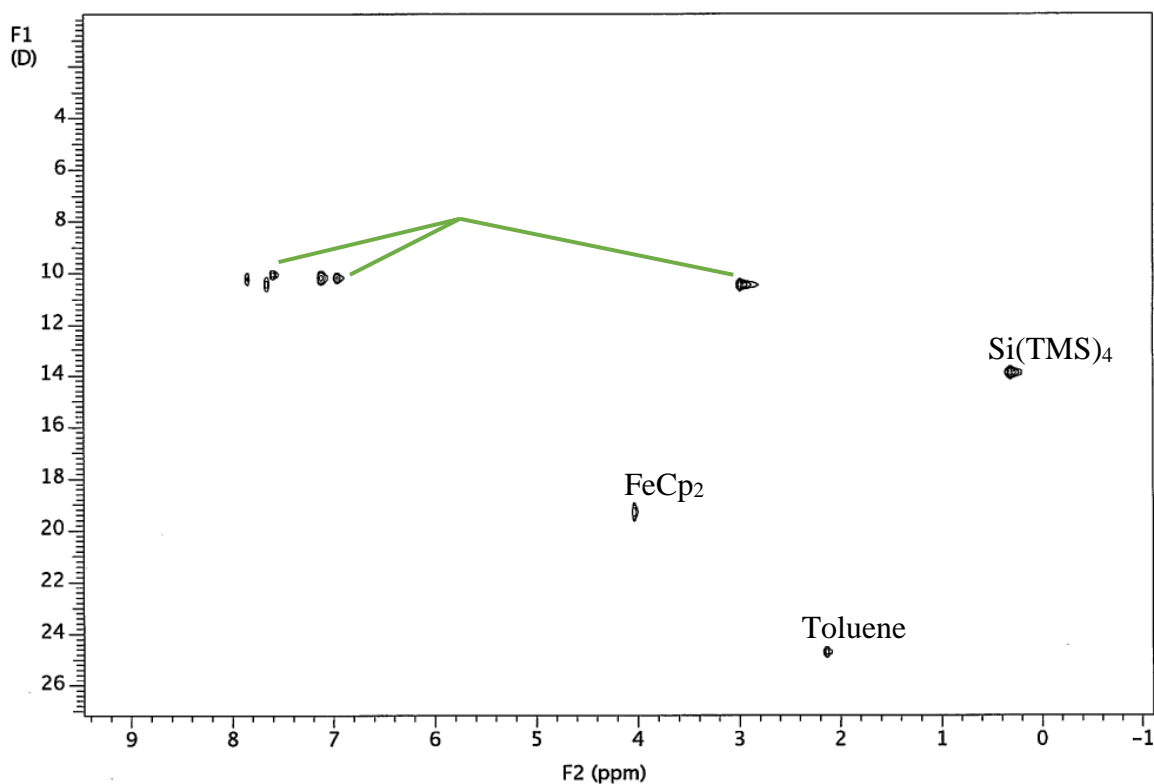


Figure 4-8. DOSY spectrum of Ti(dithioBINAP)(NMe<sub>2</sub>)<sub>2</sub> (**6**) at 25 °C.



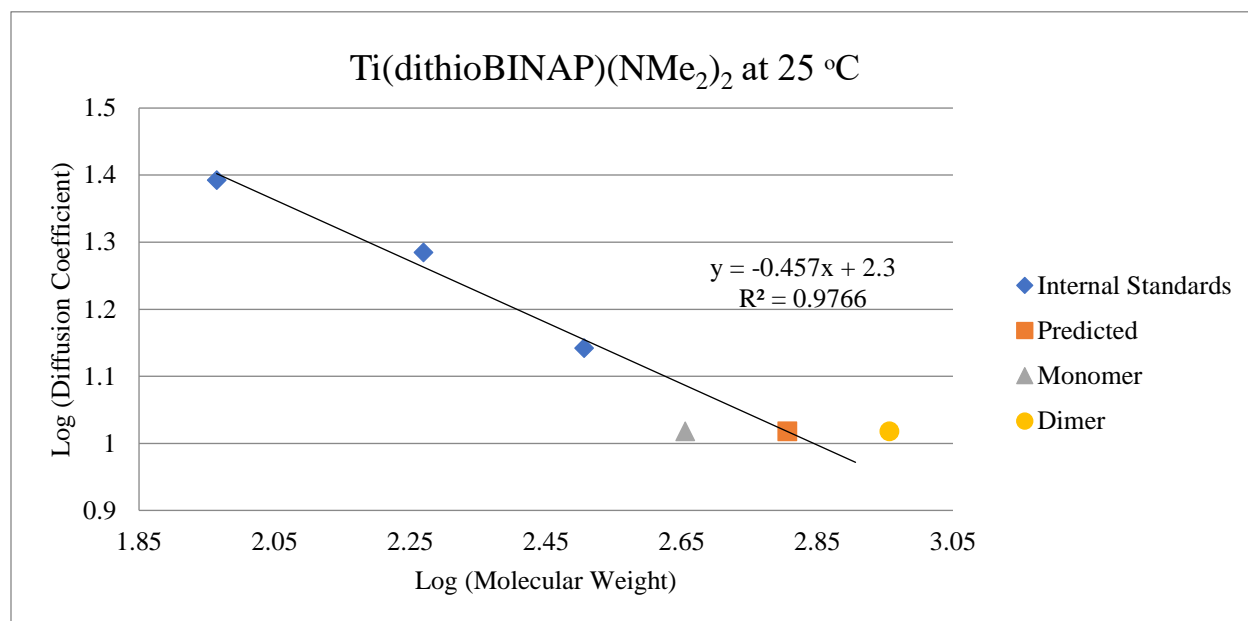
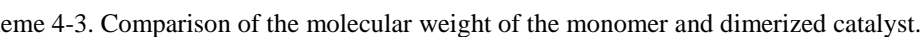


Figure 4-9. Molecular weight calibration of Ti(dithioBINAP)(NMe<sub>2</sub>)<sub>2</sub> (6) at 25 °C.

The log of diffusion coefficient vs log molecular weight plots for the internal standards FeCp<sub>2</sub>, toluene, and Si(TMS)<sub>4</sub> (show as the blue diamonds) and Ti(dithioBINAP)(NMe<sub>2</sub>)<sub>2</sub> (shown as the orange square) in toluene-d<sub>8</sub>. The calibrated molecular weight of Ti(dithioBINAP)(NMe<sub>2</sub>)<sub>2</sub> at room temperature is  $639.06 \pm 51.52$  g/mol. The expected molecular weights for the monomer (shown as the grey triangle) is 452.46 g/mol and the dimer (shown as the yellow circle) is 904.91 g/mol.

Unfortunately, the results of this experiment were inconclusive as to which species is predominant in solution. However, in the solid state, Ti(dithioBINAP)(NMe<sub>2</sub>)<sub>2</sub> was found to be dimeric. Based on these observations, Ti(dithioBINAP)(NMe<sub>2</sub>)<sub>2</sub> could possibly be in equilibrium between the monomeric and dimeric complexes, as shown in the scheme below:





179



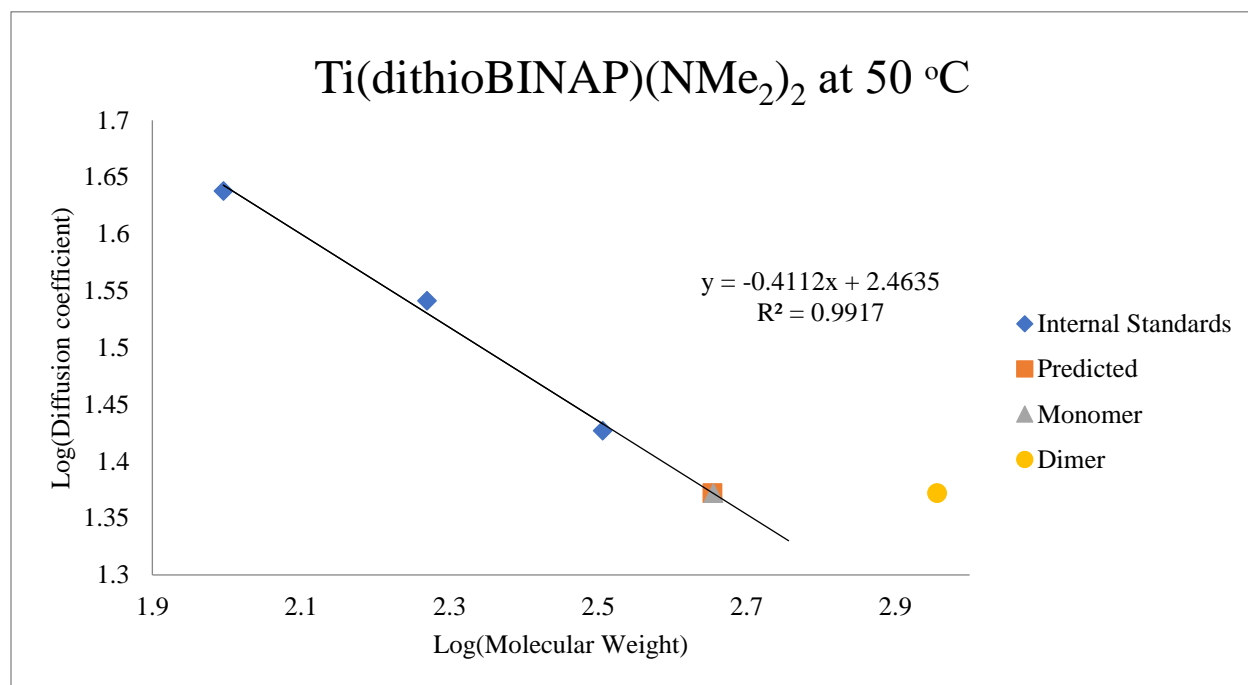


Figure 4-10. Molecular weight calibration of Ti(dithioBINAP)(NMe<sub>2</sub>)<sub>2</sub> (6) at 50 °C.

The log of diffusion coefficient vs log molecular weight plots for the internal standards FeCp<sub>2</sub>, toluene, and Si(TMS)<sub>4</sub> (show as the blue diamonds) and Ti(dithioBINAP)(NMe<sub>2</sub>)<sub>2</sub> (shown as the orange square) in toluene-d<sub>8</sub>. The predicted molecular weight of Ti(dithioBINAP)(NMe<sub>2</sub>)<sub>2</sub> at 50 °C is  $450.82 \pm 22.76$  g/mol. The expected molecular weights for the monomer (shown as the grey triangle) is 452.46 g/mol and the dimer (shown as the yellow circle) is 904.91 g/mol.

The results of this experiment suggest that, when Ti(dithioBINAP)(NMe<sub>2</sub>)<sub>2</sub> is heated to 50 °C, the predominant species in solution is monomeric. In order to get a better understanding of what was occurring during the kinetic experiments another DOSY experiment was conducted to better mimic the kinetic conditions.



Due to error caused by thermal convection, this experiment could not be measured at the same temperature as the kinetic conditions. Instead, the DOSY experiment was conducted at 50 °C, like the previous experiment. Also, in the kinetic experiments 10 equivalents of aniline is used, however, using this much aniline, the  $^1\text{H}$  NMR signals for the titanium complex and the standards are too obscured to measure an accurate diffusion coefficient. Lessening the amount of excess aniline (to 4 equivalents), the  $^1\text{H}$  NMR signals are not obscured while still providing an environment similar to the kinetic conditions. The data collected from this DOSY experiment is shown in Figure 4-11.

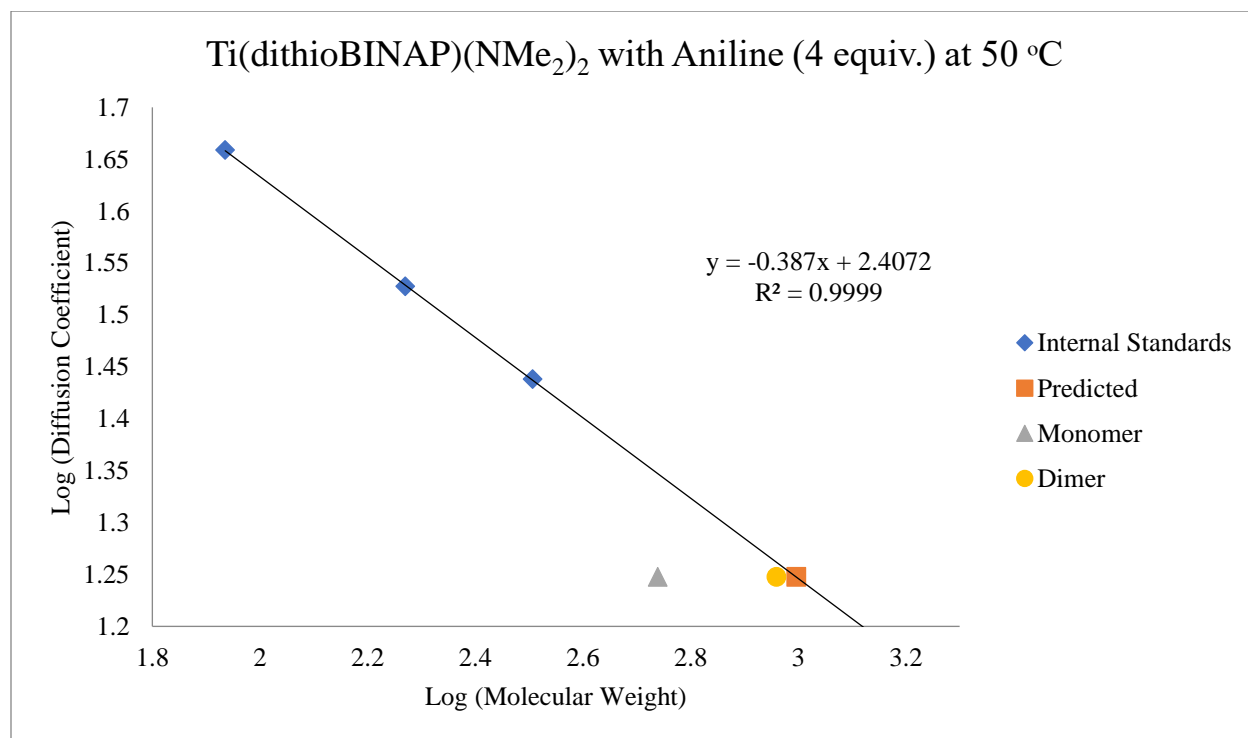


Figure 4-11. Molecular weight calibration of Ti(dithioBINAP)(NMe<sub>2</sub>)<sub>2</sub> (6) with addition of aniline (4 equiv.) at 50 °C.

The log of diffusion coefficient vs log molecular weight plots for the internal standards FeCp<sub>2</sub>, *n*-hexane, and Si(TMS)<sub>4</sub> (show as the blue diamonds) and Ti(dithioBINAP)(NMe<sub>2</sub>)<sub>2</sub> (shown as the orange square) in toluene-d<sub>8</sub>. The predicted molecular weight of Ti(dithioBINAP)(NMe<sub>2</sub>)<sub>2</sub> at 50



$^{\circ}\text{C}$  is  $992.41 \pm 48.35$  g/mol. The expected molecular weight of the monomer  $\text{Ti}(\text{dithioBINAP})(\text{NHPh})_2$  is 548.54 g/mol (shown as the grey triangle). The expected molecular weight of the dimer  $[\text{Ti}(\text{dithioBINAP})(=\text{NPh})]_2$  is 910.83 g/mol (shown as the yellow circle).

The results of this experiment suggest that even at an elevated temperature ( $50^{\circ}\text{C}$ ) in the presence of excess aniline the titanium species in solution is dimeric. If the titanium species is dimeric under the kinetic conditions then that species could be experiencing increased sterics around the metal center, as well as different electronic effects. These added effects would drastically change the catalysis and are not accounted for in our model, which is likely why it does not correlate. While some dimerization occurs with the titanium imide active species with all the catalysts, the dimerization of the thiolate species in the presence of a large excess of amine is far more profound, which leads to the large inhibition.

## Synthetic Procedures

### General Considerations

All reactions and manipulations were carried out in an MBraun glovebox under a nitrogen atmosphere and/or using standard Schlenk techniques. Diethyl ether, pentane, acetonitrile, tetrahydrofuran, benzene, *n*-hexane, and toluene were purchased from Aldrich Chemical Company. Diethyl ether, pentane, acetonitrile, and toluene were purified by passing through alumina columns to remove water after being sparged with dry nitrogen to remove oxygen. Tetrahydrofuran, benzene, and hexane were sparged with dinitrogen to remove oxygen and distilled from sodium and benzophenone.  $\text{N}(\text{Cr}(\text{N}^i\text{Pr}_2)_3)$ ,  $\text{N}(\text{Cr}(\text{N}^i\text{Pr}_2)_2(\text{OPh}))$ ,  $\text{N}(\text{Cr}(\text{N}^i\text{Pr}_2)_2\text{I})$ ,  $\text{N}(\text{Cr}(\text{N}^i\text{Pr}_2)_2(\text{Pyr}))$ , and  $\text{N}(\text{Cr}(\text{N}^i\text{Pr}_2)_2(\text{Pyr}-3-[\text{C}_6\text{H}_3(\text{CF}_3)_2]))$  were prepared using the previously reported procedures.<sup>15, 29</sup> Procedures for generation of thallium-pyrrole salts were modified from the



literature.<sup>15</sup> 2,4-dimethyl phenol, 2-*tert*-butyl-4-methyl phenol, 2,2'-methylenebis(6-*tert*-butyl-4-methylphenol), 2-methyl-4-methoxyphenol and pyrrole-2-carboxyaldehyde were purchased from Aldrich Chemical Company and used as received. 3-methylindole and 2,4,5-trimethylphenol were purchased from Alfa Aesar and used as received. 3,3'-di-*tert*-butyl-5,5'-dimethoxy-[1,1'-biphenyl]-2,2'-diol was purchased from Strem Chemicals Inc. and used as received. 3-*tert*-butyl-4-hydroxyanisole was purchased from TCI America and was used as received. 2-phenylpyrrole, 2-tolylpyrrole, 2-(3,5-trifluoromethylphenyl)pyrrole,  $\text{H}_2\text{dpm}^{2-[\text{C}_6\text{H}_3(\text{CF}_3)_2]}$ ,  $\text{Ti}(\text{NMe}_2)_2(\text{dpm}^{2-[\text{C}_6\text{H}_3(\text{CF}_3)_2]})$ ,  $\text{H}_2\text{dpm}^{3-[\text{C}_6\text{H}_3(\text{CF}_3)_2]}$ ,  $\text{Ti}(\text{NMe}_2)_2(\text{dpm}^{3-[\text{C}_6\text{H}_3(\text{CF}_3)_2]})$ ,  $\text{H}_2\text{dpm}$ ,  $\text{Ti}(\text{NMe}_2)_2(\text{dpm})$ , 2-methylpyrrole,  $\text{H}_2\text{dpm}^{2\text{Me}}$ , 3-methyl-5-fluoroindole and di(3-methylindol-2-yl)phenylmethane, 2-*tert*-butyl-4,5-dimethyl phenol, 1,1'-binaphthalene-2,2'-dithiol, 3,3'-di-*tert*-butyl-5,5'-dimethoxy-[1,1'-biphenyl]-2,2'-diol and 6-bromo-2-naphthalenthioi were prepared following their literature procedures.<sup>(2, 7, 9, 35-43)</sup> Generation of lithium salts was performed by slow addition of 2.5 M *n*-butyl lithium in hexanes to a nearly frozen solution of the ligand in ether. The lithium salts were then isolated as solids and used without further purification. To remove all water and oxygen, all ligands were dissolved in benzene, sparged with nitrogen, and refluxed in a Dean-Stark trap overnight. The benzene was then removed *in vacuo*, and the solids were taken into the nitrogen glove box.  $\text{Ti}(\text{NMe}_2)_4$  was purchased from Gelest and used as received. In many cases, due to the sensitivity of the reported complexes to air and moisture, elemental analysis could not be accurately performed. In these cases, bulk purity of the compound was determined by  $^1\text{H}$  NMR.

$\text{CDCl}_3$ ,  $\text{C}_6\text{D}_6$ , and toluene- $\text{d}_8$  were purchased from Cambridge Isotopes Laboratories, Inc. Toluene- $\text{d}_8$  and  $\text{C}_6\text{D}_6$  were sparged with dry dinitrogen and dried over 3 Å molecular sieves.  $\text{CDCl}_3$  was sparged with dinitrogen and distilled from  $\text{P}_2\text{O}_5$  prior to use. All NMR solvents were stored under an inert atmosphere. Spectra were taken on Varian instruments located in the Max T. Rogers



Instrumentation Facility at Michigan State University. These include an Agilent DDR2 500 spectrometer equipped with a 5 mm pulsed-field-gradient (PFG) OneProbe and operating at 499.955 MHz ( $^1\text{H}$ ) and 125.77 MHz ( $^{13}\text{C}$ ), a Varian Inova 600 spectrometer equipped with a 5 mm PFG switchable broadband probe operating at 599.89 MHz ( $^1\text{H}$ ) and 564.30 MHz ( $^{19}\text{F}$ ), a UNITY plus 500 spectrometer equipped with a 5 mm Pulsed-Field-Gradient (PFG) switchable broadband probe and operating at 499.955 MHz ( $^1\text{H}$ ) and 125.77 ( $^{13}\text{C}$ ), as well as a Varian Unity Plus 500 spectrometer with a low gamma broadband probe operating at 36 MHz ( $^{14}\text{N}$ ). NMR chemical shifts are reported in ppm and referenced to the solvent peaks for  $^1\text{H}$  NMR ( $\text{CDCl}_3$ ,  $\delta$  7.26 ppm;  $\text{C}_6\text{D}_6$ ,  $\delta$  7.16 ppm; toluene- $\text{d}_8$ ,  $\delta$  2.08, 6.97, 7.01, 7.09 ppm) and  $^{13}\text{C}$  NMR ( $\text{CDCl}_3$ ,  $\delta$  77.16 ppm;  $\text{C}_6\text{D}_6$ ,  $\delta$  128.06 ppm; toluene- $\text{d}_8$ ,  $\delta$  20.43, 125.13, 127.96, 128.87, 137.48 ppm).  $^{14}\text{N}$  NMR chemical shifts are reported in ppm and referenced to the dinitrogen gas dissolved in solvents ( $\text{CDCl}_3$ ,  $\delta$  310.0 ppm), which in turn has been externally referenced against neat  $\text{CH}_3\text{NO}_2$  as 381.6 ppm; this procedure places  $\text{NH}_3$  as 0 ppm. Single crystal X-ray diffraction data was collected in the Center for Crystallographic Research at MSU.

*Synthesis of  $\text{NCr}(\text{N}^i\text{Pr}_2)_2(\text{Ind}^{3\text{Me}})$ :* To a solution of  $\text{NCr}(\text{N}^i\text{Pr}_2)_2\text{OPh}$  (75 mg, 0.209 mmol) in toluene, freshly prepared  $\text{Li-Ind}^{3\text{Me}}$  (86 mg, 0.626 mmol) was added slowly. The reaction was heated to 40 °C for 18 h whereupon color changes to a dark purple. The volatiles were removed *in vacuo* and the residue extracted with pentane. The extracts were then filtered through Celite and concentrated *in vacuo*. Recrystallization was achieved by cooling the concentrated solution at –30 °C overnight. (25 mg, 0.063 mmol, 30.2%).  $^1\text{H}$  NMR (500 MHz,  $\text{CDCl}_3$ ):  $\delta$  = 8.04 (d,  $J$  = 8.2 Hz, 1H, Ind-H), 7.48 – 7.42 (m, 1H, Ind-H), 7.18 (d,  $J$  = 0.9 Hz, 1H, Ind-H), 7.15 (ddd,  $J$  = 8.2, 7.0, 1.3 Hz, 1H, Ind-H), 7.06 (ddd,  $J$  = 7.8, 7.1, 1.0 Hz, 1H, Ind-H), 5.18 (br. sept., 2H,  $\text{CH}(\text{CH}_3)_2$ ), 3.74 (br. sept., 2H,  $\text{CH}(\text{CH}_3)_2$ ), 2.33 (d,  $J$  = 1.0 Hz, 3H, Ind- $\text{CH}_3$ ), 1.74 (d,  $J$  = 1.74 Hz, 6H,



CH(CH<sub>3</sub>)<sub>2</sub>), 1.62 (d, *J* = 1.68 Hz, 6H, CH(CH<sub>3</sub>)<sub>2</sub>), 1.21 (d, *J* = 6.9 Hz, 6H, CH(CH<sub>3</sub>)<sub>2</sub>), 1.00 (s, 6H, CH(CH<sub>3</sub>)<sub>2</sub>). <sup>13</sup>C NMR (125 MHz, CDCl<sub>3</sub>): δ = 145.19, 131.48, 129.17, 120.78, 118.76, 116.84, 115.77, 111.61, 57.83, 55.59, 30.60, 30.09, 21.85, 9.96. <sup>14</sup>N NMR (36 MHz, CDCl<sub>3</sub>): 998.7, 390.5, 208.6. Elemental Analysis: Calcd. C, 63.61; H, 9.15; N, 14.13. Found: C, 63.26; H, 9.44; N, 13.97. M.p.: 200-201 °C.

*Synthesis of NCr(N<sup>i</sup>Pr<sub>2</sub>)<sub>2</sub>(Ind<sup>3Me5F</sup>):* To a solution of NCr(N<sup>i</sup>Pr<sub>2</sub>)<sub>2</sub>OPh (75 mg, 0.191 mmol) in toluene, freshly prepared Li-Ind<sup>3Me5F</sup> (89 mg, 0.572 mmol) was added slowly. The reaction was heated to 40 °C for 18 h whereupon color changed to a dark purplish color. The volatiles were removed *in vacuo* and the residue extracted with pentane. The extracts were then filtered through Celite and concentrated *in vacuo*. Recrystallization was achieved by cooling the concentrated solution at −30 °C overnight. (51.9 mg, 0.125 mmol, 65.7%). <sup>1</sup>H NMR (500 MHz, CDCl<sub>3</sub>): δ = 7.94 (dd, *J* = 8.9, 4.7 Hz, 1H, Ind-H), 7.20 (s, 1H, Ind-H), 7.07 (dd, *J* = 9.7, 2.6 Hz, 1H, Ind-H), 6.97 (d, *J* = 7.7 Hz, 1H, Ind-H), 6.87 (td, *J* = 9.2, 2.6 Hz, 1H, Ind-H), 5.17 (br. sept., 2H, CH(CH<sub>3</sub>)<sub>2</sub>), 3.76 (br. sept., 2H, CH(CH<sub>3</sub>)<sub>2</sub>), 1.69 (d, *J* = 59.8 Hz, 12H, CH(CH<sub>3</sub>)<sub>2</sub>), 1.22 (s, 6H, CH(CH<sub>3</sub>)<sub>2</sub>), 1.01 (s, 6H, CH(CH<sub>3</sub>)<sub>2</sub>). <sup>13</sup>C NMR (125 MHz, CDCl<sub>3</sub>): δ = 159.41, 157.56, 142.25, 133.45, 129.70, 129.62, 116.78, 116.70, 112.19, 112.15, 109.06, 108.85, 102.18, 101.99, 58.40, 56.14, 31.04, 30.48, 22.24, 21.99, 10.29. <sup>19</sup>F NMR (470 MHz, CDCl<sub>3</sub>): δ = −126.65 (td) <sup>14</sup>N NMR (36 MHz, CDCl<sub>3</sub>): 998.1, 392.6, 204.2 Note: Despite multiple attempts, adequate elemental analysis could not be obtained. M.p.: 206-207 °C.

*Synthesis of NCr(N<sup>i</sup>Pr<sub>2</sub>)<sub>2</sub>(Pyrr<sup>Me</sup>):* A suspension of ZnCl<sub>2</sub> (52.0 mg, 0.381 mmol) in THF was chilled to near freezing temperatures in the cold well. To this cold, stirring solution was added freshly prepared Na-Pyrr<sup>Me</sup> (79 mg, 0.763 mmol) as a chilled solution in THF. This was left to react for 2 h. After the 2 h, the solution was chilled again, and a chilled solution of NCr(N<sup>i</sup>Pr<sub>2</sub>)<sub>2</sub>I



(75 mg, 0.191 mmol) in THF was added slowly. This reaction was left to stir for 4 h, yielding a dark reddish orange solution. The volatiles were removed *in vacuo* and the residue extracted with pentane. The extracts were then filtered through Celite and concentrated *in vacuo*. Recrystallization was achieved by cooling the concentrated solution at  $-30\text{ }^{\circ}\text{C}$  overnight. (39 mg, 0.113 mmol, 59.0%).  $^1\text{H}$  NMR (500 MHz,  $\text{CDCl}_3$ ):  $\delta$  = 6.76 (s, 1H, Pyrr-H), 6.12 (t,  $J$  = 2.6 Hz, 1H, Pyrr-H), 5.91 (s, 1H, Pyrr-H), 5.16 (br. sept., 2H,  $\text{CH}(\text{CH}_3)_2$ ), 3.77 (br. sept., 2H,  $\text{CH}(\text{CH}_3)_2$ ), 2.51 (s, 3H, Pyrr- $\text{CH}_3$ ), 1.80 (d,  $J$  = 5.5 Hz, 6H,  $\text{CH}(\text{CH}_3)_2$ ), 1.60 (d,  $J$  = 5.5 Hz, 6H,  $\text{CH}(\text{CH}_3)_2$ ), 1.20 (d,  $J$  = 5.6 Hz, 6H,  $\text{CH}(\text{CH}_3)_2$ ), 1.06 (d,  $J$  = 5.6 Hz, 6H,  $\text{CH}(\text{CH}_3)_2$ ).  $^{13}\text{C}$  NMR (125 MHz,  $\text{CDCl}_3$ ):  $\delta$  = 137.35, 124.07, 107.93, 105.55, 58.64, 56.25, 30.78, 30.58, 22.27, 21.69, 17.36.  $^{14}\text{N}$  NMR (36 MHz,  $\text{CDCl}_3$ ):  $\delta$  = 999.2, 369.5, 224.0. Elemental Analysis: Calcd. C, 58.93; H, 9.89; N, 16.17. Found: C, 58.93; H, 10.08; N, 15.96. M.p.: 151-152  $^{\circ}\text{C}$ .

*Synthesis of  $\text{NCr}(\text{N}^i\text{Pr}_2)_2(\text{Pyrr}^{2-[\text{C}_6\text{H}_3(\text{CF}_3)_2]})$* : To a solution of  $\text{NCr}(\text{N}^i\text{Pr}_2)_2\text{I}$  (132 mg, 0.336 mmol) in ether, a suspension of freshly prepared  $\text{Ti-Pyrr}^{2-[\text{C}_6\text{H}_3(\text{CF}_3)_2]}$  (170 mg, 0.352 mmol) in ether was added slowly. Immediately a yellow precipitate formed. The reaction was allowed to stir for 2 h whereupon it was filtered through Celite, dried *in vacuo*, and the reddish orange solids extracted with pentane. Recrystallization was achieved by cooling a concentrated solution of the compound in HMDSO at  $-30\text{ }^{\circ}\text{C}$  overnight. (80 mg, 0.147 mmol, 44%).  $^1\text{H}$  NMR (500 MHz,  $\text{CDCl}_3$ ):  $\delta$  = 8.04 (s, 2H, Ar-H), 7.64 (s, 1H, Ar-H), 7.01 (s, 1H, Pyrr-H), 6.37 (s, 2H, Pyrr-H), 5.17 (m,  $J$  = 12.7, 2H,  $\text{CH}(\text{CH}_3)_2$ ), 3.70 (m,  $J$  = 12.5, 2H,  $\text{CH}(\text{CH}_3)_2$ ), 1.53 (d,  $J$  = 6.3 Hz, 6H,  $\text{CH}(\text{CH}_3)_2$ ), 1.48 (d,  $J$  = 6.2 Hz, 6H,  $\text{CH}(\text{CH}_3)_2$ ), 1.15 (d,  $J$  = 6.4 Hz, 6H,  $\text{CH}(\text{CH}_3)_2$ ), 1.06 (d,  $J$  = 6.3 Hz, 6H,  $\text{CH}(\text{CH}_3)_2$ ).  $^{13}\text{C}$  NMR (125 MHz,  $\text{CDCl}_3$ ):  $\delta$  = 141.09, 140.27, 131.01, 130.80, 13., 129.35, 129.32, 128.20, 119.11, 119.08, 119.0, 119.3, 110.89, 110.22, 59.04, 56.67, 30.26, 22.39, 21.96.  $^{19}\text{F}$  NMR



(470 MHz, CDCl<sub>3</sub>):  $\delta$  = -62.86. <sup>14</sup>N NMR (36 MHz, CDCl<sub>3</sub>): 1006.5, 404.4, 208.9. Elemental Analysis: Calcd. C, 52.94; H, 6.29; N, 10.29. Found: C, 52.73; H, 6.43; N, 10.15. M.p.: 40-42 °C.

*Synthesis of NCr(N<sup>i</sup>Pr<sub>2</sub>)<sub>2</sub>(Pyrr<sup>Ph</sup>):* To a solution of NCr(N<sup>i</sup>Pr<sub>2</sub>)<sub>2</sub>I (75 mg, 0.191 mmol) in ether, a suspension of freshly prepared Tl-Pyrr<sup>Ph</sup> (46.3 mg, 0.133 mmol) in ether was added slowly. Immediately a yellow precipitate formed. The reaction was allowed to stir for 2 h before being filtered through Celite. The filtrate was dried *in vacuo*, and the reddish orange solids extracted with pentane. The extracts were then concentrated *in vacuo*. Recrystallization was achieved by cooling the concentrated solution at -30 °C overnight. (52 mg, 0.127 mmol, 67%). <sup>1</sup>H NMR (500 MHz, CDCl<sub>3</sub>):  $\delta$  = 7.61 (t, 2H, Ph-H), 7.30 (m, 2H, Ph-H), 7.19 (t,  $J$  = 9.2, 4.3 Hz, 1H, Ph-H), 6.94 (t,  $J$  = 2.4, 1.4 Hz, 1H, Pyrr-H), 6.33 (t, 1H, Pyrr-H), 6.27 (m,  $J$  = 3.1, 1.4 Hz, 1H, Pyrr-H), 5.13 (sept, 2H, CH(CH<sub>3</sub>)<sub>2</sub>), 3.70 (sept, 2H, CH(CH<sub>3</sub>)<sub>2</sub>), 1.54 (d,  $J$  = 25.2, 6.3 Hz, 6H, CH(CH<sub>3</sub>)<sub>2</sub>), 1.50 (d,  $J$  = 25.2, 6.4 Hz, 6H, CH(CH<sub>3</sub>)<sub>2</sub>), 1.14 (d,  $J$  = 6.4 Hz, 6H, CH(CH<sub>3</sub>)<sub>2</sub>), 1.11 (d,  $J$  = 6.4 Hz, 6H, CH(CH<sub>3</sub>)<sub>2</sub>). <sup>13</sup>C NMR (CDCl<sub>3</sub>, 25 °C, 125 MHz):  $\delta$  = 143.58, 138.27, 129.28, 127.21, 126.64, 125.62, 109.70, 108.25, 58.49, 56.13, 29.97, 29.83, 22.6, 21.57. <sup>14</sup>N NMR (36 MHz, CDCl<sub>3</sub>):  $\delta$  = 1007.8, 402.0, 213.8. Elemental Analysis: Calcd. C, 64.84; H, 8.88; N, 13.71. Found: C, 64.89; H, 8.81; N, 13.74. M.p.: 133-135 °C.

*Synthesis of NCr(N<sup>i</sup>Pr<sub>2</sub>)<sub>2</sub>(Pyrr<sup>Tol</sup>):* To a solution of NCr(N<sup>i</sup>Pr<sub>2</sub>)<sub>2</sub>I (75 mg, 0.191 mmol) in ether, a suspension of freshly prepared Pyrr<sup>Tol</sup> (72.2 mg, 0.200 mmol) in ether was added slowly. Immediately a yellow precipitate is formed. The reaction was allowed to stir for 2 h before being filtered through Celite. The filtrate was dried *in vacuo*, and the dark orange solids extracted with pentane. The extracts were then concentrated *in vacuo*. Recrystallization was achieved by cooling the concentrated solution at -30 °C overnight. (70 mg, 0.166 mmol, 87%). <sup>1</sup>H NMR (500 MHz,



CDCl<sub>3</sub>):  $\delta$  = 7.52 (d,  $J$  = 7.6 Hz, 2H, Tol-H), 7.12 (d,  $J$  = 7.6 Hz, 2H, Tol-H), 6.95 (s, 1H, Pyrr-H), 6.33 (s, 1H, Pyrr-H), 6.25 (s, 1H, Pyrr-H), 5.17 (m,  $J$  = 12.5, 6.2 Hz, 2H, CH(CH<sub>3</sub>)<sub>2</sub>), 3.73 (m,  $J$  = 12.4, 6.1 Hz, 2H, CH(CH<sub>3</sub>)<sub>2</sub>), 2.35 (s, 3H, Tol-CH<sub>3</sub>), 1.58 (d,  $J$  = 6.2 Hz, 6H, CH(CH<sub>3</sub>)<sub>2</sub>), 1.53 (d,  $J$  = 6.2 Hz, 6H, CH(CH<sub>3</sub>)<sub>2</sub>), 1.16 (d,  $J$  = 6.3 Hz, 6H, CH(CH<sub>3</sub>)<sub>2</sub>), 1.10 (d,  $J$  = 6.2 Hz, 6H, CH(CH<sub>3</sub>)<sub>2</sub>). <sup>13</sup>C NMR (CDCl<sub>3</sub>, 25 °C, 125 MHz):  $\delta$  = 143.61, 135.47, 135.04, 129.18, 127.93, 126.23, 109.36, 107.75, 58.38, 56.08, 29.97, 29.86, 22.04, 21.57, 21.14. <sup>14</sup>N NMR (36 MHz, CDCl<sub>3</sub>):  $\delta$  = 1010.1, 399.7, 213.6. Elemental Analysis: Calcd. C, 65.37; H, 9.06; N, 13.26 Found: C, 65.33; H, 9.11; N, 13.21. M.p.: 143-144 °C.

*Synthesis of NCr(N<sup>i</sup>Pr<sub>2</sub>)<sub>2</sub>(OPh<sup>2,4-diMe</sup>):* To a nearly frozen, stirring solution of NCr(N<sup>i</sup>Pr<sub>2</sub>)<sub>3</sub> (75 mg, 0.205 mmol) in ether, an ethereal solution of the HOPh<sup>2,4-diMe</sup> (25 mg, 0.205 mmol) was added dropwise. The solution began to change to an orange color rapidly. After 2 h of stirring, the volatiles were removed *in vacuo*, and the residue extracted with pentane. The extracts were filtered over Celite and concentrated for recrystallization at -30 °C overnight. (32.5 mg, 0.084 mmol, 41%). <sup>1</sup>H NMR (500 MHz, CDCl<sub>3</sub>):  $\delta$  = 7.00 (d,  $J$  = 7.9 Hz, 1H, Ar-H), 6.85 (s, 1H, Ar-H), 6.83 (s, 1H, Ar-H), 5.04 (br. sept., 2H, CH(CH<sub>3</sub>)<sub>2</sub>), 3.75 (br. sept., 2H, CH(CH<sub>3</sub>)<sub>2</sub>), 2.22 (s, 3H, Ar-CH<sub>3</sub>), 2.14 (s, 3H, Ar-CH<sub>3</sub>), 1.84 (br. s, 6H, CH(CH<sub>3</sub>)<sub>2</sub>), 1.47 (br. s, 6H, CH(CH<sub>3</sub>)<sub>2</sub>), 1.25 (br. d,  $J$  = 61.3 Hz, 12 H CH(CH<sub>3</sub>)<sub>2</sub>). <sup>13</sup>C NMR (125 MHz, CDCl<sub>3</sub>):  $\delta$  = 163.60, 130.58, 128.56, 127.45, 125.33, 117.62, 58.64, 55.49, 30.71, 21.77, 20.92, 17.20. <sup>14</sup>N NMR (36 MHz, CDCl<sub>3</sub>):  $\delta$  = 1004.4, 379.3. Elemental Analysis: Calcd. C, 61.99; H, 9.62; N, 10.84. Found: C, 61.70; H, 9.31; N, 10.79. M.p.: 116-117 °C.

*Synthesis of NCr(N<sup>i</sup>Pr<sub>2</sub>)<sub>2</sub>(OPh<sup>2-tBu-4-Me</sup>):* To a nearly frozen, stirring solution of NCr(N<sup>i</sup>Pr<sub>2</sub>)<sub>3</sub> (75 mg, 0.205 mmol) in ether, an ethereal solution of the HOPh<sup>2-tBu-4-Me</sup> (33.6 mg, 0.205 mmol) was added dropwise. After 16 h of stirring, the volatiles were removed *in vacuo*. The orange, extremely



soluble residue was then extracted with pentane. The extracts were filtered over Celite and concentrated for recrystallization at  $-30\text{ }^{\circ}\text{C}$  overnight. (53 mg, 0.123 mmol, 60%).  $^1\text{H}$  NMR (500 MHz,  $\text{CDCl}_3$ ):  $\delta$  = 7.21 (d,  $J$  = 8.1 Hz, 1H, Ar-H), 6.98 (s, 1H, Ar-H), 6.90 (d,  $J$  = 8.0 Hz, 1H, Ar-H), 5.05 (s, 2H,  $\text{CH}(\text{CH}_3)_2$ ), 3.77 (s, 2H,  $\text{CH}(\text{CH}_3)_2$ ), 2.27 (s, 3H, Ar- $\text{CH}_3$ ), 1.86 (s, 6H,  $\text{CH}(\text{CH}_3)_2$ ), 1.54 (s, 6H,  $\text{CH}(\text{CH}_3)_2$ ), 1.37 (s, 9H,  $^t\text{Bu}$ ), 1.18 (s, 12H,  $\text{CH}(\text{CH}_3)_2$ ).  $^{13}\text{C}$  NMR (125 MHz,  $\text{CDCl}_3$ ):  $\delta$  = 163.60, 136.15, 128.22, 127.85, 126.44, 119.96, 58.81, 55.76, 35.12, 30.92, 30.44, 30.17, 22.82, 22.25, 21.28.  $^{14}\text{N}$  NMR (36 MHz,  $\text{CDCl}_3$ ):  $\delta$  = 1004.6, 380.4. Note: Due to the high affinity for solvents, adequate elemental analysis could not be obtained. M.p.: 188-191  $^{\circ}\text{C}$ .

*Synthesis of  $\text{NCr}(\text{N}^i\text{Pr}_2)_2(\text{OPh}^{2,4,5\text{-triMe}})$ :* To a nearly frozen, stirring solution of  $\text{NCr}(\text{N}^i\text{Pr}_2)_3$  (150 mg, 0.409 mmol) in ether, an ethereal solution of the  $\text{HOPh}^{2,4,5\text{-triMe}}$  (55.7 mg, 0.409 mmol) was added dropwise. The solution began to change to an orange color rapidly. After 1.5 h of stirring, the volatiles were removed *in vacuo*, and the residue extracted with pentane. The extracts were then filtered over Celite and concentrated for recrystallization at  $-30\text{ }^{\circ}\text{C}$  overnight. (129 mg, 0.321 mmol, 79%).  $^1\text{H}$  NMR (500 MHz,  $\text{CDCl}_3$ ):  $\delta$  = 6.94 (s, 1H, Ar-H), 6.81 (s, 1H, Ar-H), 5.05 (br. sept., 2H,  $\text{CH}(\text{CH}_3)_2$ ), 3.78 (br. sept., 2H,  $\text{CH}(\text{CH}_3)_2$ ), 2.17 (s, 3H, Ar- $\text{CH}_3$ ), 2.15 (s, 3H, Ar- $\text{CH}_3$ ), 2.13 (s, 3H, Ar- $\text{CH}_3$ ), 1.86 (br. s, 6H,  $\text{CH}(\text{CH}_3)_2$ ), 1.31 (br. s, 6H,  $\text{CH}(\text{CH}_3)_2$ ), 1.21 (apt. t, 12H,  $\text{CH}(\text{CH}_3)_2$ ). Note: Due to rapid exchange in the system, the integral values on the room temperature spectrum are inaccurate. As such, an integrated low temperature spectrum is included in the spectra below.  $^{13}\text{C}$  NMR (125 MHz,  $\text{CDCl}_3$ ):  $\delta$  = 163.52, 134.46, 130.87, 126.99, 122.26, 119.10, 58.41, 55.21, 30.61, 21.42, 19.61, 18.87, 16.42.  $^{14}\text{N}$  NMR (36 MHz,  $\text{CDCl}_3$ ):  $\delta$  = 1001.9, 375.8. Elemental Analysis: Calcd. C, 62.81; H, 9.79; N, 10.46. Found: C, 62.67; H, 9.90; N, 10.52. M.p.: 127-128  $^{\circ}\text{C}$ .



*Synthesis of  $\text{NCr}(\text{N}^i\text{Pr}_2)_2(\text{OPh}^{2\text{-tBu-4,5-diMe}})$ :* To a nearly frozen, stirring solution of  $\text{NCr}(\text{N}^i\text{Pr}_2)_3$  (100 mg, 0.273 mmol) in THF, a THF solution of the  $\text{HOPh}^{2\text{-tBu-4,5-diMe}}$  (48.6 mg, 0.273 mmol) was added dropwise. The solution was loaded into a pressure tube and sealed. The reaction was heated on an aluminum heating block at 50 °C for 3 h, whereupon the color changed from beet to orange. After the 3 h, the volatiles were dried *in vacuo*, and the dark residue was extracted with pentane. The extracts were then filtered over Celite and concentrated for recrystallization at –30 °C overnight. (67 mg, 0.151 mmol, 55%).  $^1\text{H}$  NMR (500 MHz,  $\text{CDCl}_3$ ):  $\delta$  = 7.12 (s, 1H, Ar-H), 6.93 (s, 1H, Ar-H), 5.05 (s, 2H,  $\text{CH}(\text{CH}_3)_2$ ), 3.79 (s, 2H,  $\text{CH}(\text{CH}_3)_2$ ), 2.18 (app. d, 6H, Ar- $\text{CH}_3$ ), 1.89 (d,  $J$  = 4.2 Hz, 6H,  $\text{CH}(\text{CH}_3)_2$ ), 1.55 (d,  $J$  = 4.3 Hz, 6H,  $\text{CH}(\text{CH}_3)_2$ ), 1.37 (s, 9H,  $^i\text{Bu}$ ), 1.19 (s, 12H,  $\text{CH}(\text{CH}_3)_2$ ).  $^{13}\text{C}$  NMR (125 MHz,  $\text{CDCl}_3$ ):  $\delta$  = 163.19, 134.86, 133.44, 126.77, 126.59, 121.54, 58.52, 55.49, 34.52, 30.69, 30.13, 30.20, 22.58, 21.99, 19.30, 19.15.  $^{14}\text{N}$  NMR (36 MHz,  $\text{CDCl}_3$ ):  $\delta$  = 1002.3, 379.1. Elemental Analysis: Calcd. C, 64.98; H, 10.22; N, 9.47. Found: C, 64.92; H, 10.33; N, 9.63. M.p.: 107-109 °C.

*Synthesis of  $\text{NCr}(\text{N}^i\text{Pr}_2)_2(\text{OPh}^{2\text{-Me-4-OMe}})$ :* To a nearly frozen, stirring solution of  $\text{NCr}(\text{N}^i\text{Pr}_2)_3$  (100 mg, 0.273 mmol) in ether, an ethereal solution of the  $\text{HOPh}^{2\text{-Me-4-OMe}}$  (37.7 mg, 0.273 mmol) was added dropwise. After stirring for 1.5 h, the color had changed from beet to orange. The volatiles were dried *in vacuo*, and the dark residue was extracted with pentane. The extracts were filtered over Celite and concentrated for recrystallization at –30 °C overnight. (44 mg, 0.109 mmol, 40%).  $^1\text{H}$  NMR (500 MHz,  $\text{CDCl}_3$ ):  $\delta$  = 7.01 (d,  $J$  = 8.6 Hz, 1H, Ar-H), 6.61 (m, 1H, Ar-H), 5.03 (br. sept., 2H,  $\text{CH}(\text{CH}_3)_2$ ), 3.76 (br. sept., 2H,  $\text{CH}(\text{CH}_3)_2$ ), 3.73 (s, 3H, O- $\text{CH}_3$ ), 2.17 (s, 3H, Ar- $\text{CH}_3$ ), 1.85 (br. s, 6H,  $\text{CH}(\text{CH}_3)_2$ ), 1.45 (br. s, 6H,  $\text{CH}(\text{CH}_3)_2$ ), 1.23 (br. s, 12H,  $\text{CH}(\text{CH}_3)_2$ ). Note: Due to rapid exchange in the system, the room temperature integral values in the spectrum are inaccurate. As such, an integrated low temperature spectrum is included in the spectra below.  $^{13}\text{C}$



NMR (125 MHz, CDCl<sub>3</sub>):  $\delta$  = 160.22, 152.89, 126.13, 117.82, 115.52, 111.55, 58.37, 55.89, 30.18, 21.53, 17.31. <sup>14</sup>N NMR (36 MHz, CDCl<sub>3</sub>):  $\delta$  = 1008.2, 377.1. Elemental Analysis: Calcd. C, 59.53; H, 9.24; N, 10.41. Found: C, 59.73; H, 9.78; N, 10.24. M.p.: 158-160 °C.

*Synthesis of NCr(N<sup>i</sup>Pr<sub>2</sub>)<sub>2</sub>(OPh<sup>2-tBu-4OMe</sup>):* To a nearly frozen, stirring solution of NCr(N<sup>i</sup>Pr<sub>2</sub>)<sub>3</sub> (100 mg, 0.273 mmol) in ether, an ethereal solution of the HOPh<sup>2-tBu-4OMe</sup> (49.2 mg, 0.273 mmol) was added dropwise. The solution was allowed to stir for 18 h with little noticeable color change. After that time, the volatiles were dried *in vacuo*, and the dark residue was extracted with pentane. The solution was filtered over Celite and once again dried. The extremely soluble residue was dissolved in a minimal amount of HMDSO for recrystallization at –30 °C overnight. (61 mg, 0.137 mmol, 50%). <sup>1</sup>H NMR (500 MHz, CDCl<sub>3</sub>):  $\delta$  = 7.22 (d, *J* = 8.7 Hz, 1H, Ar-H), 6.79 (d, *J* = 3.1 Hz, 1H, Ar-H), 6.64 (dd, *J* = 8.7, 3.1 Hz, 1H, Ar-H), 5.03 (m, 2H, CH(CH<sub>3</sub>)<sub>2</sub>), 3.77 (m, 2H, CH(CH<sub>3</sub>)<sub>2</sub>), 3.75 (s, 3H, O-CH<sub>3</sub>), 1.87 (d, *J* = 5.4 Hz, 6H, CH(CH<sub>3</sub>)<sub>2</sub>), 1.53 (d, *J* = 5.5 Hz, 6H, CH(CH<sub>3</sub>)<sub>2</sub>), 1.37 (s, 9H <sup>t</sup>Bu), 1.18 (app. t, 12H, CH(CH<sub>3</sub>)<sub>2</sub>). <sup>13</sup>C NMR (125 MHz, CDCl<sub>3</sub>):  $\delta$  = 159.60, 152.49, 137.10, 119.48, 112.54, 110.34, 58.38, 55.62, 55.26, 34.92, 30.51, 29.99, 29.54, 22.39, 21.82. <sup>14</sup>N NMR (36 MHz, CDCl<sub>3</sub>):  $\delta$  = 1004.4, 379.2. Elemental Analysis: Calcd. C, 61.99; H, 9.73; N, 9.43. Found: C, 61.66; H, 9.82; N, 9.53. M.p.: 97-100 °C.

*Synthesis of NCr(N<sup>i</sup>Pr<sub>2</sub>)<sub>2</sub>(SNap):* To a nearly frozen, stirring solution of NCr(N<sup>i</sup>Pr<sub>2</sub>)<sub>3</sub> (100 mg, 0.273 mmol) in THF, a THF solution of the HSNap (45.9 mg, 0.286 mmol) was added dropwise. The solution was allowed to stir for 18 h at 55 °C upon which time the color changed to a reddish-purple color. After that time, the volatiles were dried *in vacuo*, and the dark residue was extracted with pentane. The solution was filtered over Celite and the filtrate concentrated. The pentane solution was then left in the freezer for recrystallization at –30 °C overnight. (63.9 mg, 0.150 mmol, 55%). <sup>1</sup>H NMR (500 MHz, CDCl<sub>3</sub>)  $\delta$  8.10 (s, 1H, Ar-H), 7.76 (dd, *J* = 8.6, 1.8 Hz, 1H, Ar-



H), 7.72 (d,  $J = 8.1$  Hz, 1H, Ar-H), 7.63 (dd,  $J = 24.8, 8.3$  Hz, 2H, Ar-H), 7.41 – 7.29 (m, 2H, Ar-H), 5.28 (m, 2H, CH(CH<sub>3</sub>)<sub>2</sub>), 3.74 (m, 2H, CH(CH<sub>3</sub>)<sub>2</sub>), 1.81 (d,  $J = 6.2$  Hz, 6H, CH(CH<sub>3</sub>)<sub>2</sub>), 1.54 (d,  $J = 6.2$  Hz, 6H, CH(CH<sub>3</sub>)<sub>2</sub>), 1.16 (dd,  $J = 6.1, 2.7$  Hz, 12H, CH(CH<sub>3</sub>)<sub>2</sub>). <sup>13</sup>C NMR (125 MHz, CDCl<sub>3</sub>):  $\delta = 140.42, 134.08, 131.91, 131.25, 130.50, 127.77, 127.20, 126.99, 126.05, 124.77, 59.39, 56.39, 30.69, 30.32, 22.79, 20.79$ . <sup>14</sup>N NMR (36 MHz, CDCl<sub>3</sub>):  $\delta = 1000.5, 406.3$ . Elemental Analysis: Calcd. C, 62.09; H, 8.29; N, 9.87. Found: C, 61.96; H, 8.15; N, 9.76. M.p.: 126-127 °C.

*Synthesis of NCr(N<sup>i</sup>Pr)<sub>2</sub>(6Br-SNap)*: To a nearly frozen, stirring solution of NCr(N<sup>i</sup>Pr)<sub>3</sub> (125 mg, 0.340 mmol) in THF, a THF solution of the 6Br-HSNap (87 mg, 0.360 mmol) was added dropwise. The solution was allowed to stir for 18 h at 55 °C upon which time the color changed to a reddish-purple color. After that time, the volatiles were dried *in vacuo*, and the dark residue was extracted with ether. The solution was filtered over Celite and the filtrate concentrated. The ether solution was then left in the freezer for recrystallization at –30 °C overnight. The LDP value, which was measured but not used in this particular study, is 14.15 kcal/mol. (120 mg, 0.264 mmol, 78%). <sup>1</sup>H NMR (500 MHz, CDCl<sub>3</sub>)  $\delta = 8.09$  (s, 1H, Ar-H), 7.88 (s, 1H, Ar-H), 7.80-7.78 (m, 1H, Ar-H), 7.53-7.51 (m, 2H, Ar-H), 7.46 – 7.44 (m, 1H, Ar-H), 5.34-5.26 (sept,  $J = 6.2$  Hz, 2H, CH(CH<sub>3</sub>)<sub>2</sub>), 3.79-3.71 (sept,  $J = 6.3$  Hz, 2H, CH(CH<sub>3</sub>)<sub>2</sub>), 1.81-1.80 (d,  $J = 6.3$  Hz, 6H, CH(CH<sub>3</sub>)<sub>2</sub>), 1.55-1.54 (d,  $J = 6.3$  Hz, 6H, CH(CH<sub>3</sub>)<sub>2</sub>), 1.18-1.15 (dd,  $J = 6.5, 4.5$  Hz, 12H, CH(CH<sub>3</sub>)<sub>2</sub>). <sup>13</sup>C NMR (125 MHz, CDCl<sub>3</sub>):  $\delta = 141.06, 132.58, 132.11, 131.89, 130.09, 129.51, 129.11, 128.29, 125.92, 118.14, 59.21, 56.20, 30.43, 30.06, 21.99, 20.52$ . <sup>14</sup>N NMR (36 MHz, CDCl<sub>3</sub>):  $\delta = 996.0, 404.2$ . M.p.: 149-151 °C.

#### General Procedure for Kinetics

All manipulations were done in an inert atmosphere drybox. A 2 mL volumetric flask was loaded the catalyst (10 mol%, 0.1 mmol) and ferrocene (0.0560 g, 0.3 mmol) as an internal



standard. Next, 0.75 mL of toluene-d<sub>8</sub> was added to the volumetric flask and the solution was mixed by swirling the flask until all solids were dissolved. Once all solids were dissolved, aniline (911 µL, 10 mmol) and 1-phenylpropyne (125 µL, 1.0 mmol) were added respectively to the volumetric flask. Lastly, the solution was diluted to 2 mL with toluene-d<sub>8</sub>. The solution was mixed via pipette (i.e. the solution was drawn up into the pipette and dispensed back into the volumetric flask) five times to ensure the solution was well-mixed. An ample amount of solution (~0.75 mL) was loaded into a threaded J. Young tube that was sealed with a Teflon stopper. The tube was removed from the dry box and was heated at 75 °C in the NMR spectrometer (Varian Inova 600 spectrometer). The relative 1-phenylpropyne *versus* ferrocene concentration was monitored as a function of time. The fits are to the exponential decay of the starting material using the scientific graphing program Origin. The exact expression used to fit the data is shown below: <sup>(44)</sup>

$$Y_t = Y_\infty + (Y_0 - Y_\infty)\exp^{-k_{obs}t}$$

Where Y = [1-phenylpropyne] at time t (Y<sub>t</sub>), infinity (Y<sub>∞</sub>), or at the start of the reaction (Y<sub>0</sub>). The variables Y<sub>∞</sub>, Y<sub>0</sub>, k<sub>obs</sub>, were optimized in the fits. Each kinetic experiment was completed in triplicate.



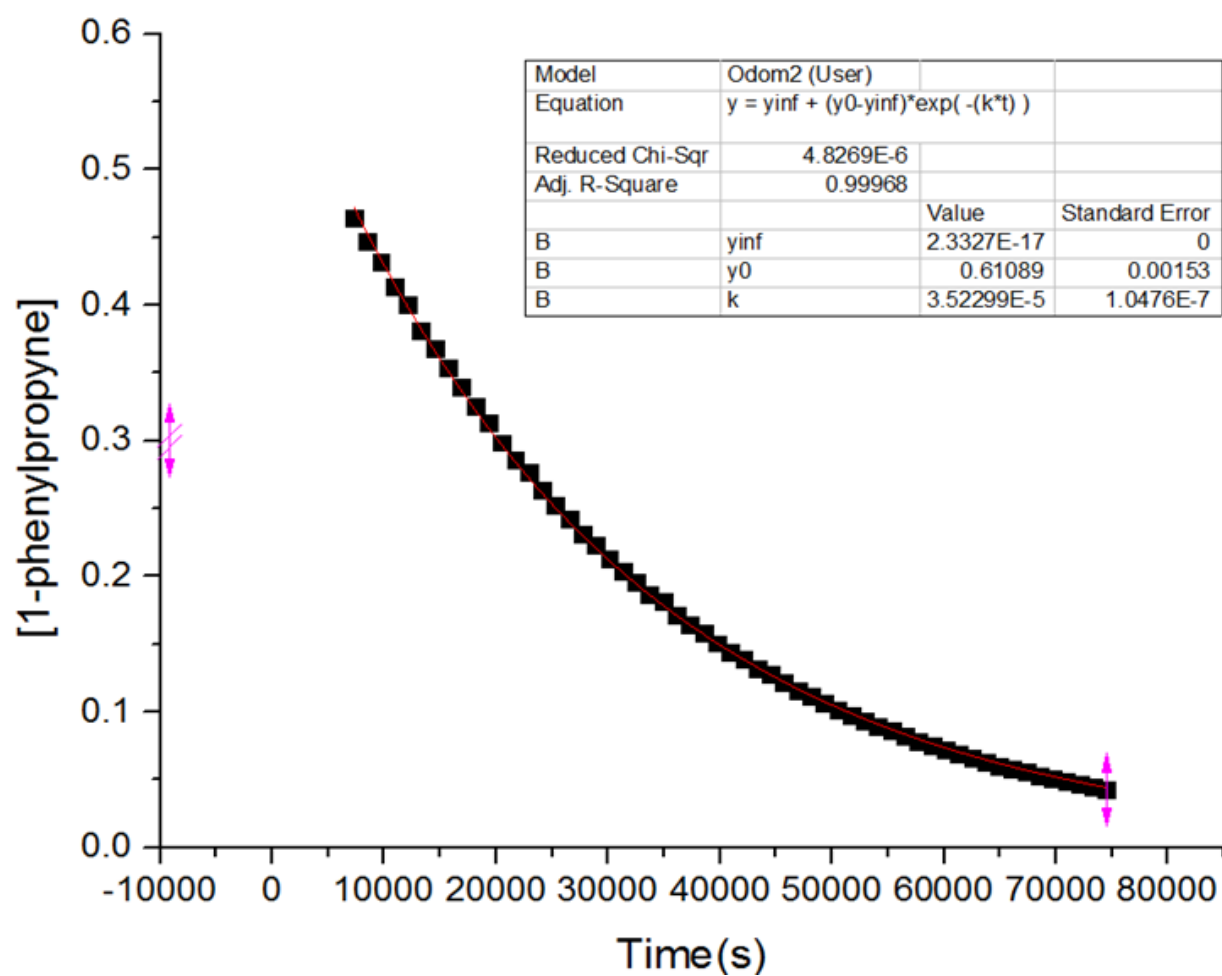


Figure 4-12. Representative Plots for Kinetics Plot of [1-phenylpropyne] vs time with  $\text{Ti}(\text{NMe}_2)_2(\text{bis-phenoxide}^{2\text{tBu-4Me}})$  (**5**)



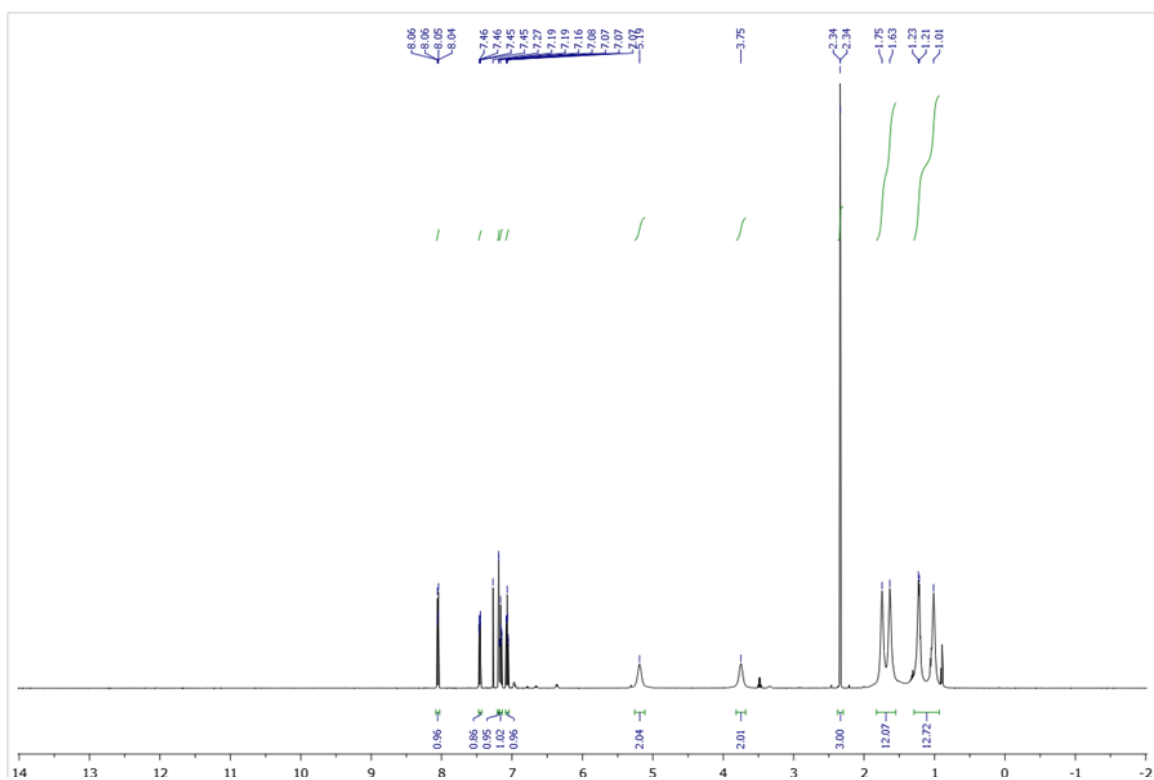


Figure 4-13.  $^1\text{H}$  NMR Spectrum of  $\text{NCr}(\text{NiPr}_2)_2(\text{Ind}^{\text{3Me}})$  in  $\text{CDCl}_3$ .



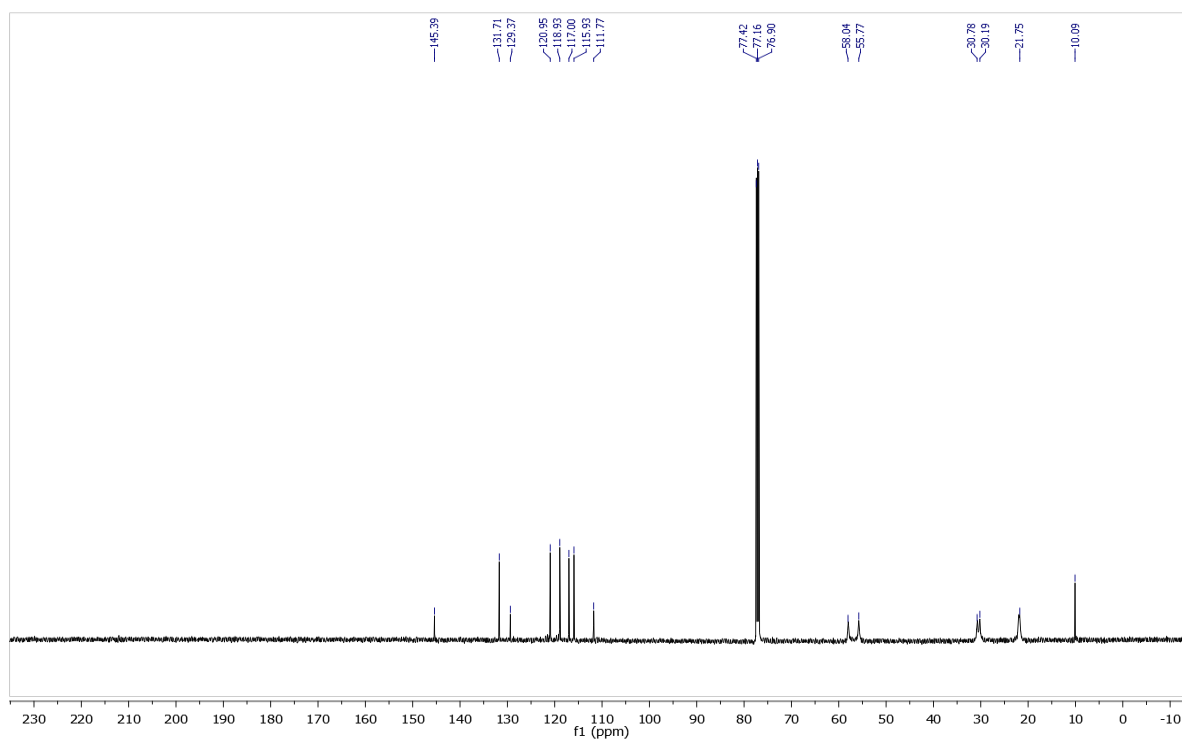


Figure 4-14.  $^{13}\text{C}$  NMR Spectrum of  $\text{NCr}(\text{N}^i\text{Pr}_2)_2(\text{Ind}^{3\text{Me}})$  in  $\text{CDCl}_3$ .



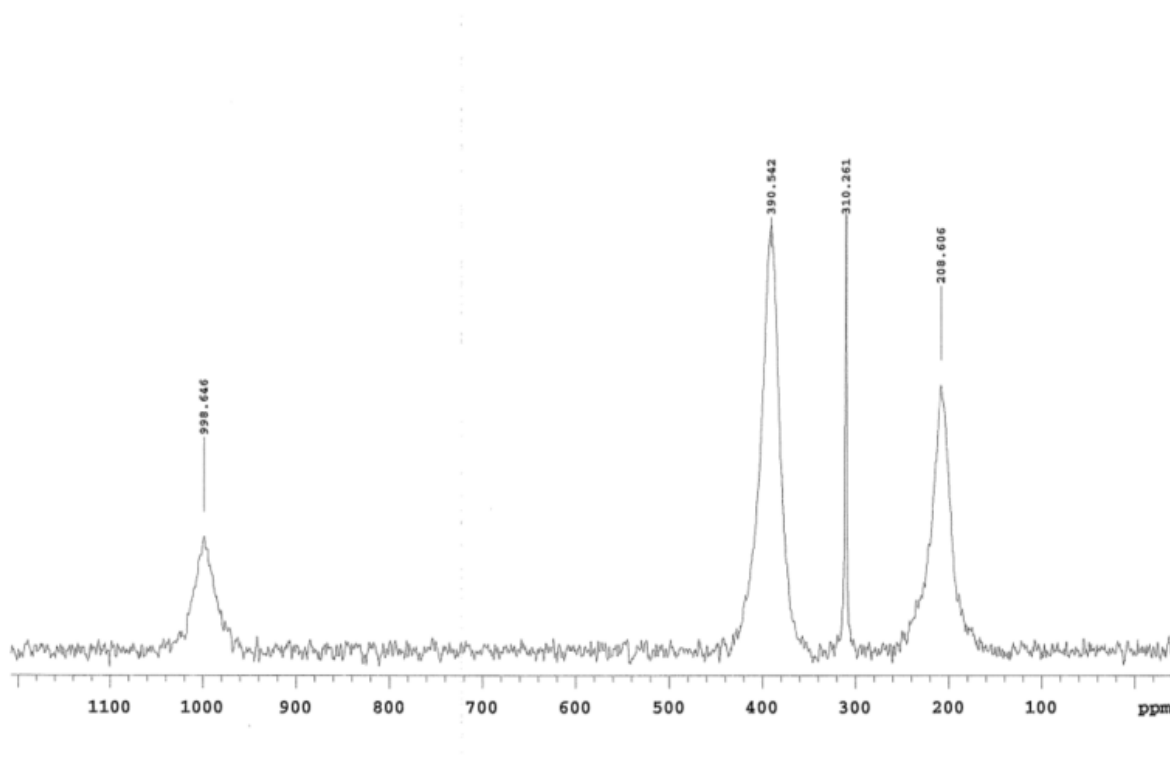


Figure 4-15.  $^{14}\text{N}$  NMR Spectrum of  $\text{NCr}(\text{N}^i\text{Pr}_2)_2(\text{Ind}^{3\text{Me}})$  in  $\text{CDCl}_3$ .



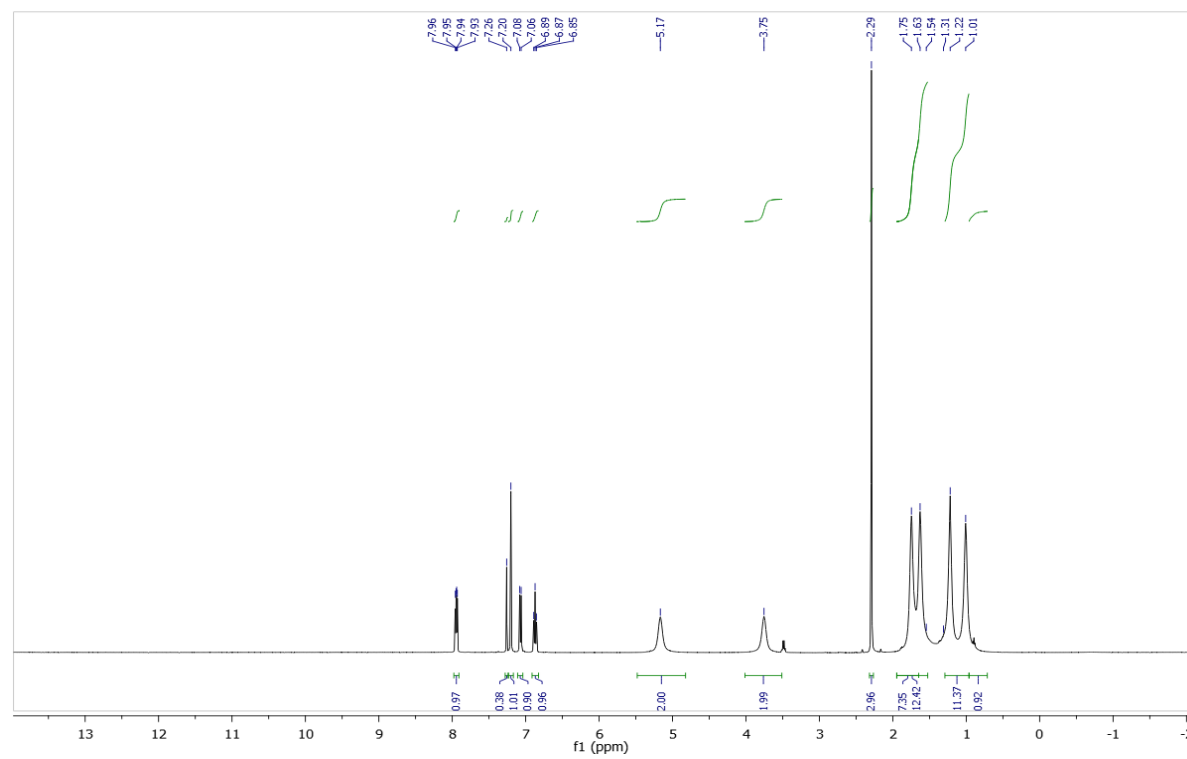


Figure 4-16.  $^1\text{H}$  NMR Spectrum of  $\text{NCr}(\text{N}^i\text{Pr}_2)_2(\text{Ind}^{3\text{Me5F}})$  in  $\text{CDCl}_3$ .



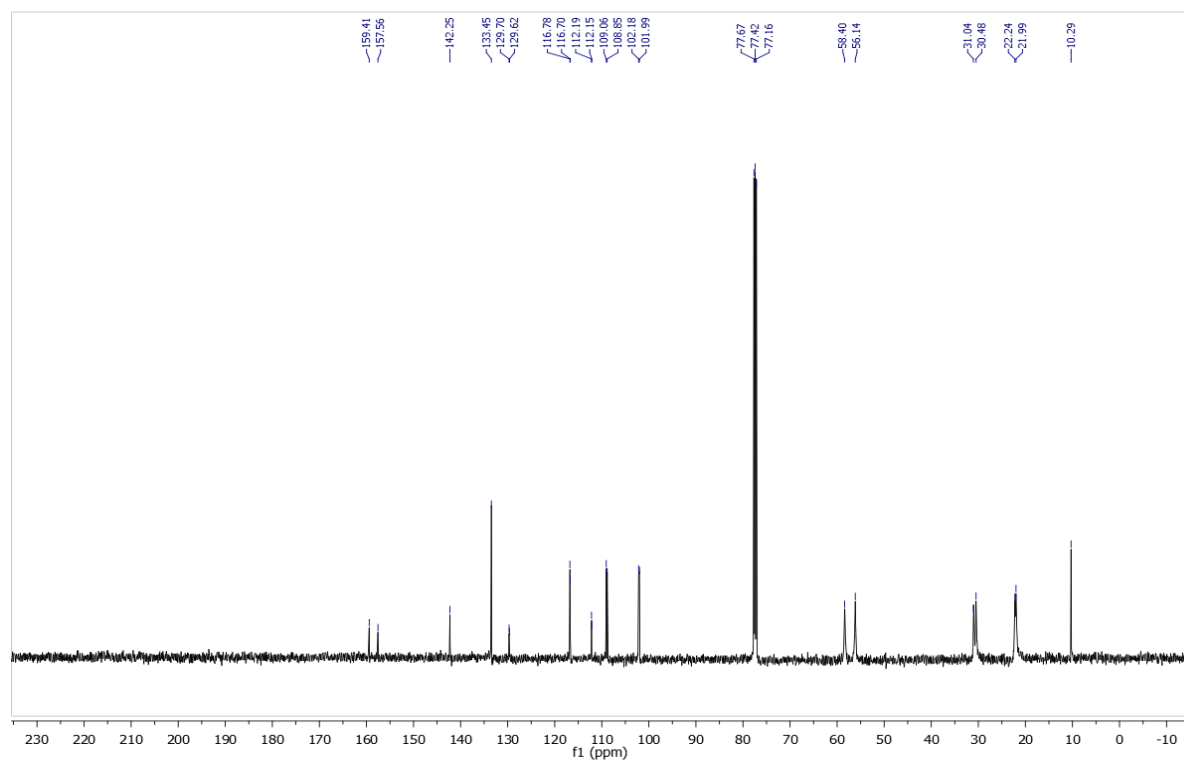


Figure 4-17.  $^{13}\text{C}$  NMR Spectrum of  $\text{NCr}(\text{N}^i\text{Pr}_2)_2(\text{Ind}^{3\text{Me5F}})$  in  $\text{CDCl}_3$ .



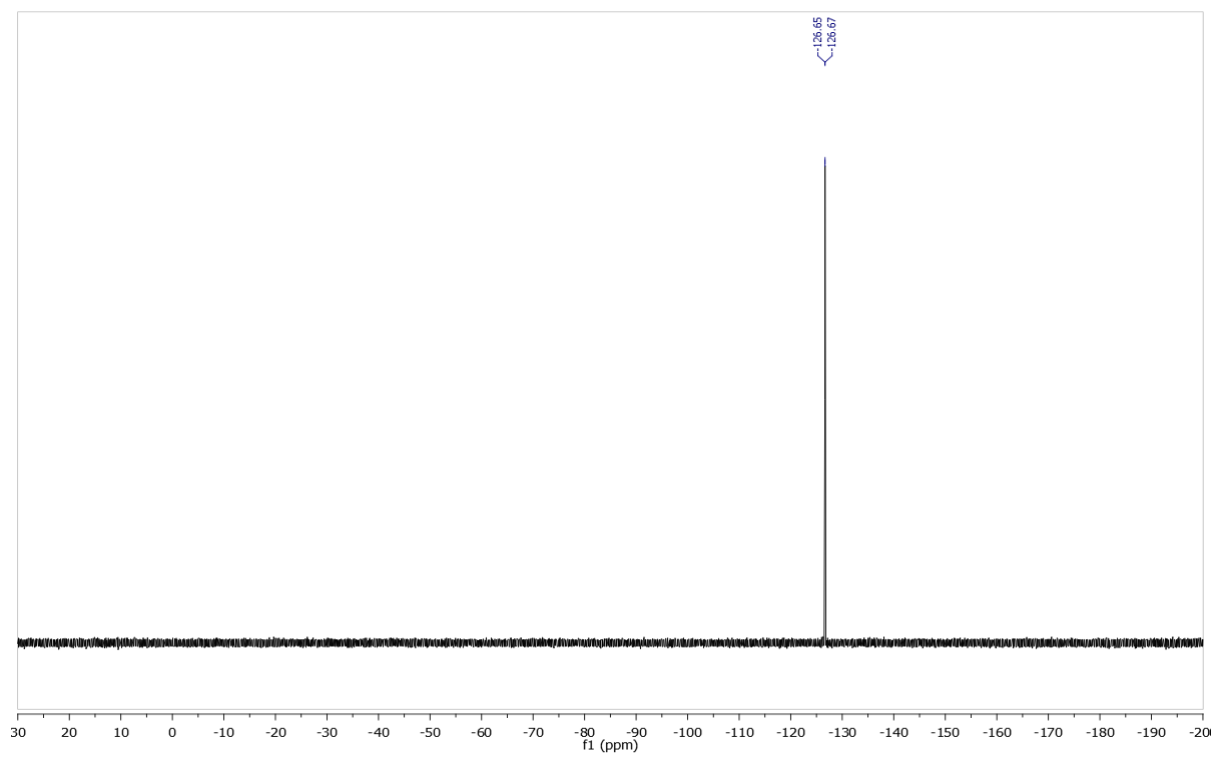


Figure 4-18.  $^{19}\text{F}$  NMR Spectrum of  $\text{NCr}(\text{N}^i\text{Pr}_2)_2(\text{Ind}^{3\text{Me}_5\text{F}})$  in  $\text{CDCl}_3$ .



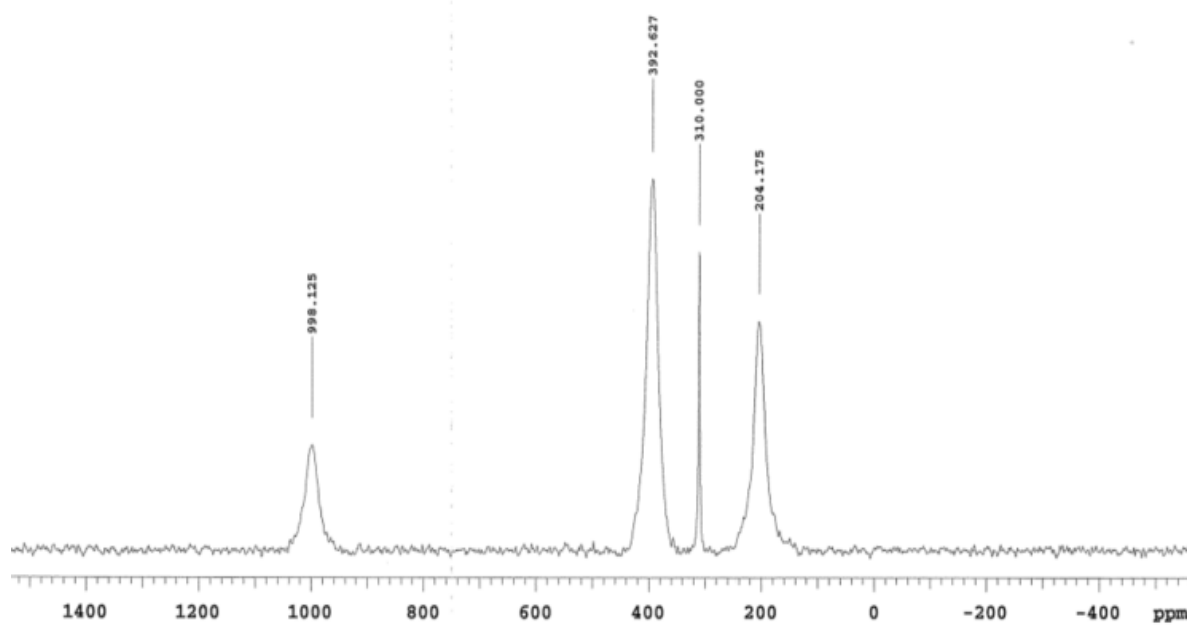


Figure 4-19.  $^{14}\text{N}$  NMR Spectrum of  $\text{NCr}(\text{N}^i\text{Pr}_2)_2(\text{Ind}^{3\text{Me}_5\text{F}})$  in  $\text{CDCl}_3$ .



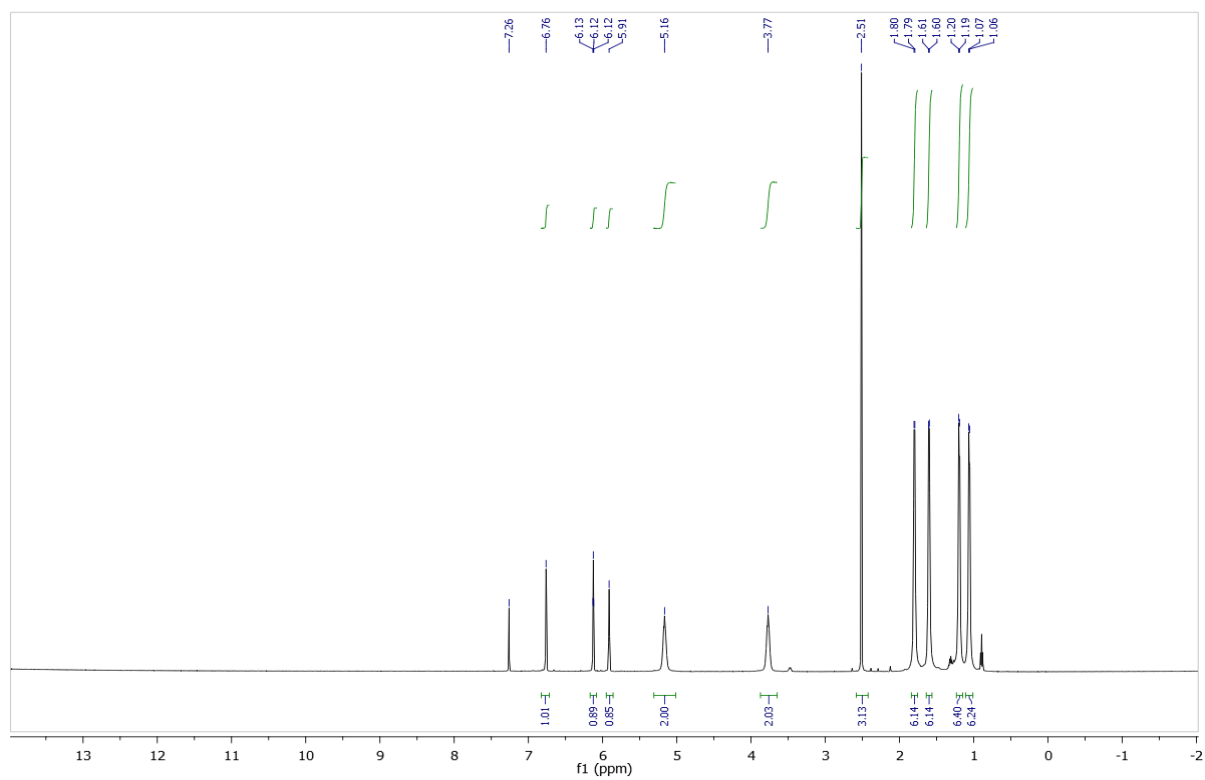


Figure 4-20.  $^1\text{H}$  NMR Spectrum of  $\text{NCr}(\text{N}^i\text{Pr}_2)_2(\text{Pyrr}^{\text{Me}})$  in  $\text{CDCl}_3$ .



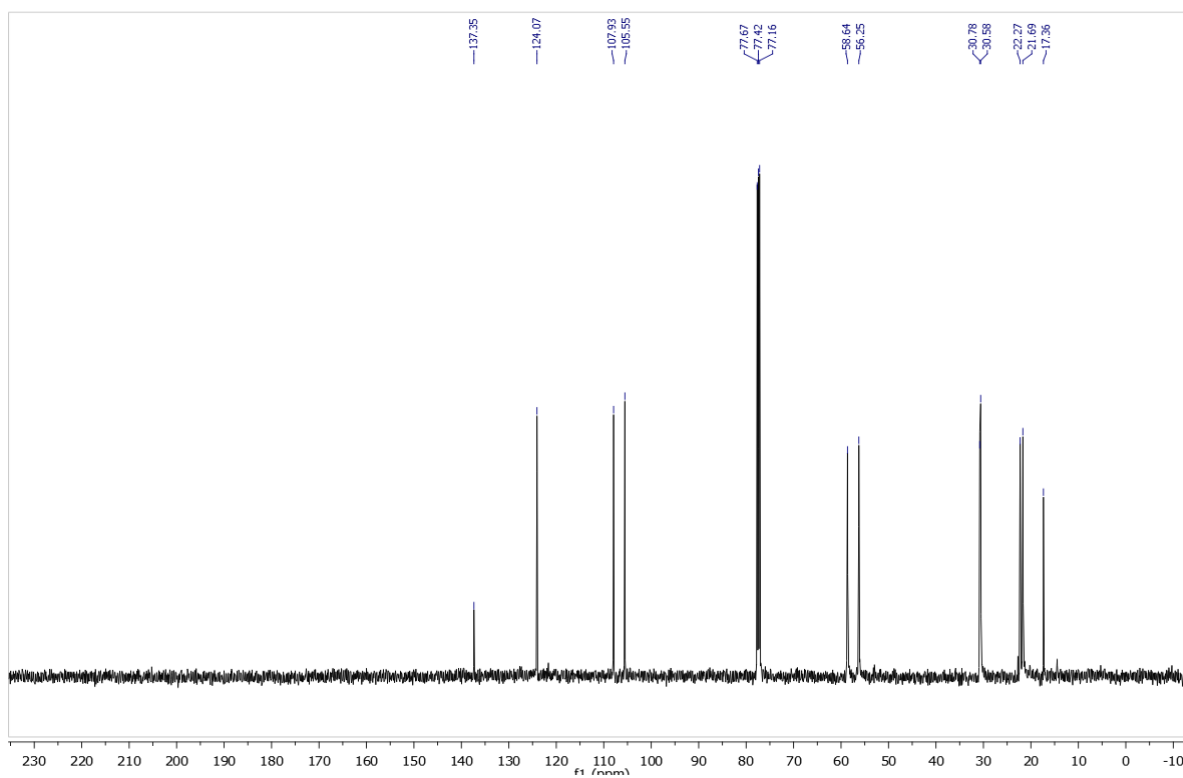


Figure 4-21.  $^{13}\text{C}$  NMR Spectrum of  $\text{NCr}(\text{NiPr}_2)_2(\text{Pyrr}^{\text{Me}})$  in  $\text{CDCl}_3$ .



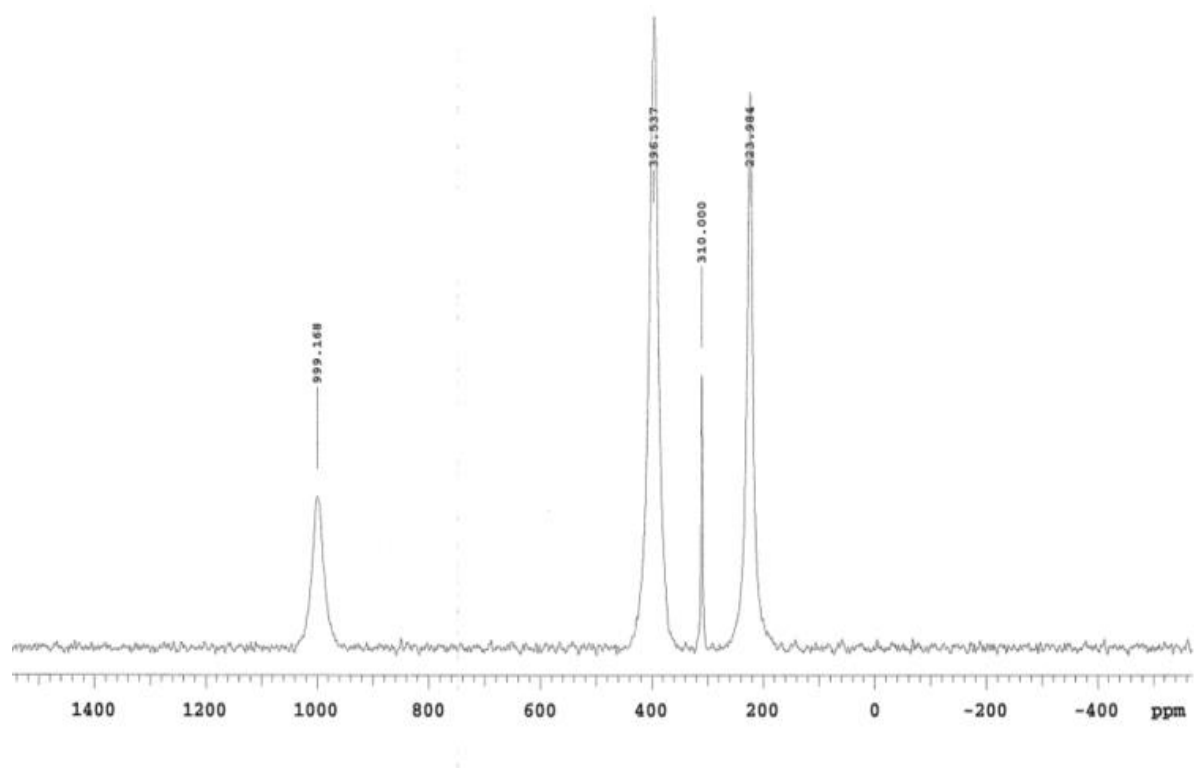


Figure 4-22.  $^{14}\text{N}$  NMR Spectrum of  $\text{NCr}(\text{N}^i\text{Pr}_2)_2(\text{Pyrr}^{\text{Me}})$  in  $\text{CDCl}_3$ .



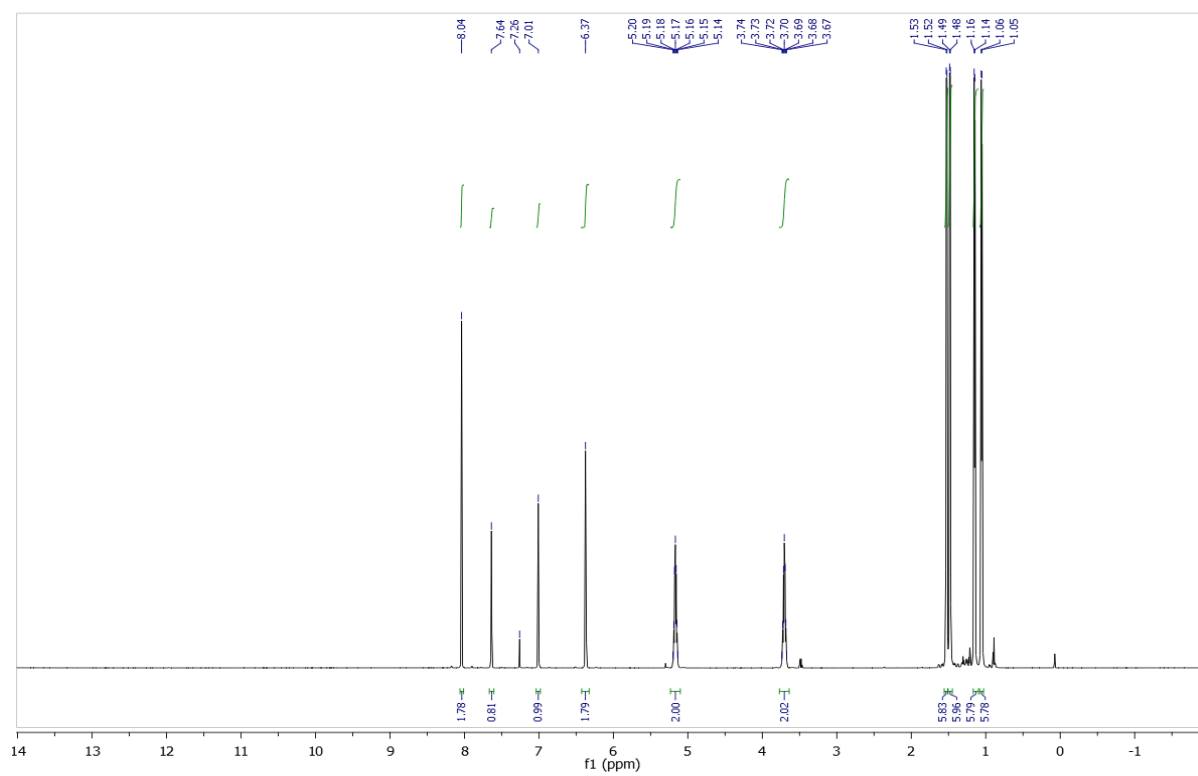


Figure 4-23.  $^1\text{H}$  NMR Spectrum of  $\text{NCr}(\text{NiPr}_2)_2(\text{Pyrr}^{2-}[\text{C}_6\text{H}_3(\text{CF}_3)_2])$  in  $\text{CDCl}_3$ .



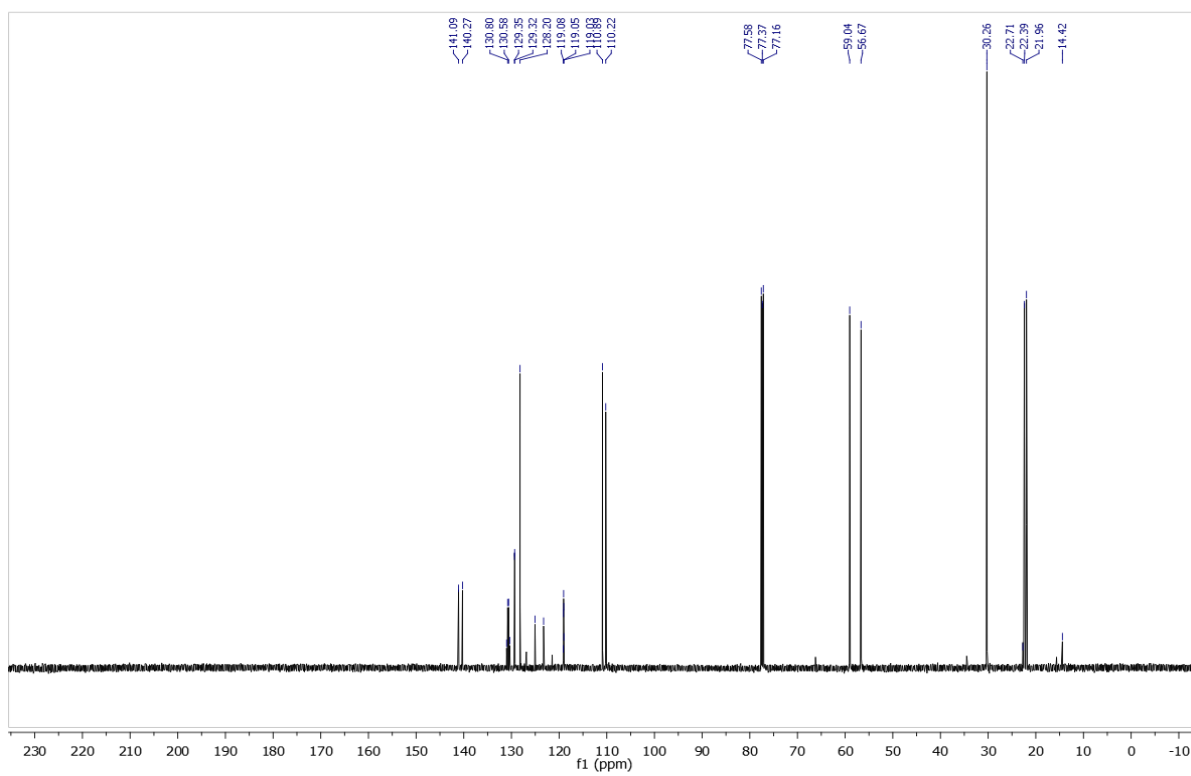


Figure 4-24.  $^{13}\text{C}$  NMR Spectrum of  $\text{NCr}(\text{N}^i\text{Pr}_2)_2(\text{Pyrr}^{2-}[\text{C}_6\text{H}_3(\text{CF}_3)_2])$  in  $\text{CDCl}_3$ .



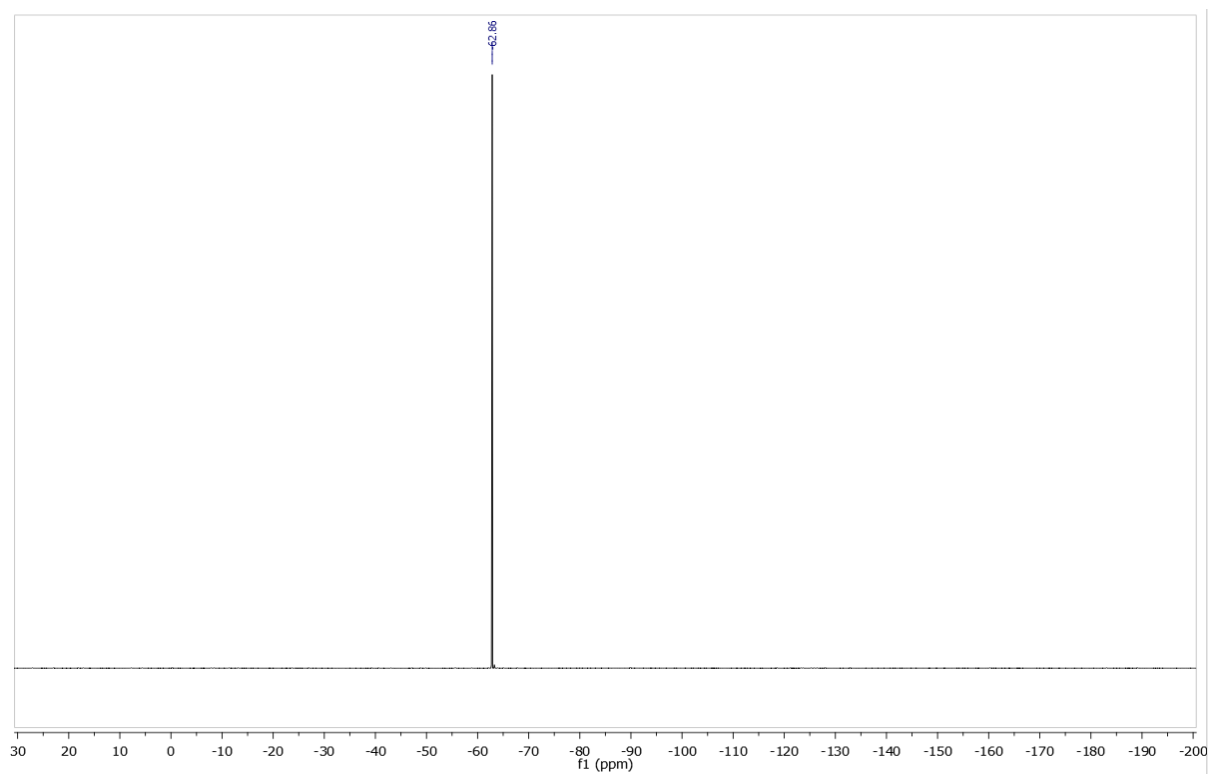


Figure 4-25.  $^{19}\text{F}$  NMR Spectrum of  $\text{NCr}(\text{N}^i\text{Pr}_2)_2(\text{Pyri}^{2-}[\text{C}_6\text{H}_3(\text{CF}_3)_2])$  in  $\text{CDCl}_3$



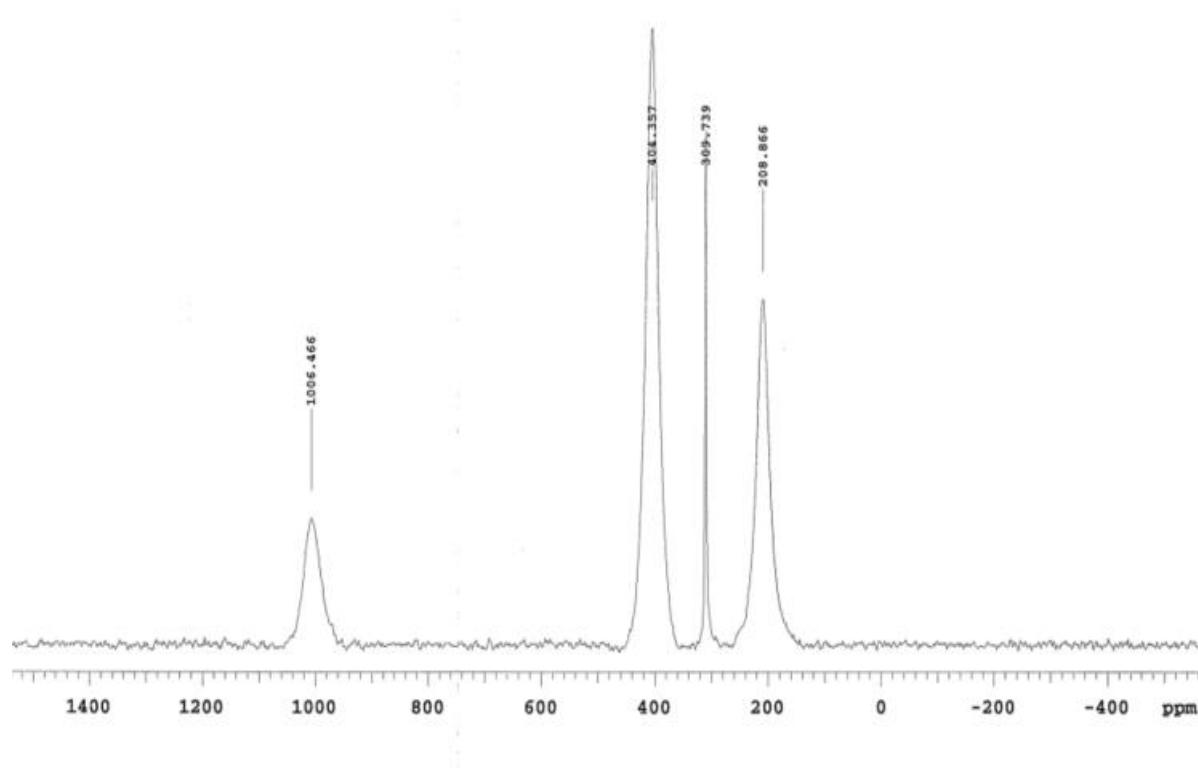


Figure 4-26.  $^{14}\text{N}$  NMR Spectrum of  $\text{NCr}(\text{N}^i\text{Pr}_2)_2(\text{Pyrr}^{2-}[\text{C}_6\text{H}_3(\text{CF}_3)_2])$  in  $\text{CDCl}_3$ .



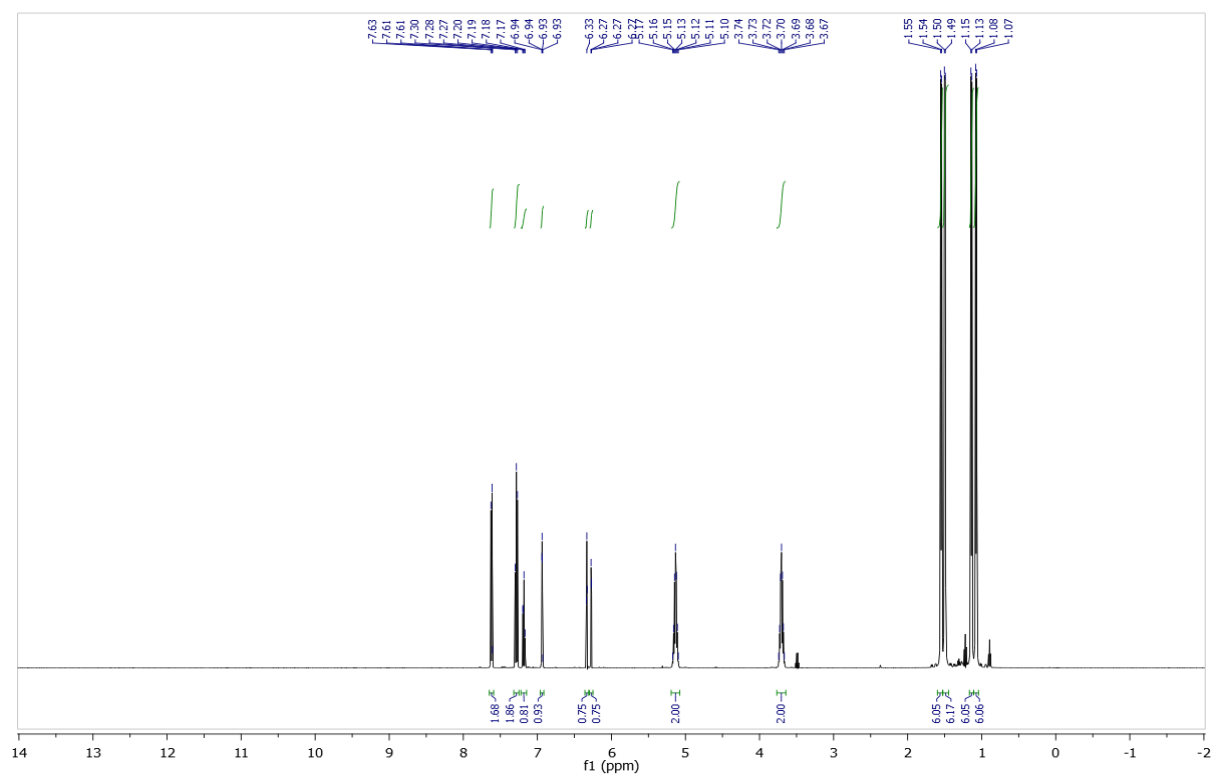


Figure 4-27.  $^1\text{H}$  NMR Spectrum of  $\text{NCr}(\text{NiPr}_2)_2(\text{Pyrr}^{\text{Ph}})$  in  $\text{CDCl}_3$ .



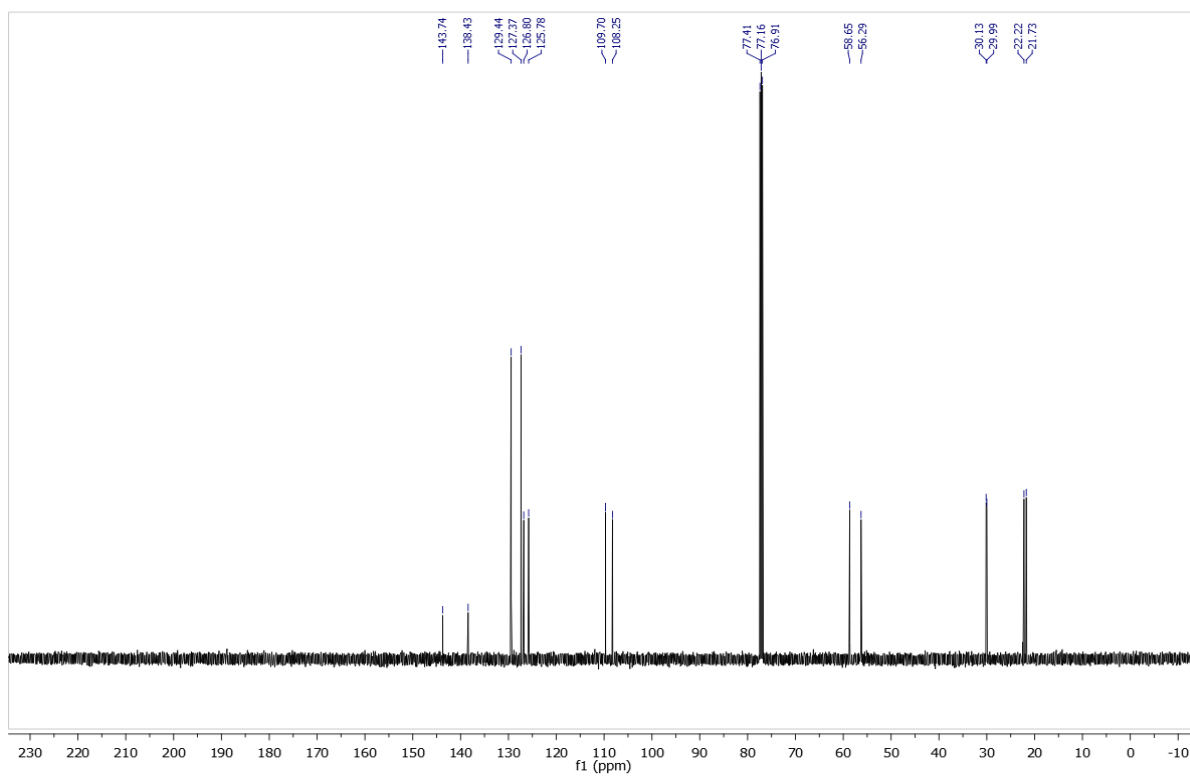


Figure 4-28.  $^{13}\text{C}$  NMR Spectrum of  $\text{NCr}(\text{NiPr}_2)_2(\text{Pyrr}^{\text{Ph}})$  in  $\text{CDCl}_3$ .



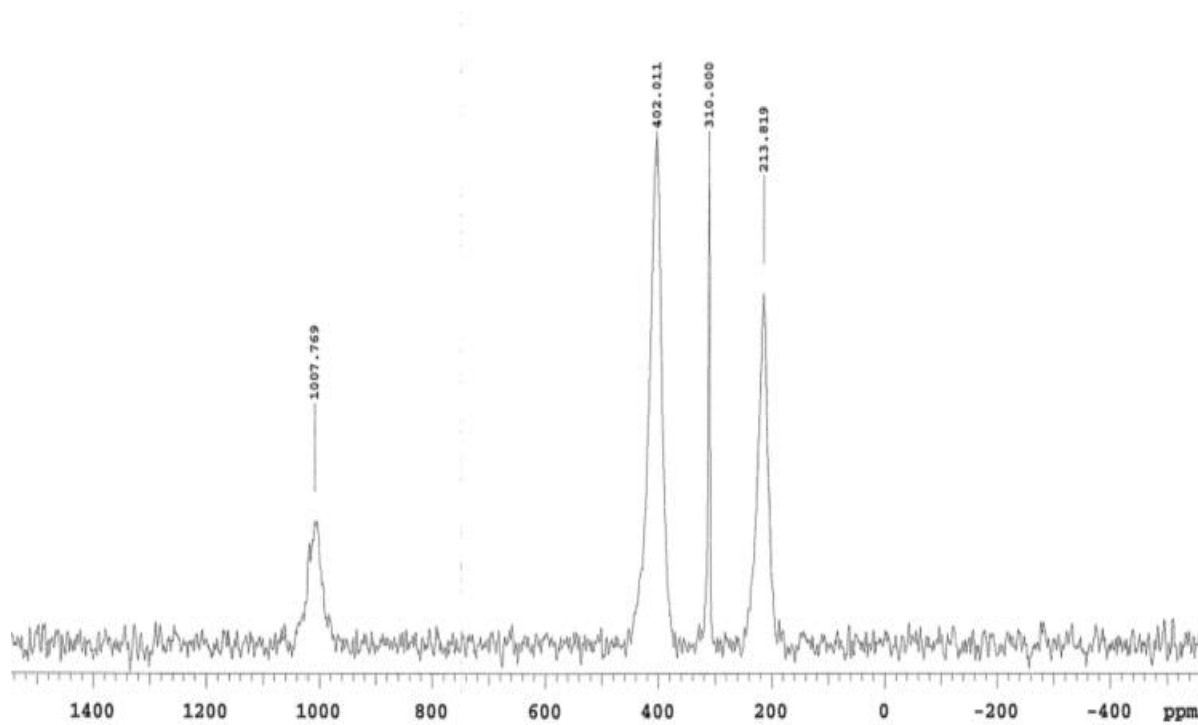


Figure 4-29.  $^{14}\text{N}$  NMR Spectrum of  $\text{NCr}(\text{N}^i\text{Pr}_2)_2(\text{Pyrr}^{\text{Ph}})$  in  $\text{CDCl}_3$ .



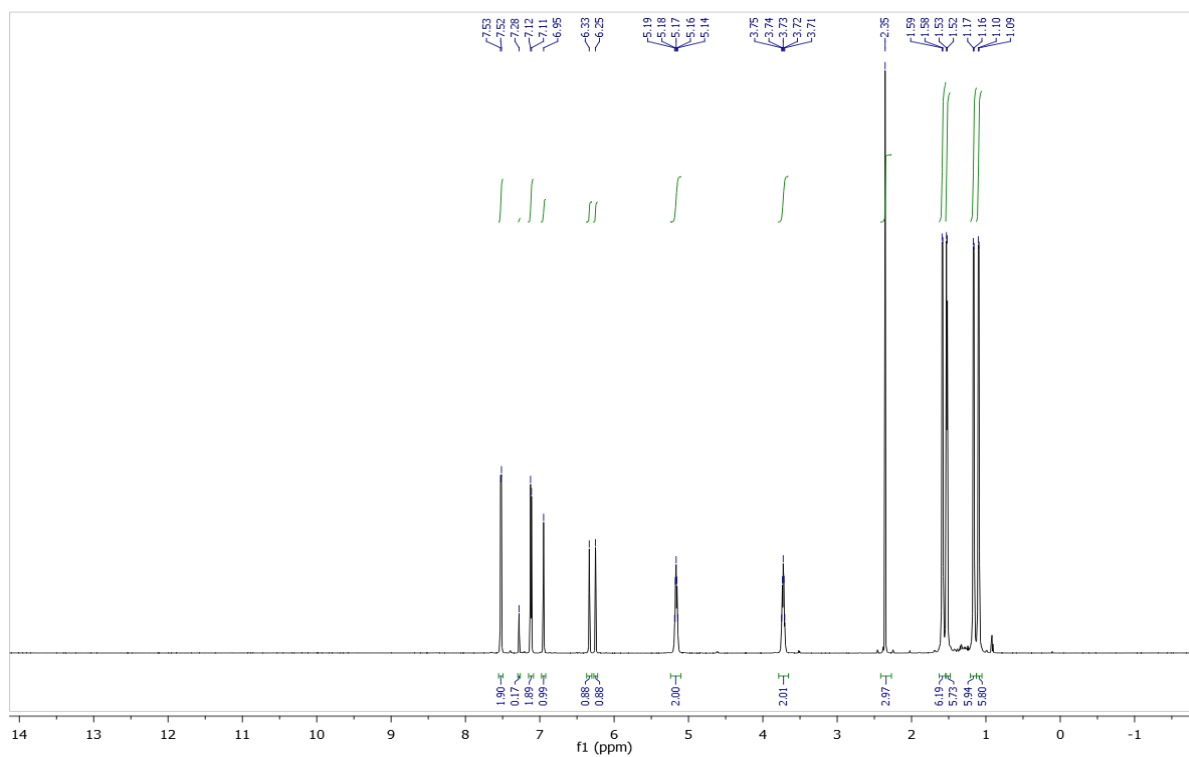


Figure 4-30.  $^1\text{H}$  NMR Spectrum of  $\text{NCr}(\text{N}^i\text{Pr}_2)_2(\text{Pyrr}^{\text{Tol}})$  in  $\text{CDCl}_3$ .



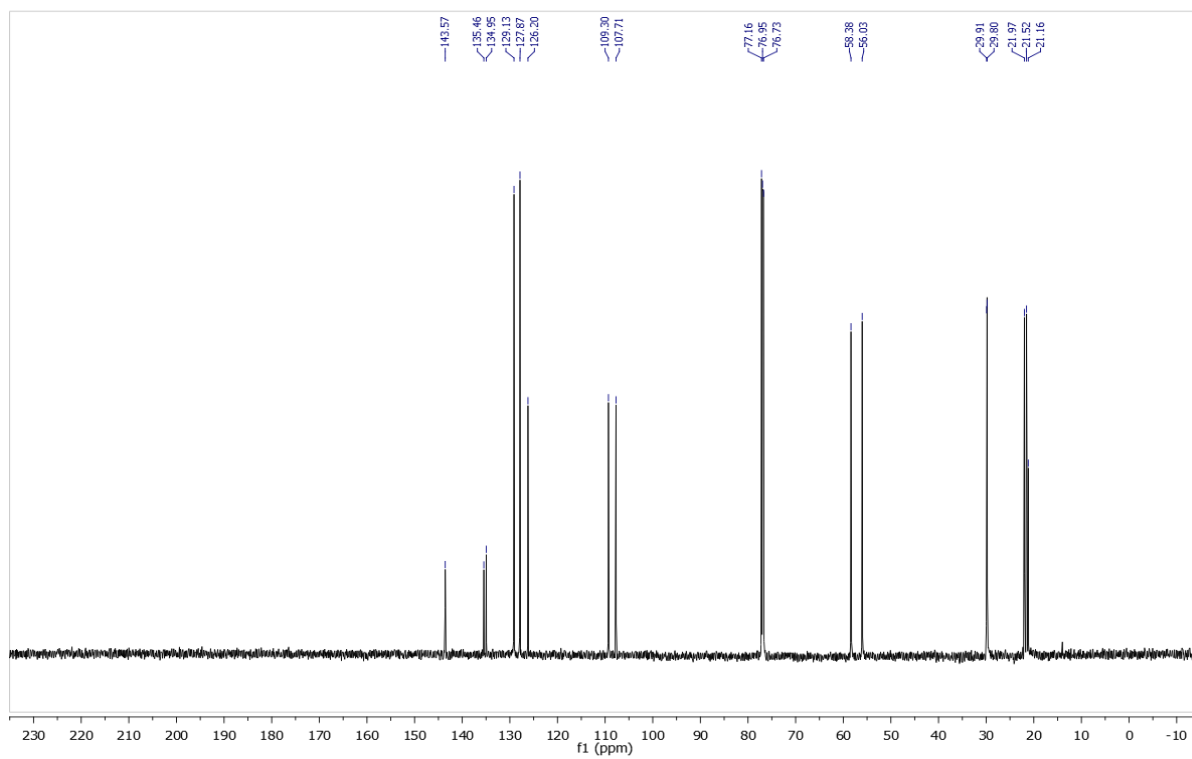


Figure 4-31.  $^{13}\text{C}$  NMR Spectrum of  $\text{NCr}(\text{NiPr}_2)_2(\text{Pyrr}^{\text{Tol}})$  in  $\text{CDCl}_3$ .



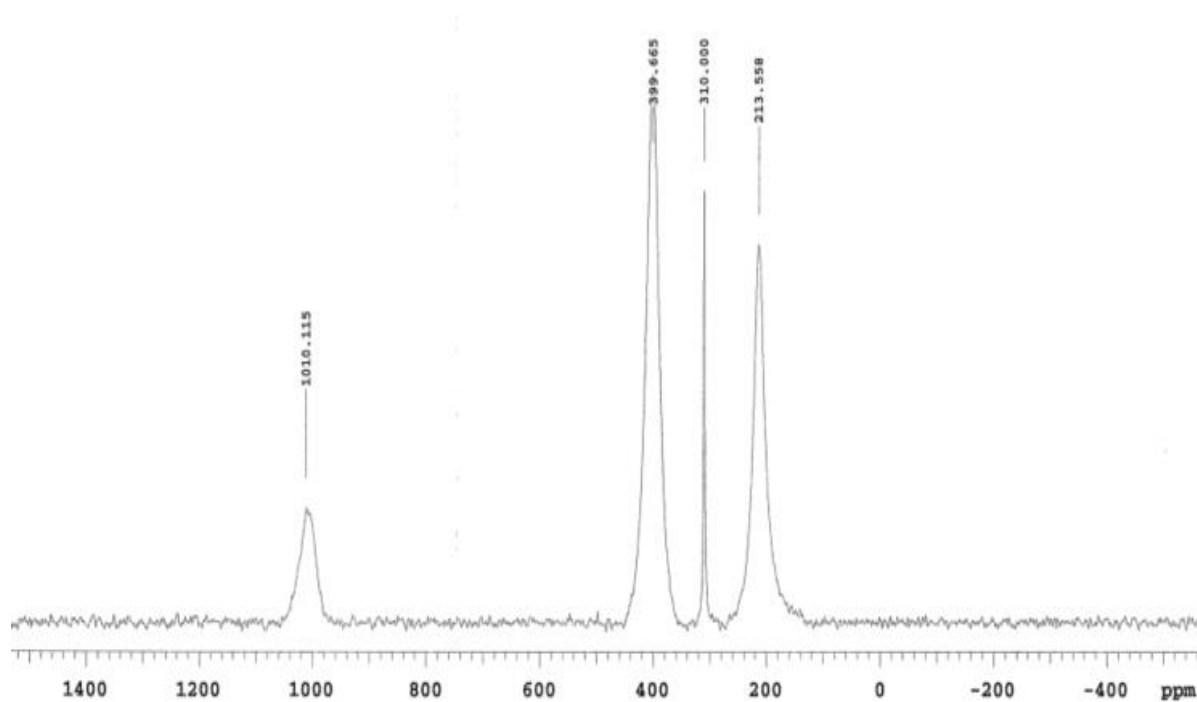


Figure 4-32.  $^{14}\text{N}$  NMR Spectrum of  $\text{NCr}(\text{NiPr}_2)_2(\text{Pyrr}^{\text{Tol}})$  in  $\text{CDCl}_3$ .



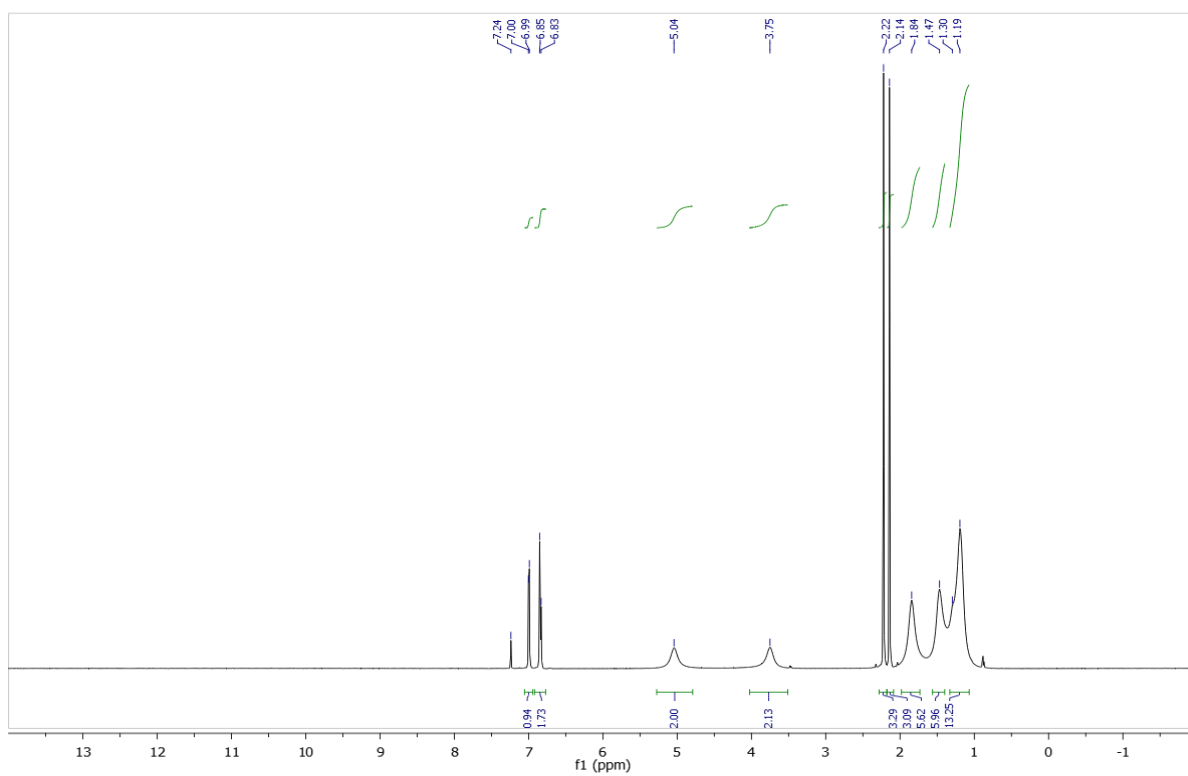


Figure 4-33.  $^1\text{H}$  NMR Spectrum of  $\text{NCr}(\text{N}^i\text{Pr}_2)_2(\text{OPh}^{2,4\text{-diMe}})$  in  $\text{CDCl}_3$ .



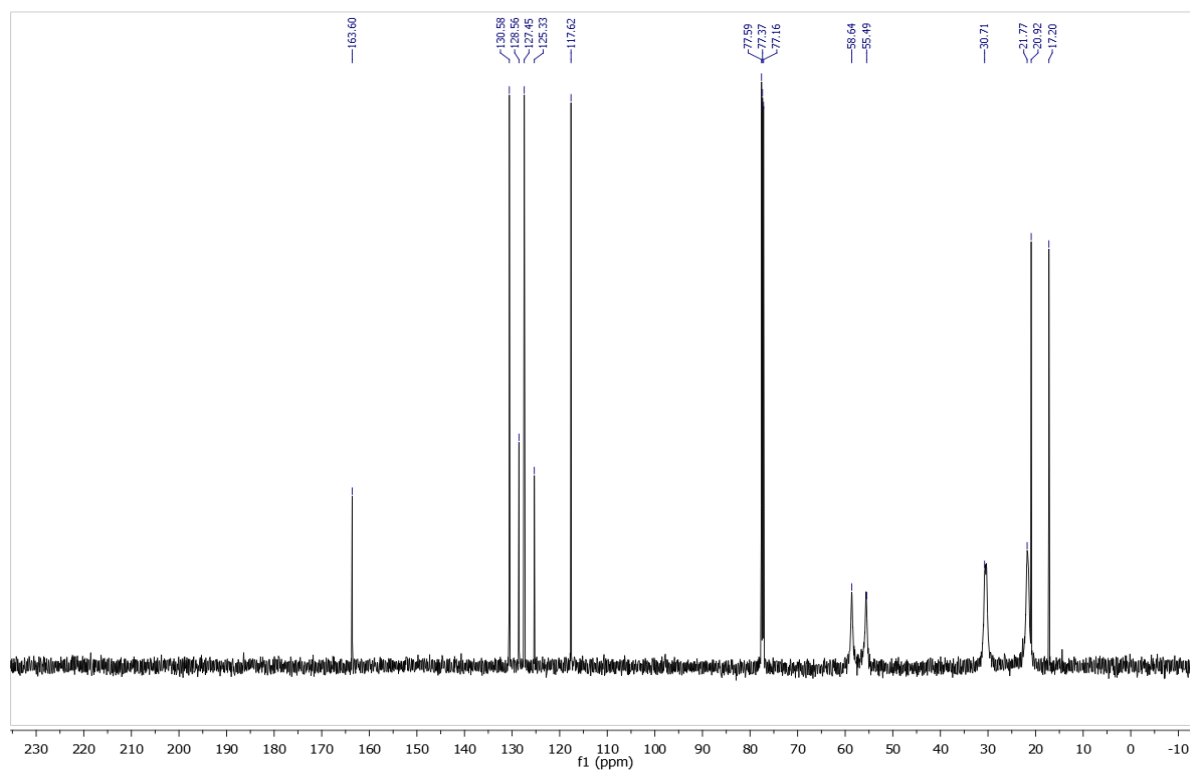


Figure 4-34.  $^{13}\text{C}$  NMR Spectrum of  $\text{NCr}(\text{N}^i\text{Pr}_2)_2(\text{OPh}^{2,4\text{-diMe}})$  in  $\text{CDCl}_3$ .



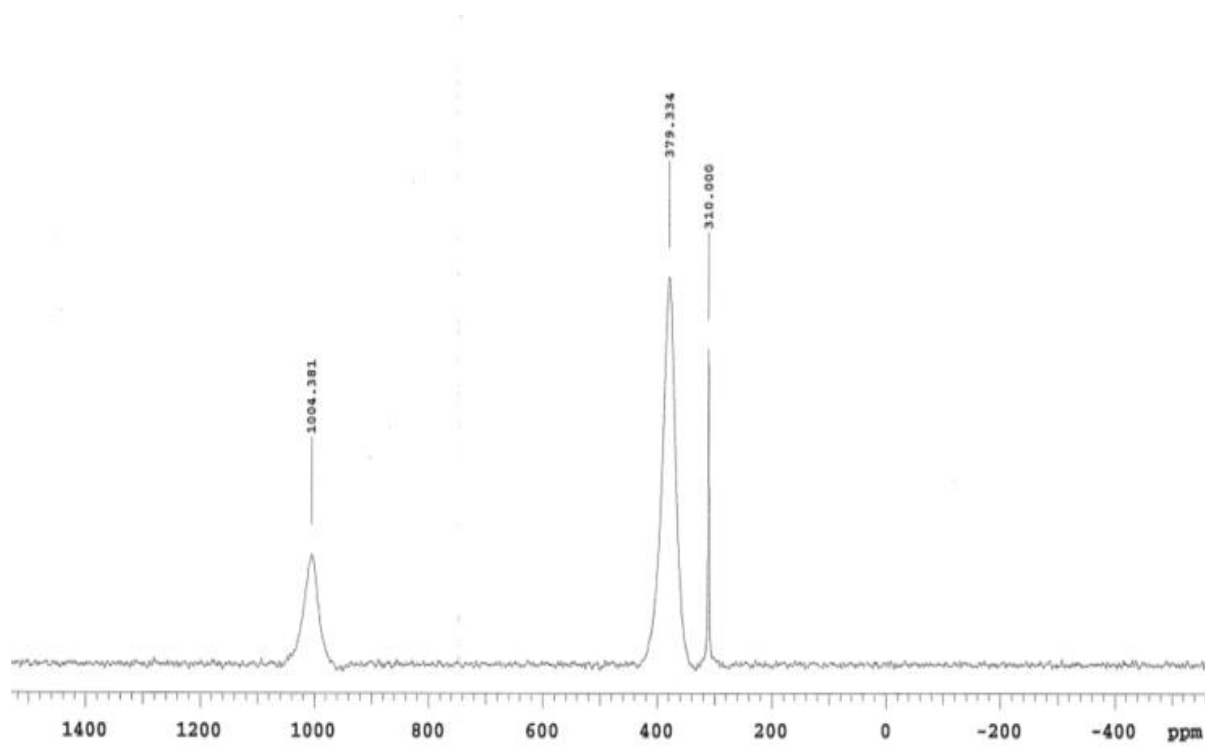


Figure 4-35.  $^{14}\text{N}$  NMR Spectrum of  $\text{NCr}(\text{N}^i\text{Pr}_2)_2(\text{OPh}^{2,4\text{-diMe}})$  in  $\text{CDCl}_3$ .



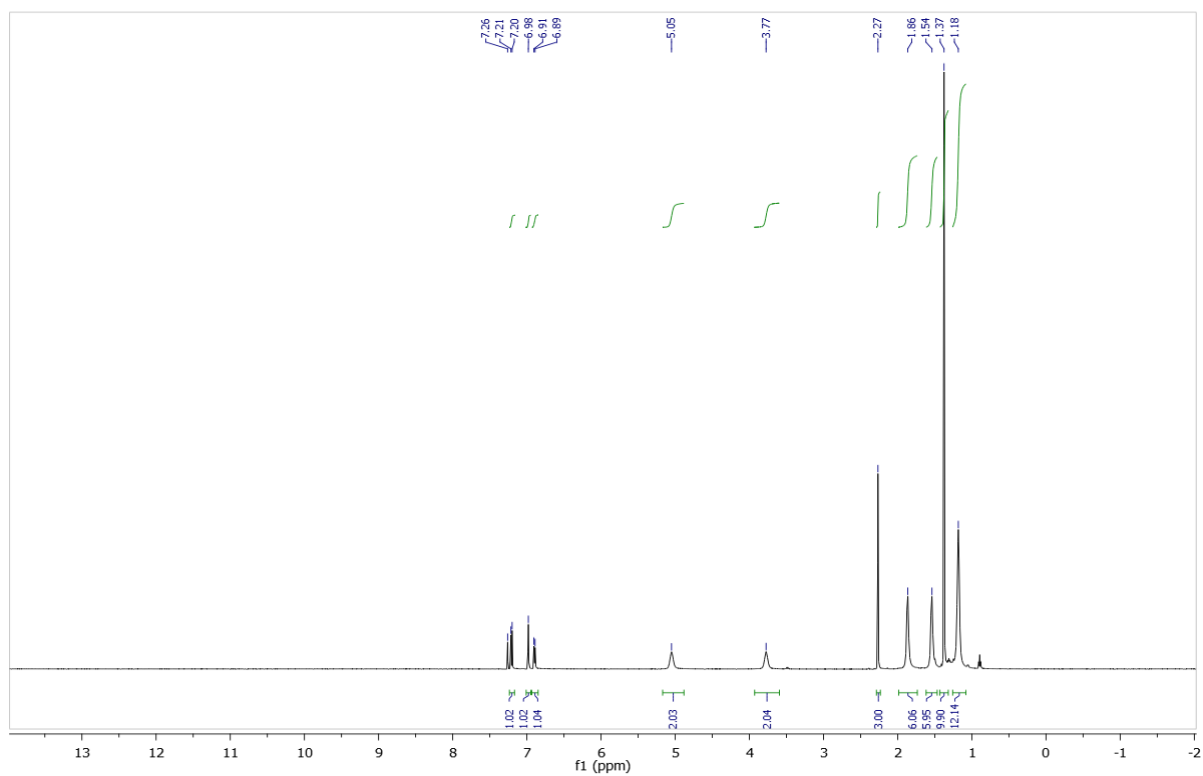


Figure 4-36.  $^1\text{H}$  NMR Spectrum of  $\text{NCr}(\text{N}^i\text{Pr}_2)_2(\text{OPh}^{2\text{-tBu-4-Me}})$  in  $\text{CDCl}_3$ .



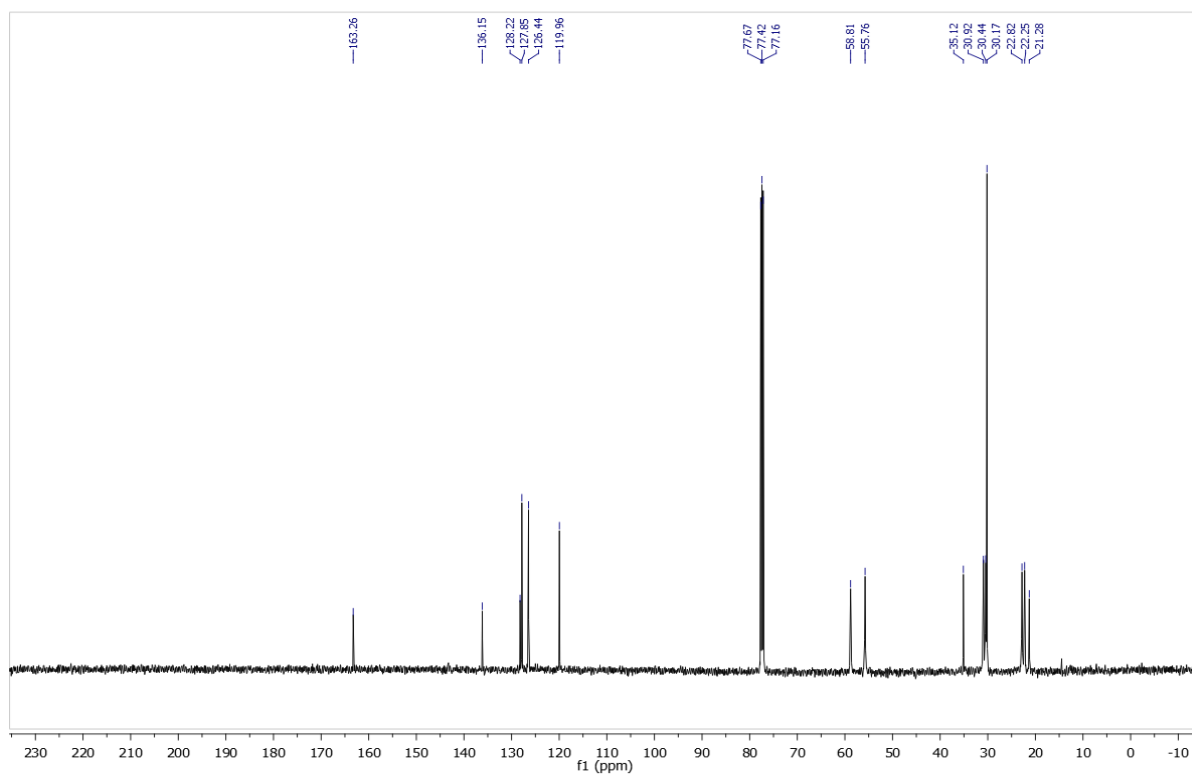


Figure 4-37.  $^{13}\text{C}$  NMR Spectrum of  $\text{NCr}(\text{N}^i\text{Pr}_2)_2(\text{OPh}^{2\text{-tBu-4-Me}})$  in  $\text{CDCl}_3$ .



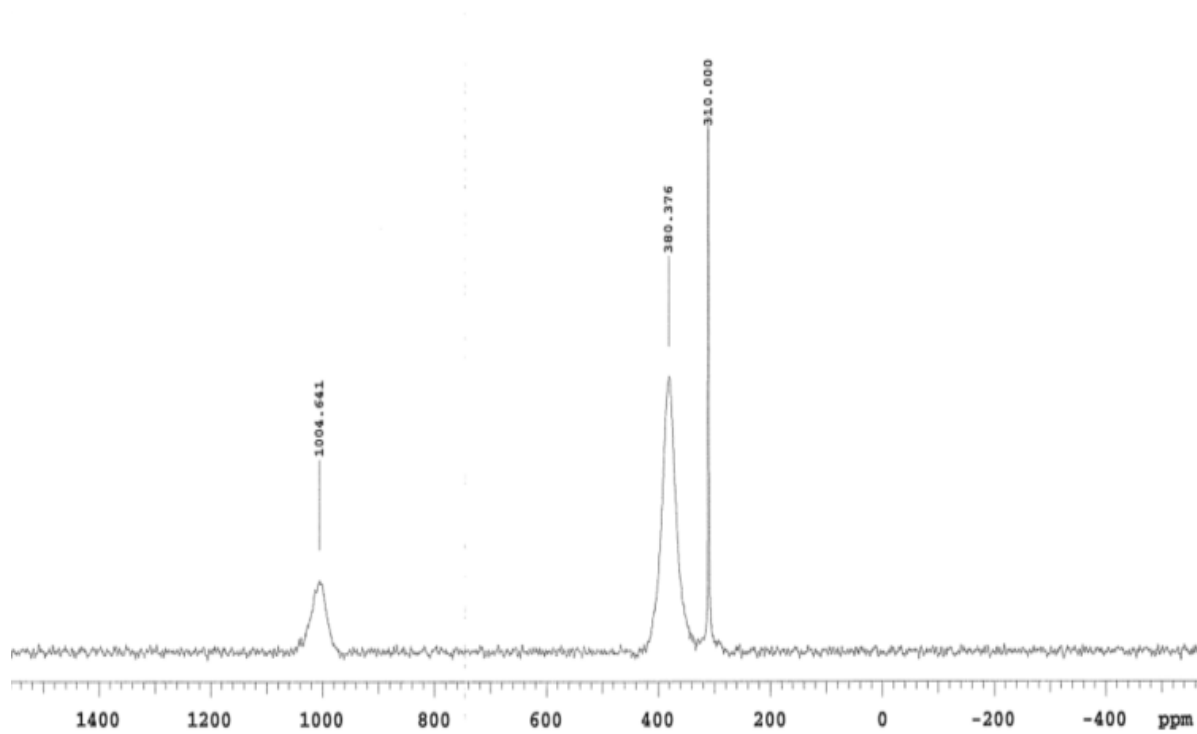


Figure 4-38.  $^{14}\text{N}$  NMR Spectrum of  $\text{NCr}(\text{N}^i\text{Pr}_2)_2(\text{OPh}^{2\text{-tBu-4-Me}})$  in  $\text{CDCl}_3$ .



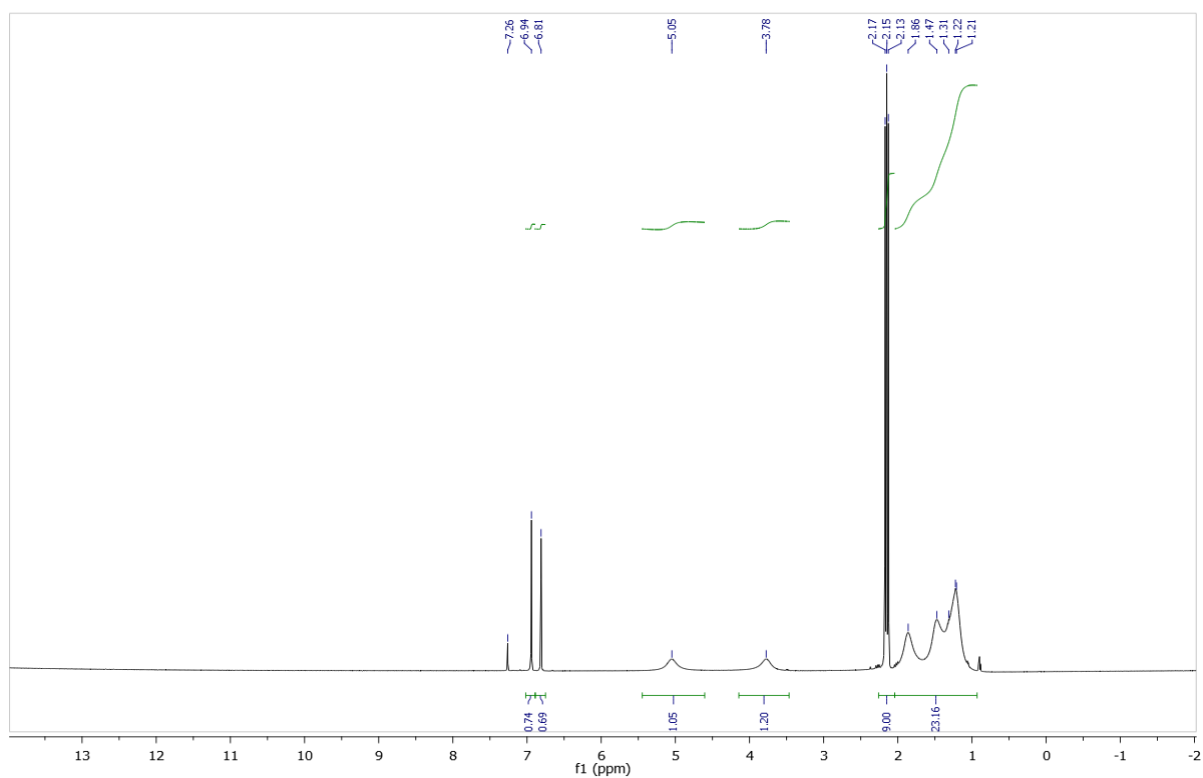


Figure 4-39. <sup>1</sup>H NMR Spectrum of  $\text{NCr}(\text{N}^i\text{Pr}_2)_2(\text{OPh}^{2,4,5\text{-triMe}})$  in  $\text{CDCl}_3$ .



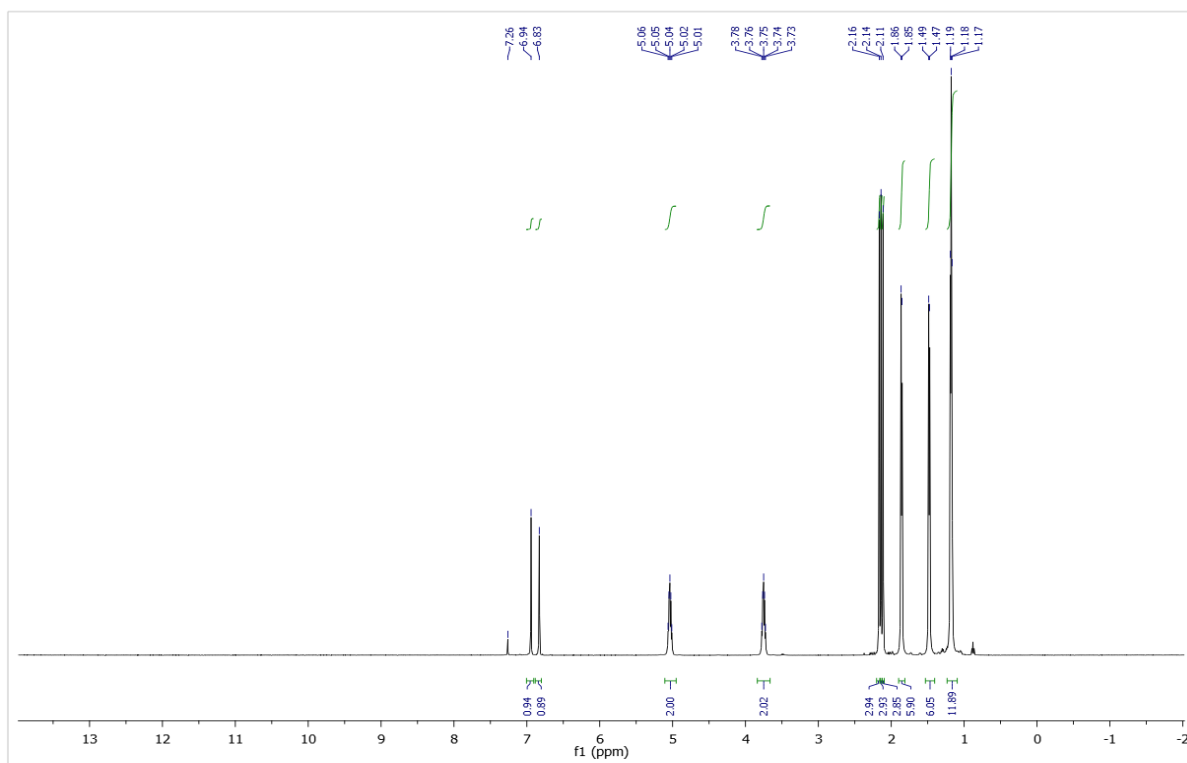


Figure 4-40.  $^1\text{H}$  NMR Spectrum of  $\text{NCr}(\text{N}^i\text{Pr}_2)_2(\text{OPh}^{2,4,5\text{-triMe}})$  in  $\text{CDCl}_3$  at  $-29^\circ\text{C}$ .



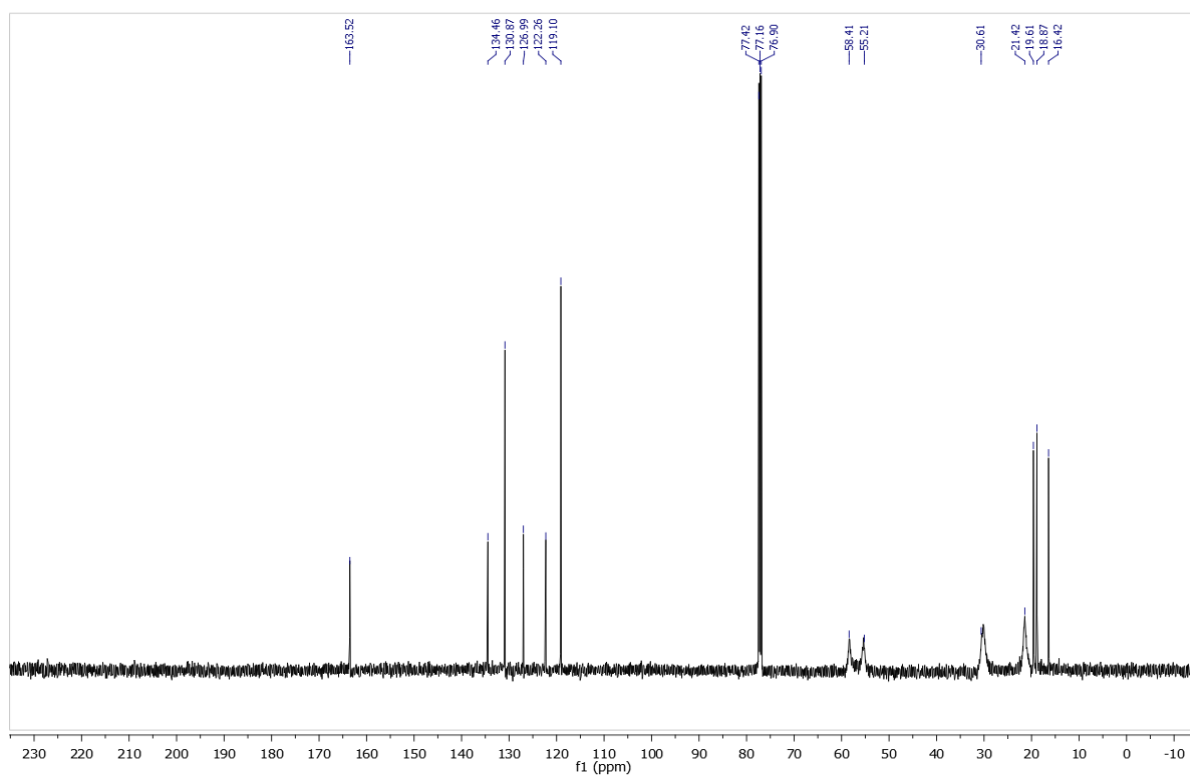


Figure 4-41.  $^1\text{H}$  NMR Spectrum of  $\text{NCr}(\text{N}^i\text{Pr}_2)_2(\text{OPh}^{2,4,5\text{-triMe}})$  in  $\text{CDCl}_3$  at  $-29^\circ\text{C}$ .



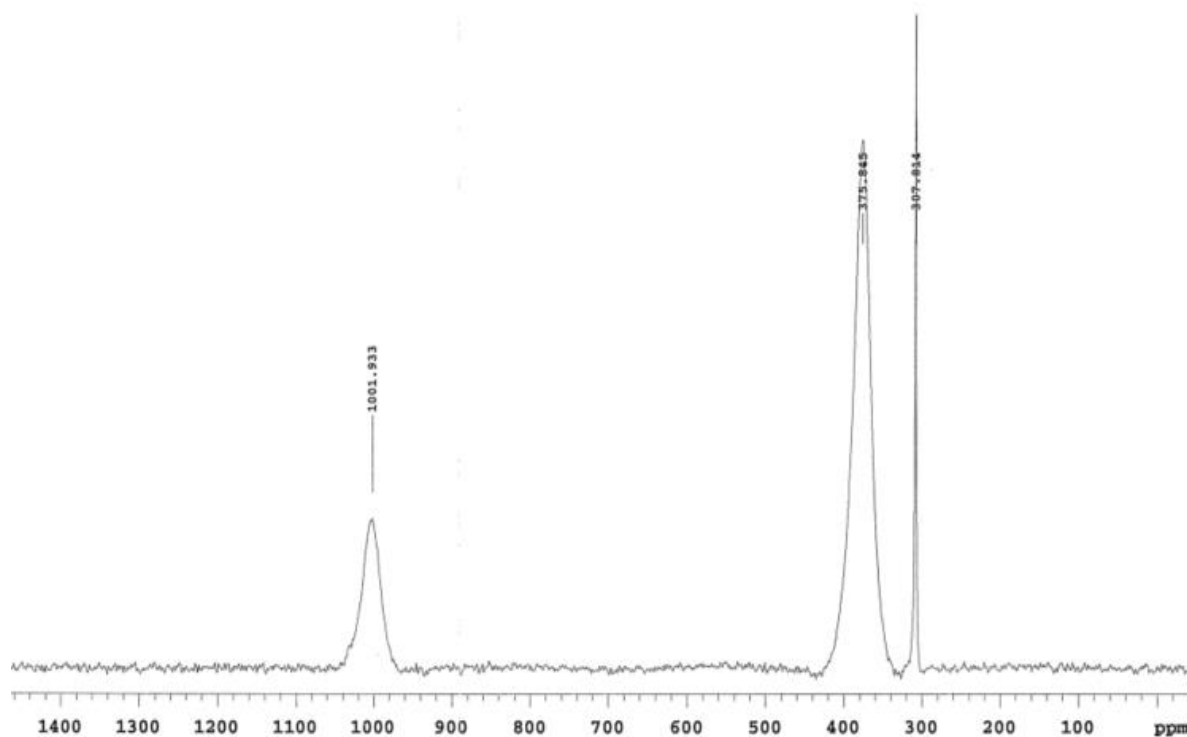


Figure 4-42.  $^{14}\text{N}$  NMR Spectrum of  $\text{NCr}(\text{N}^i\text{Pr}_2)_2(\text{OPh}^{2,4,5\text{-triMe}})$  in  $\text{CDCl}_3$ .



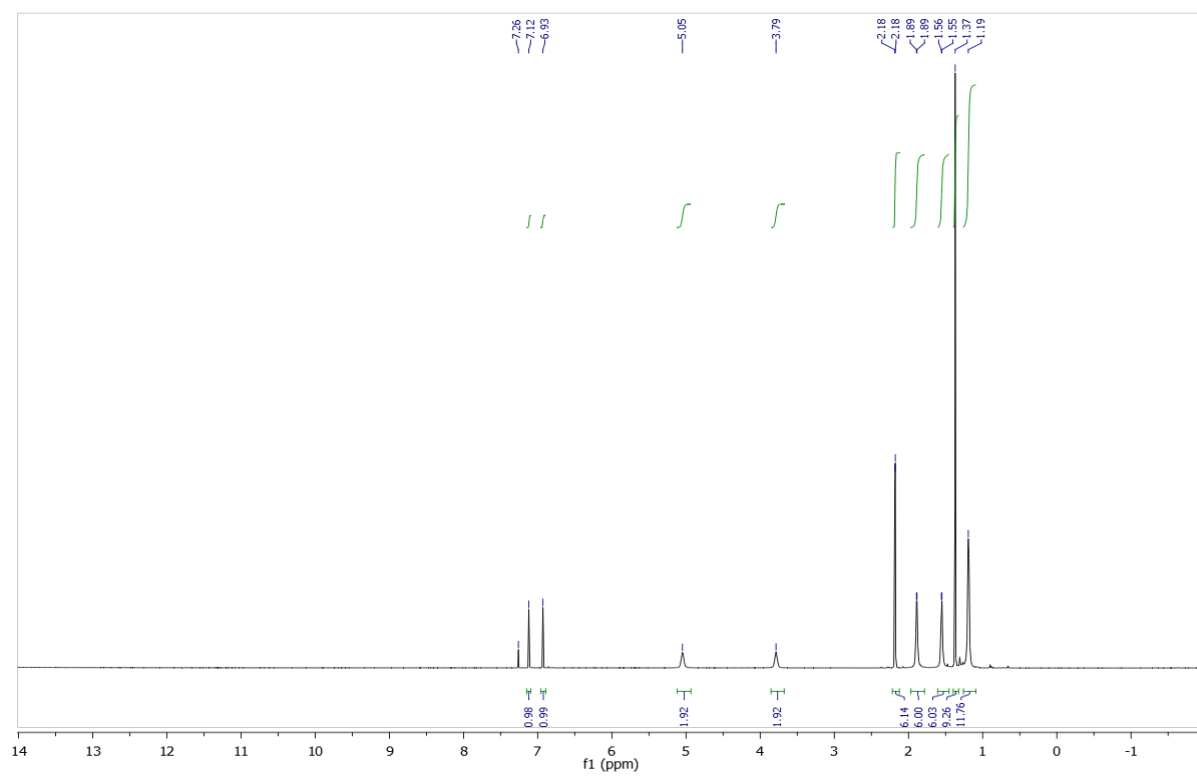


Figure 4-43.  $^1\text{H}$  NMR Spectrum of  $\text{NCr}(\text{NiPr}_2)_2(\text{OPh}^{2\text{-tBu-4,5-diMe}})$  in  $\text{CDCl}_3$ .



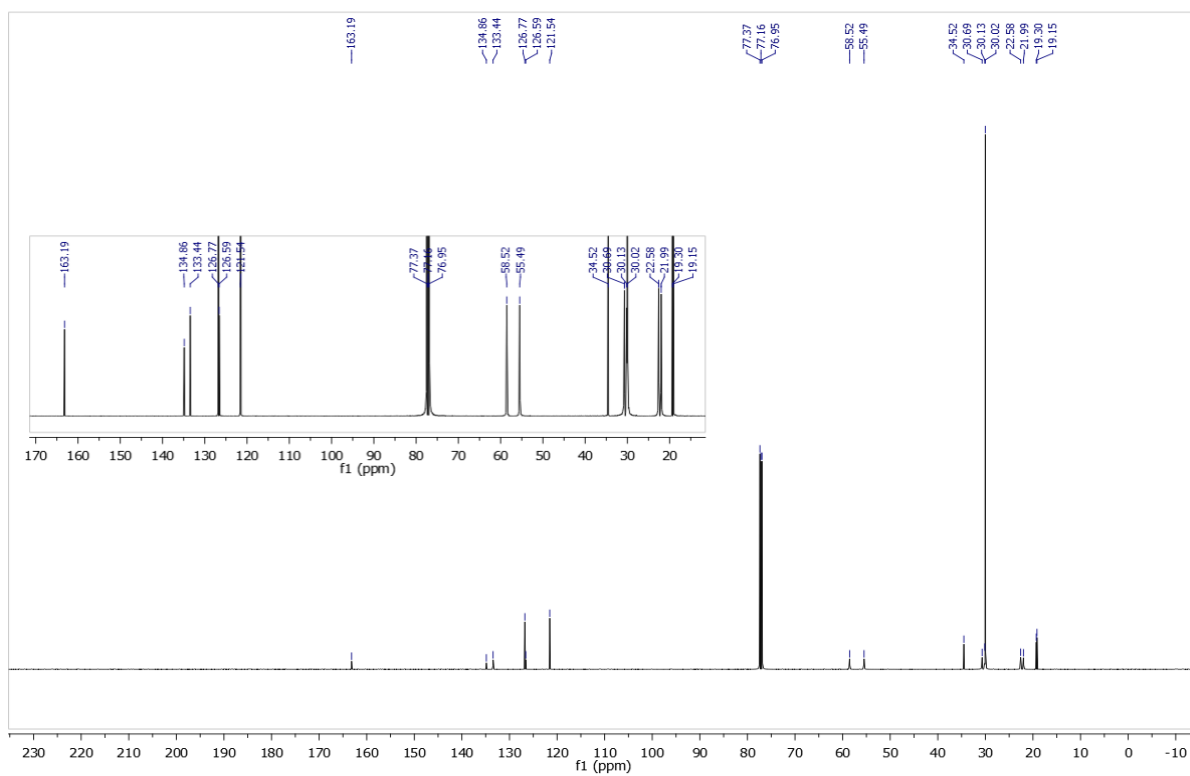


Figure 4-44.  $^{13}\text{C}$  NMR Spectrum of  $\text{NCr}(\text{N}^i\text{Pr}_2)_2(\text{OPh}^{2\text{-tBu-4,5-diMe}})$  in  $\text{CDCl}_3$ .



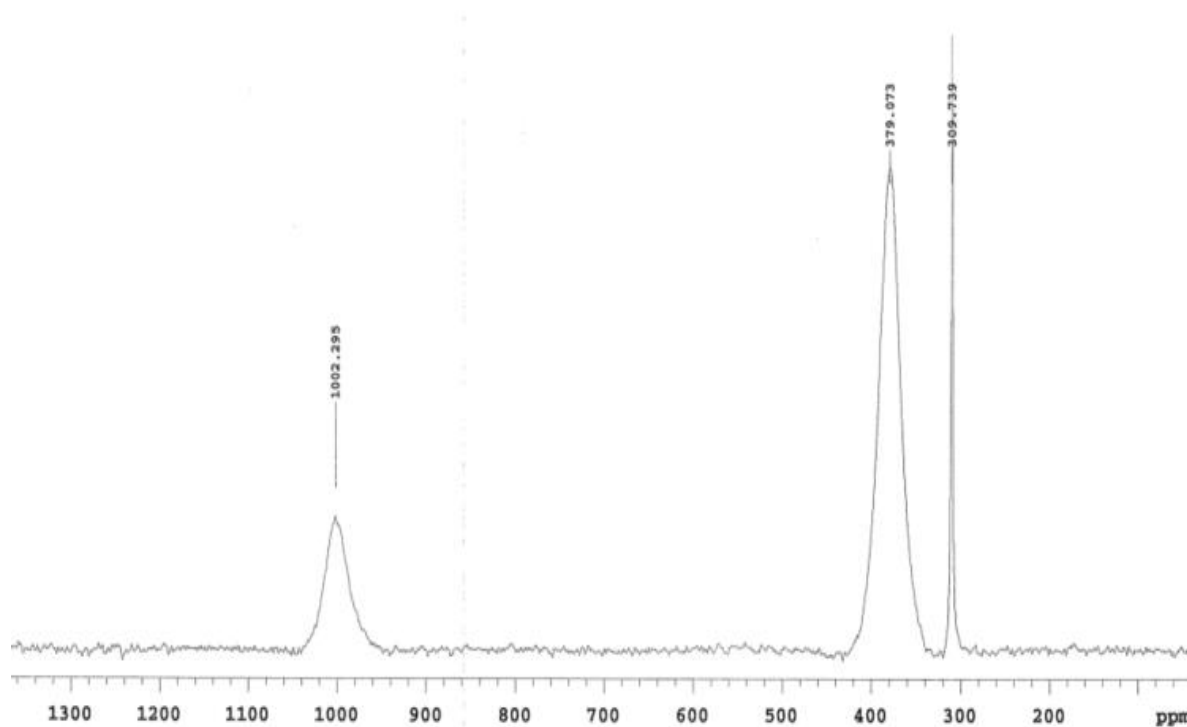


Figure 4-45.  $^{14}\text{N}$  NMR Spectrum of  $\text{NCr}(\text{N}^i\text{Pr}_2)_2(\text{OPh}^{2\text{-tBu-4,5-diMe}})$  in  $\text{CDCl}_3$ .



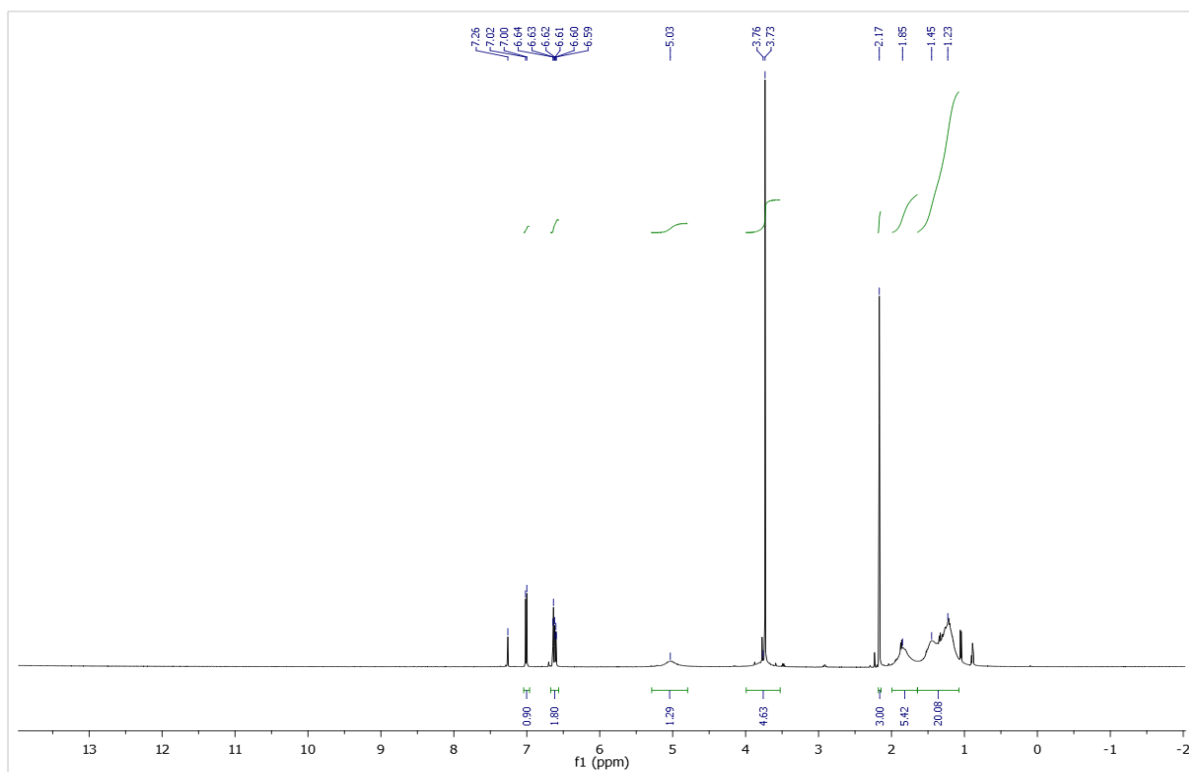


Figure 4-46.  $^1\text{H}$  NMR Spectrum of  $\text{NCr}(\text{N}^i\text{Pr}_2)_2(\text{OPh}^{2\text{-Me-4-OMe}})$  in  $\text{CDCl}_3$ .



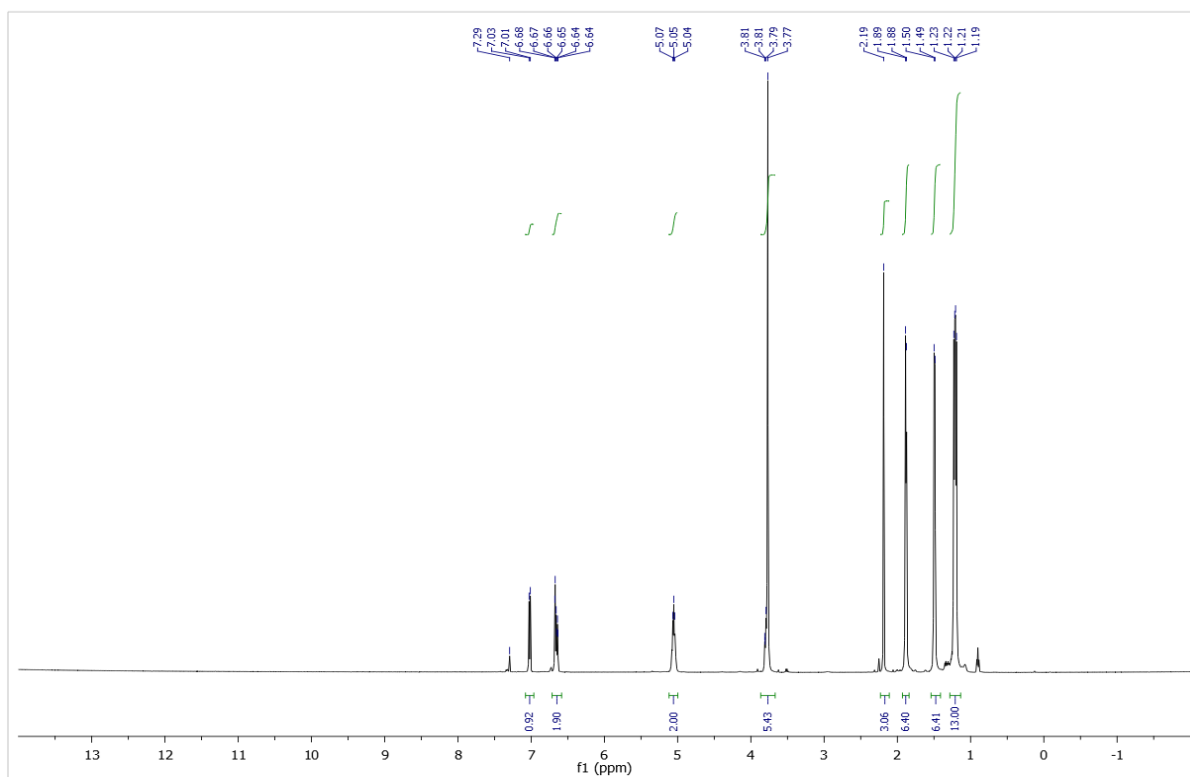


Figure 4-47.  $^1\text{H}$  NMR Spectrum of  $\text{NCr}(\text{N}^i\text{Pr}_2)_2(\text{OPh}^{2\text{-Me-4-OMe}})$  in  $\text{CDCl}_3$  at  $-26^\circ\text{C}$ .



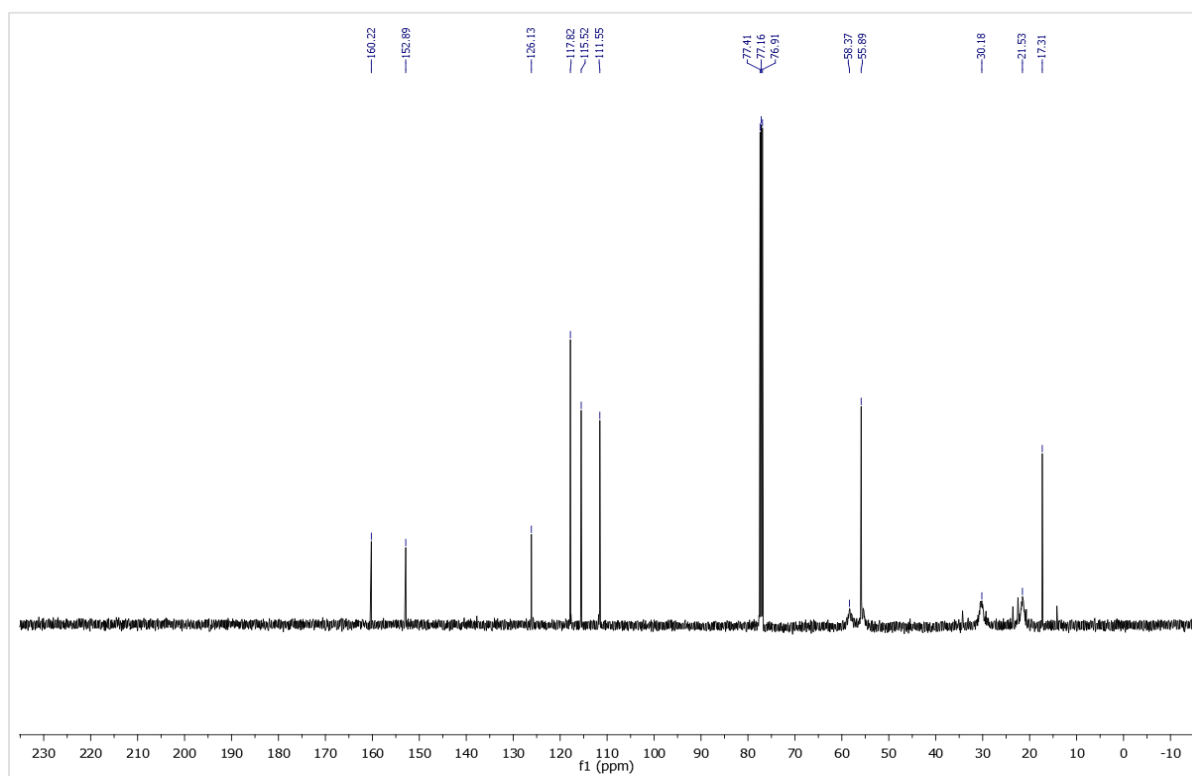


Figure 4-48.  $^{13}\text{C}$  NMR Spectrum of  $\text{NCr}(\text{N}^i\text{Pr}_2)_2(\text{OPh}^{2\text{-Me-4-OMe}})$  in  $\text{CDCl}_3$ .



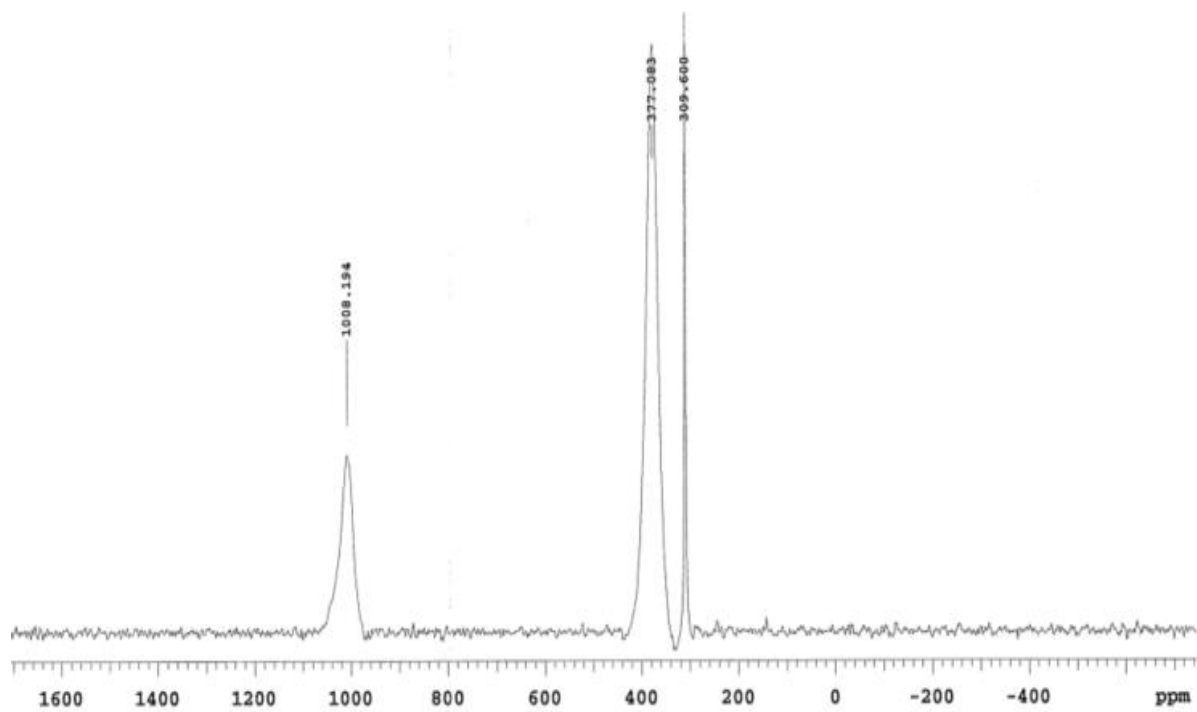


Figure 4-49.  $^{14}\text{N}$  NMR Spectrum of  $\text{NCr}(\text{N}^i\text{Pr}_2)_2(\text{OPh}^{2\text{-Me-4-OMe}})$  in  $\text{CDCl}_3$ .



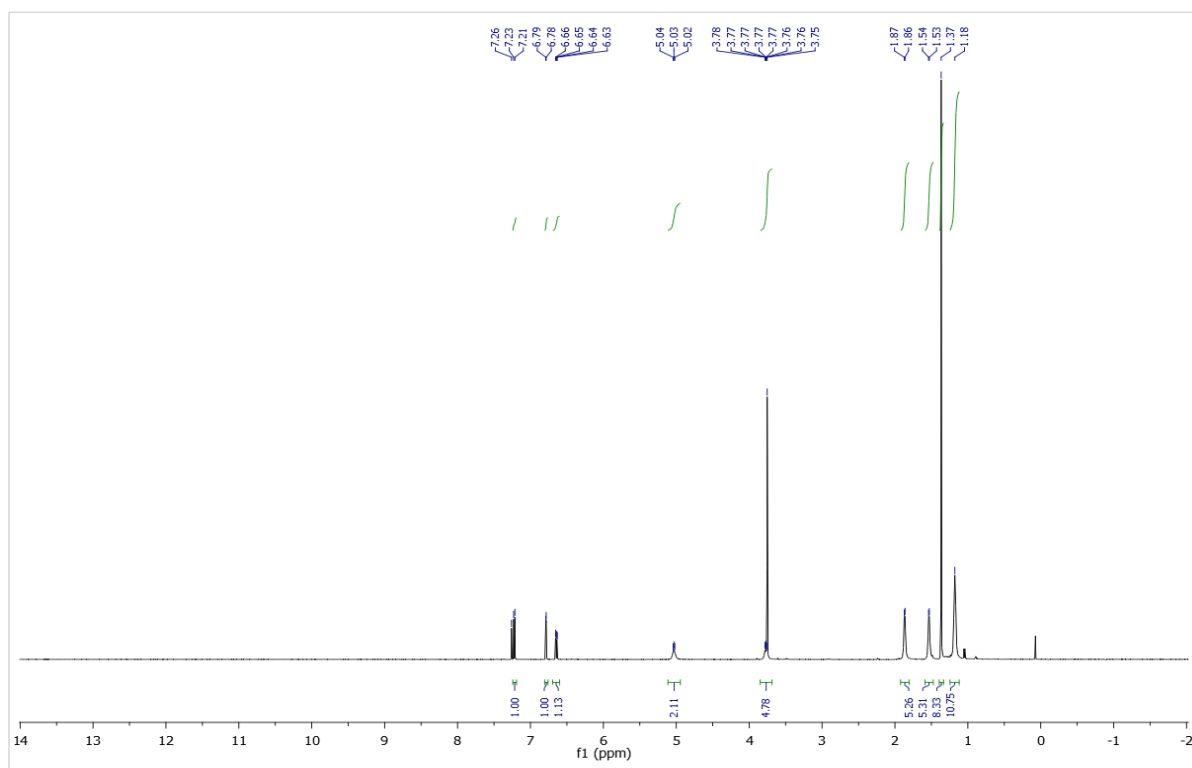


Figure 4-50.  $^1\text{H}$  NMR Spectrum of  $\text{NCr}(\text{N}^i\text{Pr}_2)_2(\text{OPh}^{2\text{-tBu-4-OMe}})$  in  $\text{CDCl}_3$ .



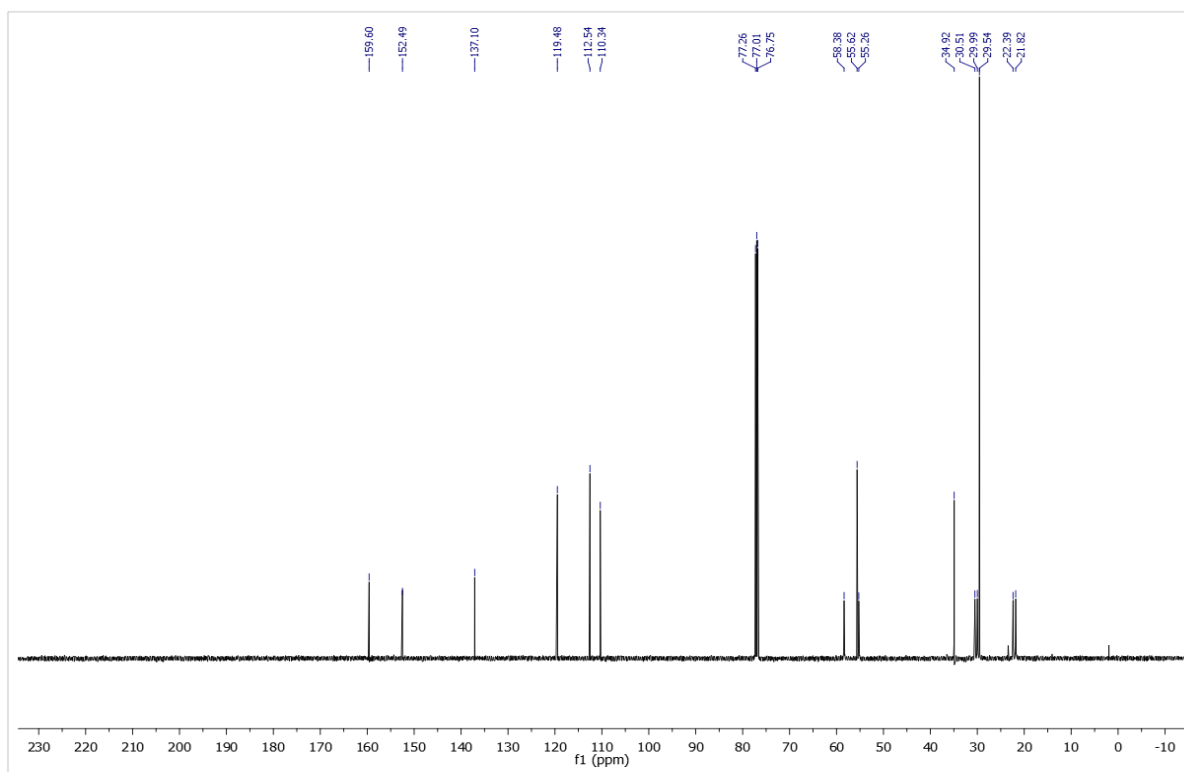


Figure 4-51.  $^{13}\text{C}$  NMR Spectrum of  $\text{NCr}(\text{N}^i\text{Pr}_2)_2(\text{OPh}^{2\text{-tBu-4-OMe}})$  in  $\text{CDCl}_3$ .



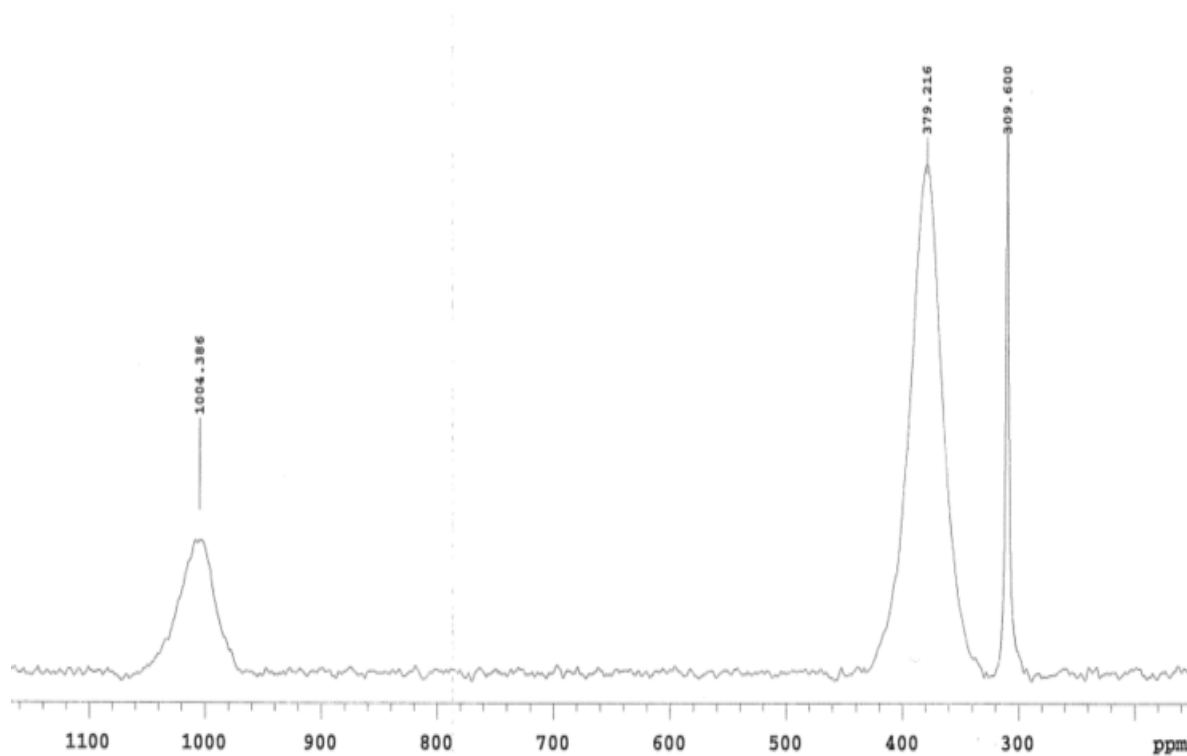


Figure 4-52.  $^{14}\text{N}$  NMR Spectrum of  $\text{NCr}(\text{N}^i\text{Pr}_2)_2(\text{OPh}^{2\text{-tBu-4-OMe}})$  in  $\text{CDCl}_3$ .



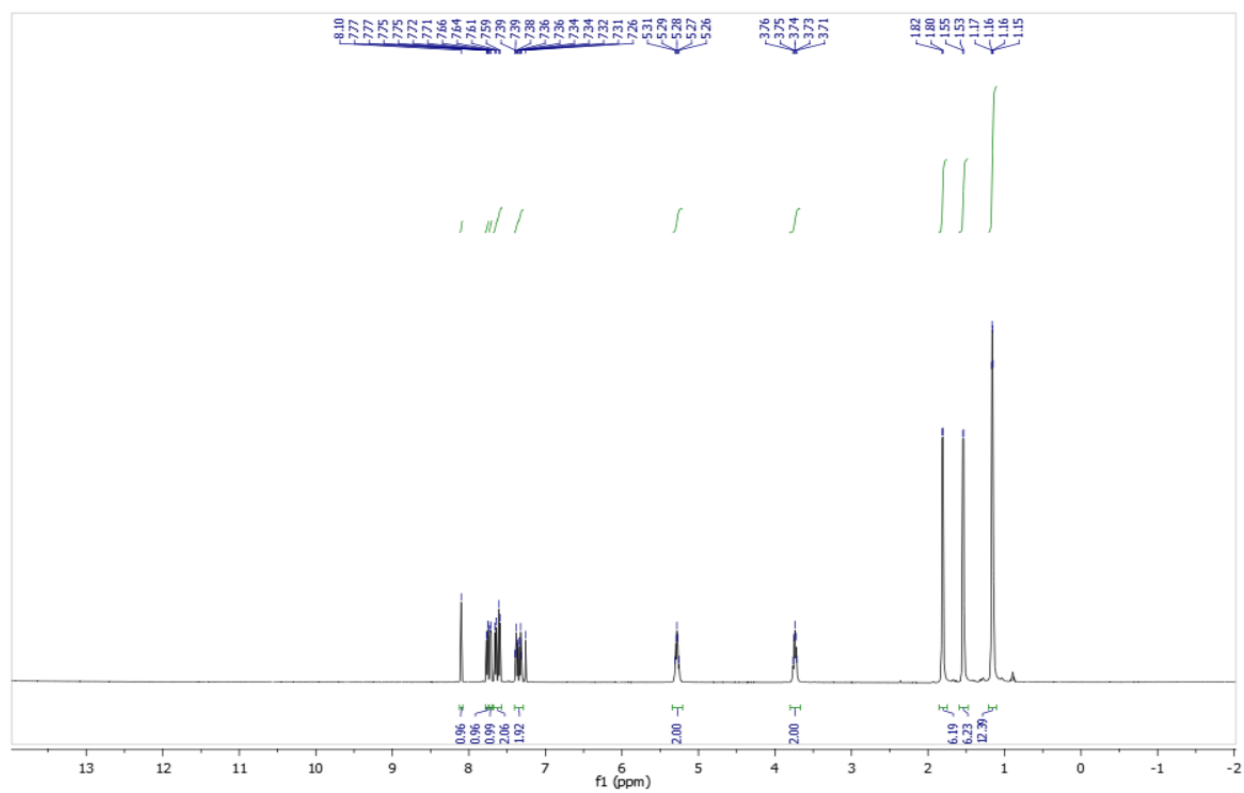


Figure 4-53.  $^1\text{H}$  NMR Spectrum of  $\text{NCr}(\text{N}^i\text{Pr}_2)_2(\text{SNap})$  in  $\text{CDCl}_3$ .



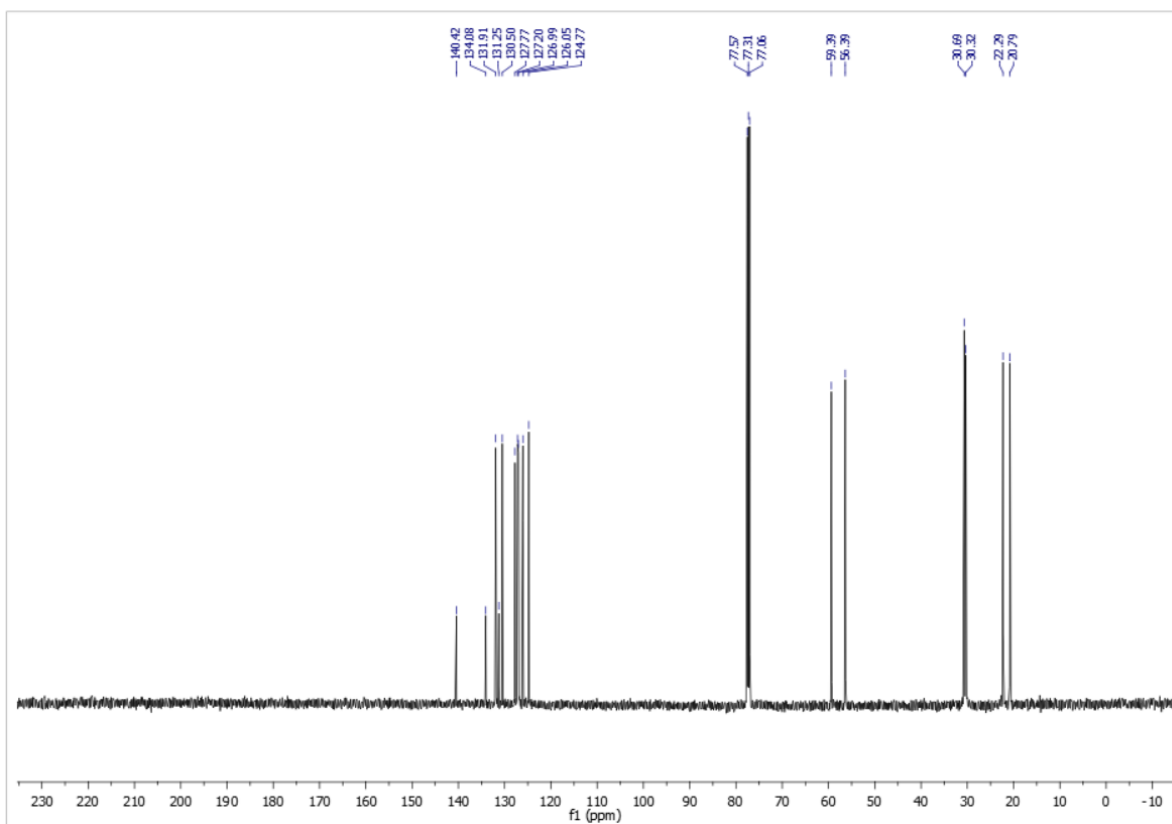


Figure 4-54.  $^{13}\text{C}$  NMR Spectrum of  $\text{NCr}(\text{N}^i\text{Pr}_2)_2(\text{SNap})$  in  $\text{CDCl}_3$ .



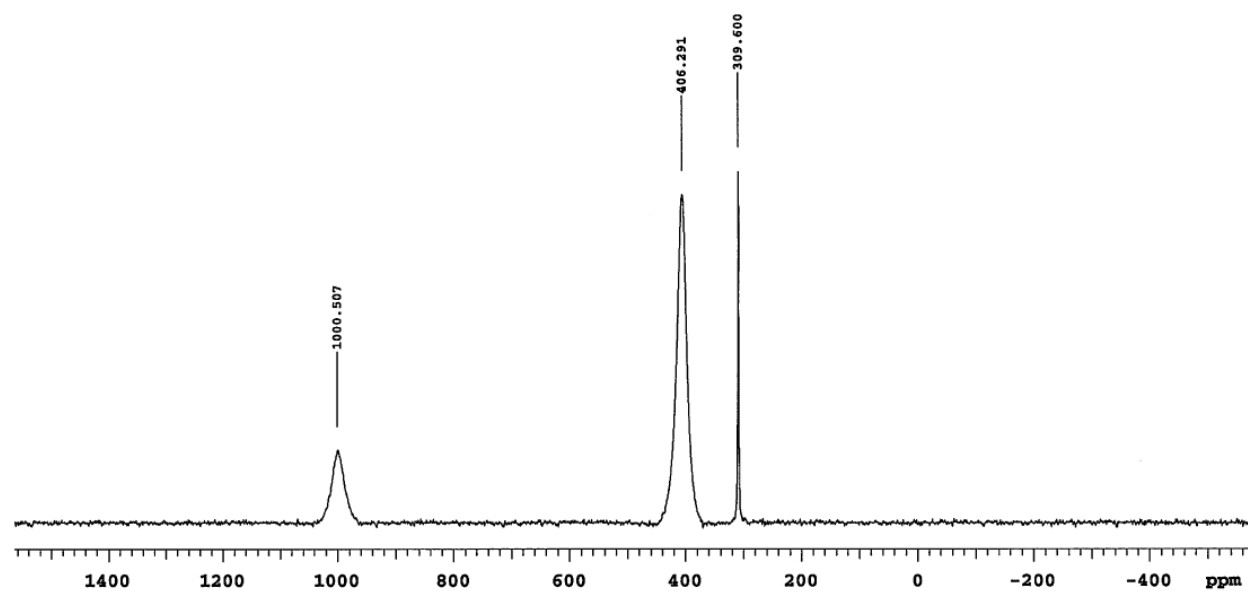


Figure 4-55.  $^{14}\text{N}$  NMR Spectrum of  $\text{NCr}(\text{N}^i\text{Pr}_2)_2(\text{SNap})$  in  $\text{CDCl}_3$ .



## REFERENCES



## REFERENCES

1. Walsh, P. J.; Baranger, A. M.; Bergman, R. G., *J. Am. Chem. Soc.* **1992**, *114* (5), 1708-1719.
2. Odom, A. L.; McDaniel, T. J., *Acc. Chem. Res.* **2015**, *48* (11), 2822-2833.
3. Ryken, S. A.; Schafer, L. L., *Acc. Chem. Res.* **2015**, *48* (9), 2576-2586.
4. Straub, B. F.; Bergman, R. G., *Angew. Chem. Int. Ed.* **2001**, *40* (24), 4632-4635.
5. Cao, C.; Ciszewski, J. T.; Odom, A. L., *Organometallics* **2001**, *20* (24), 5011-5013.
6. Mountford, P., *Chem. Commun.* **1997**, (22), 2127-2134.
7. Swartz II, D. L.; Staples, R. J.; Odom, A. L., *Dalton Trans.* **2011**, *40* (30), 7762-7768.
8. Swartz II, D. L.; Odom, A. L., *Dalton Trans.* **2008**, (32), 4254-4258.
9. Swartz, D. L.; Odom, A. L., *Organometallics* **2006**, *25* (26), 6125-6133.
10. Mikami, K.; Terada, M.; Nakai, T., *J. Am. Chem. Soc.* **1990**, *112* (10), 3949-3954.
11. Weingarten, H.; Van Wazer, J. R., *J. Am. Chem. Soc.* **1965**, *87* (4), 724-730.
12. Benzing, E.; Kornicker, W., *Chem. Ber.* **1961**, *94* (8), 2263-2267.
13. Kansal, D.; Odom, A. L., *Unpublished Results*.
14. Shi, Y.; Hall, C.; Ciszewski, J. T.; Cao, C.; Odom, A. L., *Chem. Commun.* **2003**, (5), 586-587.
15. DiFranco, S. A.; Maciulis, N. A.; Staples, R. J.; Batrice, R. J.; Odom, A. L., *Inorg. Chem.* **2012**, *51* (2), 1187-1200.
16. Tolman, C. A., *Chem. Rev.* **1977**, *77* (3), 313-348.
17. Tolman, C. A., *J. Am. Chem. Soc.* **1970**, *92* (10), 2956-2965.
18. Hirota, M.; Sakakibara, K.; Komatsuzaki, T.; Akai, I., *Comput. Chem.* **1991**, *15* (3), 241-248.
19. Taverner, B. C., *J. Comput. Chem.* **1996**, *17* (14), 1612-1623.
20. Falivene, L.; Credendino, R.; Poater, A.; Petta, A.; Serra, L.; Oliva, R.; Scarano, V.; Cavallo, L., *Organometallics* **2016**, *35* (13), 2286-2293.



21. Poater, A.; Cosenza, B.; Correa, A.; Giudice, S.; Ragone, F.; Scarano, V.; Cavallo, L., *Eur. J. Inorg. Chem.* **2009**, 2009 (13), 1759-1766.
22. Billow, B. S.; McDaniel, T. J.; Odom, A. L., *Nat. Chem.* **2017**, 9, 837-842.
23. McDaniel, T. J. Applications and Optimization of Titanium Catalysis. Michigan State University, 2017.
24. Odom, A. L.; Cummins, C. C., *Polyhedron* **1998**, 17 (5-6), 675-688.
25. Falivene, L.; Credendino, R.; Poater, A.; Petta, A.; Serra, L.; Oliva, R.; Scarano, V.; Cavallo, L., *Organometallics*, **2016**, 35(13), 2286-2293.
26. Billow, B. S.; Bemowski, R. D.; DiFranco, S. A.; Staples, R. J.; Odom, A. L., *Organometallics* **2015**, 34 (18), 4567-4573.
27. Hammett, L. P., *J. Am. Chem. Soc.* **1937**, 59 (1), 96-103.
28. Aldrich, K. E.; Billow, B. S.; Holmes, D.; Bemowski, R. D.; Odom, A. L., *Organometallics* **2017**, 36 (7), 1227-1237.
29. Bemowski, R. D.; Singh, A. K.; Bajorek, B. J.; DePorre, Y.; Odom, A. L., *Dalton. Trans.* **2014**, 43 (32), 12299-12305.
30. Shi, Y.; Ciszewski, J. T.; Odom, A. L., *Organometallics* **2001**, 20 (19), 3967-3969.
31. Li, D.; Kagan, G.; Hopson, R.; Williard, P. G., *J. Am. Chem. Soc.* **2009**, 131 (15), 5627-5634.
32. Kiraly, P.; Swan, I.; Nilsson, M.; Morris, G. A., *J. Mag. Res.* **2016**, 270, 24-30.
33. Lane, E. M.; Chapp, T. W.; Hughes, R. P.; Glueck, D. S.; Feland, B. C.; Bernard, G. M.; Wasylshen, R. E.; Rheingold, A. L., *Inorg. Chem.* **2010**, 49 (8), 3950-3957.
34. Boyle, T. J.; Barnes, D. L.; Heppert, J. A.; Morales, L.; Takusagawa, F.; Connolly, J. C., *Organometallics* **1992**, 11 (3), 1112-1126.
35. Rieth, R. D.; Mankad, N. P.; Calimano, E.; Sadighi, J. P., *Org. Lett.* **2004**, 6 (22), 3981-3983.
36. Batrice, R. J.; Kefalidis, C. E.; Maron, L.; Eisen, M. S., *J. Am. Chem. Soc.* **2016**, 138 (7), 2114-2117.
37. Su, Y.-M.; Hou, Y.; Yin, F.; Xu, Y.-M.; Li, Y.; Zheng, X.; Wang, X.-S., *Org. Lett.* **2014**, 16 (11), 2958-2961.
38. Mason, M.; Barnard, T.; Segla, M.; Xie, B.; Kirschbaum, K., *J. Chem. Crystallogr.* **2003**, 33 (7), 531-540.



39. van der Vlugt, J. I.; Hewat, A. C.; Neto, S.; Sablong, R.; Mills, A. M.; Lutz, M.; Spek, A. L.; Müller, C.; Vogt, D., *Adv. Synth. Catal.* **2004**, *346* (8), 993-1003.
40. Murat-Onana, M. L.; Berini, C.; Minassian, F.; Pelloux-Leon, N.; Denis, J.-N., *Org. Biomol. Chem.* **2010**, *8* (9), 2204-2211.
41. Alexander, J. B.; La, D. S.; Cefalo, D. R.; Hoveyda, A. H.; Schrock, R. R., *J. Am. Chem. Soc.* **1998**, *120* (16), 4041-4042.
42. Hatano, M.; Maki, T.; Moriyama, K.; Arinobe, M.; Ishihara, K., *J. Am. Chem. Soc.* **2008**, *130* (50), 16858-16860.
43. Vilches-Herrera, M.; Miranda-Sepúlveda, J.; Rebolledo-Fuentes, M.; Fierro, A.; Lühr, S.; Iturriaga-Vasquez, P.; Cassels, B. K.; Reyes-Parada, M., *Bioorg. Med. Chem.* **2009**, *17* (6), 2452-2460.
44. Espenson, J. H., *Chemical Kinetics and Reaction Mechanisms*, 2nd Edition ed.; McGraw Hill: New York, 2002.



## Chapter 5. Preliminary Investigations of Uranium-Ligand Interactions

### 5.1 Introduction

In recent decades, pushes towards alternative energy sources have led to a number of new energy production methods. One such method is nuclear power. Despite the clean energy produced by nuclear reactors, a major drawback to implementation of nuclear power has been remediation of the radioactive waste produced. A major challenge in cleaning or recycling the waste produced by nuclear reactors is the difficulty in separating the components of the mixture. Because there is often a complex mixture of lanthanides, actinides, and many other decay products, isolation of radioactive components can be extremely costly.<sup>1</sup> However, if the bonding preferences of the waste components, such as uranium, were better understood, a better procedure might be developed to separate and recycle the waste mixtures. As such, bonding interactions between f-block elements and ligands have become a popular research subject in recent decades. In contrast to transition metal systems, where bonding involving primarily *d*- and *s*-orbitals is understood. Bonding in the actinides involves varying degrees of *f*- and *d*-orbital participation depending on orbital extension and energy in the complexes making the bonding trends quite complex. Orbital participation is further complicated when considering the varying degree of covalency and ionicity in actinide bonding as well.

In 2017, a collaboration with Dr. James Boncella at Los Alamos National Lab was started through a DOE SCGSR fellowship. This collaboration was based on a proposal to treat a series of uranium catalysts as we treated the titanium hydroamination catalysts in chapter 4. Using the LDP method with systematic variation of ligand sets we aimed to elucidate some of the intricacies involved in actinide-light element bonding.



Since uranium has accessible  $\pi$ -acceptor orbitals, it was proposed that our system of ligand parameterization, based on Cr(VI), might be applicable. The electronic values are based on a metal in which bonding is heavily covalent, so the numbers could show correlation in uranium systems where covalency between uranium and its ligands is important. Interestingly, we have shown in correlation between LDP and uranium is possible. The plot in Figure 5-1 shows correlation between our LDP values and the predicted reduction potentials of  $\text{OU}(\text{NMe}_2)_3\text{X}$ .<sup>2</sup> For the OMe value, we used the LDP from OEt as an electronic surrogate. The number for CN is the only point that seems to be a poor fit. It may be that since the X ligand in the Schelter system is trans to a strongly donating oxo group,  $\pi$ -effects are important. Naturally, in the LDP system those same  $\pi$ -effects would not be present. The correlation for all of the other X ligands suggests the LDP may indeed be an adequate measure of small atom donation to a uranium center.



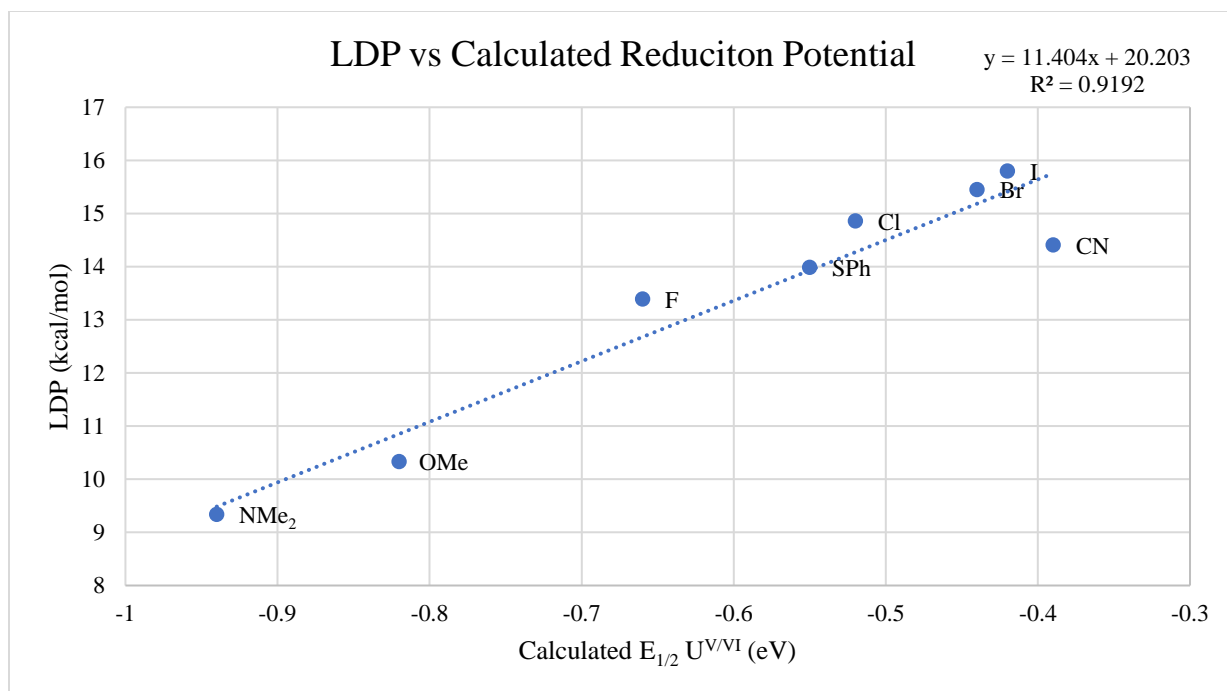


Figure 5-1. Plot of the LDP versus the  $E_{1/2}$  values of a U(V)/U(VI) redox couple for a series of ligands.

By developing a model for uranium catalysis similar to the reported titanium model, we proposed that evaluation of actinide reactivity as a function of ligand properties and covalency could be possible.<sup>3</sup>

## 5.2 Reaction Design

The decision to use catalysis to study uranium as opposed to other types of studies was an obvious one. Monitoring catalysis has many advantages over other studies. Primarily, small electronic effects at a metal center, as a result of ligand electronic changes, are hard to measure. Theory can give some insight, and there are advanced spectroscopies that would allow comparisons between ligand sets as well, but these studies are generally limited to simple systems due to complexities in the electronic structure of the actinides.<sup>4-10</sup> Rather than try to replace these types of studies, our aim was to bridge these studies to real-world reactivity using uranium-based catalysis.



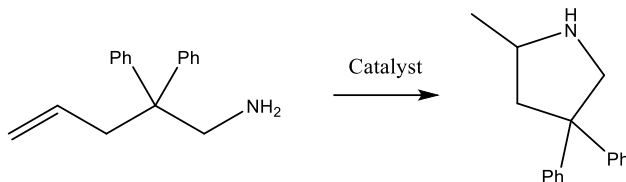
When we study a reaction using a metal complex as a catalyst, we see the direct effects of ancillary ligand changes in the reaction. And, because the complex is used for the same reaction over and over, the effects of those changes are amplified several times. For example, if we were to consider a ligand exchange reaction instead of a catalyzed transformation, the reaction happens once at each metal center. To study that reaction, we only get to observe one transformation at each metal-containing molecule. This can be more difficult to detect, but, more importantly, slight changes between reactions can go unnoticed. If we compare that to a reaction where a uranium complex catalyzes a reaction at 1 mol%, now we can observe each molecule doing one hundred reactions. The result is that any differences between various uranium catalysts are amplified by one hundred times, making those same slight differences more obvious. This makes studying small amounts of material, such as radioactive actinides, easier to do.

This approach could allow observation of the effects that minor electronic changes from the ancillary ligands have on the overall reactivity of the catalyst, providing a new mechanism of study for the tendencies of the actinide series. Since using LDP allows quantitative measure of the changes in both steric and electronic perturbations, studying the resulting effects on reactivity should be simplified. This could allow development of ideal complexing ligands for such processes as nuclear power waste remediation or medical isotope chelation.

Typically, new reactions are more exciting and, therefore, more desirable. For this study though, the reaction is somewhat unimportant. It was most critical for us to know that the reaction can work with minimal complications. Therefore, we chose to study intramolecular hydroamination (Scheme 5-1) because it is well established. Hydroamination of alkynes is a relatively simple reaction, but using the intramolecular hydroamination avoids side reactions like



alkyne oligomerizations.<sup>11</sup> Another advantage of hydroamination for this study is the existing literature precedence.



Scheme 5-1. Example of an intramolecular hydroamination.

Several groups have reported hydroamination using uranium catalysts, unfortunately none of the reported complexes would work well with the LDP system.<sup>11-15</sup> The large ionic radius and lability of uranium typically requires the ancillary ligands to be quite bulky. As we have discussed in the previous chapters, that limits our options for LDP evaluation of the ligands. In order to keep our study quantitative, we decided to design new uranium catalysts that allowed interrogation through the LDP system.

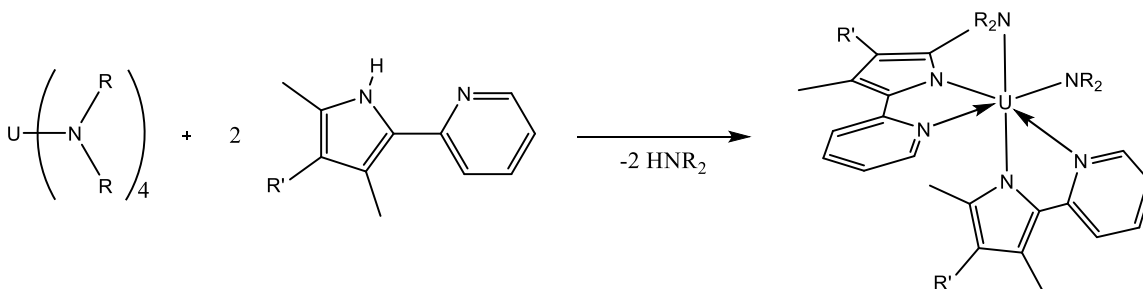
### 5.3 Catalyst Design and Synthesis

Our first design was a new series of uranium catalysts based on the 6,5'-pyridylpyrrole, or PyPyr, ligands. The pyrrole fragment allows for easy substitution on various positions of the ring.<sup>16</sup> In this way, we were able to easily manipulate both the size of the ligand, and, more importantly, the electronic properties of the ligand. Additionally, from our experience with titanium, PyPyr ligands are typically easy to bind to the metal center through acid-base reactions with  $M(NR_2)_4$  starting materials, which are known starting materials for U as well.<sup>17-20</sup> Like the linker of the ligand for our titanium catalysts, we hoped that we would be able to ignore any contributions from the pyridine, considering it as a constant.<sup>3</sup> If true, we could quantitatively measure changes to the catalyst by measuring the LDP differences of the pyrrole rings. Since our focus is the electronic bonding interactions, we also sought to keep sterics as constant as possible. To achieve this, we



used 2,4-dimethyl substituted pyrrole rings. This leaves the 3-position open for substitution of electronically different groups but maintains an almost constant steric profile at the metal center.

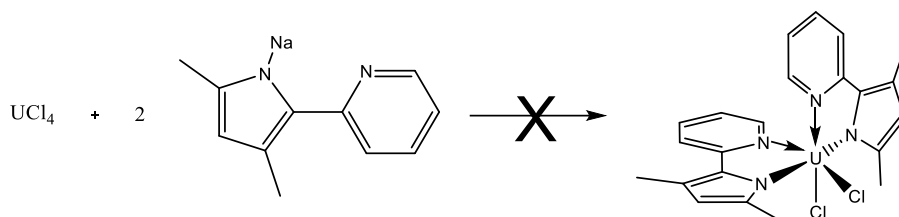
When this project began, we envisioned complexes analogous to our previously reported titanium catalysts,  $\text{U}(\text{PyPyr})_2(\text{NR}_2)_2$  type compounds (Scheme 5-2).<sup>21</sup> Since the known  $\text{U}(\text{N}(\text{SiMe}_3)_2)_4$  is reportedly very inert, and the smaller amide based starting materials are not readily available, we targeted other synthetic routes.<sup>18, 22</sup> We decided, instead of using acid-base type reactions, it might be easier to utilize transmetalations using sodium or potassium salts of the ligands with the halide based U starting materials.<sup>23-24</sup>



Scheme 5-2. Proposed synthesis of the uranium precatalysts.

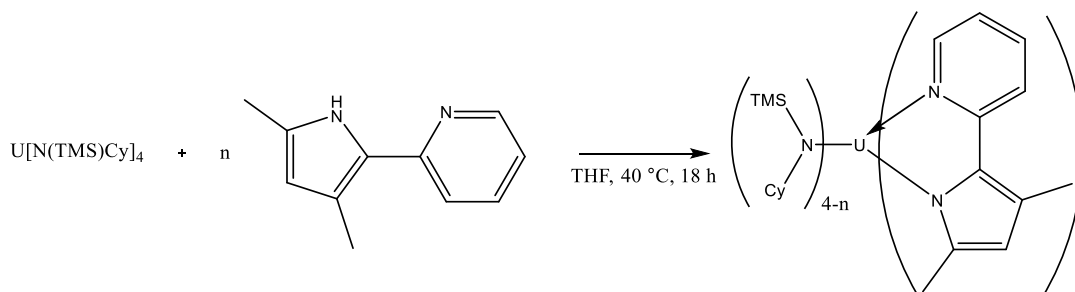
The sodium salt of  $\text{PyPyr}^{\text{Me}_2}$ , the PyPyr derivative bearing a 2,4-dimethyl pyrrole, can be easily generated by deprotonation of the ligand with  $\text{NaCH}_2\text{TMS}$  or  $\text{NaN}(\text{TMS})_2$ . Addition of two equivalents of  $\text{NaPyPyr}^{\text{Me}_2}$  to  $\text{UCl}_4$ , or  $\text{U}(\text{I})_4$ , was unsuccessful. Due to the lability of uranium complexes, the metal tends to redistribute ligands quite easily. These rearrangement reactions cause difficulties in synthesizing pure molecules. For example, when making  $\text{UCl}_2(\text{PyPyr}^{\text{Me}_2})_2$  from  $\text{UCl}_4$  and two equivalents of  $\text{NaPyPyr}^{\text{Me}_2}$ , the major products of the reaction are  $\text{U}(\text{PyPyr}^{\text{Me}_2})_4$  and  $\text{UCl}_4$  regardless of addition rate, reaction time, etc. (Scheme 5-3).





Scheme 5-3. Attempted synthesis of  $\text{U(PyPyr)}_2\text{Cl}_2$  from  $\text{UCl}_4$ .

Fortunately, Dr. Aaron Tondreau had recently prepared a series of uranium amides that were capable of producing  $\text{U}(\text{NR}_2)_2\text{Cl}_2$  molecules.<sup>20</sup> In addition to the  $\text{U}(\text{NR}_2)_2\text{Cl}_2$  molecule, the  $\text{U}(\text{NR}_2)_3\text{Cl}$  and  $\text{U}(\text{NR}_2)_4$  molecules were also stable. To us, this suggested the  $\text{N}(\text{TMS})\text{Cy}$  amides might be ideal as co-ligand in our PyPyr based catalysts. If the  $\text{N}(\text{TMS})\text{Cy}$  amides produced stability with chlorides, it would be likely to work with our PyPyr ligands too.



Scheme 5-4. Synthesis of mixed amide PyPyr compounds.

Stirring two equivalents of  $\text{HPyPyr}^{\text{Me}_2}$  and  $\text{U}[\text{N}(\text{TMS})\text{Cy}]_4$  in THF overnight at 40 °C changed the reaction color from light tan to dark red (Scheme 5-4). Crude NMR of the mixture indicated a relatively clean reaction, though, no X-ray quality crystals could be isolated from the reaction and paramagnetic shifts of in the NMR precluded adequate assignment. We decided to test the crude product, presumably  $\text{U}(\text{PyPyr}^{\text{Me}_2})_2(\text{N}(\text{TMS})\text{Cy})_2$  (**1**) for catalytic activity towards intramolecular hydroamination using 2,2-diphenyl-1-amino-4-pentene (DPAP). At 60 °C, the catalyst cyclizes >95% of the DPAP in less than 18 hours by  $^1\text{H}$  NMR (Figure 5-2). The cyclized product was



isolated by passing the reaction mixture through alumina with hexane, resulting in a colorless oil after removal of the volatiles, confirming conversion to the heterocycle.

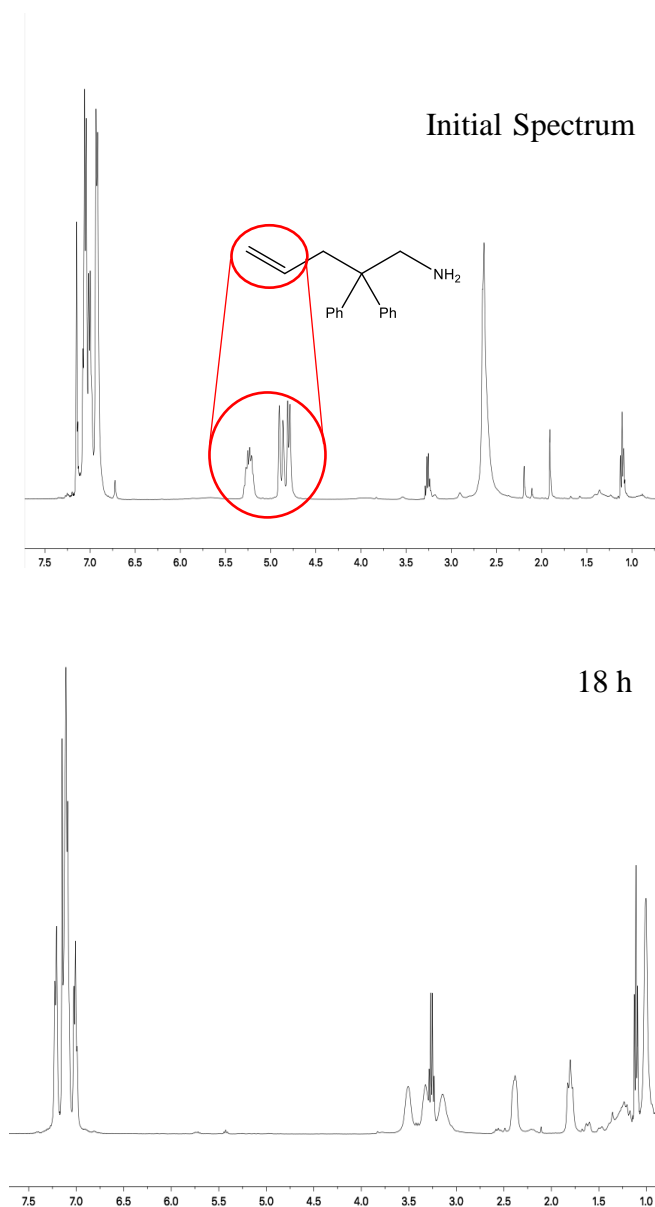


Figure 5-2. Comparison of the olefinic region of the <sup>1</sup>H NMR spectrum before (top) and after (bottom) catalysis showing complete cyclization.

As a control, we added three equivalents of HPyPyr<sup>Me2</sup> to U(N(TMS)Cy)<sub>4</sub> following the same procedure as that for **1** (Scheme 5-4). When the hydroamination reaction is performed with *in situ* generated U(PyPyr<sup>Me2</sup>)<sub>3</sub>[N(TMS)Cy] (**2**) the reaction does not proceed. Due to the nature of the



reaction we are performing, these results suggest that we are, indeed, generating **1** and **2** in the synthesis. The difference in two or three equivalents of  $\text{PyPyr}^{\text{Me}_2}$  is significant. If we assume the reaction follows the Bergman hydroamination mechanism (which Eisen suggests their U species do, but there exists some debate) the reaction needs two proteolytically cleavable sites for imido formation.<sup>11, 13-15, 25</sup> In this case the  $\text{N}(\text{TMS})\text{Cy}$  ligands are the only sites basic enough to be deprotonated by the primary amine, so the reaction cannot occur with  $\text{U}(\text{PyPyr}^{\text{Me}_2})_3[\text{N}(\text{TMS})\text{Cy}]$ . The difficulty in isolating pure catalyst, however, makes a kinetic study of the reaction dubious, especially when considering that hydroamination with  $\text{U}[\text{N}(\text{TMS})\text{Cy}]_4$  also resulted in the cyclization of DPAP, albeit at a much slower rate and with formation of byproducts by  $^1\text{H}$  NMR.



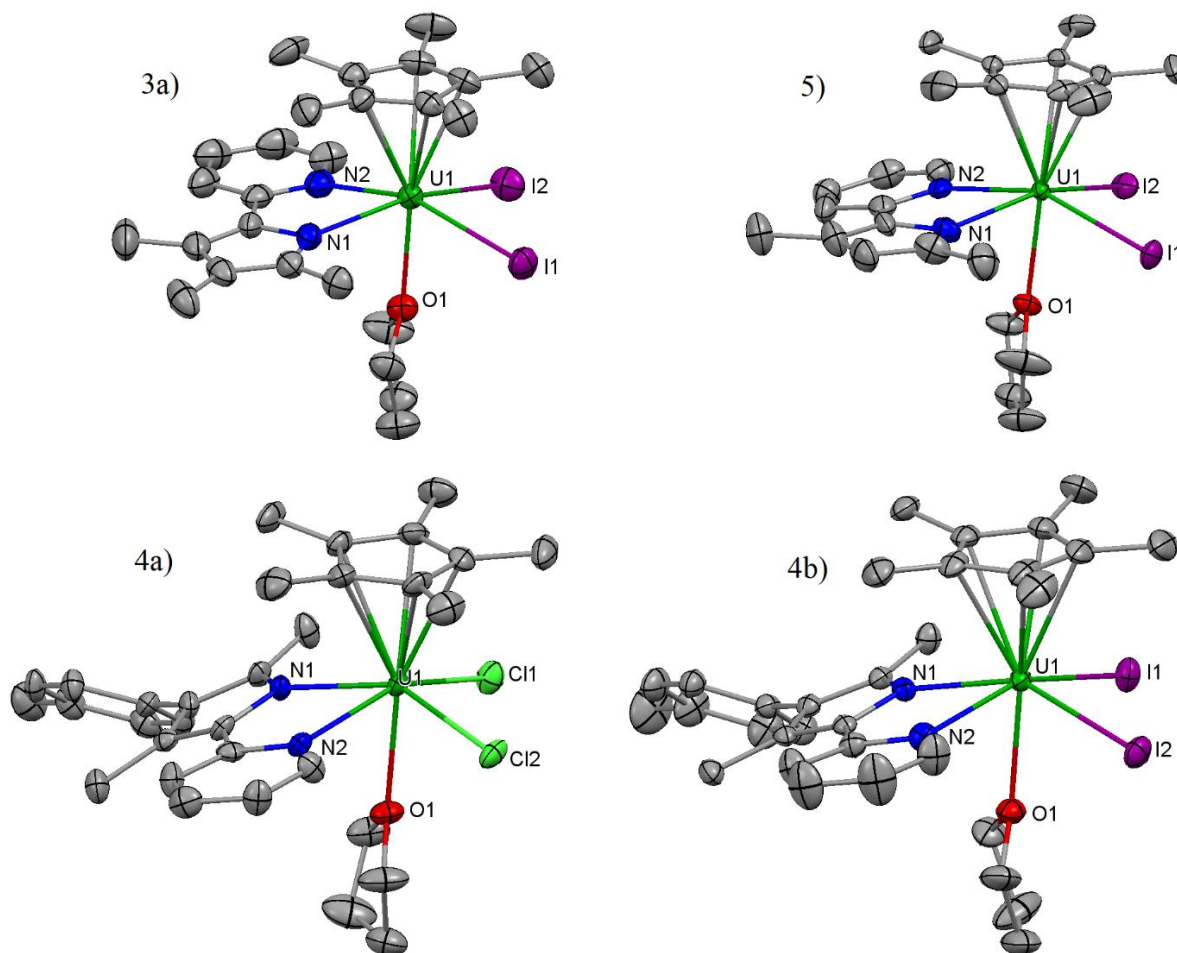
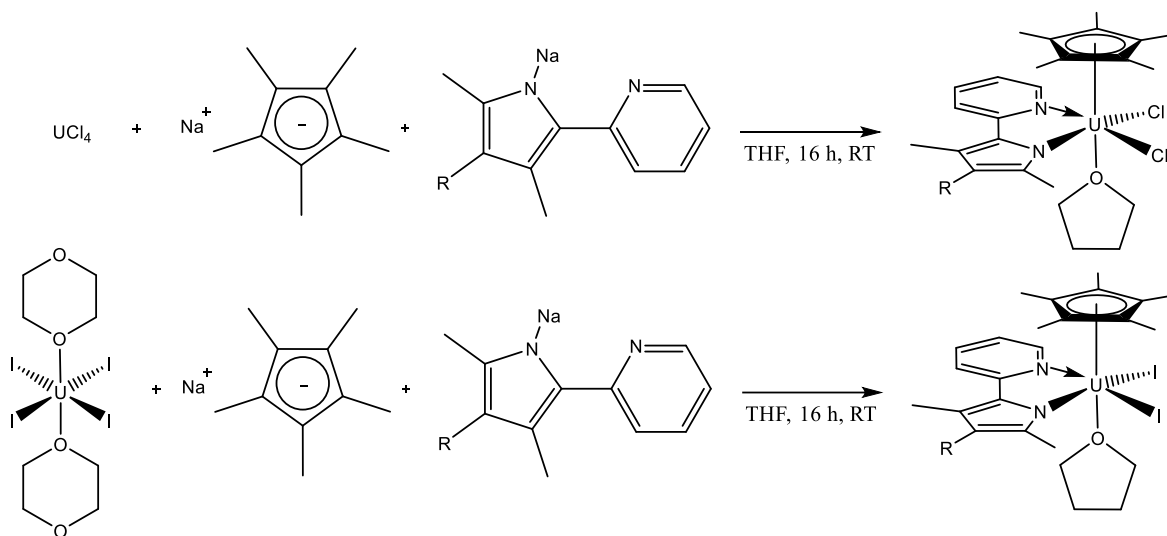


Figure 5-3. Structures of *top*:  $\text{Cp}^*\text{UI}_2(\text{PyPyr}^{\text{Me}3})(\text{thf})$  (**3a**),  $\text{Cp}^*\text{UI}_2(\text{PyPyr}^{\text{Me}2})(\text{thf})$  (**5**), *bottom*:  $\text{Cp}^*\text{UCl}_2(\text{PyPyr}^{\text{Me}2\text{Tol}})(\text{thf})$  (**4a**), and  $\text{Cp}^*\text{UI}_2(\text{PyPyr}^{\text{Me}2\text{Tol}})(\text{thf})$  (**4b**), Hydrogens and co-crystallized solvents removed for clarity.

By replacing one of the ancillary PyPyr ligands with a pentamethylcyclopentadiene, or  $\text{Cp}^*$ , we postulated that we would increase both the stability and crystallinity of the catalyst. Beginning with  $\text{UCl}_4$ , addition of  $\text{NaCp}^*$ , or  $\text{KCp}^*$ , in a THF solution presumably generates  $\text{Cp}^*\text{UCl}_3$ . The generated  $\text{Cp}^*\text{UCl}_3$  is not isolable and decomposes upon attempts at isolation, but subsequent addition of  $\text{NaPyPyr}$  (Scheme 5-5) to the solution produces a reddish orange color, which, after workup, can be crystallized to yield  $\text{Cp}^*\text{UCl}_2(\text{PyPyr})(\text{thf})$  ( $\text{PyPyr}^{\text{Me}3}$  **3a**,  $\text{PyPyr}^{\text{Me}2\text{Tol}}$  **4a**). Likewise, the same reaction procedure starting from  $\text{UI}_4$  produces  $\text{Cp}^*\text{UI}_2(\text{PyPyr})(\text{thf})$ , ( $\text{PyPyr}^{\text{Me}3}$  **3b**,  $\text{PyPyr}^{\text{Me}2\text{Tol}}$  **4b**,  $\text{PyPyr}^{\text{Me}2}$  **5**), also shown in Scheme 5-5. Surprisingly, despite lower yield relative



to the chloride compounds, the  $\text{Cp}^*\text{UI}_2(\text{PyPyr})$  molecules crystallized easier with the methyl substituted PyPyr ligands, the structures are shown in Figure 5-3.



Scheme 5-5. Synthesis of  $\text{Cp}^*\text{UX}_2(\text{PyPyr})(\text{thf})$  from  $\text{UX}_4$  starting materials.

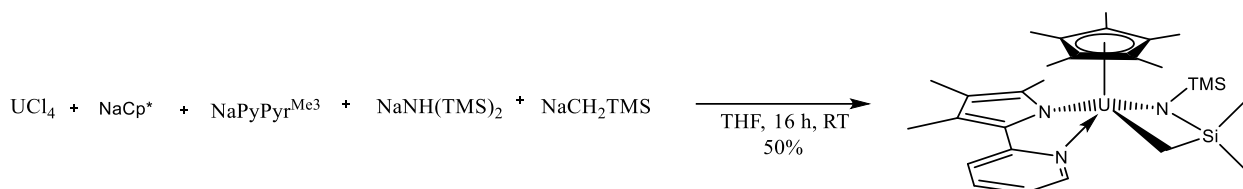
We then attempted substitution of the halides to create active sites for the catalysis. Attempts with small amides, bulky amides, alkyl groups, and alkoxy groups were all met with failure. Attempted formation of an imido group was equally unsuccessful due to ligand redistribution reactions. These redistribution reactions led to the exciting chemistry that will be discussed in chapter 6, but never to a competent catalyst.

## 5.4 Catalysis

We finally found success using  $\text{NaN}(\text{TMS})_2$  and  $\text{NaCH}_2\text{TMS}$ . Sequential addition of  $\text{NaCp}^*$ ,  $\text{NaPyPyr}^{\text{Me}^3}$ ,  $\text{NaN}(\text{TMS})_2$ , and  $\text{NaCH}_2\text{TMS}$  to a solution of  $\text{UCl}_4$  in THF results in a cyclometalated,  $\kappa^2(\text{N-C})\text{-N}(\text{TMS})(\text{CH}_2\text{SiMe}_2)$  ligand (Scheme 5-6). The resulting  $(\kappa^2(\text{N-C})\text{-CH}_2\text{SiMe}_2\text{NTMS})\text{U}(\text{Cp}^*)(\text{PyPyr}^{\text{Me}^3})$  (**6**) was more crystalline than the *bis*-PyPyr based catalysts, and X-ray quality crystals were isolated.



We were unsure what to expect for the competency of these catalysts towards hydroamination. Surprisingly, with 10 mol% catalyst loading at 65 °C the catalysis was rather rapid, with the reaction reaching completion in under 3 h. Using **6** at 5% catalyst loading and a reaction temperature of 65 °C, the reaction reached completion (by  $^1\text{H}$  NMR) in under 6 hours. Analysis of the  $^1\text{H}$  NMR spectrum indicates that, after heating, the catalyst structure seems to remain constant (i.e. there appear to be no peaks for disproportionation products).



Scheme 5-6. Synthesis of  $(\kappa^2(\text{N-C})\text{-CH}_2\text{SiMe}_2\text{NTMS})\text{U}(\text{Cp}^*)(\text{PyPyr}^{\text{Me}_3})$  (**6**) from  $\text{UCl}_4$ .

Having established a baseline with a catalyst that seemed stable with regard to ligand redistribution, we sought to produce a derivative using a different PyPyr ligand. Using the same synthetic procedure,  $(\kappa^2(\text{N-C})\text{-CH}_2\text{SiMe}_2\text{NTMS})\text{U}(\text{Cp}^*)(\text{PyPyr}^{\text{Me}_2})$  (**7**) can be produced. Interestingly, with just a change in the 3-position of the pyrrole from Me to H, the catalyst has a different coordination geometry due to incorporation of an equivalent of THF. The crystal structures of **6** and **7** are compared in Figure 5-4.

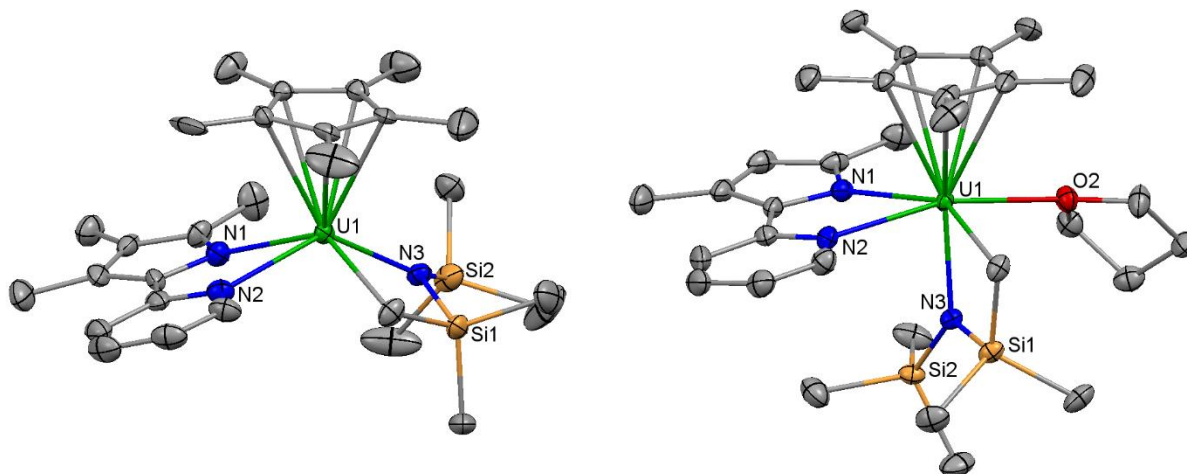




Figure 5-4. Comparison of the solid-state structures of ( $\kappa^2$ (N-C)-CH<sub>2</sub>SiMe<sub>2</sub>NTMS)U(Cp\*)(PyPyr<sup>Me3</sup>) (**6**) (left) and ( $\kappa^2$ (N-C)-CH<sub>2</sub>SiMe<sub>2</sub>NTMS)U(Cp\*)(PyPyr<sup>Me2</sup>) (**7**) (right).

Rather than the pseudo-square pyramidal geometry observed in **6**, the structure in **7** has a pseudo-octahedral ligand arrangement. The coordination of THF is not surprising, but the position relative to the other ligands is. If we define a z-axis along the U-Cp\* bond vector, rather than filling in the open axial coordination site of the square pyramid trans to the Cp\* ligand (which is the location of the THF in **3-5** and the open site in **6**), the THF molecule is bound in the equatorial plane. This places the N3 amide trans to the Cp\* ligand, effectively putting the two strongest donors trans to one another.<sup>26</sup> This phenomenon is not necessarily uncommon in actinide chemistry, but might be a significant difference between **6** and **7**.<sup>27-31</sup>

When the hydroamination of DPAP was run with **7**, using 5 mol% loading at 65 °C, the catalysis was complete in just over 3 hours. It is worth restating, the only difference between the ancillary ligands is a Me group in the 3-position of the pyrrole ring, yet the catalysis is nearly twice as fast. Importantly, though, the two PyPyr ligands remain essentially isosteric. If we assume the THF in **7** dissociates during the catalysis, this is the same trend seen with the titanium catalysis. Minor changes in the electronic structure of the ligand play large roles in reactivity differences. While drawing conclusions based on two qualitative points would be careless, the results of the experiment were exciting. We also attempted to produce the analogous catalysts of **6** and **7** using halides and aryl groups in the 3-position of the pyrrole ring, but isolation of those catalysts was unsuccessful.

## 5.5 Future Work

Regrettably, synthesis of the catalysts is not very reproducible. The yields of the reaction vary and, after moving back to MSU, we were unable to isolate the species from U<sub>4</sub> starting materials. One issue affecting the isolation of the catalysts from U<sub>4</sub> starting materials is ligand redistribution



reactions. Reactions where the catalysts were made using the one pot procedure always show production of redistribution reaction products, commonly  $\text{U}(\text{PyPyr})_4$  and  $\text{Cp}^*\text{U}(\text{NTMS}_2)(\kappa^2(\text{N-C})\text{-CH}_2\text{SiMe}_2\text{NTMS})$ . Even stepwise synthesis reactions to produce the isolable intermediate  $\text{Cp}^*\text{U}(\text{PyPyr})\text{I}_2$  results in formation of a significant quantity of the  $\text{U}(\text{PyPyr})_4$  compounds shown in Figure 5-5, which may explain the poor yield of **3b**. Perhaps simply acquiring some  $\text{UCl}_4$  is the solution to our issues, but currently that is not a material we have access to.

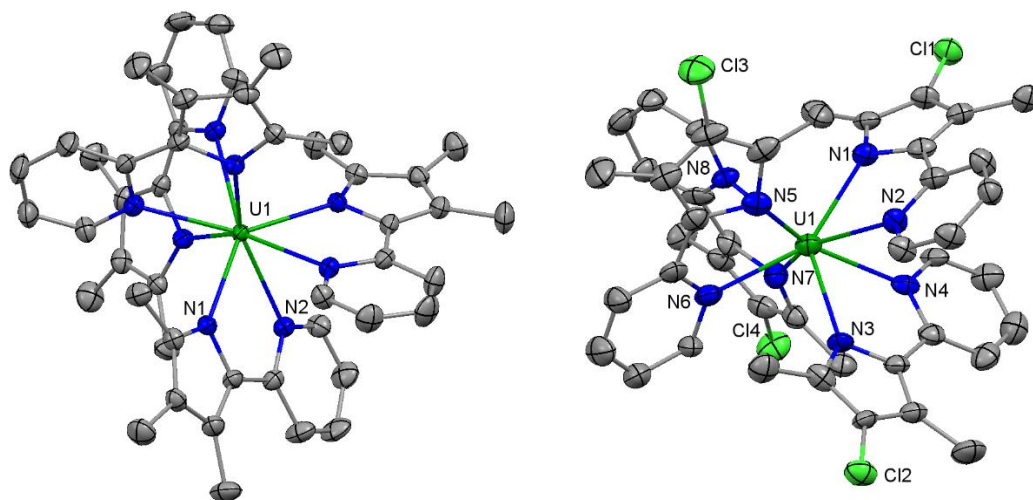


Figure 5-5. Crystals structures of  $\text{U}(\text{PyPyr}^{\text{Me}_3})_4$  and  $\text{U}(\text{PyPyr}^{\text{Me}_2\text{Cl}})_4$  byproducts. The structure of  $\text{U}(\text{PyPyr}^{\text{Me}_3})_4$  crystallizes with four-fold symmetry, the grown structure is shown. Hydrogens and co-crystallized solvents removed for purity.



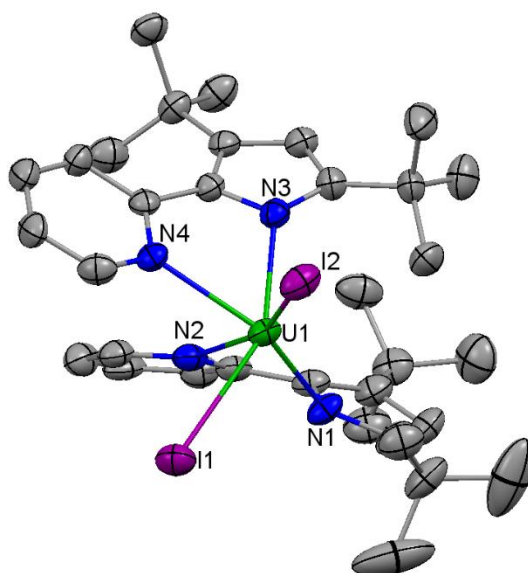


Figure 5-6. Crystal structure of  $\text{UI}_2(\text{PyPyr}^{\text{tBu}2})_2$  (**6**). Hydrogens and co-crystallized diethyl ether molecules removed for clarity.

We wondered if adding more steric bulk to the PyPyr in the 2-position might slow some of the redistribution of ligands. To achieve this, we synthesized the 2,4-di<sup>t</sup>Bu-PyPyr ( $\text{PyPyr}^{\text{tBu}2}$ ) ligand.<sup>16</sup> The pyrrole was then deprotonated and added with  $\text{NaCp}^*$  to  $\text{UI}_4(\text{thf})_2$  following the analogous procedure to synthesize **3-5**. Still though, significant quantities of unwanted byproducts were produced, and the primary isolated species was  $\text{UI}_2(\text{PyPyr}^{\text{tBu}2})_2$ , **8** (Figure 5-4). We have not thoroughly explored or characterized **8**, but  $\text{PyPyr}^{\text{tBu}2}$  could potentially work as an ancillary ligand in the  $(\text{PyPyr})_2\text{U}(\text{NR}_2)_2$ -type catalysts due to the increased steric bulk.

In trying to sort out the synthesis of adequate catalysts, we produced a number of interesting U-PyPyr molecules. An in-depth analysis of some of the molecules discovered may prove useful in moving forward. Specifically, compounds **3-5** are quite interesting. The  $^1\text{H}$  NMR spectra of **3a/4a** and **3b/4b** show a significant dependence on halide bound to uranium. It could be that making a series of halides, including Br, with various PyPyr ligands might give another indication on how the electronic structure of the uranium atom is affected as a function of LDP. Since the



NMR data are quite clean, NMR may be an easy way to investigate the changing structure similar to the correlations that have been shown with NMR shift and ligand donor abilities previously.<sup>26,</sup>

<sup>32</sup> By comparing both the series of PyPyr ligands against one another for each type of dihalide (i.e. comparing compounds **3a** and **4a**) and comparing the halides with each PyPyr ligand (i.e. comparing compounds **3a** and **3b**), we could interrogate the U atom as a function of the LDP of each the PyPyr ligands and changing the halide. While this does not use catalysis, it might provide more insight into the effects of the PyPyr substituents on the electronic structure of uranium.

Additionally, when more catalysts can be prepared, in addition to determining typical kinetic data, such as rate dependence on substrate and catalyst, a dependence on THF should also be investigated. This might be a way to interrogate whether the coordinated THF molecule in ( $\kappa^2$ (N-C)-CH<sub>2</sub>SiMe<sub>2</sub>NTMS)UCp\*(PyPyr<sup>Me2</sup>) (**7**) is significant, or if it is simply displaced during the catalysis.

## 5.6 Conclusions

The synthesis of complexes **6** and **7**, and their reactivity towards cyclization of the hydroamination substrate, was a minor success. Unfortunately, time and equipment constraints at Los Alamos, and starting material limitations at MSU meant those were the only active molecules isolated. Looking forward, more derivatives of each catalyst are necessary to confirm reactivity trends. Moreover, the catalyst behavior needs to be thoroughly examined during the reaction. The ligand redistribution reactions that we have observed, and the lability of uranium necessitate detailed analysis to be sure the hydroamination reaction is proceeding normally and catalyst decomposition is not an issue. In the two catalytic runs we performed in this study, no hints of catalyst side reactions were observed, but more evidence is necessary to prove the differences in reaction rate are a function of ligand substitutions and not adventitious reactions.



## 5.7 Experimental

All reactions and manipulations were carried out in an MBraun glovebox under an inert atmosphere and/or using standard Schlenk techniques. Diethyl ether, pentane, tetrahydrofuran, and hexane were purchased from Aldrich Chemical Company. Diethyl ether and pentane were purified by passing through alumina columns to remove water after being sparged with dry nitrogen to remove oxygen. Tetrahydrofuran and hexane were sparged with dinitrogen to remove oxygen and distilled from sodium and benzophenone. C<sub>6</sub>D<sub>6</sub>, THF-d<sub>8</sub>, and toluene-d<sub>8</sub> were purchased from Cambridge Isotopes Laboratories, Inc or Aldrich Chemical Company. Toluene-d<sub>8</sub> and THF-d<sub>8</sub> were sparged with dry dinitrogen and dried over 4 Å molecular sieves. Before use, each solvent was passed through a plug of activated alumina to filter the solvent and to ensure dryness. C<sub>6</sub>D<sub>6</sub> was sparged with dry dinitrogen and distilled from CaH<sub>2</sub> before use. All NMR solvents were stored under an inert atmosphere away from light. Depleted uranium turnings were purchased from Manufacturing Sciences Corporation. Synthesis of UCl<sub>4</sub>, UI<sub>4</sub>(dioxane)<sub>2</sub>, PyPyr ligands, U(N(TMS)Cy)<sub>4</sub>, NaCH<sub>2</sub>TMS, and 2,2-diphenyl-1-amino-4-pentene were prepared according to literature procedures.<sup>16, 20, 23-24, 33-34</sup> The PyPyr and Cp\* ligands were deprotonated in hexane with stoichiometric NaCH<sub>2</sub>TMS or NaN(TMS)<sub>2</sub> over 16 h. The reaction generates an off-white precipitate which can be collected by filtration. The precipitate was washed with several aliquots of hexane and used as is. Elemental Analysis was performed by Atlantic Microlab in Norcross, GA using a He filled glovebag to handle the compounds.

### Synthesis

*Caution! Depleted uranium (primary isotope <sup>238</sup>U) is a weak α-emitter (4.197 MeV) with a half-life of 4.47x10<sup>9</sup> years; manipulations and reactions should be carried out in monitored fume*



hoods or in an inert atmosphere drybox in a radiation laboratory equipped with  $\alpha$ - and  $\beta$ -counting equipment

*Oxide-Free Uranium Metal Turnings: Cautionary Note: Uranium is pyrophoric when finely divided; caution is recommended in the washing process to avoid exposure to air.* This is a modification of the literature procedure.<sup>23</sup> Depleted uranium turnings were received in mineral oil from Manufacturing Sciences Corporation. The turnings (~10 g) were carefully transferred to a 500 mL side arm flask which was fitted with a hose flowing dry dinitrogen or dry argon gas. The turnings were washed with hexanes (3 x 150 mL), acetone (3 x 150 mL), then water (3 x 150 mL). The flask was then filled with enough water to fully cover the turnings (~100 mL). Concentrated nitric acid was then added by pipette while gently swirling the flask until removal of the black oxide layer was achieved and the turnings became metallic in color. The amount of concentrated acid necessary can vary significantly depending on the quality of turnings, but typically ~20 mL is sufficient. Cleaning of the oxide layer can be accompanied by warming of the solution as well as NO<sub>2</sub> gas generation, observable as a brown gas. Once the turnings appear shiny and metallic, the acid solution is carefully decanted. The turnings are then washed again with water (3 x 150 mL) and acetone (3 x 150 mL). After the final wash, the turnings were dried under reduced pressure and transferred to the drybox.

*In-situ preparation of  $U(N(TMS)Cy)_2(PyPyr^{Me_2})_2$  (**1**):* In a 20 mL scintillation vial,  $U(N(TMS)Cy)_4$  (200 mg, 0.218 mmol) was loaded with a stir bar and THF (5 mL). The solution was stirred with a magnetic stir plate. To the stirring solution was added  $HPyPyr^{Me_2}$  (75 mg, 0.435 mmol). The vial was heated to 40 °C. The vial was then capped and allowed to stir for 18 h, during which, the solution changed color from tan to dark red. **1** was never isolated as a pure product, but the crude NMR is displayed in Figure 5-7, below.



*In-situ preparation of  $U(PyPyr^{Me2})_3(N(TMS)Cy)$  (2):* In a 20 mL scintillation vial,  $U(N(TMS)Cy)_4$  (200 mg, 0.218 mmol) was loaded with a stir bar and THF (5 mL). The solution was stirred with a magnetic stir plate. To the stirring solution was added  $HPyPyr^{Me2}$  (112 mg, 0.653 mmol). The vial was heated to 40 °C. The vial was then capped and allowed to stir for 18 h, during which, the solution changed color from tan to dark red. **2** was never isolated as a pure product, but the crude NMR is displayed in Figure 5-8, below.

*Synthesis of  $Cp^*UCl_2PyPyr^{Me3}(thf)$  (3a):* In a 20 mL scintillation vial,  $UCl_4$  (200 mg, 0.527 mmol) was loaded with a stir bar and THF (5 mL). The solution was stirred with a magnetic stir plate. To the stirring solution was added  $NaCp^*$  (83 mg, 0.527 mmol). The solution rapidly darkened. Next,  $NaPyPyr^{Me3}$  (109 mg, 0.527 mmol) was added as a solution in THF (1 mL). The solution was left to stir for 2 h whereupon the color had turned to a dark brown/yellow. The solution was then dried of the volatiles. The solids were extracted with diethyl ether (~10 mL) and filtered using Celite as a filtering agent. The filtrate was concentrated to ~1 mL and put in the freezer at -30 °C overnight for recrystallization.  $^1H$  NMR (400 MHz,  $C_6D_6$ ):  $\delta$  = 49.28 (s, 2H, thf), 48.32 (s, 2H, thf), 24.26 (s, 4H thf), 9.37 (s, 15H,  $Cp^*$ ), 1.46 (s, 3H, Me), 1.02 (s, 3H, Me), -1.03 (s, 1H, Ar), -5.29 (s, 1H, Ar), -14.15 (s, 1H, Ar), -25.89 (s, 3H, Me), -67.31 (s, 1H, Ar).

*Synthesis of  $Cp^*UI_2PyPyr^{Me3}(thf)$  (3b):* In a 20 mL scintillation vial,  $UI_4(dioxane)_2$  (250 mg, 0.271 mmol) was loaded with a stir bar and THF (5 mL). The solution was stirred over a magnetic stir plate. To the stirring solution was added  $NaCp^*$  (43 mg, 0.271 mmol). The solution rapidly darkened. Next,  $NaPyPyr^{Me3}$  (56 mg, 0.271 mmol) was added as a solution in THF (1 mL). The solution was left to stir for 2 h whereupon the color had turned to a dark brown/yellow. The solution was then dried of the volatiles. The solids were extracted with diethyl ether (~10 mL) and filtered using Celite as a filtering agent. The filtrate was concentrated to ~1 mL and put in the



freezer at -30 °C overnight for recrystallization. Yield: 19 mg (8%).  $^1\text{H}$  NMR (600 MHz, toluene- $d_8$ ):  $\delta$  = 71.76 (s, 2H, thf), 68.72 (s, 2H, thf), 35.38 (s, 4H thf), 15.04 (s, 15H, Cp\*), 0.42 (s, 3H, Me), -1.29 (s, 3H, Me), -3.72 (s, 1H, Ar), -7.95 (s, 1H, Ar), -17.78 (s, 1H, Ar), -41.07 (s, 3H, Me), -88.90 (s, 1H, Ar).

*Synthesis of  $\text{Cp}^*\text{UCl}_2\text{PyPyr}^{\text{Me}_2\text{Tol}}(\text{thf})$  (4a):* In a 20 mL scintillation vial,  $\text{UCl}_4$  (200 mg, 0.527 mmol) was loaded with a stir bar and THF (5 mL). The solution was stirred over a magnetic stir plate. To the stirring solution was added  $\text{NaCp}^*$  (83 mg, 0.527 mmol). The solution rapidly darkened. Next,  $\text{NaPyPyr}^{\text{Me}_2\text{Tol}}$  (150 mg, 0.527 mmol) was added as a solution in THF (1 mL). The solution was left to stir for 2 h whereupon the color had turned to a dark brown/yellow. The solution was then dried of the volatiles. The solids were extracted with diethyl ether (~10 mL) and filtered using Celite as a filter agent. The filtrate was concentrated to ~1 mL and put in the freezer at -30 °C overnight for recrystallization.  $^1\text{H}$  NMR (400 MHz,  $\text{C}_6\text{D}_6$ ):  $\delta$  = 52.76 (s, 2H, thf), 51.81 (s, 2H, thf), 26.14 (s, 4H thf), 9.84 (s, 15H, Cp\*), 6.38 (s, 2H, Tol), 5.97 (s, 2H, Tol), 1.61 (s, 3H, Me), 0.00 (s, 3H, Me), -1.17 (s, 1H, Ar), -5.95 (s, 1H, Ar), -14.08 (s, 1H, Ar), -28.81 (s, 3H, Me), -68.57 (s, 1H, Ar).

*Synthesis of  $\text{Cp}^*\text{UI}_2\text{PyPyr}^{\text{Me}_2\text{Tol}}(\text{thf})$  (4b):* In a 20 mL scintillation vial,  $\text{UI}_4(\text{dioxane})_2$  (250 mg, 0.271 mmol) was loaded with a stir bar and THF (5 mL). The solution was stirred over a magnetic stir plate. To the stirring solution was added  $\text{NaCp}^*$  (43 mg, 0.271 mmol). The solution rapidly darkened. Next,  $\text{NaPyPyr}^{\text{Me}_2\text{Tol}}$  (77 mg, 0.271 mmol) was added as a solution in THF (1 mL). The solution was left to stir for 2 h whereupon the color had turned to a dark brown/yellow. The solution was then dried of the volatiles. The solids were extracted with diethyl ether (~10 mL) and filtered using Celite as a filtering agent. The filtrate was concentrated to ~1 mL and put in the freezer at -30 °C overnight for recrystallization producing small quantities of X-ray quality



crystals.  $^1\text{H}$  NMR (400 MHz,  $\text{C}_6\text{D}_6$ ):  $\delta$  = 75.40 (s, 2H, thf), 72.49 (s, 2H, thf), 37.29 (s, 4H thf), 15.88 (s, 15H,  $\text{Cp}^*$ ), 5.25 (d,  $J$  = 8.4 Hz, 2H, Tol), 3.50(d,  $J$  = 8.2 Hz, 2H, Tol), 0.90 (s, 3H, Me),  $-0.55$  (s, 3H, Me),  $-4.05$  (s, 1H, Ar),  $-8.81$  (d,  $J$  = 9.9 Hz, 1H, Ar),  $-17.94$  (s, 1H, Ar),  $-44.22$ (s, 3H, Me),  $-90.74$  (d,  $J$  = 6.8, 1H, Ar).

*Synthesis of  $\text{Cp}^*\text{UI}_2\text{PyPyr}^{\text{Me}_2}(\text{thf})$  (5):* In a 20 mL scintillation vial,  $\text{UI}_4(\text{dioxane})_2$  (250 mg, 0.271 mmol) was loaded with a stir bar and THF (5 mL). The solution was stirred over a magnetic stir plate. To the stirring solution was added  $\text{NaCp}^*$  (43 mg, 0.271 mmol). The solution rapidly darkened. Next,  $\text{NaPyPyr}^{\text{Me}_2}$  (40 mg, 0.271 mmol) was added as a solution in THF (1 mL). The solution was left to stir for 2 h whereupon the color had turned to a dark brown/yellow. The solution was then dried of the volatiles. The solids were extracted with diethyl ether (~10 mL) and filtered using Celite as a filter agent. The filtrate was concentrated to ~1 mL and put in the freezer at  $-30\text{ }^\circ\text{C}$  overnight for recrystallization producing small quantities of X-ray quality crystals.  $^1\text{H}$  NMR (400 MHz,  $\text{C}_6\text{D}_6$ ):  $\delta$  = 74.81 (s, 2H, thf), 71.79 (s, 2H, thf), 36.88 (s, 4H thf), 15.57 (s, 15H,  $\text{Cp}^*$ ), 0.98 (s, 1H, Ar),  $-0.63$  (s, 3H, Me),  $-4.49$  (s, 1H, Ar),  $-9.24$  (d,  $J$  = 9.7 Hz, 1H, Ar),  $-18.17$  (s, 1H, Ar),  $-41.09$  (s, 3H, Me),  $-90.42$  (d,  $J$  = 7.3 Hz, 1H, Ar).

*Preliminary synthesis ( $\kappa^2(\text{N-C})\text{-CH}_2\text{SiMe}_2\text{NTMS})\text{U}(\text{Cp}^*)(\text{PyPyr}^{\text{Me}_3})$  (6):* In a 20 mL scintillation vial,  $\text{UCl}_4$  (200 mg, 0.527 mmol) was loaded with a stir bar and THF (5 mL). The solution was stirred with a magnetic stir plate. To the stirring solution was added  $\text{NaCp}^*$ (83 mg, 0.527 mmol). The solution rapidly darkened. Next,  $\text{NaPyPyr}^{\text{Me}_3}$  (109 mg, 0.527) was added as a solution in THF (1 mL). Following that,  $\text{NaHMDS}$  (96 mg, 0.527 mmol) was added as a solid. Finally,  $\text{NaCH}_2\text{TMS}$  (58 mg, 0.526 mmol) was added as a solution in THF (1 mL). The solution was left to stir for 18 h whereupon the color had turned from green to dark brown/red. The solution was then dried of the volatiles *in vacuo*. The solids were extracted with *n*-hexane (~10 mL) and



filtered using Celite as a filtering agent. The filtrate was concentrated to ~1 mL and put in the freezer at -30 °C overnight for recrystallization. Crystals grown were of X-ray quality and contained no solvent, however, extra unassignable peaks in the  $^1\text{H}$  NMR spectrum suggest in solution **5** may coordinate a solvent molecule. Yield 188 mg (50%)  $^1\text{H}$  NMR (400 MHz,  $\text{C}_6\text{D}_6$ ):  $\delta$  = 32.71 (s, 9H), 21.68 (s, 3H), 21.46 (s, 3H), 10.29 (s, 15H, Cp\*), 7.43 (s, 1H), 3.04 (s, 1H), 2.87 (s, 1H), 2.12 (s, 1H), 0.13 (s, 1H), -5.79 (br s, 3H), -9.03 (br s, 3H), -10.58 (br s, 3H), -33.89 (br), -54.71 (br).

*Preliminary synthesis* ( $\kappa^2(\text{N-C})\text{-CH}_2\text{SiMe}_2\text{NTMS}$ ) $\text{U}(\text{Cp}^*)(\text{PyPyr}^{\text{Me}_2})(\text{thf})$  (**7**): In a 20 mL scintillation vial,  $\text{UCl}_4$  (200 mg, 0.527 mmol) was loaded with a stir bar and THF (5 mL). The solution was stirred with a magnetic stir plate. To the stirring solution was added  $\text{NaCp}^*$  (83 mg, 0.527 mmol). The solution rapidly darkened. Next,  $\text{NaPyPyr}^{\text{Me}_2}$  (102 mg, 0.527) was added as a solution in THF (1 mL). Following that,  $\text{NaHMDS}$  (96 mg, 0.527 mmol) was added as a solid. Finally,  $\text{NaCH}_2\text{TMS}$  (58 mg, 0.526 mmol) was added as a solution in THF (1 mL). The solution was left to stir for 18 h whereupon the color had turned from green to dark brown/red. The solution was then dried of the volatiles *in vacuo*. The solids were extracted with *n*-hexane (~10 mL) and filtered using Celite as a filtering agent. The filtrate was concentrated to ~1 mL and put in the freezer at -30 °C overnight for recrystallization. Yield 102 mg (25%)  $^1\text{H}$  NMR (400 MHz,  $\text{C}_6\text{D}_6$ ):  $\delta$  = 33.41 (s, 9H), 21.76 (s, 3H), 21.63 (s, 3H), 10.84 (br s, 15H, Cp\*), 7.43 (s, 1H), 2.12 (s, 1H), 2.05 (s, 1H), 1.79 (s, 1H), 1.69 (s, 1H), 0.12 (s, 1H), 0.02 (s, 1H), -5.94 (br, 3H), -10.32 (br, 3H), -10.58 (br s, 3H), -33.25 (br), -54.47 (br).



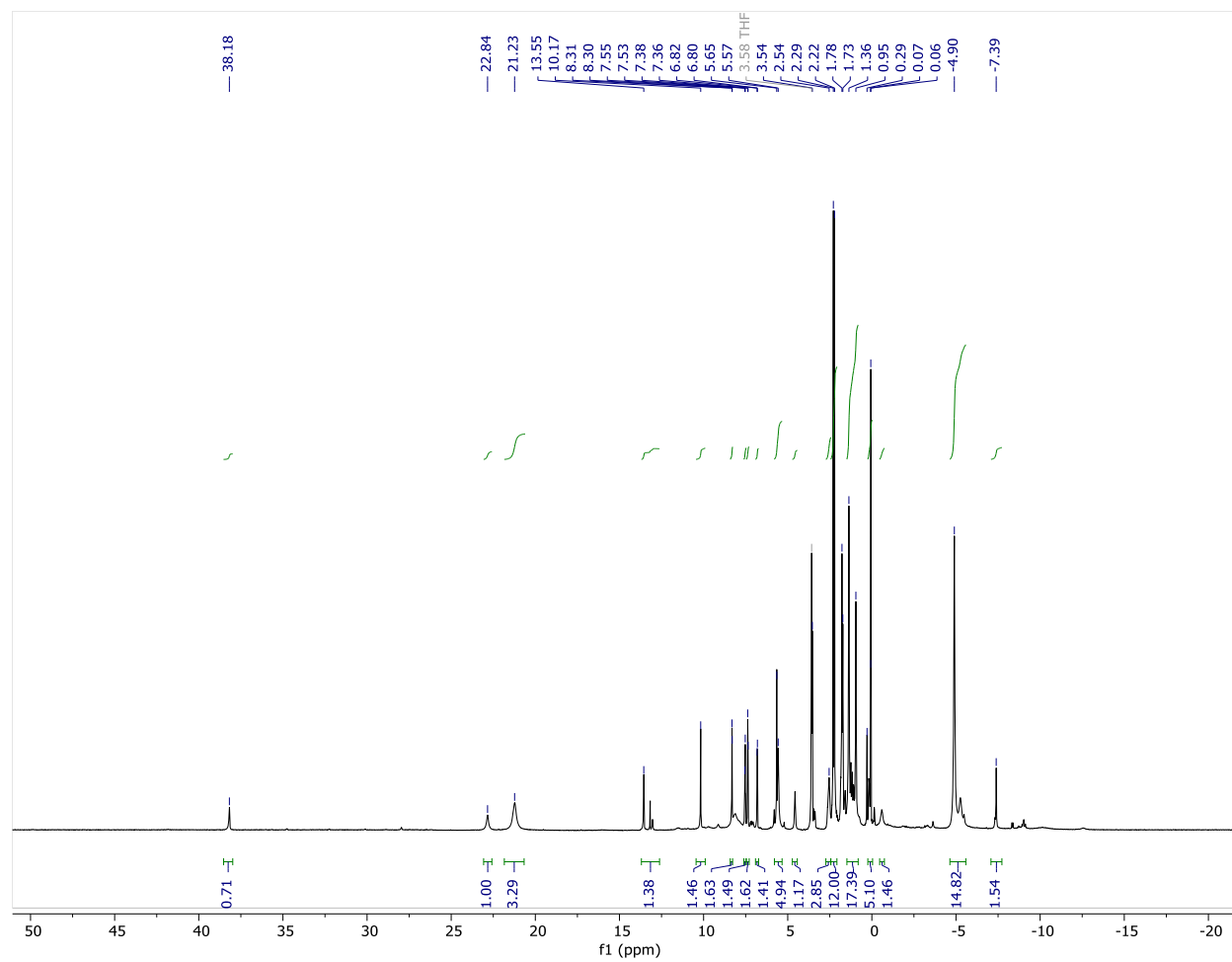


Figure S-7. Crude  $^1\text{H}$  NMR of  $[\text{N}(\text{TMS})\text{Cy}]_2\text{U}(\text{PyPyr}^{\text{Me}_2})_2$ , **1**.



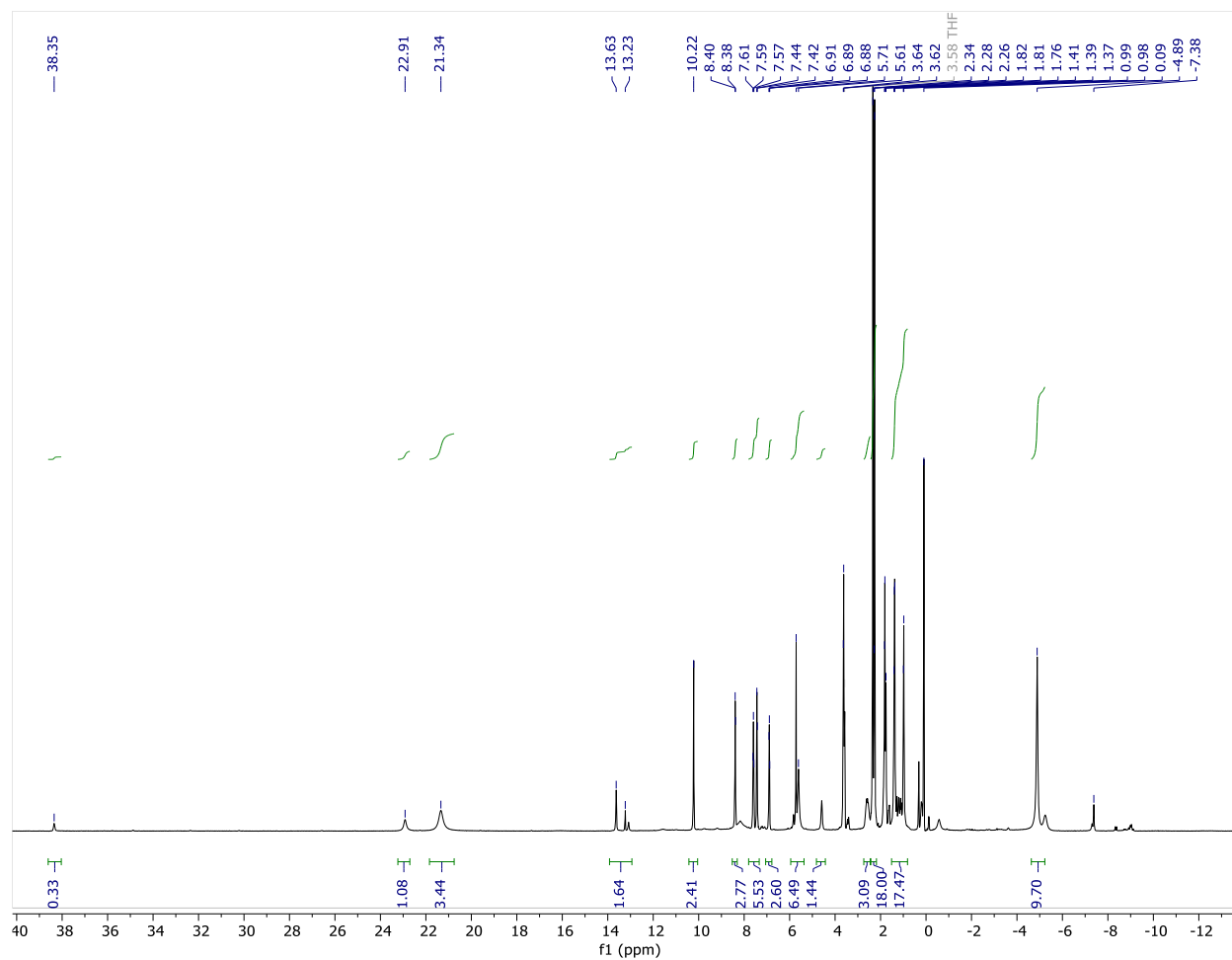


Figure 5-8. Crude  $^1\text{H}$  NMR of  $[\text{N}(\text{TMS})\text{Cy}]\text{U}(\text{PyPyr}^{\text{Me}_2})_3$ , **2**.



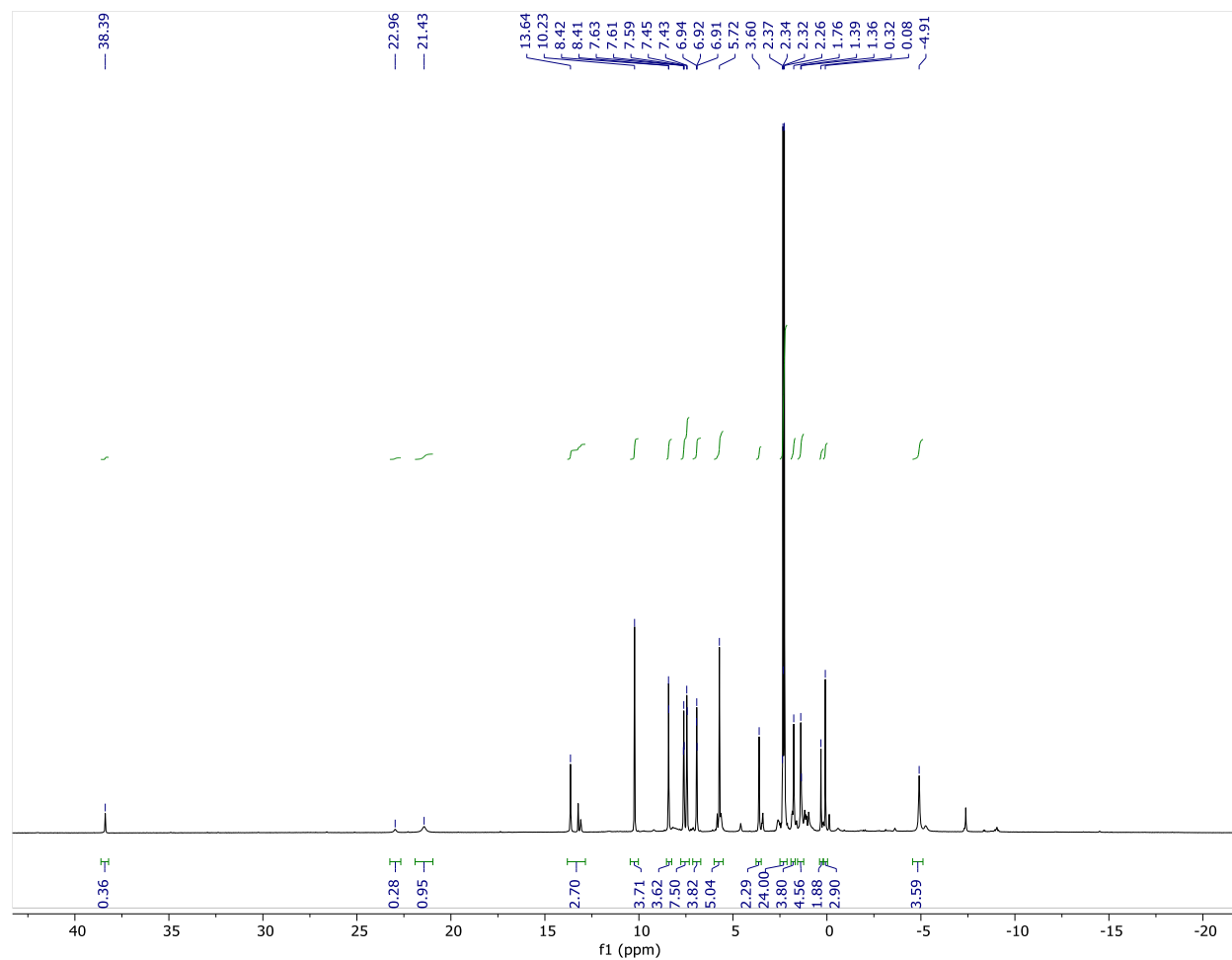


Figure 5-9. Crude  $^1\text{H}$  NMR of  $\text{U}(\text{PyPyr}^{\text{Me}_2})_4$ . There are still signals present for **2**, but the majority of the  $\text{N}(\text{TMS})\text{Cy}$  amides have been displaced.



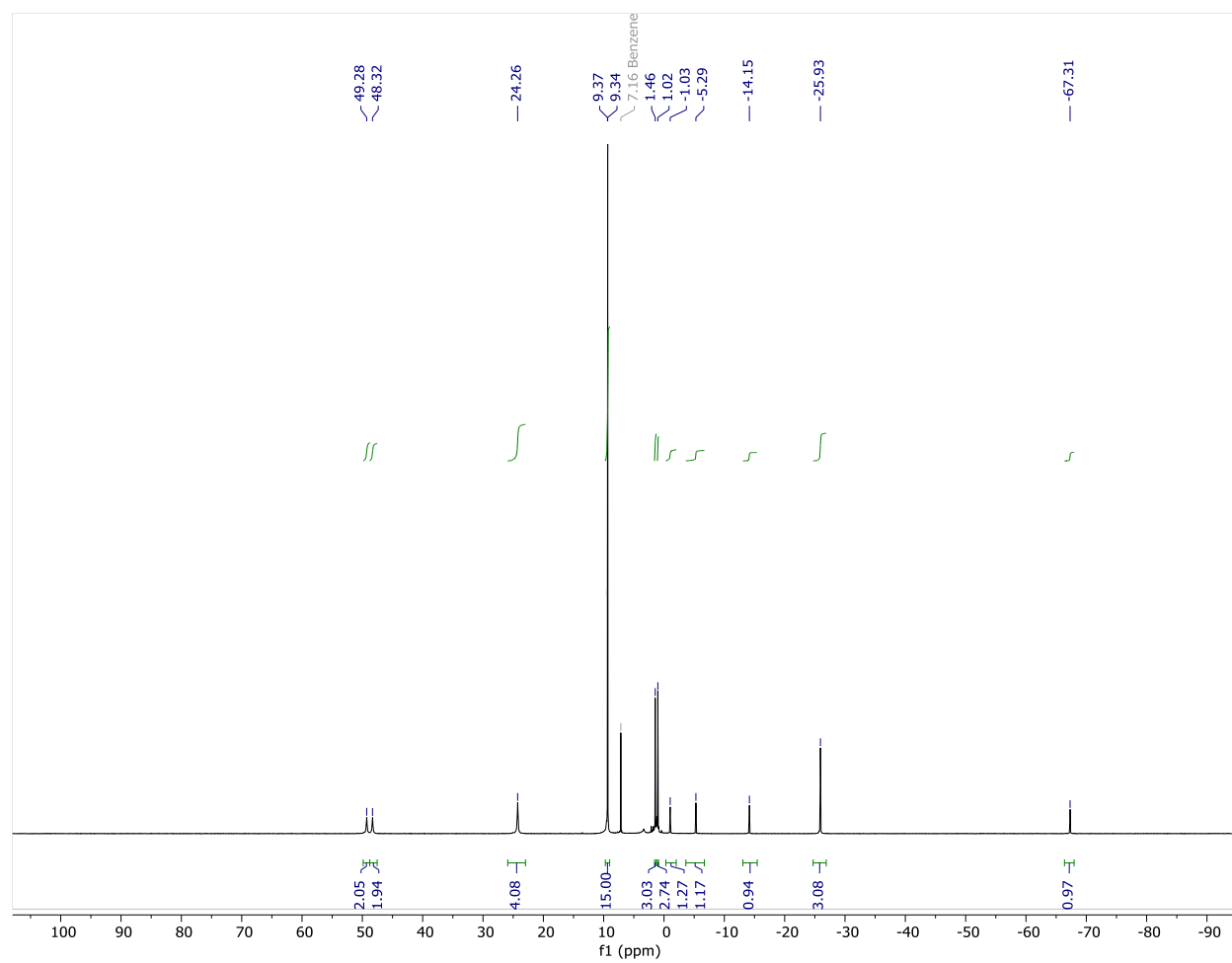


Figure 5-10.  $^1\text{H}$  NMR of  $\text{Cp}^*\text{UCl}_2(\text{PyPyr}^{\text{Me}_3})(\text{thf})$  (**3a**).



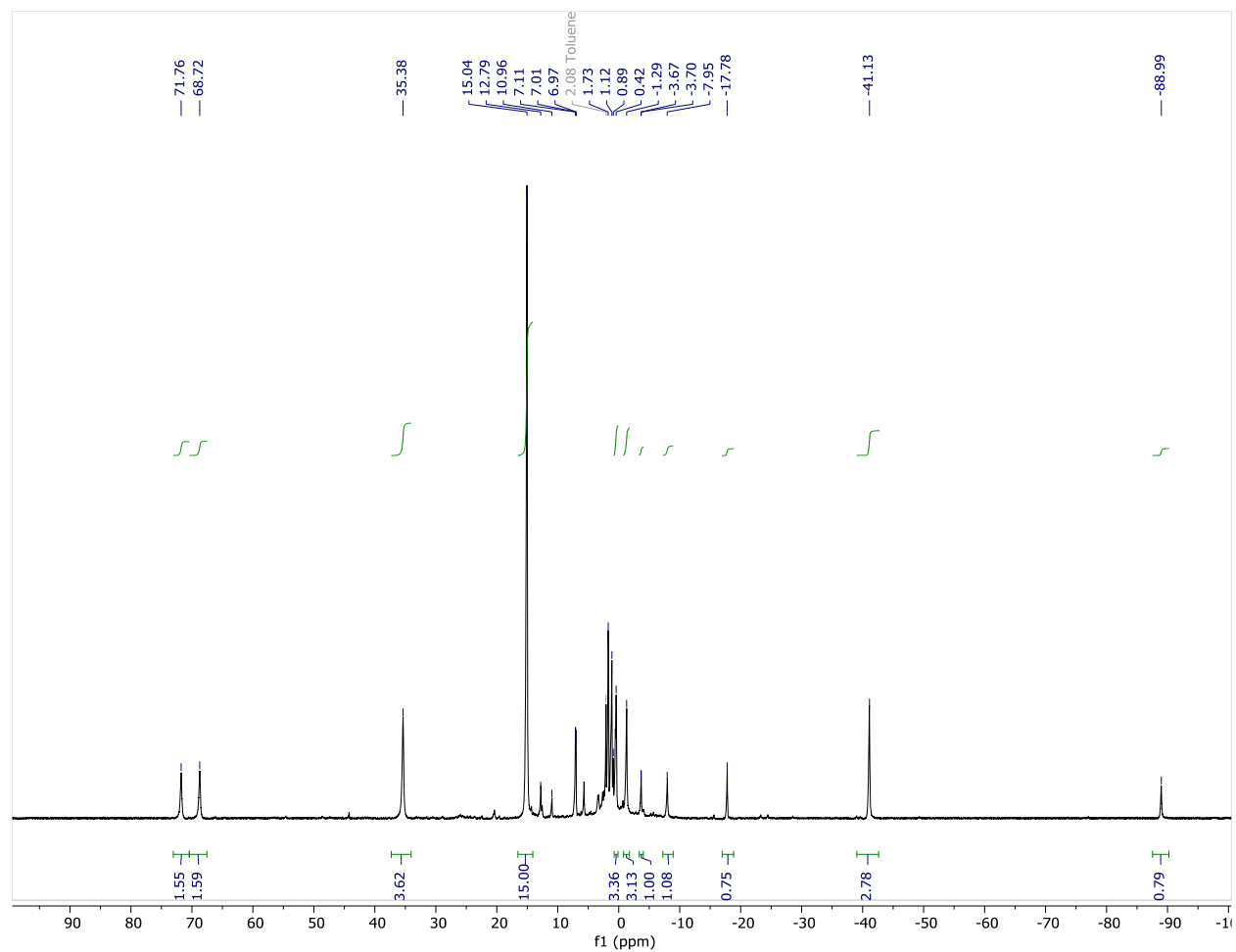


Figure 5-11. Best  $^1\text{H}$  NMR of  $\text{Cp}^*\text{UI}_2(\text{PyPyr}^{\text{Me}_3})(\text{thf})$ , (**3b**). The spectrum contains impurities from unknown species that are not removed by recrystallization.



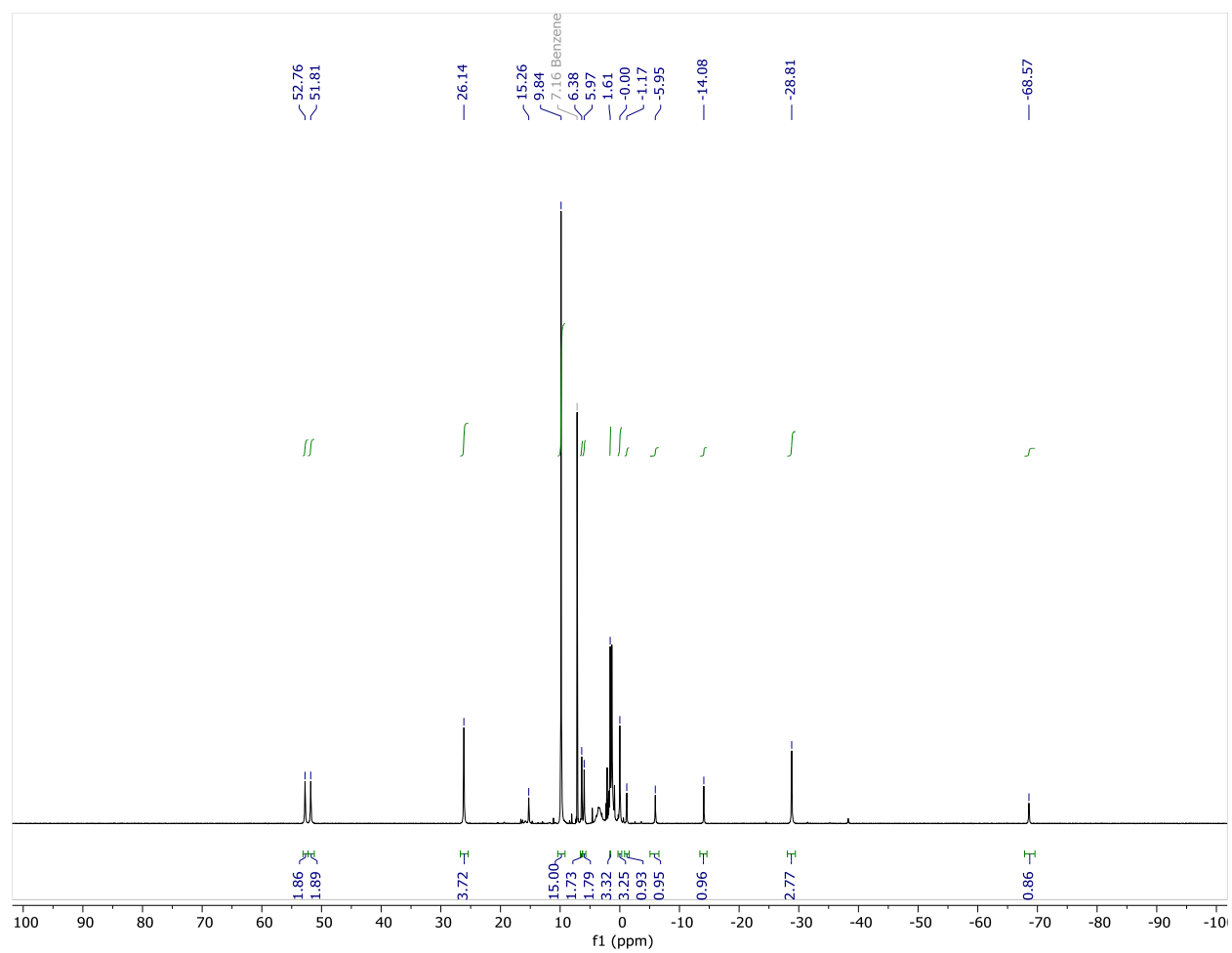


Figure 5-12. <sup>1</sup>H NMR of Cp\*UCl<sub>2</sub>(PyPyr<sup>Me2Tol</sup>)(thf), (4a).



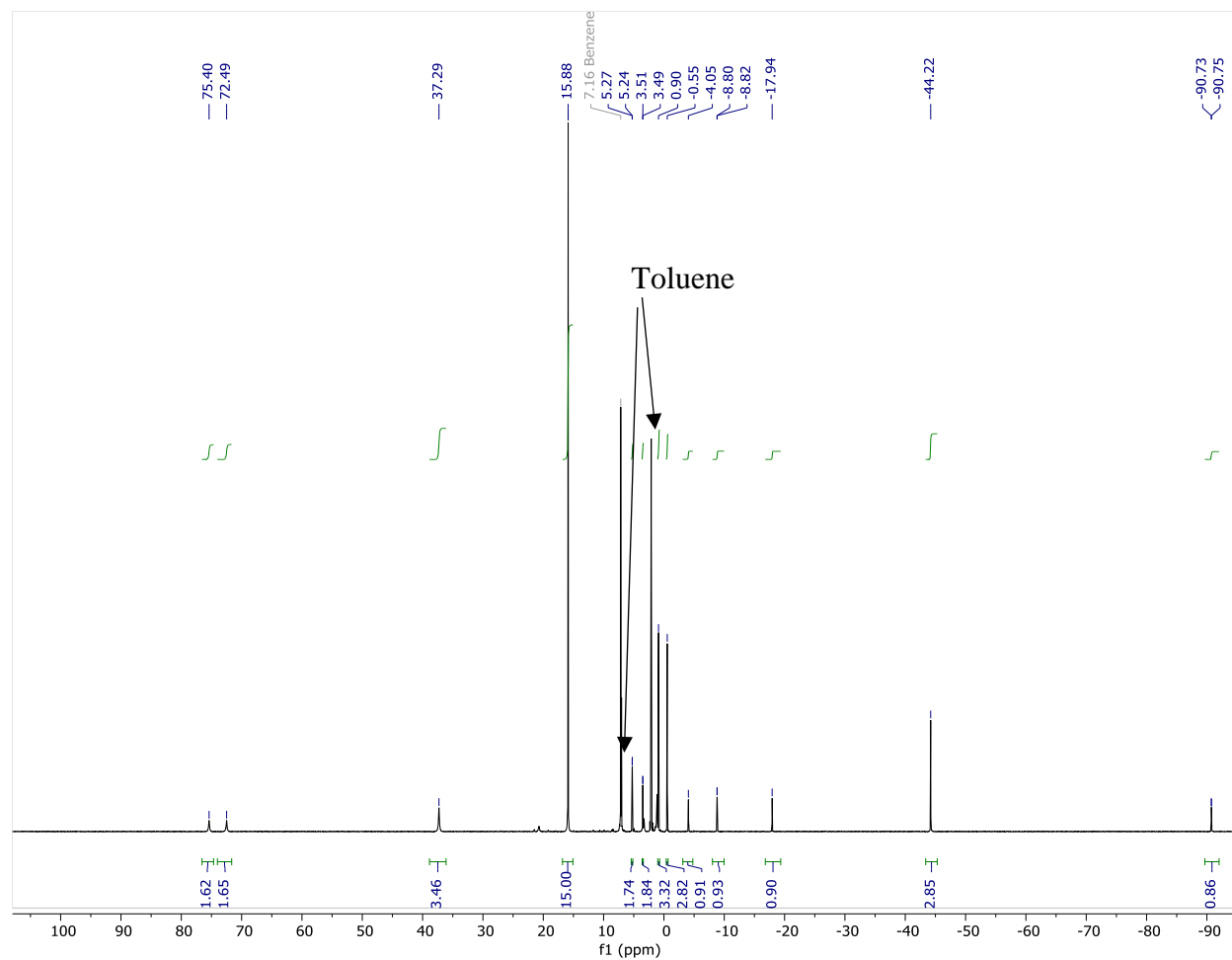


Figure 5-13.  $^1\text{H}$  NMR of  $\text{Cp}^*\text{UI}_2(\text{PyPyr}^{\text{Me}_2\text{Tol}})(\text{thf})$  (**4b**).



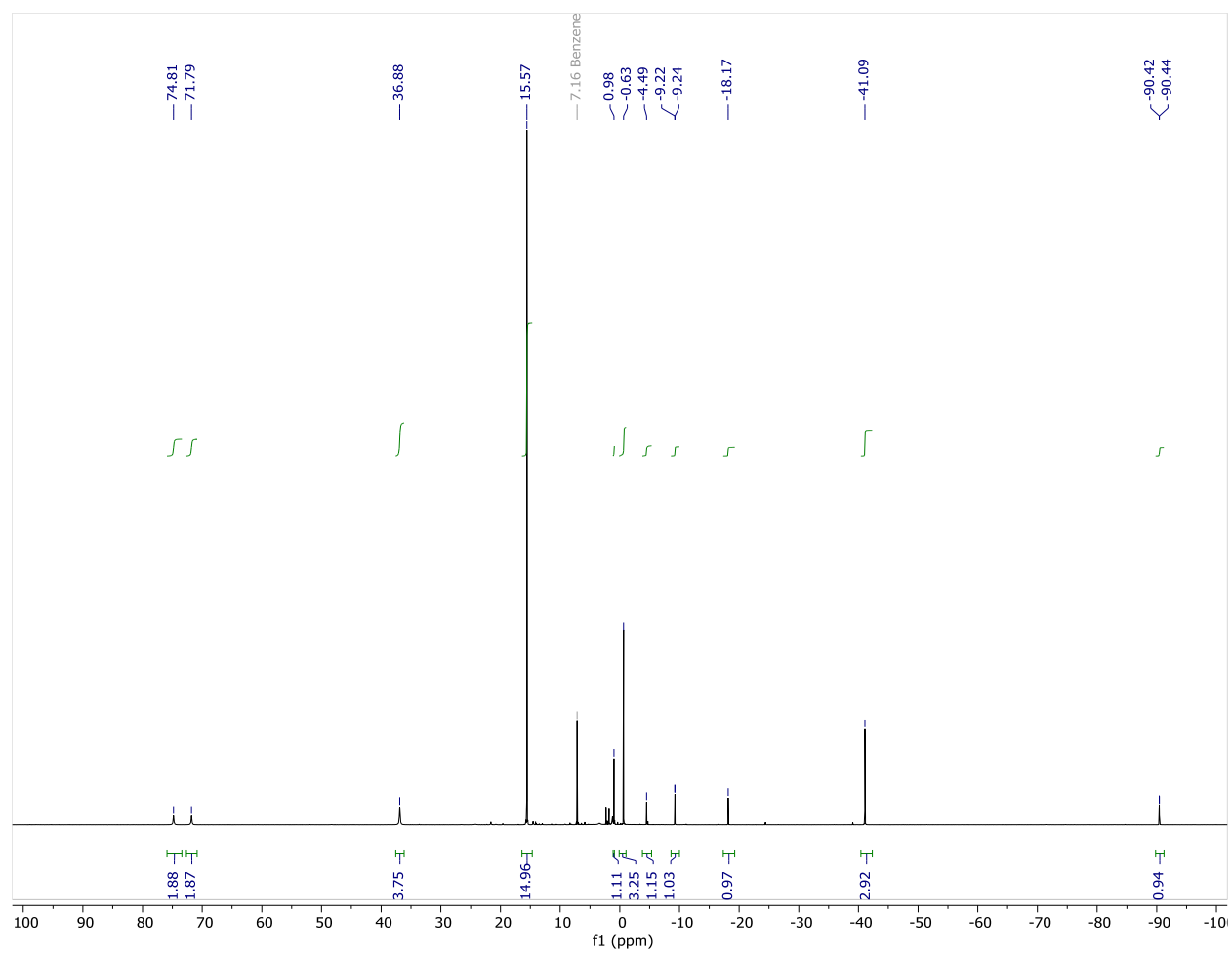


Figure 5-14. <sup>1</sup>H NMR of Cp\*UI<sub>2</sub>(PyPyr<sup>Me2</sup>)(thf) (**5**).



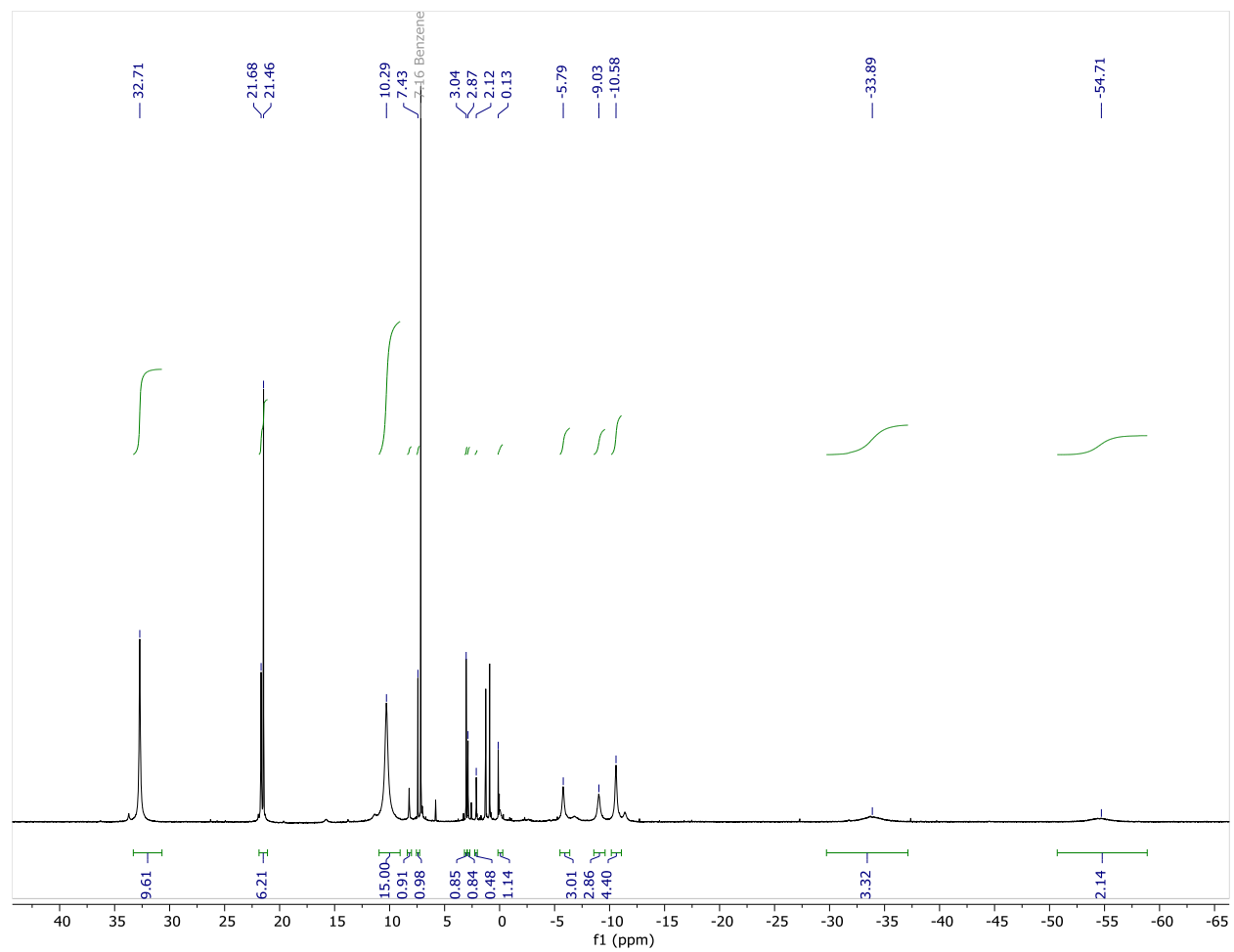


Figure 5-15. <sup>1</sup>H NMR of  $(\kappa^2(\text{N-C})\text{-CH}_2\text{SiMe}_2\text{NTMS})\text{U}(\text{Cp}^*)(\text{PyPyr}^{\text{Me}^3})$  (**6**).



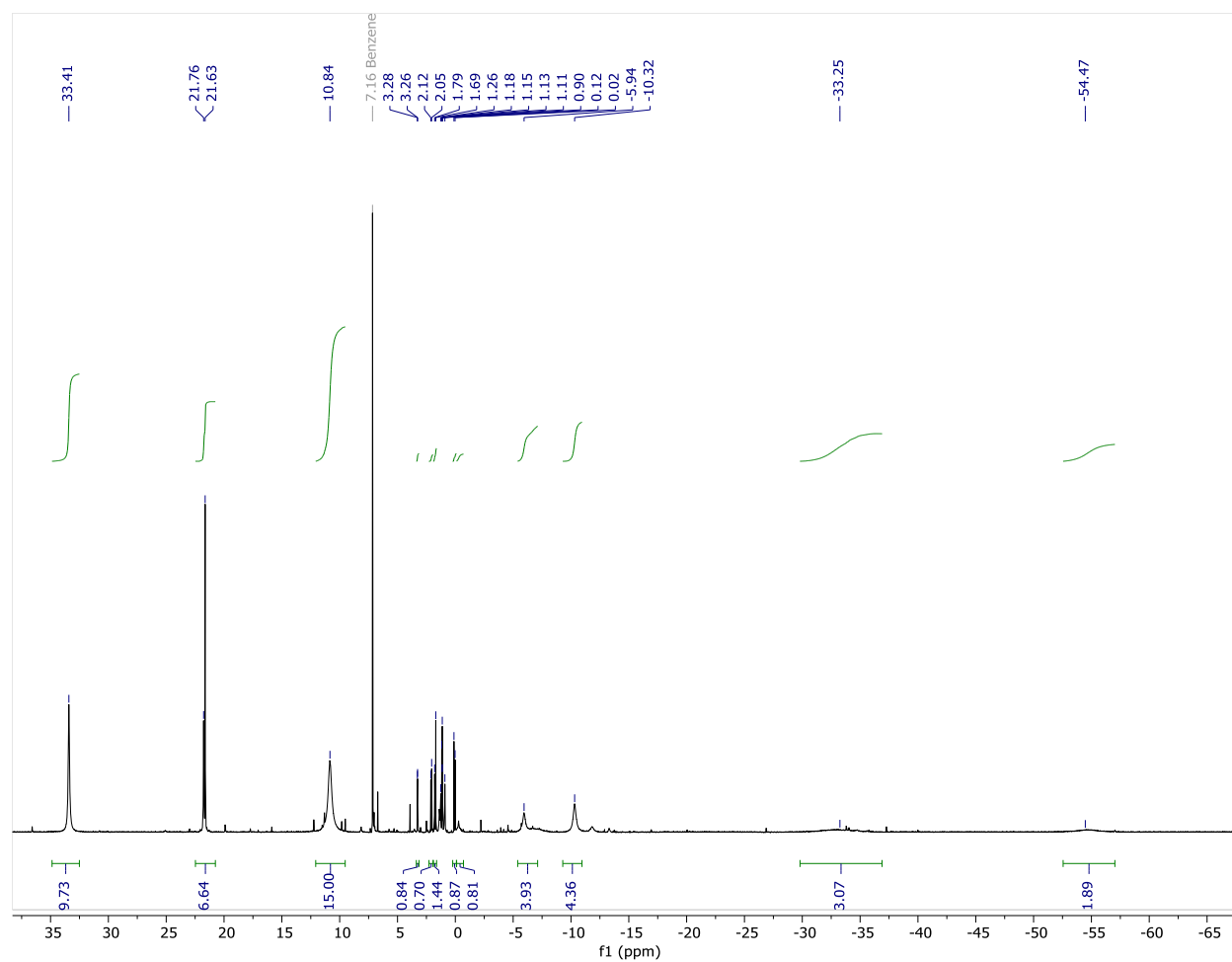


Figure S-16. Crude <sup>1</sup>H NMR of (κ<sup>2</sup>(N-C)-CH<sub>2</sub>SiMe<sub>2</sub>NTMS)U(Cp\*)(PyPyr<sup>Me2</sup>) (7).



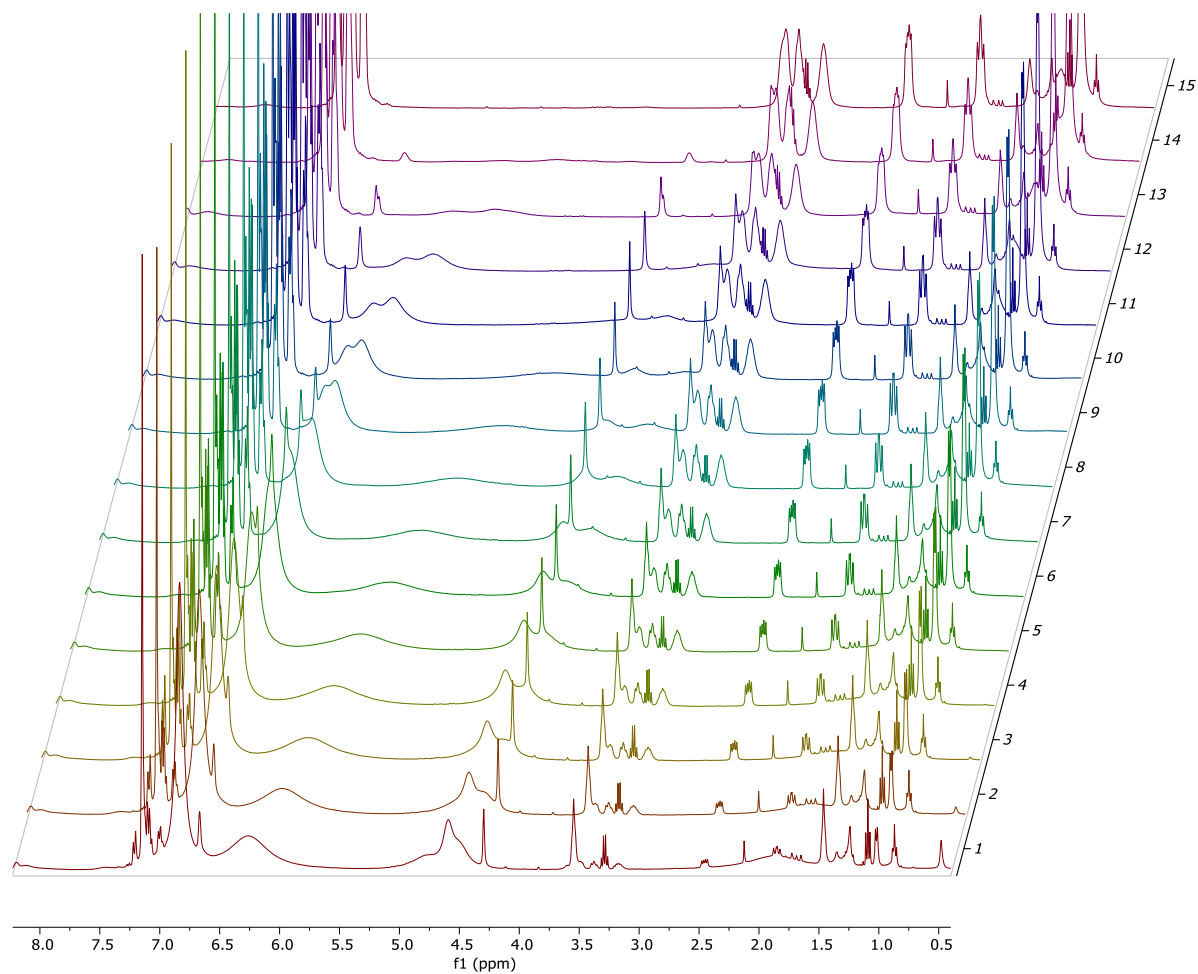


Figure 5-17. Arrayed Spectra from the catalysis of **6** (10 mol%, 65 °C, C<sub>6</sub>D<sub>6</sub>) with DPAP. Each spectrum was taken in 10-minute intervals. The reaction appears to be complete after ~150 minutes (spectrum 15).



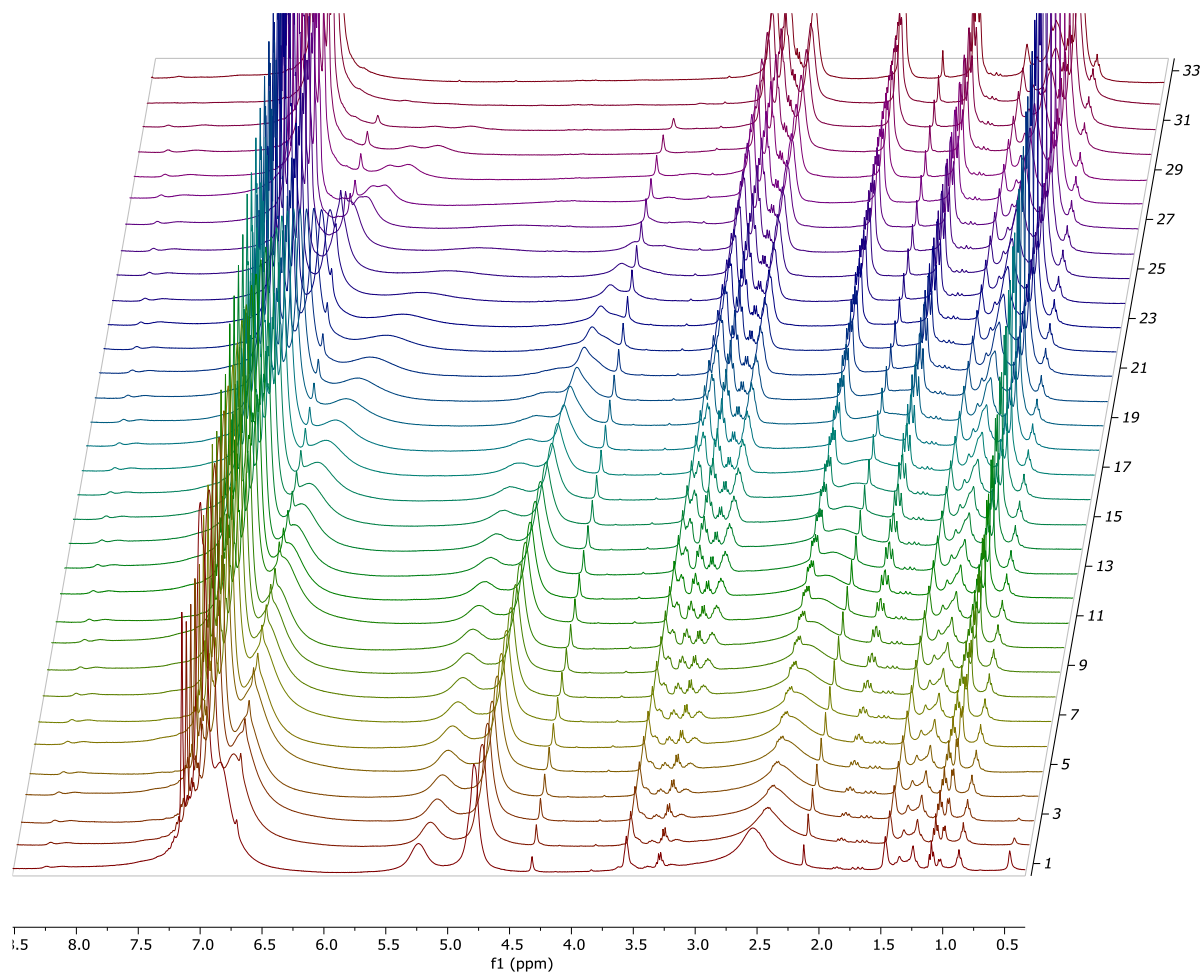


Figure 5-18. Arrayed Spectra from the catalysis of **6** (5 mol%, 65 °C, C<sub>6</sub>D<sub>6</sub>) with DPAP. Each spectrum was taken in 10-minute intervals. The reaction appears to be complete after ~330 minutes (spectrum 33).



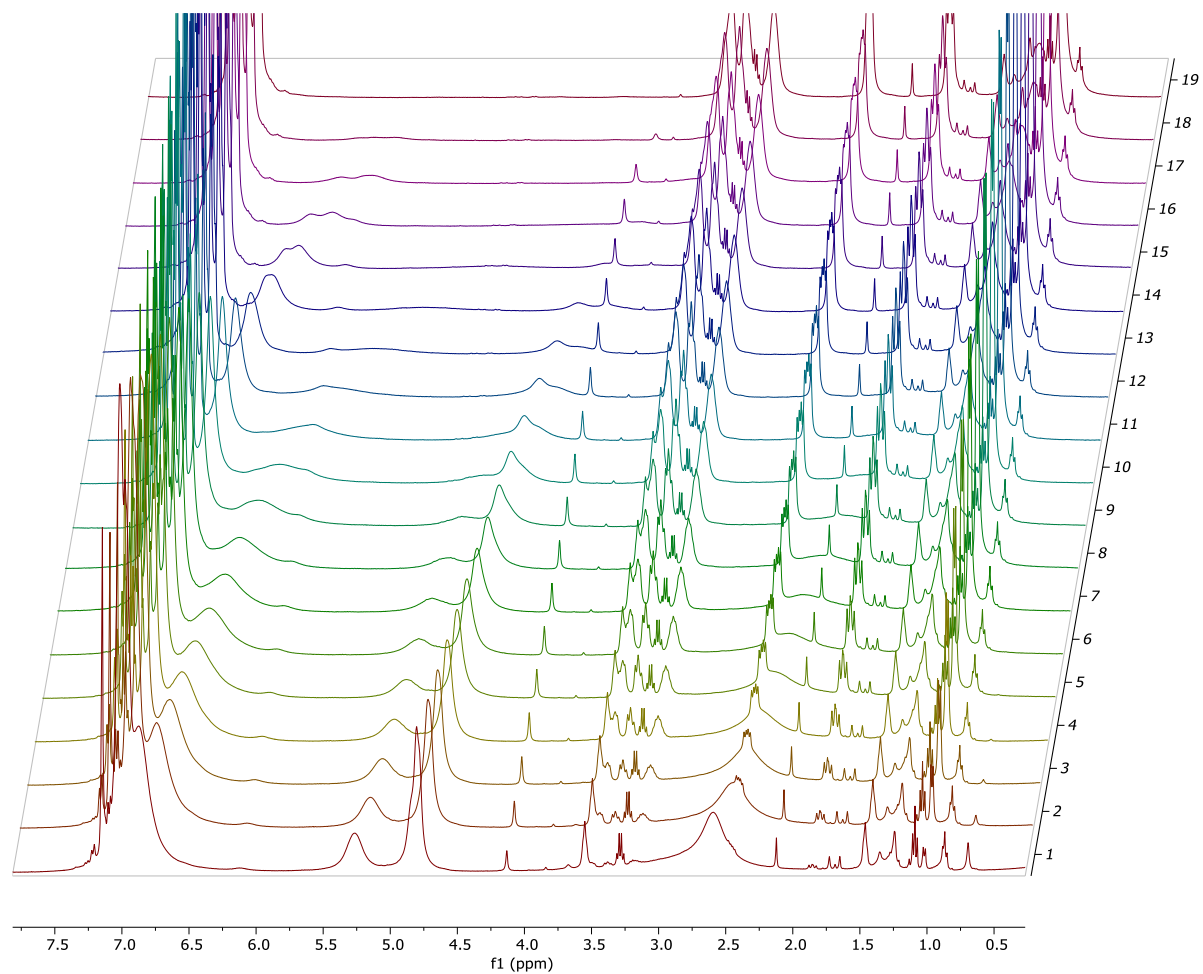


Figure 5-19. Arrayed Spectra from the catalysis of **7** (5 mol%, 65 °C, C<sub>6</sub>D<sub>6</sub>) with DPAP. Each spectrum was taken in 10-minute intervals. The reaction appears to be complete after ~190 minutes (spectrum 19).



## REFERENCES



## REFERENCES

1. Economic Assessment of Used Nuclear Fuel Management in the United States. **2006**.
2. Lewis, A. J.; Carroll, P. J.; Schelter, E. J., *J. Am. Chem. Soc.* **2013**, *135* (35), 13185-13192.
3. Billow, B. S.; McDaniel, T. J.; Odom, A. L., *Nat. Chem.* **2017**, *9*, 837-842.
4. Pepper, M.; Bursten, B. E., *Chem. Rev.* **1991**, *91* (5), 719-741.
5. Allen, P. G.; Shuh, D. K.; Bucher, J. J.; Edelstein, N. M.; Reich, T.; Denecke, M. A.; Nitsche, H., *Inorg. Chem.* **1996**, *35* (3), 784-787.
6. Denecke, M. A., *Coord. Chem. Rev.* **2006**, *250* (7), 730-754.
7. Graves, C. R.; Yang, P.; Kozimor, S. A.; Vaughn, A. E.; Clark, D. L.; Conradson, S. D.; Schelter, E. J.; Scott, B. L.; Thompson, J. D.; Hay, P. J.; Morris, D. E.; Kiplinger, J. L., *J. Am. Chem. Soc.* **2008**, *130* (15), 5272-5285.
8. Lan, J.-H.; Shi, W.-Q.; Yuan, L.-Y.; Li, J.; Zhao, Y.-L.; Chai, Z.-F., *Coord. Chem. Rev.* **2012**, *256* (13), 1406-1417.
9. Minasian, S. G.; Keith, J. M.; Batista, E. R.; Boland, K. S.; Clark, D. L.; Conradson, S. D.; Kozimor, S. A.; Martin, R. L.; Schwarz, D. E.; Shuh, D. K.; Wagner, G. L.; Wilkerson, M. P.; Wolfsberg, L. E.; Yang, P., *J. Am. Chem. Soc.* **2012**, *134* (12), 5586-5597.
10. Gagliardi, L.; Truhlar, D. G.; Li Manni, G.; Carlson, R. K.; Hoyer, C. E.; Bao, J. L., *Acc. Chem. Res.* **2017**, *50* (1), 66-73.
11. Wang, J.; Dash, A. K.; Kapon, M.; Berthet, J.-C.; Ephritikhine, M.; Eisen, M. S., *Chem. Eur. J.* **2002**, *8* (23), 5384-5396.
12. Haskel, A.; Straub, T.; Eisen, M. S., *Organometallics* **1996**, *15* (18), 3773-3775.
13. Stubbert, B. D.; Marks, T. J., *J. Am. Chem. Soc.* **2007**, *129* (14), 4253-4271.
14. Broderick, E. M.; Gutzwiller, N. P.; Diaconescu, P. L., *Organometallics* **2010**, *29* (15), 3242-3251.
15. Hayes, C. E.; Platel, R. H.; Schafer, L. L.; Leznoff, D. B., *Organometallics* **2012**, *31* (19), 6732-6740.
16. Klappa, J. J.; Rich, A. E.; McNeill, K., *Org. Lett.* **2002**, *4* (3), 435-437.
17. Wang, J. Q.; Dash, A. K.; Berthet, J. C.; Ephritikhine, M.; Eisen, M. S., *Organometallics* **1999**, *18* (13), 2407-2409.



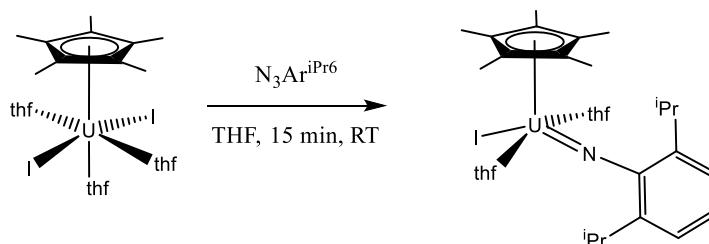
18. Berthet, J.-C.; Ephritikhine, M., *J. Chem. Soc. Chem. Commun.* **1993**, (20), 1566-1567.
19. Mansell, S. M.; Perandones, B. F.; Arnold, P. L., *J. Organomet. Chem.* **2010**, 695 (25), 2814-2821.
20. Tondreau, A. M.; Duignan, T. J.; Stein, B. W.; Fleischauer, V. E.; Autschbach, J.; Batista, E. R.; Boncella, J. M.; Ferrier, M. G.; Kozimor, S. A.; Mocko, V.; Neidig, M. L.; Cary, S. K.; Yang, P., *Inorg. Chem.* **2018**, 57 (14), 8106-8115.
21. Dissanayake, A. A.; Odom, A. L., *Chem. Commun.* **2012**, 48 (3), 440-442.
22. Lewis, A. J.; Williams, U. J.; Carroll, P. J.; Schelter, E. J., *Inorg. Chem.* **2013**, 52 (13), 7326-7328.
23. Monreal, M. J.; Thomson, R. K.; Cantat, T.; Travia, N. E.; Scott, B. L.; Kiplinger, J. L., *Organometallics* **2011**, 30 (7), 2031-2038.
24. Kiplinger, J. L.; Morris, D. E.; Scott, B. L.; Burns, C. J., *Organometallics* **2002**, 21 (26), 5978-5982.
25. Straub, T.; Haskel, A.; Neyroud, T. G.; Kapon, M.; Botoshansky, M.; Eisen, M. S., *Organometallics* **2001**, 20 (24), 5017-5035.
26. DiFranco, S. A.; Maciulis, N. A.; Staples, R. J.; Batrice, R. J.; Odom, A. L., *Inorg. Chem.* **2012**, 51 (2), 1187-200.
27. Lewis, A. J.; Mullane, K. C.; Nakamaru-Ogiso, E.; Carroll, P. J.; Schelter, E. J., *Inorg. cHem.* **2014**, 53 (13), 6944-6953.
28. La Pierre, H. S.; Meyer, K., *Inorg. Chem.* **2013**, 52 (2), 529-539.
29. Kosog, B.; La Pierre, H. S.; Heinemann, F. W.; Liddle, S. T.; Meyer, K., *J. Am. Chem. Soc.* **2012**, 134 (11), 5284-5289.
30. Kaltsoyannis, N., *Chem. Soc. Rev.* **2003**, 32 (1), 9-16.
31. O'Grady, E.; Kaltsoyannis, N., *J. Chem. Soc. Dalton Trans.* **2002**, (6), 1233-1239.
32. Huynh, H. V.; Han, Y.; Jothibasu, R.; Yang, J. A., *Organometallics* **2009**, 28 (18), 5395-5404.
33. Clegg, W.; Conway, B.; Kennedy, A. R.; Klett, J.; Mulvey, R. E.; Russo, L., *Eur. J. of Inorg. Chem.* **2011**, 2011 (5), 721-726.
34. Motolko, K. S. A.; Emslie, D. J. H.; Jenkins, H. A., *Organometallics* **2017**, 36 (8), 1601-1608.



## Chapter 6. Synthesis and Characterization of Uranium-Terphenyl Complexes

### 6.1 Investigating Imido Synthesis

As was mentioned briefly in chapter 5, we were attempting experiments aimed at isolating uranium(IV) monoimido compounds. More specifically, we were attempting diisopropylphenyl (DiPP) imido synthesis using azide and  $\text{KC}_8$ , analogous to the reports recently published by the Bart group.<sup>1-2</sup> Starting from a THF solution of  $(\text{Cp}^*)\text{U}(\text{I})_2(\text{thf})_3$ , where  $\text{Cp}^* =$  pentamethylcyclopentadiene,  $\text{N}_3\text{DiPP}$  was added (Scheme 6-1).



Scheme 6-1. Reaction of  $(\text{Cp}^*)\text{U}(\text{I})_2(\text{thf})_3$  with  $\text{DiPPN}_3$ .

In contrast to reports from the Bart group, where  $\text{U}(\text{I})_3(\text{thf})_4$  and azide can be added together without reaction, when azide is added to  $(\text{Cp}^*)\text{U}(\text{I})_2(\text{thf})_3$ , immediate, vigorous bubbling occurs. We expected formation of a U(V) imido compound since U(III) was reacting with just  $\text{N}_3\text{DiPP}$ . Surprisingly, crystals isolated from the reaction mixture were identified by X-ray diffraction as  $(\text{Cp}^*)\text{U}(\text{I})_3(\text{thf})_2$  (**1**). Presumably, the strongly electron donating  $\text{Cp}^*$  makes the U(III) metal center reducing enough to react with the azide without the addition of  $\text{KC}_8$ . The compounds should have reacted to form a U(V) imido, but perhaps the instability of the product caused disproportionation into a mixture of compounds. Unfortunately, no other products were isolable.



This reaction made us wonder if it would be possible to stabilize the U(V) imido (**[Int]** in Scheme 6-1) using sterically crowded ligands. We proposed that if the aryl azide were much larger, the intermediate, **[Int]**, of the reaction shown in Scheme 6-1 might be isolable. Toward this end, we began investigations using the extremely bulky terphenyl ligands.<sup>3</sup> There are surprisingly few reported compounds of uranium with terphenyl substituents.<sup>4-6</sup> However, as will be discussed in detail below, these terphenyl ligands proved to be ideal ligands for uranium, and provided access to some exciting low valent uranium species.

## 6.2 Steric Bulk as a Method to Slow Ligand Redistribution

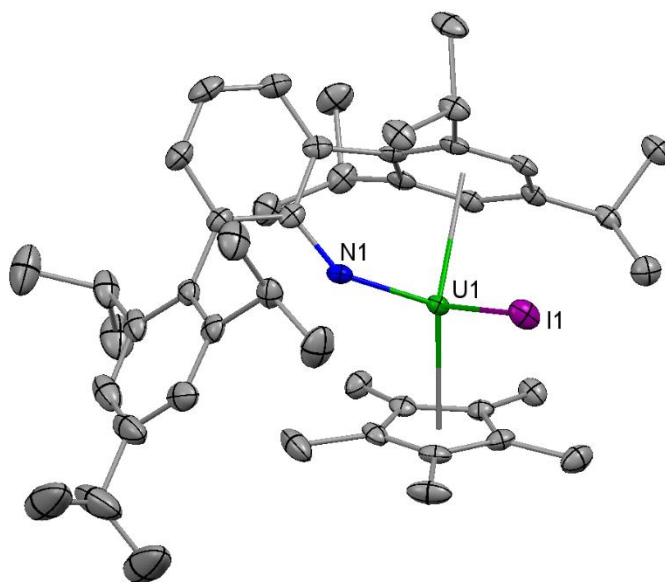
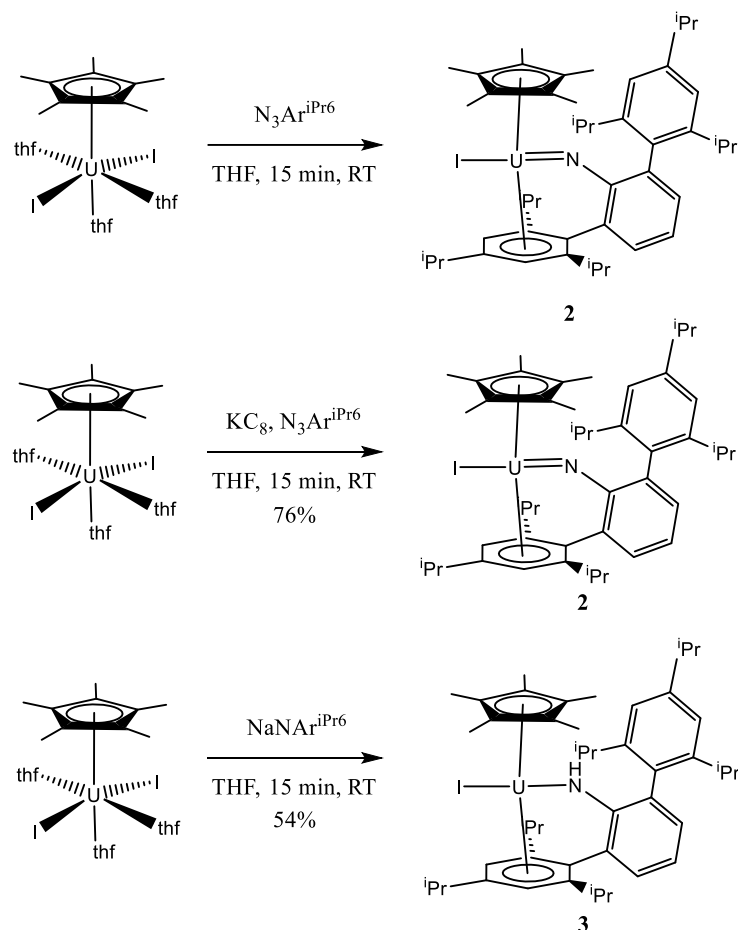


Figure 6-1. Single crystal structure of (Cp\*)UI(NAr<sup>iPr6</sup>) (**2**). Solvent molecules and hydrogens removed for clarity.

Following the same procedure in Scheme 6-1, when 2,6-bis(2,4,6-triisopropylphenyl)-phenyl azide (N<sub>3</sub>Ar<sup>iPr6</sup>) was added to a THF solution of (Cp\*)U(I)<sub>2</sub>(thf)<sub>3</sub> (Scheme 6-2, top), the reaction mixture immediately bubbles and changes color from turquoise to a deep red. Upon crystallization of the product, deep red colored blocks were obtained. Single crystal X-ray diffraction analysis of these crystals identified the product as (Cp\*)UI(NAr<sup>iPr6</sup>) (**2**), Figure 6-1.





Scheme 6-2. Top. Discovery of  $(\text{Cp}^*)\text{UI}(\text{NAr}^{i\text{Pr}_6})$  (**2**) from  $(\text{Cp}^*)\text{U}(\text{I})_2(\text{thf})_3$  and  $\text{N}_3\text{Ar}^{i\text{Pr}_6}$  disproportionation. Middle. Rational synthesis of **2**. Bottom. Synthesis of  $(\text{Cp}^*)\text{UI}(\text{NHAr}^{i\text{Pr}_6})$  (**3**) from  $(\text{Cp}^*)\text{U}(\text{I})_2(\text{thf})_3$  and  $\text{NaNAr}^{i\text{Pr}_6}$

Unfortunately, the bulky azide was only partially successful at stopping the disproportionation. Electron transfer reactions must have still occurred since the oxidation state of the uranium center in **2** is U(IV). But, in contrast to the reactions with  $\text{N}_3\text{DiPP}$  from Scheme 6-1, the ligand stoichiometry was retained. Rational synthesis of **2** was achieved by adding an equivalent of  $\text{KC}_8$  to  $(\text{Cp}^*)\text{U}(\text{I})_2(\text{thf})_3$  before addition of the  $\text{N}_3\text{Ar}^{i\text{Pr}_6}$ . Using this procedure, the U(IV) imido complex, **2**, could be isolated in reasonable yields (Scheme 6-2, middle).



In the crystal structure, **2** has a pronounced  $\eta^6$ -interaction between the *ortho*-arene substituent of the  $\text{Ar}^{i\text{Pr}_6}$  and uranium. This interaction gives the molecule a geometry similar to classic  $(\text{Cp}^*)_2\text{U}(\text{X})_2$  compounds.<sup>7</sup> Because of the  $\eta^6$ -arene interaction, the U-N-C bond angle of the imido is uncharacteristically bent at  $145.0(3)^\circ$ .<sup>1-2, 8-9</sup> The N-U bond length of  $1.977(4)$  Å, however, is consistent with the assignment of N1 as an imido. UV-vis/NIR spectroscopy is also consistent with assignment of **2** as a U(IV) imido.

It has long been established that uranium species can be stabilized through interaction with arenes.<sup>10-19</sup> Given the definite arene interaction in compound **2**, we postulated the steric bulk and arene capping ability of the  $\text{Ar}^{i\text{Pr}_6}$  ligand may lead to stabilization of some exciting uranium species. Specifically, we wondered if these bulky nitrogen-based ligands presented here would allow access to low oxidation state uranium species.

### 6.3 Comparisons Between Amide and Imides of Bulky Ligands

In order to compare **2** to an analogous uranium  $\text{Ar}^{i\text{Pr}_6}$  amide as well as producing uranium compounds in lower oxidation states, the synthesis of  $(\text{Cp}^*)\text{UI}(\text{NHAr}^{i\text{Pr}_6})$  (**3**) was pursued. Simple precipitation of NaI by reacting  $(\text{Cp}^*)\text{U}(\text{I})_2(\text{thf})_3$  and  $\text{NaNHAr}^{i\text{Pr}_6}$  in THF results in a color change from turquoise to black, producing **3** (Scheme 6-2, bottom). In the crystal structure of **3** (Figure 6-2), the U-N-C bond is substantially more bent at  $132.9(2)^\circ$ , and the U-N bond is significantly longer,  $2.277(3)$  Å compared to  $1.977(4)$  Å in the imido. Compound **3** displays a similar  $\eta^6$ -interaction between the *ortho*-arene substituent of the  $\text{Ar}^{i\text{Pr}_6}$  and the uranium atom. Aside from the bond length differences, the crystal structures of the two molecules are quite similar, and unit cell dimensions indicate the two molecules are isostructural despite the difference in formal oxidation state. Interestingly, the  $\eta^6$ -arene in **3** has a distance from uranium to the centroid of the arene of  $2.482(2)$  Å, compared to the U-arene interaction in **2** which is substantially longer, at  $2.594(1)$  Å.



While there are a number of possible explanations for this phenomenon, to us, this suggests a stronger back bonding interaction from U(III) to the arene.<sup>15, 19</sup>

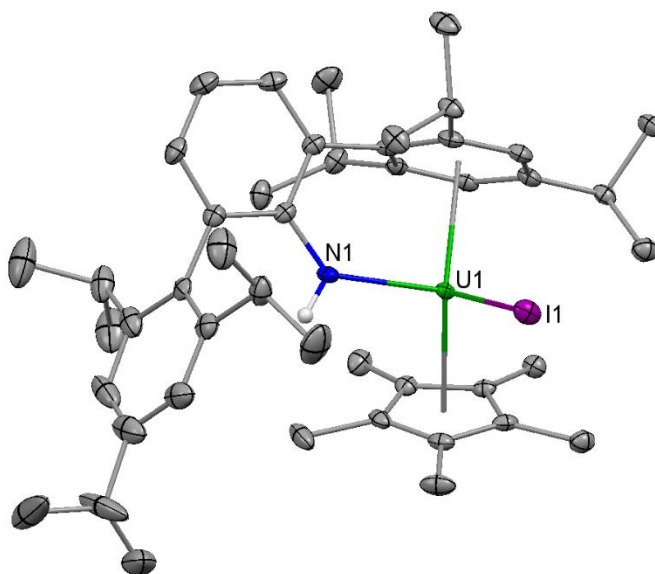


Figure 6-2. Single crystal structure of (Cp\*)UI(NHAr<sup>iPr6</sup>) (**3**). Hydrogens (except NH) and solvent removed for clarity.

Initial reactivity studies of both **2** and **3** show that the Ar<sup>iPr6</sup> substituent confers a remarkable degree of kinetic stability to these molecules, which could be ideal to access low valent uranium. Attempts at reduction of **2** using KC<sub>8</sub> and decamethylcobaltacene did result in color change of the solutions, but no clean products were isolable; <sup>1</sup>H NMR indicated messy reactions, and the only isolable crystals of X-ray quality were the starting material, **2**. Likewise, even simple deprotonations of the **3** were unsuccessful with a number of bases, presumably due to the extraordinary steric bulk of the Ar<sup>iPr6</sup> substituent. These results were promising inasmuch that the terphenyl group may stabilize what would normally be very reactive uranium species, but, ironically, those same groups were also hindering our ability to make the reactive species in the first place.



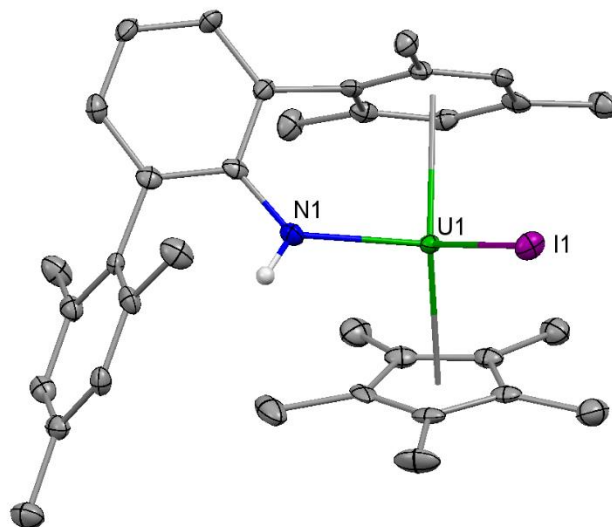
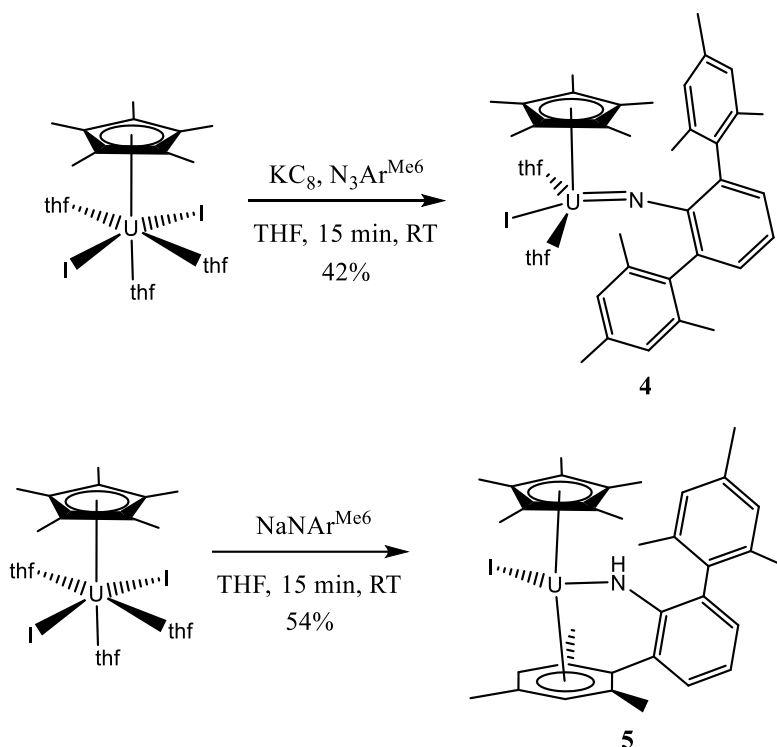


Figure 6-3. Single crystal structure of (Cp\*)UI(NHAr<sup>Me6</sup>) (**5**). Hydrogens (except NH) removed for clarity.

We postulated that perhaps reducing the steric bulk of the ligand somewhat but maintaining an  $\eta^6$ -arene interaction might allow for a balance between ligand redistribution reactivity, stability of the molecules, and subsequent reactivity. By exchanging the Ar<sup>iPr6</sup> group for a smaller terphenyl group, NAr<sup>Me6</sup>, we reduced steric bulk on the ligand, but retained 2,6-arene substituents available for  $\eta^6$ -arene interactions with the metal center. Syntheses similar to those for **2** and **3** produced the analogous (Cp\*)UI(NAr<sup>Me6</sup>) (**4**) and (Cp\*)UI(NHAr<sup>Me6</sup>) (**5**) Ar<sup>Me6</sup> compounds (Scheme 6-3).





Scheme 6-3. Synthesis of (Cp\*)UI(NAr<sup>Me6</sup>) (**4**) and (Cp\*)UI(NHAr<sup>Me6</sup>) (**5**).

As expected, **5**, shown in Figure 6-3, has the same basic geometry as **2** and **3** with a U-N-C bond angle of 132.4(3)° and a U-N bond length of 2.315(4) Å. The centroid of the arene in **5** is 2.501(3) Å from the uranium center, almost identical to **3**. This suggests similar uranium-arene interaction.

In contrast, compound **4**, shown in Figure 6-4, has no η<sup>6</sup>-arene interaction. Instead, two THF molecules are bound to the uranium and the U-N-C angle is 169.3(2)°, an angle much more typical of uranium imidos. Still, the U-N bond length of **4** is typical of similar to **2** at 2.006(3) Å. In an effort to encourage an η<sup>6</sup>-arene interaction and geometry analogous to **2**, attempts were made to synthesize the adduct-free analogue of **4** by performing the reaction in solvents other than THF. When the reaction was performed in diethyl ether, **4** was still the primary product. Seemingly, the THF molecules bound to the starting (Cp\*)U(I)<sub>2</sub>(thf)<sub>3</sub> are never displaced.



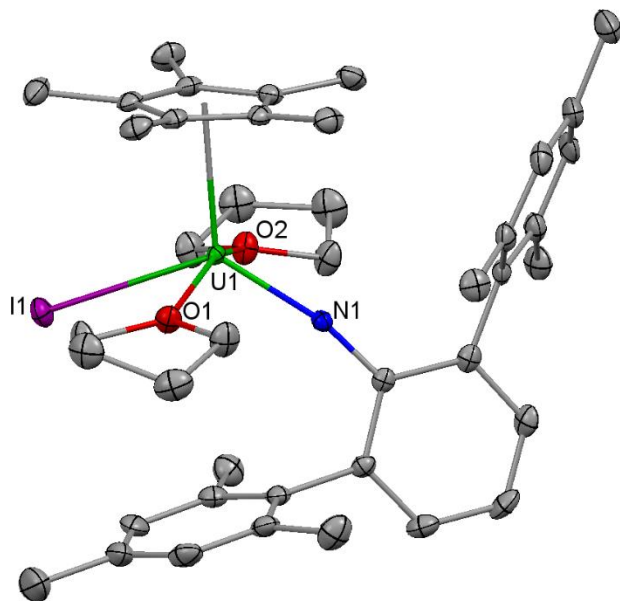
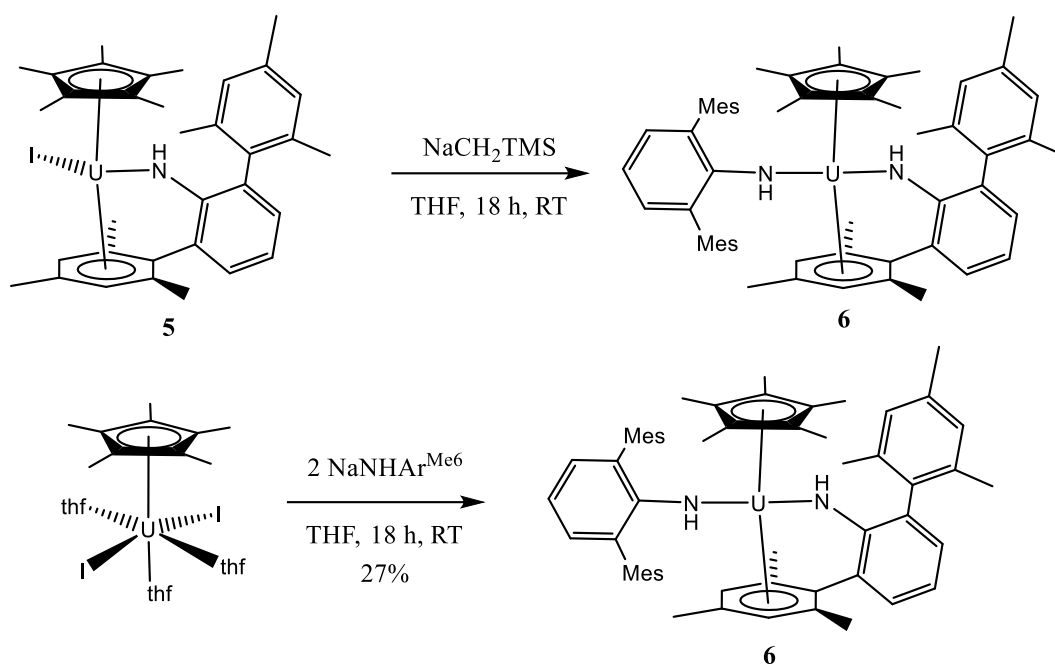


Figure 6-4. Single crystal structure of  $(\text{Cp}^*)\text{UI}(\text{NAr}^{\text{Me6}})(\text{thf})_2$ , **4**. Hydrogens (except NH) removed for clarity.

In an effort to test the reactivity of the *m*-terphenyl amides, we attempted deprotonation of **5** using (trimethylsilyl)methyl sodium. Instead of the desired U(III) imido, we isolated  $(\text{Cp}^*)\text{U}(\text{NAr}^{\text{Mes2}})_2$  (**6**). **6** can be generated through a more rational route by adding two equivalents of  $\text{NaNHAr}^{\text{Mes2}}$  to a stirring solution of  $(\text{Cp}^*)\text{U}(\text{I})_2(\text{thf})_3$  in THF (Scheme 6-4), but the reaction always contains impurities of free  $\text{H}_2\text{NAr}^{\text{Me6}}$ , among other things, which are not removed by recrystallization.





Scheme 6-4. Synthesis of  $(\text{Cp}^*)\text{U}(\text{NHAr}^{\text{Me6}})_2$  (**6**).

Interestingly, in the crystal structure of **6** (Figure 6-5), the two amide ligands are inequivalent. The U-N1-C bend is similar to the other U(III) amides, **3** and **5**, at  $132.1(2)^\circ$ . Compound **6** also has an  $\eta^6$ -mesityl group bound to the uranium center making the coordination sphere of **6** similar to the above compounds **2**, **3**, and **5**. Here the centroid of the  $\eta^6$ -mesityl is again at a distance of  $2.497(3) \text{ \AA}$ , identical to the  $\eta^6$ -arene-U distances in **3** and **5**. This observation is surprising considering the large difference between an ancillary iodide in **3** and **5** and the ancillary *m*-terphenyl amide in **6**. The N2 amide of **6**, however, is surprisingly linear, likely as a result of the steric hindrance around the uranium center with a U-N2-C angle of  $162.4(2)$ . Despite this linear bond angle, the bond length of  $2.336(3) \text{ \AA}$  suggests this nitrogen is still a monoanionic amide ligand. Additionally, UV-vis/NIR spectroscopy of a crude sample of **6** is consistent with the assignment of the metal center as a U(III), supporting the identity of both N1 and N2 as monoanionic amide ligands.<sup>20</sup> Still, since analytically pure **6** could not be generated, these assertions should not be considered definite.



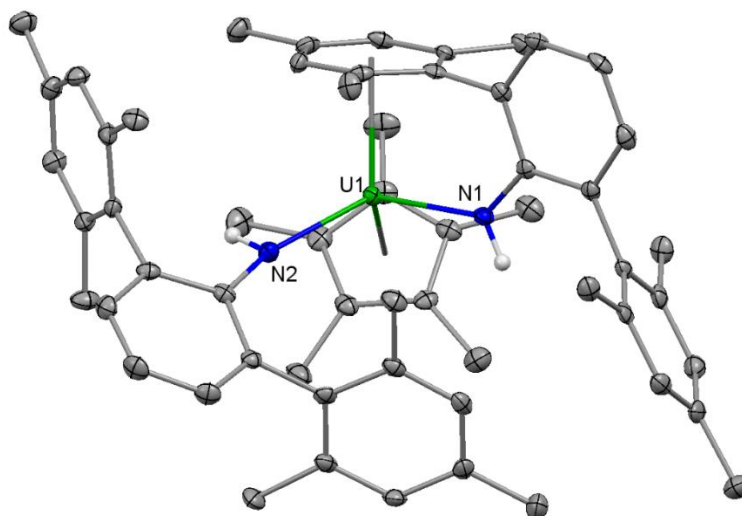


Figure 6-5. Single crystal structure of  $(\text{Cp}^*)\text{U}(\text{NHAr}^{\text{Me}_6})_2$ , **6**. Hydrogens (except NH) removed for clarity.

Nevertheless, discovery of **6** was very unexpected. We knew the ionic radius of uranium is large and can accommodate very bulky ligands; still we did not expect that two terphenyl groups could fit. This realization led to an idea, if we could fit two terphenyl groups around uranium, we might also be able to encourage a  $\text{bis}(\eta^6\text{-arene})\text{-U}$  complex with two amides. This way, we would produce a coordinatively saturated (formally 8 coordinate) uranium species with only two anionic ligands.



## 6.4 Bis(Amide) Species as a Way to Access Low Valent Uranium

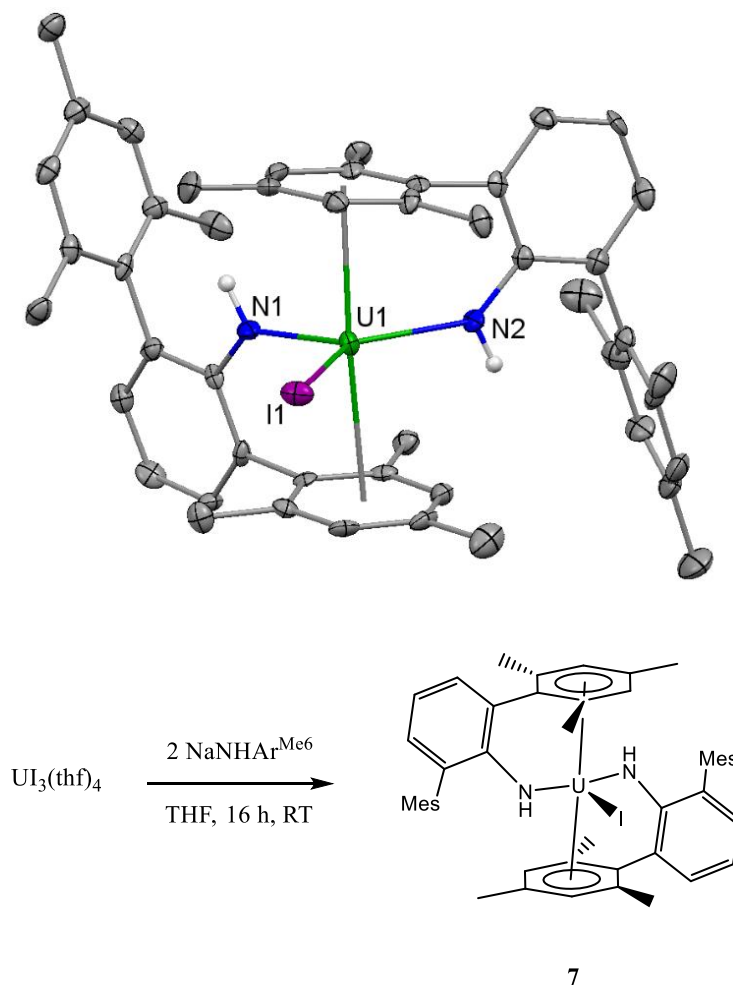


Figure 6-6. *Top*: Single crystal structure of **7**. Hydrogens (except NH's) removed for clarity. *Bottom*: Synthesis of  $\text{UI}(\text{NHAr}^{\text{Me6}})_2$  **7**.

Addition of two equivalents of  $\text{NaNHAr}^{\text{Mes2}}$  to  $\text{UI}_3(\text{thf})_4$  in THF gives  $\text{UI}(\text{NHAr}^{\text{Mes2}})_2$  (**7**), in decent yield (Figure 6-6). The single crystal X-ray diffraction structure of **7** displays the postulated bis( $\eta^6$ -arene) coordination. Unlike the analogous  $(\text{Cp}^*)_2$  complexes, the  $\eta^6$ -arene substituents adopt a more classical sandwich structure, i.e., the centroid-U-centroid angle is  $174.5(1)^\circ$ . As a result of the orientation of the ligands, **7** is almost  $C_2$  symmetric through the U-I bond vector. In the solid state the two amides are slightly inequivalent. The bond length of N1-U1 is  $2.316(6)$  Å compared to the N2-U2 length of  $2.349(6)$  Å. The U-N-C bond angles, though, are identical at



136.5(5)°. The largest disparity between the two amides is in the uranium-arene distances. Despite the slightly longer N-U bond, the  $\eta^6$ -mesityl group from N2 is  $\sim 0.08$  Å closer to uranium than the arene from N1, 2.754(3) Å compared to 2.825(3) Å. The  $^1\text{H}$  NMR spectrum of **7** displays very few well-resolved signals. Many of the signals observed are very broad, likely due to fluctuation in the U-arene bonds. This could be consistent with the inequivalent bond lengths to the arenes of N1 and N2 in the solid state.

By performing a reaction analogous to that shown in Figure 6-6 with the bulkier  $\text{Ar}^{\text{iPr}_6}$  amide, we were able to produce the analogous *bis*-( $\text{Ar}^{\text{iPr}_6}$ -arene) complex. Reaction of  $\text{UI}_3(\text{thf})_4$  with two equivalents of  $\text{NaNHAr}^{\text{iPr}_6}$  in THF overnight, produces  $\text{UI}(\text{NHAr}^{\text{iPr}_6})_2$  (**8**) (Figure 6-7, *Bottom*). In the crystal structure of **8**, the  $\eta^6$ -arene substituents are farther from the metal than in **7** at 2.788(1) Å and 2.897(1) Å for the arenes coordinated to N1 and N2, respectively. This is likely a result of the increased steric bulk of the isopropyl groups on the arene substituents in **8** relative to **7**. Additionally, the ligands are arranged in a fashion typical of  $\text{U}(\text{X})_2(\text{Cp}^*)_2$  compounds, with the centroids making an angle of 158.78(2)° with respect to uranium. This is likely a result of the closely packed arrangement of isopropyl groups surrounding the iodide ligand. The N-U bond distances are similar to **7** with both N1-U and N2-U at 2.354(2) Å and 2.365(2) Å. The U-N-C bond angles are slightly more obtuse than **7** at 138.7(2)° and 139.5(2)° for N1 and N2, respectively, which is expected given the greater arene-U distances.

In the solid state, **8** appears  $C_2$  symmetric with the rotational axis along the U-I bond vector (Figure 6-7). The two amide nitrogens and the iodide constitute an equatorial plane with the sum of angles totaling 359.88(5)°. Additionally, one triisopropylphenyl group from each amide substituent is  $\eta^6$ -arene capped in an axial position. The U-N-C bond angles and U-N bond lengths



are all consistent with monoanionic amide ligands. Furthermore, the quality of the data obtained in the crystal structure allowed location and refinement of the N-H hydrogen positions.

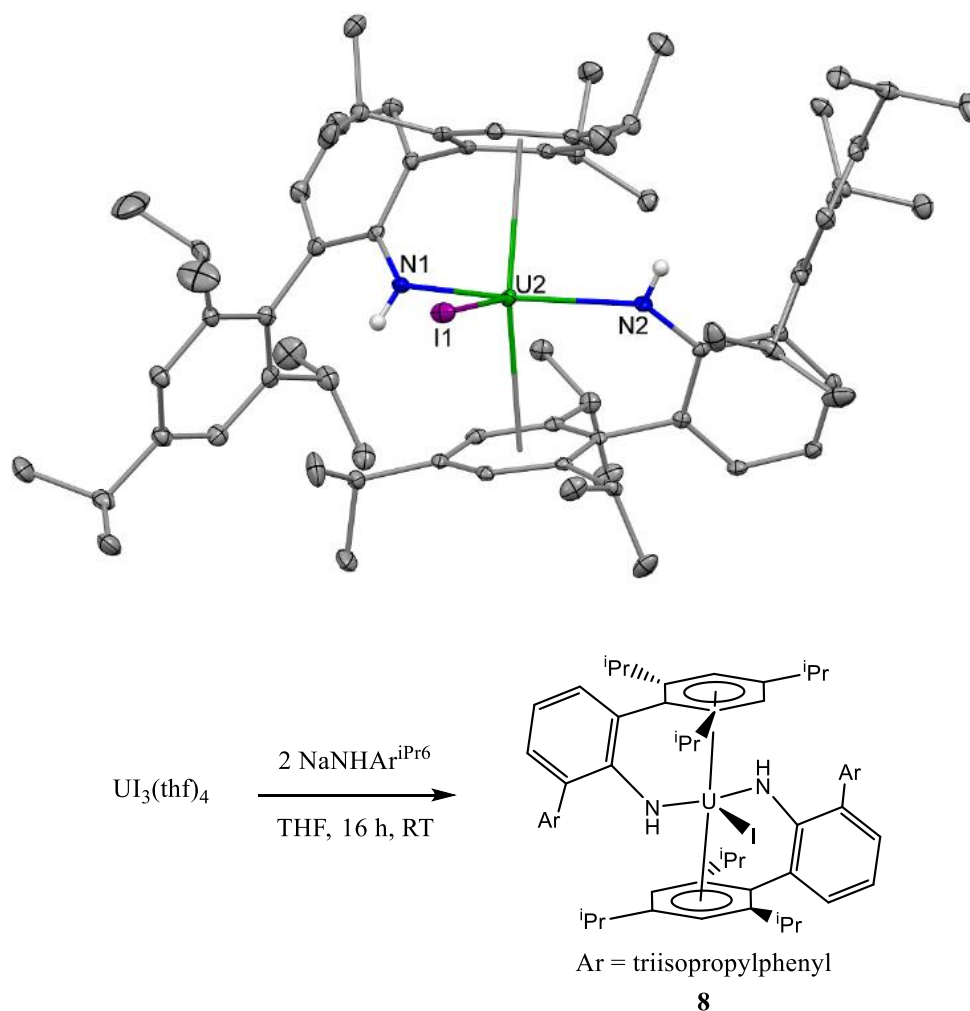


Figure 6-7. *Top*: Crystal structure of  $\text{UI}(\text{NHAr}^{\text{iPr6}})_2$  **8**. Hydrogens (excepts N-H's) and solvent molecule removed for clarity. *Bottom*: Synthesis of  $(\text{IU}(\text{NHAr}^{\text{iPr6}})_2)$  (**8**).

Surprisingly, the structure of **8** varies somewhat depending on the solvent of crystallization. As mentioned above, when crystallized from diethyl ether, **8** gives a solid-state structure with a molecule of ether in the asymmetric unit, and the distance from the metal center to arene centroids are significantly different, at 2.788(1) Å and 2.897(1) Å, similar to what was seen in **7**. However, when the crystals are grown from concentrated *n*-hexane and a molecule of hexane appears in the



asymmetric unit, the cell changes, and the U-centroid distances are similar at 2.790(1) Å and 2.776(1) Å. The U-C bonds to the arene are also different by a significant amount from an average of 3.120(2) Å and 3.217(2) Å to 3.122(4) Å and 3.111(4) Å. This phenomenon is consistent with weak U-arene interactions, as small packing forces with the different solvent molecules are apparently enough to disrupt the structure slightly, see Figure 6-8.

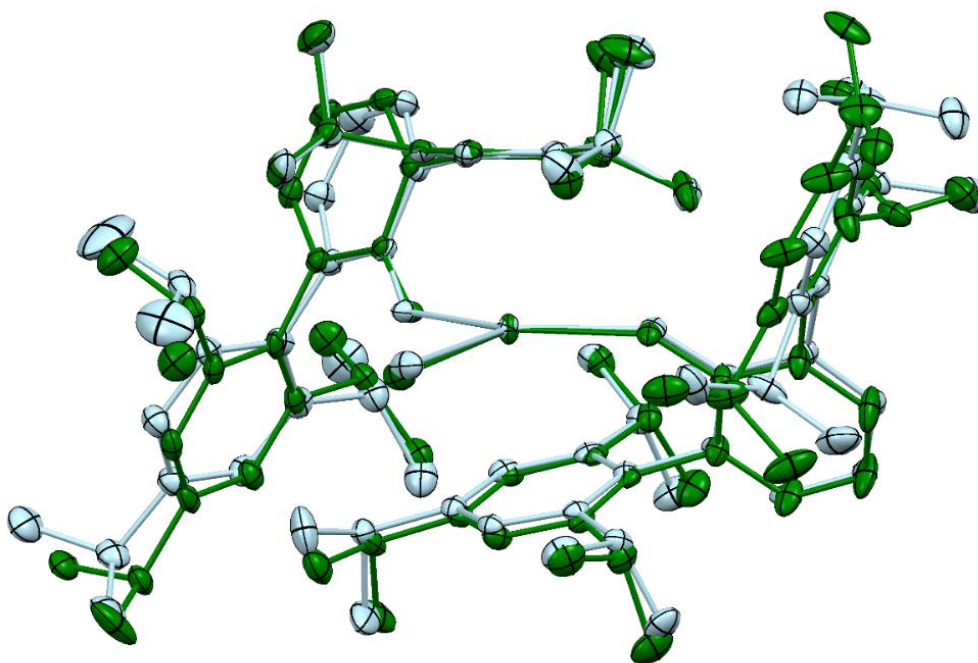


Figure 6-8. Contrasting solid state structures of **8** when crystallized from diethyl ether (green) and n-hexane (light blue).

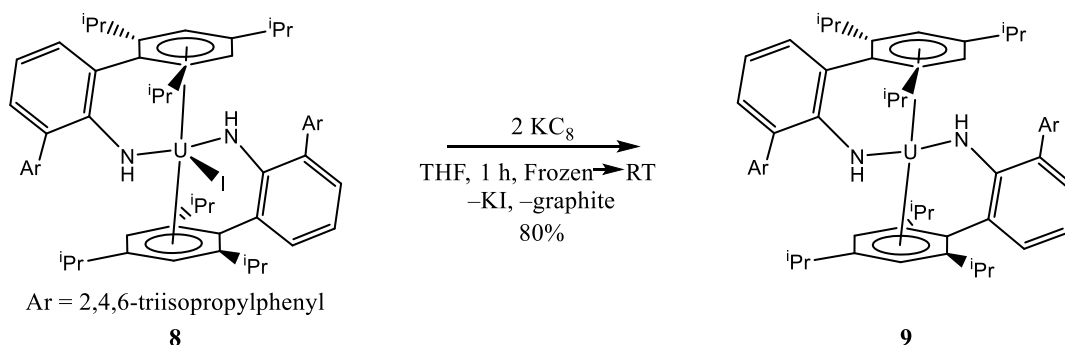
The weak interaction is confirmed in the solution state. Ambient temperature  $^1\text{H}$  NMR only shows signals for the solvent that crystallizes in the lattice, a singlet at 12.97 ppm, a broad singlet at 9.1 ppm, and a very broad signal from ~6 to –10 ppm. The signals are even less resolved than in the NMR of **7**. However, on cooling the solution to –30 °C, the expected number of signals for the  $C_2$  symmetric molecule become distinguishable between 87 ppm and –82 ppm. As we



suspected, this behavior is consistent with fluxionality of the arene substituents resulting from a weak uranium-arene interaction.

Compound **8** was also investigated with absorption spectroscopy in the visible and near-infrared. A large absorption in the visible region along with broad but distinct *f-f* transitions in the near-IR are consistent with this assignment of **8** as a U(III) species (*vide infra*).<sup>20</sup>

### 6.5 Generation of a Neutral Uranium(II)



Scheme 6-5. Synthesis of  $\text{U}(\text{NHAr}^{\text{iPr}_6})_2$  (**9**) from **8**.

Common techniques for abstraction of iodide from **8**, such as precipitation by silver or sodium salts, were fruitless. However, reduction of **8** with excess  $\text{KC}_8$  in THF (Scheme 6-5) results in precipitation of KI and graphite with generation of green  $\text{U}(\text{NHAr}^{\text{iPr}_6})_2$  (**9**). This is in contrast to the reactions performed with  $(\text{Cp}^*)\text{UI}(\text{NAr}^{\text{iPr}_6})$  (**2**), where no tractable products could be obtained. Compound **9** was the first example of a neutral uranium organometallic species in the +2-oxidation state.<sup>21-24</sup> Compound **9** was also the third U(II) moiety. This is particularly significant due to reportedly differing valence electron configurations in the original two studies. In the tris(cyclopentadienyl) systems reported by the Evans group, the geometry of the complex enforces a  $5f^3d^1$  electron configuration.<sup>24</sup> In the tris(aryloxide)-arene system reported by Meyer, a  $5f^46d^0$  electronic configuration was determined.<sup>19</sup> Compound **9** is essentially set up to be a tie breaker to confirm the more common valence electron configuration of U(II).



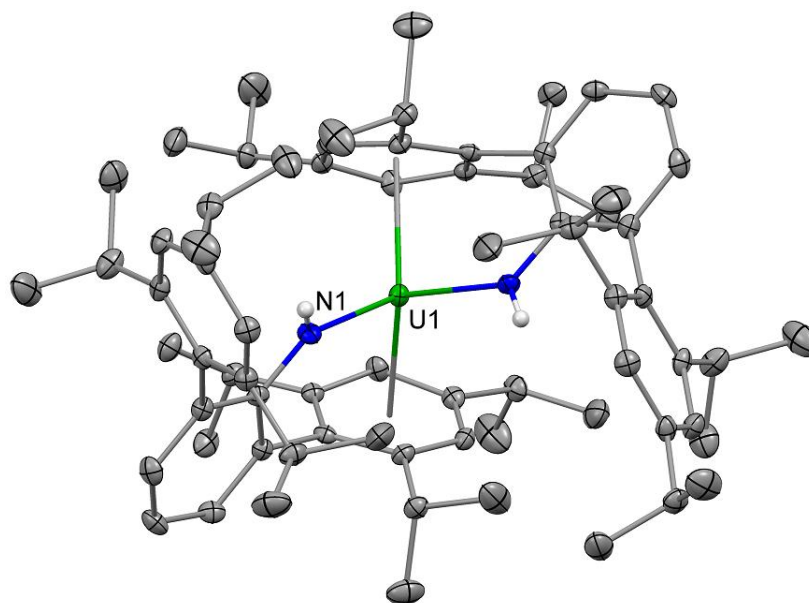


Figure 6-9. Crystal structure of  $\text{U}(\text{NHAr}^{\text{iPr6}})_2$  (**9**). Hydrogens, except N-H's, and solvent molecule removed for clarity. The structure is grown to show the full molecule, but **9** crystallizes as half of the molecule with a 2-fold rotational axis.

Fortunately, the structural data of **9** was also high enough quality to locate and refine the N-H hydrogen. This combined with, the U-N bond of  $2.330(2)$  Å and U-N-C bond angle of  $130.2(2)^\circ$  are consistent with the assignment of N1 as a mono anionic amide ligand.

The geometry of **8** (Figure 6-7) and **9** (Figure 6-9) vary significantly in the solid-state structures. The U(II) compound **9** crystallizes as a  $C_2$  symmetric molecule with only half of the molecule occupying the asymmetric unit. Upon removal of iodide and formal reduction of the complex, the U-centroid bond distances shortened significantly, from  $2.843(1)$  Å (avg.) in **8** to  $2.405(1)$  Å in **9**. The contraction is consistent with increased backbonding interactions between a formally reduced metal center and the arene. An alternative explanation involves increased ionic interaction between a reduced arene and the metal center; however, the data presented here are more consistent with a U(II) species interacting with a neutral arene (*vide infra*). Indeed, analysis of the C-C bond lengths in the coordinated arene of **9** shows an avg. C-C bond length of  $1.415(4)$  Å. This is essentially unchanged from both **8** (avg. C-C  $1.402(5)$  Å) and from free  $\text{H}_2\text{NAr}^{\text{iPr6}}$ .<sup>25</sup>



Also noteworthy in the comparison of the solid-state structures of **8** and **9** are the differences in arene-U-arene angles. Going from **8** to **9**, the centroid-U-centroid angle decreases from 158.785(2)° to 134.240(9)°, respectively. Additionally, the N-U-N angle decreases from 149.92(7)° to 99.22(11)°.

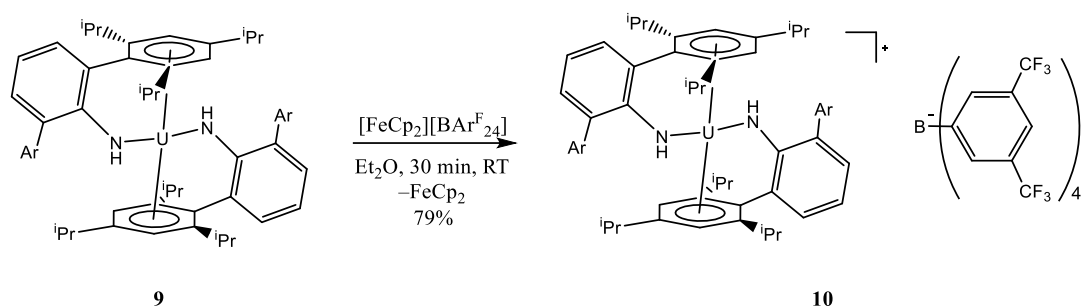
The  $^1\text{H}$  NMR of **9** displays sharp signals at room temperature, confirming stronger interaction in the U-arene bonds relative to **8**. Assignment of the NMR spectrum of **9** was not possible due to the paramagnetic shifts, but the number of peaks is consistent with a  $C_2$  symmetric molecule with static U-arene bonds on the NMR timescale and diastereotopic methyl groups in the *iso*-propyl groups, consistent with the solid-state structure.

Absorption spectroscopy in the visible to near-IR on **9** in diethyl ether is mostly featureless except for strong absorption at 400 nm and a very broad absorption at ~600 nm. The spectrum of **9** is similar to that observed by the Meyer group in their report of a uranium(II) species.<sup>19</sup>

Compared to previous reports of U(II) species, **9** is more robust.<sup>19, 24</sup> The room temperature synthesis and characterization of **9** display reasonable thermal stability, for instance, the visible to near-IR absorption spectrum was taken by serial dilution over ~5 h at room temperature with no signs of decomposition. Extended storage of **9** in the glovebox freezer (-35 °C) is also possible, provided the sample is pure.



## 6.6 Oxidation of the Uranium(II)



Scheme 6-6. Synthesis of  $[\text{U}(\text{NHAr}^{\text{iPr}6})_2][\text{BAR}^{\text{F}}_{24}]$  (**10**) from **9**.

Reaction of **9** in ether with  $[\text{FeCp}_2][\text{BAR}^{\text{F}}_{24}]$  (Scheme 6-6) results in a rapid color change from green to brown. After removal of volatiles and a hexane wash,  $[\text{U}(\text{NHAr}^{\text{iPr}6})_2][\text{BAR}^{\text{F}}_{24}]$  (**10**) can be isolated. Recrystallization from concentrated ether results in diffraction quality crystals of **10**.

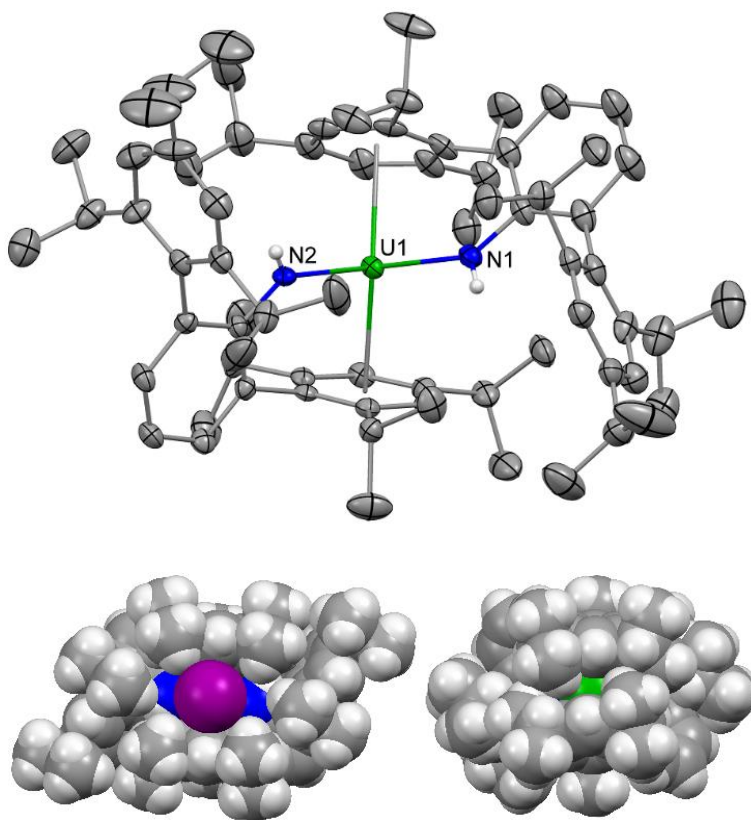


Figure 6-10. *Top*: Crystal structure of  $[\text{U}(\text{NHAr}^{\text{iPr}6})_2][\text{BAR}^{\text{F}}_{24}]$  (**10**) Hydrogens, except N-H's, anion, disorder, and solvent molecule removed for clarity. *Bottom*: Space filling structures of **8** (left) and **10** (right).



Structurally (Figure 6-10 *Top*), **10** is between **8** and **9**. The distance between uranium and the  $\eta^6$ -arene centroids are 2.570(3) and 2.583(3) Å. The centroid-U-centroid and N-U-N angles also falls between those of **8** and **9** at 145.8(1)° and 111.2(2)°, respectively. The uranium arene distances in **10** confirm that both the large radius of the iodide and the bulk of the  $\text{Ar}^{\text{iPr}_6}$  groups play a significant role in the large change in uranium-arene distances between compounds **8** to **10** (Figure 6-10 *Bottom*).

The  $^1\text{H}$  NMR spectrum of **10**, contrary to **8**, shows the expected resonances at room temperature. It is worth mentioning, however, that the solubility of **10** required the use of THF- $d_8$ , and, over the course of extended experiments, the compound reacts with this solvent.

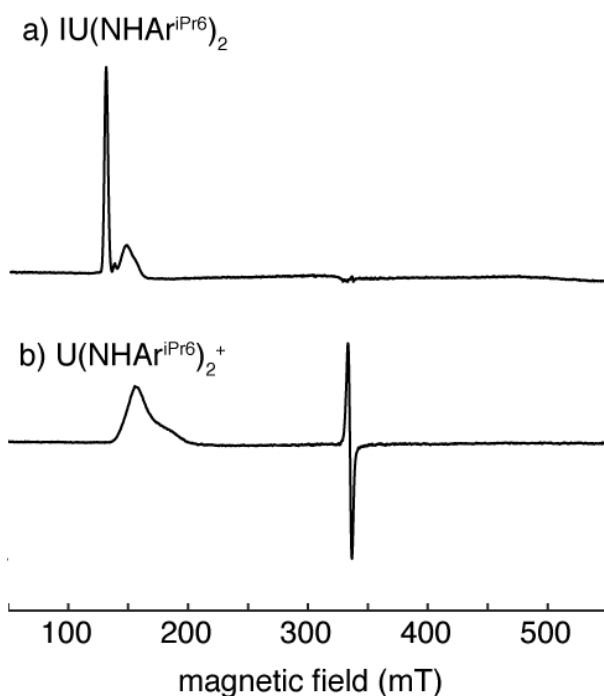


Figure 6-11. EPR spectra of (a)  $(\text{I})\text{U}(\text{NHAr}^{\text{iPr}_6})_2$  (**8**) and (b)  $[\text{U}(\text{NHAr}^{\text{iPr}_6})_2][\text{BAr}^{\text{F}_{24}}]$  (**10**). Measurement parameters for both spectra were: microwave frequency, 9.40 GHz; microwave power, 0.79 mW; field modulation amplitude, 1 mT; and sample temperature, 6 K.

Dissolving **10** in THF at room temperature results in an extremely viscous liquid, this is not altogether unexpected. Surprisingly though, dissolving **10** in toluene results in a color change from



brown to bright red. The cause of the color change is unclear; however, attempts at crystallization of the products did yield colorless crystals containing the  $\text{BAr}^{\text{F}}_{24}$  anion with an unresolvable cation, as well as crystals of free  $\text{H}_2\text{NAr}^{\text{iPr6}}$ .

## 6.7 Spectroscopic Analysis

The X-band EPR spectrum of **8** collected at 6 K (Figure 6-11a) shows well-resolved peaks at  $g = 5.17$  and  $g = 4.56$ . These were the only peaks resolved over a field range that extended from 50-850 mT ( $g = 13$  to  $g = 0.8$ ). While broad features at higher fields were observed in our spectra (Figure 6-11a), they could not be distinguished from typical baseline distortions that remain after subtracting background contributions.

No EPR response was detected for **9** in either perpendicular or parallel detection modes at 6 K. Absence of a signal here supports our assignment of **9** as a U(II) species with neutral arene substituents.

The EPR spectrum of **10** collected at 6 K is provided in Figure 6-11 and shows a broad peak at  $g = 4.3$  with a shoulder at  $g = 3.6$ . A resonance with a narrower line shape was also resolved at  $g = 2.003$ . The resonance at  $g = 2.003$  is unusual because its narrow line shape makes it unlikely that it arises from the U(III) paramagnetic center. This signal was observed in three separate preparations of **10** that were carried out in two different solvents. It is possible that oxidation of **9** resulted in a species best described as a U(III) center, but with a small contribution of U(II) and ligand radical, or a small contribution from solvent radical.

Solution state magnetic susceptibility studies were carried out on **9** using the Evans method.<sup>30</sup> The resulting temperature dependent paramagnetism was determined in 10 K intervals from 299-219 K in toluene- $d_8$  with hexamethyldisiloxane as a reference. At room temperature the effective



magnetic moment value of **9** is  $0.78 \text{ cm}^3\text{Kmol}^{-1}$  ( $\mu_{\text{eff}} = 2.50$ ), which decreases slightly to  $0.72 \text{ cm}^3\text{Kmol}^{-1}$  ( $\mu_{\text{eff}} = 2.40$ ) at 219 K.

Solid-state magnetic properties of **8-10** were also probed by SQUID magnetometry (Figure 6-5).<sup>21, 23</sup> Focusing on the divalent species, **9**, at 300 K  $\chi_{\text{M}}T = 0.67 \text{ cm}^3 \text{ K mol}^{-1}$  ( $\mu_{\text{eff}} = 2.32$ ). Upon decreasing the temperature, the  $\chi_{\text{M}}T$  value decreases monotonically until  $\sim 100 \text{ K}$ , where the decrease becomes more dramatic; at  $2 \text{ K}$ ,  $\chi_{\text{M}}T = 0 \text{ cm}^3 \text{ K mol}^{-1}$  ( $\mu_{\text{eff}} = 0$ ). The temperature dependent profile of **9** tracks lower in the solid state than in solution. Differences observed between solution and solid-state behavior are common given the very different environments. For the one other U(II) species where magnetic studies were done in solution and the solid state, the solid state susceptibilities also tracked lower than the solution values.<sup>21</sup> The solid-state behavior is similar to what was observed for previously published U(II) complexes, although the downturns for the other U(II) complexes are observed at lower temperatures ( $\sim 15\text{-}20 \text{ K}$ ) compared to **9**.<sup>21, 23</sup> Similar to the other two complexes reported previously, the magnetic susceptibility approaches  $0 \text{ cm}^3 \text{ K mol}^{-1}$  ( $\mu_{\text{eff}} = 0$ ) at low temperature, suggestive of an integer spin system where spin-orbit coupling leads to a ground state singlet. This agrees with the absence of an EPR signal in **9**. While not diagnostic, the temperature profile for **9** is qualitatively similar to Meyer's U(II) complex with a  $5f^46d^0$  electronic configuration.<sup>21</sup>



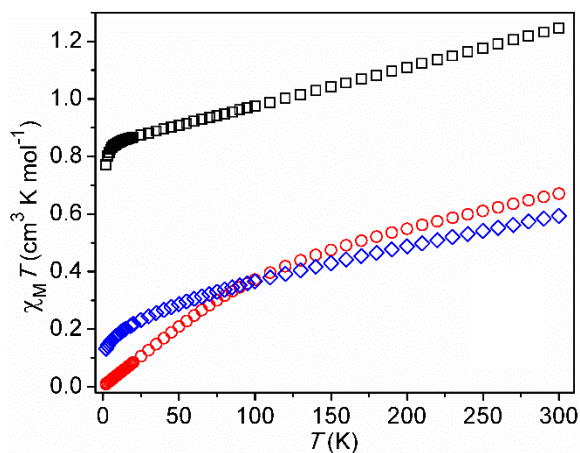


Figure 6-12. Temperature dependence of the magnetic susceptibility for  $\text{U}(\text{NHA}^{\text{iPr}_6})_2$  (**8**) (black squares),  $\text{U}(\text{NHA}^{\text{iPr}_6})_2$  (**9**) (red circles), and  $[\text{U}(\text{NHA}^{\text{iPr}_6})_2][\text{BAr}^{\text{F}_{24}}]$  (**10**) (blue diamonds) collected at 5000 Oe.

## 6.8 Conclusions

In summary, the terphenyl groups proved to be ideal ligand partners for low valent uranium. The  $\text{Ar}^{\text{iPr}_6}$  ligands allowed isolation of a neutral U(II) complex,  $\text{U}(\text{NHA}^{\text{iPr}_6})_2$  (**9**), where the large arenes act as  $\eta^6$ -donors towards the metal center. Analysis of **9** by visible-NIR absorption spectroscopy, SQUID magnetometry, and EPR spectroscopy are consistent with a  $5f^4 6d^0$  electron configuration. EPR spectroscopy and magnetometry studies clearly display integer spin properties expected from a U(II) center. This suggests that the three-fold symmetrical tris(cyclopentadienyl) coordination environments employed by the Evan's group may impart the unexpected  $5f^3 6d^1$  electronic configuration in  $\text{U}(\text{cyclopentadienyl})_3^-$ .<sup>22-24</sup> Additionally, we synthesized a series of U(IV), U(III), and U(II) arene complexes. The uranium(II) complex has metrical parameters consistent with much stronger U-arene interactions than the U(III) complexes, which, likewise, are stronger than the U(IV) arene interactions. This is presumably due to stronger metal-arene backbonding in the lower oxidation state complexes. Hopefully, the complexes presented here will pave the way to new and exciting low valent uranium reactivity.

## 6.9 Experimental



All reactions and manipulations were carried out in an MBraun glovebox under a nitrogen atmosphere and/or using standard Schlenk techniques. Diethyl ether, pentane, tetrahydrofuran, and hexane were purchased from Aldrich Chemical Company. Diethyl ether and pentane were purified by passing through alumina columns to remove water after being sparged with dry nitrogen to remove oxygen. Tetrahydrofuran and hexane were sparged with dinitrogen to remove oxygen and distilled from sodium and benzophenone. C<sub>6</sub>D<sub>6</sub>, THF-d<sub>8</sub>, and toluene-d<sub>8</sub> were purchased from Cambridge Isotopes Laboratories, Inc or Aldrich Chemical Company. Toluene-d<sub>8</sub> and THF-d<sub>8</sub> were sparged with dry dinitrogen and dried over 4 Å molecular sieves. Before use, each solvent was passed through a plug of activated alumina to filter the solvent and to ensure dryness. C<sub>6</sub>D<sub>6</sub> was sparged with dry dinitrogen and distilled from CaH<sub>2</sub> before use. All NMR solvents were stored under an inert atmosphere away from light. Depleted uranium turnings were purchased from Manufacturing Sciences Corporation. Synthesis of UI<sub>3</sub>(THF)<sub>4</sub>, KC<sub>8</sub>, IAr<sup>iPr<sub>6</sub></sup>, N<sub>3</sub>Ar<sup>iPr<sub>6</sub></sup>, H<sub>2</sub>Ar<sup>iPr<sub>6</sub></sup>, and [FeCp<sub>2</sub>]<sup>+</sup> BAr<sup>F<sub>24</sub></sup><sup>-</sup> was done according to the literature procedures.<sup>3, 31-33</sup> H<sub>2</sub>Ar<sup>iPr<sub>6</sub></sup> was deprotonated in hexane with stoichiometric NaCH<sub>2</sub>TMS over 16 h. The reaction generates an off-white precipitate which can be collected by filtration. The precipitate was washed with several aliquots of hexane and used as is. Elemental Analysis was performed by Atlantic Microlab in Norcross, GA using a He filled glovebag to handle the compounds.

### Synthesis of Compounds

Caution! Depleted uranium (primary isotope <sup>238</sup>U) is a weak α-emitter (4.197 MeV) with a half-life of 4.47x10<sup>9</sup> years; manipulations and reactions should be carried out in monitored fume hoods or in an inert atmosphere drybox in a radiation laboratory equipped with α- and β-counting equipment



*Oxide-Free Uranium Metal Turnings:* Cautionary Note: Uranium is pyrophoric when finely divided; caution is recommended in the washing process to avoid exposure to air. This is a modification of the literature procedure.<sup>31</sup> Depleted uranium turnings were received in mineral oil from Manufacturing Sciences Corporation. The turnings (~10 g) were carefully transferred to a 500 mL side armed flask which was fitted with a hose flowing dry dinitrogen or dry argon gas. The turnings were washed with hexanes (3 x 150 mL), acetone (3 x 150 mL), then water (3 x 150 mL). The flask was then filled with enough water to fully cover the turnings (~100 mL). Concentrated nitric acid was then added by pipette while gently swirling the flask until removal of the black oxide layer was achieved and the turnings were becoming metallic in color. The amount of concentrated acid necessary can vary significantly depending on the quality of turnings, but typically ~20 mL is sufficient. Cleaning of the oxide layer can be accompanied by warming of the solution as well as NO<sub>2</sub> gas generation. Once the turnings appear shiny and metallic, the acid solution is carefully decanted. The turnings are then washed again with water (3 x 150 mL) and acetone (3 x 150 mL). After the final wash, the turnings were dried under reduced pressure and transferred to the drybox.

*Synthesis of (Cp\*)UI(NAr<sup>iPr6</sup>) (2):* A 20 mL scintillation vial was loaded with (Cp\*)U(I)<sub>2</sub>(thf)<sub>3</sub> (300 mg, 0.356mmol), 4 mL THF, and a magnetic stir bar. The solution was stirred vigorously. To the stirring solution was added KC<sub>8</sub> (48 mg, 0.356 mmol) as a solid in small portions. The solution immediately darkened in color. Next, N<sub>3</sub>Ar<sup>iPr6</sup> (187 mg, 0.356 mmol) was added as a solid in small portions, causing immediate, vigorous bubbling, and turning the solution a dark red color. The reaction was loosely capped and left to stir for approximately 30 minutes before being dried of the volatiles under reduced pressure. The remaining residue was extracted with approximately 5 mL *n*-hexane. The extracts were filtered through Celite and the filtrate concentrated to a volume of



approximately 1 mL. The deep red solution was chilled in the freezer at -30 °C overnight yielding small dark red X-ray quality crystals (270 mg, 76%). Additional crops of crystals can be obtained by concentrating the mother liquor further and chilling. Elemental Analysis Calculated  $C_{46}H_{64}IN_2U$  (0.5  $C_6H_{14}$  from X-ray): C 55.47(56.59), H 6.48(6.98), N 1.41(1.35); Found C 56.22, H 7.06, N 0.94.  $^1H$  NMR (400 MHz, 25 °C,  $C_6D_6$ ):  $\delta$  = 17.04 (br s), 16.11 (br s), 14.38 (br s), 12.62 (br s), 10.10 (s), 7.92 (s), 4.30 (br), 3.24 (br), 3.00 (s), 2.84 (s), 1.26 (s), -0.46 (s), -1.21 (s), -3.22 (s), -3.79 (s), -7.14 (s), -8.57 (br), -15.47 (br), -20.48 (br s), -34.14 (br s), -51.20 (br s), -59.44 (br).

*Synthesis of  $(Cp^*)UI(NHAr^{iPr6})$  (3):* A 20 mL scintillation vial was loaded with  $(Cp^*)U(I)_2(thf)_3$  (300 mg, 0.356mmol), 3 mL THF, and a magnetic stir bar. The solution was stirred vigorously. To the stirring solution was added  $NaNHAr^{iPr6}$  (185 mg, 0.356 mmol) in THF dropwise. The solution slowly darkened in color to black. The solution was left to stir for approximately 6 h before being dried of volatiles under reduced pressure. The remaining dark residue was extracted with approximately 4 mL *n*-hexane. The extracts were filtered through Celite and concentrated to a volume of approximately 1 mL. The concentrated solution was put in the freezer and chilled at -30 °C overnight, yielding dark black X-ray quality crystals (171mg, 54%) Elemental Analysis Calculated  $C_{46}H_{65}INU$ : C 55.42, H 6.57, N 1.40; Found C 54.24, H 6.57, N 1.20.  $^1H$  NMR (400 MHz, 25 °C,  $C_6D_6$ ):  $\delta$  = 62.13 (br), 51.90 (br d), 29.09 (br s), 27.20 (s), 17.35 (br s), 14.30 (br s), 12.78 (br), 9.88 (br), 8.36 (br), 6.93 (s), -2.26 (br), -2.87 (br), -4.76 (br), -7.99 (br), -21.84 (br), -37.51 (br), -74.50 (br), -100.56 (br).

*Synthesis of  $(Cp^*)UI(NAr^{Me6})(thf)_2$  (4):* A 20 mL scintillation vial was loaded with  $(Cp^*)U(I)_2(thf)_3$  (300 mg, 0.356mmol), 4 mL THF, and a magnetic stir bar. The solution was stirred vigorously. To the stirring solution was added  $KC_8$  (48 mg, 0.356 mmol) as a solid in small



portions. The solution immediately darkened in color. Next,  $\text{N}_3\text{Ar}^{\text{Me}_6}$  (127 mg, 0.356 mmol) was added as a solid in small portions, causing immediate, vigorous bubbling, and turning the solution a dark red color. The reaction was loosely capped and left to stir for approximately 30 minutes before being dried of the volatiles under reduced pressure. The remaining residue was extracted with a 1:1 mixture of *n*-hexane: diethyl ether. The extracts were filtered through Celite and the volatiles were removed once again. The residue was dissolved in a minimal amount of diethyl ether, approximately 1 mL, and chilled in the freezer at  $-30\text{ }^\circ\text{C}$  overnight for recrystallization yielding deep red X-ray quality crystals (144 mg, 41.7%). Elemental Analysis Calculated  $\text{C}_{42}\text{H}_{56}\text{INO}_2\text{U}$ : C 51.91, H 5.81, N 1.41; Found C 49.98, H 5.77, N 1.41.  $^1\text{H}$  NMR (400 MHz,  $25\text{ }^\circ\text{C}$ ,  $\text{C}_6\text{D}_6$ ):  $\delta$  = 48.03 (br), 24.86 (br), 13.40 (s), 12.83 (s), 5.83 (s), 2.17 (m),  $-2.91$  (s),  $-3.60$  (s),  $-7.44$  (br).

*Synthesis of  $(\text{Cp}^*)\text{U}(\text{I})(\text{NHA}^{\text{Me}_6})$  (5):* A 20 mL scintillation vial was loaded with  $(\text{Cp}^*)\text{U}(\text{I})_2(\text{thf})_3$  (300 mg, 0.356mmol), 3 mL THF, and a magnetic stir bar. The solution was stirred vigorously. To the stirring solution was added a solution of  $\text{NaNHA}^{\text{Me}_6}$  (185 mg, 0.356 mmol) in THF dropwise. The solution slowly darkened in color to a black solution. The solution was left to stir for approximately 6 h before being dried of volatiles under reduced pressure. The remaining dark residue was extracted with approximately 4 mL of 1:1 *n*-hexane: diethyl ether. The extracts were filtered through Celite and again, the volatiles were removed. The residue was dissolved in a minimal amount of diethyl ether, approximately 1 mL, and chilled in the freezer at  $-30\text{ }^\circ\text{C}$  overnight for recrystallization yielding dark black X-ray quality crystals (160 mg, 54.3%). Analytically pure sample could not be obtained. Crude  $^1\text{H}$  NMR (400 MHz,  $25\text{ }^\circ\text{C}$ ,  $\text{C}_6\text{D}_6$ ):  $\delta$  = 15.35 (br s), 11.10 (br), 10.86 (bri), 8.48 (br s), 5.74 (s), 2.36 (s), 2.14 (br), 0.25 (s),  $-3.05$  (s),  $-5.48$  (m),  $-10.16$  (br d),  $-27.68$  (br s),  $-38.55$  (br s),  $-56.85$  (br s),  $-58.71$  (br s).



*Synthesis of (Cp\*)U(NHAr<sup>Me6</sup>)<sub>2</sub> (6):* A 20 mL scintillation vial was loaded with (Cp\*)U(I)<sub>2</sub>(thf)<sub>3</sub> (300 mg, 0.356 mmol), 3 mL THF, and a magnetic stir bar. The solution was stirred with a stir plate. To the stirring solution was added NaNHAr<sup>Me6</sup> (251 mg, 0.712 mmol) in THF (~2 mL) dropwise. The solution was allowed to stir at room temperature for approximately 18 h before being dried in vacuo. The remaining dark residue was extracted with *n*-hexane. The extracts were filtered through Celite, and the volatiles removed in vacuo. The remaining solids were dissolved in a minimal amount of hexane for recrystallization. Synthesis of (Cp\*)U(NHAr<sup>Me6</sup>)<sub>2</sub> without impurity was never achieved. Crude yield of (Cp\*)U(NHAr<sup>Me6</sup>)<sub>2</sub> was 92 mg (27.4%).

*Synthesis of UI(NHAr<sup>Me6</sup>)<sub>2</sub> (7):* In the drybox, UI<sub>3</sub>(THF)<sub>4</sub> (250 mg, 0.276 mmol) was weighed into a 20 mL glass scintillation vial. The vial was charged with ~5 mL diethyl ether and a magnetic stir bar. The vial was then placed in a liquid nitrogen cooled cold well until frozen. Once frozen, the vial was removed from the cold well and suspended above a magnetic stir plate. When the solution had thawed enough to stir, a solution of NaNHAr<sup>Me6</sup> (194 mg, 0.551 mmol) in diethyl ether (~2 mL) was added dropwise. The solution was left to warm to room temperature and stirred for 16 h, whereupon the solution changed color from dark blue to dark purple. The volatiles were then removed under reduced pressure. The residue was then extracted with several aliquots of *n*-hexane until colorless. The extracts were then filtered using Celite as a filtering agent. The filtrate was then concentrated to ~1-2 mL under reduced pressure and chilled to –35 °C overnight to produce dark crystals of **7** (184 mg, 65.2%). X-ray quality crystals were grown from a concentrated solution of **7** in a –35 °C freezer overnight. Elemental Analysis Calculated C<sub>48</sub>H<sub>52</sub>IN<sub>2</sub>U: C 56.42, H 5.13, N 2.74; Found C 56.40, H 5.24, N 2.73. <sup>1</sup>H NMR (600 MHz, 25 °C, C<sub>6</sub>D<sub>6</sub>): δ = 27.76 (br),



20.09 (br), 13.33 (br s), 8.87 (s), 6.88 (s), 5.92 (br), 3.28 (s), 3.26 (s), 2.21 (s), 2.13 (s), 1.77 (v br), -14.89 (br), -19.29 (br), -28.31 (br), -43.66 (br).

*Synthesis of  $UI(NHAr^{iPr6})_2$  (**8**):* In the drybox,  $UI_3(THF)_4$  (250 mg, 0.276 mmol) was weighed into a 20 mL glass scintillation vial. The vial was charged with ~5 mL diethyl ether and a magnetic stir bar. The vial was then placed in a liquid nitrogen cooled cold well until frozen. Once frozen, the vial was removed from the cold well and suspended above a magnetic stir plate. When the solution had thawed enough to stir, a solution of  $NaNHAr^{iPr6}$  (287 mg, 0.551 mmol) in diethyl ether (~2 mL) was added dropwise. The solution was left to warm to room temperature and stirred for 16 h whereupon the solution changed from dark blue to dark purple. The volatiles were then removed under reduced pressure. The residue was then extracted with several aliquots of *n*-hexane until colorless. The extracts were then filtered using Celite as a filtering agent. The filtrate was then concentrated to ~1-2 mL under reduced pressure and chilled to -35 °C overnight to produce dark crystals of **10** (262 mg, 66.5%). Note: Crystals of **8** contain 1 molecule of solvent depending on which solvent it is crystallized from, hexane or ether. X-ray quality crystals were grown from a concentrated solution of **10** in a -35 °C freezer overnight. Elemental Analysis Calculated  $C_{72}H_{100}IN_2U$ : C 63.66, H 7.42, N 2.06; Found C 63.08, H 7.75, N 1.90.  $^1H$  NMR (600 MHz, -30 °C, toluene- $d_8$ ):  $\delta$  = 87.02 (br), 56.22 (br), 38.01 (br s), 35.92 (s), 28.04 (s), 24.73 (s), 24.06 (br), 20.85 (br), 16.88(s), 15.56 (s), 10.65 (s), 9.42 (s), 6.87 (s), 6.51 (s), 1.18 (s), -1.58 (s), -3.24 (br), -5.30 (br), -11.76 (s), -22.44 (s), -31.96 (br), -43.51 (br), -50.74 (br), -82.02 (br).

*Synthesis of  $U(NHAr^{iPr6})_2$  (**9**):* In the drybox, crystals of **8** (210 mg, 0.147 mmol) were weighed into a 20 mL glass scintillation vial. The vial was charged with ~5 mL THF and a magnetic stir bar. The vial was then placed in a liquid nitrogen cooled cold well until the solution froze. Once frozen, the vial was removed from the cold well and suspended above a magnetic stir plate. When



the solution had thawed enough to stir, a suspension of  $\text{KC}_8$  (40 mg, 0.296 mmol) in THF (1 mL) was added. The solution turned color from deep purple to dark green rapidly. The solution was stirred for 1 h at room temperature. The volatiles were then removed under reduced pressure, and the remaining residue dissolved in ~5 mL diethyl ether. The ether solution was stirred for ~5 min before being filtered using Celite as a filtering agent. The remaining residue was washed with an additional aliquot of diethyl ether (~3 mL) and the extracts filtered. The combined filtrate was then dried of the volatiles. The remaining dark green residue was dissolved in *n*-pentane and filtered using Celite as a filtering agent once more. Crude **9** can be isolated and used for further reactivity by removal of the pentane (145 mg, 80.3%). Otherwise, X-ray quality single crystals can be produced by chilling a concentrated pentane solution of **9** in a -35 °C freezer overnight. The yield of recrystallization is only slightly worse over two crops (130mg, 80%). Elemental Analysis Calculated  $\text{C}_{72}\text{H}_{100}\text{N}_2\text{U}$ : C 70.21, H 8.18, N 2.27; Found C 68.66, H 8.38, N 2.13.  $^1\text{H}$  NMR (600 MHz, 25 °C, toluene- $d_8$ )  $\delta$  = 12.38 (s), 9.55 (s), 8.85 (d,  $J$  = 7.4 Hz), 7.37 (s), 6.82 (s), 6.54 (s), 5.44 (s), 4.41 (s), 3.59 – 3.50 (m), 3.48 (br), 3.34 (t,  $J$  = 7.4 Hz), 2.74 (s), 1.82 (d,  $J$  = 10.2 Hz), 1.75 (d,  $J$  = 6.9 Hz), 1.62 (s), 1.26 (dd,  $J$  = 19.3, 7.0 Hz), 1.18 (d,  $J$  = 7.0 Hz), 0.75 (s), 0.52 (d,  $J$  = 118.4 Hz), -0.38 (d,  $J$  = 42.2 Hz), -1.55 (d,  $J$  = 131.5 Hz), -6.52 (s), -14.97 (s), -25.82 (s).

*Synthesis of  $[\text{U}(\text{NHA}r^{i\text{Pr}6})_2]^+ \text{BA}r^{\text{F}}_{24}^-$  (**10**):* In the drybox, **9** (70 mg, 0.057 mmol) was weighed into a 20 mL glass scintillation vial. The vial was charged with diethyl ether (~3 mL) and a magnetic stir bar. The solution was then stirred on a magnetic stir plate. To the stirring solution,  $[\text{FeCp}_2]^+ \text{BA}r^{\text{F}}_{24}^-$  (60 mg, 0.057 mmol) in diethyl ether (1 mL) was added dropwise. The green solution rapidly turned a reddish-brown color. The solution was left to stir for 30 min. The volatiles were then removed in vacuo. The residue was then washed with hexane (3 mL), and the residue dried again in vacuo. Diethyl ether (~3 mL) was then added to the vial. The solution was then



filtered using Celite as a filtering agent. The filtrate was concentrated to ~1 mL and chilled in a – 35 °C freezer overnight. X-ray quality crystals were observed over three crops of crystals totaling 94 mg (79%). Elemental Analysis Calculated C<sub>104</sub>H<sub>112</sub>BF<sub>24</sub>N<sub>2</sub>U: C 59.63, H 5.39, N 1.34; Found C 53.82, H 4.85, N 1.33. <sup>1</sup>H NMR (600 MHz, 25 °C, THF-d<sub>8</sub>) δ = 37.22 (br s), 26.72 (br s), 18.42 (s), 14.90 (s), 13.68 (s), 11.52 (br), 10.82 (s), 8.49 (s), 8.28 (br s), 7.57 (s), 7.40 (s), 5.97 (br), 2.63 (br), 1.30 (br), 1.11 (br), 0.89 (br), 0.48 (br), –6.69 (br), –6.94 (br), –7.66 (br), –13.25 (s), –16.16 (br), –17.11 (br s), –21.57 (s), –26.89 (br s), –33.91 (br s).

### <sup>1</sup>H NMR Spectra

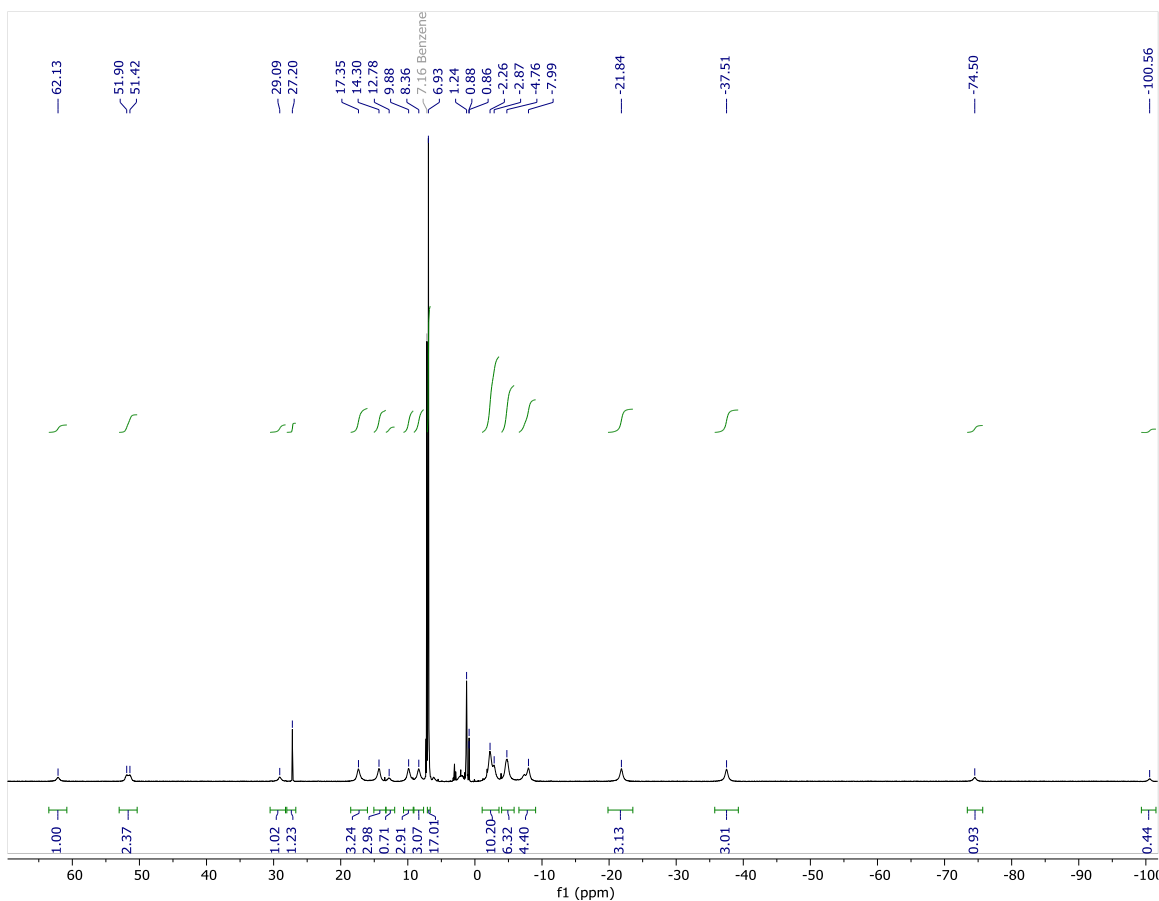


Figure 6-13. <sup>1</sup>H NMR spectrum of (Cp\*)UI(NAr<sup>iPr6</sup>) in C<sub>6</sub>D<sub>6</sub>



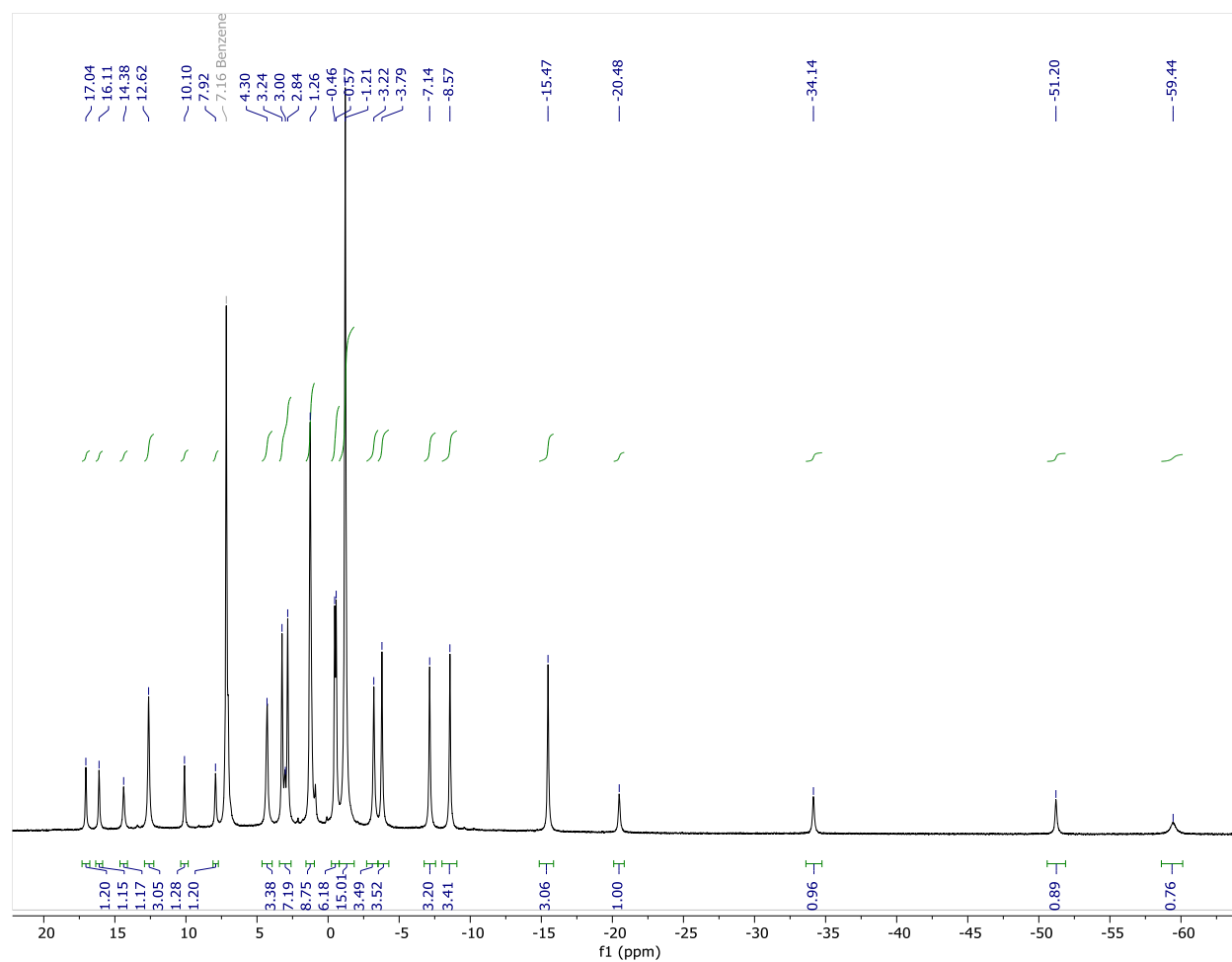


Figure 6-14.  $^1\text{H}$  NMR spectrum of  $(\text{Cp}^*)\text{UI}(\text{NHAr}^{\text{iPr}_6})$  in  $\text{C}_6\text{D}_6$



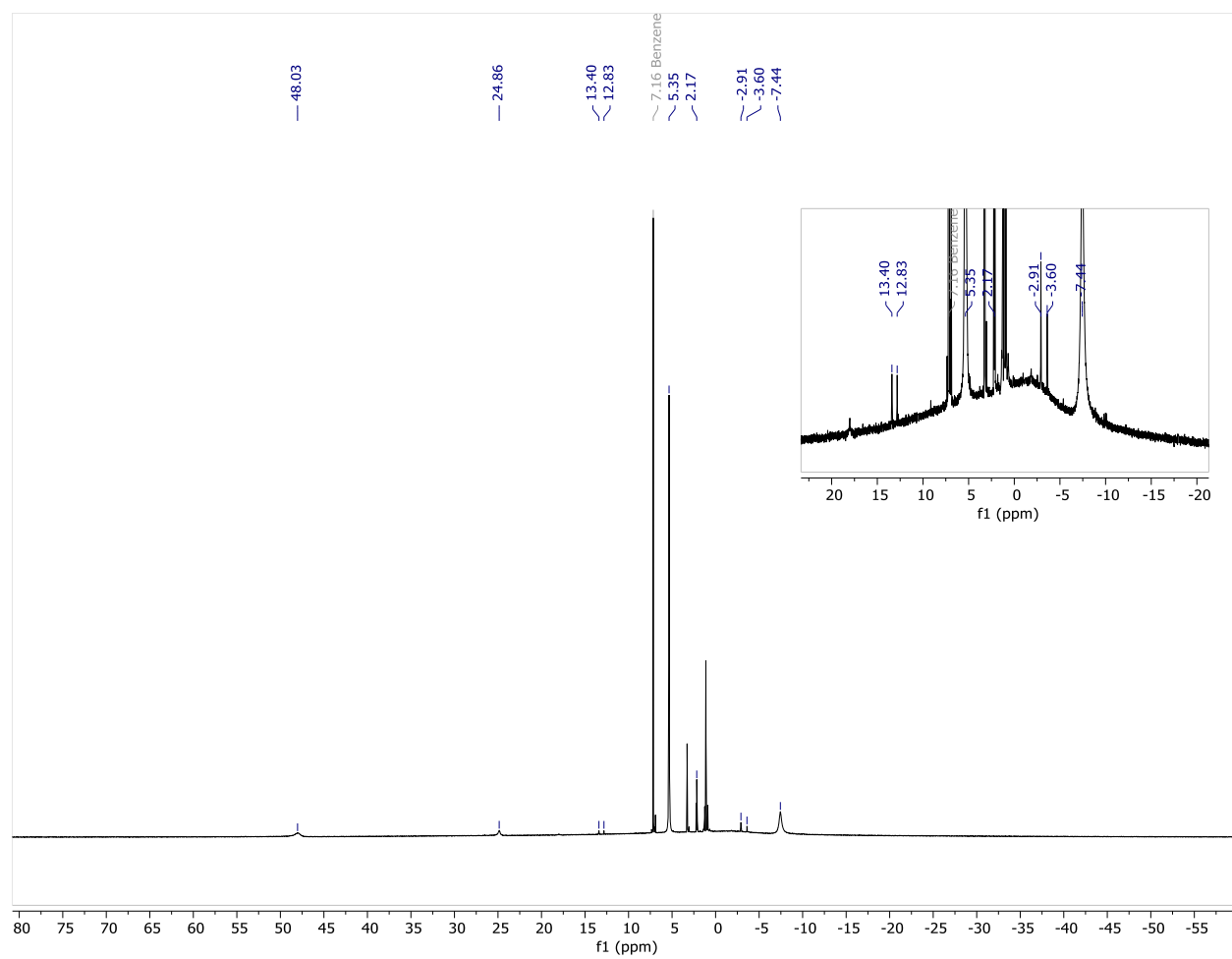


Figure 6-15.  $^1\text{H}$  NMR spectrum of  $(\text{Cp}^*)\text{UI}(\text{NAr}^{\text{Me}_6})$  in  $\text{C}_6\text{D}_6$



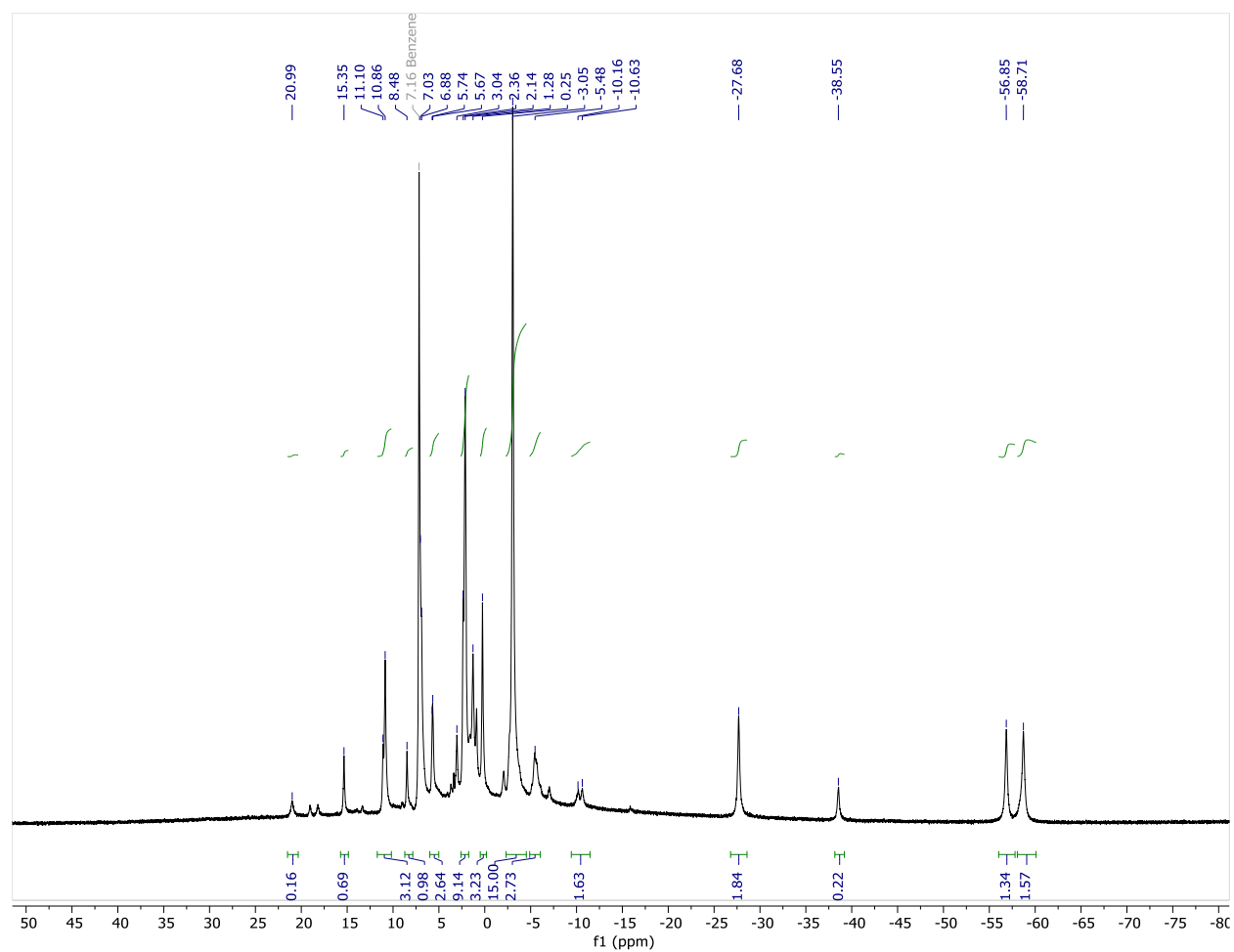


Figure 6-16. Crude  $^1\text{H}$  NMR spectrum of  $(\text{Cp}^*)\text{UI}(\text{NHAr}^{\text{Me6}})$  in  $\text{C}_6\text{D}_6$



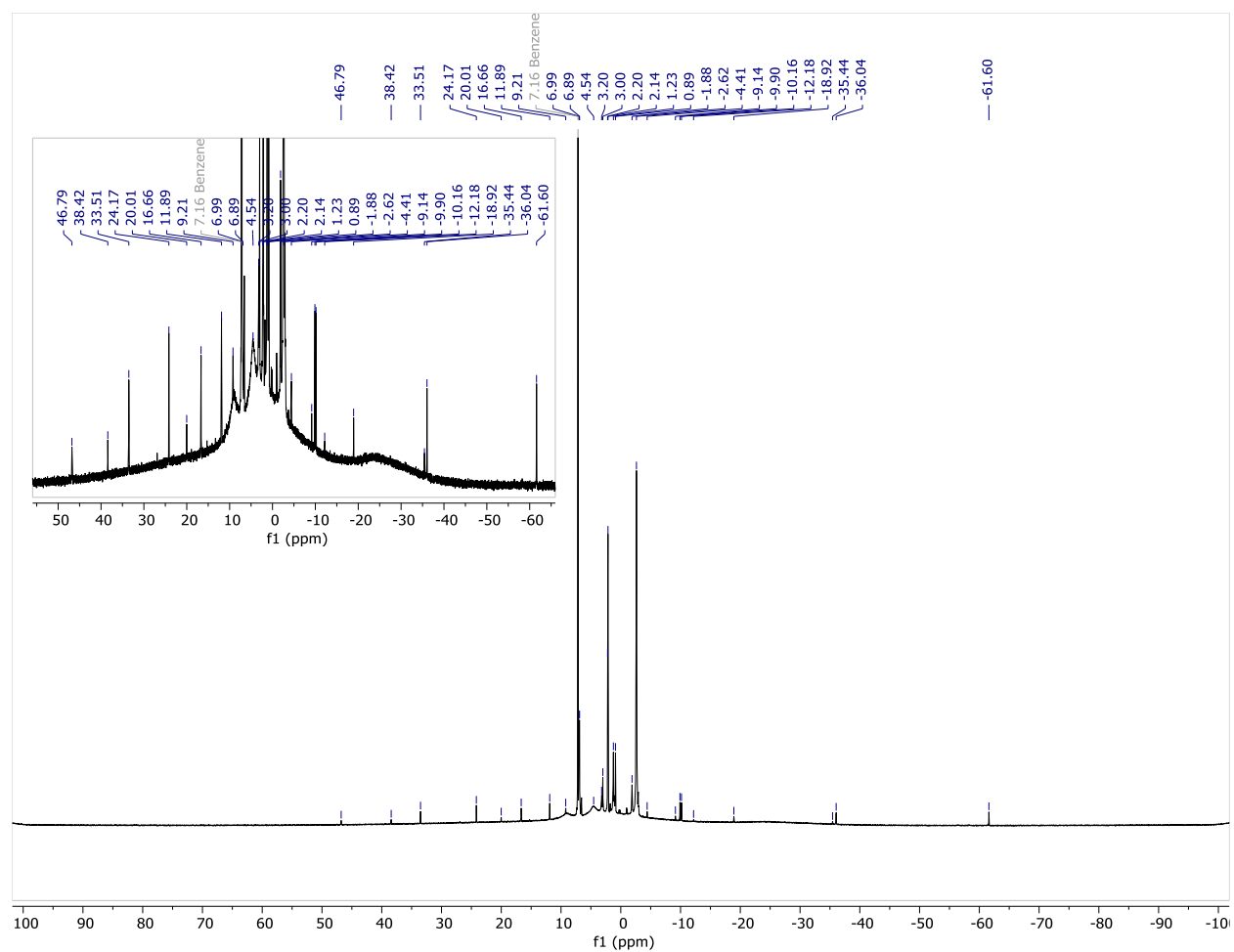


Figure 6-17. Crude  $^1\text{H}$  NMR of  $(\text{Cp}^*)\text{U}(\text{NHAr}^{\text{Me}_6})_2$  in  $\text{C}_6\text{D}_6$ . Inset shows the broad peaks attributed to fluxionality.



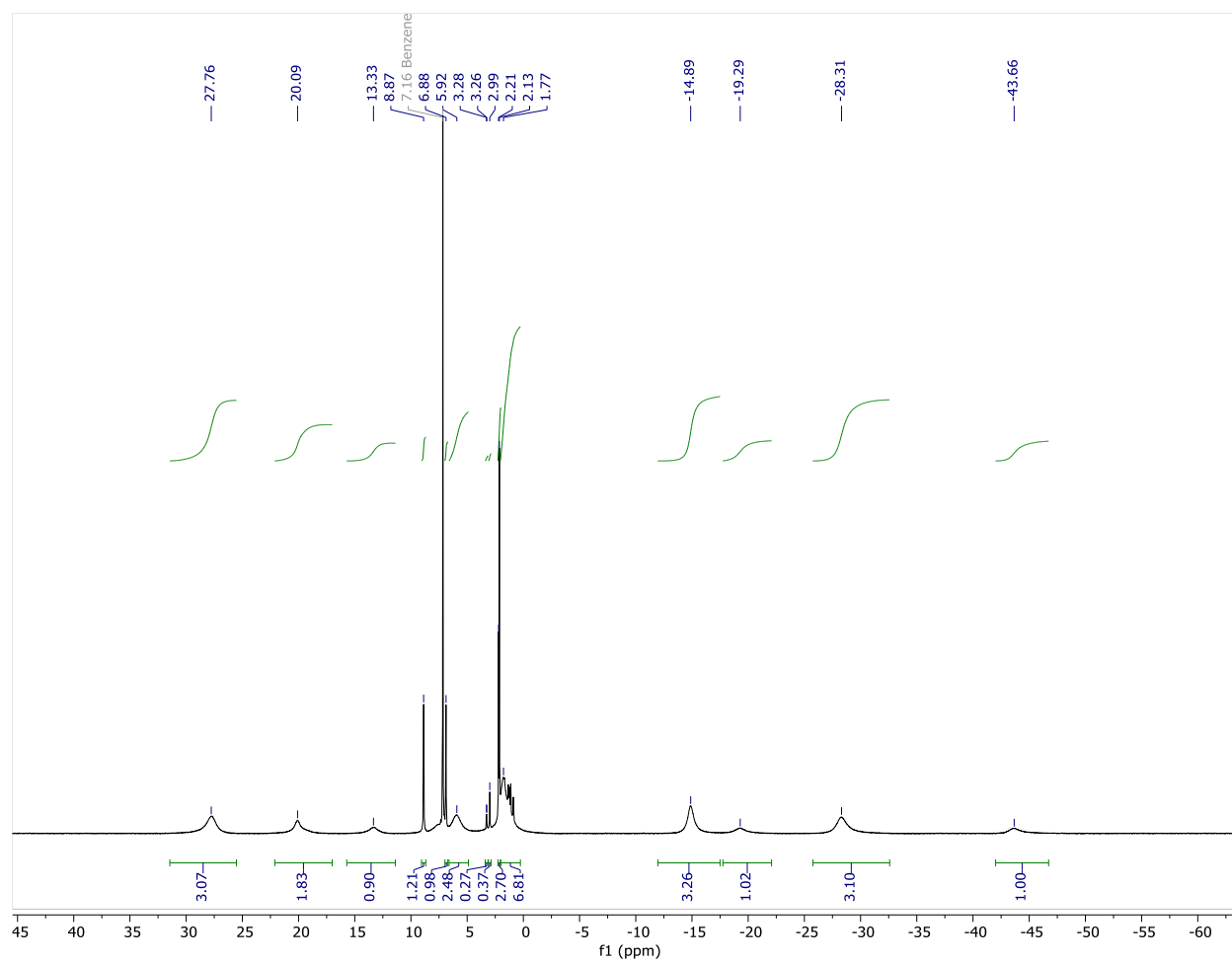


Figure 6-18. <sup>1</sup>H NMR spectrum of UI(NHAr<sup>Me6</sup>)<sub>2</sub> in C<sub>6</sub>D<sub>6</sub>



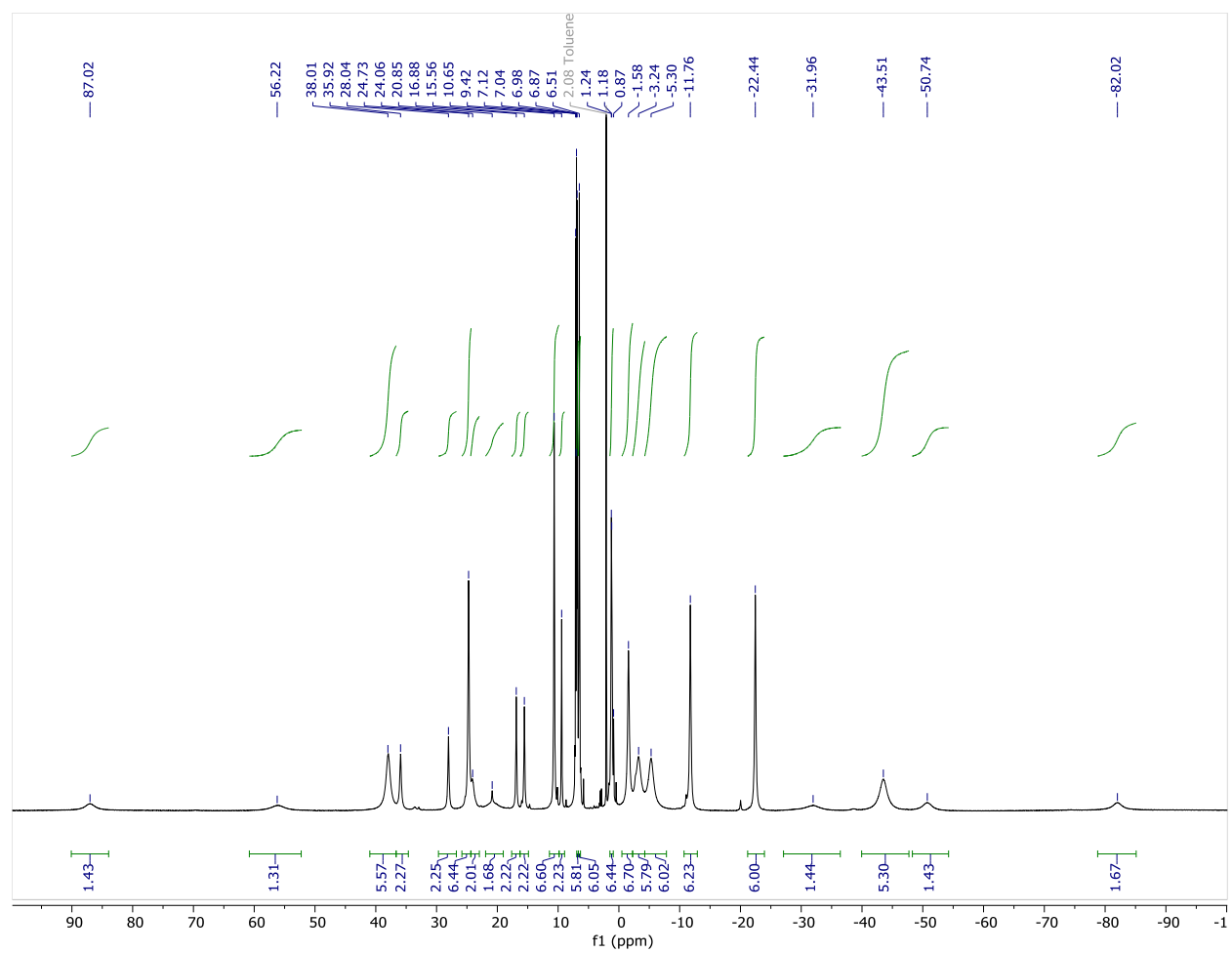


Figure 6-19.  $^1\text{H}$  NMR Spectrum of  $\text{UI}(\text{NHAr}^{\text{iPr}_6})_2$  (**8**) at  $-30\text{ }^\circ\text{C}$  in toluene- $\text{d}_8$



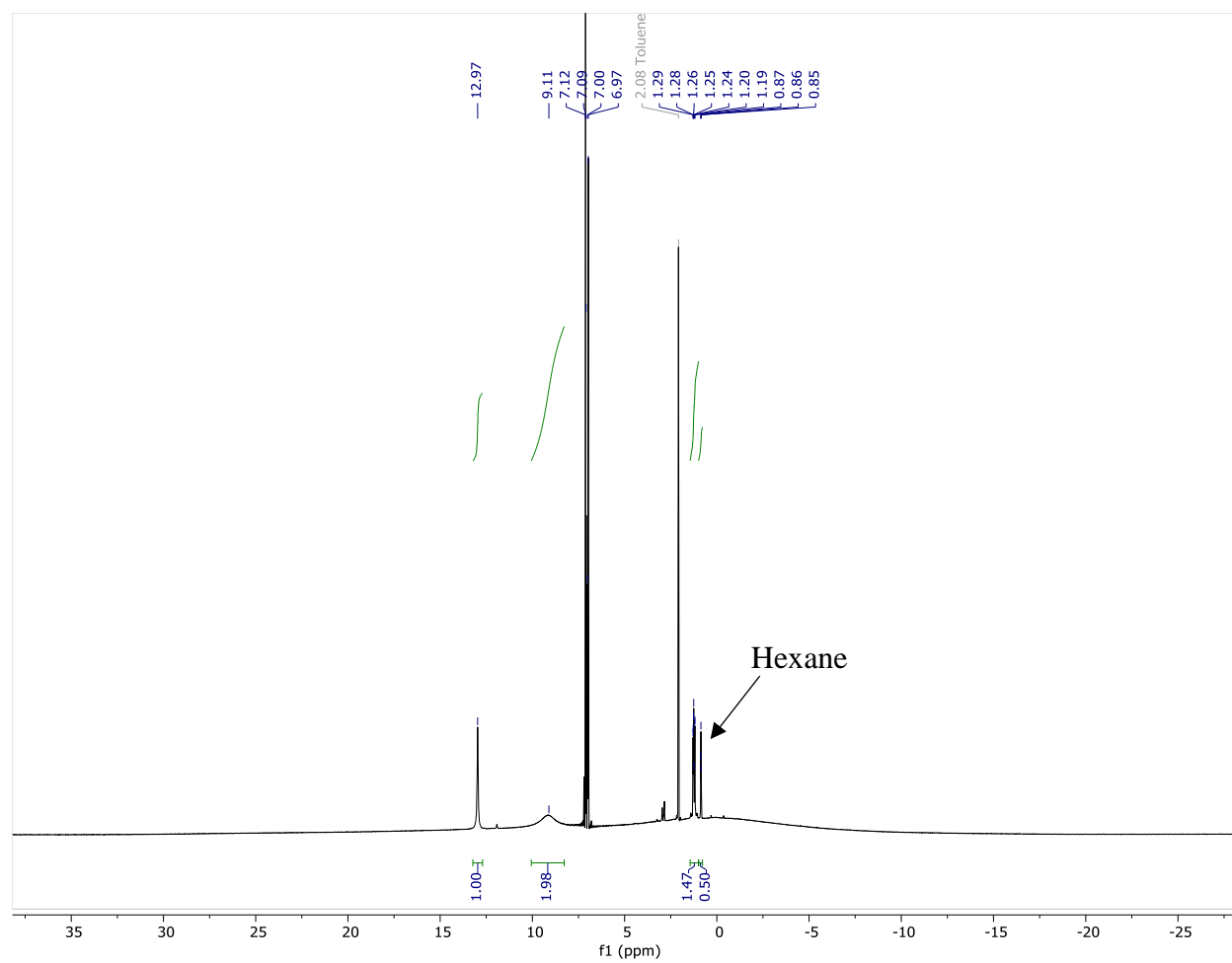


Figure 6-20.  $^1\text{H}$  NMR Spectrum of  $\text{UI}(\text{NHAr}^{\text{iPr}_6})_2$  (**8**) at ambient temperature in  $\text{toluene-d}_8$



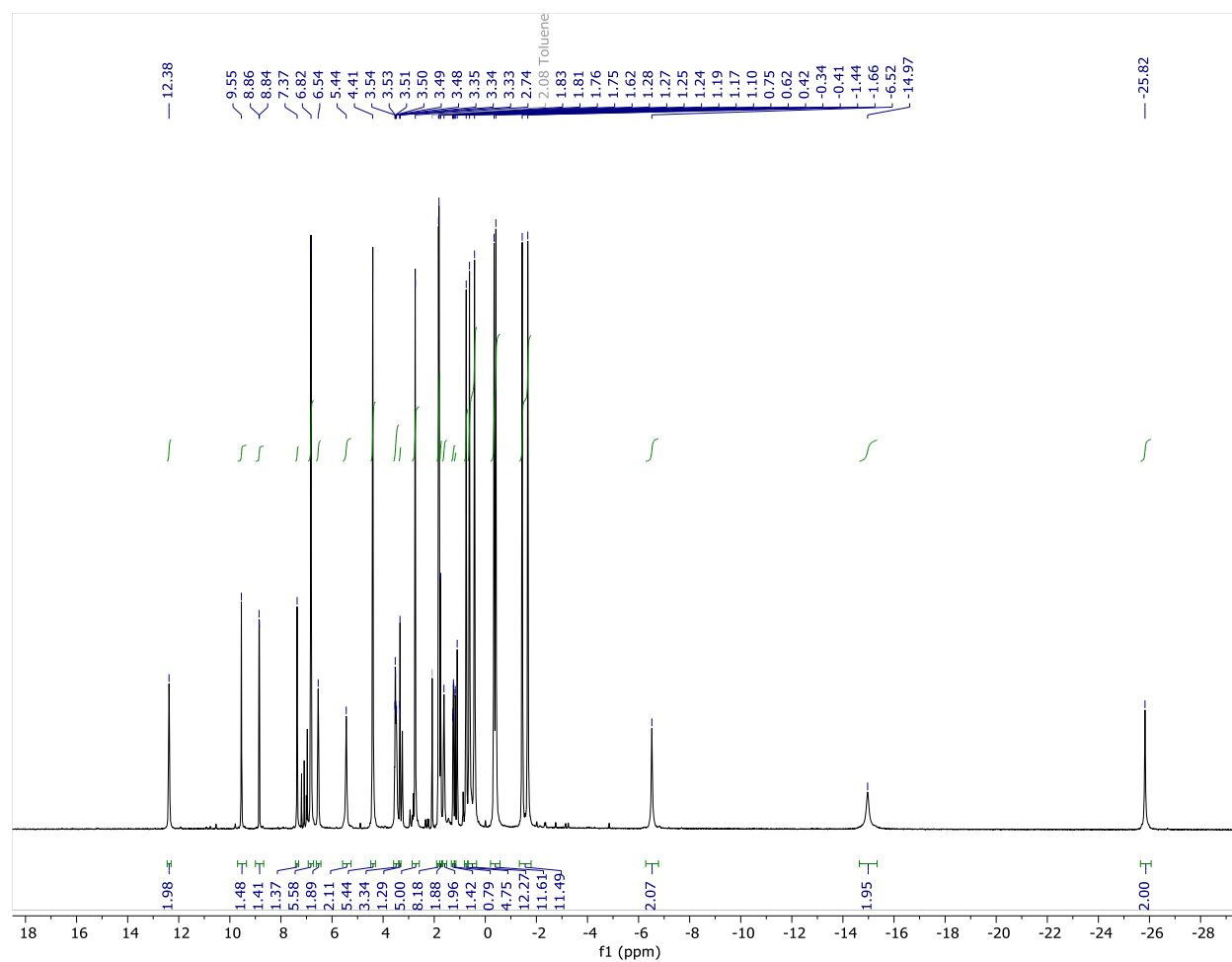


Figure 6-21. <sup>1</sup>H NMR Spectrum of U(NHAr<sup>i</sup>Pr<sub>6</sub>)<sub>2</sub> (**9**) at 25 °C in toluene-d<sub>8</sub>



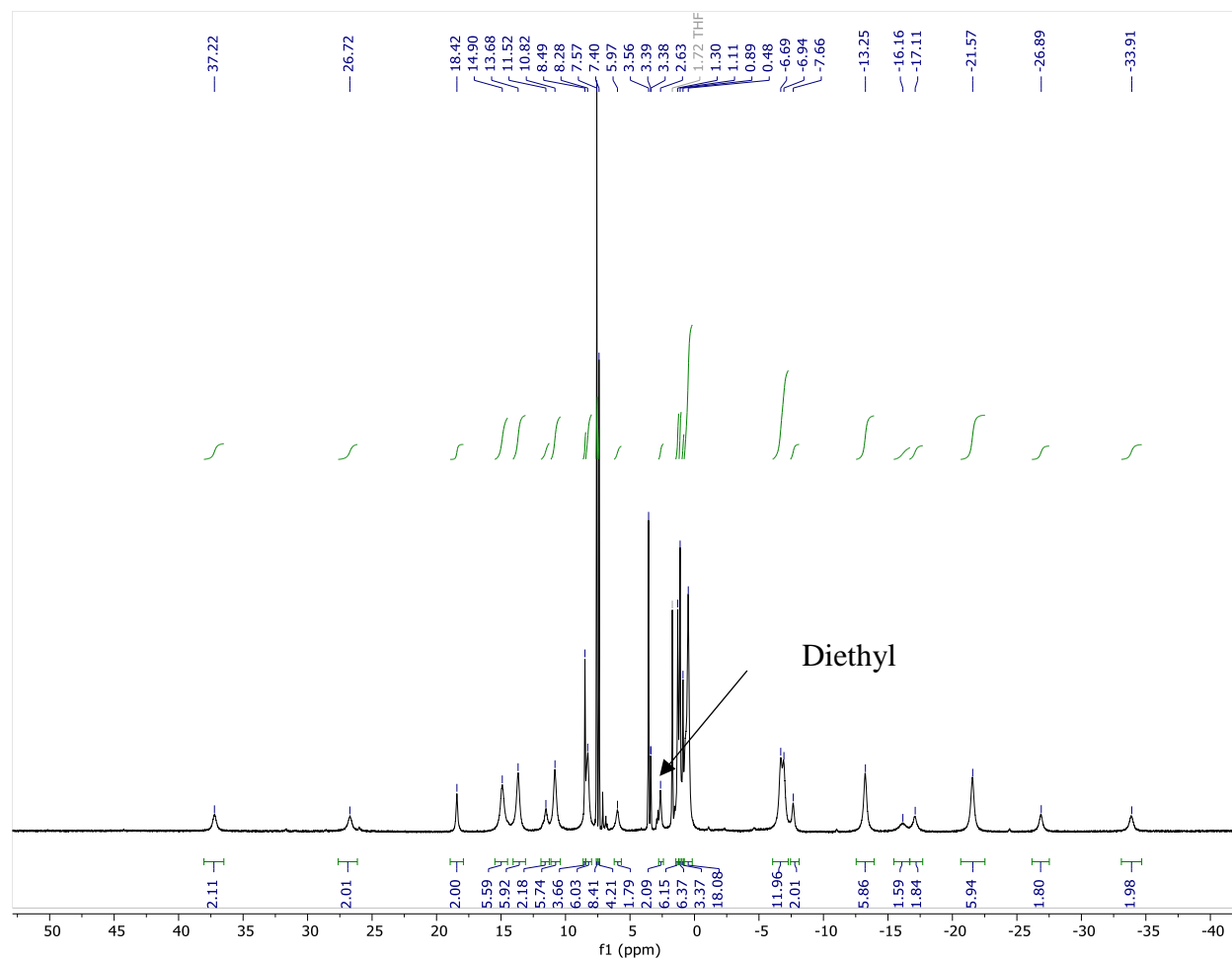


Figure 6-22.  $^1\text{H}$  NMR Spectrum of  $[\text{U}(\text{NHAr}^{\text{iPr}_6})_2]^+ [\text{BAr}^{\text{F}_{24}}]^-$  (10) at  $25^\circ\text{C}$  in  $\text{THF-d}_8$



## Vis-near IR Spectra

Preparation of samples was performed in the glovebox using dry, degassed diethyl ether. Spectra are baseline corrected for a blank sample of diethyl ether in the quartz cuvette used for data collection. Data were collected at ambient temperature. All molar absorptivity values should only be considered approximate as the values are based off of a single concentration rather than averaged over a series of concentrations.

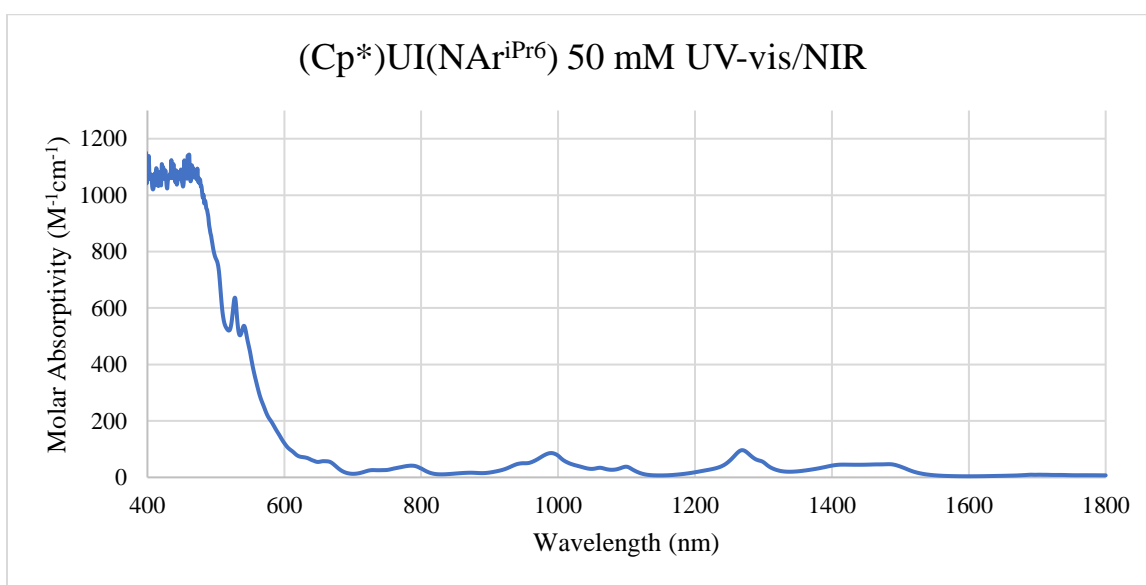


Figure 6-23. UV-vis/NIR spectrum of **2** in 1 mm cuvette



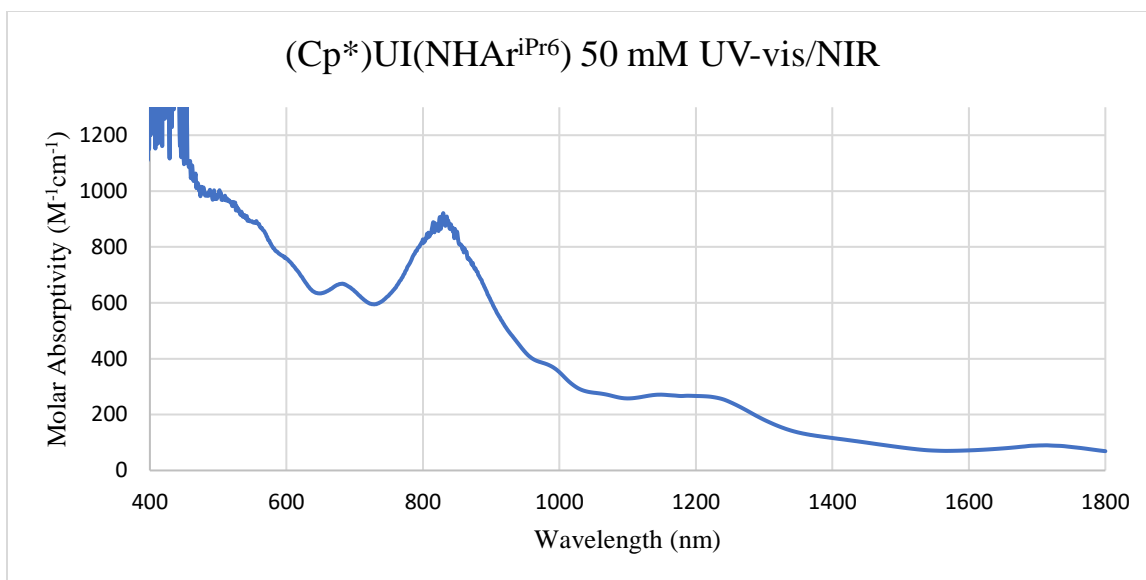


Figure 6-24. UV-vis/NIR spectrum of **3** in 1 mm cuvette

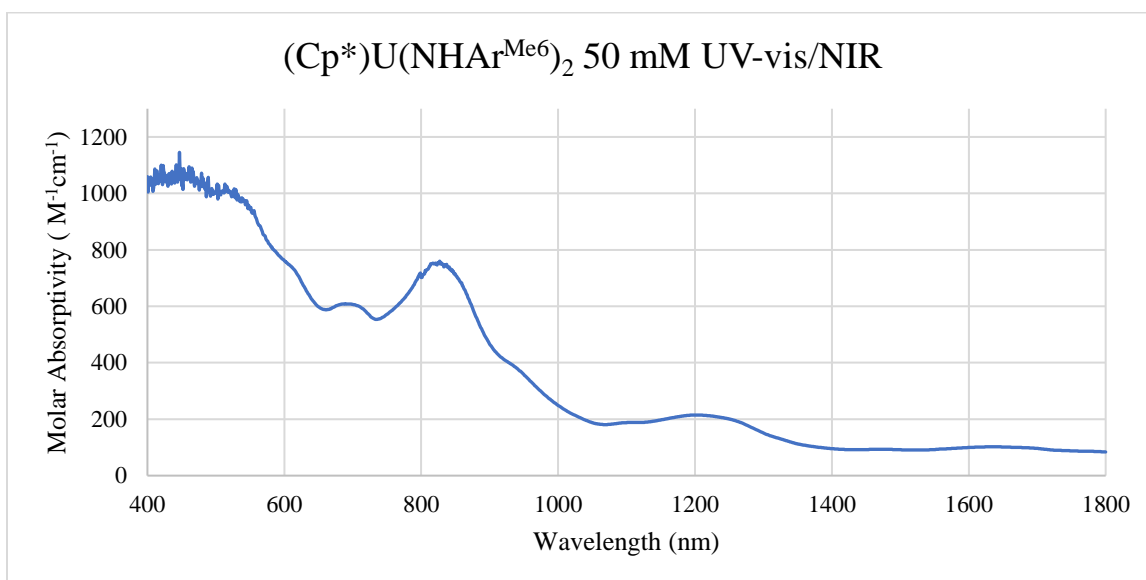


Figure 6-25. UV-vis/NIR spectrum of **6** in 1 mm cuvette.



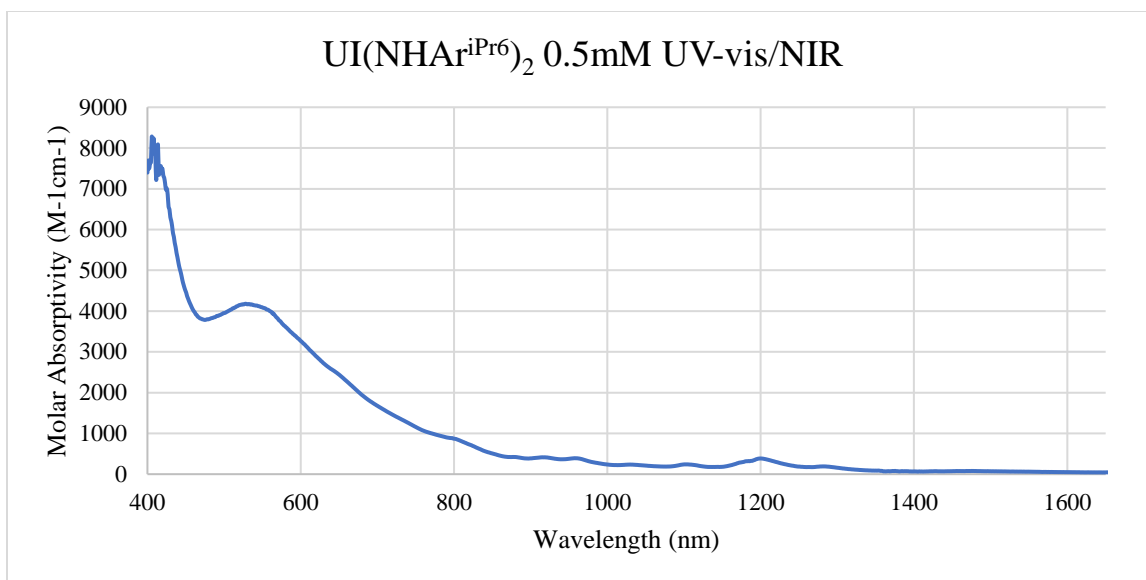


Figure 6-26. UV-vis/NIR spectrum of **8** at low concentration (~0.5 mM).

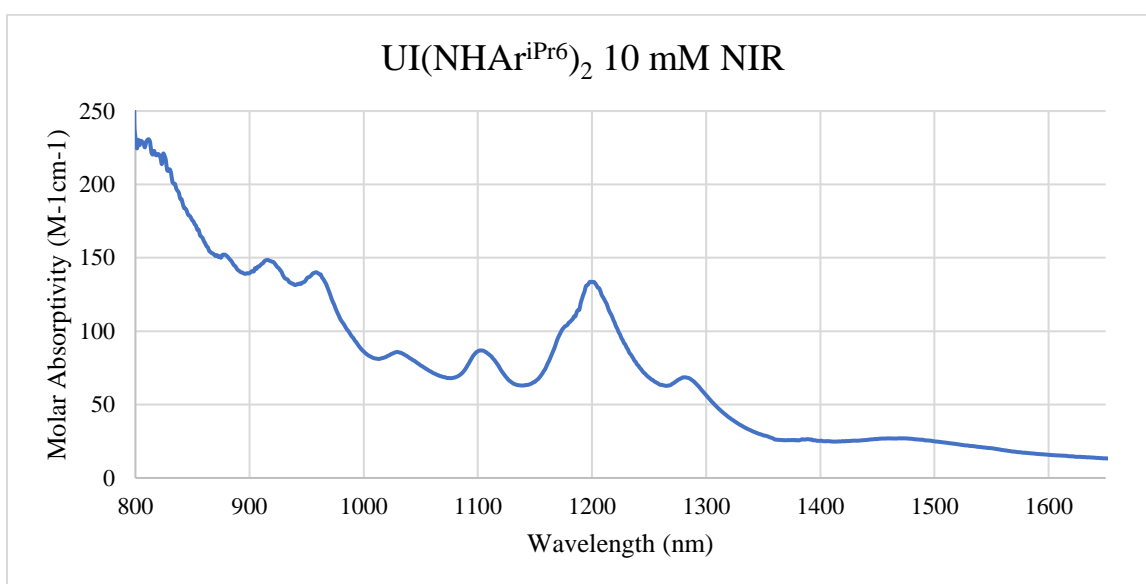


Figure 6-27. NIR spectrum of **8** at high concentration (~10 mM).



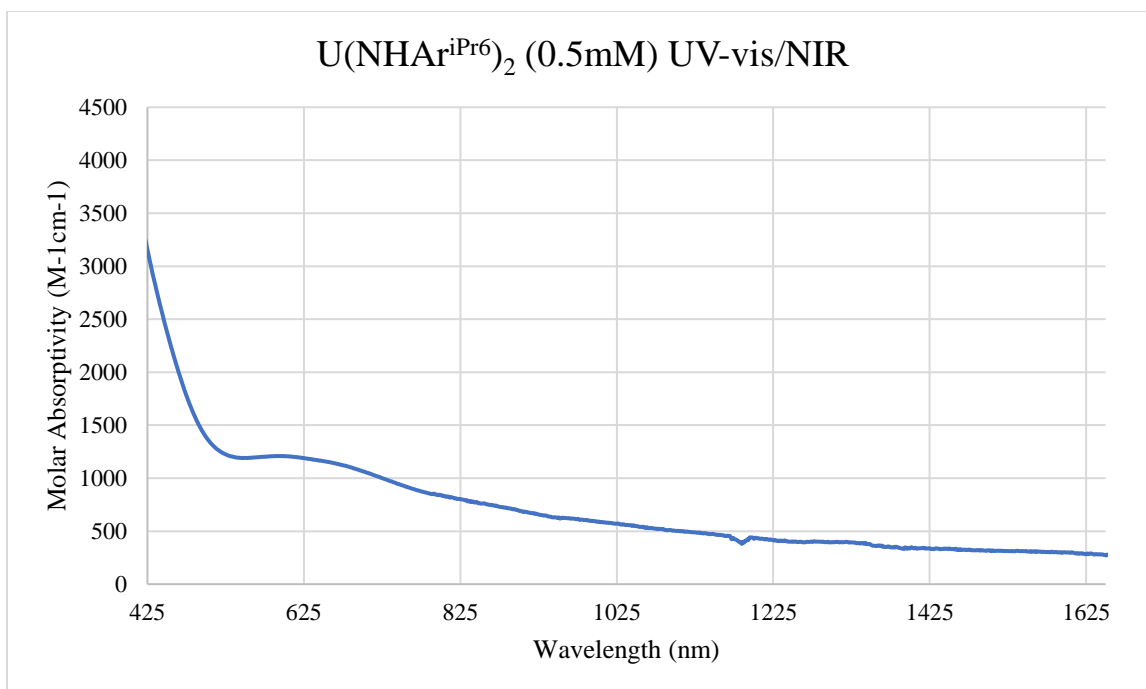


Figure 6-28. UV-vis/NIR spectrum of **9** at low concentration (~0.5 mM).

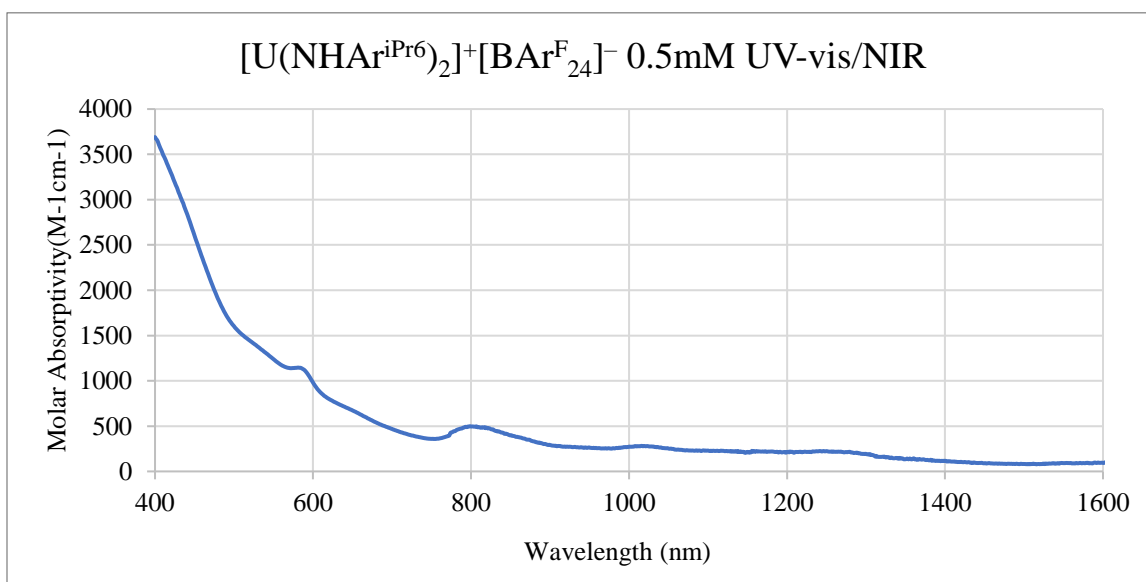


Figure 6-29. UV-vis/NIR spectrum of **10** at low concentration (~0.5 mM).



## EPR Spectroscopy

Samples were prepared for EPR spectroscopy in the drybox using either dry degassed diethyl ether or toluene. The samples were loaded as a solution into a quartz EPR tube and sealed using a rubber septum and PTFE tape. The samples were then rapidly taken from the drybox and submerged into a Dewar flask containing liquid nitrogen.

The X-band EPR spectra were collected at 6 K. For all scans, the data were corrected for background contributions by subtracting EPR spectra obtained for a blank quartz tube containing only solvent. For some scans, the baselines were leveled by subtracting a first or second-degree polynomial after the background correction was done. The data for **9** collected using a SHQ-E probe are shown below plotted on the same scale as **8** and **10** shown in the manuscript. The data for **9** were collected under the same conditions: microwave frequency, 9.40 GHz; microwave power, 0.8 mW; field modulation amplitude, 1.0 mT; and sample temperature, 6K. We collected these data on the second day that we ran in July. The data were collected on a Bruker E-680X EPR spectrometer equipped with an Oxford ESR-900 liquid helium cryostat.



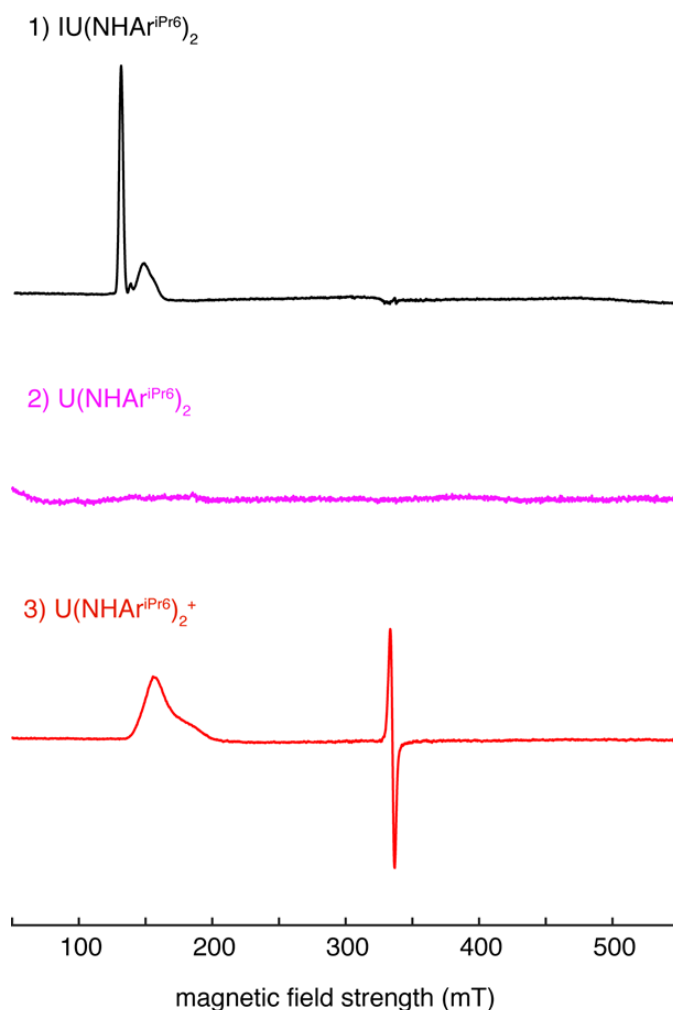


Figure 6-30. EPR spectra of (I)U(NHAr<sup>iPr6</sup>)<sub>2</sub> (**8**), U(NHAr<sup>iPr6</sup>)<sub>2</sub> (**9**), and U(NHAr<sup>iPr6</sup>)<sub>2</sub><sup>+</sup> (**10**). Measurement parameters for both spectra were: microwave frequency = 9.40 GHz, microwave power = 0.79 mW, field modulation amplitude = 1 mT, and sample temperature = 6 K.

The data collected with the DM-4116 parallel mode cavity are shown below for both parallel and perpendicular modes. For the perpendicular mode spectrum, the background contribution from the cryostat was subtracted and the baseline was then corrected by subtracting a second-degree polynomial. For parallel mode, no background correction was needed, but a 3<sup>rd</sup> degree polynomial was subtracted from the baseline to flatten it.



$\text{U}(\text{NHAr}^{\text{iPr}_6})_2$  : DM 4116 probe

a) perpendicular mode



b) parallel mode

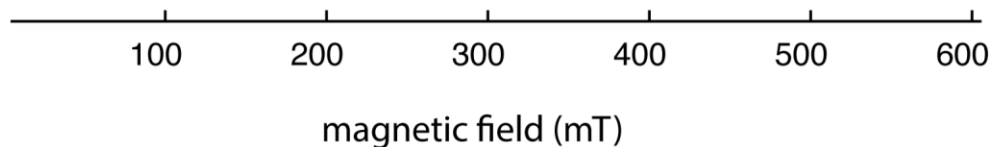


Figure 6-31. Parallel and perpendicular EPR spectra for **8**. Instrument conditions for these scans were: (a) perpendicular mode: microwave frequency = 9.643 GHz, and (b) parallel mode: microwave frequency = 9.441 GHz. Conditions common to the two spectra are: microwave power = 1.0 mW, field modulation amplitude = 1.6 mT, field modulation frequency = 10 kHz, and sample temperature = 5 K.

### Magnetism Details

SQUID magnetization data were recorded using a Quantum Design SQUID magnetometer at 5 kOe. Data were recorded at 1 K intervals from 2 to 20 K, 5 K intervals from 20 to 100 K, and 10 K intervals from 100 to 300 K. Each measurement was checked by following the same temperature program in reverse. Several batches of the samples were measured, and the most self-consistent data was chosen for this publication. Data were corrected for magnetization of the sample holder by subtracting the susceptibility of an empty container and for diamagnetic contributions of the sample using Pascal's constants.<sup>34</sup>

Samples for SQUID magnetometry were all prepared using the following method. Using a vacuum sealer, vacuum-sealable polyethylene bags (bags with opposing diagonal lines) were



sealed to form narrow bags approximately 1 cm in width and 8 cm in length. In an inert atmosphere glovebox, the uranium samples were loaded into the bottom of the narrow bags using a straw to avoid contamination on the sides of the bag. Once loaded, the bags were vacuum sealed at the end of the bag, leaving a substantial amount of bag between where the vacuum is pulled and the sample. With the bag sealed under vacuum, the sample chamber was reduced in size by sealing the bag as close to the sample as possible while avoiding sealing any sample in the seam. The excess bag was then cut off and the size of the bag was reduced to less than 1 cm<sup>2</sup> (by mass the bags weighed ~57 mg). The bag was then folded into a small ball, loaded into a straw, and transferred to the SQUID magnetometer.

Solution state magnetic susceptibility studies were carried out on **9** using the Evans method. The resulting temperature dependent paramagnetism was determined in 10 K intervals from 299-219 K. The sample of **2** was 20 mM in toluene-*d*<sub>8</sub> with a sealed capillary containing 20 mM hexamethyldisiloxane as a reference. At room temperature the effective magnetic moment value of **2** is 0.78 cm<sup>3</sup>Kmol<sup>-1</sup> ( $\mu_{\text{eff}} = 2.50$ ), which decreases slightly to 0.72 cm<sup>3</sup>Kmol<sup>-1</sup> ( $\mu_{\text{eff}} = 2.40$ ) at 219 K. Data were corrected for diamagnetic contributions of the sample using Pascal's constants.

<sup>34</sup> No approximation was included for the temperature dependence of toluene-*d*<sub>8</sub> density.



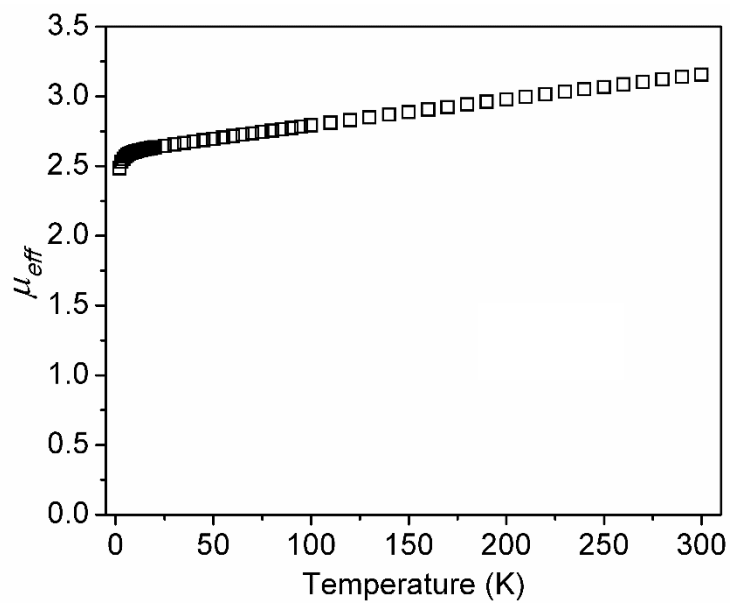


Figure 6-32. Temperature dependence of magnetic susceptibility ( $\mu_{\text{eff}}$ ) for **8** collected at 5000 Oe.

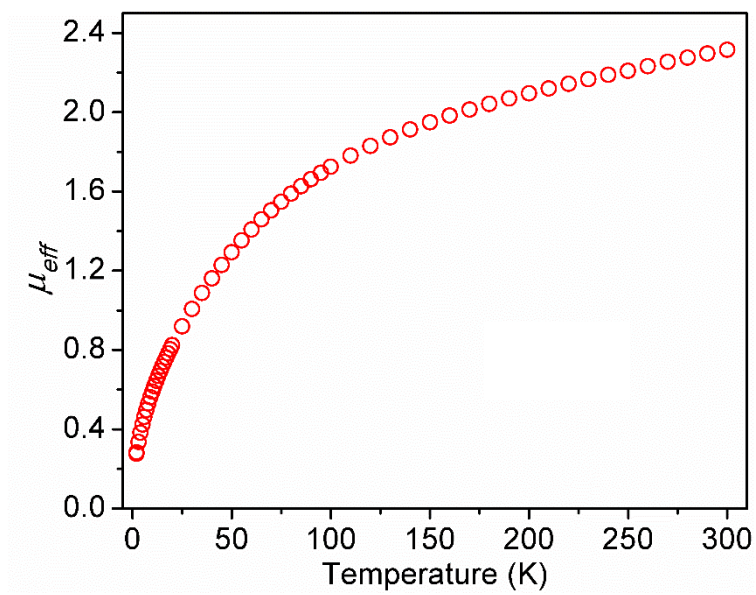


Figure 6-33. Temperature dependence of magnetic susceptibility ( $\mu_{\text{eff}}$ ) for **9** collected at 5000 Oe.



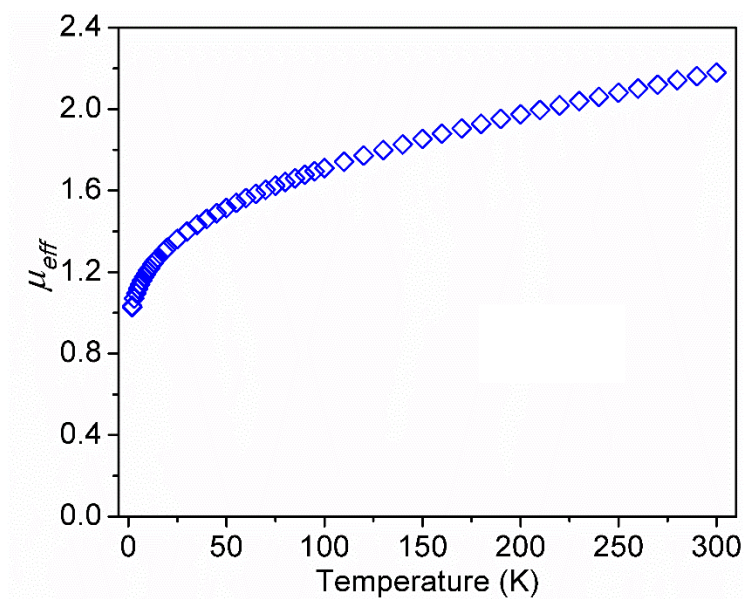


Figure 6-34. Temperature dependence of magnetic susceptibility ( $\mu_{\text{eff}}$ ) for **10** collected at 5000 Oe.

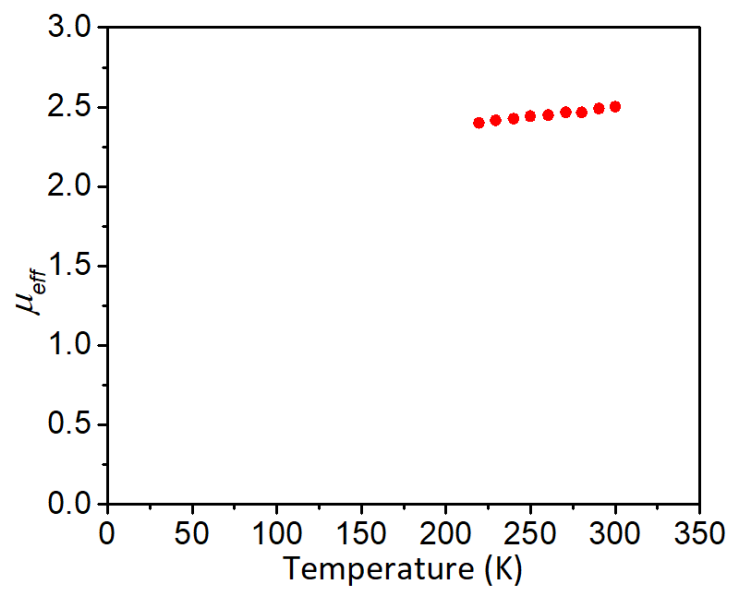


Figure 6-35. Temperature dependence of solution state magnetic susceptibility ( $\mu_{\text{eff}}$ ) for **9**.



# X-ray Crystallographic Details

Complex	(Cp*)UI(NAr <sup>iP</sup> <sub>r6</sub> ) <b>2</b>	(Cp*)UI(NHAr <sup>iP</sup> <sub>r6</sub> ) <b>3</b>	(Cp*)UI(NAr <sup>Me6</sup> )(thf) <sub>2</sub> <b>4</b>	(Cp*)UI(NHAr <sup>M</sup> <sub>e6</sub> ) <b>5</b>	(Cp*)U(NHAr <sup>Me</sup> <sub>6</sub> ) <sub>2</sub> <b>6</b>	UI(NHAr <sup>Me6</sup> ) <sub>2</sub> <b>7</b>
U-N	1.977(4)	2.277(3)	2.006(3)	2.315(4)	2.356(3), 2.336(3)	2.349(6), 2.316(6)
U-N-C	145.0(3)	132.9(2)	163.9(2)	132.4(3)	162.4(2), 132.1(2)	136.5(5), 136.5(5)
N-U-N	--	--	--	--	110.8(1)	113.2(2)
U-Ar <sub>cent</sub>	2.594(1)	2.482(2)	--	2.501(3)	2.497(3)	2.754(3), 2.843(3)
<sup>a</sup> Cent-U-Cent	136.4(3)	137.2(08)	--	136.9(1)	125.9(08)	174.5(1)
Cp* <sub>cent</sub> -U	2.462(2)	2.469(2)	2.500(4)	2.466(3)	2.496(2)	--

Table 6-1. Selected bond lengths and angles. <sup>a</sup>The centroid refers to the Cp\* centroid-U-Arene centroid angle in **2-6**, and the Arene centroid-U-Arene centroid angle in **7**.



Complex	UI(NHAr <sup>iPr</sup> ) <sub>2</sub> <b>8</b> <sup>a</sup>	U(NHAr <sup>iPr</sup> ) <sub>2</sub> <b>9</b>	U(NHAr <sup>iPr</sup> ) <sub>2</sub> BAr <sup>F</sup> <b>10</b>
<b>U-N</b>	2.390(3), 2.372(3)	2.330(2)	2.283(6), 2.282(6)
	2.355(2), 2.366(2)		
<b>U-N-C</b>	137.5(2), 135.6(2)	130.26(2)	133.5(5), 131.6(5)
	139.43(2), 138.53(2)		
<b>N-U-N</b>	149.07(1)	99.24(1)	111.2(2)
	149.92(7)		
<b>U-Ar<sub>cent</sub></b>	2.777(1), 2.790(1)	2.405(1)	2.573(3), 2.583(3)
	2.8968(9), 2.7878(9)		
<b>Ar<sub>cent</sub>-U-Ar<sub>cent</sub></b>	158.28(4)	134.23(5)	145.8(1)
	158.78(3)		
<b>U-Carene</b>	3.147(3), 3.208(3), 3.143(3), 3.080(3), 3.043(3), 3.109(3), 3.147(3), 3.178(3), 3.135(3), 3.069(3), 3.020(3), 3.114(3)	2.735(3), 2.730(3), 2.869(3), 2.725(3), 2.770(3), 2.903(3)	2.945(7), 3.008(7), 2.953(7), 2.902(7), 2.842(7), 2.908(7), 3.061(9), 2.993(8), 2.940(7), 2.828(6), 2.869(7), 2.947(8)
	3.182(2), 3.177(2), 3.091(2), 3.039(2), 3.058(2), 3.175(2), 3.314(2), 3.310(2), 3.191(2), 3.106(2), 3.116(2), 3.264(2)		
<b>Avg. C<sub>Ar</sub>-C<sub>Ar</sub> bond</b>	1.402	1.415333333	1.403
	1.403		

Table 6-2. Selected bond lengths and angles. <sup>a</sup>The white rows are the values from the diethyl ether crystallized structure, the grey rows are from the hexane crystallized structure.



Single crystal diffraction data were collected Bruker APEX-II CCD diffractometers using either MoK $\alpha$  or CuK $\alpha$ . Single crystals were mounted on glass fiber loops using either N-paratone oil or Krytox grease. Data collection was done at either 100 K or 173 K under a liquid nitrogen cold stream. Using Olex2, the structures were solved with the ShelXT solution program using intrinsic phasing and refined with the XL refinement package using least squares minimization.<sup>35-</sup>

37

Crystal data and structure refinement for (Cp\*)UI(NAr<sup>iPr6</sup>) (2)

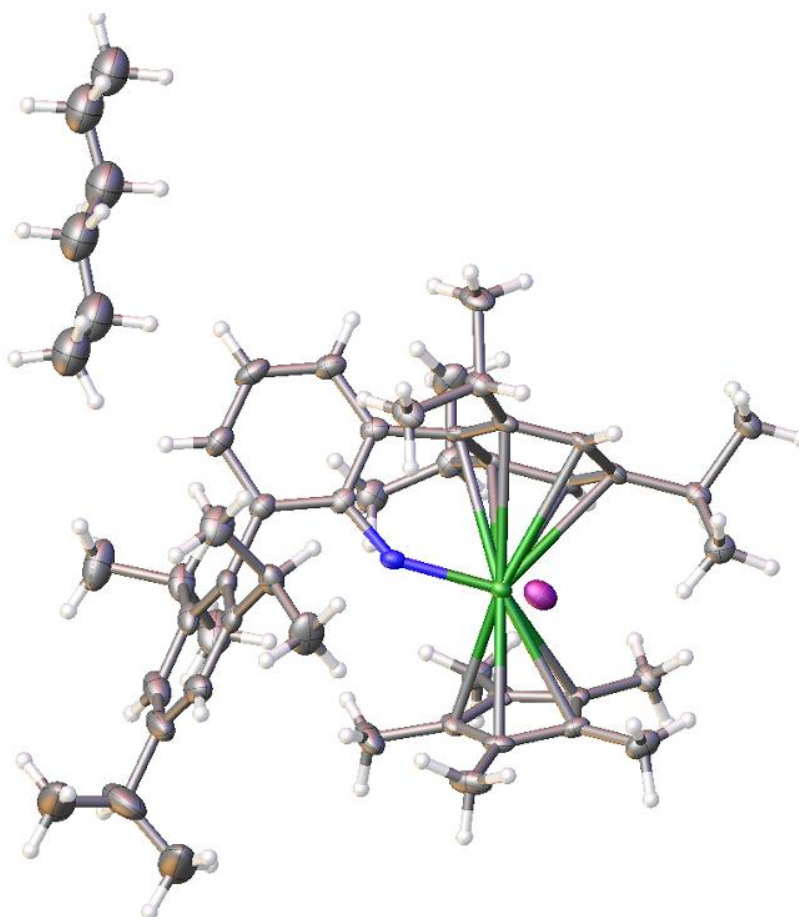


Figure 6-36. Full structure of (2) including solvent

Identification code (Cp\*)UINTriPP



Empirical formula	C <sub>49</sub> H <sub>71</sub> INU
Formula weight	1038.99
Temperature/K	100.0
Crystal system	monoclinic
Space group	P2 <sub>1</sub> /c
a/Å	17.797(11)
b/Å	17.303(11)
c/Å	16.558(10)
α/°	90
β/°	103.395(7)
γ/°	90
Volume/Å <sup>3</sup>	4960(5)
Z	4
ρ <sub>calc</sub> /g/cm <sup>3</sup>	1.391
μ/mm <sup>-1</sup>	3.924
F(000)	2068.0
Crystal size/mm <sup>3</sup>	0.27 × 0.25 × 0.06
Radiation	MoKα (λ = 0.71073)
2Θ range for data collection/°	5.058 to 54.206
Index ranges	-22 ≤ h ≤ 22, -22 ≤ k ≤ 22, -21 ≤ l ≤ 21
Reflections collected	54710
Independent reflections	10926 [R <sub>int</sub> = 0.0564, R <sub>sigma</sub> = 0.0438]
Data/restraints/parameters	10926/2/479
Goodness-of-fit on F <sup>2</sup>	1.029
Final R indexes [I ≥ 2σ (I)]	R <sub>1</sub> = 0.0326, wR <sub>2</sub> = 0.0779
Final R indexes [all data]	R <sub>1</sub> = 0.0523, wR <sub>2</sub> = 0.0869



Largest diff. peak/hole / e Å<sup>-3</sup> 1.46/-0.97

Crystal data and structure refinement for (Cp\*)UI(NHAr<sup>iPr</sup><sub>6</sub>) (**3**)

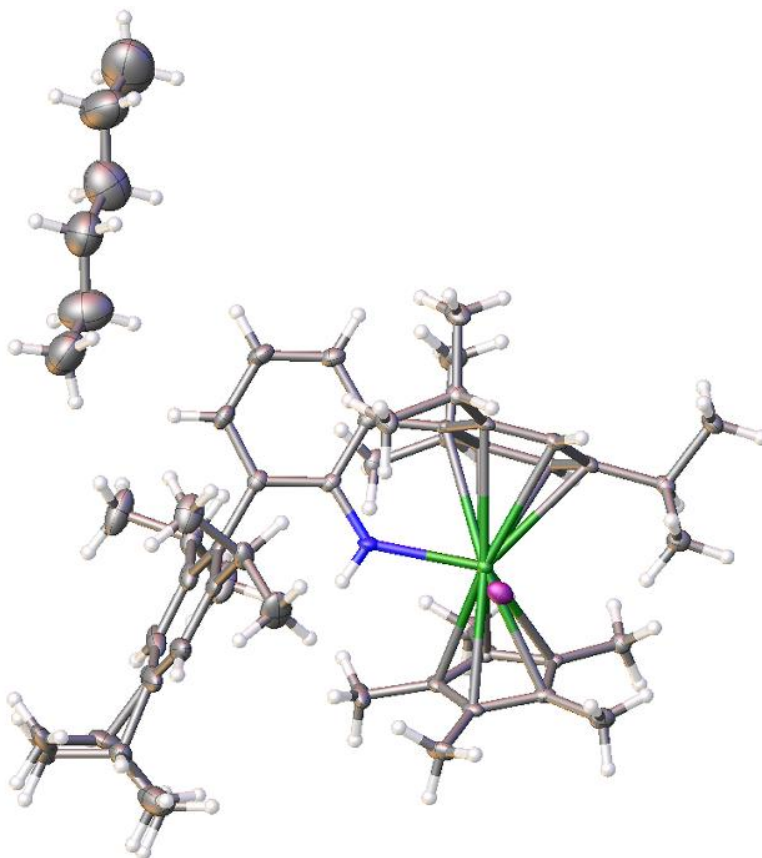


Figure 6-37. Full structure of (**3**) including solvent and molecular disorder

Identification code	CpstarUINHTriPP
Empirical formula	C <sub>52</sub> H <sub>79</sub> INU
Formula weight	1083.09
Temperature/K	103.0
Crystal system	monoclinic
Space group	P2 <sub>1</sub> /c
a/Å	18.0138(13)



b/Å	17.3681(13)
c/Å	16.4608(12)
$\alpha/^\circ$	90
$\beta/^\circ$	103.183(2)
$\gamma/^\circ$	90
Volume/Å <sup>3</sup>	5014.3(6)
Z	4
$\rho_{\text{calc}}/\text{g}/\text{cm}^3$	1.435
$\mu/\text{mm}^{-1}$	3.885
F(000)	2172.0
Crystal size/mm <sup>3</sup>	0.42 × 0.42 × 0.11
Radiation	MoK $\alpha$ ( $\lambda$ = 0.71073)
2 $\Theta$ range for data collection/ $^\circ$	5.204 to 55.752
Index ranges	-23 ≤ h ≤ 23, -22 ≤ k ≤ 22, -21 ≤ l ≤ 21
Reflections collected	76155
Independent reflections	11949 [ $R_{\text{int}}$ = 0.0465, $R_{\text{sigma}}$ = 0.0294]
Data/restraints/parameters	11949/4/544
Goodness-of-fit on F <sup>2</sup>	1.024
Final R indexes [ $I \geq 2\sigma(I)$ ]	$R_1$ = 0.0250, $wR_2$ = 0.0528
Final R indexes [all data]	$R_1$ = 0.0395, $wR_2$ = 0.0579
Largest diff. peak/hole / e Å <sup>-3</sup>	1.16/-0.66

Crystal data and structure refinement for (Cp\*)UI(NAr<sup>Me6</sup>)(thf)<sub>2</sub> (**4**)



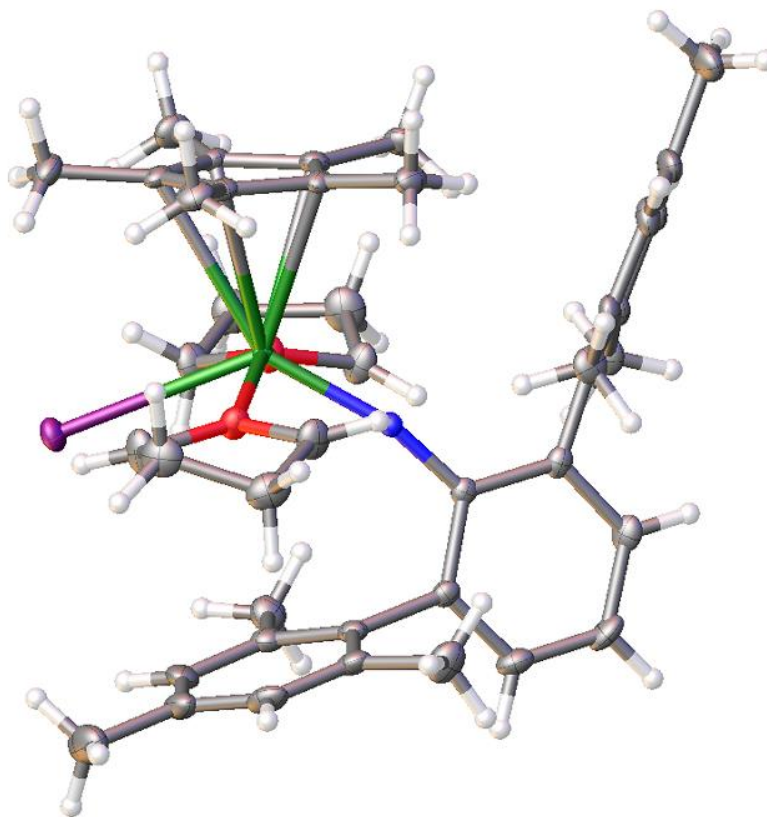


Figure 6-38. Full structure of (4)

Identification code	Mes2ArNUCpstarIthf2
Empirical formula	C <sub>42</sub> H <sub>53</sub> INO <sub>2</sub> U
Formula weight	968.83
Temperature/K	296.15
Crystal system	monoclinic
Space group	P2 <sub>1</sub> /c
a/Å	10.6120(18)
b/Å	12.157(2)
c/Å	29.815(5)
$\alpha$ /°	90
$\beta$ /°	95.774(2)



$\gamma/^\circ$	90
Volume/ $\text{\AA}^3$	3826.9(11)
Z	4
$\rho_{\text{calc}}/\text{g}/\text{cm}^3$	1.6814
$\mu/\text{mm}^{-1}$	5.085
F(000)	1850.6
Crystal size/ $\text{mm}^3$	$0.19 \times 0.17 \times 0.07$
Radiation	Mo K $\alpha$ ( $\lambda = 0.71073$ )
$2\Theta$ range for data collection/ $^\circ$	4.96 to 55.66
Index ranges	$-13 \leq h \leq 13, -15 \leq k \leq 15, -39 \leq l \leq 39$
Reflections collected	44555
Independent reflections	9053 [ $R_{\text{int}} = 0.0432, R_{\text{sigma}} = 0.0331$ ]
Data/restraints/parameters	9053/0/434
Goodness-of-fit on $F^2$	1.063
Final R indexes [ $I \geq 2\sigma(I)$ ]	$R_1 = 0.0258, wR_2 = 0.0568$
Final R indexes [all data]	$R_1 = 0.0319, wR_2 = 0.0592$
Largest diff. peak/hole / $e \text{\AA}^{-3}$	1.01/-1.25

Crystal data and structure refinement for (Cp\*)UI(NHAr<sup>Me6</sup>) (**5**)



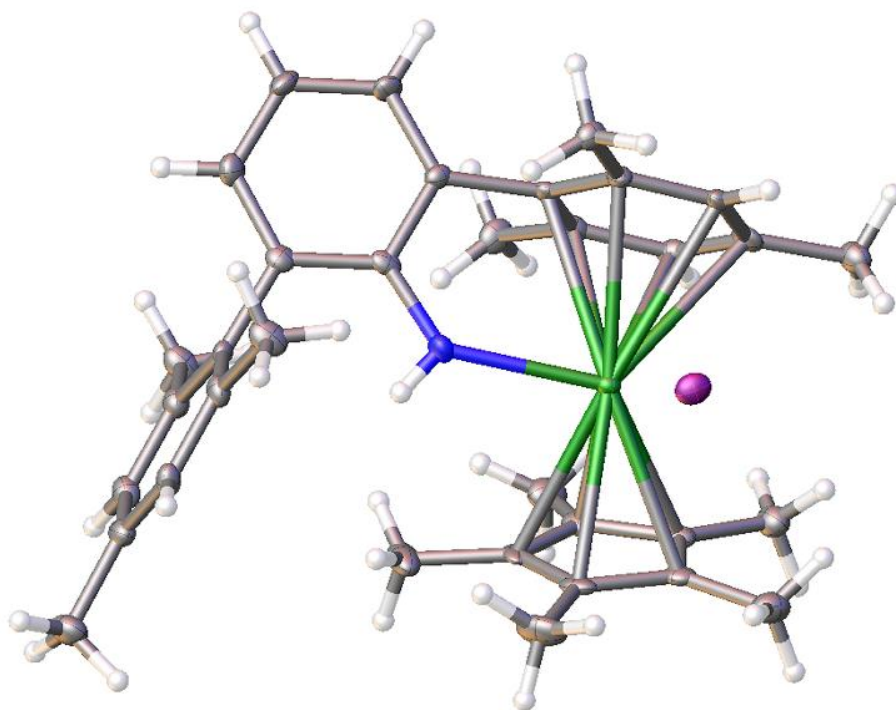


Figure 6-39. Full structure of **(5)**

Identification code	Mes2ArNHUICpstar
Empirical formula	C <sub>34</sub> H <sub>41</sub> INU
Formula weight	828.61
Temperature/K	100.0
Crystal system	monoclinic
Space group	P2 <sub>1</sub> /c
a/Å	21.313(2)
b/Å	8.7053(10)
c/Å	17.0261(19)
$\alpha$ /°	90
$\beta$ /°	101.810(2)
$\gamma$ /°	90
Volume/Å <sup>3</sup>	3092.0(6)



Z	4
$\rho_{\text{calc}}/\text{cm}^3$	1.780
$\mu/\text{mm}^{-1}$	6.270
F(000)	1588.0
Crystal size/ $\text{mm}^3$	$0.34 \times 0.33 \times 0.02$
Radiation	MoK $\alpha$ ( $\lambda = 0.71073$ )
2 $\Theta$ range for data collection/ $^\circ$	5.28 to 57.452
Index ranges	$-28 \leq h \leq 27, -11 \leq k \leq 10, -21 \leq l \leq 23$
Reflections collected	22223
Independent reflections	7990 [ $R_{\text{int}} = 0.0412, R_{\text{sigma}} = 0.0498$ ]
Data/restraints/parameters	7990/0/348
Goodness-of-fit on $F^2$	1.030
Final R indexes [ $I \geq 2\sigma(I)$ ]	$R_1 = 0.0347, wR_2 = 0.0706$
Final R indexes [all data]	$R_1 = 0.0517, wR_2 = 0.0780$
Largest diff. peak/hole / $e \text{ \AA}^{-3}$	2.84/-1.79



Crystal data and structure refinement for (Cp\*)U(NHAr<sup>Me6</sup>)<sub>2</sub> (**6**)

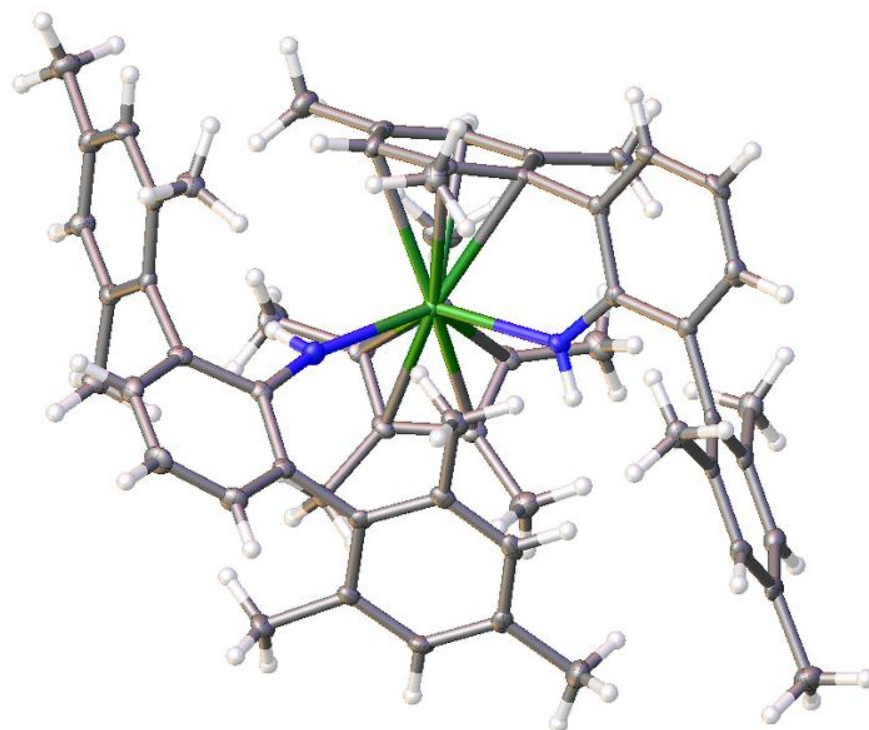


Figure 6-40. Full structure of (**6**)

Identification code	CpstarUNArMes2_2
Empirical formula	C <sub>58</sub> H <sub>67</sub> N <sub>2</sub> U
Formula weight	1030.22
Temperature/K	100.01
Crystal system	monoclinic
Space group	P2 <sub>1</sub> /c
a/Å	11.2677(12)
b/Å	27.403(3)
c/Å	15.9408(17)
$\alpha$ /°	90



$\beta/^\circ$	110.049(2)
$\gamma/^\circ$	90
Volume/ $\text{\AA}^3$	4623.7(9)
Z	4
$\rho_{\text{calc}}/\text{g}/\text{cm}^3$	1.4798
$\mu/\text{mm}^{-1}$	3.552
F(000)	2044.1
Crystal size/ $\text{mm}^3$	$0.17 \times 0.06 \times 0.05$
Radiation	Mo K $\alpha$ ( $\lambda = 0.71073$ )
$2\Theta$ range for data collection/ $^\circ$	4.86 to 55.98
Index ranges	$-14 \leq h \leq 14, -36 \leq k \leq 36, -21 \leq l \leq 21$
Reflections collected	65480
Independent reflections	11109 [ $R_{\text{int}} = 0.0593, R_{\text{sigma}} = 0.0388$ ]
Data/restraints/parameters	11109/0/566
Goodness-of-fit on $F^2$	1.056
Final R indexes [ $I \geq 2\sigma(I)$ ]	$R_1 = 0.0330, wR_2 = 0.0693$
Final R indexes [all data]	$R_1 = 0.0478, wR_2 = 0.0749$
Largest diff. peak/hole / $e \text{\AA}^{-3}$	2.00/-0.99

Crystal data and structure refinement for  $\text{UI}(\text{NHAr}^{\text{Me6}})_2$  (**7**)



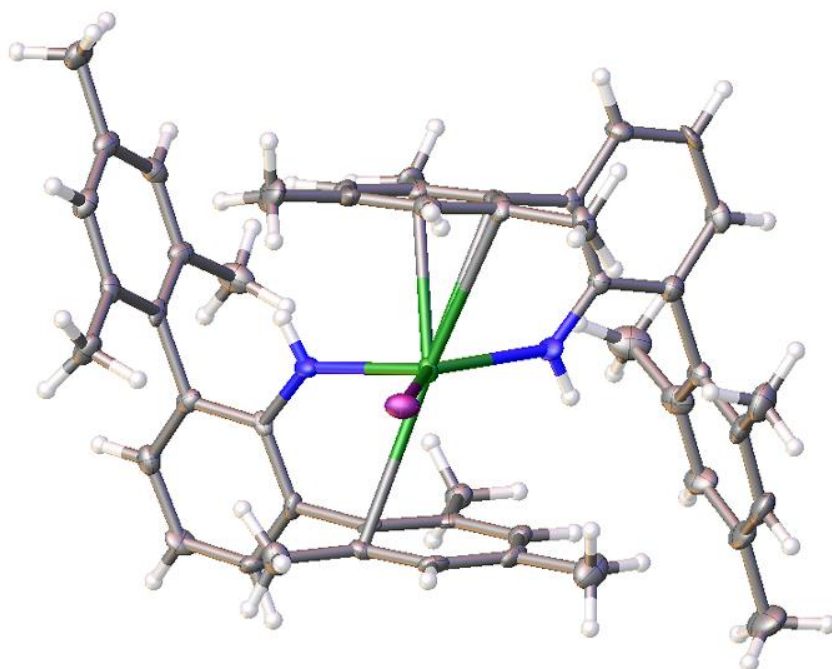


Figure 6-41. Full structure of (7)

Identification code	Mes2ArNH2UI
Empirical formula	C <sub>48</sub> H <sub>52</sub> IN <sub>2</sub> U
Formula weight	1021.89
Temperature/K	104.34
Crystal system	monoclinic
Space group	P2 <sub>1</sub> /c
a/Å	19.2948(18)
b/Å	13.1778(12)
c/Å	17.2207(16)
$\alpha$ /°	90
$\beta$ /°	104.958(2)
$\gamma$ /°	90
Volume/Å <sup>3</sup>	4230.2(7)
Z	4



$\rho_{\text{calc}}/\text{cm}^3$	1.6044
$\mu/\text{mm}^{-1}$	4.602
F(000)	1954.5
Crystal size/ $\text{mm}^3$	$0.19 \times 0.19 \times 0.15$
Radiation	Mo K $\alpha$ ( $\lambda = 0.71073$ )
2 $\Theta$ range for data collection/ $^\circ$	5.8 to 52.72
Index ranges	$0 \leq h \leq 25, -17 \leq k \leq 0, -22 \leq l \leq 21$
Reflections collected	9882
Independent reflections	8465 [ $R_{\text{int}} = 0.0000, R_{\text{sigma}} = 0.0532$ ]
Data/restraints/parameters	8465/0/480
Goodness-of-fit on $F^2$	1.054
Final R indexes [ $I \geq 2\sigma(I)$ ]	$R_1 = 0.0503, wR_2 = 0.1049$
Final R indexes [all data]	$R_1 = 0.0727, wR_2 = 0.1145$
Largest diff. peak/hole / $e \text{ \AA}^{-3}$	2.55/-1.61



Crystal data and structure refinement for  $\text{UI}(\text{NHAr}^{\text{iPr6}})_2$  (**8**) crystallized from ether

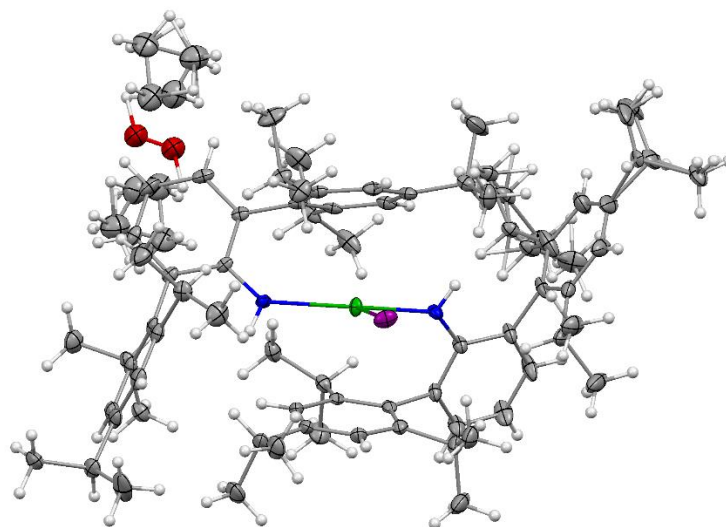


Figure 6-42. Full structure of (**8**) solvent and molecular disorder

Identification code	TriPPNH2UI
Empirical formula	$\text{C}_{74}\text{H}_{105}\text{IN}_2\text{O}_{0.5}\text{U}$
Formula weight	1395.52
Temperature/K	100(2)
Crystal system	monoclinic
Space group	$\text{P2}_1/\text{n}$
$a/\text{\AA}$	15.2986(7)
$b/\text{\AA}$	23.8567(11)
$c/\text{\AA}$	18.6523(9)
$\alpha/^\circ$	90
$\beta/^\circ$	96.0070(10)
$\gamma/^\circ$	90
Volume/ $\text{\AA}^3$	6770.2(5)
Z	4
$\rho_{\text{calc}}/\text{cm}^3$	1.369



$\mu/\text{mm}^{-1}$	2.895
F(000)	2848.0
Crystal size/ $\text{mm}^3$	$0.18 \times 0.15 \times 0.15$
Radiation	MoK $\alpha$ ( $\lambda = 0.71073$ )
$2\Theta$ range for data collection/ $^\circ$	4.712 to 56.564
Index ranges	$-20 \leq h \leq 20, -31 \leq k \leq 31, -24 \leq l \leq 24$
Reflections collected	82390
Independent reflections	16801 [ $R_{\text{int}} = 0.0388, R_{\text{sigma}} = 0.0323$ ]
Data/restraints/parameters	16801/48/803
Goodness-of-fit on $F^2$	1.014
Final R indexes [ $I \geq 2\sigma(I)$ ]	$R_1 = 0.0268, wR_2 = 0.0552$
Final R indexes [all data]	$R_1 = 0.0401, wR_2 = 0.0594$
Largest diff. peak/hole / $e \text{ \AA}^{-3}$	0.70/−0.54



Crystal data and structure refinement for  $\text{UI}(\text{NHAr}^{\text{iPr}_6})_2$  (**8**) with *n*-hexane co-crystallized.

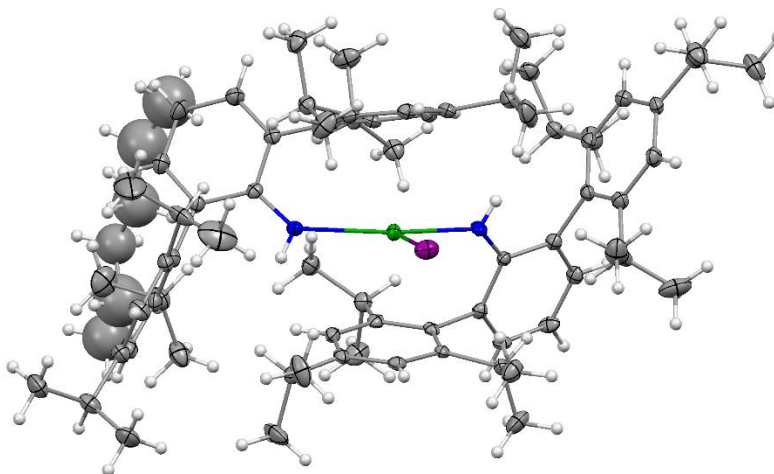


Figure 6-43. Full structure of (**8**) including solvent and molecular disorder

Identification code	TriPPNH2UI_hexane
Empirical formula	$\text{C}_{78}\text{H}_{114}\text{IN}_2\text{U}$
Formula weight	1444.64
Temperature/K	296.15
Crystal system	monoclinic
Space group	$\text{P2}_1/\text{n}$
$a/\text{\AA}$	13.3008(15)
$b/\text{\AA}$	15.0013(17)
$c/\text{\AA}$	36.190(4)
$\alpha/^\circ$	90
$\beta/^\circ$	94.3230(10)
$\gamma/^\circ$	90
Volume/ $\text{\AA}^3$	7200.4(14)
Z	4



$\rho_{\text{calc}}/\text{cm}^3$	1.333
$\mu/\text{mm}^{-1}$	2.724
F(000)	2964.0
Crystal size/ $\text{mm}^3$	$0.22 \times 0.22 \times 0.07$
Radiation	MoK $\alpha$ ( $\lambda = 0.71073$ )
$2\Theta$ range for data collection/ $^\circ$	4.74 to 54.314
Index ranges	$-16 \leq h \leq 17, -19 \leq k \leq 19, -46 \leq l \leq 46$
Reflections collected	80270
Independent reflections	15912 [ $R_{\text{int}} = 0.0470, R_{\text{sigma}} = 0.0376$ ]
Data/restraints/parameters	15912/21/743
Goodness-of-fit on $F^2$	1.037
Final R indexes [ $I \geq 2\sigma(I)$ ]	$R_1 = 0.0345, wR_2 = 0.0770$
Final R indexes [all data]	$R_1 = 0.0464, wR_2 = 0.0812$
Largest diff. peak/hole / $\text{e } \text{\AA}^{-3}$	1.70/−0.85

Crystal data and structure refinement for  $\text{U}(\text{NHAr}^{\text{iPr6}})_2$  (**9**).



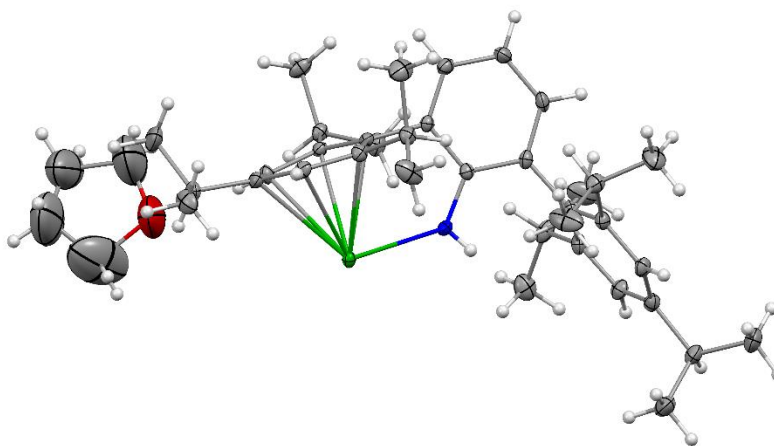


Figure 6-44. Full structure of (9) including solvent.

Identification code	UNHTriPP2
Empirical formula	C <sub>76</sub> H <sub>106</sub> N <sub>2</sub> O <sub>U</sub>
Formula weight	1301.65
Temperature/K	100(2)
Crystal system	monoclinic
Space group	C2/c
a/Å	18.0536(13)
b/Å	16.8949(12)
c/Å	22.7572(16)
$\alpha$ /°	90
$\beta$ /°	106.9720(10)
$\gamma$ /°	90
Volume/Å <sup>3</sup>	6638.9(8)
Z	4
$\rho_{\text{calc}}/\text{cm}^3$	1.302
$\mu/\text{mm}^{-1}$	2.489
F(000)	2704.0



Crystal size/mm <sup>3</sup>	0.26 × 0.22 × 0.12
Radiation	MoK $\alpha$ ( $\lambda$ = 0.71073)
2 $\Theta$ range for data collection/°	4.718 to 55.67
Index ranges	$-23 \leq h \leq 23$ , $-22 \leq k \leq 22$ , $-29 \leq l \leq 29$
Reflections collected	39160
Independent reflections	7874 [ $R_{\text{int}} = 0.0396$ , $R_{\text{sigma}} = 0.0311$ ]
Data/restraints/parameters	7874/66/390
Goodness-of-fit on $F^2$	1.072
Final R indexes [ $I \geq 2\sigma(I)$ ]	$R_1 = 0.0275$ , $wR_2 = 0.0690$
Final R indexes [all data]	$R_1 = 0.0318$ , $wR_2 = 0.0711$
Largest diff. peak/hole / e Å <sup>-3</sup>	1.06/−0.66



Crystal data and structure refinement for  $[\text{U}(\text{NHA}^{\text{iPr}_6})_2]^+[\text{BAr}^{\text{F}_{24}}]^-$  (**10**).

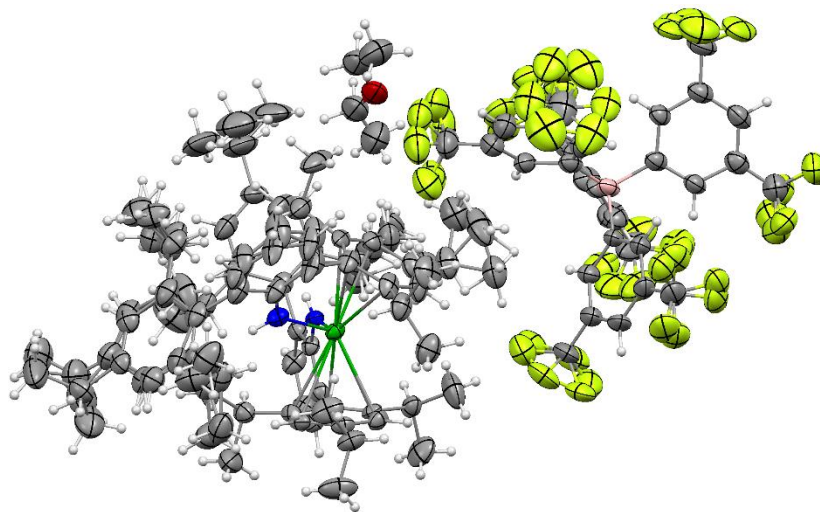


Figure 6-45. Full structure of (**10**) including anion, solvent, and molecular disorder

Identification code	UNHTriPP2BArF
Empirical formula	C <sub>105</sub> H <sub>114.5</sub> BF <sub>24</sub> N <sub>2</sub> O <sub>0.25</sub> U
Formula weight	2113.32
Temperature/K	172.98
Crystal system	monoclinic
Space group	P2 <sub>1</sub> /c
a/Å	14.7775(2)
b/Å	16.4035(2)
c/Å	41.8881(6)
α/°	90
β/°	90.8930(10)
γ/°	90
Volume/Å <sup>3</sup>	10152.6(2)



Z	4
$\rho_{\text{calc}}/\text{cm}^3$	1.383
$\mu/\text{mm}^{-1}$	5.277
F(000)	4294.0
Crystal size/ $\text{mm}^3$	$0.258 \times 0.106 \times 0.062$
Radiation	$\text{CuK}\alpha$ ( $\lambda = 1.54178$ )
$2\Theta$ range for data collection/ $^\circ$	4.22 to 144.264
Index ranges	$-17 \leq h \leq 18, -20 \leq k \leq 19, -51 \leq l \leq 51$
Reflections collected	78623
Independent reflections	19461 [ $R_{\text{int}} = 0.1307, R_{\text{sigma}} = 0.0952$ ]
Data/restraints/parameters	19461/934/1530
Goodness-of-fit on $F^2$	1.014
Final R indexes [ $I \geq 2\sigma(I)$ ]	$R_1 = 0.0572, wR_2 = 0.1242$
Final R indexes [all data]	$R_1 = 0.0954, wR_2 = 0.1415$
Largest diff. peak/hole / $\text{e } \text{\AA}^{-3}$	1.40/−1.23



## REFERENCES



## REFERENCES

1. Anderson, N. H.; Xie, J.; Ray, D.; Zeller, M.; Gagliardi, L.; Bart, S. C., *Nat. Chem.* **2017**, *9*, 850.
2. Anderson, N. H.; Odoh, S. O.; Yao, Y.; Williams, U. J.; Schaefer, B. A.; Kiernicki, J. J.; Lewis, A. J.; Goshert, M. D.; Fanwick, P. E.; Schelter, E. J.; Walensky, J. R.; Gagliardi, L.; Bart, S. C., *Nat. Chem.* **2014**, *6*, 919.
3. Schiemenz, B.; Power, P. P., *Organometallics* **1996**, *15* (3), 958-964.
4. Boreen, M. A.; Parker, B. F.; Lohrey, T. D.; Arnold, J., *J. Am. Chem. Soc.* **2016**, *138* (49), 15865-15868.
5. Boreen, M. A.; Arnold, J., *Polyhedron* **2018**, *155*, 149-152.
6. Diaconescu, P. L.; Cummins, C. C., *Inorg. Chem.* **2012**, *51* (5), 2902-2916.
7. Manriquez, J. M.; Fagan, P. J.; Marks, T. J., *J. Am. Chem. Soc.* **1978**, *100* (12), 3939-3941.
8. Warner, B. P.; Scott, B. L.; Burns, C. J., *Angew. Chem. Int. Ed.* **1998**, *37* (7), 959-960.
9. Hayton, T. W.; Boncella, J. M.; Scott, B. L.; Palmer, P. D.; Batista, E. R.; Hay, P. J., *Science* **2005**, *310* (5756), 1941-1943.
10. Cesari, M.; Pedretti, U.; Zazzetta, Z.; Lugli, g.; Marconi, W., *Inorg. Chim. Acta* **1971**, *5*, 439-444.
11. Cotton, F. A.; Schwotzer, W., *Organometallics* **1985**, *4* (5), 942-943.
12. Baudry, D.; Bulot, E.; Ephritikhine, M., *J. Chem. Soc. Chem. Commun.* **1988**, (20), 1369-1370.
13. Van der Sluys, W. G.; Burns, C. J.; Huffman, J. C.; Sattelberger, A. P., *J. Am. Chem. Soc.* **1988**, *110* (17), 5924-5925.
14. Arliguie, T.; Lance, M.; Nierlich, M.; Vigner, J.; Ephritikhine, M., *J. Chem. Soc. Chem. Commun.* **1994**, (7), 847-848.
15. Diaconescu, P. L.; Arnold, P. L.; Baker, T. A.; Mindiola, D. J.; Cummins, C. C., *J. Am. Chem. Soc.* **2000**, *122* (25), 6108-6109.
16. Evans, W. J.; Kozimor, S. A.; Ziller, J. W., *Chem Commun.* **2005**, (37), 4681-4683.
17. Bart, S. C.; Heinemann, F. W.; Anthon, C.; Hauser, C.; Meyer, K., *Inorg. Chem.* **2009**, *48* (19), 9419-9426.



18. Halter, D. P.; Heinemann, F. W.; Maron, L.; Meyer, K., *Nat. Chem.* **2017**, *10*, 259-267.
19. S., L. P. H.; Andreas, S.; W., H. F.; Wolfgang, H.; Karsten, M., *Angew. Chem. Int. Ed.* **2014**, *53* (28), 7158-7162.
20. Cantat, T.; Scott, B. L.; Morris, D. E.; Kiplinger, J. L., *Inorg. Chem.* **2009**, *48* (5), 2114-2127.
21. La Pierre, H. S.; Scheurer, A.; Heinemann, F. W.; Hieringer, W.; Meyer, K., **2014**, *53* (28), 7158-7162.
22. Huh, D. N.; Ziller, J. W.; Evans, W. J., *Inorg. Chem.* **2018**, *57* (18), 11809-11814.
23. Windorff, C. J.; MacDonald, M. R.; Meihaus, K. R.; Ziller, J. W.; Long, J. R.; Evans, W. J., *Chem. Eur. J.*, **2016**, *22* (2), 772-782.
24. MacDonald, M. R.; Fieser, M. E.; Bates, J. E.; Ziller, J. W.; Furche, F.; Evans, W. J., *J. Am. Chem. Soc.* **2013**, *135* (36), 13310-13313.
25. Twamley, B.; Hwang, C.-S.; Hardman, N. J.; Power, P. P., *J. Organomet. Chem.* **2000**, *609* (1), 152-160.
26. Stoll, S.; Schweiger, A., *J. Magn. Reson.* **2006**, *178* (1), 42-55.
27. Atherton, N. M., Ellis Horwood : PTR Prentice Hall: New York, 1993.
28. Blumberg, W. E., In *Magnetic Resonance in Biological Systems*, Ehrenberg, A.; Malmstrom, B. G.; Vanngard, T., Eds. Pergamon: 1967.
29. Boatner, L. A.; Abraham, M. M., *Reports on Progress in Physics* **1978**, *41* (1), 87.
30. Evans, D. F., *J. Chem. Soc.* **1959**, (0), 2003-2005.
31. Monreal, M. J.; Thomson, R. K.; Cantat, T.; Travia, N. E.; Scott, B. L.; Kiplinger, J. L., *Organometallics* **2011**, *30* (7), 2031-2038.
32. Gavenonis, J.; Tilley, T. D., *Organometallics* **2004**, *23* (1), 31-43.
33. Chávez, I.; Alvarez-Carena, A.; Molins\*, E.; Roig, A.; Maniukiewicz, W.; Arancibia, A.; Arancibia, V.; Brand, H.; Manuel Manríquez\*, J., *J. Organomet. Chem.* **2000**, *601* (1), 126-132.
34. Bain, G. A.; Berry, J. F., *J. Chem. Ed.* **2008**, *85* (4), 532-536.
35. Sheldrick, G., *Acta Crystallogr., Sect. C: Cryst. Struct. Commun.* **2015**, *71* (1), 3-8.
36. Sheldrick, G., *Acta Crystallogr., Sect. A: Found. Crystallogr.* **2008**, *64* (1), 112-122.
37. Dolomanov, O. V.; Bourhis, L. J.; Gildea, R. J.; Howard, J. A. K.; Puschmann, H., *J. Appl. Crystallogr.* **2009**, *42* (2), 339-341.



## Chapter 7. Reduction of Dinitrogen to Hydrazine

### 7.1 Introduction

In recent years the temperature of the planet has begun rising steadily.<sup>1</sup> Both land and ocean temperatures have seen record high temperatures, and, in fact, all five hottest years on record (since 1880) have occurred since 2010.<sup>1</sup> High carbon dioxide (CO<sub>2</sub>) concentrations in the atmosphere are likely a contributing factor. CO<sub>2</sub> is a very efficient greenhouse gas due to its high transparency to solar radiation and its high absorptivity of infrared radiation emitted from the earth.<sup>2</sup> Over the last 420,000 years, CO<sub>2</sub> concentrations in the atmosphere have been in equilibrium between 200-300 ppm.<sup>3</sup> Recently, this equilibrium has been shattered as concentrations of CO<sub>2</sub> have climbed over 400 ppm (Figure 7-1).<sup>4</sup>

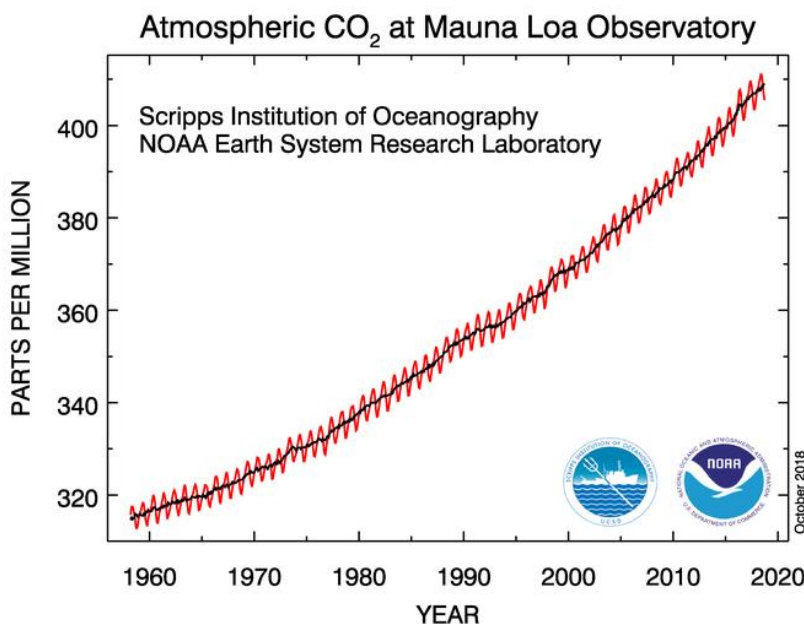


Figure 7-1. Concentration of CO<sub>2</sub> in the atmosphere measured from 1958 to 2018 at the Manua Loa Observatory.  
Figure taken from reference 3.



These recent increases in concentration are almost certainly due to human influence. One indication of human influence is that the increase in concentration of  $\text{CO}_2$  is accompanied by a reduction in the concentration of  $^{13}\text{C}$  in the atmosphere, likely from burning  $^{13}\text{C}$  deficient fossil fuels.<sup>5-8</sup>

The trend in using fossil fuels as an energy source has shown little indication of slowing.<sup>9</sup> Fossil fuels are predicted to account for over 70% of the world's energy source in 2040. In fact, the only fossil fuel source with a predicted plateau in growth rate is coal, while natural gas is predicted to grow even faster than renewable energy sources.

A major hurdle in implementation of renewable energy sources is the often-intermittent energy supply. For example, solar power may be a worthwhile investment in southern states with consistent exposure to sun, but in the northern states short and cloudy days during winter make solar energy unreliable.<sup>10</sup> We need to find a method to make renewable energy sources, like solar, viable in all areas of the world. In order to solve this problem, we need to find a method of energy storage that has a similar to fossil fuels. Better energy storage solutions would allow full utilization of things like solar energy when they are available. For example, we could use solar energy to charge a battery during the day, then use the battery to power lights at night.

One potential source we could take advantage of is hydrogen gas ( $\text{H}_2$ ).  $\text{H}_2$  is a clean energy source since the only combustion byproduct is water ( $\text{H}_2\text{O}$ ). The issue when considering  $\text{H}_2$  as a fuel source is its energy density (per unit volume). Even using the best-case scenario storage tanks for fuel cell-based vehicles, the maximum energy density of  $\text{H}_2$  is 5.3 MJ/L.<sup>11</sup> When compared to something like gasoline, which has an energy density of 34.4 MJ/L,  $\text{H}_2$  is hardly viable.<sup>11</sup>



## 7.2 Ammonia as an Energy Storage Solution

One possible solution to the energy density of  $H_2$  is ammonia ( $NH_3$ ). Ammonia can be considered a carrier of  $H_2$  but has a higher energy density. In fact,  $NH_3$  has a higher energy density than even natural gas, at 13.6 MJ/L for ammonia compared to 10.4 MJ/L in natural gas.<sup>11</sup> Ammonia is already produced, stored, and transported on a massive scale. Holding tanks on the 50,000-ton scale, dedicated pipelines, and easy conversion of natural gas infrastructure are all a testament to the ease with which we could convert to ammonia based fuels.<sup>12</sup> Even aspects such as safety assessments of  $NH_3$  as a fuel source have been conducted, concluding equal or lower risk when compared to current fossil fuels.<sup>13-14</sup>

Part of what makes this infrastructure possible is the simple liquification of  $NH_3$ . At just under 10 atm of pressure  $NH_3$  liquifies, producing high energy density compared to  $H_2$ . This liquified ammonia could then be easily transported and used either directly as a fuel source or split into  $H_2$  and  $N_2$  so that the  $H_2$  can be used as fuel.<sup>15-16</sup> One might have cause to wonder, if  $NH_3$  is such a perfect solution, why is it not already in use?

To answer that question, we must look to the production methods currently employed for ammonia synthesis: the Haber-Bosch process.<sup>17-18</sup> Currently the Haber-Bosch process is run on a ~175 million metric ton scale annually to meet demands of compounds like ammonium salts, nitrates, and ureas.<sup>19</sup> But, due to the high activation energy of the N-N triple bond in dinitrogen, this process is extremely energy intensive. At current production levels, the Haber-Bosch process produces 1-2% of the entire world's greenhouse gases.<sup>20</sup> Its worth mentioning, though, that the Haber-Bosch process supports an estimated 52% of the world's population through fertilizer production, so the energy demand is justified.<sup>21</sup> Still, the demand for nitrogen fixation is



extraordinary and will only continue to grow.<sup>22</sup> Even if  $\text{NH}_3$  isn't the next gasoline alternative, the demand for fertilizers is unlikely to stop growing.<sup>20-21</sup>

### 7.3 Alternative Methods for Nitrogen Fixation

In recent years there has been a surge in efforts to fix dinitrogen using a variety of catalysts.<sup>19, 23-29</sup> In particular, the data presented by Shilov is very intriguing. Shilov's group has produced a number of research articles spanning several decades highlighting their work on fixation of dinitrogen. Their report in *Nature* in 1971 highlighted a few notable experiments.<sup>30</sup> Shilov's group demonstrated  $\text{N}_2$  could be reduced to hydrazine or ammonia by a mixture of V(II) in  $\text{H}_2\text{O}$  or Cr(II) in  $\text{MeOH}/\text{H}_2\text{O}$ . Both of these experiments produce hydrazine in substoichiometric amounts. In the same report though, they produce hydrazine using Ti(III) as a reductant. In this system, when there is Ti(III),  $\text{MgCl}_2$ , and KOH at elevated pressure and temperature, very small quantities of hydrazine are produced. When Mo is added, in the form of  $\text{MoOCl}_3$  or  $\text{MoO}_4^{2-}$ , the reaction produces noticeably more hydrazine, and, in fact, is catalytic in Mo obtaining ~87 turnovers.<sup>30</sup>

In the following years, the Shilov system developed and the reaction changed in almost every aspect. They changed Ti(III) to sodium-mercury amalgam or an electrode,<sup>31-32</sup> added L- $\alpha$ -dipalmitoylphosphatidylcholine (PC) as a surfactant,<sup>33</sup> added phosphine to the system,<sup>32</sup> reduced the extremity of the conditions to ambient temperature and pressure, and, in the process, increased the yield of hydrazine produced per Mo to ~120 turnovers.<sup>29, 34-35</sup>

Probably the most notable advancement in the Shilov system was the discovery of an active heterometallic  $\text{Mo}_8\text{Mg}_2$  cluster.<sup>36-37</sup> The cluster, shown in Figure 7-2, is a dianionic cluster consisting of bridging oxygen-based ligands ranging from datively coordinated methanol to oxo ligands, and has an outer sphere magnesium ion.



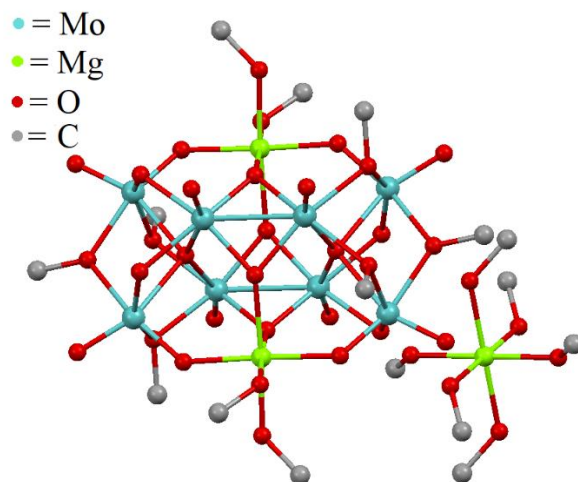


Figure 7-2. Heterometallic cluster reported by Shilov to be the active species in his dinitrogen reduction system.<sup>36</sup>

Using the  $\text{Mo}_8\text{Mg}_2$  cluster above, Shilov was able to increase the production of hydrazine up to 1600 turnovers per Mo at 1 atm  $\text{N}_2$  and ambient temperature.<sup>35</sup> The number of turnovers could be increased up to  $10^4$  turnovers if the system was pressurized with 70 atm  $\text{N}_2$ .<sup>29</sup>

While the Shilov system does not reliably produce  $\text{NH}_3$ , initial cleavage of the N-N triple bond is, perhaps, the most difficult step, especially since hydrazine cleavage has been reported.<sup>38-40</sup> Part of the energy intensity of the Haber-Bosch process is that it requires a stream of  $\text{H}_2$  gas. Since the Shilov system only requires  $\text{N}_2$  and aqueous media, the proton source is presumably  $\text{H}_2\text{O}$ .<sup>29, 34</sup>

Unfortunately, implementation of the Shilov system has not been achieved to date. One potential reason is the lack of detailed synthetic procedures. In Shilov's report of the cluster synthesis, the procedure reads as follows:

“For the synthesis of polynuclear mixed valence  $\text{Mo(V-VI)}$  complex a sample was used containing 30% of  $\text{Mo(VI)}$ . The sample was left standing in the presence of air for a long time and presumably  $\text{Mo(VI)}$  was formed in the process of oxidation.” -A. E. Shilov 1989



The above procedure is the method to produce the starting Mo compound for synthesis of the cluster. There is no analysis of the resulting compound, only an estimated composition of Mo(V) vs. Mo(VI). The duration of the reaction is specified as “a long time” which could be hours, days, weeks, or longer. There are no details about the humidity (MoCl<sub>5</sub> reacts vigorously with H<sub>2</sub>O from the author’s personal experience) to indicate what sort of Mo complex the starting material is. In brief, there is no detail at all. The lack of detail continues through the rest of the experimental in the paper, as well as the experimental in Shilov’s other reports of nitrogen reduction.<sup>30-33, 36-37</sup> The lack of experimental rigor is exacerbated by the sensitivity of the cluster synthesis. As evidenced by recent reports, an extremely wide variety of products can be obtained through similar reactions.<sup>41-45</sup>

#### **7.4 Reproduction of Shilov’s Results**

Given the promise of Shilov’s reports and the necessity for the world’s energy demand problems to be solved, we set out to try and replicate the results Shilov had reported. We avoided, at first, using the complete system including the phosphatidylcholine and amalgam to try and simplify and more systematically characterize the system.

Shortly after Shilov’s report in *Nature*, Hill and Richards published a report using <sup>15</sup>N<sub>2</sub> to validate Shilov’s results using both Mo and V as catalysts for N<sub>2</sub> reduction.<sup>46</sup> Confirming the results reported by Shilov, the system produced <sup>15</sup>N containing hydrazine.<sup>30</sup> Like the original report by Shilov, they found the reaction was substoichiometric, but went on to conclude that modification of the Shilov system could yield useful systems for dinitrogen activation.<sup>30, 46</sup> Because the system was less complex than the later Shilov systems, and because there were additional reports of its success, we set out to study the TiCl<sub>3</sub> reductant system.



Due to the high pressure of N<sub>2</sub> required for the reactions, Shilov employed a specialized reactor.<sup>33,47</sup> The diagrams of the reactor they employed were difficult to interpret. Given that their N<sub>2</sub> pressures exceeded 100 atm, we used a Parr pressure reactor. The reactor was fit with a Teflon-coated mechanical stirrer, a Teflon liner, thermocouple, two pressure sensors (one electronic and one standard gauge), a burst disc set to 2000 psi, and a custom fit heating mantle. We hoped using Teflon liners wherever possible would avoid the corrosive solution leaching any metal from the reactor walls. For the thermocouple, which could not be coated with Teflon due to thermal conductivity concerns, we used a narrow glass sleeve filled with MeOH. This way, the thermocouple maintained thermal contact with the solution but was isolated from the reaction mixture. The system was set up so that reactions could be transported to and from a glove bag while remaining sealed under a nitrogen atmosphere.

Over a series of attempts to produce hydrazine using the general method reported by Shilov, we did eventually manage to find a system that produced some quantities of N<sub>2</sub>H<sub>4</sub>. Our reaction was done using 12% TiCl<sub>3</sub> in HCl with a solution of 15 mL H<sub>2</sub>O and 100 mL MeOH, KOH, MgCl<sub>2</sub> · 6H<sub>2</sub>O, MoCl<sub>5</sub> (see experimental for details). Over a number of reactions, heating the Parr bomb containing those reagents to 85 °C with >800 psi N<sub>2</sub> produced small, but measurable quantities of N<sub>2</sub>H<sub>4</sub>. We were unable to detect any amount of NH<sub>3</sub> in any of the reactions. This reaction, when performed with the specific sequence outlined in the experimental, was reproducible (in the sense that, qualitatively, detectable hydrazine was produced each time) by our group, as well as Dr. Dan Little and Dillon Edwards following the same procedure in the Hamann lab.

## 7.5 Monitoring Hydrazine Formation

We attempted quantification of the hydrazine using the *p*-dimethylaminobenzaldehyde (PDMAB) indicator solution, but the solution was unreliable, especially with the complex, colored



reaction mixture.<sup>48</sup> From our experience, the indicator can reliably be used to produce qualitative color changes which can indicate the presence of  $\text{N}_2\text{H}_4$ , but quantitation was not possible. As a substitute, we explored other aldehydes that might allow isolation of the hydrazone product.

We attempted hydrazine to hydrazone conversion using several different benzaldehydes, including phthaldialdehyde (o-benzene-1,2-dicarboxaldehyde). Unfortunately, most reactions with the aldehydes we tested did not seem to lead to quantitative conversion to the hydrazone, or, as was the case with phthaldialdehyde, the reaction was rather slow. To our surprise, when a small aliquot of the reaction mixture from the Parr reactor is added to a solution containing benzaldehyde, GC/MS analysis of the resulting mixture indicates the presence of stilbene. When reaction mixtures from the reactor that do not show production of  $\text{N}_2\text{H}_4$  by the PDMAB indicator are added to the benzaldehyde solution, no stilbene is observed. We thought this might be a possible method of quantification, so we took two samples from the reactor and added each to separate vials containing a solution of benzaldehyde. The first was analyzed by GC/MS as is, the second was spiked with a known quantity of hydrazine hydrate. From the relative difference in peak areas in the GC traces, we estimated the amount of hydrazine present in the first vial.

It is important to note, we say “estimated” here. The method, in practice, seemed more reliable than the PDMAB indicator solution, but given the complexity of the transformations, it is unlikely to be a perfect quantitative measure. Attempts at elucidating the mechanism of conversion of the aldehyde to stilbene were fruitless as reaction of hydrazine hydrate and benzaldehyde in the presence of anything other than the complete reaction mixture, failed to produce stilbene.

Still, our estimated production of hydrazine was usually substoichiometric relative to Mo. Only in one experiment were we able to produce  $\text{N}_2\text{H}_4$  in excess of the amount of Mo added (0.09 mmol  $\text{N}_2\text{H}_4$  relative to 0.08 mmol Mo added). Given that we cannot assign error bars to the measurement,



we hesitate to call this a turnover of Mo. Regardless, the system using Mo and Ti, as Shilov reported, does reduce  $\text{N}_2$  to  $\text{N}_2\text{H}_4$ .

## 7.6 Moving to More Complex Systems

In light of the success with the Ti system, we sought to move to the more complex Shilov systems that were more productive.<sup>32, 49</sup> Unfortunately, as mentioned above, this meant the reaction mixture had to be even more complicated. Specifically, in addition to the amounts of Mo, Mg, KOH, MeOH:H<sub>2</sub>O ratio, pressure, stir rate, and temperature, we now also had to worry about amalgam concentration, phosphine concentration, phospholipid choice (since changing the structure of the phospholipid can completely deactivate catalysis), and catalyst preparation.<sup>49</sup> Unsurprisingly, despite a wide variety of conditions, the more complex reaction mixture was completely unsuccessful in every attempt.

There are simply too many variables, and Shilov's reports are only speculative at the action of each. Take for example the phospholipid. The proposal Shilov put forward for the action of PC in the reaction mixture was as a surfactant to keep the amalgam surface area high.<sup>34, 49</sup> They report that when PC is added to the solutions containing amalgam, they get finely divided beads of amalgam that are stable enough to be measured for size distribution. Yet, somehow, the increased activity on addition of phosphine ligand to the solution is dependent on the presence of the phospholipid, and the addition of phosphatidylcholine suppresses production of  $\text{NH}_3$ , making  $\text{N}_2\text{H}_4$  the sole product.<sup>49</sup> The reported procedure for the catalyst, too, is disturbing (this procedure was published before the isolation of the  $\text{Mo}_8\text{Mg}_2$  cluster discussed above but is equally unhelpful). In the report they suggest that the catalyst solution was vastly improved by subsequent acidification by HCl and basification by  $\text{NaOCH}_3$ . In the process, molybdenum is reported to precipitate, but the remaining solution displayed more catalytic activity.<sup>49</sup> Much like the other



experimental reports, concentrations of the acid and base are not given, pH of the solution at any point is not given, reaction times are not given, and Mo concentration after the precipitation is unknown.

In an effort with the Hamann group, we also tried to replace chemical reductants with electrodes. Here too, all efforts at dinitrogen reduction were unsuccessful despite a variety of electrodes, potentials, and catalyst preparations.

## 7.7 Catalyst Synthesis

In our opinion, the most room for error in the systems where we saw hydrazine production is in the catalyst solution preparation. In our procedure, we make a methanolic solution of  $\text{MgCl}_2$  and add it to  $\text{MoCl}_5$ . There is a rapid series of color changes and evolution of  $\text{HCl}$  gas. This was our best guess at mimicking the Shilov procedure, and it seemed to work to some degree, but given how rapid the reaction is, it almost certainly leads to a variety of products. We cannot even say what the approximate concentrations of catalyst in our experiments are because we have no idea what the active species is and how much is present.

Much like Shilov, we sought to pre-form a catalyst to use in these reactions.<sup>36</sup> In an ideal situation, we could isolate a catalyst, then add it directly to the reductant solution, and start the reaction. We also hoped we could more completely characterize the complex and develop a reproducible method for its production. As mentioned earlier, though, we are not the first to attempt synthesis of Mo-Mg clusters in methanolic media. The Bazhenova and Kuznetsov group have published a series of reports outlining just how many products are possible.<sup>41-45, 50</sup>

We made several attempts at isolation of complexes. We used anhydrous  $\text{MeOH}$  and  $\text{MgCl}_2$ , more rigorous air-free techniques, and controlled reaction times. In most cases, the resulting



mixtures were unstable species that were intractable. One minor success was had in the isolation of crystals of the complex in Figure 7-3. While the complex bears resemblance to those in the recent literature, it is not identical.

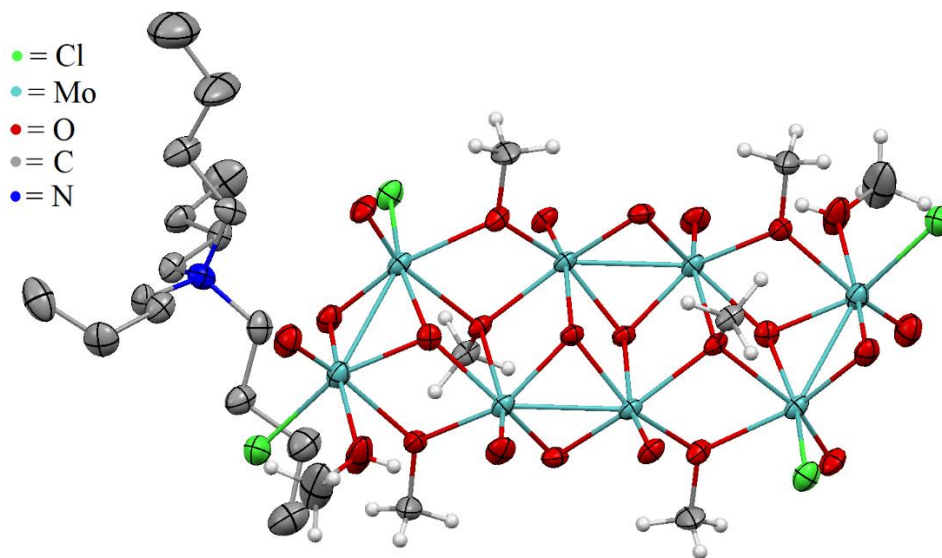


Figure 7-3. Molybdenum cluster isolated from attempts at catalyst synthesis. Hydrogens are removed from the tetrabutyl ammonium for clarity.

We postulated one problem in the synthesis of Shilov's cluster is formation of the cation and anion pair. We hoped we could make more stable complexes using discrete cation units such as  $\text{NBu}_4^+$ . Besides the incorporation of the ammonium, the complex is far from that reported by Shilov. Among other things, it is not heterometallic, it did not achieve complete hydrolysis, and the charge is not correct. Not surprisingly, the cluster in Figure 7-3 is not competent for the catalysis.

## 7.8 Looking Forward

It is the author's opinion that developing a controlled synthesis to produce active MoMg clusters should be the primary goal in this research. There are simply too many other variables at work in the complete reaction mixture to analyze each part systematically. That said, cluster



synthesis should be approached with caution. Most importantly, I think, the pH of the solution should be controlled carefully. The chemistry of these cluster formations is likely to be extremely sensitive to pH, solution conductivity, and concentration. In hindsight, I suspect this was my biggest shortcoming in attempts at cluster synthesis.

Additionally, if possible, a different Mo source may afford more control over the reaction.  $\text{MoCl}_5$  is extremely reactive with methanol and water. Because of the immediate release of  $\text{HCl}$  on contact with the solvents, control over the reaction properties mentioned above will be difficult. We attempted some synthesis from other Mo starting materials, such as amides and oxides, but only briefly and with little success.

## 7.9 Conclusions

The Shilov group published a number of reports spanning several decades.<sup>29</sup> We have managed to lend only some to the simplest research presented in those reports. Unfortunately, a lack of experimental detail and an overwhelming complexity precluded reproduction of the interesting results. Still, the challenge of nitrogen fixation is yet to be solved, as such, every effort to solve this problem is welcome and necessary.

## 7.10 Experimental

### General Considerations

$\text{TiCl}_3$  solution,  $\text{MgCl}_2$  hydrate,  $\text{KOH}$  pellets, benzaldehyde, and hydrazine hydrate were purchased from Sigma Aldrich as used as received.  $\text{MoCl}_5$  was purchased from Strem and used as received. Methanol was distilled from  $\text{Mg}$  before use.

All productive reactions followed the general procedure below.



All required chemical, glassware, and reactor vessel were loaded into a glovebag. The glovebag was purged several times with dry N<sub>2</sub> gas before being sealed. Once sealed, 12% TiCl<sub>3</sub> in HCl (9.6 mL, ~7.5 mmol) was loaded into the Teflon lined reactor. In a vial, KOH (0.702 g, 12.5 mmol) was dissolved in 15.5 mL H<sub>2</sub>O. The contents of the vial were then added to the reactor. In a separate vial, MgCl<sub>2</sub>•6H<sub>2</sub>O (0.771 g, 3.8 mmol) was dissolved in MeOH (15 mL). This solution was added to another vial containing MoCl<sub>5</sub> (20.5 mg, 0.08 mmol). The solution rapidly changed color and white fumes were emitted from the vial. This solution was capped and swirled by hand gently before being added to the reactor. A narrow tube filled with clean MeOH was also loaded into the reactor. The reactor cap was then put on, being careful to keep the thermocouple in the MeOH filled tube away from the corrosive reaction mixture. The reactor was sealed and transported to the holder. A line from a N<sub>2</sub> tank was fixed while flowing <14 psi N<sub>2</sub> gas so the line was purged of any air or moisture. The vessel was filled to 50 psi of N<sub>2</sub> gas and the headspace was carefully purged using the pressure relief valve. Caution was taken to avoid the pressure falling below 50 psi (this was again to ensure a clean atmosphere of N<sub>2</sub> gas in the reactor. Once purged, the vessel was sealed, and the thermocouple, stirrer, and pressure sensor were fitted. The heating mantle was put in place and the stirrer was switched on. The vessel was then slowly pressurized with N<sub>2</sub> and heated. For reactions that were heated, the timing was started once they reached temperature. All reactions were allowed to cool once the reaction time was complete by removing the heating mantle. Caution is emphasized in opening the reactor due to the corrosivity of the mixture. Qualitative analysis is performed by adding a small drop to the hydrazine indicator solution.<sup>48</sup>

#### Mass Spec Analysis of the Reaction Solution



Two 500  $\mu\text{L}$  aliquots of reaction solution was loaded into two separate GC vials. To each vial was added a THF solution containing excess benzaldehyde. The first vial was analyzed by GC/MS as is while the second vial was spiked with 4  $\mu\text{L}$  of 50 ppm hydrazine hydrate solution before analysis. In the GC trace the peak for stilbene was integrated in each spectrum. The concentration of hydrazine in the unspiked vial was solved using the difference in peak area between the first and second vial as the known amount of hydrazine added. The number of mols in the GC vial sample was then scaled to the volume of the reactor solution (125 mL) to solve for the total hydrazine production.

### Cluster Synthesis

In a glovebag under nitrogen,  $\text{MgSO}_4$  (13.22 mg, 0.183 mmol) was dissolved in MeOH (~5 mL). The solution was added to a vial containing  $\text{MoCl}_5$  (50 mg, 0.183 mmol). Immediately a green color was formed as well as smoke, presumably HCl gas. The solution was stirred for ~10 minutes. The solution was then neutralized (determined by sampling on a pH test strip) with a 1M methanolic solution of NaOH whereupon the color changed from green to orange/red. After neutralization  $\text{NBu}_4\text{Cl}$  (203.4 mg, 0.732 mmol). The solution was concentrated, hexanes added, and the white precipitate filtered. Ether was added to the filtrate causing an orange precipitate to crash out, the solution was centrifuged and the solvent decanted. The solid was washed with 50:50 methanol: ether, and centrifuged and decanted again. The remaining solid was dissolved in minimal amounts of MeOH and put in a  $-20\text{ }^\circ\text{C}$  freezer for recrystallization. Orange X-ray quality crystals were produced after 2 days (30 mg, 10%). The X-ray analysis was the only characterization technique performed as the synthesis was not reproducible.



Representative GC/MS traces for the successful N<sub>2</sub> reduction reactions.

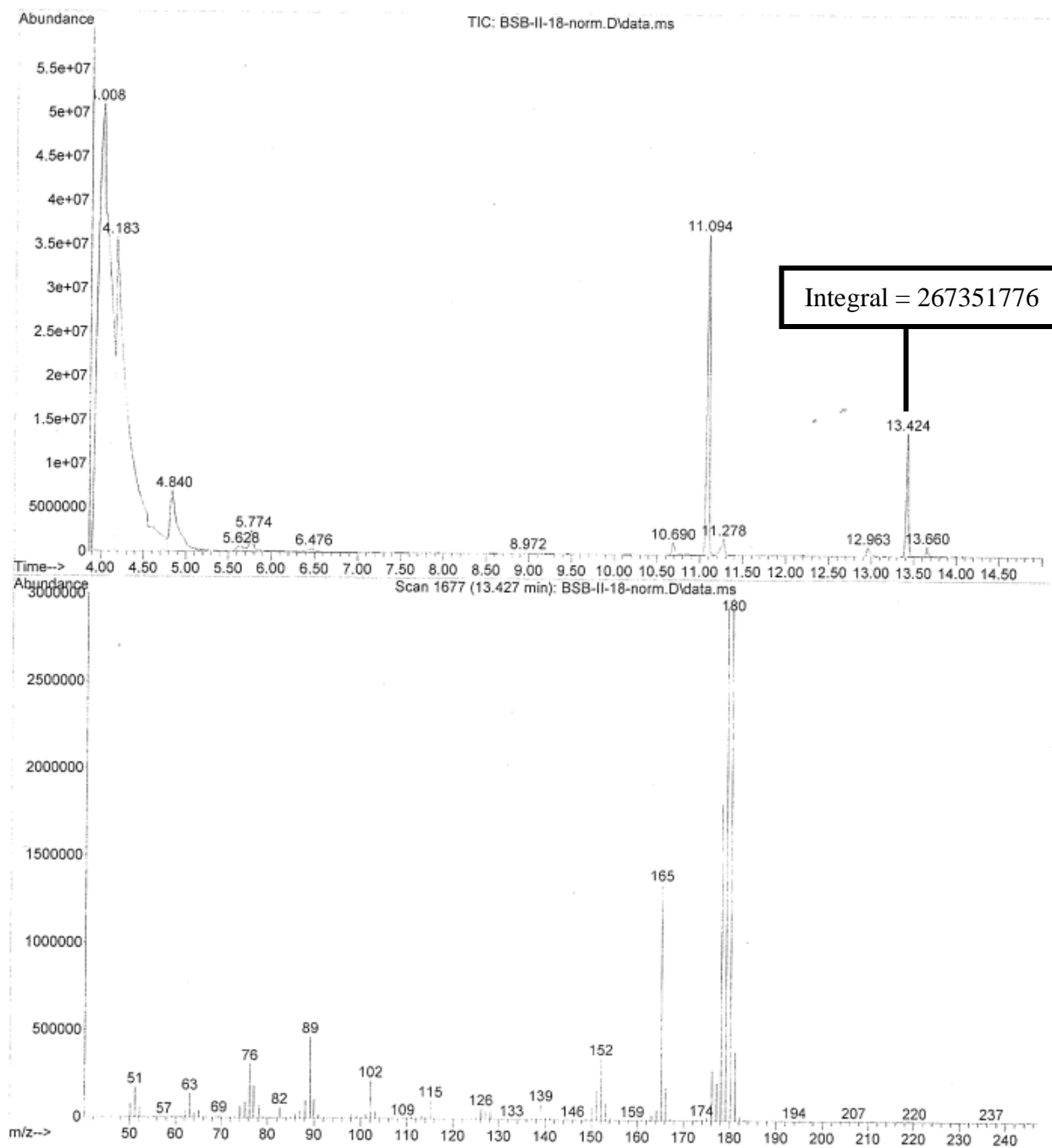


Figure 7-4. GC/MS trace of an aliquot of the reaction solution from a reaction that produced hydrazine according to the indicator solution.<sup>48</sup> The indicated peak at 13.424 represents the peak for stilbene.



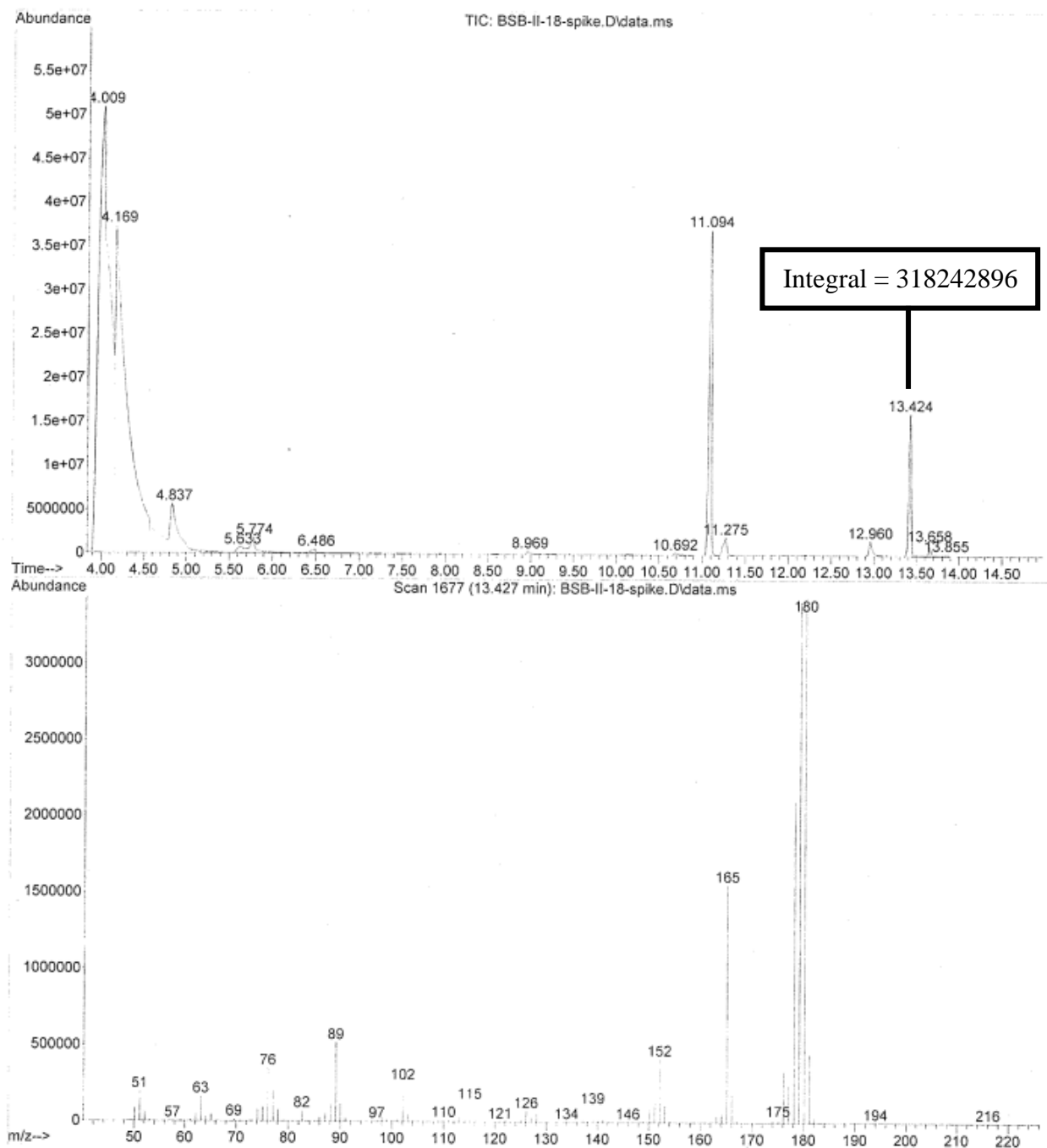


Figure 7-5 GC/MS trace of an equal aliquot from the same solution shown in Figure 7-4 spiked with 0.25  $\mu\text{g}$  hydrazine (added as hydrate).<sup>48</sup> The indicated peak at 13.424 represents the peak for stilbene.



## REFERENCES



## REFERENCES

1. State of the Climate: Global Climate Report for August 2018. National Ocean and Atmospheric Administration National Centers for Environmental Information: **2018**.
2. Harries, J. E.; Brindley, H. E.; Sagoo, P. J.; Bantges, R. J., *Nature* **2001**, *410*, 355-357.
3. Petit, J. R.; Jouzel, J.; Raynaud, D.; Barkov, N. I.; Barnola, J. M.; Basile, I.; Bender, M.; Chappellaz, J.; Davis, M.; Delaygue, G.; Delmotte, M.; Kotlyakov, V. M.; Legrand, M.; Lipenkov, V. Y.; Lorius, C.; PÉpin, L.; Ritz, C.; Saltzman, E.; Stievenard, M., *Nature* **1999**, *399*, 429-436.
4. Tans, P. K., R. Trends in Atmospheric Carbon Dioxide. National Ocean and Atmospheric Administration Earth System Research Laboratory: **2018**.
5. White, J. W. C. V., B.H.; Michel, S.E. Stable Isotopic Composition of Atmospheric Carbon Dioxide (<sup>13</sup>c and <sup>18</sup>o) from the Noaa Esrl Carbon Cycle Cooperative Global Air Sampling Network. National Ocean and Atmospheric Administration Earth System Research Laboratory: 2015, **2015**.
6. Quay, P. D.; Tilbrook, B.; Wong, C. S., *Science* **1992**, *256* (5053), 74-79.
7. Stuiver, M.; Burk, R. L.; Quay, P. D., *J. Geophys. Res. Atmos.* **1984**, *89* (D7), 11731-11748.
8. Francey, R. J.; Allison, C. E.; Etheridge, D. M.; Trudinger, C. M.; Enting, I. G.; Leuenberger, M.; Langenfelds, R. L.; Michel, E.; Steele, L. P., *Tellus B Chem Phys Meteorol.* **1999**, *51* (2), 170-193.
9. International Energy Outlook 2017. US Energy Information Administration: **2017**.
10. National Ocean and Atmospheric Administration National Center for Environmental Information: 2004.
11. Zamfirescu, C.; Dincer, I., *J. Power Sources* **2008**, *185* (1), 459-465.
12. Bartels, J. R. A Feasibility Study of Implementing an Ammonia Economy. Iowa State Univserity, 2008.
13. Duijm, N. J.; Markert, F.; Paulsen, J. L. 87-550-3415-2; Safety Assessment of Ammonia as a Transport Fuel. **2005**.
14. Comparative Quantitative Risk Analysis of Motor Gasoline, Lpg, and Anhydrous Ammonia as an Automotive Fuel. Quest Consultants Inc.: Norman, OK **2009**.
15. Afif, A.; Radenahmad, N.; Cheok, Q.; Shams, S.; Kim, J. H.; Azad, A. K., *Renew. Sust. Energ. Rev.* **2016**, *60*, 822-835.



16. Boggs, B. K.; Botte, G. G., *J. Power Sources* **2009**, *192* (2), 573-581.
17. Haber, F.; Van Oordt, G., *Z. Anorg. Chem.* **1905**, *43* (1), 111-115.
18. Haber, F.; Van Oordt, G., *Z. Anorg. Chem.* **1905**, *44* (1), 341-378.
19. Tanabe, Y.; Nishibayashi, Y., *The Chemical Record* **2016**, *16* (3), 1549-1577.
20. Fertilizers, Climate Change and Enhancing Agricultural Productivity Sustainably. International Fertilizer Industry Association: **2009**.
21. Erisman, J. W.; Sutton, M. A.; Galloway, J.; Klimont, Z.; Winiwarter, W., *Nat. Geosci.* **2008**, *1*, 636-639.
22. Annual Energy Outlook 2015 with Projections to 2040. US Energy Information Administration, US Department of Energy: **2015**.
23. Hazari, N., *Chem. Soc. Rev.* **2010**, *39* (11), 4044-4056.
24. Bjornsson, R.; Neese, F.; Schrock, R. R.; Einsle, O.; DeBeer, S., *J. Bio. Inorg. Chem.* **2015**, *20* (2), 447-460.
25. Hoffman, B. M.; Lukoyanov, D.; Yang, Z.-Y.; Dean, D. R.; Seefeldt, L. C., *Chem. Rev.* **2014**, *114* (8), 4041-4062.
26. Fryzuk, M. D., *Acc. Chem. Res.* **2009**, *42* (1), 127-133.
27. Gambarotta, S.; Scott, J., *Angew. Chem. Int. Ed.* **2004**, *43* (40), 5298-5308.
28. Howard, J. B.; Rees, D. C., *Chem. Rev.* **1996**, *96* (7), 2965-2982.
29. Shilov, A. E., *Russ. Chem. Bull.* **2003**, *52* (12), 2555-2562.
30. Shilov, A.; Denisov, N.; Efimov, O.; Shuvalov, N.; Shuvalova, N.; Shilova, A., *Nature* **1971**, *231*, 460-461.
31. Didenko, L. P. O., A. G.; Shilov, A. E.; Shilova, A. K., *Kinet. Catal.* **1977**, *18* (1078), 887-888.
32. Didenko, L. P.; Gavrilov, A. B.; Shilova, A. K.; Strelets, V. V.; Tsarev, V. N.; Shilov, A. E.; Makhaev, V. D.; Banerjee, A. K.; Pospíšil, L., *Nouveau Journal de Chimie* **1986**, *10*, 583-588.
33. Didenko, L. P.; Gavrilina, O. K.; Yablonskaya, E. E.; Shilova, A. k.; Shilov, A. E., *Nouveau Journal de Chimie* **1983**, *7*, 605-611.
34. Bazhenova, T. A.; Shilov, A. E., *Coord. Chem. Rev.* **1995**, *144* (0), 69-145.
35. Shilova, A. K.; Efimov, O. N.; Makhaev, V. D.; Shilov, A. E., *Kinet. Catal.* **1995**, *36* (2), 228-231.



36. Antipin, M. Y.; Didenko, L. P.; Kachapina, L. M.; Shilov, A. E.; Shilova, A. K.; Struchkov, Y. T., *J. Chem. Soc. Chem. Commun.* **1989**, (19), 1467-1468.
37. Antipin, M.; Struchkov, Y.; Shilov, A.; Shilova, A., *Gazz. Chim. Ital.* **1993**, *123*, 265-270.
38. DiFranco, S. A.; Staples, R. J.; Odom, A. L., *Dalton Trans.* **2013**, *42* (7), 2530-2539.
39. Malinak, S. M.; Demadis, K. D.; Coucouvanis, D., *J. Am. Chem. Soc.* **1995**, *117* (11), 3126-3133.
40. Chu, W.-C.; Wu, C.-C.; Hsu, H.-F., *Inorg. Chem.* **2006**, *45* (8), 3164-3166.
41. Kuznetsov, D. A.; Fedyanin, I. V.; Komarova, N. y. S.; Shilov, G. V.; Martynenko, V. M.; Vasil'ev, S. G.; Krivenko, A. G.; Lyssenko, K. A.; Bazhenova, T. A., *Eur. J. of Inorg. Chem.* **2015**, *2015* (4), 715-724.
42. Kuznetsov, D. A.; Kovaleva, N. V.; Fedyanin, I. V.; Lyssenko, K. A.; Bazhenova, T. A., *Polyhedron* **2015**, *85* (0), 809-813.
43. Manakin, Y. V.; Kuznetsov, D. A.; Fedyanin, I. V.; Lyssenko, K. A.; Kovaleva, N. V.; Kulikov, A. V.; Bazhenova, T. A., *Russ. Chem. Bull.* **2014**, *62* (8), 1843-1851.
44. Bazhenova, T. A.; Lyssenko, K. A.; Kuznetsov, D. A.; Kovaleva, N. V.; Manakin, Y. V.; Savinykh, T. A.; Shestakov, A. F., *Polyhedron* **2014**, *76* (0), 108-116.
45. Kuznetsov, D. A.; Bazhenova, T. A.; Fedyanin, I. V.; Martynenko, V. M.; Shestakov, A. F.; Petrova, G. N.; Komarova, N. y. S., *Dalton Trans.* **2016**, *45* (41), 16309-16316.
46. Hill, R. E. E.; Richards, R. L., *Nature* **1971**, *233*, 114-115.
47. Shilov, A. E.; Shilova, A. K.; Vorontsova, T. A., *React. Kinet. Catal. Lett.* **1975**, *3* (2), 143-148.
48. Watt, G. W.; Chrisp, J. D., *Anal. Chem.* **1952**, *24* (12), 2006-2008.
49. Shilov, A. E., *J. Mol. Catal.* **1987**, *41* (1-2), 221-234.
50. Kuznetsov, D. A.; Fedyanin, I. V.; Lyssenko, K. A.; Bazhenova, T. A., *Dalton Trans.* **2014**, *43* (34), 12876-12885.